ADVANCED FINITE ELEMENT MODELLING OF COUPLED TRAIN-TRACK SYSTEMS:

A GEOTECHNICAL PERSPECTIVE

by

Meysam Banimahd

Submitted for the degree of Doctor of Philosophy

Heriot-Watt University

School of the Built Environment

March 2008

ABSTRACT

In this thesis, a series of models have been developed based on the finite element method to study coupled train-railway track systems. In particular a three dimensional dynamic model, which incorporates all track components such as multi-layered ground, sleepers and rails, has been developed. In this model, absorbing boundaries are implemented to prevent artificial wave reflection at the domain boundaries. Nonlinearity of the soil is taken into account by implementing several nonlinear constitutive models into the numerical code. The train is modelled as a combination of rigid masses, dashpots and springs. The train and track are coupled at the wheel-rail contact points, employing a nonlinear-contact theory that incorporates the rail surface irregularities and the possibility of wheel-rail separation. The dynamic problem of the coupled track-train system is solved in the time domain using a modified explicit integration technique. Using the developed three-dimensional model, the effects of train speed and soil nonlinearity are investigated in terms of the track displacement and the stress & vibration level in the sub-soil. Based on these studies, a modified design algorithm is suggested for high speed tracks to minimize railway track maintenance levels.

The problem of stiffness transition near bridges and tunnels is also investigated, using the three-dimensional finite element model, in terms of applied load/stress on the track and passenger comfort. A train-track irregularity model, which is developed to compute the response of a train to a given track irregularity, is also employed to perform parametric studies on transition problems. Relationships between dynamic load amplification in the transition zone and geometrical properties of the transitions, for different train speeds, are accordingly given. The design principles for transition zones are critically reviewed against the outcome of transition studies conducted in this research, and modifications are suggested toward the sustainable design of transitions.

With ever-increasing train speeds, heavier axle loads and mixed passenger-freight traffic, the track sub-soil is experiencing complicated stress paths at relatively high stress levels. Such a stress regime would generate considerable track settlement and even cause foundation failure in a worst-case scenario. The soil behaviour under such stress regimes

can be represented only by complicated constitutive models which simulate cyclic, as well as monotonic, soil elastic-plastic behaviour appropriately. An example of such constitutive soil models, called ALTERNAT, is given. Unlike simple elastic-plastic models, ALTERNAT realistically accounts for stress dependency of the friction angle, strain softening–hardening and non-associativity. In order to develop a good understanding of railway track response affected by complex soil behaviour, the monotonic response of shallow foundations, which can represent a railway track, is extensively studied using a finite element code incorporating ALTERNAT. To determine the parameters in ALTERNAT, a calibration procedure is also developed based on an optimization technique, namely a micro genetic algorithm. The effect of footing size, shape, relative density and roughness on the ultimate bearing capacity and settlement characteristics are studied, and the computed results compare very favourably with the experimental trends. It is also shown that ALTERNAT can simulate the basic features of the cyclic response of granular soils, which occurs under train loading. It is therefore suggested that the ALTERNAT cyclic model and the three dimensional finite element model can be used together towards the prediction of the long-term performance of railway tracks.

Dedicated to my beloved parents

for their continuous support and encouragement

ACKNOWLEDGMENTS

I would like to express my sincere gratitude and appreciation to Dr. Peter K. Woodward for his continuous support, supervision and enthusiasm during the course of this study.

I would also like to specially thank my parents and brothers for their continued support and encouragement throughout the period of this study.

Special thanks to my friend Justin Kennedy who read the manuscript of this thesis and helped the manuscript be edited. I would also like to extend my thanks to all my friends and colleagues in the School of the Built Environment for their help and support.

ACADEMIC REGISTRY
Research Thesis Submission

Name:	MEYSAM BANIMAHD		
School/PGI:	School of the Built Environment		
Version: *(i.e. First, Resubmission, Final)*	Final	Degree Sought:	PhD

Declaration

In accordance with the appropriate regulations I hereby submit my thesis and I declare that:

1) the thesis embodies the results of my own work and has been composed by myself
2) where appropriate, I have made acknowledgement of the work of others and have made reference to work carried out in collaboration with other persons
3) the thesis is the correct version of the thesis for submission and is the same version as any electronic versions submitted*.
4) my thesis for the award referred to, deposited in the Heriot-Watt University Library, should be made available for loan or photocopying and be available via the Institutional Repository, subject to such conditions as the Librarian may require
5) I understand that as a student of the University I am required to abide by the Regulations of the University and to conform to its discipline.

* *Please note that it is the responsibility of the candidate to ensure that the correct version of the thesis is submitted.*

Signature of Candidate:	M. Banimahd	Date:	06.06.08

Submission

Submitted By *(name in capitals)*:	Meysam Banimahd
Signature of Individual Submitting:	M. Banimahd
Date Submitted:	06.06.08

For Completion in Academic Registry

Received in the Academic Registry by *(name in capitals)*:	CAROLINE COOKE		
Method of Submission *(Handed in to Academic Registry; posted through internal/external mail)*:	HANDED IN		
E-thesis Submitted			
Signature	C.J. Cooke	Date:	6/6/08

TABLE OF CONTENT

LIST OF RELATED PUBLICATIONS

Banimahd, M., and Woodward, P.K., 2006. Load-displacement and bearing capacity of foundations on granular soils using a multi-surface kinematic constitutive soil model. International Journal for Numerical and Analytical Methods in Geomechanics, 30(9): 865 - 886.

Banimahd, M., and Woodward, P.K., 2007. 3-dimensional finite element modelling of railway transitions, Proceedings of 9th International Confrence on Railway Engineering, London, UK.

Banimahd, M., and Woodward, P.K., 2007. Numerical study of train speed effect on railway track response, Proceedings of 9th International Conference on Railway Engineering, London, UK.

Woodward, P.K., Zettor, B., Kaddouri, A., and Banimahd, M., 2005. Advanced nonlinear dynamic finite element modelling of railway track behaviour, Proceedings of 8th International Conference on Railway Engineering, London, UK.

Woodward, P.K., Thompson, D., and Banimahd M., 2007. Geocomposite technology: reducing railway maintenance. Proceedings of the Institution of Civil Engineers: Transport, TR3: 109-115.

Woodward, P.K., Boyd, P., and Banimahd M., 2007a. XiTRACK reinforcement of tunnel railway tracks from floating to fixed geometry in a day, 9th International Conference on Railway Engineering, London, UK.

Woodward, P.K., Boyd, P. , Spiers, J. and Banimahd, M., 2007b. XiTRACK reinforcement of Keadby canal drawbridge, 9th International Conference on Railway Engineering, London, UK.

CHAPTER 1

INTRODUCTION

1.1 General Considerations

In recent decades, railways have regained their importance as a result of their efficiency and environmental friendly technologies. High speed trains are now integrated into the transportation strategies of all the developed (and fast developing) countries. In a survey published in the latest Railway Gazette International, Takagi (2005) named 10 countries in which trains have passed an average speed of 150 km/h, and stated that high speed operations are becoming widespread in other countries as well. Furthermore, according to Takagi (2005), the fastest speed of any scheduled service on conventional railways, up to 2005, was 330 km/h in Germany on the Cologne-Rhein/Main NBS. At present, the fastest train in the UK runs at 186 mph (300 km/h) on CTRL.

High speed trains have, however, brought a number of challenges to traditional railway track engineering, specifically to track geotechnics. Most of the railway tracks in use are relatively old and have not been designed specifically for present axial loads and train speed. These tracks consequently require a high level of maintenance to provide a safe and comfortable ride under the present operating conditions. It has been observed that running high speed trains on railway tracks constructed on soft soils induces high levels of vibration in the track and the surrounding ground. These vibrations can result in rapid deterioration of the track structure, causing derailment and ground failure in the worst cases.

In addition, even if the train speed is kept lower than the so-called critical velocity, more frequent passage of trains will subject the track to permanent settlements at a faster rate. Under the train load the sub-soils are subjected to a series of loading, unloading and

reloading. After each loading cycle, the track returns to approximately the initial geometry, but not exactly, i.e. very small permanent settlements are generated. These small settlements accumulate over thousands and thousands of cycles; this makes the rail lose its geometry and alignment. On the other hand, the irregularity generated on the surface of the rail itself increases the dynamic train load and consequently accelerates the track deterioration even more.

The presence of structural irregularities will also induce high dynamic loads under a high speed train. Such a high dynamic load is responsible for high levels of maintenance in the vicinity of irregularities. A typical example of such irregularities is stiffness transition near bridges and tunnels, which is usually associated with the high level of maintenance required to keep the track geometry acceptable for high speed trains.

1.2 Research Objectives

Despite all of the geotechnical complexities associated with high speed tracks, the design and maintenance of the track is still strongly based on empirical relationships and simple models. As will be discussed in the following chapters, these types of models are not able to represent appropriately the mechanics of the track, especially under a high speed regime. A high speed railway track model should address the three dimensional nature of track response, multi-layered substructure, nonlinearity of soil behaviour, train-track interaction, and structural/geometrical irregularities.

The main objective of this research is to develop computational models, namely a three-dimensional finite element train-track model and train-irregularity model, to study coupled train-track response under different geotechnical and operational conditions. The three-dimensional finite element coupled train-track model represents track components placed on a multi-layered ground system and incorporates soil stiffness nonlinearity, absorbing boundary conditions and train-track interaction. A train-irregularity model is developed to compute the train response to any given irregularity such as a stiffness transition, and is used to study train excitation caused by different levels of differential deflection (induced

in the vicinity of stiffness transitions). The effect of train speed, soil stiffness nonlinearity and the presence of a stiffness transition on track response and maintenance levels are studied; the developed results are then used to improve design practice in terms of track maintenance levels for plain tracks and in transition tracks.

In addition, the necessity of using an advanced elastic-plastic constitutive soil model to represent monotonic and cyclic behaviour of track sub-soil is also discussed. In accordance, the application of an advanced nonlinear elastic-plastic multi surface kinematic constitutive soil model, called ALTERNAT, is presented with special reference to the surface foundation problem. Such an application can easily be extended to the estimation of bearing capacity and settlement of railway track systems in cases of high train speeds or high axle loads. The effect of footing size, shape, relative density and roughness on the ultimate bearing capacity and settlement characteristics are studied, and the computed results compare very favourably with the experimental trends. Some features of cyclic behaviour of granular soil under repeated train loading are also investigated using ALTERNAT. This advanced constitutive model, if used along with an advanced three-dimensional dynamic railway track model, is also applicable in the simulation of the long-term settlement of railway track. Table (1.1) shows the models developed and used in the current study, along with the chapters in which they are addressed.

1.3 Thesis Outline

As this thesis addresses different aspects of track geotechnics, the literature review is not presented in one single chapter and hence the relevant literature review is given instead in its corresponding chapter. The thesis is organized into the following chapters:

Chapter 1 Introduction.

Chapter 2 gives a basic overview of railway track mechanics. Track components and their functions are first briefly described; track stiffness is then explored through the definition of the track modulus. Train loading is discussed in terms of the dynamic amplification

factor related to different track conditions and train speed. Wave propagation phenomena and track vibration are studied next. Different possible failure mechanisms in the track support geo-system are also presented, followed by an overview of empirical relationships to predict the long-term settlement of track.

Computational models and procedures	**Chapter**
3D dynamic finite element models for train-track coupled systems	3,4,5,6
Train-irregularity model	6
2D finite element model for axi-symmetric and strip foundations, incorporating ALTERNAT	7
2D/3D finite element model for cyclic behaviour of granular layers, incorporating ALTERNAT	7
A calibration procedure based on a micro-genetic algorithm for advanced constitutive models such as ALTERNAT	7

Table 1.1 List of computational models and procedures developed and used in the present research

Chapter 3 presents the development of a high speed track model based on three-dimensional dynamic finite element methods. Different aspects of the developed model are illustrated in terms of representations of track components, boundary conditions, time integrations, train loading and material damping. Finally, the performance of the model is discussed when compared to actual site measurements and experimental trends.

In Chapter 4, the effect of train speed on railway track response is studied numerically for a multi-layered ground track system using the developed three-dimensional dynamic finite

element models. The effect of differing subgrade stiffness, ballast depth and stiffness are addressed; the track maintenance level is also related to the stress level in subgrade and stress & vibration in the ballast layer. The track design methods are reviewed and a design method, based on dynamic finite element analysis, is proposed which aims at protecting the subgrade from deterioration and decreasing the level of ballast maintenance.

Chapter 5 addresses nonlinearity in the resilient behaviour of ballast and clayey subgrade. Several constitutive relationships are presented to capture the resilient nonlinearity, and their implementations in the dynamic finite element model are also discussed in detail. The three-dimensional finite element model, with incorporated substructure nonlinearity, is then used to investigate the effect of nonlinearity of the ballast and subgrade on the response of the track and on the track maintenance level.

In Chapter 6, the train-track interaction problem is investigated. Different train models are studied and formulated within the finite element framework. The train models are then coupled with the three-dimensional track models through the employment of a nonlinear contact theory. The interaction problem between the track and train is solved in the time domain, using explicit time integration schemes. Performances of these algorithms compare very favourably against an analytical solution to a typical benchmark problem. Different types of irregularities are discussed in detail and their representations in the coupled train-track models are presented.

A type of geotechnical irregularity, i.e. the stiffness transition between plain track and a bridge abutment/ tunnel base, is studied in detail. Using the 3D finite element model, the effect of the subgrade stiffness in the transition zone and the train speed on the track-train performance are investigated in terms of the rail-wheel interaction force and the train body acceleration, which is used as a measure of passenger comfort. The presence of a track fault in the transition zone is also considered and the effect of track faults, at different train speeds, is simulated. A detailed study of the train-track interaction force and train body excitation in the transition zone is also conducted using the train-irregularity model, which gives a useful insight into the effects of transition length, train speed and differential deflection o n the train-track response. Relationships between the spatial derivatives of transition curves, caused by the differential deflection in the vicinity of a transition and

dynamic force, are investigated for different train speeds. The outcomes of the numerical simulations, presented in this chapter, are then critically reviewed in comparison with site observations to improve transition design practice.

In Chapter 7 an advanced constitutive model which can be used to simulate static and cyclic behaviour of granular soil under train loading is described. The capabilities of ALTERNAT are extensively investigated through studying surface footing problems, which can be representative of the track foundation system under monotonic loading. The footing problem is numerically studied in terms of both bearing capacity and settlement characteristics. It is also demonstrated that ALTERNAT is able to simulate the essential features of cyclic behaviour of granular bodies such as ballast. Finally, an approach which can integrate the dynamic train-track coupled model and ALTERNAT to simulate life-long performance of railway tracks is proposed for future studies.

Chapter 8 presents the main conclusions drawn from each chapter, and contains suggested recommendations for future work.

CHAPTER 2

TRACK MECHANICS

2.1 Introduction

In this chapter, a basic overview of railway track mechanics is given. Track components and their functions are first briefly described; track stiffness is then explored through the definition of the track modulus. Train loading is discussed in terms of the dynamic amplification factor, which is related to different track conditions and train speeds. Next, wave propagation phenomena and track vibration are studied. Different possible failure mechanisms in the track support geo-systems are also presented, followed by an overview of empirical relationships to predict long-term track settlement.

2.2 Ballasted Track Components

A conventional railway track normally consists of rails, sleepers, railpads, fasteners, ballast, subballast and subgrade (Figure 2.1). In this thesis, ballast, subballast and subgrade are classified as sub-structure, and the sleepers, railpad/fasteners and rails are classified as super-structure.

Rails guide the wheel sets in the direction of the track and carry the horizontal and vertical loads of the train, distributing these over the sleepers. Railpads improve the flexibility of the system and therefore lead to better distribution of the train loads. In addition, soft railpads prevent high frequency vibrations from propagating into the sleeper and further down into the ballast. They also prevent or reduce rail/sleeper contact attrition and provide electrical insulation of the track signal circuits. The purpose of the fastening system is to

hold the rails against the sleepers and resist vertical, lateral, longitudinal and overturning movements of the rail. The forces generating these movements are from the wheels and from temperature changes within the rails. Sleepers hold the fastening system to maintain proper track gauge. In addition, they restrain the lateral, longitudinal and vertical rail movements by anchoring the superstructure in the ballast (Selig and Waters, 1994).

Ballast layers keep the rails and sleepers at the required position by resisting the vertical, transverse and longitudinal forces transmitted by the sleepers. The ballast also distributes the loads to the layers below, protecting the subgrade from high stresses, and attenuates the vibration in addition to providing immediate drainage. It also facilitates track maintenance. The subballast is a granular layer between the ballast and subgrade which also helps in reducing the traffic induced stresses to acceptable levels in the subgrade, and facilitates drainage. In addition, it protects the upper surface of subgrade from the intrusion of ballast stones, and acts as an inverted filter in the case of mud pumping.

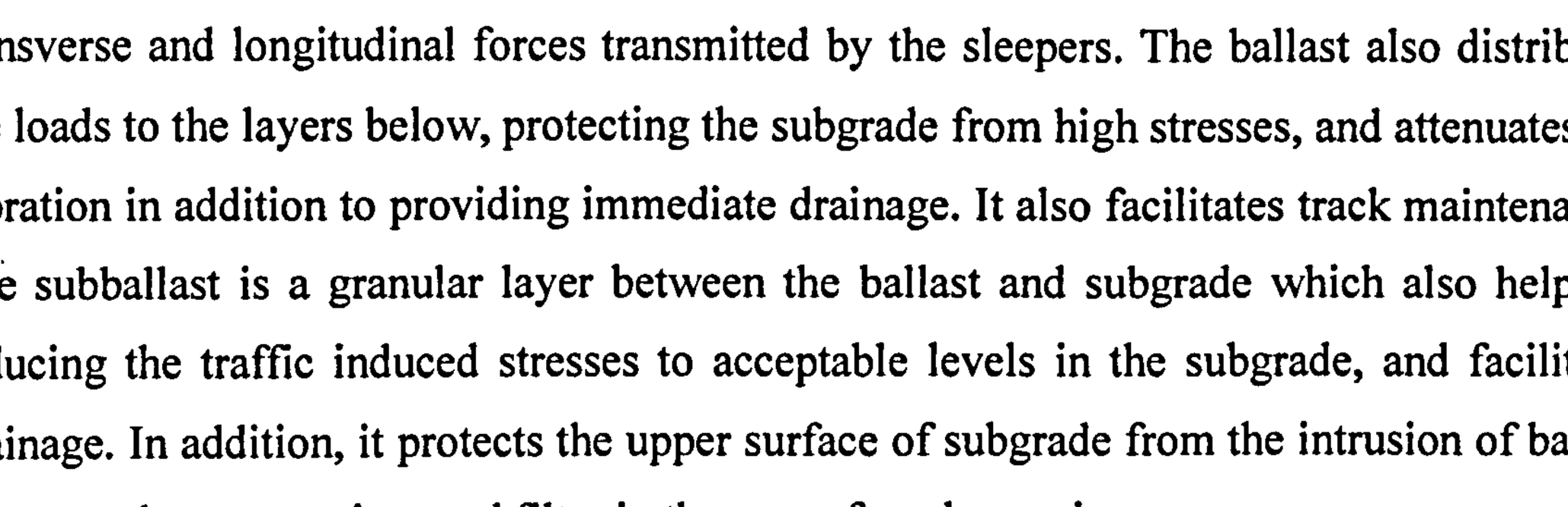

Figure 2.1. Railway track components (Dahlberg, 2006)

2.3 Track Support Stiffness

Track support stiffness is usually characterized via the track modulus. The track modulus is defined as the supporting force per unit length of rail per unit deflection of the rail (Selig and Waters, 1994). A beam on springs can be assumed to represent the railway track

(Figure 2.2), in which the beam represents the rail and the springs represent the foundation, combining the effects of railpad/fastener, sleepers, ballast, subballast and subgrade. The following differential equation governs the static response of the beam:

$$EI\frac{\partial^4 w(x)}{\partial x^4}+kw(x)=P(x) \tag{2.1}$$

where $w(x)$ is the vertical deflection of the beam at distance x, EI is the vertical flexural stiffness of the rail, $P(x)$ is the vertical load on the beam (induced by the wheels) and k is the track modulus. For a single load of magnitude P, as shown in Figure (2.2):

$$w(x_v)=\frac{P}{2kL}e^{-|x_v/L|}(\cos|x_v/L|+\sin|x_v/L|) \tag{2.2}$$

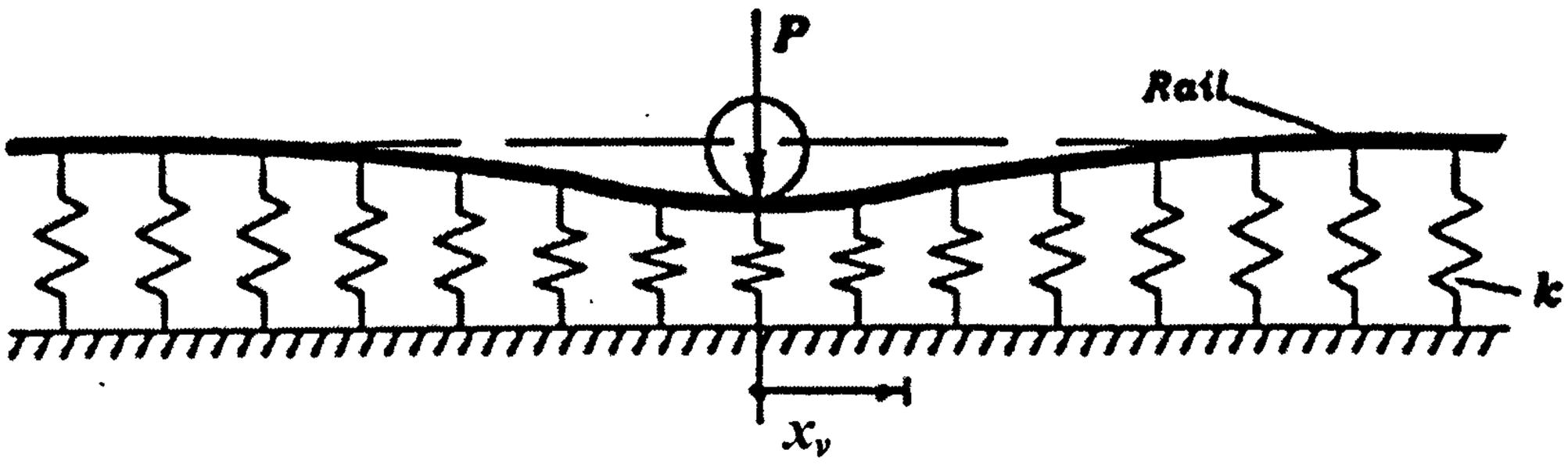

Figure 2.2. A rail subjected to a wheel load (Kerr, 2000)

in which

$$L=\sqrt[4]{\frac{4EI}{k}} \tag{2.3}$$

According to Equation (2.2), if the rail displacement is known under a single load (w_m), the track modulus can be calculated as follows

$$k = \frac{1}{4}\sqrt[3]{\frac{(\frac{P}{w_m})^4}{EI}} \tag{2.4}$$

This relationship can be used to establish a simple method to measure the track modulus. Timoshenko and Langer (1932) applied a one-axle load and, by measuring the rail deflection directly under the load, they calculated the track modulus using the above equation. This method requires a special test to be set up with a one-axle load. However, such one-axle loading devices are not generally available to railway engineers and researchers. On this basis, other procedures were developed to retain the simplicity of the above method, but are better able to utilize any available car or locomotive (two or three axle trucks) as a loading device (e.g. see Kerr, 1987). A comprehensive overview of the measurement of track modulus is given by Kerr (2000).

On the other hand, Cai *et al.* (1994) proposed a method by which the track modulus was calculated using the elastic properties of individual track components. Such a method has the advantage of eliminating the need to carry out relatively expensive field tests. This method considers railpads, sleepers, ballast/subballast and multi-layered subgrades. The method can be thought of as an extension to the fundamental relationship given by several researchers to estimate the foundation spring stiffness coefficient from the half-space elastic properties (e.g. see Vesic and Johnson, 1963).

Irrespective of what procedure is used to calculate the track modulus, several difficulties are encountered with respect to the calculation and application of the track modulus. The track modulus is likely to vary substantially at different locations along the track, as a result of variations in ballast/subgrade properties and uneven construction effects. When the ballast is disturbed (e.g. by tamping), the track modulus will change. The modulus is also affected by the accumulated tonnage of passing trains. The track modulus can also be expected to vary seasonally, owing to the effect of freeze and thaw cycles on the ballast/subgrade (Cai *et al.*, 1994). Changes in water content can also affect the track modulus and the nonlinear response of the track should also be taken into account. On this basis, Mair (1976) and Kerr and Eberhardt (1992) suggested that the track modulus should be calculated based on a load level representing the service load. However, this proves

difficult if mixed traffic is considered. In addition, if the dynamics of train-track interactions are considered, the train loads change owing to stiffness/geometrical irregularities and the track modulus changes accordingly. Limitations regarding the application of the track modulus to investigate the dynamics of railway track are discussed in more detail in Chapter 4.

2.4 Loading on Track

The forces acting on the track as a direct result of the train load have three different components, namely vertical, transversal and longitudinal loads. In the present research, horizontal components of loads are not considered and therefore are not covered as this research is only concerned with dynamic vertical loads. The vertical load is the sum of the static load, as a result of the train weight and the dynamic loads induced, for example, by track-wheel stiffness/geometrical irregularities. To take the dynamic loads into account, it is common practice to increase the static load by a factor called the Dynamic Amplification Factor (*DAF*). These impact factors are multipliers of the static loads (Equation 2.5), which are used to determine dynamic load magnifications caused primarily by irregularity of the track and operating conditions, such as train speed.

$$F_{dyn} = DAF.F_{stat} \tag{2.5}$$

where F_{stat} and F_{dyn} are static and dynamic loads respectively. Several simple empirical formulas which aim to assess the dynamic train-track interaction force have been proposed. Eisenman's dynamic amplification factor (Esveld, 2001) is one of the most well known:

$$\begin{cases} DAF = 1 + t\varphi & V < 60 \\ DAF = 1 + t\varphi(1 + \dfrac{V-60}{140}) & 60 \le V \le 200 \end{cases} \tag{2.6}$$

where t is a multiplication factor depending on the confidence interval. φ is an empirical factor depending on the track quality and V is the train speed (km/hr). The values for these

empirical factors are given in Table (2.1). According to Eisenman's dynamic amplification factor, higher dynamic loads are applied to the track as the train speed increases and track quality deteriorates.

Probability	t	Application	Track condition	φ
68.3%	1	Contact stress, subgrade	Very good	0.1
95.4%	2	Lateral load, ballast bed	Good	0.2
99.7%	3	Rail stresses, fastenings, supports	Bad	0.3

Table 2.1. Parameters for Eisenman's dynamic amplification factor (Esveld, 2001)

AREA (1984) suggested the following DAF:

$$DAF = 1 + \frac{5.2V}{D_w} \tag{2.7}$$

where V is train speed (km/hr) and D_w is the wheel diameter in millimetres. This relationship has some similarities to an earlier formulation proposed by Talbot (1918, 1920):

$$DAF = 1 + 0.0062(V - 8) \tag{2.8}$$

Some other researchers linked the dynamic amplification factor to the track supporting stiffness through the track modulus. Clarke (1957) proposed the following relationship for a wooden sleeper system:

$$DAF = 1 + \frac{19.65V}{D_w\sqrt{k}} \tag{2.9}$$

k is the track modulus (MN/m/m). Stewart and O'Rourke (1988) suggested typical values of 7, 14, 21 MN/m/m for poor, average and good quality tracks respectively. Indian railways (Sirinivasan, 1969) use the following DAF:

$$DAF = 1 + \frac{0.017V}{\sqrt{k}} \tag{2.10}$$

The dynamic amplification of loads in the presence of isolated irregularities has also been studied. Jenkins *et al.* (1974) studied dipped joint problems and observed two different loads, namely high frequency component (P_1) and low frequency component (P_2), as shown in Figure (2.3).

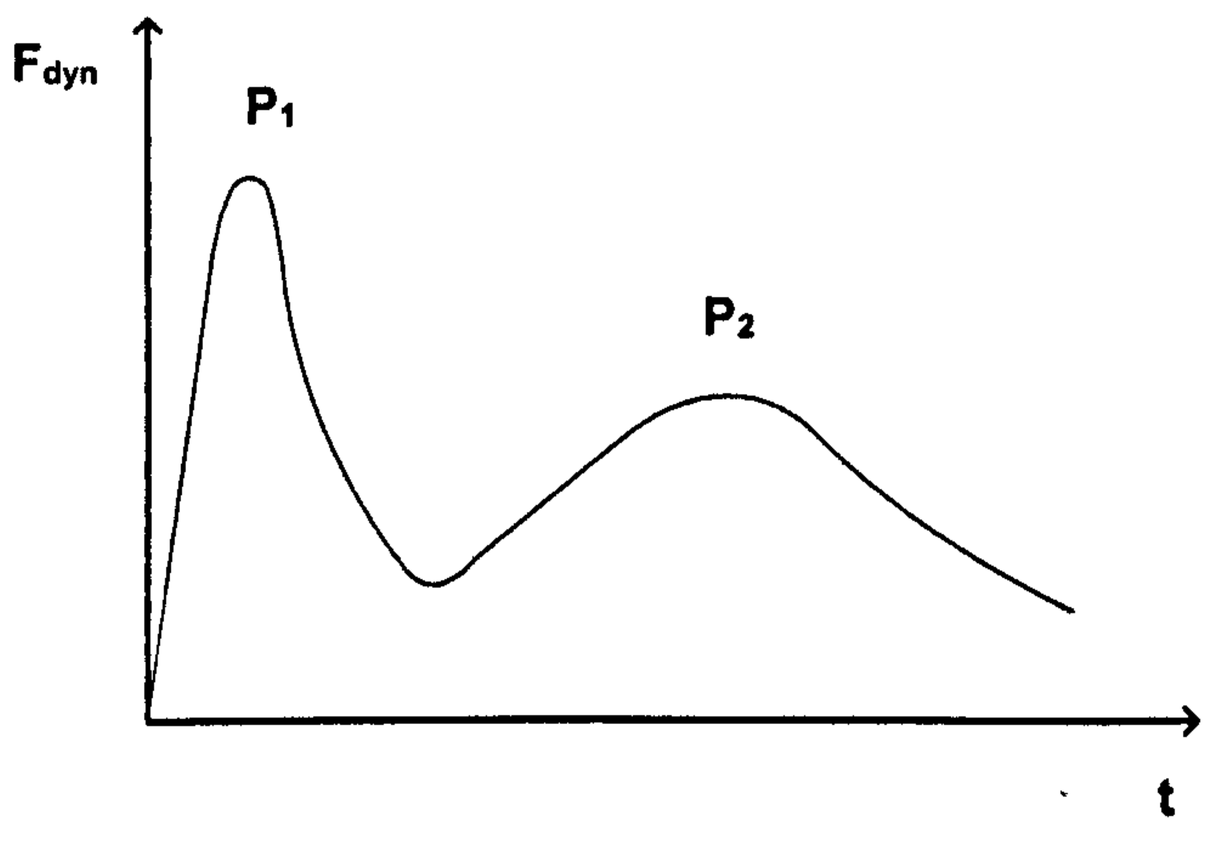

Figure 2.3. Schematic presentation of loads at a dipped joint (Jenkins *et al.*, 1974)

As will be discussed in Chapter 6, the general consensus regarding these forces is that the P_1 forces are largely filtered out by attenuation in the rail, railpad and sleeper (Frederick and Round, 1984) so that the P_2 forces are the important ones when dealing with stresses in the track foundation. The P_1 (kN) and P_2 (kN) forces can be estimated as below (Jenkins *et al.*, 1974):

$$P_1 = P_{stat} + 2\alpha\sqrt{\frac{K_{wr}M_{T1}}{1 + M_{T1}/M_u}} \tag{2.11}$$

$$P_2 = P_{stat} + 2\alpha V\sqrt{\frac{M_u}{M_u + M_{T2}}}\left[1 - \frac{C_T\pi}{\sqrt{K_T(M_u + M_{T2})}}\right]\sqrt{K_T M_u} \tag{2.12}$$

in which

2α is the total dip angle at joint in radians

K_{wr} is the linearized Hertzian wheel/rail contact stiffness (See Chapter 6) in N/m

M_{T1} is the effective track mass for P_1 calculation in kg

M_{T2} is the effective track mass for P_2 calculation in kg

M_u is the unsprung mass of the wheel in kg

K_T is the track stiffness in N/m

Track stiffness (K_T) can be related to the track modulus using the following equation:

$$K_T = (64EIk^3)^{0.25} \tag{2.13}$$

See Jenkins *et al.* (1974) for more details.

Frederick and Round (1984) and Lane (1982) simplified Equation (2.11) for the P_2 force, into the following form:

$$P_2 = P_{stat} + 2\alpha V\sqrt{K_T M_u} \tag{2.14}$$

These formulas are mostly a rough approximation of reality as they do not address the train-track interaction mechanism appropriately. However, they provide a simple approach towards designing the railway track and therefore have gained wide use in the railway industry. Using a mathematically sound approach, such as the dynamic coupled train-track model as developed in this research, should provide better insights into the dynamic train-track interaction problem; which will be the subject of study in Chapter 6.

2.5 Vibration in Railway Track

2.5.1 Source of Vibration

When a train stands motionless on the track, a stress pattern generated by its weight is produced in the ground beneath and around the train. As the train moves, the stress pattern moves with it. This moving stress pattern will cause a varying ground reaction that induces stress waves into the surrounding soil. This mechanism is the main source of train-induced ground vibrations (when geometrical irregularities are not present) and hence will induce stress waves, even in the absence of imperfections or periodic irregularities in the vehicle or the track. The track structural response induced by a moving train depends on parameters such as the spacing of the wheel axles, the axle weight and the speed of the train.

There are many other secondary sources of vibration caused by the moving stress pattern. Any unsteady riding of the vehicle caused by wheel defects may cause fluctuating forces on the railway track. The track itself provides non-uniform supports. The rails are supported on sleepers placed at regular intervals and the sleepers are placed on a ballast bed which provides variable support and geometry. Different sources of vibration are summarized in Table (2.2).

2.5.2 Wave Propagation Phenomena

Once stress variations are produced in the ground beneath the track, they will propagate away from the source as stress waves, causing vibrations in the surrounding soil. The degree to which these ground vibrations will spread depends upon the geometry and stiffness of the surrounding soil. A variety of stress waves are induced: compression waves, shear waves and Rayleigh waves. Each of these waves has different propagation velocities and hence will attenuate differently with increasing distance from the source. The propagation of different stress waves is further complicated by refraction and reflection as the propagating stress waves pass through soils with different geometries and mechanical properties. The distribution of ground-born energy also differs between the wave types, and

depends strongly upon the magnitude of the excitation. If the excitation is localized on the surface of an area which has a relatively small size when compared to the shear wave wavelength, as is the case for railway track, then the Rayleigh wave will carry most of the energy. If however, the excitation area is large, the body wave will be dominant. According to Miller and Pursey (1954), 67% of the energy from a circular disc oscillating vertically on the surface of an isotropic homogenous half-space is propagated as Rayleigh waves, 26% as shear waves and 7% as compression waves (Figure 2.4).

Stress waves induced by the track structural response • axle weight • spacing of wheel axles • speed of train
Vibration source at wheel-rail interface • unsteady riding of the vehicle (bouncing, rolling, pitching) • dynamic properties of the vehicle bogie • wheels defects (eccentricity. imbalance, flats) • misalignment of motors • acceleration and deceleration of train
Discontinuity on the track • rail defects (unevenness, waviness) • spacing and interval of rail joints • switches • curves and tilting track (centrifugal forces)
Variable support • geometry, stiffness and spacing of sleepers • geometry, stiffness and heterogeneity of the ballast • stiffness and geometry of the ground

Table 2.2. Different source of railway track vibration (Hall, 2000)

Compression and shear waves are termed body waves and the Rayleigh wave is classified as a surface wave. The speed at which body and surface body waves travel varies with the stiffness of the materials through which they pass. At any point on the ground the compressive wave arrives first, followed by shear wave and then the Rayleigh wave. The compression, shear and Rayleigh wave velocities in an elastic medium can be calculated from the following equations respectively:

$$V_p = \sqrt{\frac{E(1-\nu)}{\rho(1+\nu)(1-2\nu)}} \qquad (2.15)$$

$$V_s = \sqrt{\frac{E}{2\rho(1+\nu)}} \qquad (2.16)$$

$$V_R \approx \frac{0.87+1.12\nu}{1+\nu} V_S \qquad (2.17)$$

where E , ν and ρ are elasticity modulus, Poisson's ratio and density of the elastic medium respectively.

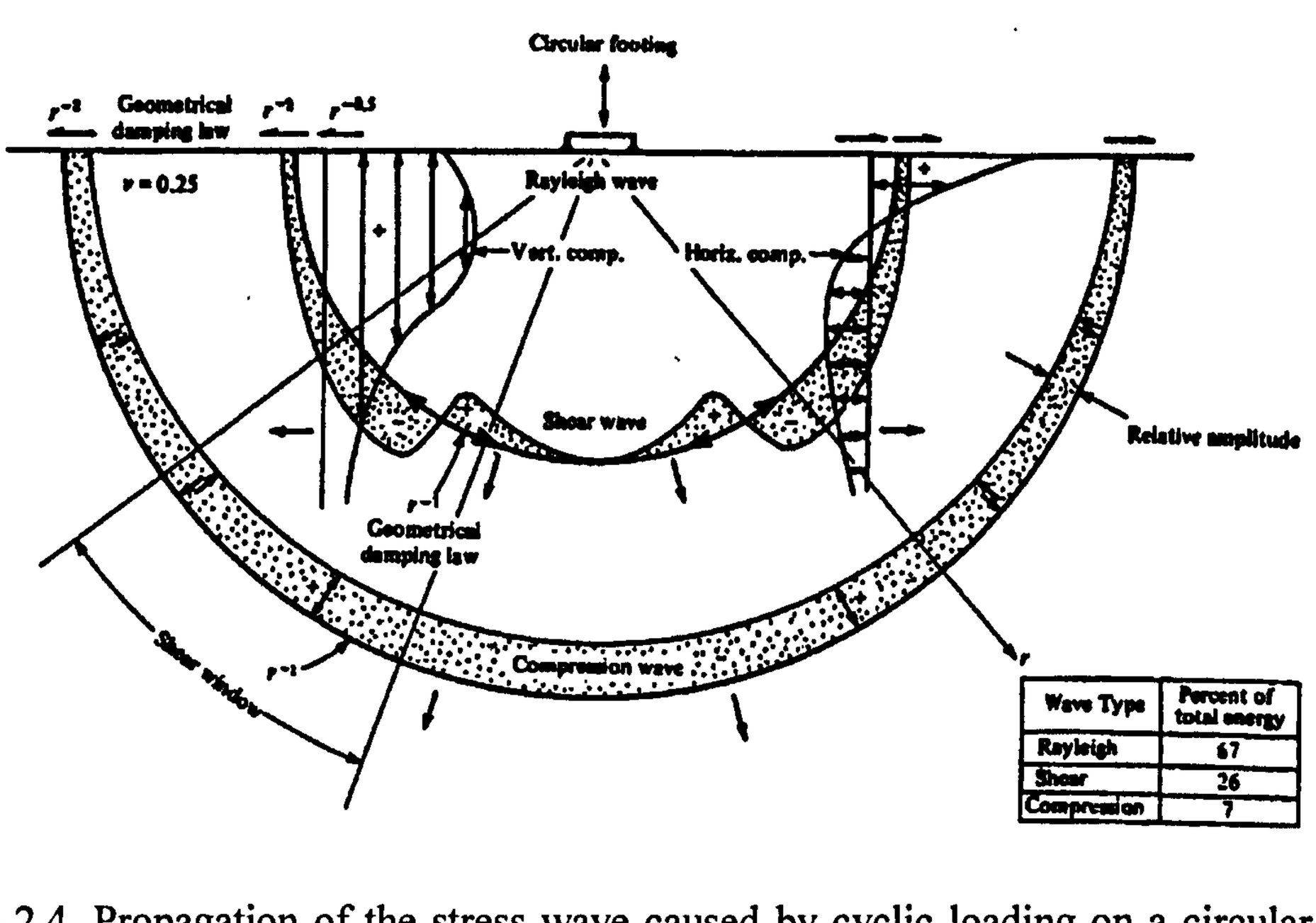

Figure 2.4. Propagation of the stress wave caused by cyclic loading on a circular footing over a homogeneous, isotropic elastic half-space (Wood, 1968)

The frequency content originating in a track-train structure is summarised in Table (2.3). The ground vibration induced by railway traffic is mainly of a low frequency character

(mostly under 20 Hz, according to Hall, 2000). Higher frequency pulses, which are generated by wheel-rail imperfection and unsteady riding of the vehicle, are mainly filtered by attenuation of the super-structure. They are also filtered by the ballast bed, with the dimension of ballast particles being the same as, or larger than, the wave length of such high frequency vibration (Bodare, 1993; Hall, 2000).

Frequency Range	**Low**	**Medium**	**High**
Threshold	0-40 Hz	40-400 Hz	400-1500 Hz
Part of track	Substructure	Superstructure excluding rail	rail
Human perception and discomfort			
Local resident	Vibrations and contact noise(buildings)	Radiated sound/noise	Radiated sound/noise
Passenger	Vibrations and contact noise (vehicle)	Radiated sound/noise	Radiated sound/noise
Structural damage			
Track	Damage of substructure and engineering structure	Damage of superstructure	Damage of rails
Vehicle	Damage of carriages, bogies, axles and wheels	Damage of wheels	Damage of wheels

Table 2.3. The frequency range in railway track-vehicles (De Man, 2002)

2.6 Substructure Failure Mechanisms

Different failure mechanisms can be formed in the subgrade and granular ballast/subballast layers. The most important substructure failure modes are subgrade surface attrition, mud pumping into ballast, massive shear failure, progressive shear failure of subgrade and the excessive subgrade plastic deformation which creates ballast pockets (Selig and Water, 1994; Li and Selig, 1998a; Brough *et al.*, 2003). Attrition of the subgrade by the overlying ballast in the presence of water can result in the formation of slurry at the ballast/subgrade

interface. Under certain conditions, cyclic loading associated with passing traffic can cause this slurry to be pumped up to the surface of the ballast. Such failures are normally associated with hard, fine grained materials, such as clay and soft rocks such as chalk (Selig and Water, 1994).

When the slurry reaches the sleeper/ballast interface, cyclic movements of the sleeper within the ballast bed result in the slurry being ejected from beneath the sleeper onto the surface of the ballast. The slurry, in this case from the subgrade attrition, ultimately finds its way into the trackside drainage system which can result in premature blocking. Because of its association with high subgrade stresses and large sleeper movements, subgrade attrition failure is frequently found to originate at these sleepers associated with rail joints (Selig and Water, 1994).

The mud formed can also consist of the products of the ballast and subballast breakdown. Under the action of loading and mechanical maintenance (such as tamping), the ballast particles may break down and fill the voids up with fines. Fines may also be deposited by wind and spillages from freight trains. This will affect the appropriate drainage, cause excessive pore water pressure generation and also accelerate the attrition of the subgrade (the pumping problem) and hence weakening of the subgrade.

Local subgrade failure, accompanied by pumping, can lead to a loss of lateral track restraint, which in turn can lead to a loss of correct horizontal and vertical track alignment. This can result in the displacement of ballast from around the sleeper by the jetting action of the slurry during its ejection from beneath the sleeper. Lubrication of the ballast/sleeper interface results in a reduction in sliding friction between the sleeper and the ballast. Lubrication of the ballast particle also results in a reduction in the shear strength of the supporting and shoulder ballast. A local depression of the subgrade results from a loss of material associated with the erosion of the subgrade and possible ponding of water within the depression. To prevent the occurrence of subgrade attrition failure, subbballast can be interposed between the ballast and the subgrade.

Regarding the massive shear failure of the substructure, the driving forces are the axle weights from the train and the track superstructure. The resisting force is from the

substructure shearing resistance. Because most of the failure zone is in the subgrade, the subgrade strength properties have a major effect on the factor of safety against massive shear failure. Massive failure in the subgrade under repeated loading generally occurs at stress levels higher than that which causes progressive shear failure (Burrow *et al.*, 2007). Thus massive failure is likely to be a problem only when subgrade strength diminishes because of increasing water content. This may occur at times of heavy rainfall and flooding, for example. In such situations, failure may occur even without train loading being present. Increasing granular layer thickness is not the approach to prevent this type of failure.

Stresses imposed on the subgrade by the axle loads may be large enough to cause progressive shear failure. This condition will most likely develop in the top of the subgrade where the traffic induced stresses are highest. Overstressed soil will be squeezed sideways from beneath the track and upwards to give a bearing capacity failure (cess heave). Figure (2.5a) shows schematically how overstressed clay is progressively squeezed sideways and upwards. The heaved soils in the ballast shoulder may hinder the track drainage system which in turn will weaken the soil and aggravate the problem. The depression beneath the track traps the water entering from the above granular layer, thus accelerating the subgrade failure. Because progressive shear failure develops at the subgrade surface, any subgrade with a soft layer on the top is susceptible to this failure. The probability of cess heave developing can be minimized by ensuring that an adequate depth of load distributing material exists between the underside of the sleeper and the surface of the subgrade (formation), and that the drainage system maintains a low water table level. The heave of the material at the line side is matched by a corresponding depression in the track, which is corrected by the addition of ballast beneath the track. This measure results in an increase in ballast depth and a corresponding reduction in soil stress at the formation level, which tends to improve stability. However, the depression traps water which tends to reduce the potential improvement.

Progressive subgrade failure occurs only in fine grained materials exhibiting low values of internal friction. In coarse grained materials, exhibiting high values of internal friction, the increase in shear strength associated with the applied normal stress exceeds the increase in associated shear stresses. The resistance of the subgrade to a progressive failure can be achieved by applying a general ballast lift to the track and thereby increasing the depth of

ballast between the underside of the sleeper and the surface of the subgrade. This reduces the intensity of stress applied. Such a measure is of value if the stress levels imposed on the subgrade are to be increased, for example, as a result of increased axle loads. Other possible solutions could be the removal of the ballast layer, excavation of the subgrade to a reduced elevation and replacing ballast and subballast up to their original levels (Selig and Waters, 1994).

Another source of subgrade failure may come from excessive plastic deformation, which results in ballast pocket, as shown in Figure (2.5b). Although the ballast pocket formation may be accompanied by progressive shear failure, it results essentially from the vertical component of permanent deformation (Selig and Waters, 1994). These progressive shear failure and excessive plastic deformations are not completely independent. They both occur as a result of soft subgrade soils subjected to large repeated stress applications. However, progressive shear failure can be considered to be mainly a subgrade surface (formation) failure, whereas excessive plastic deformation can be considered a failure that is influenced by a substantial depth of subgrade. A subgrade with large ballast pockets often has soft soils extending to substantial depth.

It should be noted that, in addition to subgrade strength, subgrade stiffness plays a very important role in track deterioration. Using a static finite element model, Shahu *et al.* (1999) showed that subgrade stiffness has a considerably important effect on overall track response. As the subgrade stiffness decreased, they reported that sleeper deflection increased dramatically and concluded that the track settlement and consequently the track maintenance would be critical factors for tracks built on soft subgrade. They also indicated that subgrade stiffness has the maximum influence on the track modulus when compared to the effects of ballast and subballast stiffnesses. Eberson *et al.* (1993) also confirmed the effect of track stiffness on track deterioration, reporting that a track section with a track modulus of 14 MPa required 183% more maintenance than one with a track modulus of 27 MPa.

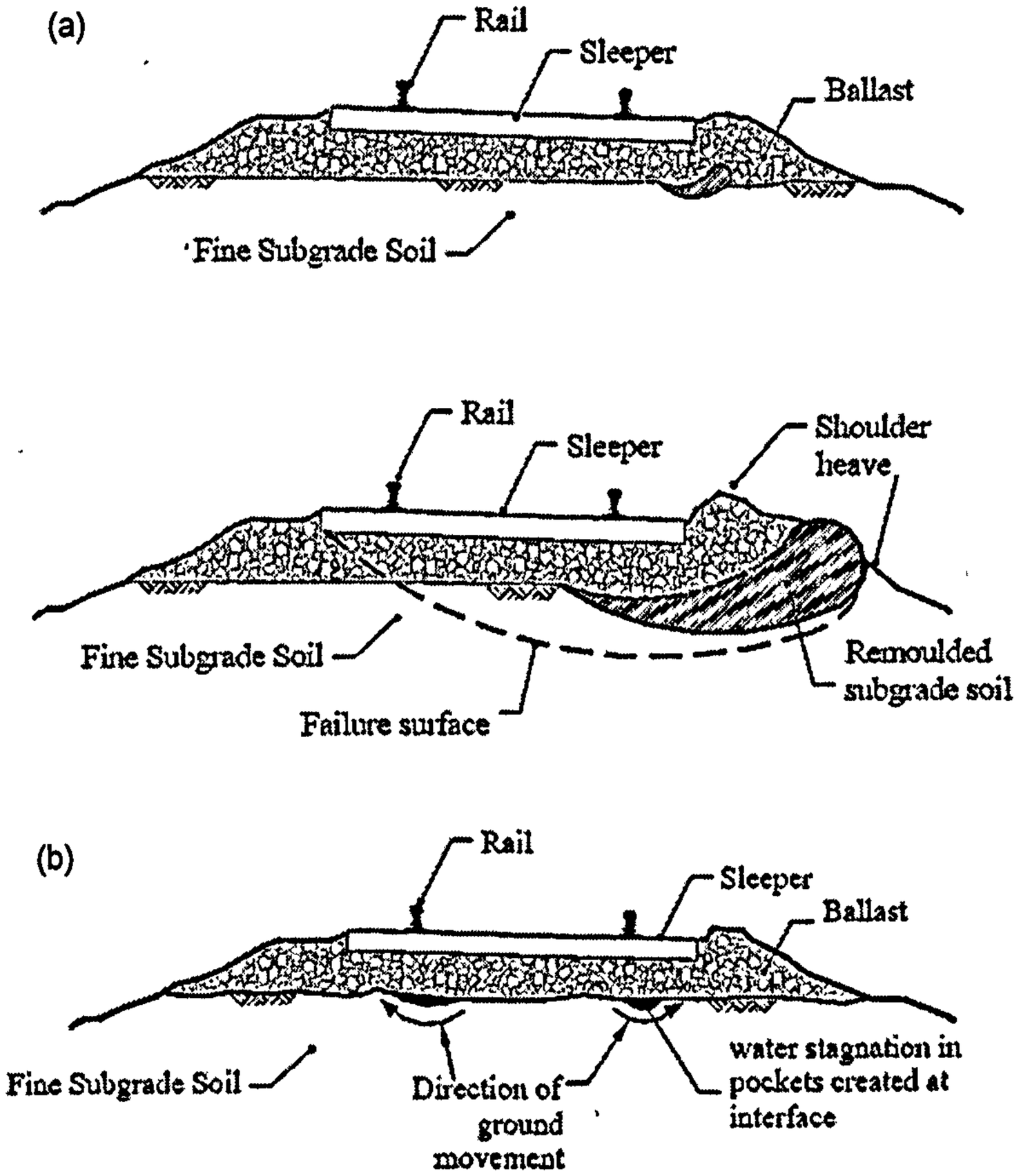

Figure 2.5. Illustrations of subgrade progressive shear failure (a); and ballast pocket formation (b) (Radampola, 2006)

2.7 Long-Term Settlement

2.7.1 Settlement in Ballast and Granular Soil

Settlement of ballast occurs in two major phases: a relatively fast settlement directly after tamping, until the ballast is consolidated, and a slow settlement afterwards. The second phase is affected by several factors (Dahlberg, 2001):

- A continued densification caused by particle rearrangement produced by repeated train loading
- Subballast or subgrade penetration into the ballast voids. This causes the ballast to penetrate into the subballast and subgrade
- Volume reduction by breakdown and/or abrasive wear of ballast particles
- Lateral, and possibly also longitudinal, movement of the sleepers causes the ballast beneath the sleeper to be pushed away and the sleeper will penetrate deeper into the ballast.

Relationships that have been exclusively developed for ballast settlement are limited; however, the models developed for granular soils can be equally used for ballast, provided they have been calibrated to the ballast. In this section, empirical relationships for the prediction of ballast and, more generally granular soil, are reviewed.

Alva-Hurtado and Selig (1981) developed an empirical model to calculate the permanent strain in the ballast layer based on the number of load cycles (N):

$$\varepsilon_p = \varepsilon_1[1 + c\log(N)] \tag{2.18}$$

where ε_p is the total permanent strain, ε_1 is the permanent strain after the first load cycle and c is a dimensionless constant controlling the rate of growth of deformation. Such a relationship suffers from several limitations as it does not address either the strength of the ballast or the stress level in the ballast layer directly.

The presence of a threshold stress for granular soils has been discussed by several researchers. Reviewing the researches on development of permanent strain in granular

soils, Lekarp *et al.*, (2000b) concluded that at a low shear stress levels, the permanent strain development is slow and is towards an asymptotic state, however, at higher stresses the strain may increase continually, resulting in an incremental failure. This shows the possibility of a critical stress level, separating the stable and unstable behaviour of granular soil. Wolf (1992) reported works done by Maree *et al.* (1982) in which he studied the cyclic behaviour of gravel and crushed stone. He reported that, under a constant confinement, the permanent settlement is stabilized if the deviator stress is below a certain threshold. Maree (1982) found this threshold to be 0.58-0.98 of the maximum static strength of the soil. Boyce *et al.* (1976) had suggested 70% of failure stress as a threshold for granular soil; this has recently been referred to as the "shakedown" limit. From their experiments, Lekarp and Dawson (1998) clearly showed the indication of the shakedown limit, however, they pointed out that more research is required to determine the shakedown limit properly. Irrespective of discrepancies regarding shakedown limit, these observations suggest that permanent settlement is governed by some form of stress ratio, combining the effect of both deviatoric and confining stresses (mean stress). Barksdale (1972) studied the cyclic behaviour of several granular soils using a conventional triaxial test and drew the conclusion that permanent axial strain increases with decreasing confining pressure and increasing deviator stress (Figure 2.6). He developed the following relationship for permanent axial strain under a conventional triaxial loading regime:

$$\varepsilon_{1,p} = \frac{q/a\sigma_3^b}{1-\left[\frac{Rq/2(C\cos\phi+\sigma_3\sin\phi}{(1-\sin\phi)}\right]} \tag{2.19}$$

where q is the deviator stress, σ_3 is the confining pressure, ϕ is the internal friction angle and C is the cohesion. Lenz and Baladi (1981) employed the static strain-stress test results of sand samples to estimate the cumulative permanent strain of identical samples for repeated loading:

$$\varepsilon_{1,p} = \varepsilon_{0.95S}\ln(1-q/s)^{-0.15} + \left\{\frac{a(q/S)}{1-b(q/S)}\right\}\ln(N) \tag{2.20}$$

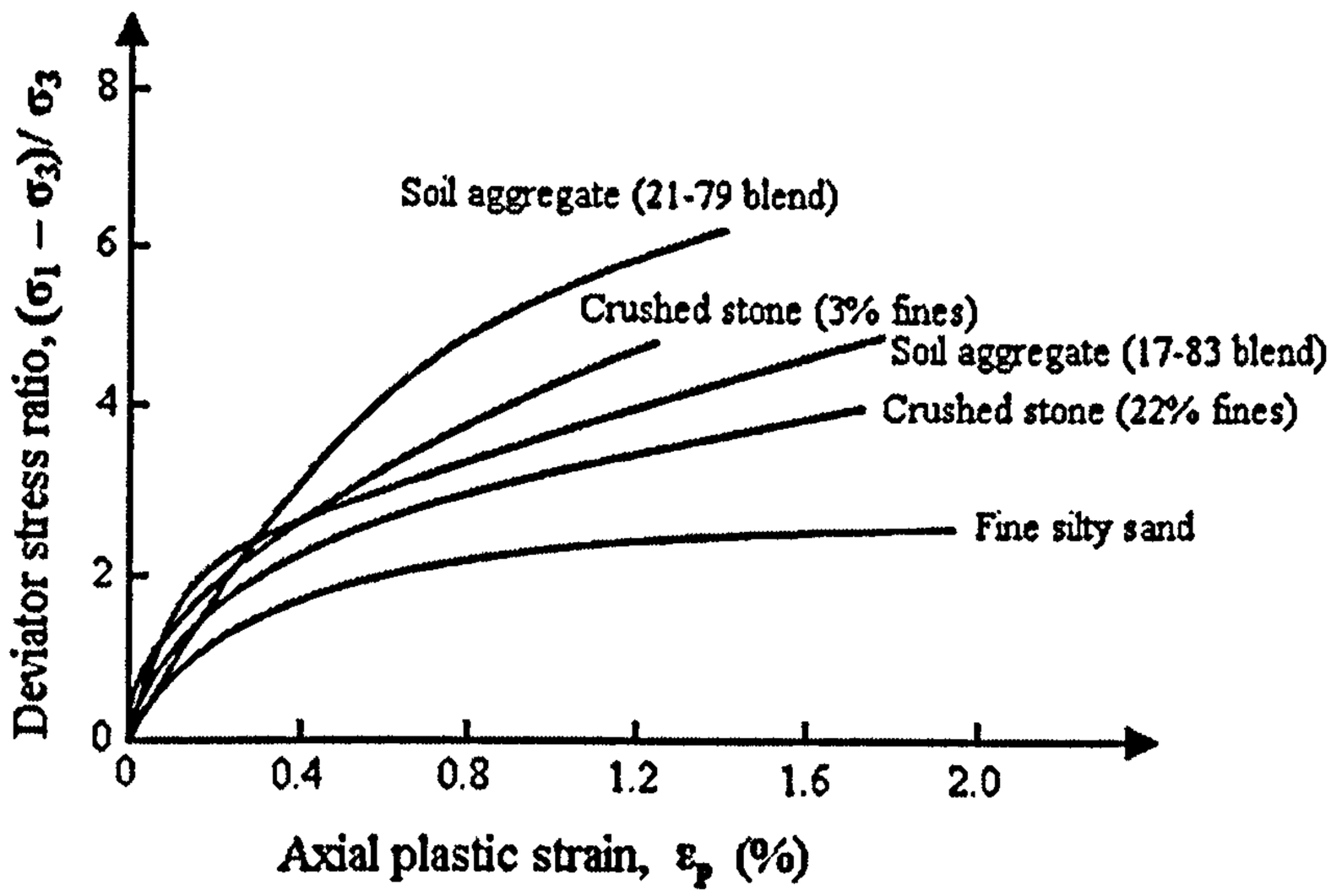

Figure 2.6. Plastic stress-strain characteristics of some of the materials investigated by Barksdale (Barksdale, 1972)

where N is the number of load cycles, S is the static strength, n, m are constants and $\varepsilon_{0.95S}$ static strain at 95% of static strength.

In a recent study, Paute *et al.* (1996) suggested that generally the permanent strain increases gradually towards an asymptotic value. He proposed the following relationship for accumulated strain after an initial period of 100 cycles ($\varepsilon^*_{1,p}$):

$$\varepsilon^*_{1,p} = A.(1-(\frac{N}{100})^{-B}) \tag{2.21}$$

where A and B are material parameters. According to this equation $\varepsilon^*_{1,p}$ approaches a limit value of A as N goes to infinity. Parameter A was related to the shear stress level given by:

$$A = \frac{\frac{q_{max}}{(p_{max} + p^*)}}{b.(m - \frac{q_{max}}{(p_{max} + p^*)})} \tag{2.22}$$

q_{max} and p_{max} are the maximum deviator and mean stresses respectively. p^* is the stress parameter defined by the intersection of the static failure line, p-axis in p-q space. b is a material parameter and m is the slope of the static failure line.

Utilizing the shakedown theorem, Lekarp and Dawson (1998) proposed the following relationship for permanent settlement for different stress paths:

$$\varepsilon_{1,p} = a.(\frac{L}{P_0}).(\frac{q}{p})^b_{max} \tag{2.23}$$

in which $\varepsilon_{1,p}$ is accumulated permanent axial strain at a given number of cycles (>100). L is the length of stress path in p-q space. a and b are material parameters. P_0 is a reference stress.

This model represents the shakedown concept; if there is a low stress ratio, the growth of permanent strain was shown to level off. On the other hand, if the stress ratio was high, the accumulation of permanent strain was progressive, resulting in a gradual deterioration of the granular layer (Lekarp and Dawson, 1998).

A comprehensive overview of empirical relationships for the prediction of permanent strain is given by Lekarp *et al.* (2000b) and Brecciaroli and Kolisoja (2006).

2.7.2 Settlement in Fine-Grained Soil

Li and Selig (1996) studied the permanent plastic deformation in fine-grained subgrade. Mechanisms of plastic deformation in the subgrade from repeated loading include cumulative plastic shear strain, cumulative consolidation and cumulative compaction. A fourth mechanism is ballast void infiltration by subgrade particles resulting from the lack of a filter layer. The resulting track settlement is usually non-uniform along the track and hence excessive subgrade settlement can lead to unacceptable track geometry change. The wavelength of the geometry change depends on the source of the settlement and its pattern (Selig and Waters, 1994).

Various models have been developed for predicting cumulative plastic strain in fine-grain subgrade soil under repeated loading. However, the most commonly used is the following power model (e.g., Monismith *et al.*, 1975; Li and Selig, 1996)

$$\varepsilon_p = AN^b \tag{2.24}$$

where ε_p and N are the cumulative plastic strain and the number of load cycles respectively. A and b are the model parameters depending on soil properties and stress state. Li and Selig (1996) indicated that the power model, given in Equation (2.24), represents the relationship between the cumulative plastic strain and number of repeated stress applications for most fine-grained soils. As well as the number of load cycles, it was discussed that three other factors will also affect the cumulative strain, namely stress state, soil physical state and soil type. For stress state, many experimental researches suggest that the deviator stress (q), in a conventional compression triaxial space, is the main stress factor influencing development of plastic strain in fine-grained soils. The physical state of the soil (water content and density) is known to affect the development of plastic strain. An increase in moisture content will increase the plastic strain accumulation. Studies by Monismoth *et al.* (1975) showed that the exponent b was independent of deviator stress. Studying the experimental data available in the literature, Li and Selig (1996) confirmed that the exponent is independent of deviator stress and also the soil physical state. They determined that it is only related to soil type.

Coefficient A however, strongly depends on the soil stress and physical state, as indicated by Li and Selig (1996). The relationship between parameters A and q was found to be similar to the relationship between ε_p and q. They argued that it is neither convenient nor common to introduce moisture content and dry density directly into the equation. A soil-strength parameter under static loading can indirectly represent the influence of the soil physical state on A. They proposed the following relationship for A.

$$A = a\left(\frac{q}{q_s}\right)^m \tag{2.25}$$

where a and m are material parameters and q_s is the soil static strength (Li and Selig, 1996). Such a relationship resembles the stress threshold concept discussed for granular soils. In fact, it has also been indicated that a critical level of repeated deviator stress also exists for fine-grained soils above which the soil plastic deformation increases rapidly with cyclic loading. At low deviator stress levels, permanent deformation has been shown to increase with the logarithm of the number of cycles, the rate of accumulation of permanent strain increasing as the stress increases. This eventually leads to a deviator stress level, denoted the "threshold stress", above which the rate of accumulation of deformation increases exponentially (Frost *et al.*, 2004). This response has been shown to be related to the stress history and water content of the material, and thus shear strength. Brown (1996) therefore suggested that the dominant factor in determining permanent deformation for fine grain soil is the relationship between applied shear stress (q) and the shear strength of the soil, i.e. (q/q_{max}). Cheung (1994) suggested the concept of a limiting value of q/q_{max}, i.e., $q_{threshold}/q_{max}$ above which plastic deformation increases relatively rapidly. According to this relationship, the accumulation of permanent strain should be approximately linear with the logarithm of the number of load applications for stress ratios that lie below the threshold stress ratio. If q becomes greater than threshold stress, then the permanent strain increases at a markedly increased rate. There is however no agreement on how to define a threshold stress for fine grain soil. Brown and Dawson (1992) suggest that for design purposes this threshold should be taken at a deviator stress equivalent to 50% of the soil's measured suction. However, Cheung (1994) suggested that the threshold stress occurs at the

deviator stress required to generate 1% permanent strain in a sample following 1,000 cyclic load applications. Experimental studies conducted by Frost *et al.* (2004) confirmed the dependency of the permanent strain on deviator stress level, as shown in Figure (2.7). In Figure (2.7), S1-9 denotes clay samples with different moisture contents (w).

It was also indicated that the permanent strain increases slightly with stress level, followed by a sharp exponential increase in permanent settlement as the stress level passes the so-called threshold stress. The threshold stress was approximated to 50% of the deviator stress at static failure (Frost *et al.*, 2004).

2.7.3 Settlement in Railway Track

Railway track will settle as a result of permanent deformation in the ballast and underlying soil. Once the permanent vertical strain ($\varepsilon_{1,p}$) is known over the depth H, then the track settlement (δ) can be estimated from the permanent axial strain (estimated to a depth of H), as given below:

$$\delta = \int_0^H \varepsilon_{1,p} dh \tag{2.26}$$

Based on experimental observations, some relationships have also been proposed to estimate track settlement directly. Sato (1995) suggested track settlement which can be expressed in the following form:

$$\delta = \gamma(1 - e^{-\alpha P}) + \beta P \tag{2.27}$$

where P represents the loading on the track. The loading factor, P, could be expressed either as the number of load cycles of the track or as the tonnage carried by the track. If this equation is used, no distinction is made between different cycles of different magnitude. Sato (1997) proposed another model which takes the sleeper-contact pressure P into account:

$$\delta = a(P - P_t)^m \quad \text{For } P > P_t \tag{2.28}$$

where P_t is a threshold stress value before which no settlement occurs. a and m are the empirical coefficients which can be obtained by regression from experimental data. Shenton (1985) developed the following relationship:

$$\delta = K_1 N^{0.2} + K_2 N \tag{2.29}$$

where K_1 and K_2 are material constants, the values of which depend on a number of factors, such as axle load, rail section, sleeper spacing and track stiffness. Shenton (1985) also indicated that axle load is probably one of the most influencing factors affecting track settlement (see Dahlberg (2001) for an extended overview of railway track settlement models).

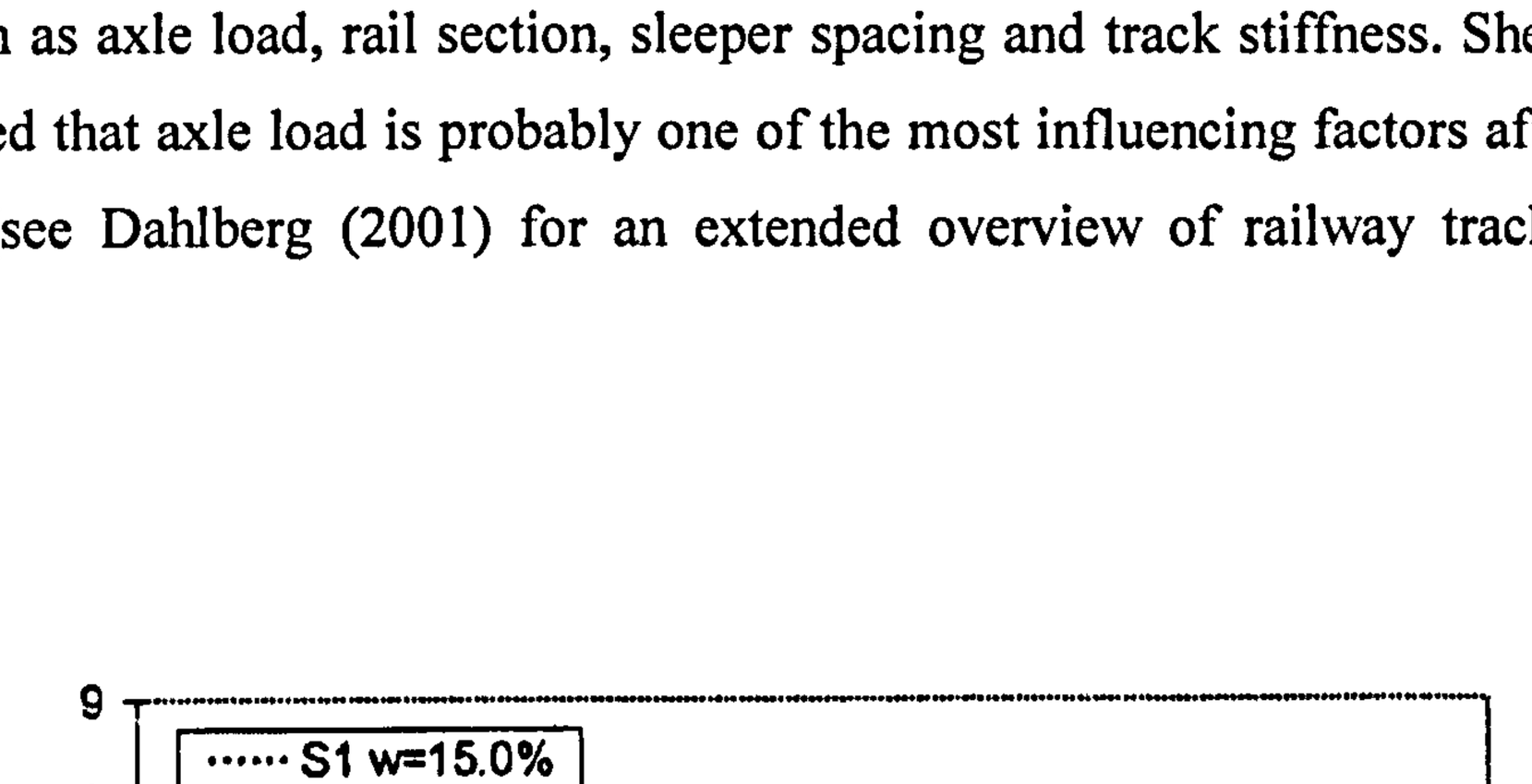

Figure 2.7. Typical relationship between permanent strain and deviator stress for clays with different water contents (Frost *et al.*, 2004)

Despite the widespread use of empirical models, they tend to be over-simplified and do not usually consider the change in track, soil property and loading mechanism within the soil. Dahlberg (2001) argued that many models used to describe the long-term behaviour of a railroad track focus on the loading of the track (number of loading cycle and/or passed tonnage). The strength/stiffness of the substructure often has not been taken into account appropriately. He suggested using a yield limit or a fatigue limit for the ballast which should be considered in any dynamic model. Accordingly, Dahlberg (2001) proposed a beam on spring model supported by a finite element block which behaves like a linear elastic-perfect plastic material (Figure 2.8). Settlement will occur if the stress in that element exceeds the yield limit of the material. The track model is excited by a moving wheel which is loaded by a constant force.

Despite some improvement over traditional models, such as considering the inertia effect and using a rigorous mathematical framework for soil behaviour, it will be argued in Chapter 7 that such a simple constitutive relationship (elastic-perfect plastic) cannot represent the complex behaviour of the granular soil (here ballast) under repeated train loading, and an advanced constitutive model is required to be used, an example of which is described in Chapter 7.

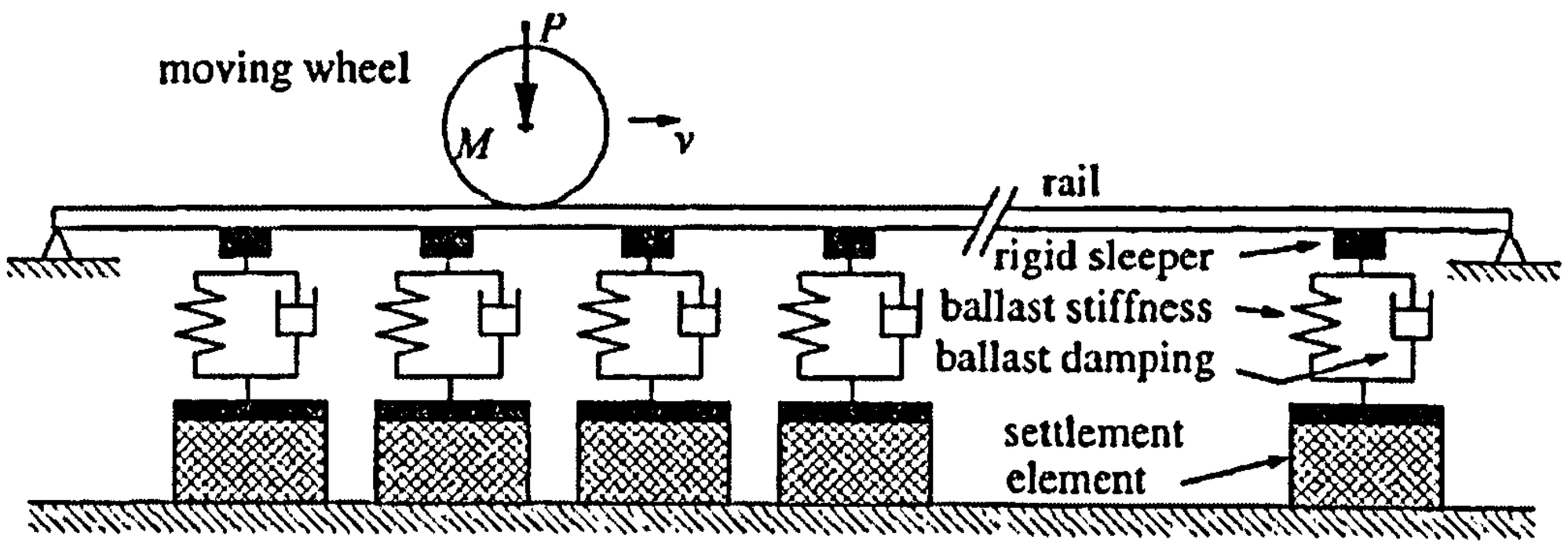

Figure 2.8. A railway model presenting both resilient and permanent behaviour of the substructure as proposed by Dahlberg (2001)

2.8 Conclusion

In this chapter different aspects of track mechanics were presented. Measuring track stiffness through a track modulus was discussed. Track loading was also explored and the different relationships to account for dynamic amplification were investigated. It was indicated that dynamic amplification of the train load is affected by train speed and by track quality. Track vibrations, their sources and induced frequencies were also captured. It was discussed that vibration in the substructure is of low frequency in nature, whereas high frequency vibration exists mainly in the upper structure. Long-term settlement of ballast, granular soil and fine-grained subgrade was also discussed in detail. It was concluded, that for both fine-grained and coarse grained soils, that there is a threshold stress after which the permanent settlement increases rapidly, which may result in incremental failure. Therefore it can be argued, as suggested by some researchers, that the stress level in the ballast and subgrade should be kept lower than the threshold stress. It was also shown that, for granular soil, the permanent settlement strongly depends on mean stress level (confining stress) and therefore the permanent settlement is a function of stress ratio, i.e. the ratio between deviatoric stress (in conventional triaxial space, the deviator stress) to mean stress. However, the permanent settlement is primarily a function of deviatoric stress for fine-grained soils.

CHAPTER 3

DEVELOPMENT OF A THREE-DIMENSIONAL FINITE ELEMENT MODEL FOR RAILWAY TRACK

3.1 Introduction

In recent decades, several models with different degrees of complexities have been developed to study railway track performance under train loading. In this chapter, an overview of such models is given and their limitations are discussed. The development of the high speed track model based on three-dimensional dynamic finite element methods is discussed next. Different aspects of the developed model are illustrated in terms of representations of the track components, boundary conditions, time integration, train loading and material damping. Finally, the performance of the model is discussed and compared against actual site measurements. This chapter describes different aspects of the basic model; further developments of the model, to include nonlinear constitutive relationships of the substructure and train-track interaction, are presented in Chapters 5 and 6 respectively.

3.2 Railway Track Modelling Philosophy

In order to design a safe and cost effective railway track, it is imperative to have an appropriate track model which realistically represents the actual behaviour of the railway track system subjected to vehicle loading. The model should simulate the mechanics of sleeper-ballast interaction, the spread of the load onto a number of adjacent sleepers, through the rail and subsequently into the multi-layered sub-structure, and the dynamic

nature of train loading. An appropriate model should also be able to represent different geometries and reflect the nonlinear behaviour of track components.

In terms of track-substructure presentation, the available models can be classified into two main categories, namely "beam on spring" and "beam on continuum half space" models, as schematically shown in Figure (3.1). Chang *et al.* (1980) reviewed several beam on spring type models. In beam spring models, the beam mainly represents the rail, and springs present the support, including the rail pad, sleepers, ballast and the multi-layered subgrade. They concluded that these models do not represent the track mechanics properly and hence proposed a three dimensional static GEOTRACK model which incorporates the analytical solution for a multi-layered elastic system as given by Burmister (1945). Static models have also been developed using finite element methods such as the two dimensional KENTRACK (Huang *et al.*, 1984) and the three dimensional model developed by Shahu *et al.* (1999) as shown in Figure (3.2). However, as will be discussed in the next chapter, track response to a moving train is essentially a dynamic problem, especially for high-speed trains.

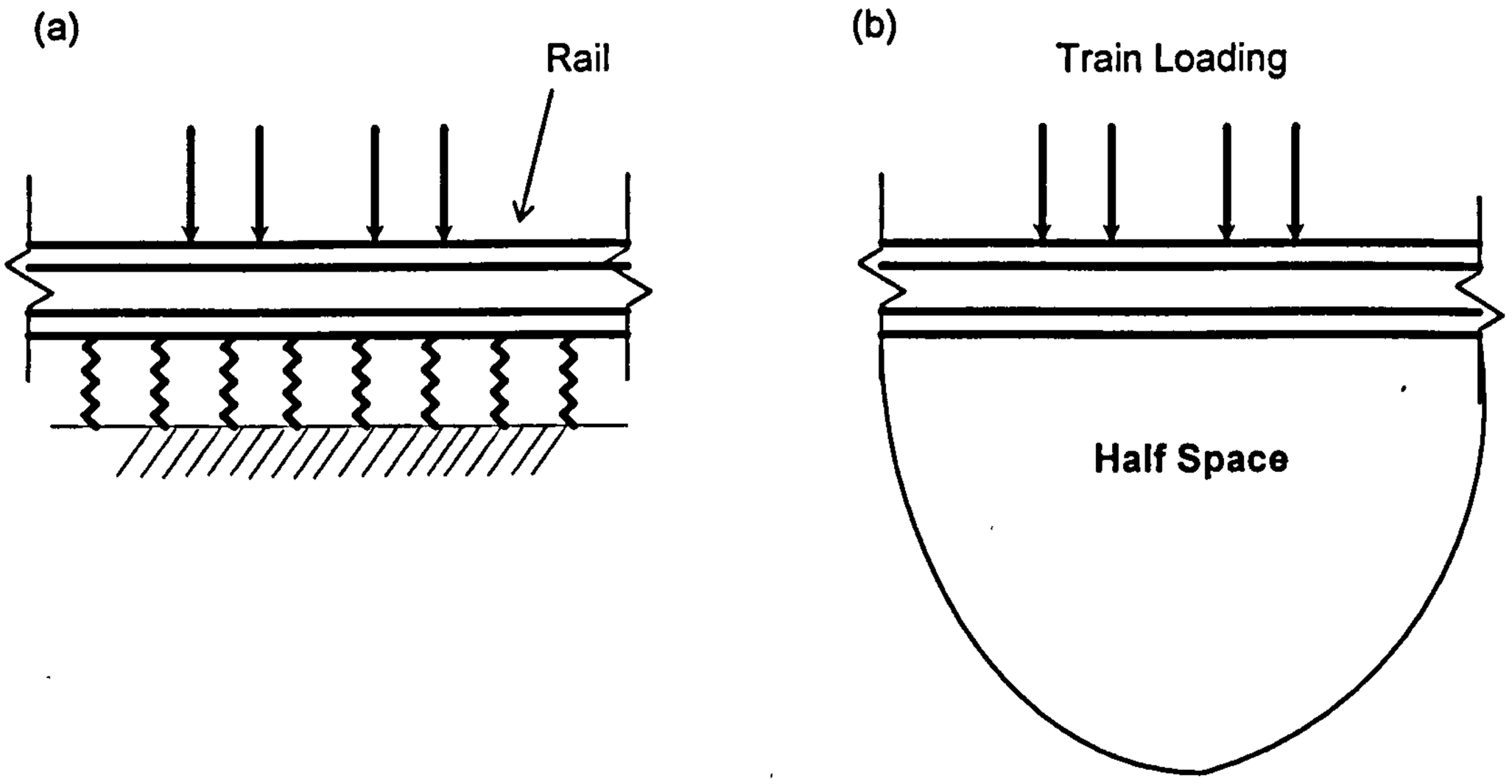

Figure 3.1. Schematic representations of "Beam on spring" (a) and "Beam on half space" (b) models

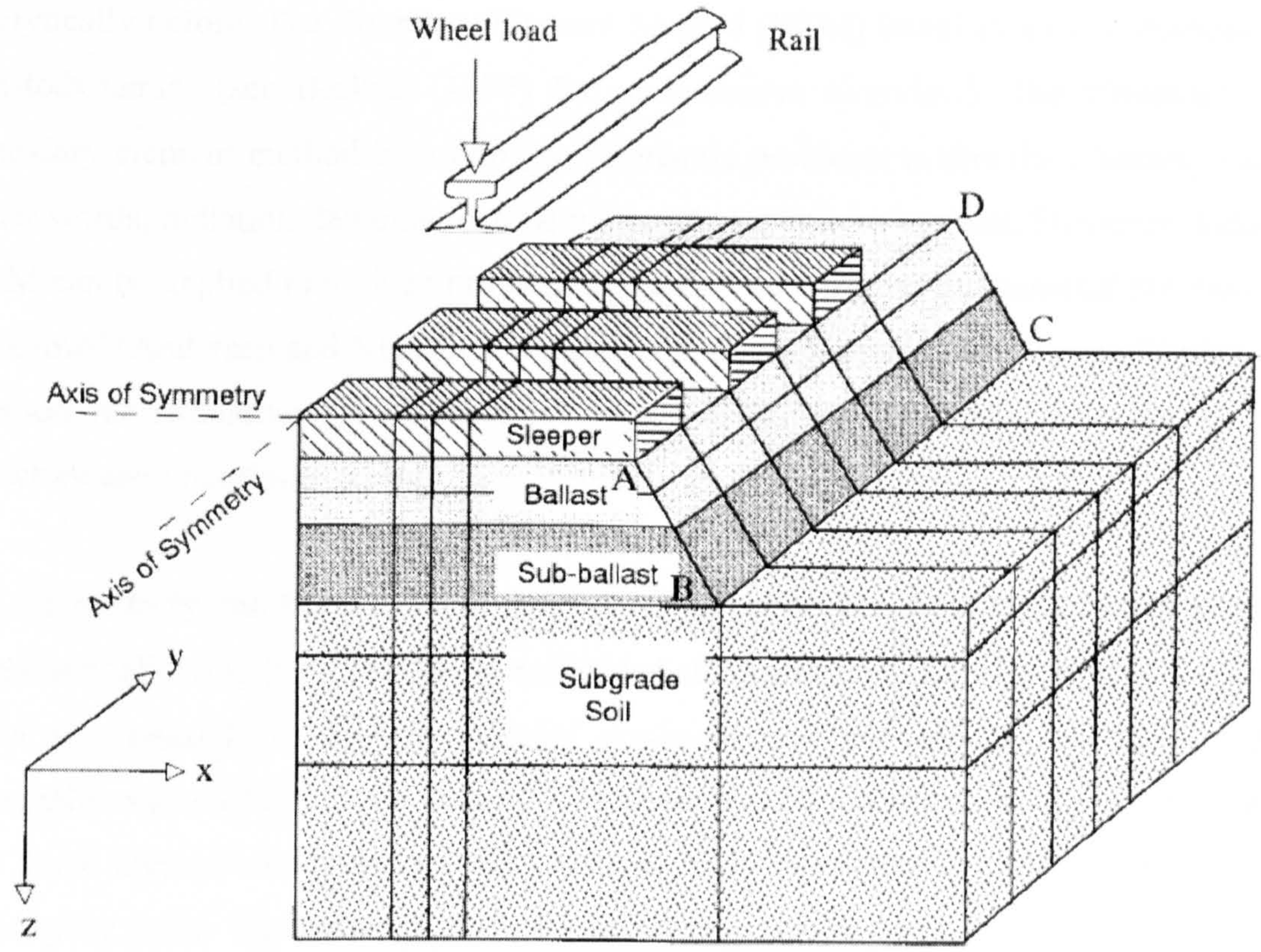

Figure 3.2. Layout of a static three dimensional finite element model of railway track (Shahu *et al.*, 1999)

To circumvent the limitations regarding static and "Beam on spring" models, a dynamic "Beam on continuum half space" model has been developed using analytical or numerical approaches. Singh and Kuo (1970) studied analytically the response of an elastic half-space under a moving circular load. Jones *et al.* (1998) obtained the analytical solution of an elastic half-space under a moving rectangular harmonic force; this was later extended by Sheng *et al.* (1999) to study the railway track on a layered ground with horizontal surfaces. In order to obtain such analytical solutions, restrictions need to be imposed on the geometry and material properties of the problem considered, as closed-form solutions cannot be easily obtained for other complex conditions (Hung and Yang, 2001).

With the advent of computers, various numerical methods, including the finite element method, the boundary element method and their variants, began to emerge as effective tools for solving problems that were not previously possible (or were difficult) to solve

analytically before. The Boundary Element Method (BEM) found extensive applications in Elastodynamics (see Beskos, (1997) for an extensive overview). The advantage of the boundary element method in solving soil dynamic problems is that the radiating wave, in other words, radiation damping, can be inherently taken into account. However, before the BEM can be applied to a given problem, the green function, or fundamental solution, must be known (Andersen and Nielsen, 2003). This imposes limitations on the application of the method for simulation of irregularities in the geometry and material properties of the structure and underlying soils.

On the contrary, the finite element method is applicable to almost any arbitrary geometric condition, allowing the inclusion of embedded structures and multi-layering of the ground. It is also possible to include material nonlinearity which affects the track response, especially under a high speed loading regime, as will be discussed in Chapter 5. However, the finite element method does not consider radiation damping of the wave energy to infinity by itself. The radiation damping to infinity can be taken into account through the implementation of a boundary condition which absorbs the travelling wave energy from the source (e.g. viscous boundaries (Lysmer and Kuhlemeyee, 1969). Alternatively, a hybrid approach can be taken in which the near field is modelled by finite elements and the far field is established through an impedance matrix relating the nodal force to the nodal displacement at the far-field near-field interface (Hung and Yang, 2001). In a hybrid approach, the far field can be modelled by methods, such as boundary element or infinite element methods, which acount for radial damping (e.g. see Chuhan and Chongbin, 1987). A discussion of different methodologies to represent the far-field can be found in Wolf and Song (1996).

In terms of the "dimension" of the railway track dynamic problem, two dimensional models have been extensively developed (e.g. Suiker and Esveld, 1997; Kaynia *et al.*, 2000; Picoux, 2003). Even if the railway system is identical in terms of material properties and geometry, in the direction perpendicular (or along) the railway track, as the train speed increases, two dimensional models become inadequate for the simulation of the railway track dynamics problem (due to the result of the wave propagation phenomenon). In other words, this particular problem may be two dimensional in geometry but three dimensional in physics (Hung and Yung, 2001).

Although three-dimensional finite element analyses have attracted considerable applications in different branches of geotechnical/structural engineering, three-dimensional dynamic modelling of railway track is still limited. Lei and Mao (2001) studied the track structure using a three-dimensional finite element model. Using a "beam on spring" type model, the loading spectrum on the sleepers was first derived. Then this load spectrum was input into the three-dimensional finite element model to study the dynamic response of the track. An increase in vibration level in the ballast was observed with the increase in train speed. Similar studies had also been conducted by Luo *et al.* (1996); in which they extended the finite element boundaries to be far enough from the domain of interest, instead of employing any absorbing boundary. Using ABAQUS, Hall (2000, 2003) conducted a limited number of three-dimensional finite element simulations of railway track and simulated the displacement of railway track at different track speeds. In this analysis, the train was modelled as a sequence of loads and dashpots was placed on the boundaries to avoid any fictitious wave reflections. Ju and Lin (2004) developed a three-dimensional finite element model and studied railways on a homogenous substructure. They reported that the vibration level in the area surroundings the track rises as the train speed increases. Furthermore, the change in displacement pattern under the train, when the train speed approaches the so-called critical track velocity, was simulated. Ju (2007) also used a similar model to study vibration in a building near a railway bridge.

In the present research, a three-dimensional finite element model is developed to simulate the dynamic response of railway track. This model incorporates multi-layered ground, material nonlinearity, material damping, stiffness/geometrical irregularity in the track and train-track interaction. The ability of the developed model to look at train-track-ground interaction in three-dimensions represents a major step forward in railway track analysis and simulation. Details of the basic model will be given in subsequent sections. As mentioned before, further developments of the model, to include nonlinear constitutive relationships of the substructure and train-track interaction, are presented elsewhere in Chapters 5 and 6 respectively.

3.3 Three-Dimensional Finite Element Model

3.3.1 Model Configurations

The sleeper, ballast, sub-ballast and ground are discretized using 20 noded brick elements. Three-dimensional beam-column elements are employed to represent the rail; this element incorporates 6 degrees of freedom (3 translations, 3 rotations) at every node. Rail pad elements are also implemented using a spring-damper combination. A schematic representation of the different types of elements used in the present research is given in Figure (3.3). Figure (3.4) depicts the finite element discretization representing the full width track. Because of symmetry around the centreline of the railway track, the finite element model is reduced to half of this system, i.e. a single rail, only half of the sleepers & ballast/subballast and ground are considered in the simulation, as shown in Figure (3.5). The dimensions of a typical symmetric model (Figure 3.5), which is used throughout this research, is 60m* 15m* 35m (length (Y direction)*width (X direction) *depth (Z direction)). As shown in Figure (3.5), more elements are used along the track, than those in directions perpendicular to the track, which are kept to a minimum to decrease the running time. 151 elements are used in Y direction (along the rail), 2 rows of elements in X direction and 5 rows of elements in vertical direction, representing sleepers, and ballast and subgrade layers. More complicated geometries can also be produced using the developed model as shown in Figures (3.6) and (3.7).

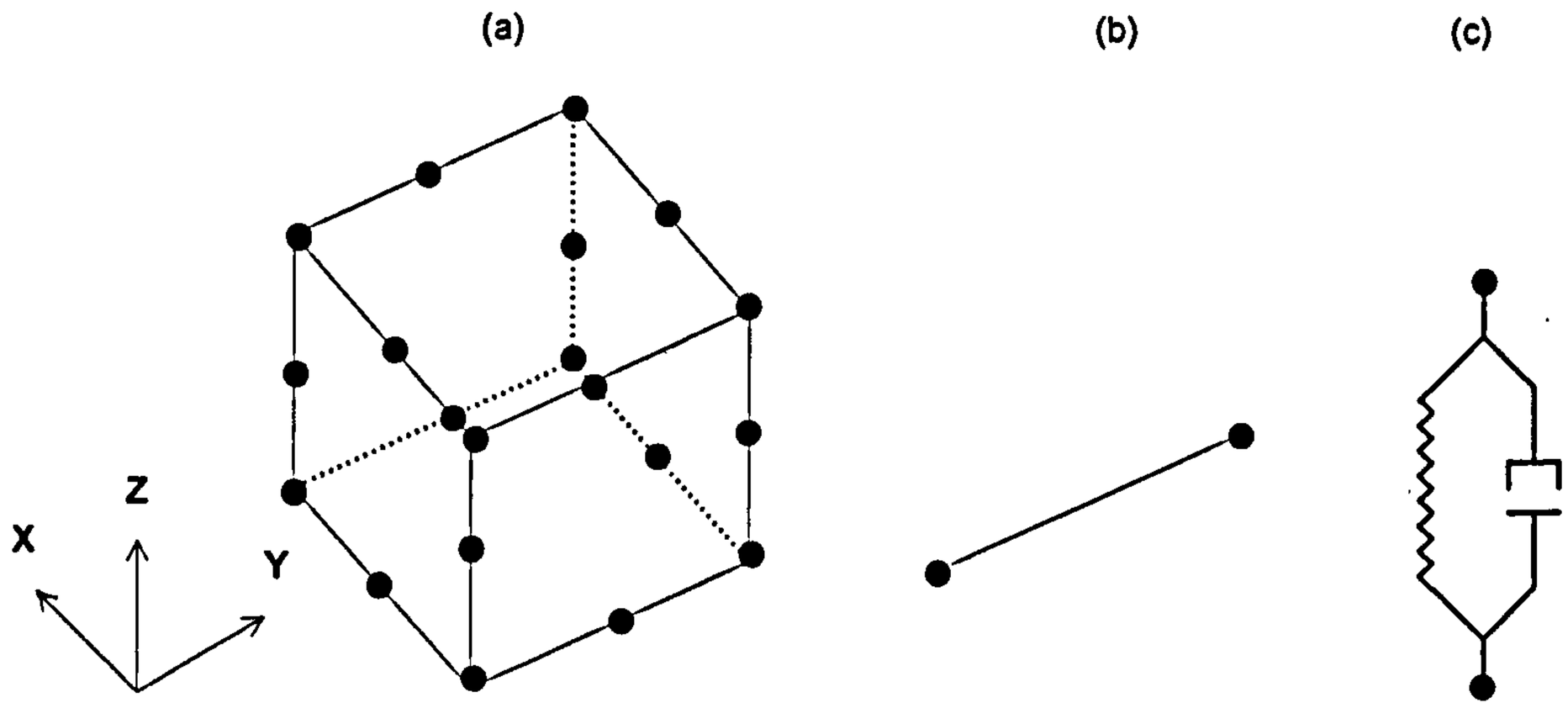

Figure 3.3 Elements used to represent track components (a) Brick element (b) Beam-column element (c) Spring-damper element

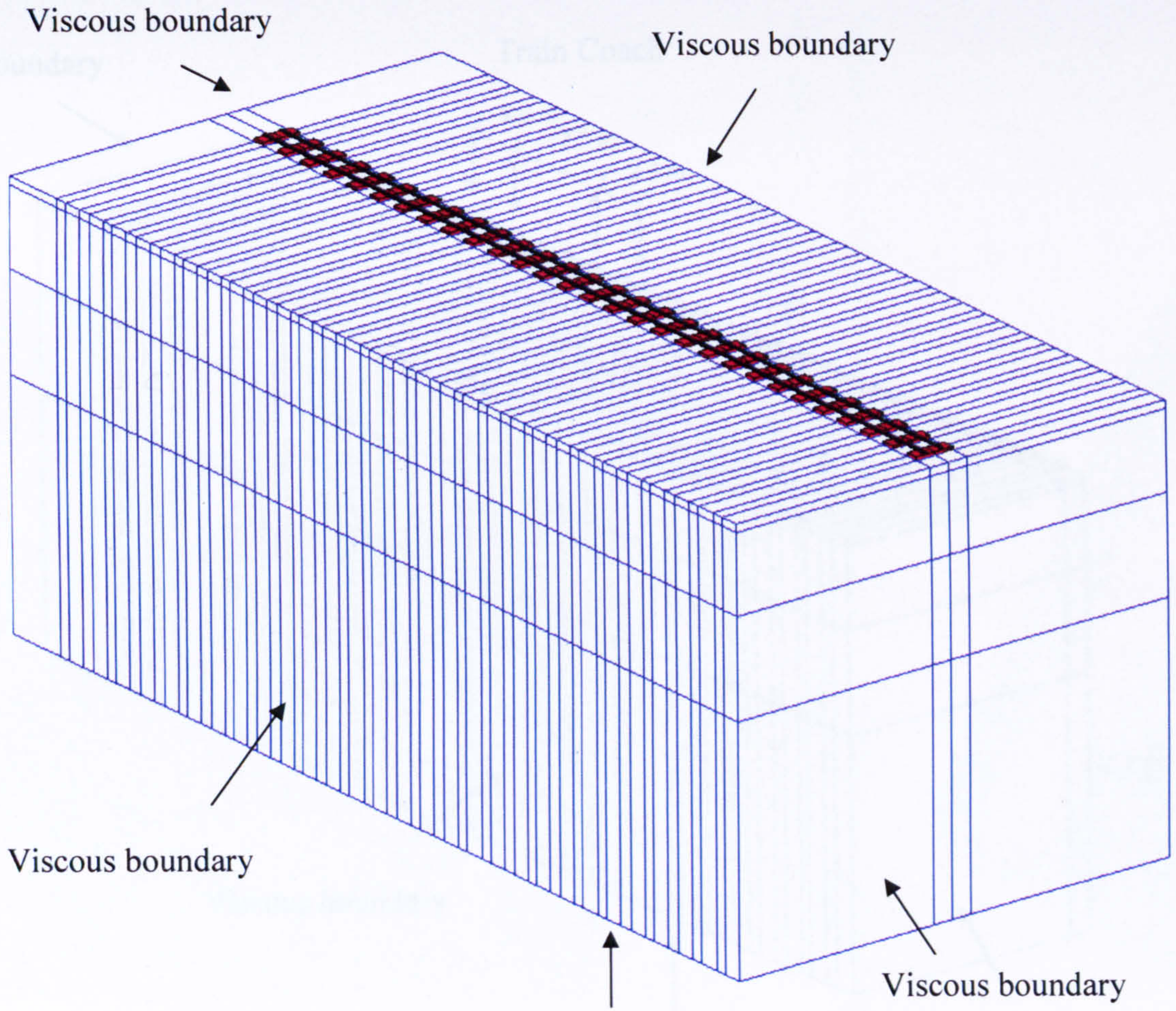

Figure 3.4 Representation of full width track by the proposed three-dimensional finite element model (only 59 rows of the total 151 elements are shown along the track)

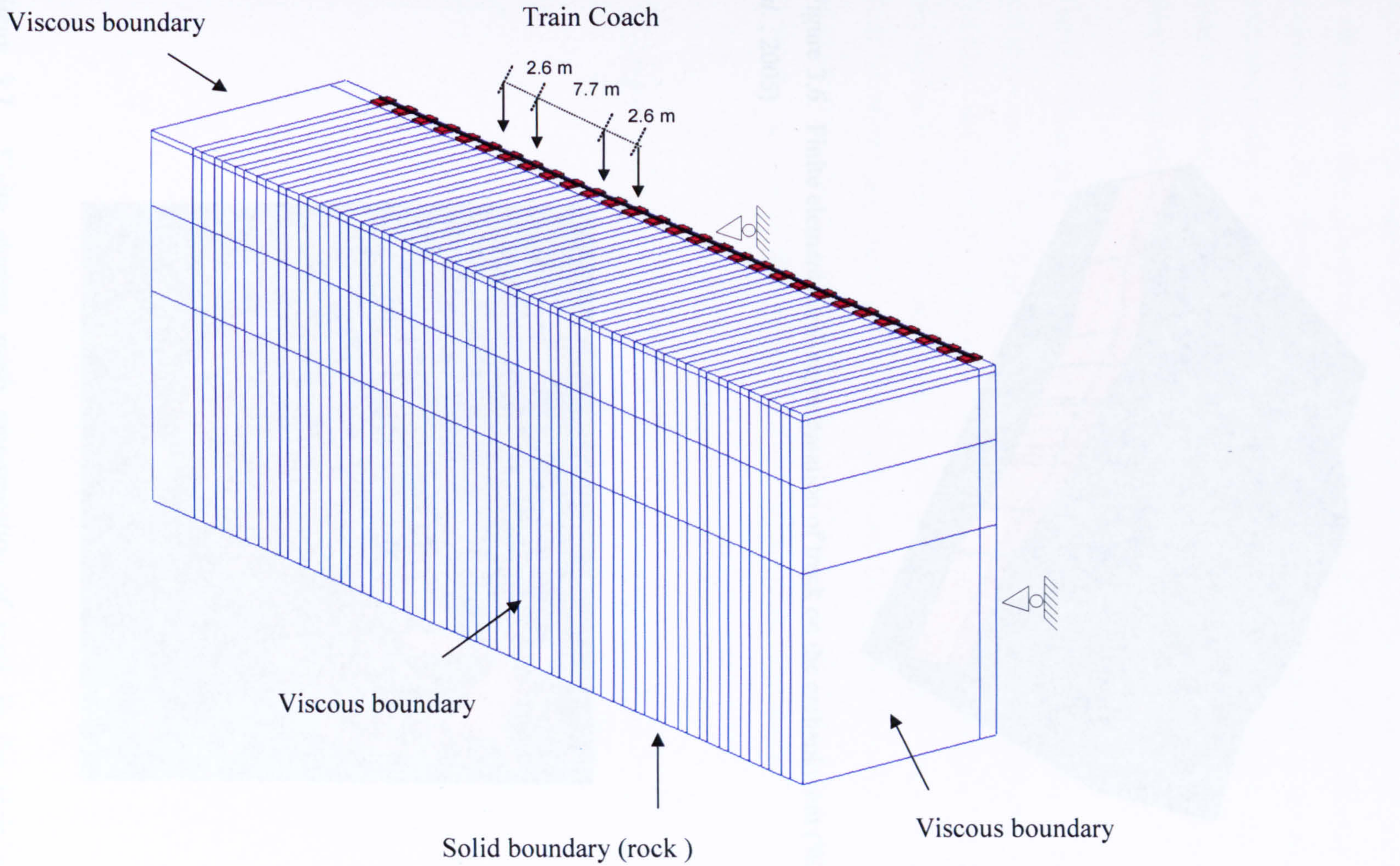

Figure 3.5. A symmetric representation of the track used in the simulations in the present research (only 59 rows of the total 151 elements are shown along the track)

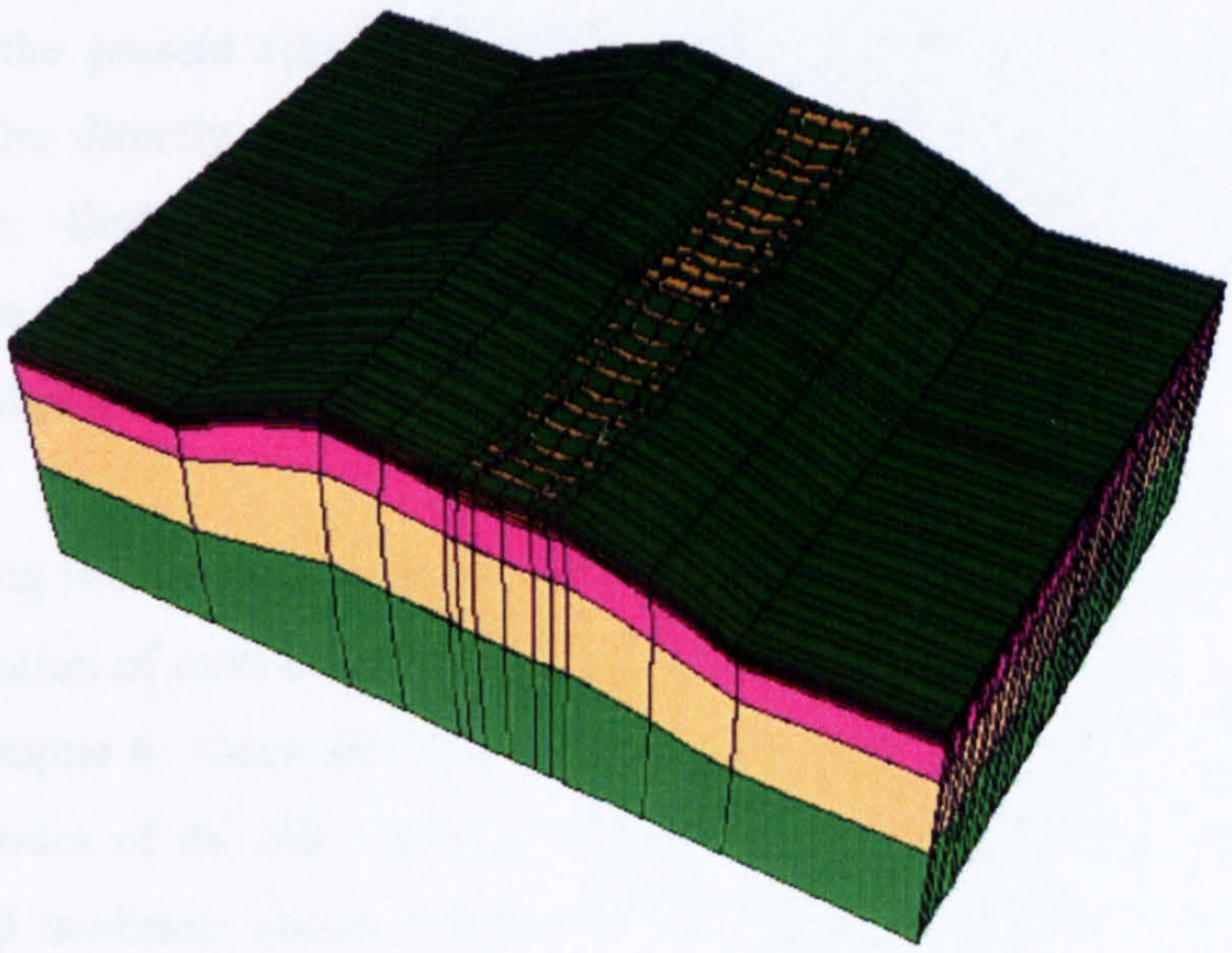

Figure 3.6. Finite element mesh representation of track on the embankment (Woodward *et al.* , 2005)

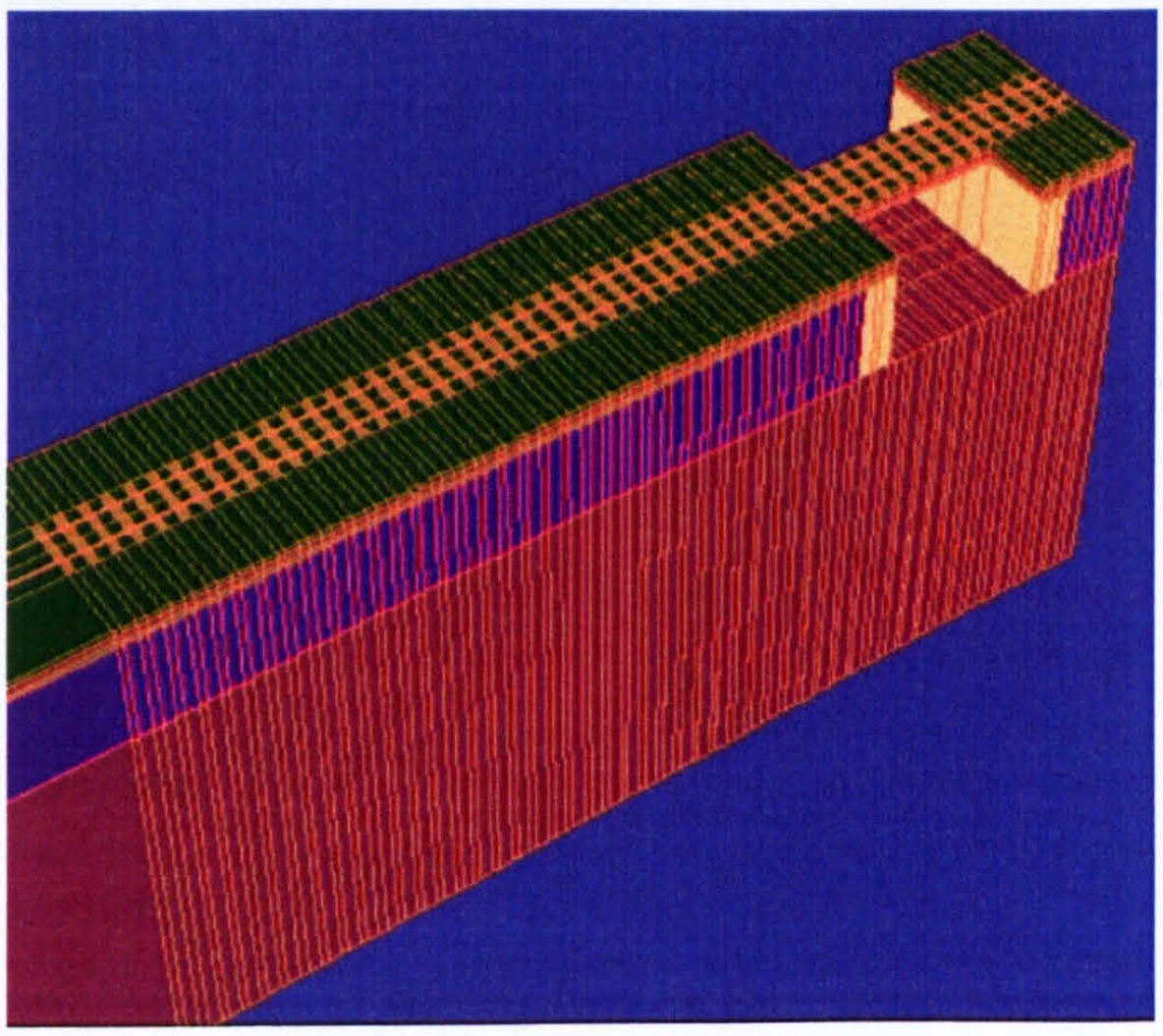

Figure 3.7. Finite element mesh representation of track in the vicinity of bridge (Woodward *et al.*, 2005)

In the model, the beam may be connected to a sleeper either through a rail pad or directly to a sleeper. As the present research was focused on substructure performance, a rail is considered to be directly connected to sleepers, and the effect of the rail pad is not considered here. Earlier studies found this approach was reasonable if the subgrade and ballast response are of main concern (low frequency response). Table (3.1) gives the sleepers and rail properties used throughout this thesis.

The train loading is introduced using two different methods: a sequence of constant loads and implementation of train models. The train models and their interactions with track are described in Chapter 6. Once the train load is known in every time step, it is distributed to two adjacent nodes of the rail, which acts as an external load in finite element analysis. Both linear and nonlinear elastic constitutive relationships are considered for ballast and subgrade soil, whereas rail and sleepers are considered to be linear elastic (see Chapter 5 for more details on constitutive relationship considered for substructure).

Component	Parameter	Value	Component	Parameter	Value
Rail	Elasticity modulus (E)	210.0 GPa	Sleeper	Elasticity modulus (E)	20.00 GPa
	Poisson's ratio (μ)	0.25		Poisson's ratio (μ)	0.3
	Bending stiffness around x (I_x)	1.2449E-5 m^4		Thickness	0.2 m
	Bending stiffness around z (I_z)	4.5261E-6 m^4		Width	0.30 m
	Torsional stiffness around y (J_y)	1.6975E-5 m^4		Length	2.40 m
	Area	6.5538E-3 m^2		Spacing	0.77 m
	Unit weight	7897 kg/ m^3		Unit weight	1000 kg/ m^3

Table 3.1. Specification of sleepers and rail used in the present research

In order to facilitate the fast inversion of the mass matrix in the time integration procedure, lumped mass matrices are employed for each element. HRZ Scheme (Hinton *et al.*, 1976) is used to produce a diagonal mass matrix from the corresponding consistent mass matrix. An HRZ Scheme based procedure to compute lumped mass matrix, from a consistent mass matrix, is given in Cook *et al.* (2002). Elaboration of the finite element procedure is not given here and can be found in numerous text books (e.g. Smith and Griffith, 1997; Cook *et al.*, 2002).

3.3.2 Boundary Conditions

In a dynamic finite element problem, defining boundary conditions becomes complicated owing to the existence of stress waves. As a stress wave propagates from its source into the media, it will experience radiation or geometric damping as it is radiated into the far field. If the far field is not modelled adequately, the wave energy will be reflected back into the finite element mesh and a spurious response will occur. The wave energy has to be absorbed at the boundary in order to prevent these phenomena from occurring. Several methods for absorbing these energies, such as infinite elements, viscous boundaries and superposition boundaries, have been employed (see e.g. Cundall *et al.*, 1978; Jones *et. al.*, 1994; Hung and Yang, 2001; Yerli *et al.*, 2003)

The simplest approach is to place boundaries far enough away so that the time taken for the fastest reflected waves to propagate back to the region of interest is longer than the period of interest. This means that the finite element meshes become very large, requiring a large amount of memory and excessive computation time.

Viscous boundaries, which absorb the energy of the impinging waves, can also be placed. The standard viscous boundary was mathematically described by Lysmer and Kuhlemeyer (1969):

$$\sigma_n = \alpha \rho V_p \frac{\partial u_n}{\partial t} \tag{3.1}$$

$$\sigma_t = \beta \rho V_S \frac{\partial u_t}{\partial t} \tag{3.2}$$

where σ_n and σ_t are the normal and shear stresses at the boundary respectively. $\frac{\partial u_n}{\partial t}$ and $\frac{\partial u_t}{\partial t}$ are normal and tangential velocities respectively. V_p and V_S are compression and shear wave velocities respectively. According to this definition, it can be said that the boundary is supported by infinitesimal dashpots, both normal and tangential to the boundary as shown in Figure (3.8).

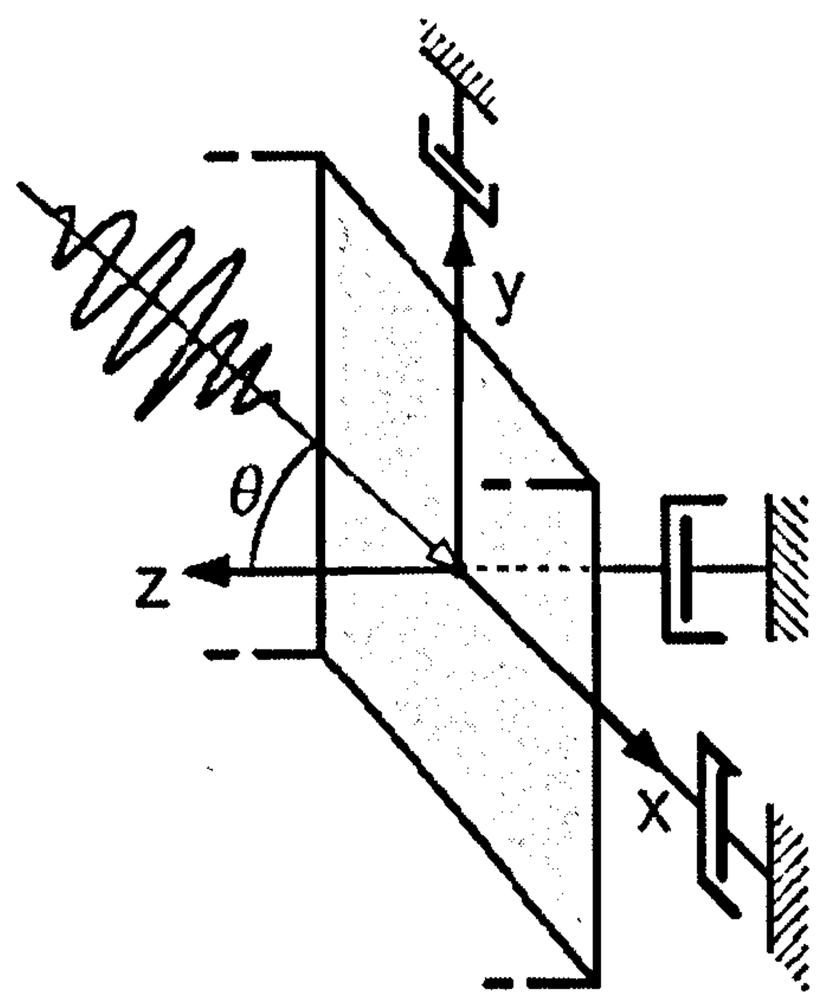

Figure 3.8. Schematic representation of a three-dimensional viscous boundary condition

The implementation of viscous boundary is described by Woodward (1993). The viscous boundary force can be calculated as follows:

$$f = \int_A [N]^T \{\sigma\} dA \tag{3.3}$$

N is the boundary element shape function. A is area of the boundary element. The stress caused by the travelling wave transmitting through the boundary can be written as

$$\{\sigma\}=[C^V]\left\{\frac{\partial u}{\partial t}\right\} \tag{3.4}$$

$$[C^V]=\begin{bmatrix}\alpha\rho V_p & 0 & 0\\ 0 & \beta\rho V_s & 0\\ 0 & 0 & \beta\rho V_s\end{bmatrix}$$

(3.5)

$$\left\{\frac{\partial u}{\partial t}\right\}=[N]\left\{\frac{\partial u}{\partial t}\right\}_n \tag{3.6}$$

where $\left\{\frac{\partial u}{\partial t}\right\}_n$ is the vector of nodal velocity for a particular boundary element (here an 8 noded quadrilateral). The force vector now becomes

$$f=\int_A [N]^T[C^V][N]\left\{\frac{\partial u}{\partial t}\right\}_n dA \tag{3.7}$$

The boundary element consistent viscous damping matrix can then be written:

$$[C^b]=\int_A [N]^T[C^V][N]dA \tag{3.8}$$

The boundary element consistent viscous damping matrix $[C^b]$ is added to the associated material damping matrix to form the global damping matrix.

In order to show the effect of a viscous boundary on incident stress waves, a three-dimensional rod is considered, as given in Figure (3.9). The elasticity modulus and Poisson's ratio of the rod are 75 MPa and 0.3 respectively. The unit weight of the rod is 1800 kg/m^3. The rod is descretized using brick elements and is subjected to two separate

force impulses, as shown in Figure (3.9), inducing a compression wave and a shear wave. The dynamic equation is solved in the time domain employing a classical explicit scheme (see Section 3.3.4) with a time increment of 15E-6 s. Figures (3.10) and (3.11) show the displacement time histories at the centre of the rod for two stress waves. The open boundary causes the reflected stress waves to be in-phase with the incident stress waves. The closed boundary causes the reflected stress waves to be out of phase with the incident stress waves. The viscous boundary, however, causes only a small amount of stress wave reflection, hence only a small change in displacement.

It should be noted that the wave energy absorption in the Lysmer and Kuhlemeyer viscous boundary depends on the angle upon which the waves hit the boundary (angle of incidence). This type of boundary does not completely absorb the Rayleigh wave either (Lysmer and Kuhlemeyer, 1969). Despite all these limitations, the viscous boundary offers a convenient and practical way of modelling the infinite media and is therefore employed in the present research.

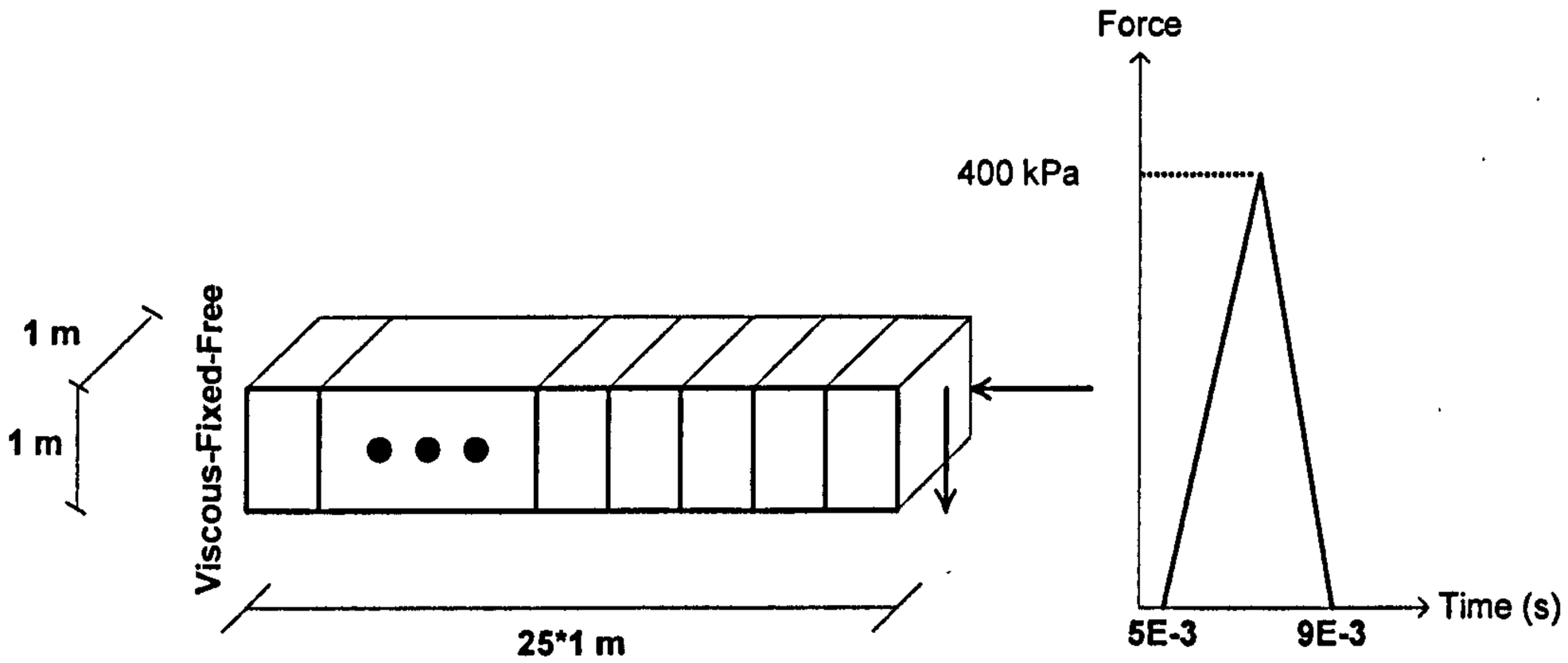

Figure 3.9. Compressive and shear impulses applied to a beam with different boundary conditions

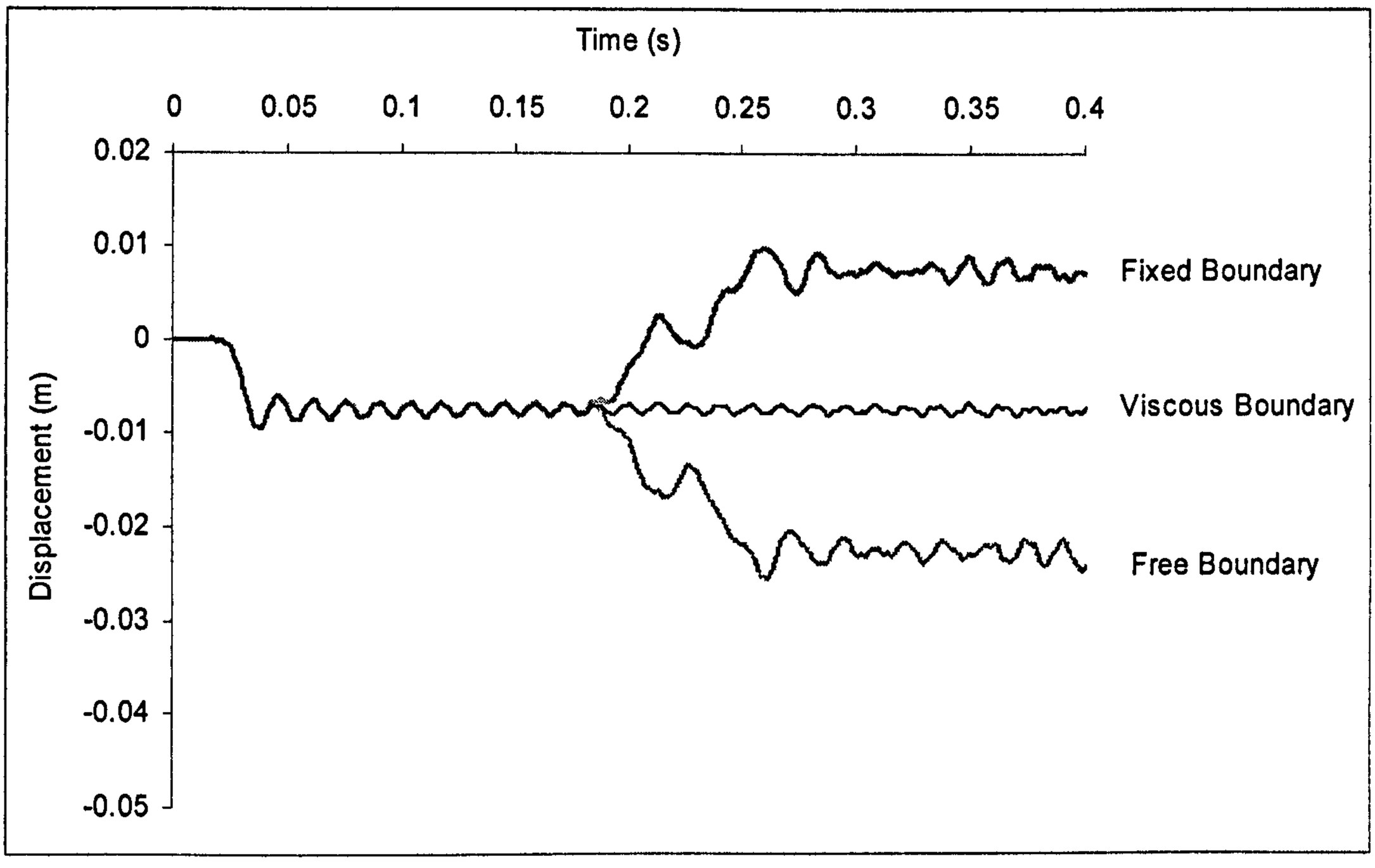

Figure 3.10. Displacement response at the middle of the beam with different boundary conditions under a compressive impulse

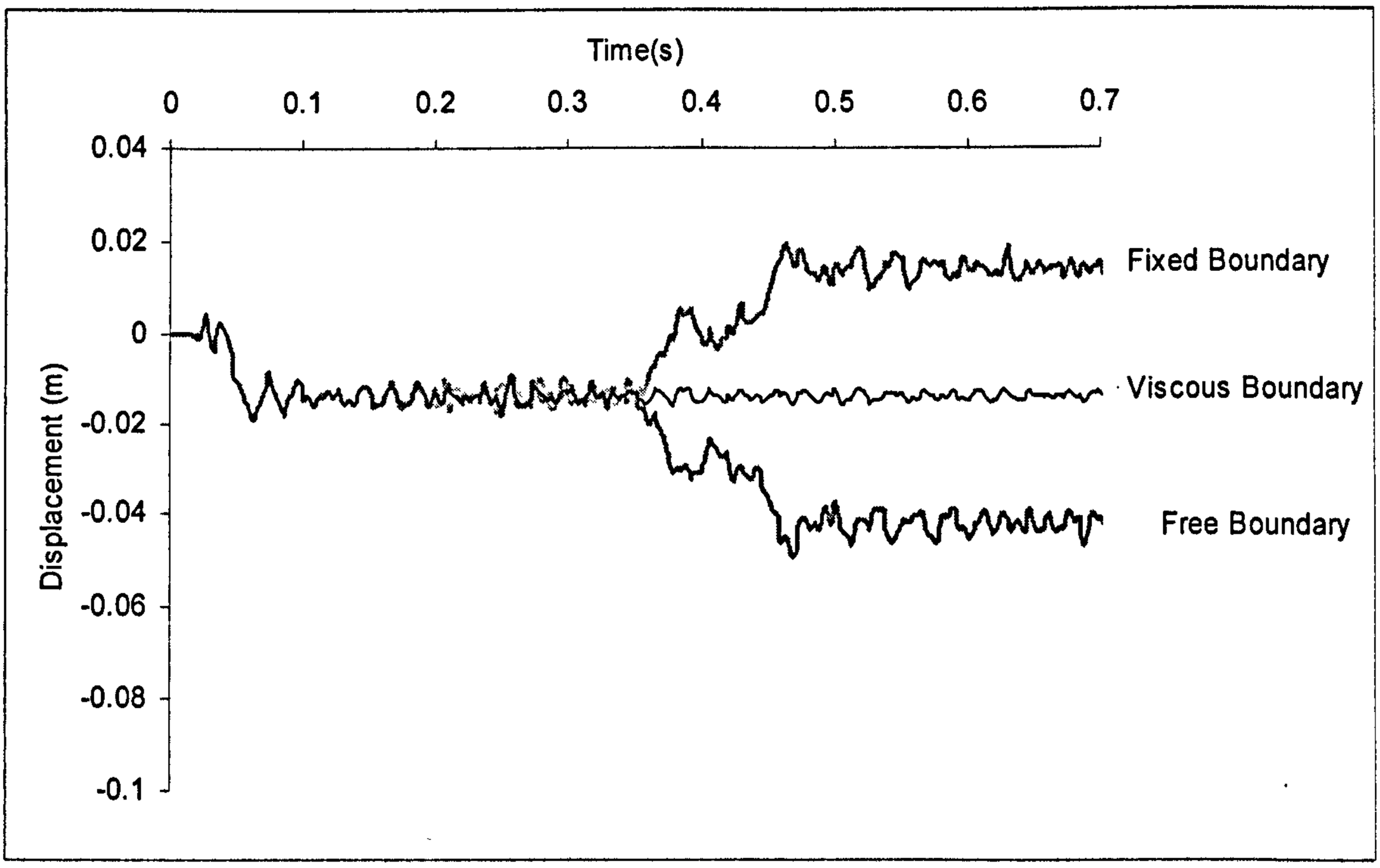

Figure 3.11. Displacement response at the middle of the beam with different boundary conditions under a shear impulse

3.3.3 Material Damping

Caughey (1960) stated that the damping matrix could be expressed as a linear combination of the mass and stiffness matrices. This type of damping is referred to as Rayleigh damping and is given by Zerwer *et al.* (2002):

$$[C]=[M]\sum_{k=0}^{p}\eta_{k+1}(\frac{[K]}{[M]})^{k} \tag{3.9}$$

η is constant. By setting p=1, the standard Rayleigh damping equation is obtained:

$$[C]=\eta_1[M]+\eta_2[K] \tag{3.10}$$

where η_1 and η_2 are constants. The relationship between damping ratio (D) and Rayleigh damping is given by

$$D=\frac{1}{2}(\frac{\eta_1}{\omega}+\eta_2\omega) \tag{3.11}$$

In order to incorporate linear damping into a finite element code, the approach is to curve fit η_1 and η_2 values to model the damping of the predominant vibration modes. Therefore,

$$\eta_1=\frac{2Dw_1w_n}{w_1+w_n} \tag{3.12}$$

$$\eta_2=\frac{2D}{w_1+w_n} \tag{3.13}$$

where w_1 and w_n are generally taken as the first natural frequency and the highest natural frequency of the vibration modes with the highest contribution to the response. The relationship between the Rayleigh damping parameters and damping ratio is given in Figure

(3.12). It is seen that mass damping is more important at lower frequencies, whereas stiffness damping becomes dominant at higher frequencies.

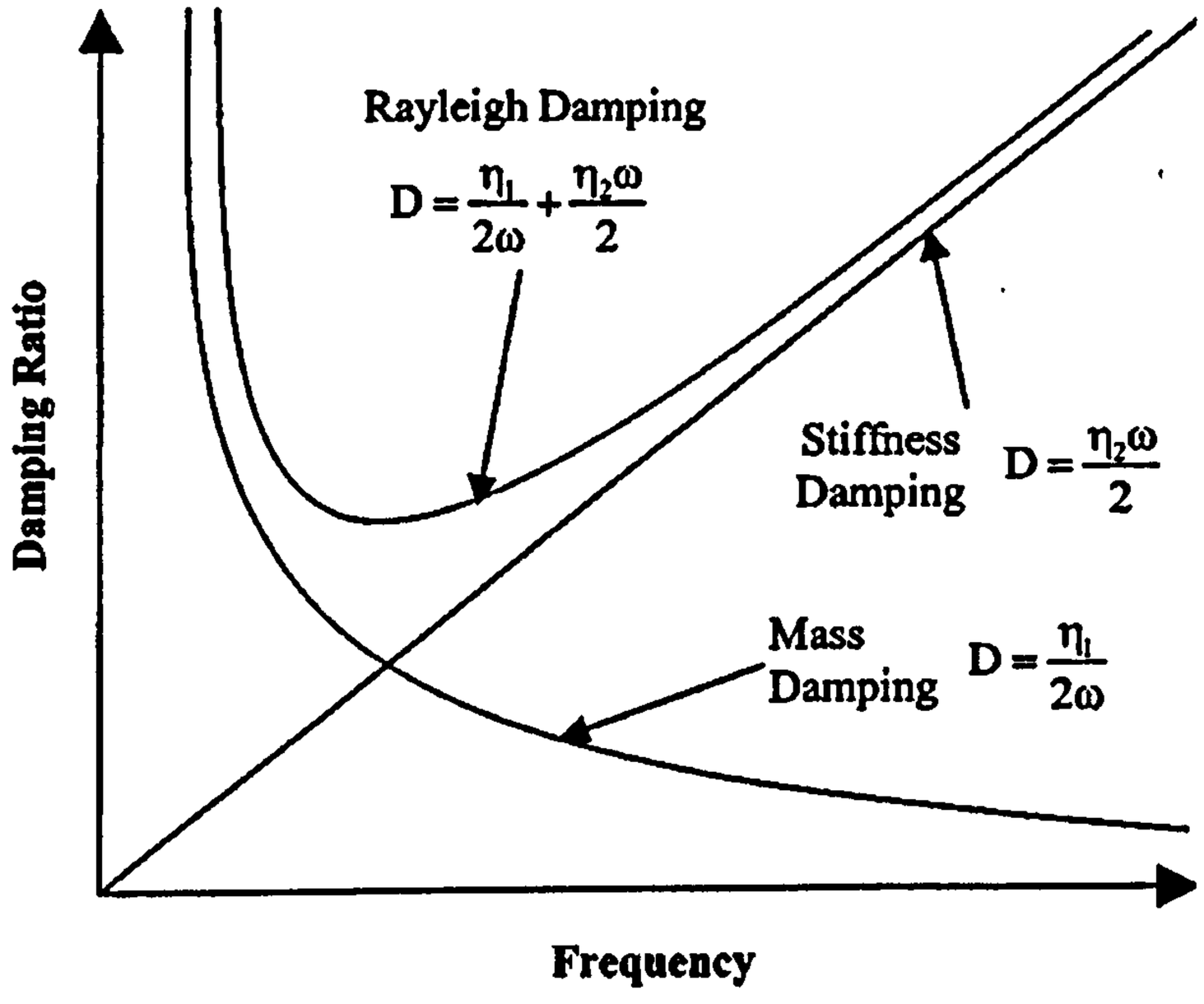

Figure 3.12. Relationship between Rayleigh damping parameters and damping ratio (Zerwer *et al.*, 2002)

Damping ratio is theoretically defined in Chapter 4 (Equation 4.6). The damping ratio can be found from the hystersis loop using the following relationship (Kramer, 1996):

$$D = \frac{A_{Loop}}{4\pi A_s} \tag{3.14}$$

in which A_{Loop} is an area inside the loop representing dissipated energy and A_s is the area representing maximum strain energy, as shown in Figure (3.13).

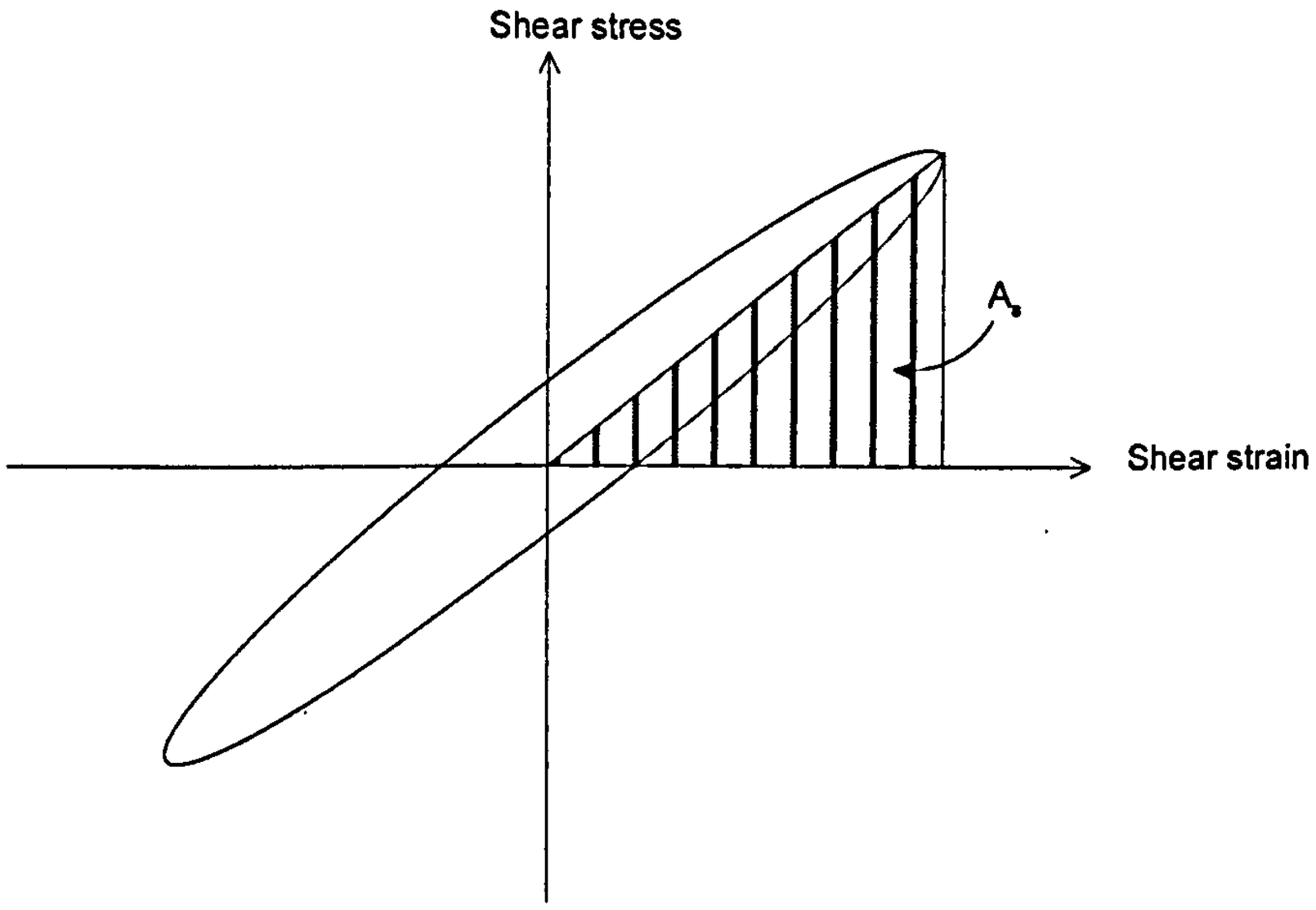

Figure 3.13. Schematic representation of a hysteretic loop

Damping ratio is affected by several factors. At low strain, theoretically no hystertic dissipation of energy takes place. However experimental evidence shows some energy dissipation, although the mechanism is not well understood. At higher strains, the breadth of the hystersis loop (exhibited by a cyclically loaded soil) increases with cyclic strain amplitude (Kramer, 1996). It indicates that the damping ratio increases with increasing strain amplitude. The damping ratio is also influenced by the soil plasticity. Damping ratios of highly plastic soils are lower than those of low plasticity soils at similar cyclic strain amplitudes (Dobry and Vucetic, 1987; Vucetic and Dobry, 1991; Kokushu *et al.*, 1992; Kramer, 1996). Damping behaviour is also affected by confining pressure, particularly for soils of low plasticity. Ishibashi and Zang (1993) developed the following empirical relationship for the damping ratio of plastic and non-plastic soils.

$$D = 0.333\frac{1+\exp(-0.0145PI^{1.3})}{2}[0.586(\frac{G}{G_{max}})^2 - 1.547\frac{G}{G_{max}} + 1] \qquad (3.15)$$

The shear modulus ratio ($\frac{G}{G_{max}}$) depends on the cyclic shear strain, confining pressure and the soil plasticity according to Equation (5.28).

3.3.4 Time Integration

The dynamic equation of the system is represented below:

$$[M]\{\ddot{u}\}+[K]\{\dot{u}\}+[C]\{u\}=\{F_{ext}\} \tag{3.16}$$

where $\{\ddot{u}\}$, $\{\dot{u}\}$and $\{u\}$ are acceleration, velocity and displacement vectors respectively. $\{F_{ext}\}$ is the external load vector. This equation can be solved in either frequency or time domains. To solve the equation in frequency domain, it needs to be initially transformed into the frequency domain and then the solution inversely transformed into the time domain. If the frequency domain technique is adopted, only a linear system can be treated, and also track response is assumed to be stationary. It implies that the singular events along the track, such as isolated irregularities and stiffness transitions, cannot be addressed. On this basis the dynamic equation of the railway track is solved in the time domain in the persent study .

As explicit time integration methods are adopted in this study, no equation is needed to be solved at every time step and the integration may be performed more efficiently when compared to implicit methods. Since the mass is lumped, inversion of the mass matrix can be done at very cheap computational cost. In the present research two different explicit integration schemes are implemented namely classical explicit and modified explicit schemes (Zhai, 1996). The classical explicit scheme is summarised as below (Smith and Griffith, 1997):

$$\{u\}^{t+1} = \{u\}^{t} + \Delta t\{\dot{u}\}^{t} + 0.5\Delta t^{2}\{\ddot{u}\}^{t} \tag{3.17}$$

$$\{\ddot{u}\}^{t+1} = [M]^{-1}(\{F_{ext}\}^{t+1} - [C]\{\dot{u}\}^{t} - [K]\{u\}^{t+1}) \tag{3.18}$$

$$\{\dot{u}\}^{t+1} = \{\dot{u}\}^{t} + 0.5(\{\ddot{u}\}^{t} + \{\ddot{u}\}^{t+1})\Delta t \tag{3.19}$$

Zhai (1996) proposed an explicit scheme with a higher accuracy when compared with the classical explicit scheme as given below:

$$\{u\}^{t+1} = \{u\}^t + \Delta t\{\dot{u}\}^t + (0.5+\psi)\Delta t^2\{\ddot{u}\}^t - \psi\Delta t^2\{\ddot{u}\}^{t-1} \tag{3.20}$$

$$\{\dot{u}\}^{t+1} = \{\dot{u}\}^t + (1+\varphi)\Delta t\{\ddot{u}\}^t - \varphi\Delta t\{\ddot{u}\}^{t-1} \tag{3.21}$$

$$\{\ddot{u}\}^{t+1} = [M]^{-1}(\{F_{ext}\}^{t+1} - [C]\dot{u}^{t+1} - [K]\{u\}^{t+1}) \tag{3.22}$$

ψ and φ are free parameters that control stability and numerical dissipation of the algorithm. To start the integration procedure, it is considered that $\varphi = \psi = 0$ at the first time step. In subsequent steps, $\varphi = \psi = 0.5$ is considered, which eliminates numerical dissipation (Zhai, 1996).

The dynamic response of a plain-stain cantilever beam to a cyclic concentrated load is modelled using both explicit schemes, and is compared against an implicit solution given by Smith and Griffith (1997). Smith and Griffith (1997) used Newmark implicit integration with a time increment of 0.05 s (see Smith and Griffith (1997) for the Newmark parameters used in the simulation). The beam is a cantilever (fixed at one end) which is discretised by brick elements. As can be seen in Figure (3.14), both integration schemes give a reasonable response which is favourably comparable to the given solution, with the Zhai modified scheme performing slightly better. As will also be shown in Chapter 6 for a track-train interaction example, it can be judged that Zhai's method is more accurate, particularly if the time step chosen is large. In this research a time increment of 15E-6 is considered unless otherwise stated.

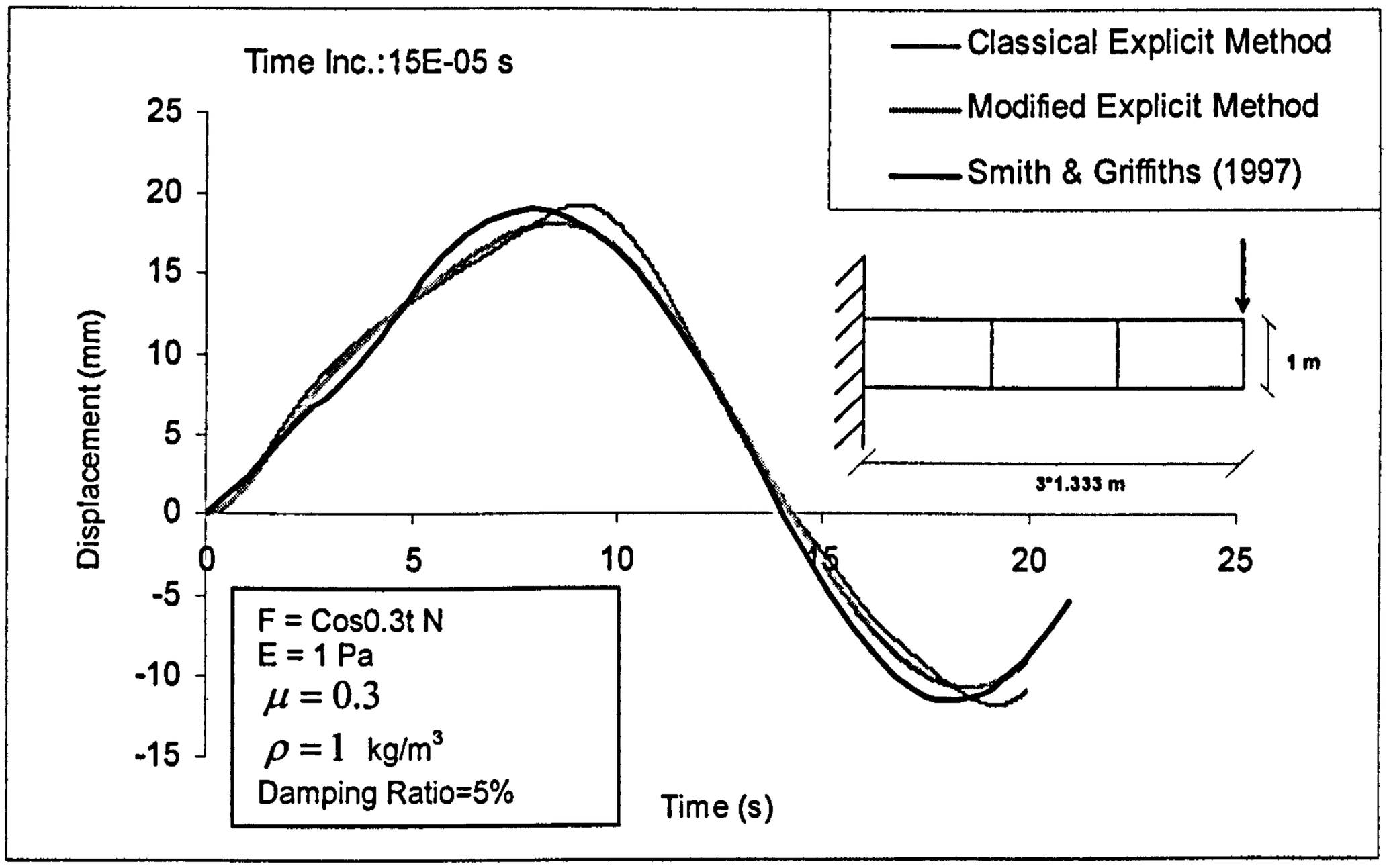

Figure 3.14. Performance of two explicit schemes for a beam problem compared to an implicit scheme

3.3.5 Model Performance

Figure (3.15) depicts a typical displacement under a sleeper when a train coach (with an axle load of 17.4 T) passes over a sleeper (ES=15 MPa, EB=120 MPa, BD=300 mm, V=30 m/s, ES, EB, BD and V stands for elasticity modulus of subgrade, elasticity modulus of ballast, ballast depth and train speed respectively). As can clearly be seen in this case, every wheel has its own footprint. Moreover, the affected area is larger than the coach length, which is related to the flexural stiffness of rail and also the elasticity of the substructure, as assumed here. The slight asymmetry seen in the response may come partly from the side viscous boundary effects. When the load is close to the boundary, some artificial displacement can be generated, since a viscous boundary cannot take any static load (the boundary provides no stiffness); such effect is minimized as the load moves further from the boundaries. After an initial investigation, it was judged that the boundary effect is not significant for the purpose of this research.

As a train passes over track it excites different frequencies, depending on the configuration of the train and track. The FFT analysis of the displacement trace (Figure 3.16) clearly represents the forced frequencies related to the wheel, bogie distances and also the extent of the affected area, as illustrated in Figures (3.15) and (3.16).

Woodward *et al.* (2004) reported the rail track displacement measured at Points 215D near Blechley Station on the West Coast Mainline, UK, under a high speed train (HST) at a speed of 110 mph. The comparison between displacement predicted by the developed model and the measurement is shown in Figure (3.17). The soil parameters are chosen based on the site investigation data available (Woodward *et al.*, 2004). According to this Figure, one can say that the model has satisfactorily simulated the displacement field under the HST train as favourable agreement between simulated and measured displacement trace is observed. It is again seen that every wheel has its own footprint, and the locomotive wheels with higher axle loads (left hand side of the Figure) experience higher displacement when compared with the coach wheels with lower axle loads.

The stress levels under the sleepers, caused by the passage of a train coach, are also simulated reasonably well, as shown in Figure (3.18). See Woodward *et al.* (2004, 2005) for more details on the track and site specifications.

3.4 Conclusion

In this chapter, available track models in the literature were discussed. A new three-dimensional track model was proposed, incorporating a multi-layered ground system, non-reflecting boundary conditions and soil material damping. The model specification was presented in detail, and it was shown that it can simulate a typical track response reasonably well. This chapter gave the basic background to the numerical simulation of a railway track. Detailed investigations of the model performance will be given in the following chapters. In addition, the model will be further developed in Chapters 5 and 6 to account for nonlinearity in the constitutive behaviour of the substructure (ballast and subgrade) and the train-track interaction respectively.

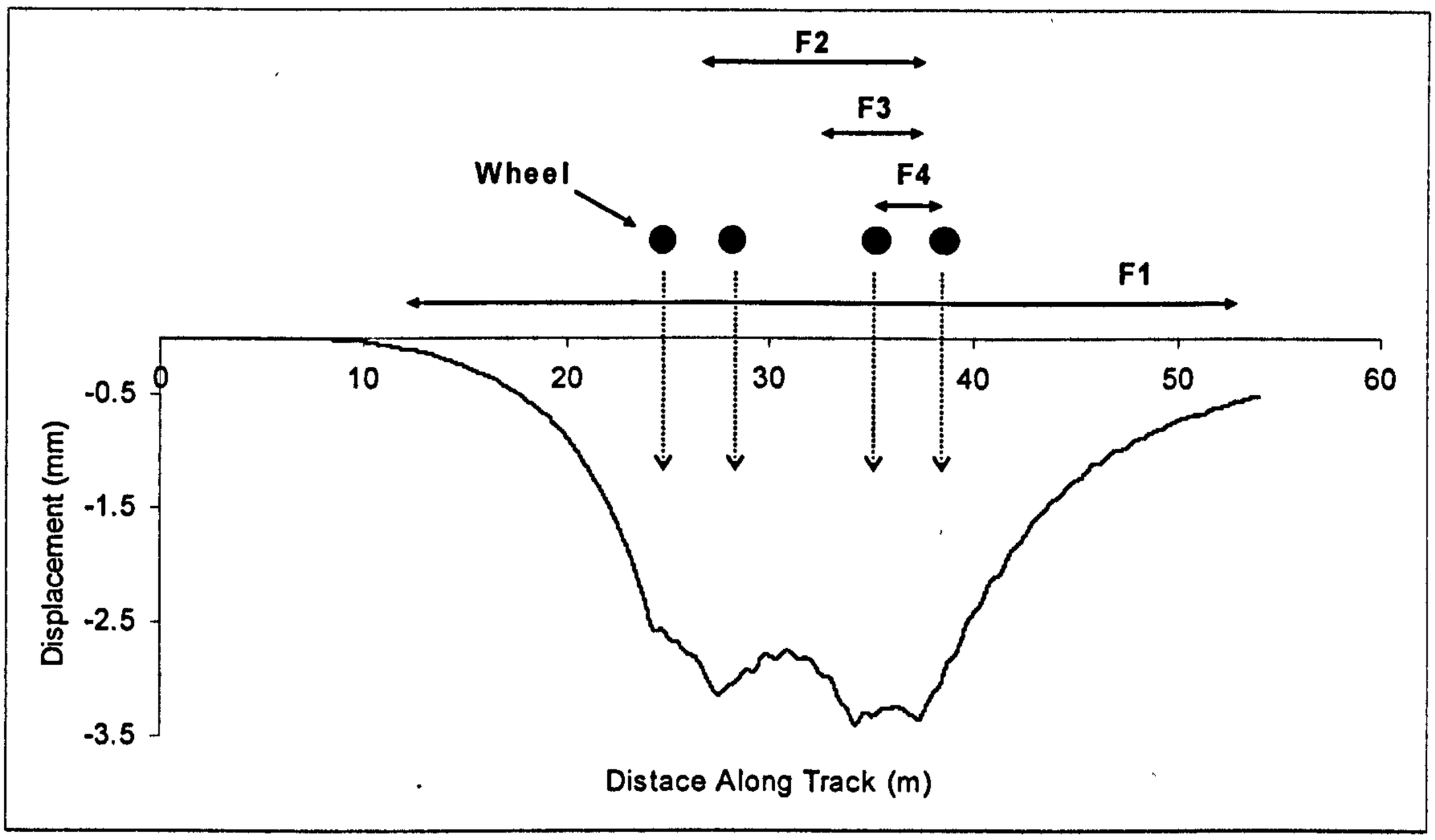

Figure 3.15. Typical sleeper displacement under a train coach (ES=15 MPa, EB=120 MPa, BD=300 mm, V=30 m/s)

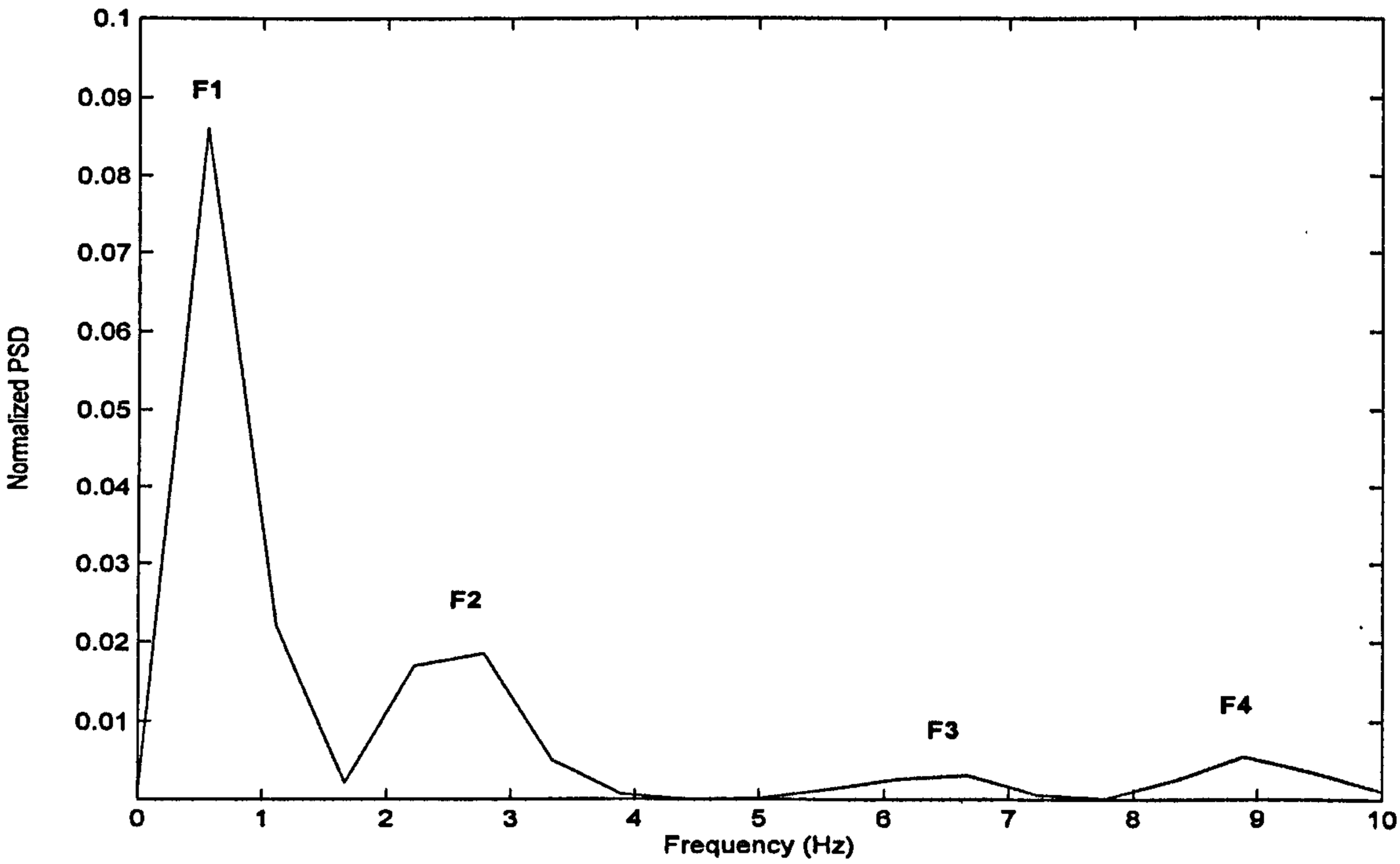

Figure 3.16. Frequency content of a sleeper displacement under the passage of a train coach (ES=15 MPa, EB=120 MPa, BD=300 mm, V=30 m/s)

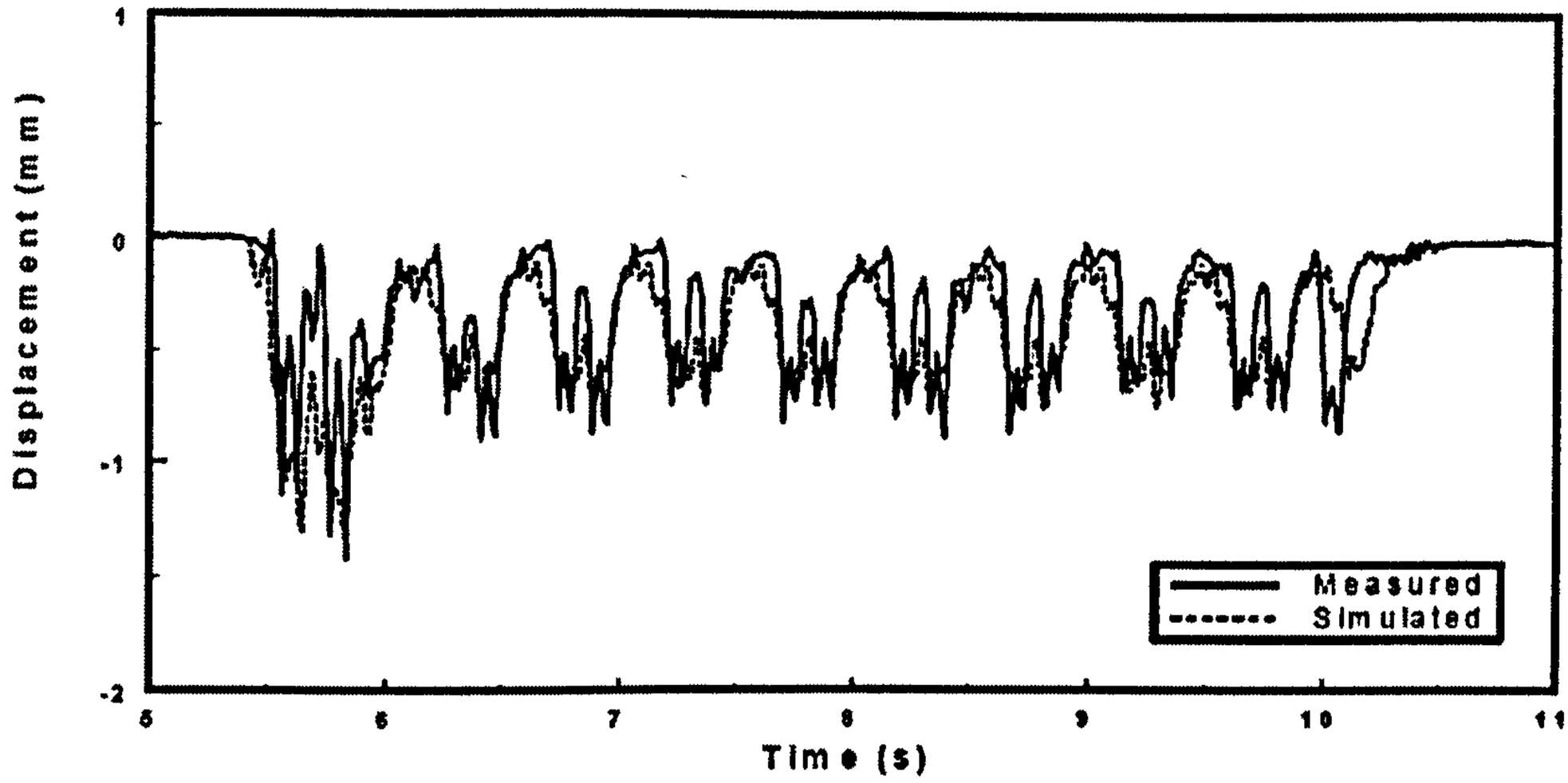

Figure 3.17. Comparison of the simulated and measured displacement under an HST train, West Coast Mainline, Bletchley station (Woodward *et al.*, 2005)

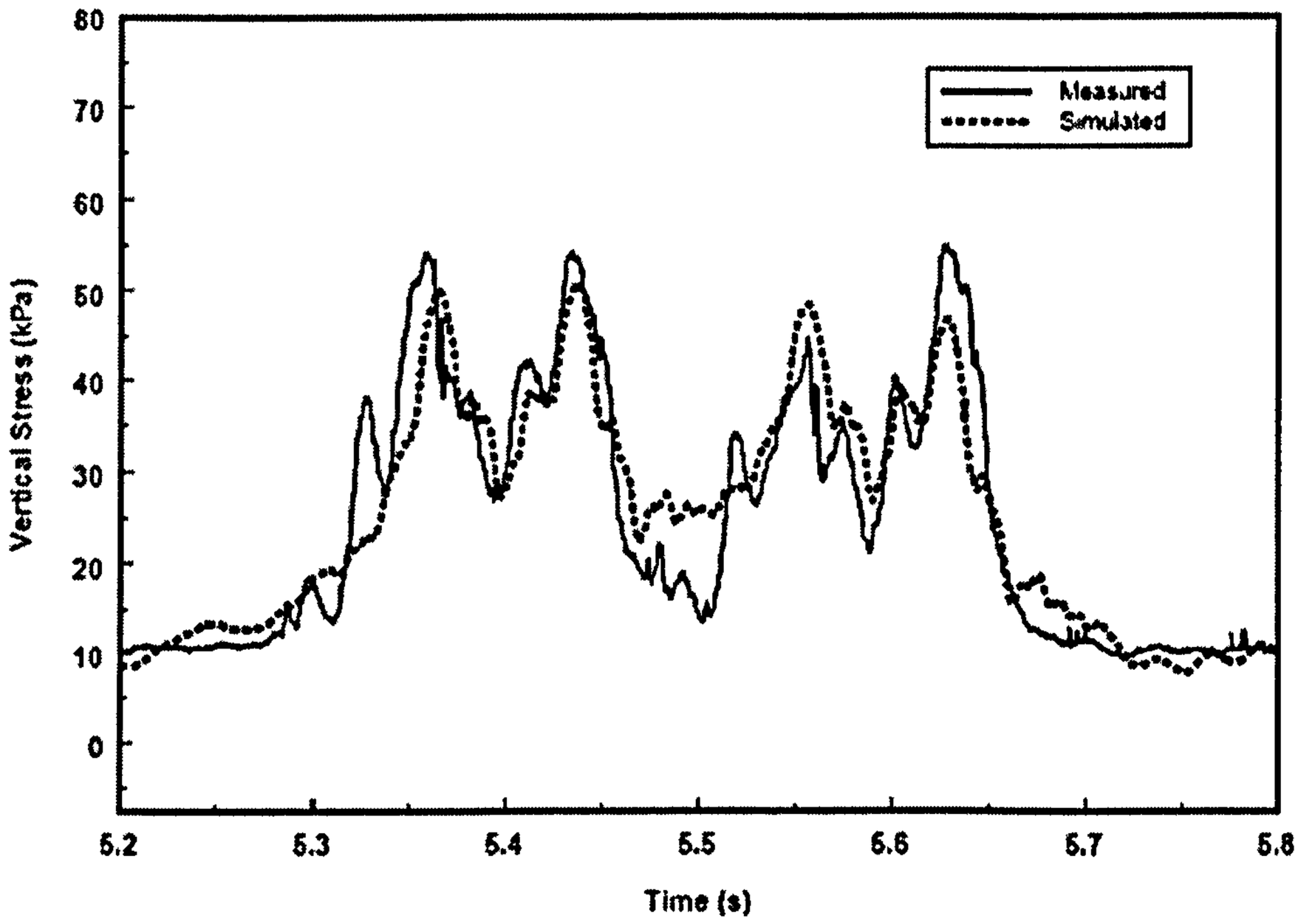

Figure 3.18. Comparison of the measured and simulated vertical stress for a single coach over a transition near a timber deck bridge (Woodward *et al*, 2005)

CHAPTER 4

TRAIN SPEED EFFECT

4.1 Introduction

It is well known that as the train speed approaches a threshold value, namely the track critical velocity, track deflections increase considerably, leading to the need for frequent maintenance and the possibility of train derailment in the worst cases. In this chapter, different types of models for the investigation of the train speed effect on the track response are discussed. The effects of train speed on railway track response are studied numerically for a multi-layered ground track system using the developed three-dimensional dynamic finite element model. The effects of differing subgrade stiffness, ballast depth and stiffness are addressed, and the track maintenance level is related to the stress level in subgrade, and the stress & vibration in the ballast layer. Track design methods are also reviewed and a design method based on the dynamic finite element analysis is proposed which aims at protecting the subgrade from deterioration and decreasing the level of ballast maintenance.

It should be noted here that the wave propagation mechanism being discussed in this chapter is solely related to the train speed effect. Other mechanisms of wave propagation and track ground vibration, which were summarized in Chapter 2, are not the subject of this chapter.

4.2 "Beam-Spring" Models

The railway track system has often been modelled as a beam lying on elastic foundations. The foundation is usually modelled as a series of springs and dampers. The train load has been usually modelled as a constant load or an oscillating load, depending on the complexity of the model. The analyses of railway track systems using beam models have attracted much interest since 1950. Kenney (1954) was among the first researchers to present an analytical solution for beams on elastic foundations under a moving load. He considered the damping effects and presented a relationship of critical velocity for the beam–foundation system. Since the analytical solution gives a useful insight into the fundamentals of speed effects on railway track behaviour, it is discussed in detail in this section.

The differential equation for the beam lying on a Winkler foundation can be expressed as follows:

$$EI\frac{\partial^4 w}{\partial x^4}+kw+c\frac{\partial w}{\partial t}+\rho\frac{\partial^2 w}{\partial t^2}=P(x,t) \tag{4.1}$$

where E and I are the elasticity and moment of inertia of the beam. w is the beam deflection at a distance along beam, x, and time t. $P(x,t)$ is the applied load and k is the modulus of the foundation. c is the damping of the foundation. ρ is the mass per unit length of the beam.

Assuming P and w are not time dependent and no damping is present, Timoshenko (1926) presented a static solution of Equation (4.1), namely the displacement at a distance of x_v from the loading point under a concentrated static load, P (See Equation 2.2). This static solution may be used to estimate the displacement of the rail under the moving load, but it has serious limitations, especially at higher speeds, since it does not take into account the inertia effect. A coordination system moving with load ($x_v = x - Vt$) can be defined to facilitate using Equation (4.1) for a moving load with a constant load speed of V. For a

beam on an elastic foundation under a moving load, the governing equation can therefore take the following form:

$$EI\frac{\partial^4 w}{\partial x_v^{\,4}} + kw + cV\frac{\partial w}{\partial x_v} + \rho V^2\frac{\partial^2 w}{\partial x_v^{\,2}} = P(x_v)\delta(x_v) \tag{4.2}$$

δ is kronker delta. This differential equation was solved by Kenney (1954) and presented in the following forms:

$$x_v < 0 \tag{4.3}$$

$$w = \frac{PL}{2k}\left[\frac{\eta\exp(\eta L x_v)}{\eta^4 + (\eta\theta)^2 + \frac{1}{2}(\frac{\theta\beta}{\eta})^2}\right]\left\{\begin{array}{l}\dfrac{-(\frac{\theta\beta}{\eta}+\eta^2)\sin((2\theta^2+\eta^2-2\theta\beta/\eta)^{0.5}Lx_v}{\eta(2\theta^2+\eta^2-\frac{2\theta\beta}{\eta})^{0.5}} \\ +\cos((2\theta^2+\eta^2-\frac{2\theta\beta}{\eta})^{0.5}Lx_v)\end{array}\right\}$$

$$x_v > 0 \tag{4.4}$$

$$w = \frac{PL}{2k}\left[\frac{\eta\exp(-\eta L x_v)}{\eta^4 + (\eta\theta)^2 + \frac{1}{2}(\frac{\theta\beta}{\eta})^2}\right]\left\{\begin{array}{l}\dfrac{-(\frac{\theta\beta}{\eta}+\eta^2)\sin((2\theta^2+\eta^2+2\theta\beta/\eta)^{0.5}Lx_v}{\eta(2\theta^2+\eta^2+\frac{2\theta\beta}{\eta})^{0.5}} \\ +\cos((2\theta^2+\eta^2+\frac{2\theta\beta}{\eta})^{0.5}Lx_v)\end{array}\right\}$$

where η is the positive real root of the following equation,

$$\eta^6 + 2\theta^2\eta^4 + (\theta^4 - 1)\eta^2 - \theta^2\beta^2 = 0 \tag{4.5}$$

L is the effective length which was defined in Equation (2.3). β is the damping ratio:

$$\beta = \frac{c}{c_{cr}} \tag{4.6}$$

and θ is the velocity ratio:

$$\theta = \frac{V}{V_{cr}} \tag{4.7}$$

The critical velocity (V_{cr}) is defined as:

$$V_{cr} = \sqrt[4]{(\frac{4kEI}{\rho^2})} \tag{4.8}$$

Critical velocity is the lowest velocity at which a free wave might propagate as defined by Kenney (1954).

Like the simple mass-spring system critical damping is defined as

$$c_{cr} = 2(k\rho)^{0.5} \tag{4.9}$$

Kenney (1954) demonstrated that the general solution given by Equations (4.3) and (4.4) does not contain the solution for β larger than a critical damping ratio (β_{cr}), for $x_v < 0$. In this case the solution is as follows:

$x_v < 0$ & $\beta > \beta_{cr}$

$$w = \frac{PL}{2k}\left[\frac{\eta \exp(\eta L x_v)}{\eta^4 + (\eta\theta)^2 + \frac{1}{2}(\frac{\theta\beta}{\eta})^2}\right]\left\{\begin{array}{l} \dfrac{-(\frac{\theta\beta}{\eta} + \eta^2)\sinh((\left|2\theta^2 + \eta^2 - 2\theta\beta/\eta\right|)^{0.5} L x_v)}{\eta(\left|2\theta^2 + \eta^2 - \frac{2\theta\beta}{\eta}\right|)^{0.5}} \\ + \cosh((\left|2\theta^2 + \eta^2 - \frac{2\theta\beta}{\eta}\right|)^{0.5} L x_v) \end{array}\right\} \tag{4.10}$$

where β_{cr} equals

$$\beta_{cr} = \frac{1}{3}\left\{2\left[\frac{1+(1+\frac{3}{\theta^4})^{0.5}}{2}\right]^{0.5} + \frac{1}{\left[\frac{1+(1+\frac{3}{\theta^4})^{0.5}}{2}\right]^{0.5}}\right\} \tag{4.11}$$

For the specific case of no damping, the solution takes the following explicit forms:

$x_v < 0 \quad \& \quad \theta < 1$

$$w = \frac{p}{2kL\alpha}.\exp(\frac{\alpha}{L}x_v).\left[\frac{-\alpha}{\beta}\sin(\frac{\varphi}{L}x_v) + \cos(\frac{\varphi}{L}x_v)\right] \tag{4.12}$$

$x_v > 0 \quad \& \quad \theta < 1$

$$w = \frac{p}{2kL\alpha}.\exp(\frac{-\varphi}{L}x_v).\left[\frac{\alpha}{\varphi}\sin(\frac{\varphi}{L}x_v) + \cos(\frac{\varphi}{L}x_v)\right] \tag{4.13}$$

$x_v < 0 \quad \& \quad \theta > 1$

$$w = \frac{p}{2kL}.\left[\frac{-2\sin(\frac{\varphi-\gamma}{L}x_v)}{\eta(\varphi-\gamma)}\right] \tag{4.14}$$

$x_v > 0 \quad \& \quad \theta > 1$

$$w = \frac{p}{2kL}.\left[\frac{-2\sin(\frac{\varphi+\gamma}{L}x_v)}{\eta(\varphi+\gamma)}\right] \tag{4.15}$$

where $\alpha = [1-(\theta)^2]^{0.5}$, $\varphi = [1+(\theta)^2]^{0.5}$ and $\gamma = [(\theta)^2 - 1]^{0.5}$.

The ratio of maximum deflection to static deflection is depicted against the velocity ratio in Figure (4.1). It is clearly seen that, as the train speed approaches the critical velocity (V_{cr}), track displacement increases dramatically without bound in the undamped case, as can be expected theoretically at the point of resonance. The inclusion of damping limits the response amplitude at the point of resonance ($V = V_{cr}$). For a lightly damped system, the beam deflection is sufficiently similar to undamped ones in the vicinity of critical velocity. However, the difference between the damped and undamped responses becomes greater with increasing damping ratio. As shown in Figure (4.2), the wave in the beam starts to propagate when the load velocity exceeds the critical velocity of the beam-spring-damper system with a different frequency & wave length ahead and behind the moving load.

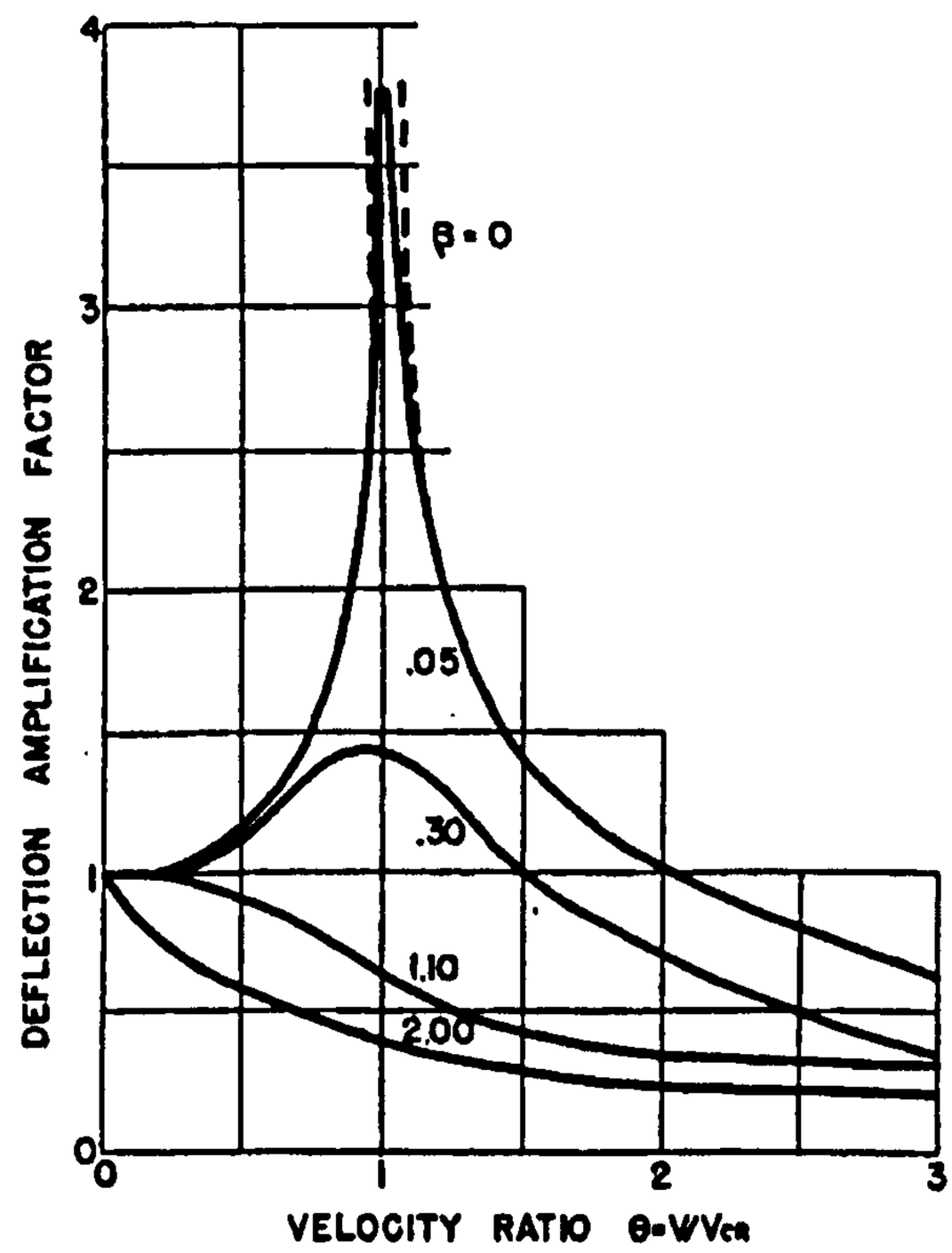

Figure 4.1. Maximum deflection versus load speed (Kenney, 1954)

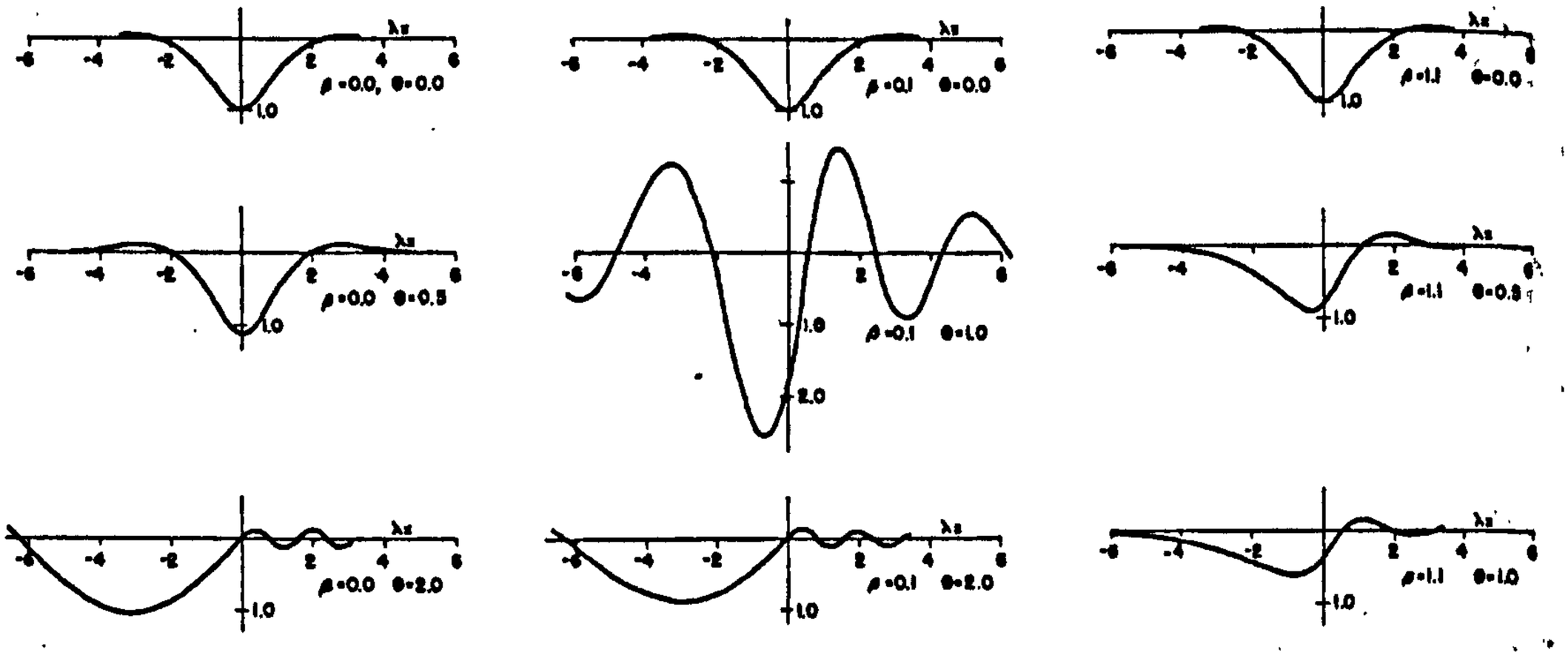

Figure 4.2. Beam displacement for different loading speeds and support damping (Kenney, 1954)

Fryba (1999) used Fourier integral transformation to solve a similar beam-spring-damper problem while considering the different range of speeds and values of viscous damping. A critical velocity was identified at which the response of the undamped beam goes to infinity. For load speeds lower than the critical velocity, it was found that the largest displacement occurs near the point of loading, while for load speeds higher than the critical velocity, the waves moving ahead of the load are significantly smaller in amplitude and wave length than those behind the load. These observations also confirmed the presence of a critical velocity, as pointed out by Kenney (1954). These types of models, solved analytically or numerically, have been extensively used for decades to study the dynamic behaviour of railway tracks. They have, however, several drawbacks. They do not consider the continuity of soil medium, so they do not capture the propagation of three dimensional stress waves in the soil properly. They do not take into account the inertia of the sleeper, ballast and ground layers. Moreover assuming a continuous support, as in Kenny's model, the discrete nature of the sleeper support to the rail is not addressed and consequently the pin-to-pin frequency cannot be captured.

In the framework of the "beam-spring type" model, attempts have been made to address these limitations. To include the pin-to-pin frequency, the continuous beam should be supported at discrete points on the sleepers. Moreover, the masses of the sleeper and ballast and subgrade should be added as lumped rigid masses to take into account their

effects in low frequency ground vibrations. The masses can also be interconnected using shear spring and dampers to mimic the continuity of the soil medium and facilitate the wave propagation in the ground system.

Malik *et al.* (2006) studied the steady-state response of a beam placed on a Pasternak foundation (with two parameters, i.e. spring constant and shear parameter), and presented the following relationship for critical velocity:

$$V_{cr} = \left[\frac{\sqrt{4EIk} + k_1}{\rho} \right]^{0.5} \tag{4.16}$$

where k and k_1 are the spring constant (N/m^2) and the shear constant (N). It was observed that the point of maximum deflection shifts behind the load with increasing speed and damping. The increase in asymmetry of the response with damping and load speed was also confirmed by Sun (2002). Zhai *et al.* (2004) considered the masses of the ballast & sleeper, shear damping and stiffness of ballast, as shown in Figure (4.3). Favourable agreement between the measurements and simulations was reported and the necessity of considering shear coupling in the ballast was emphasized.

Jones and Block (1996) took into account the ground, embankment and ballast stiffness separately (Figure 4.4) and simulated the ground vibration emitted from heavy freight trains. It was shown that the model prediction is in good agreement with experimental observations in the frequency range of 5-30 Hz. It was also found that vibrations, with frequencies lower than 5 Hz, depend mainly on the embankment stiffness parameters.

4.3 "Beam on Continuum Medium" Models

It can be said that the 1990s marked the origin of intensive investigations of 2D/3D models for railway track. The principle reason for developing such models has been the rapid

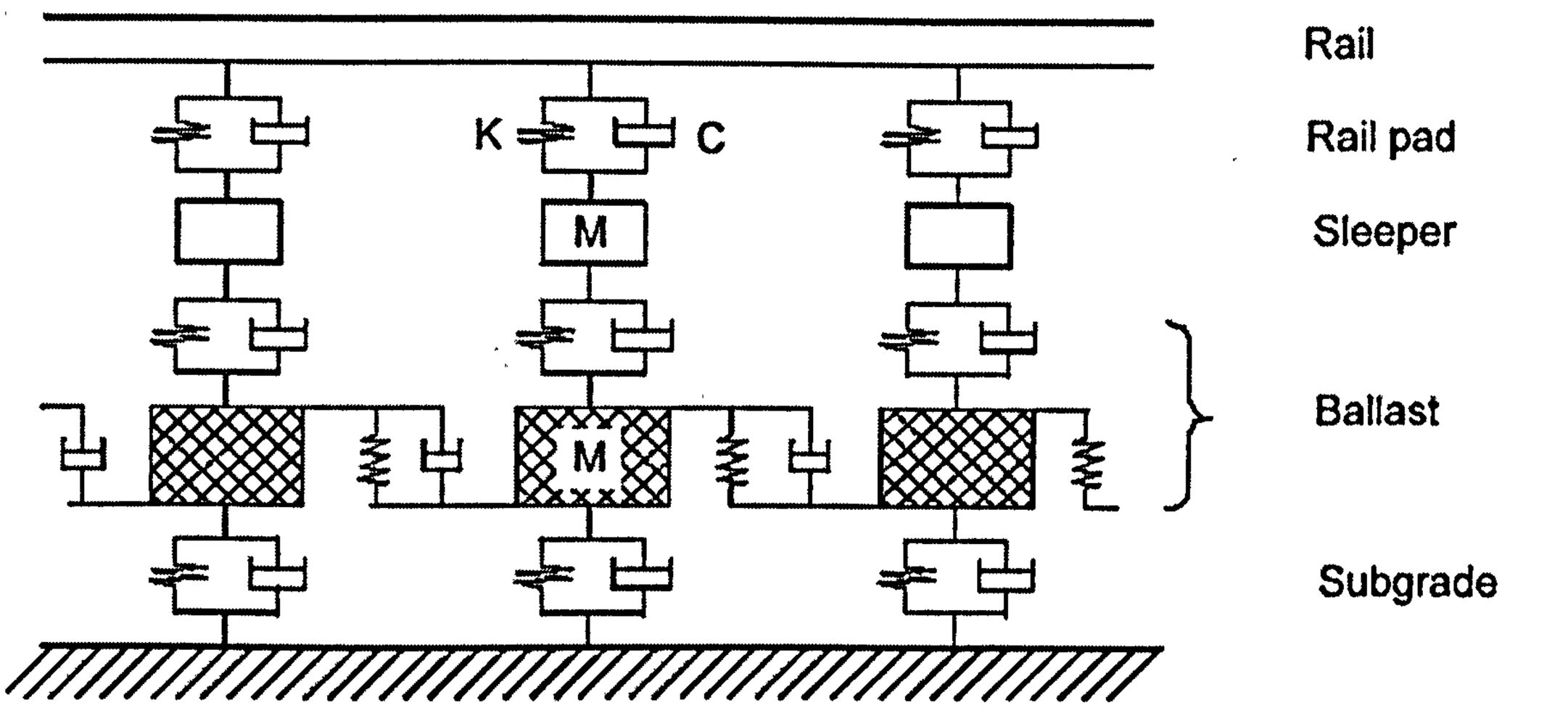

Figure 4.3. A track model taking into account mass and stiffness of ballast and sleeper (Zhai *et al.*, 2004)

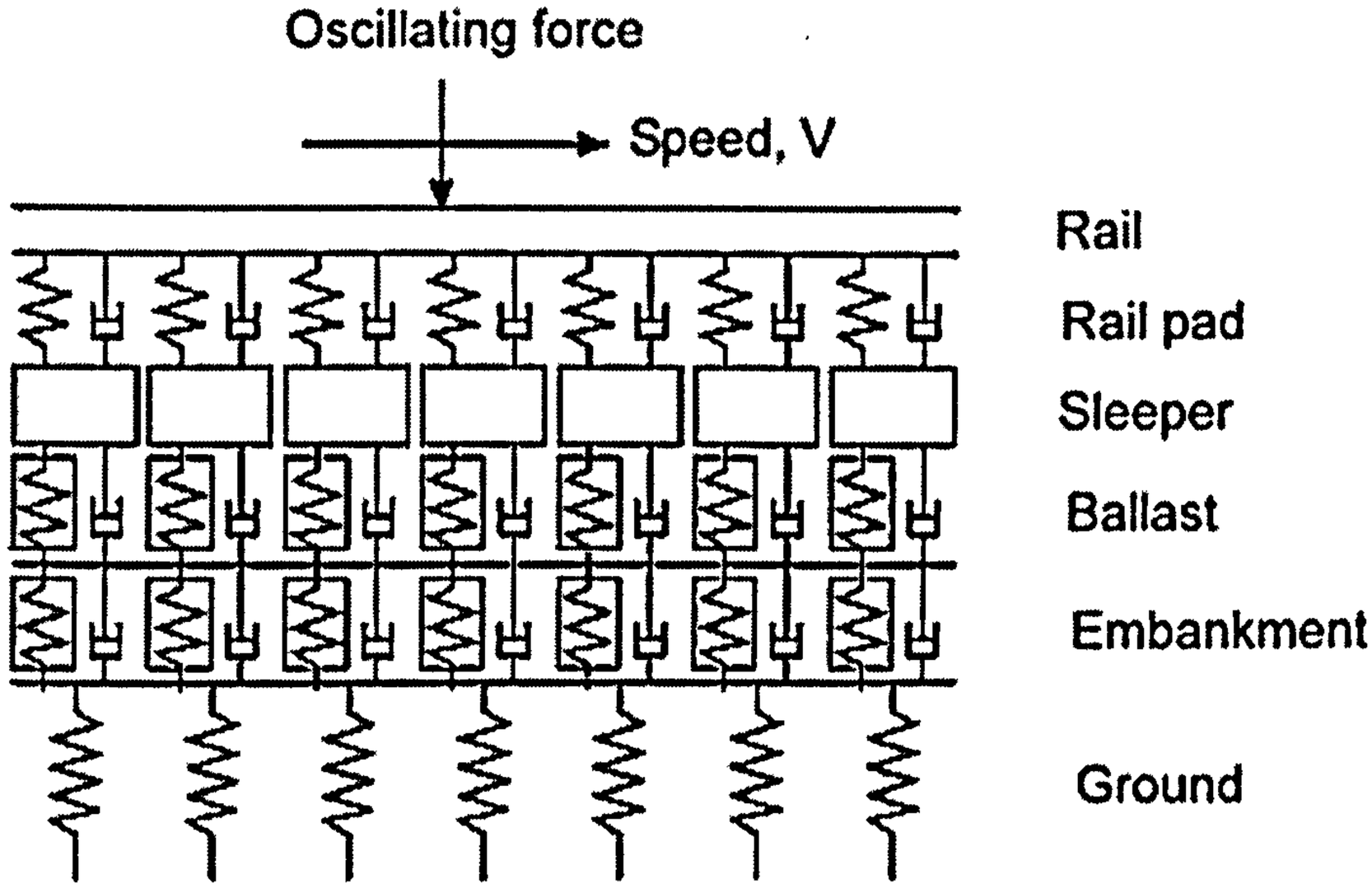

Figure 4.4. A track model taking into account mass and stiffness of ballast and sleeper and embankment (Jones and Block, 1996)

introduction of high-speed trains and the inapplicability of the simple beam-spring-damper models in high train speed simulations. A considerable effort has been devoted to deriving analytical/semi-analytical and numerical solutions for beams on elastic half-space problems (e.g. Dieterman and Metrikine, 1997; Kaynia *et al.*, 2000; Paolucci and Spinelli, 2006). Picoux *et al.* (2003) introduced a semi-analytical wave propagation model subjected to a set of harmonic moving loadings. Sub-critical ($V<V_{cr}$) and super-critical ($V>V_{cr}$) regimes were studied. The increase of displacement with load speed was shown and it was indicated that in a super-critical regime the displacement behind the load is greater; oscillating mach cone shape waves are also seen to propagate behind the load in the super-critical regime when the load speed is higher than the ground Rayleigh wave velocity (Figure 4.5). The presence of mach cone type wave propagation beneath the load in a super-critical regime has also been shown by Ju and Lin (2004) employing three dimensional finite element models to study beams on a homogonous elastic foundation under moving loads.

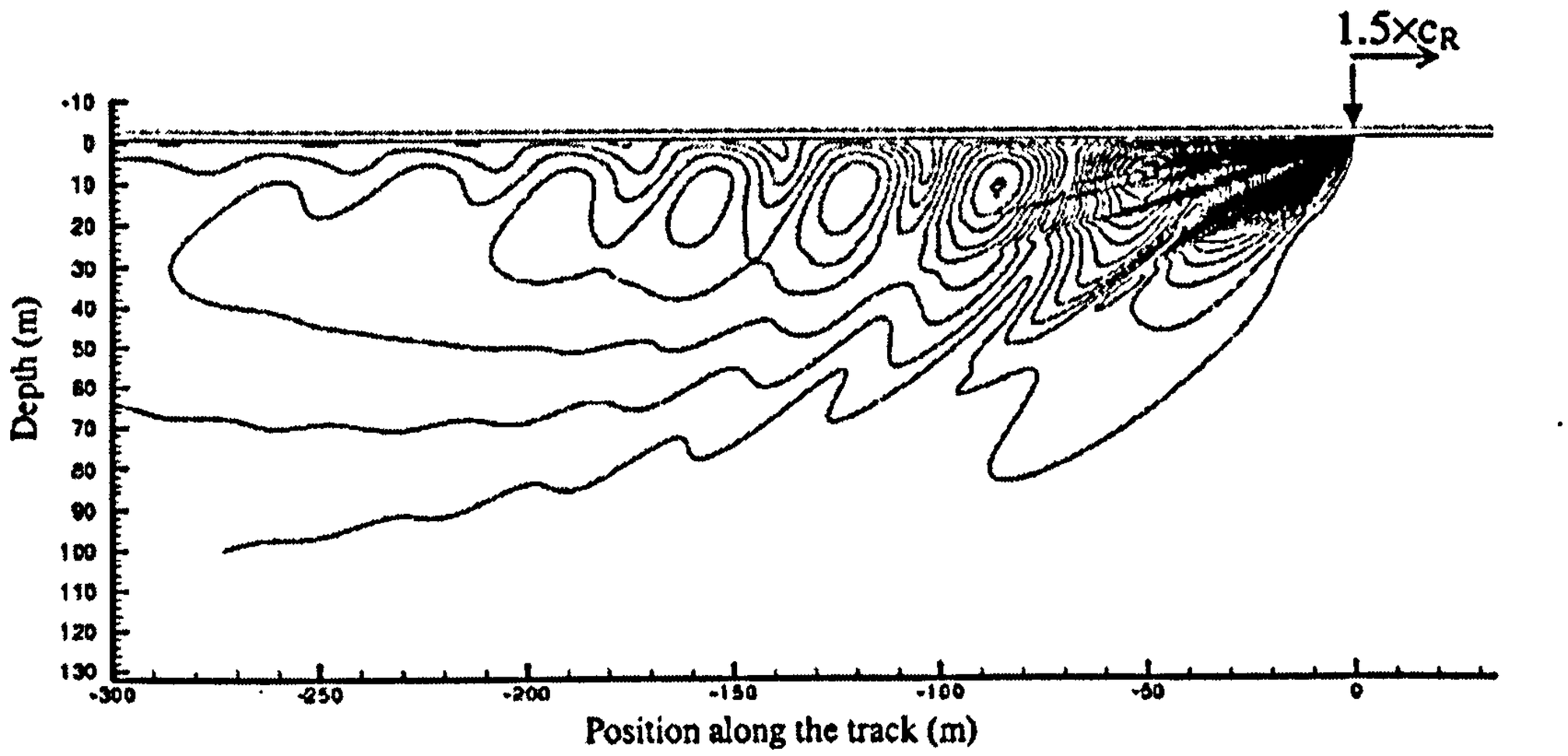

Figure 4.5. Contours of displacements against depth in super-Rayleigh regime (Picoux *et al.*, 2003)

Considering an elastic half space loaded by a set of concentrated loads with a constant speed, Krylov *et al.* (2000) pointed out that there are two main critical velocities, namely the Rayleigh surface wave in the ground and the speed of the lowest phase-wave in the beam. If the train speed exceeds the Rayleigh surface wave velocity, then a boom

associated with a very large increase in generated ground vibrations occurs. If the speed increases further and approaches the second critical velocity, very large rail deflections are theoretically predicted with their associated derailment risks.

Suiker and De Borst (1999) studied the response of two-dimensional stratified half spaces consisting of a granular layer resting on elastic subgrade under a moving harmonically varying load. They showed that, for (thin) soft granular layers resting on a stiff substratum the lowest critical state partly depends on excitation sources such as the sleeper distance. For a typical configuration (i.e. stiff ballast layer on soft subgrade) the lowest critical state is determined by the load speed only. The load speed was shown to become critical when it equals the Rayleigh wave velocity of subgrade.

Suiker (2002) studied Timoshenko's beam response under harmonic moving loads, which had been placed on an elastic half space, and observed several critical velocities. In this study, the beam represented a combination of rail, ballast and embankment. While the critical velocity values were slightly dependent on interaction effects between the beam and half space, they were all centred about the Rayleigh wave velocity of the ground (Equation 2.17). As discussed by Suiker (2002), it should be noted that since the "beam spring" model cannot represent transmission of waves in the ground, it could underestimate the dynamic speed effect by predicting an artificially high track critical velocity. In practice, the lowest critical velocity is only of interest in defining the speed limit at which the train can travel. This velocity is hereby termed "Track Critical Velocity".

4.4 Experimental Evidences of Train Speed Effect

As early as 1938, De Nie (cited from Woldrigth and New, 1999) observed dynamic deflection increases caused by speed effects in combination with poor geotechnical subgrade conditions. The dependency of track vibration on train speed was also reported by Hunt (1994), Madshus and Kaynia (2000) and Kaynia *et al.*(2000).

In the UK, at a railway track south of Peterborough over Stilton Fen, rail deflection measurements were carried out for trains running at different speeds (Hunt, 1994). A significant increase in track deflection was observed with increasing speed; it reached 12 mm, around three times the static track deflection, when the train speed approached 185 km/h. The presence of a deep soft subgrade was considered to be responsible for dynamic amplification of the track response at higher train speeds. Madshus and Kaynia (2000) and Kaynia *et al.*(2000) presented a well-documented case in Sweden. The Swedish national rail administration opened a service with the X-2000 high speed train between Götenberg and Malmö early in 1997. Shortly after starting the service, excessive vibrations of the railway embankment, surrounding soil and over-head power lines in Ledsgård were detected. Extensive site investigation and measurements were conducted. At train speeds of about 45 mph the displacement had a quasi-static pattern and was mainly symmetrical and essentially identical to the displacement measured at lower speed. As the train speed increased towards the track critical velocity, the response completely changed character; at a train speed of 115 mph the displacement amplitude drastically increased and the displacement pattern became asymmetrical with a tail of free oscillations following the train. Site investigations revealed the presence of soft clay and consequently low Rayleigh wave velocity of the track system resulting in a low track critical velocity of the site.

A study of the track response in Ledsgård (among other sites) reveals that below a certain train speed, no wave was essentially propagated (displacement field moving with train was similar to the static displacement field under the train self-weight). As soon as this speed limit was passed, ground waves were generated and the track response was amplified at an increasing rate (Madshus and Kaynia, 2000; Madshus *et al.*, 2004). The dependency of the track response on the train speed is illustrated in Figure (4.6).

4.5 Determination of Track Critical Velocity; 3D Finite Element Modelling

A ballasted track with differing depths and stiffness of the ballast layer is considered for the study. The track is on a layered soil system consisting of 7 metres of soft-to-medium stiff

soil placed on a relatively stiff layer extending to a depth of 35 metres. A set of four constant loads, which represents a passenger coach with an axle load of 17.4 T, is adopted here to simulate the train load on the track. The track meshing and train model details are given in Figure (3.5). More details on the model configuration can be found in Section 3.3.

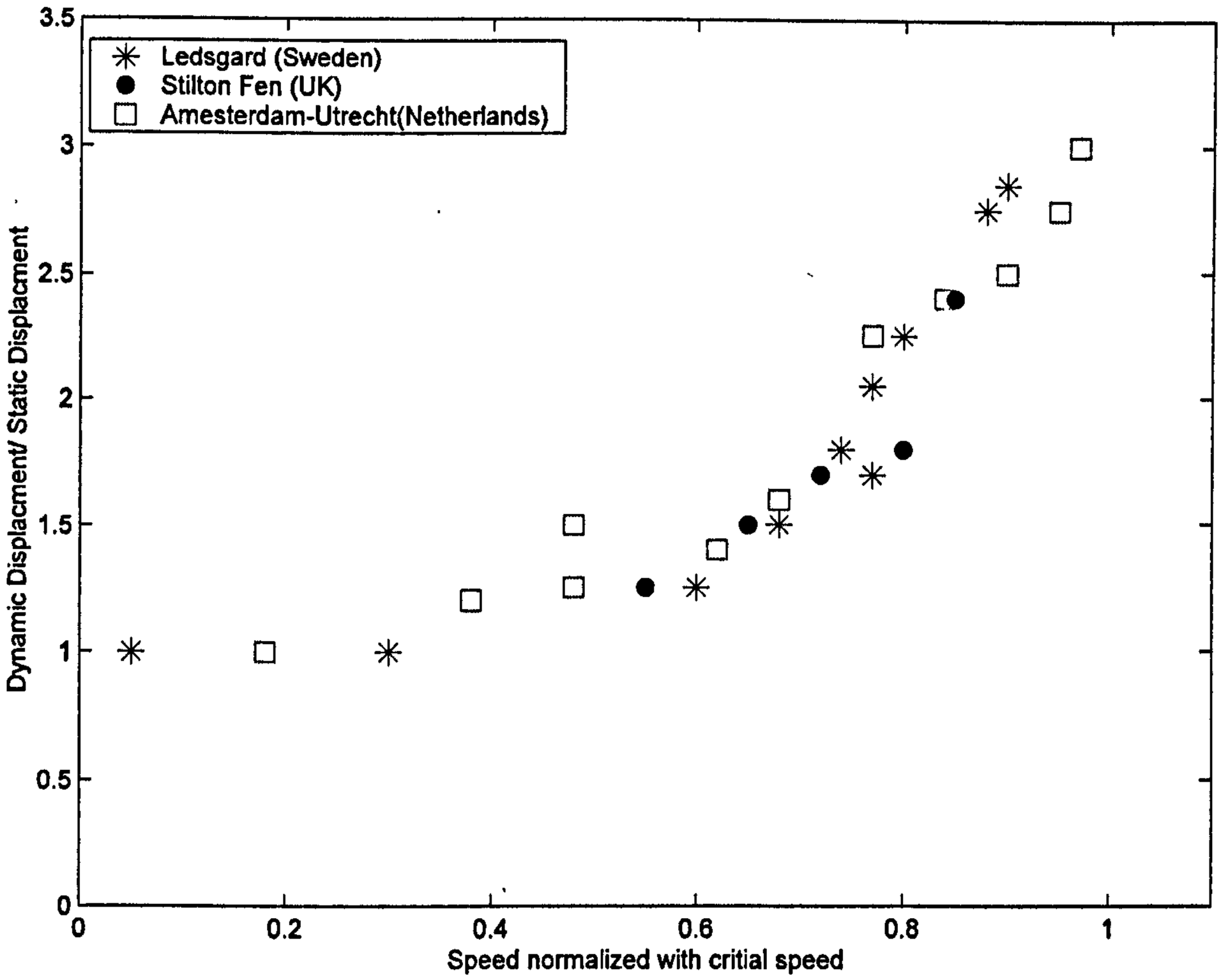

Figure 4.6. Maximum measured normalized displacement versus normalized speed (Madshus *et al.*, 2004)

Several simulations are conducted to study track response under different train speeds. Different track conditions, in terms of the subgrade stiffness (ES subgrade resilient modulus), ballast stiffness (EB ballast resilient modulus) and ballast depth (BD) are investigated. Figures (4.7- 4.11) depict a typical simulated track response (ES=15 MPa, EB=120 MPa, BD=300 mm) under a sleeper at two different train speeds, namely V=30 m/s and 60 m/s. Figures (4.7a) and (4.7b) compare simulated sleeper displacements for a

track at train speeds of 30 and 60 m/s respectively. A considerable increase in displacement is

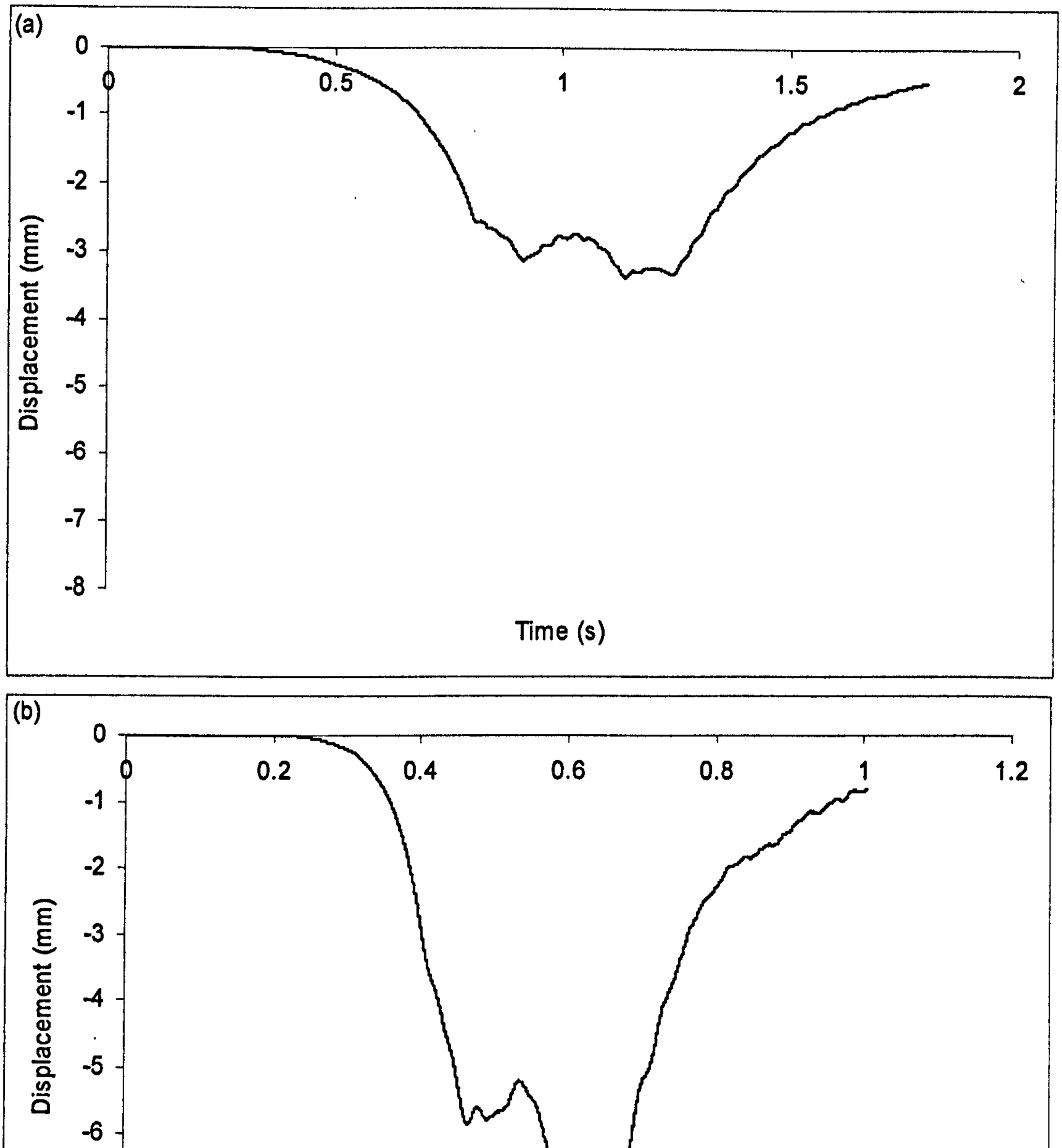

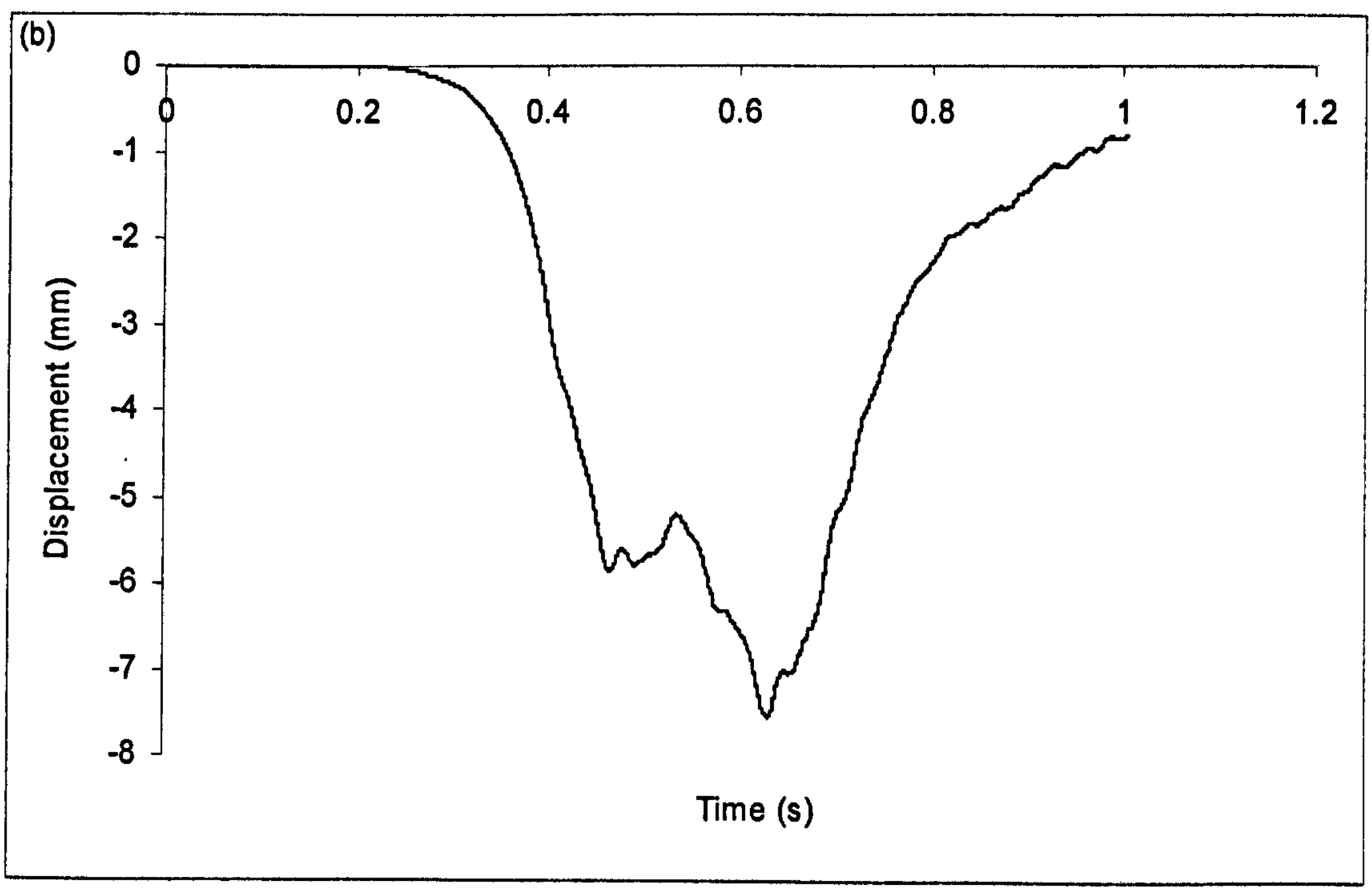

Figure 4.7. Sleeper displacement under a train coach (ES=15 MPa , EB=120 MPa, BD=300 mm) (a) V=30 m/s (b) V=60 m/s

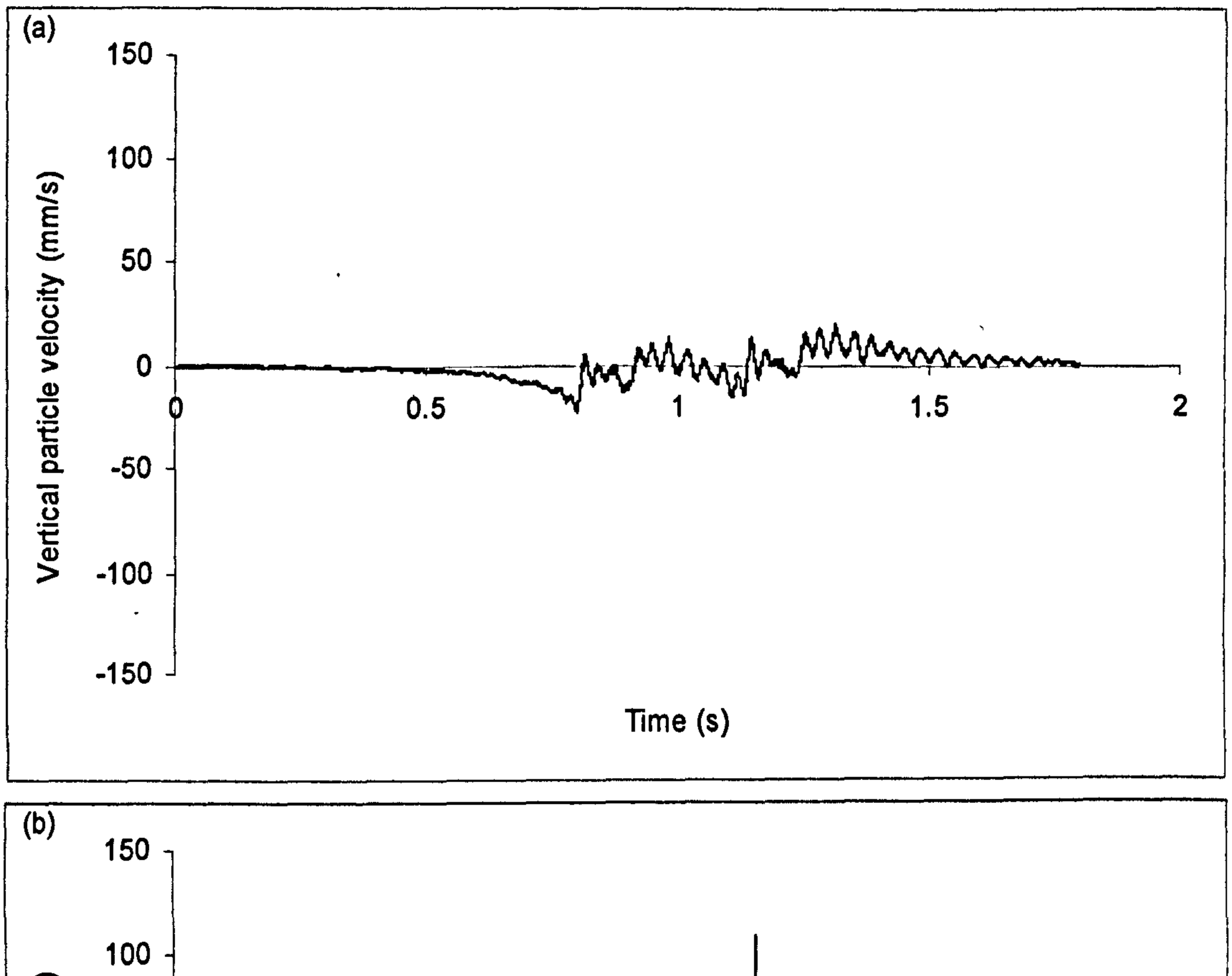

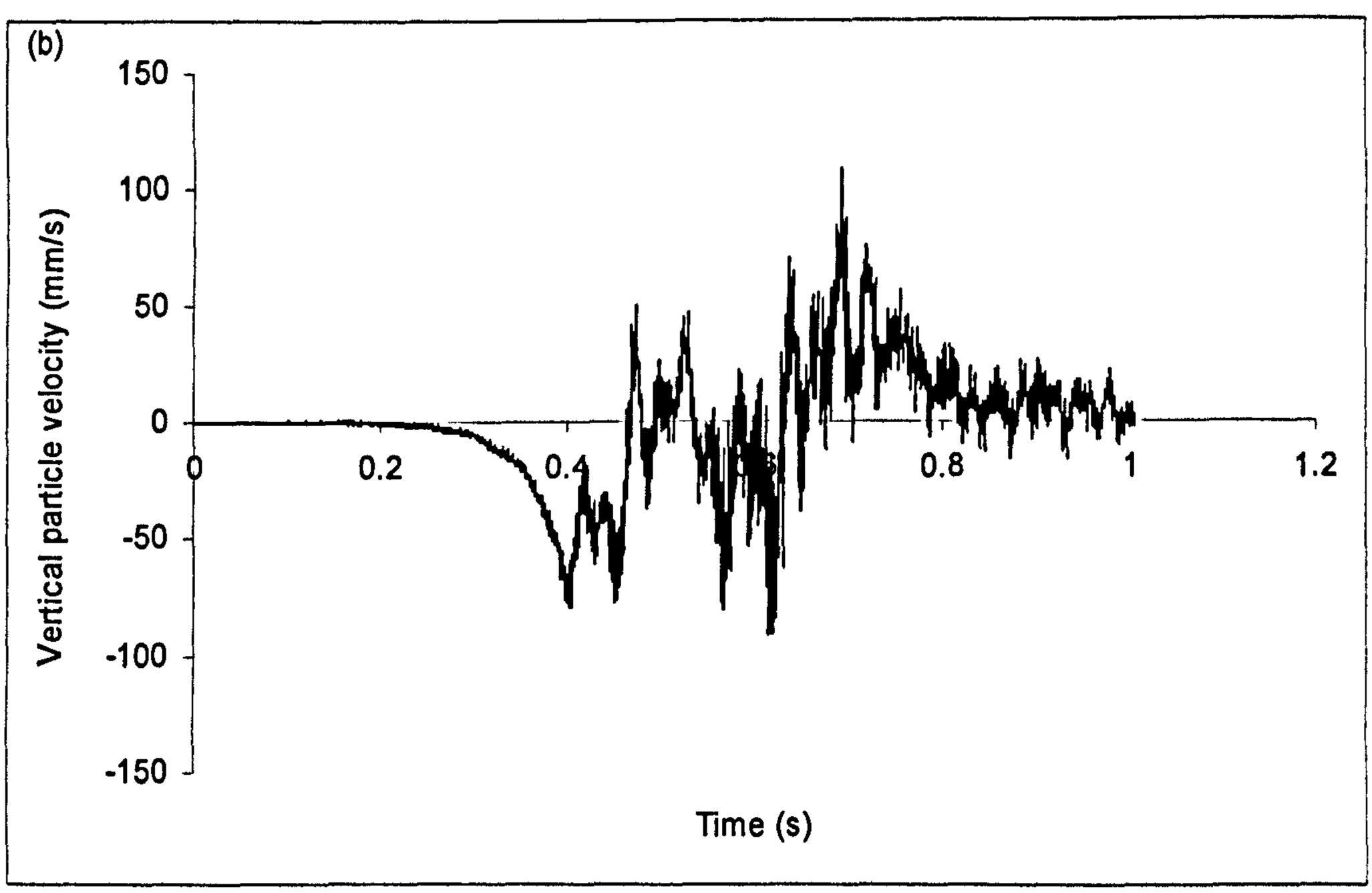

Figure 4.8. Ballast particle velocity under passage of a train coach (ES=15 MPa, EB=120 MPa, BD=300 mm)(a) V=30 m/s (b) V=60 m/s

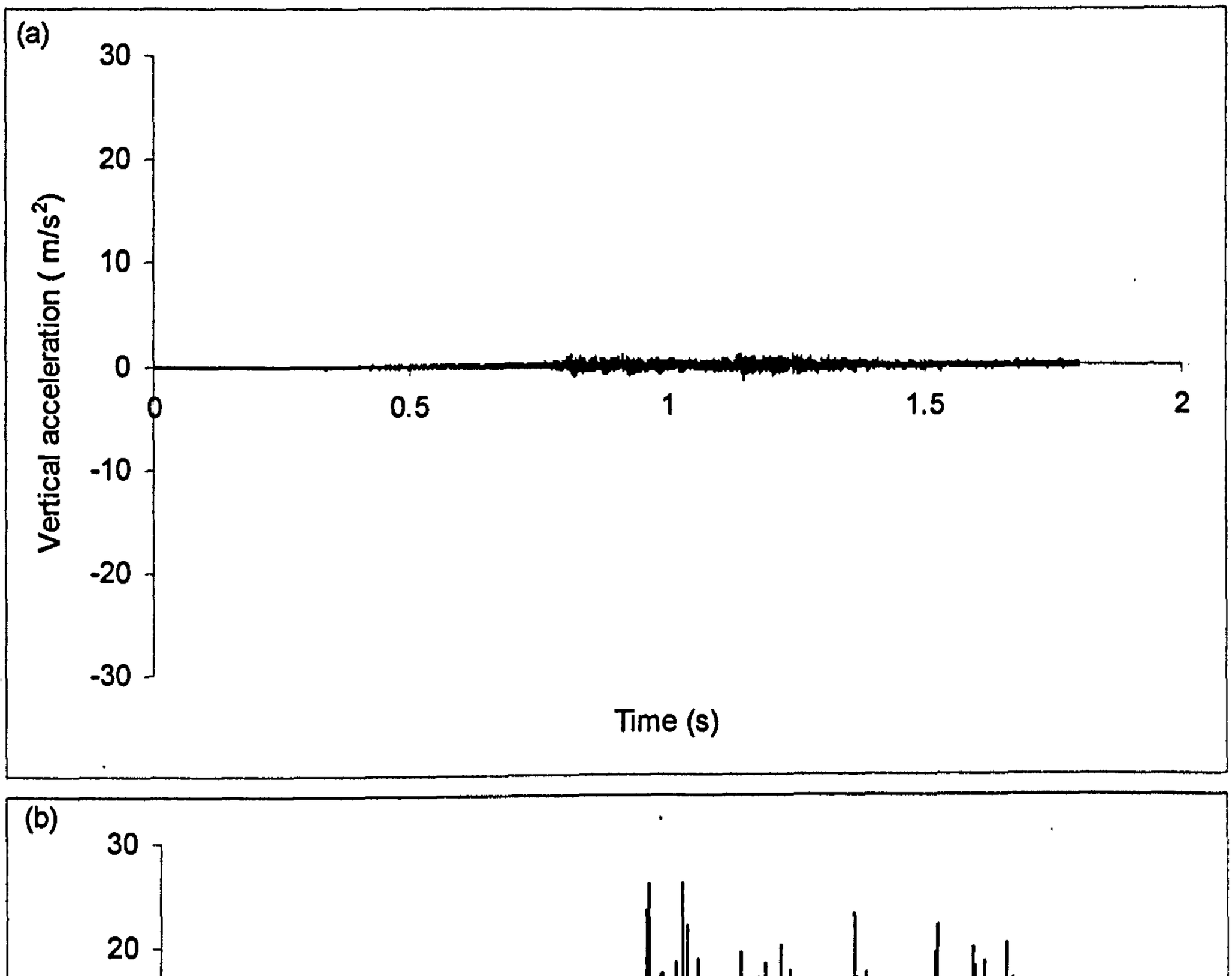

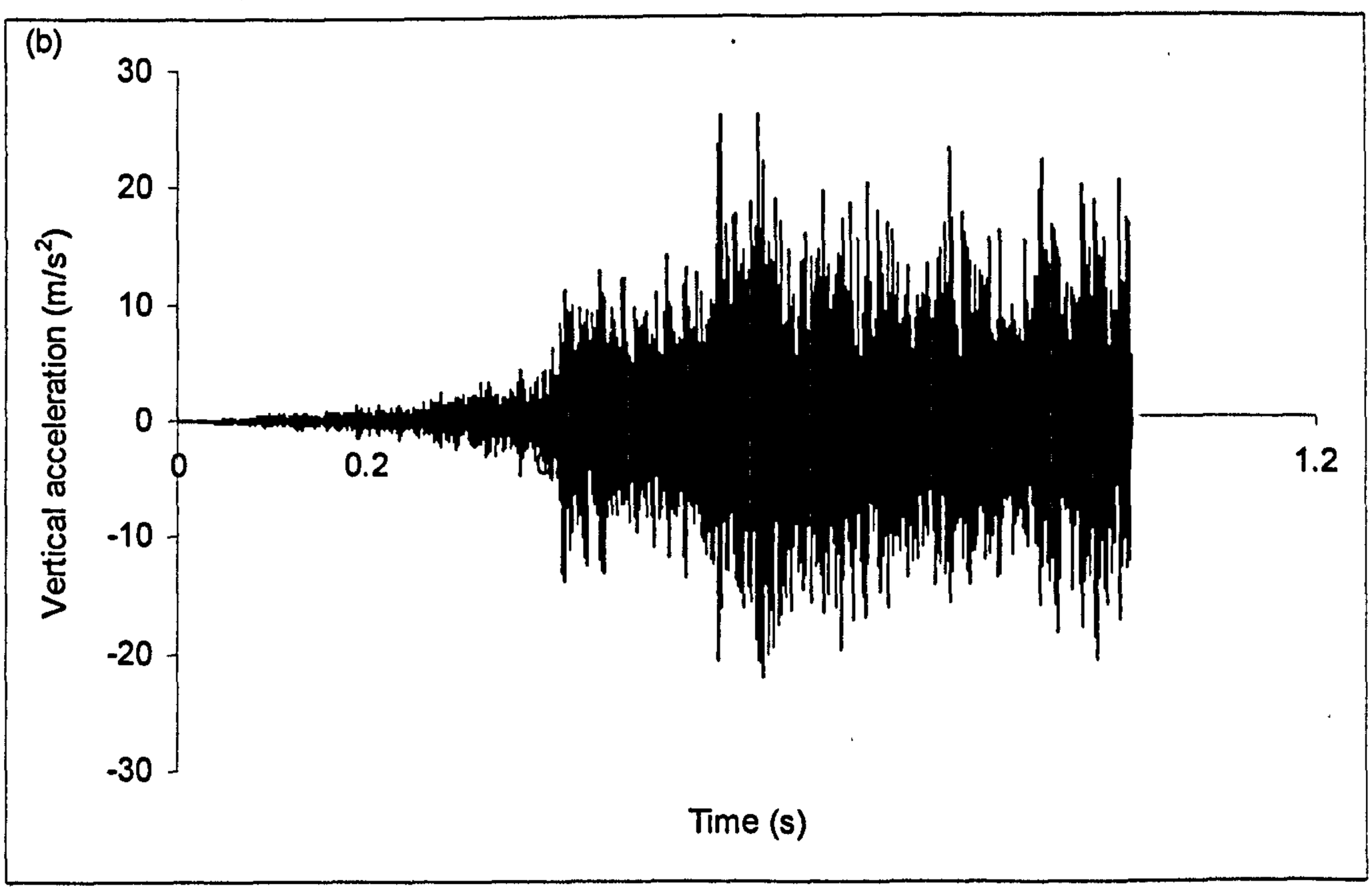

Figure 4.9. Ballast particle acceleration under passage of a train coach (ES=15 MPa, EB=120 MPa, BD=300 mm) (a) V=30 m/s (b) V=60 m/s

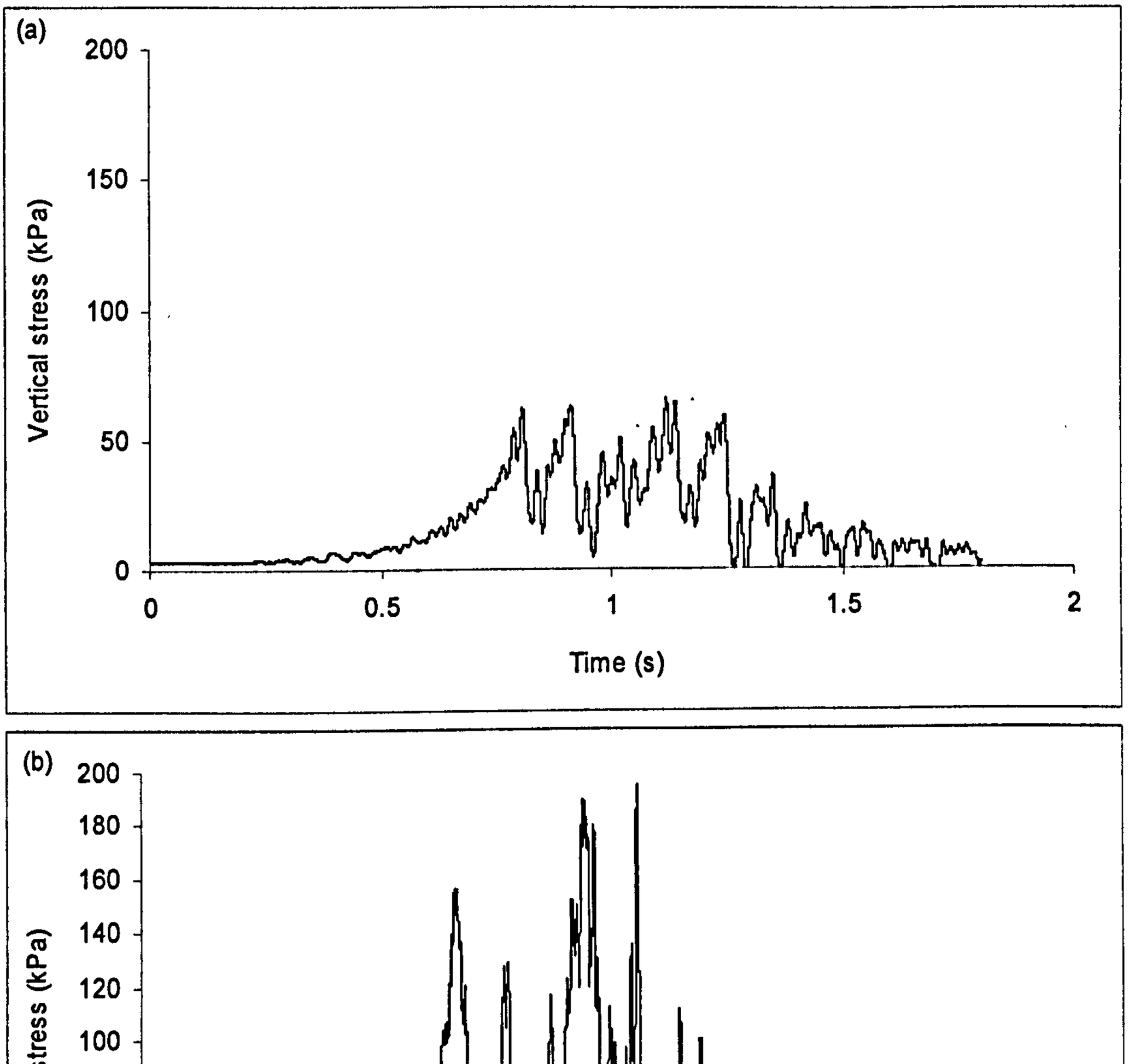

Figure 4.10. Vertical stress on top of ballast layer under passage of a train coach (ES=15 MPa, EB=120 MPa, BD=300 mm) (a) V=30 m/s (b) V=60 m/s

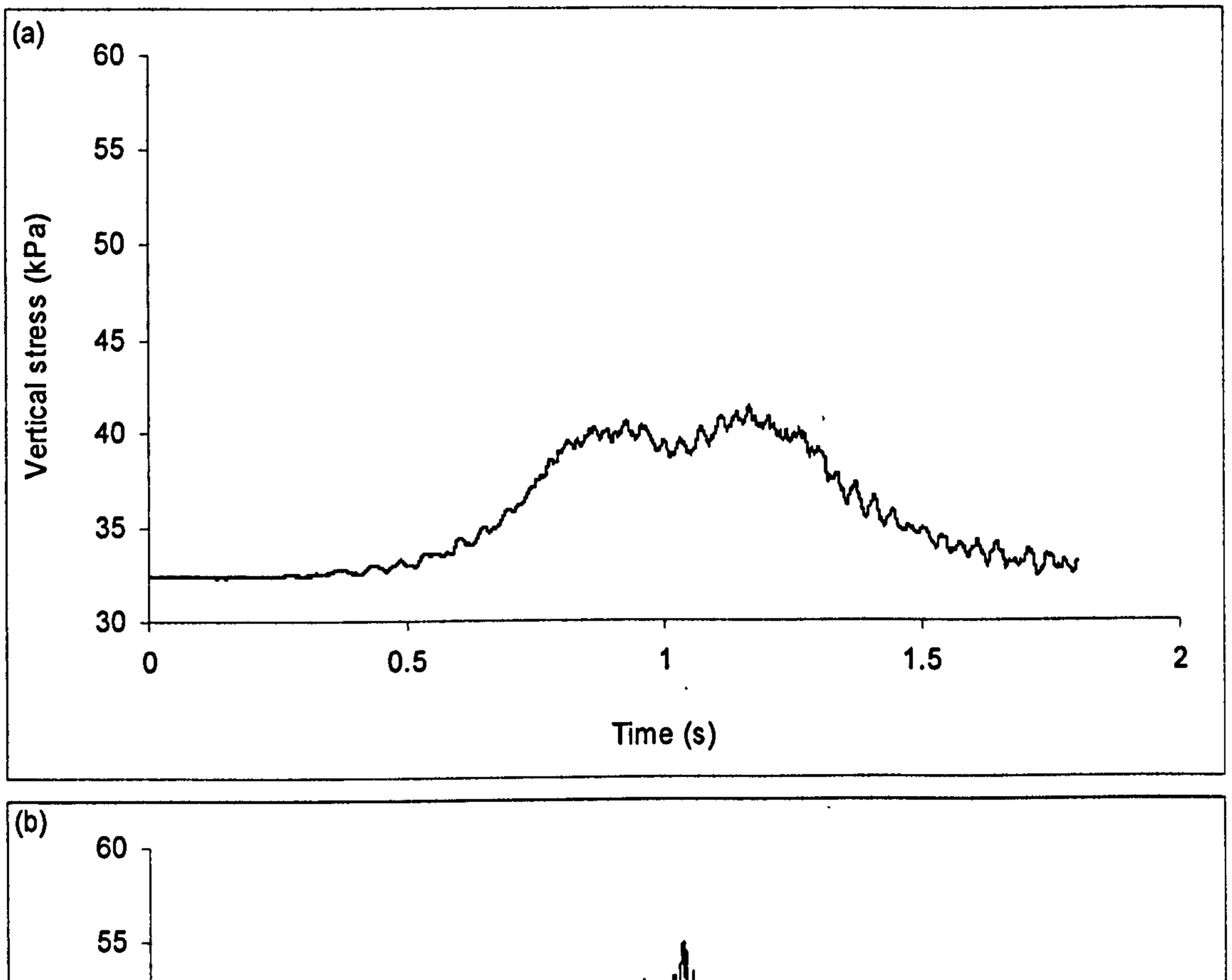

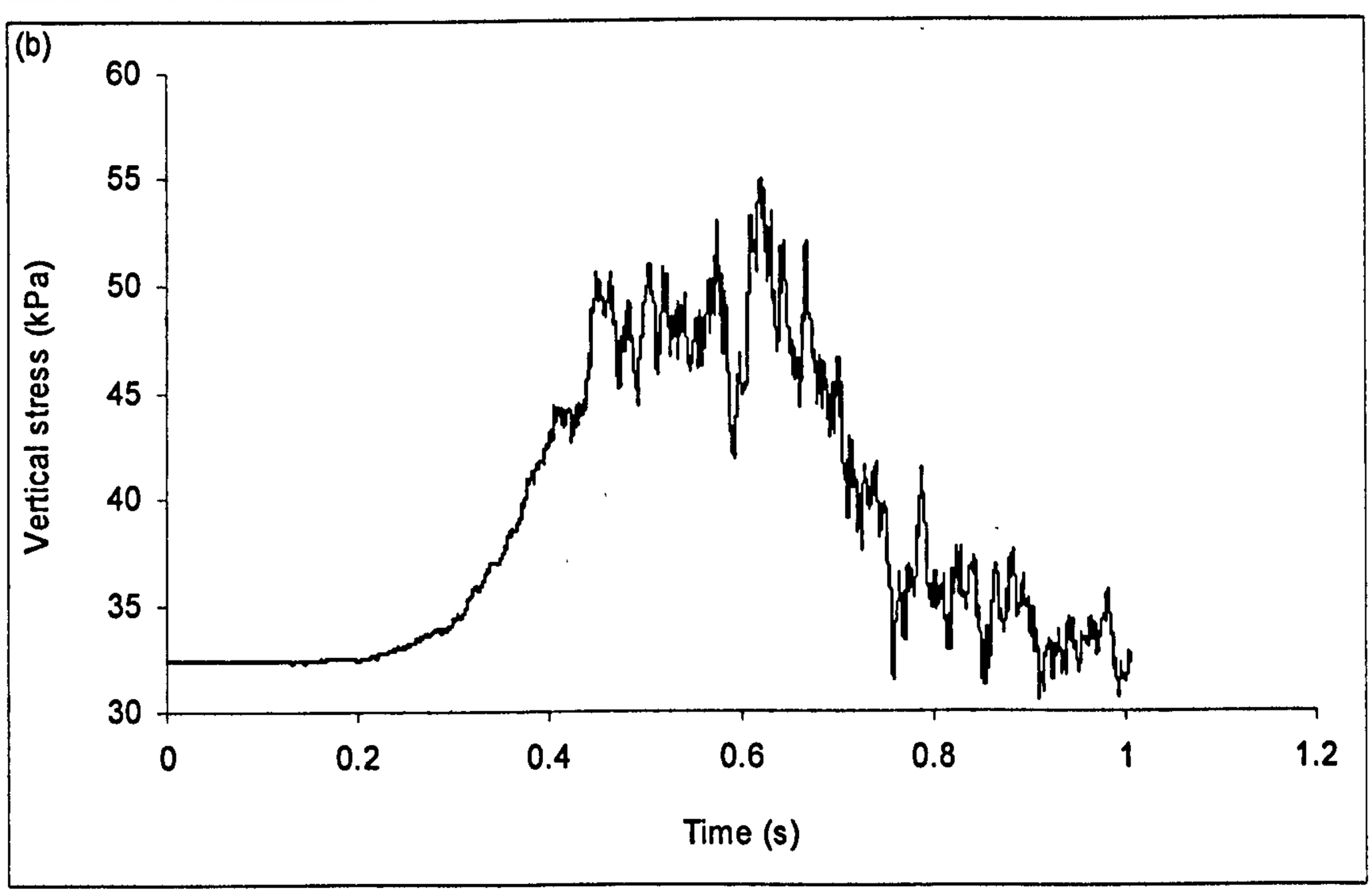

Figure 4.11. Vertical stress in the subgrade (At depth=1.8 m) under passage of a train coach (ES=15 MPa, EB=120 MPa, BD=300 mm) (a) V=30 m/s (b) V=60 m/s

clearly seen with the increase in train speed. In addition, the displacement response becomes more asymmetrical as the train speed increases. The vibration levels, in terms of vertical velocity and acceleration in the ballast layer, also rise considerably with an increase in train speed, as shown in Figures (4.8) and (4.9). Train speed also affects the stress level in the ballast and subgrade layers, as shown in Figures (4.10) and (4.11); the stresses in both ballast and subgrade increase considerably with an increase in train speed. At lower train speeds (V=30 m/s), it is also seen that the induced stresses in the ballast clearly reflect all the wheel footprints (Figures 4.10a). For the subgrade, the footprints of single wheels are not distinguishable; however the bogies' footprints are clearly seen in the induced stress time history (Figures 4.11a). As the train speed increases from 30 m/s to 60 m/s, the wheel traces (or even bogie traces) become less distinguishable in the induced stress time history (Figures 4.10b and 4.11b).

Figures (4.12-4.15) show the displacement contours on the surface and at depth for different subgrade conditions (ES=15 MPa and ES= 40 MPa) at train speeds of 30, 50 and 70 m/s. Depending on the subgrade stiffness and train speed, the track responses have different characteristic features. At low speeds ($V<=0.5V_r$, V_r is Rayleigh wave velocity of subgrade), the displacement pattern is mainly symmetric; every wheel has its own footprint and the displacement field moves with the train (Figures 4.14a and 4.15a). The displacement pattern resembles the static response of track under static train loading. As the train speed increases ($0.5V_r<V<V_r$), the displacement field still moves with the train, but it is now clearly becoming asymmetrical (Figures 4.12a, 4.12b, 4.13a, 4.13b, 4.14b, 4.14c, 4.15b and 4.15c). When the train speed exceeds the wave velocity in the ground ($V_r<V$), it is observed that the train is moving ahead of the displacement field, which is a natural consequence of the train moving faster than the subgrade stress waves (Figures 4.12c, 4.13c).

The effect of ballast depth and stiffness are also studied in Figures (4.16-4.19). In comparison to a railway on stiff ballast (EB=300 MPa), a railway system on soft ballast (EB=30 MPa) results in significantly more asymmetrical displacement patterns with higher displacements at high speeds (V=70 m/s), as seen when comparing Figure (4.17a) to Figure (4.17b). At lower speeds (V=30 m/s), a shallow depth stiff layer on the soft subgrade seems, however, to have a limited effect on the track response (Figures 4.16a and 4.16b).

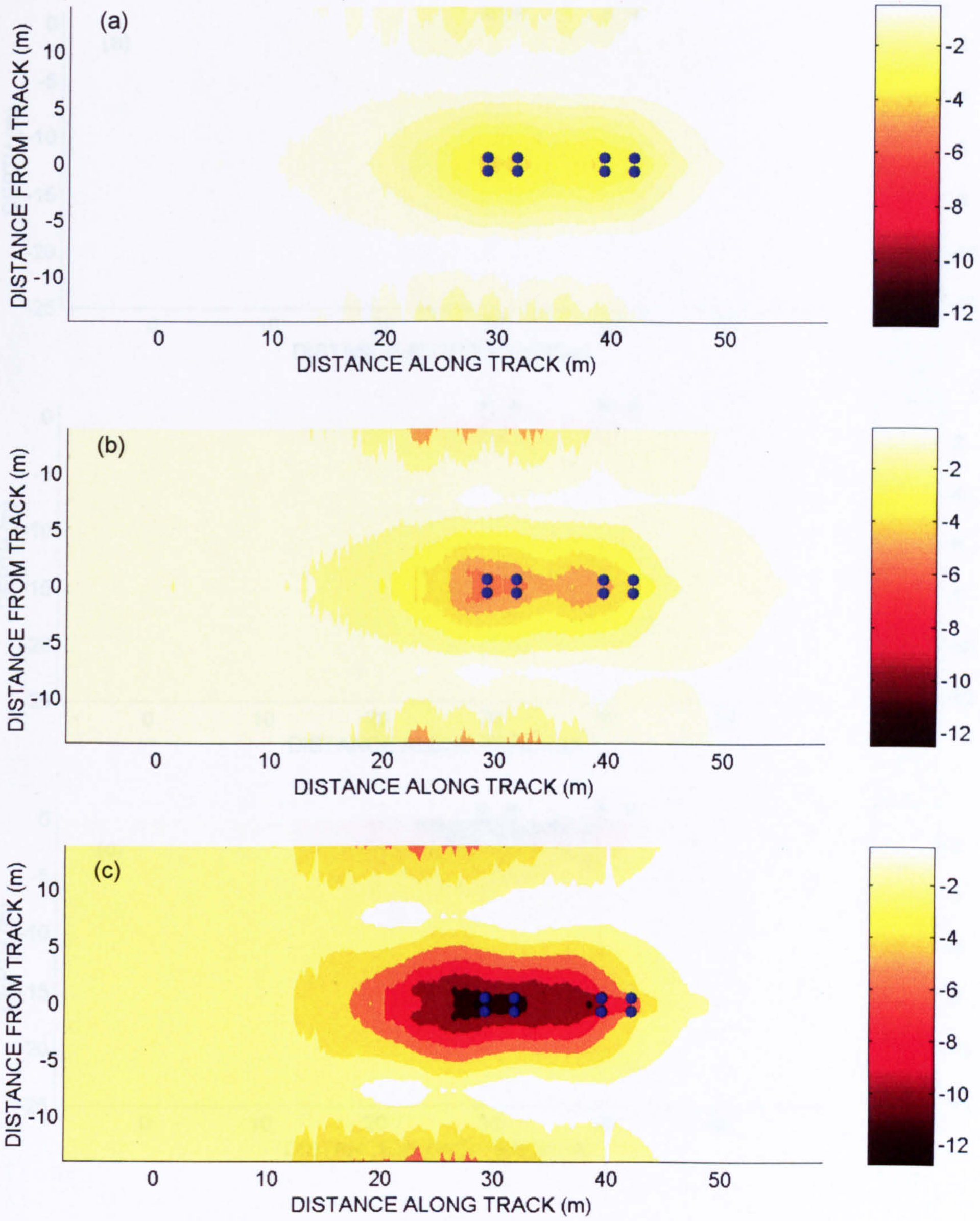

Figure 4.12. Plan views of track displacement responses on soft soil (ES=15 MPa, EB=120 MPa BD=300mm) at (a) V=30 m/s ($0.57V_r$), (b) V=50 m/s ($0.96V_r$), (c) V=70 m/s ($1.34V_r$) (contours in mm)

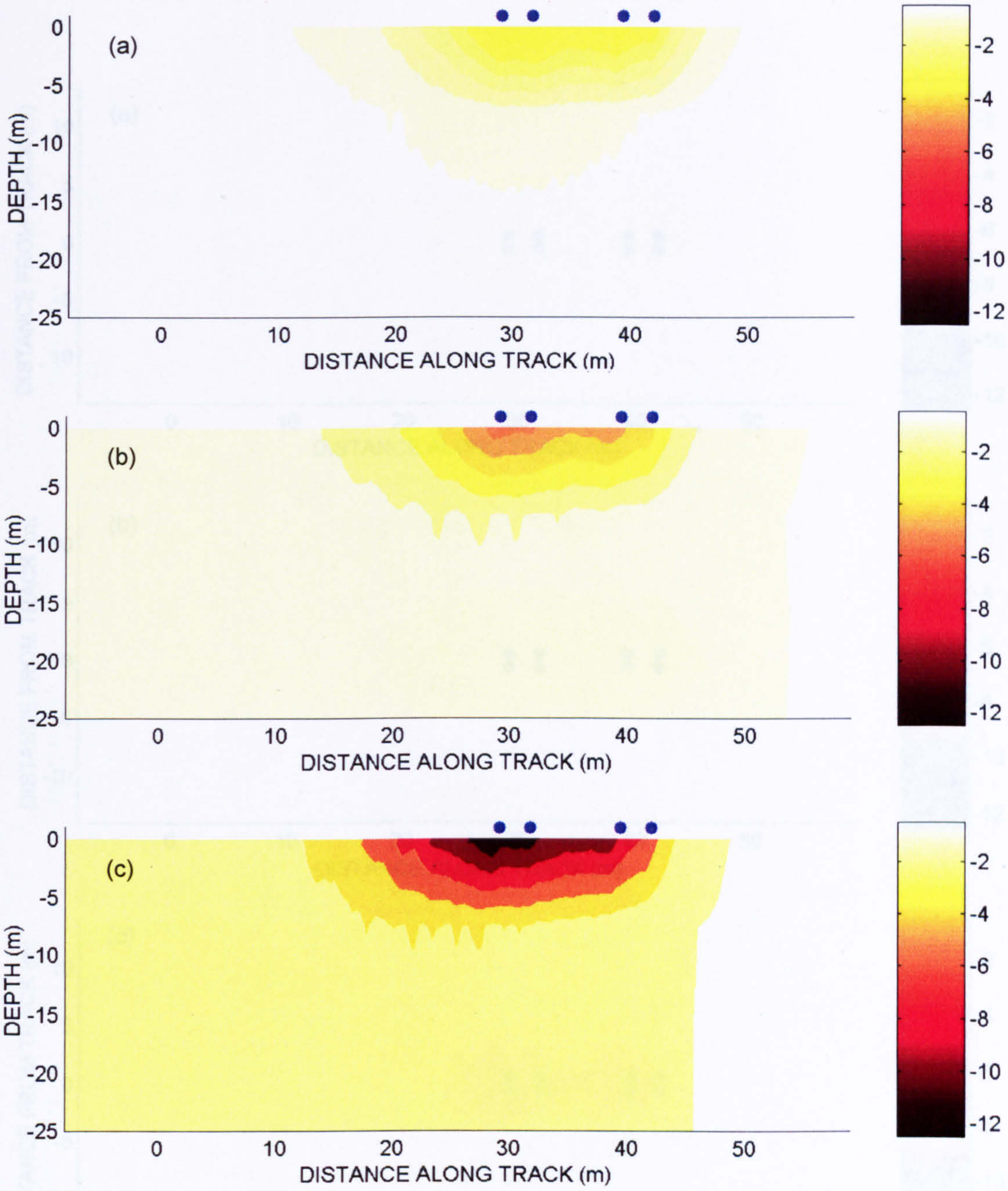

Figure 4.13. At depth views of track displacement responses on soft soil (ES=15 MPa, EB=120 MPa, BD=300mm) at (a) V=30 m/s ($0.57V_r$), (b) V=50 m/s ($0.96V_r$), (c) V=70 m/s ($1.34V_r$) (contours in mm)

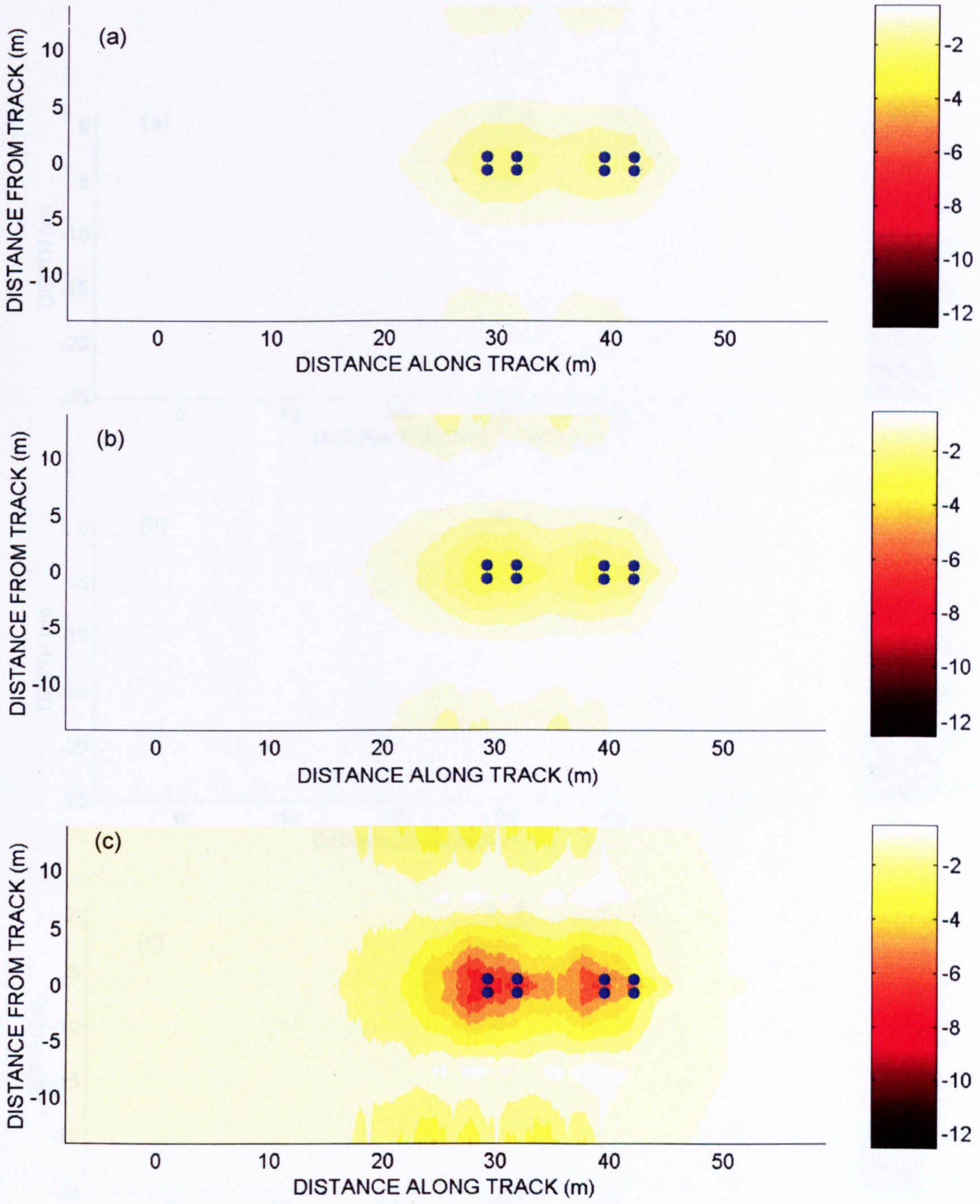

Figure 4.14. Plan views of track displacement responses on medium soil (ES=40 MPa, EB=120 MPa, BD=300mm) at (a) V=30 m/s ($0.35V_r$), (b) V=50 m/s ($0.58V_r$), (c) V=70 m/s ($0.82V_r$) (contours in mm)

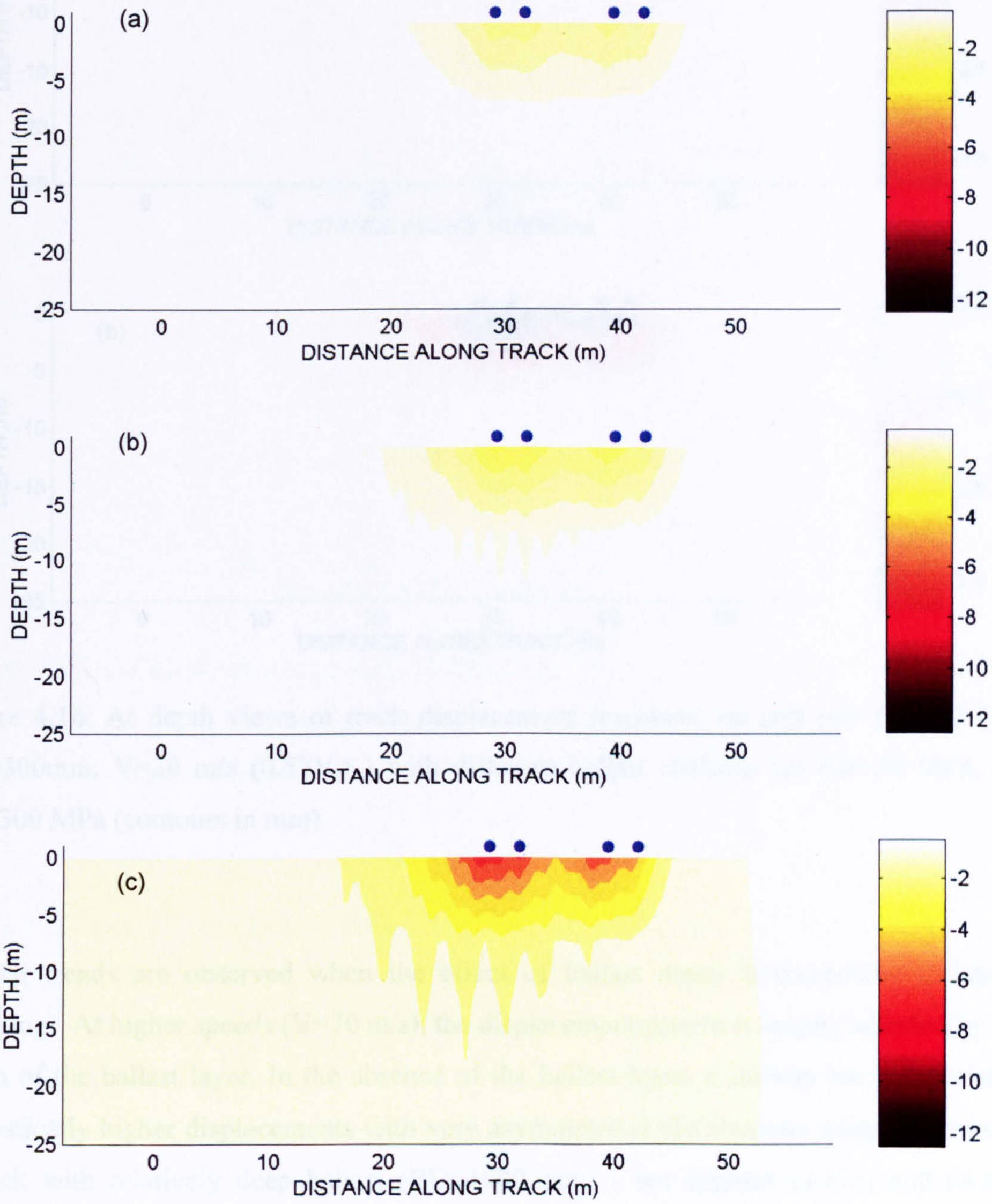

Figure 4.15. At depth views of track displacement responses on medium soil (ES=40 MPa, EB=120 MPa, BD=300mm) at (a) V=30 m/s ($0.35V_r$), (b) V=50 m/s ($0.58V_r$), (c) V=70 m/s ($0.82V_r$) (contours in mm)

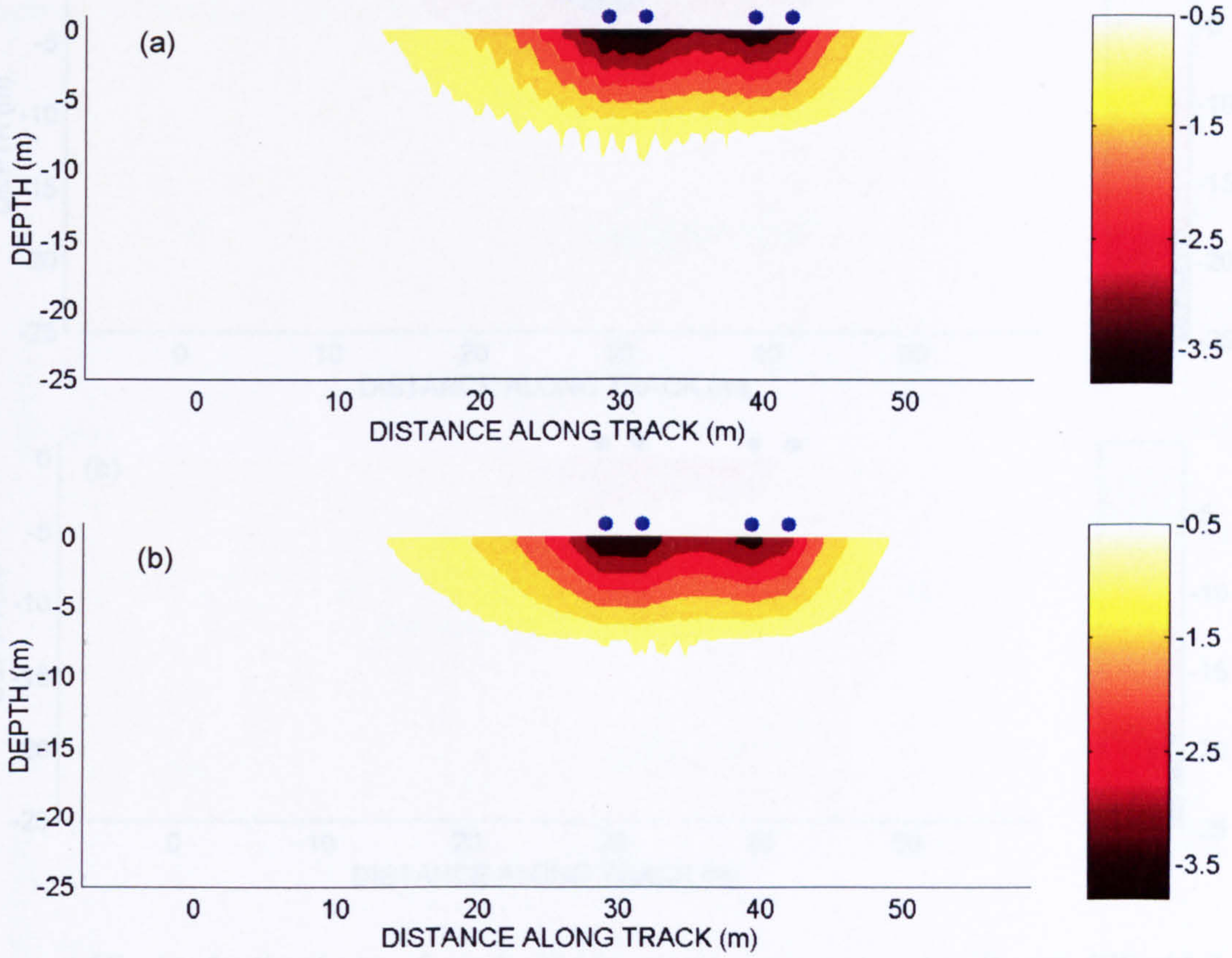

Figure 4.16. At depth views of track displacement responses on soft soil (ES=15 MPa, BD=300mm, V=30 m/s ($0.57V_r$)) with different ballast stiffness (a) EB=30 MPa, (b) EB=300 MPa (contours in mm)

Similar trends are observed when the effect of ballast depth is considered (relatively speaking). At higher speeds (V=70 m/s), the displacement pattern is largely affected by the depth of the ballast layer. In the absence of the ballast layer, a railway track experiences dramatically higher displacements with very asymmetrical distributions when compared to a track with relatively deep ballast (BD=1000 mm) - see Figures (4.17a) and (4.17b). Comparing Figures (4.18a) and (4.18b), the effect of the ballast depth is, however, seen to be limited for track on soft subgrade at lower train speeds (V=30 m/s).

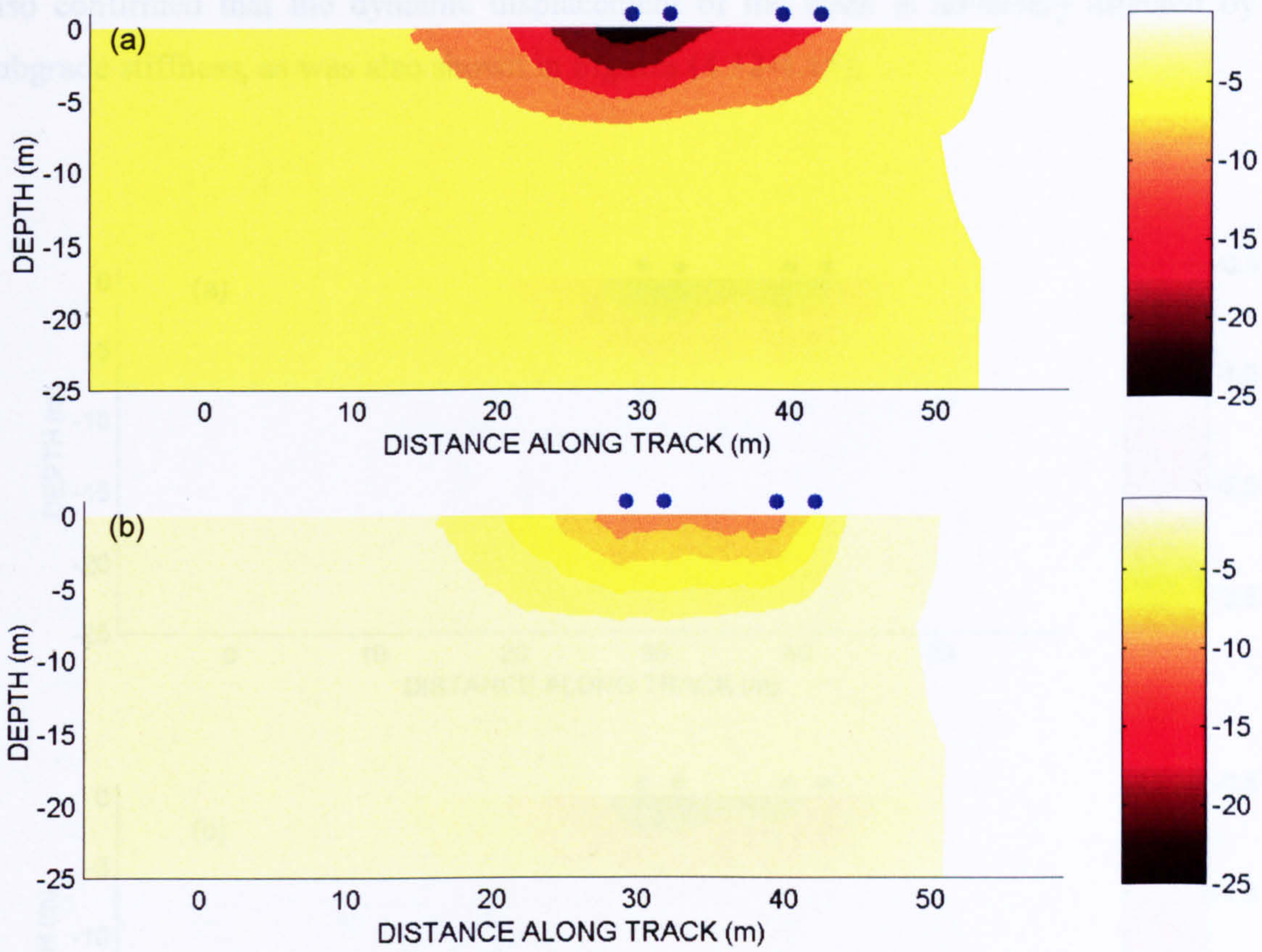

Figure 4.17. At depth views of track displacement responses on soft soil (ES=15 MPa, BD=300mm, V=70 m/s ($1.34V_r$)) with different ballast stiffness (a) EB=30 MPa, (b) EB=300 MPa (contours in mm)

It can therefore be concluded that the presence of a deep stiff ballast layer on the soft ground could reduce the displacement level significantly as the train speed increases and passes the characteristic wave velocity of the soft subgrade. In spite of that, any improvement deriving from a stiffer and a deeper ballast layer, in the high speed range, may not be as high as expected owing to the tensionless nature of ballast, stiffness degradation (e.g. because of mud pumping) and also stiffness nonlinearity of the ballast. This will be discussed in Chapter 5.

The computed maximum dynamic displacement for different track condition is plotted against train speed in Figure (4.20). Irrespective of ballast and subgrade conditions, an increase in the displacement is observed as the train speed increases. At a given speed, it is

also confirmed that the dynamic displacement of the track is adversely affected by the subgrade stiffness, as was also shown in Figures (4.12-4.15).

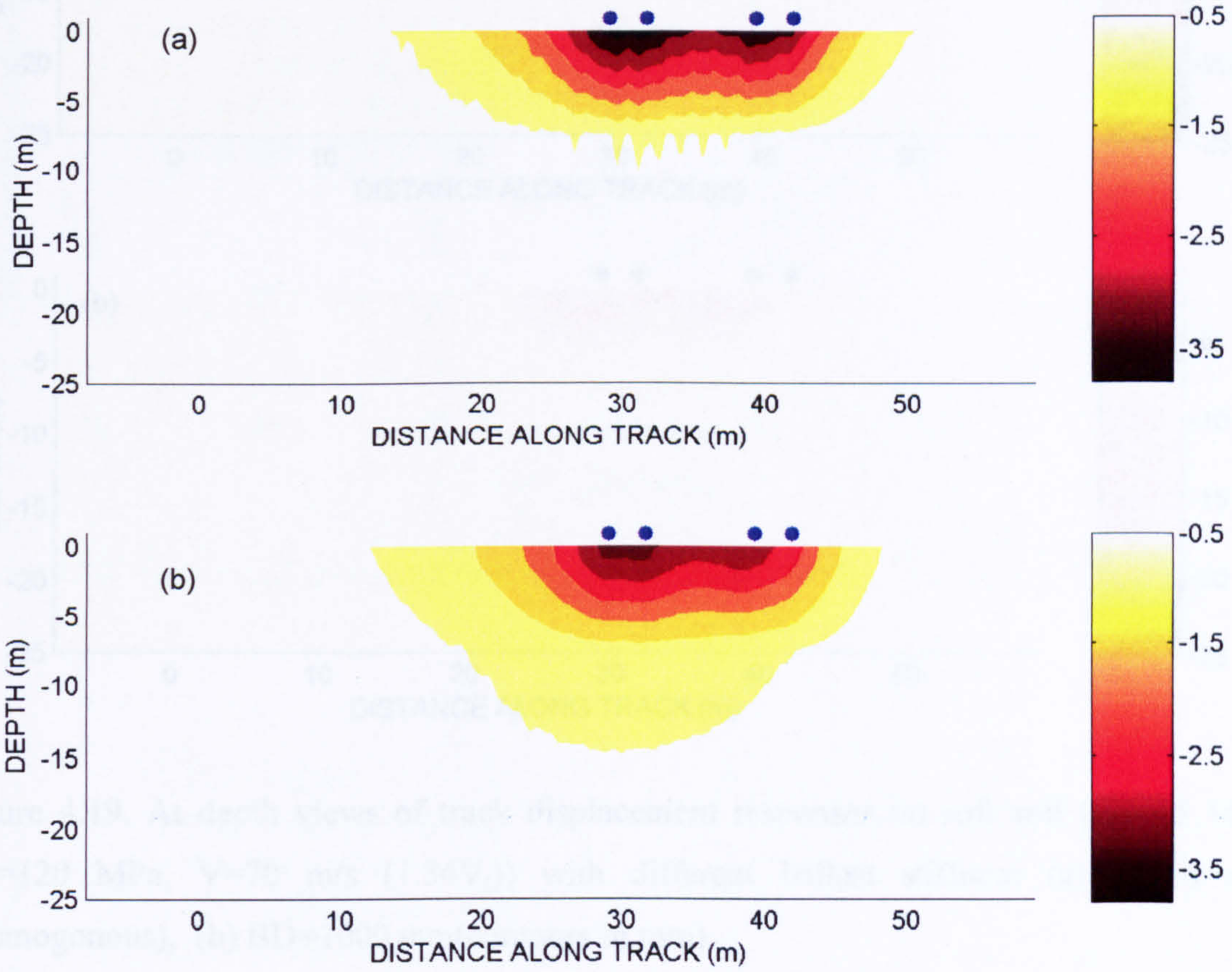

Figure 4.18. At depth views of track displacement responses on soft soil (ES=15 MPa, EB=120 MPa, V=30 m/s ($0.57V_r$)) with different ballast stiffness (a) BD=0 mm (homogonous), (b) BD=1000 mm (contours in mm)

Figures (4.21) shows the normalized speed (normalized to Rayleigh wave velocity of subgrade) versus the maximum normalized displacement obtained numerically for different subgrade stiffness, ballast depths & stiffness. It is generally seen that, as the train speed approaches the subgrade Rayleigh wave velocity (V_r), the displacement increases dramatically. For studied cases, the dynamic displacement may be more than three times the maximum static displacement when the train speed equals the subgrade Rayleigh wave velocity (V_r). As discussed before, the presence of a deeper and stiffer ballast layer can

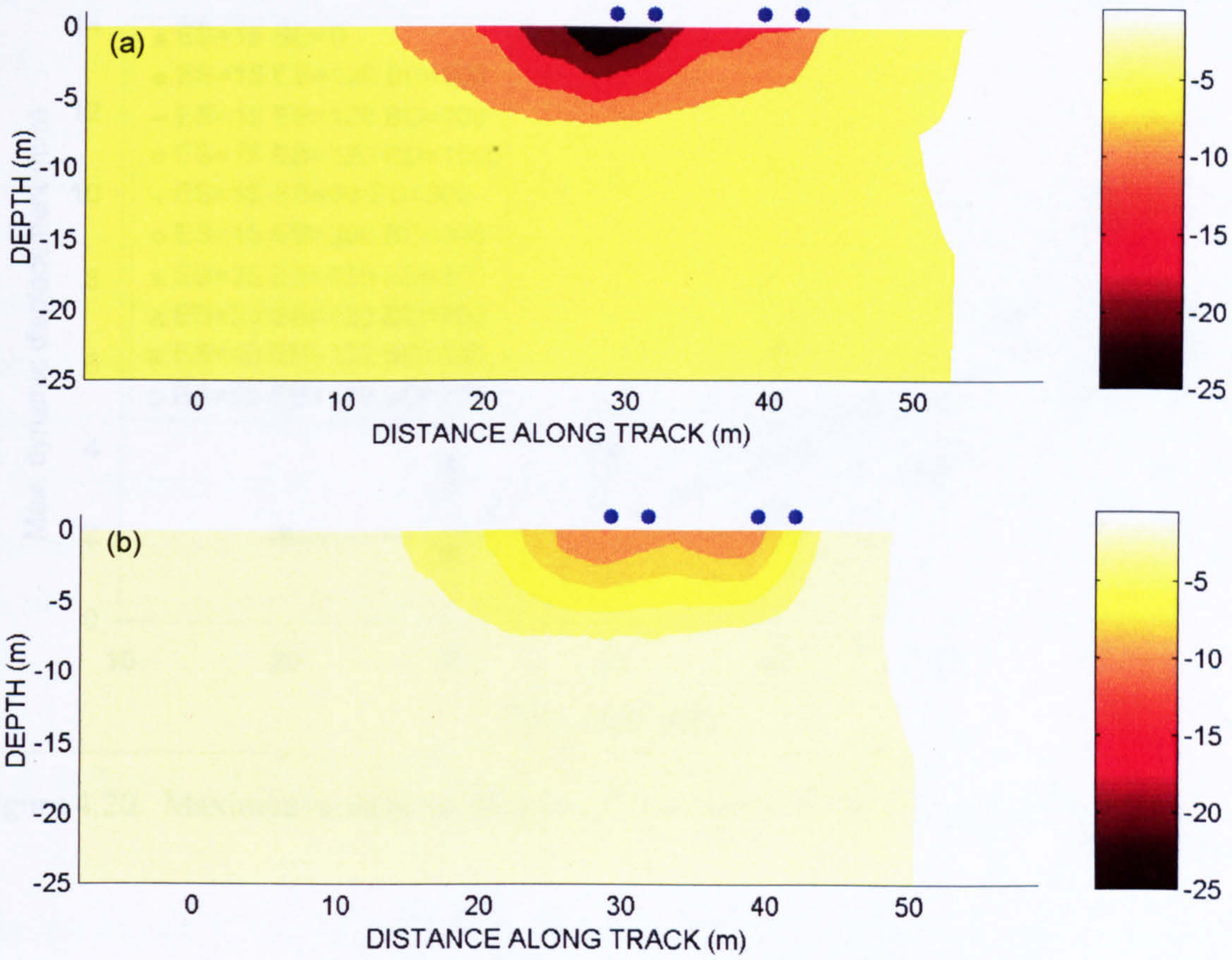

Figure 4.19. At depth views of track displacement responses on soft soil (ES=15 MPa, EB=120 MPa, V=70 m/s ($1.34V_r$)) with different ballast stiffness (a) BD=0 mm (Homogonous), (b) BD=1000 mm(contours in mm)

reduce track displacement at high speeds, suggesting that the track critical velocity may be shifted to a slightly higher value with increasing ballast layer depth and stiffness. It can be attributed to a better distribution of train loading, higher bending stiffness of the modelled ballast layer and a shift in the system natural frequency. Because of the discrete tensionless nature of the ballast, the bending stiffness of the ballast layer is low; hence the corresponding modification of the track critical velocity may be considerably lower than expected. Irrespective of ballast depth and stiffness, it can therefore be said that the Rayleigh wave velocity of the subgrade can be practically considered as the track critical velocity of the railway track system for conventional ballasted track systems. Figure (4.21) also confirms that the displacement response is essentially static for train speeds lower than

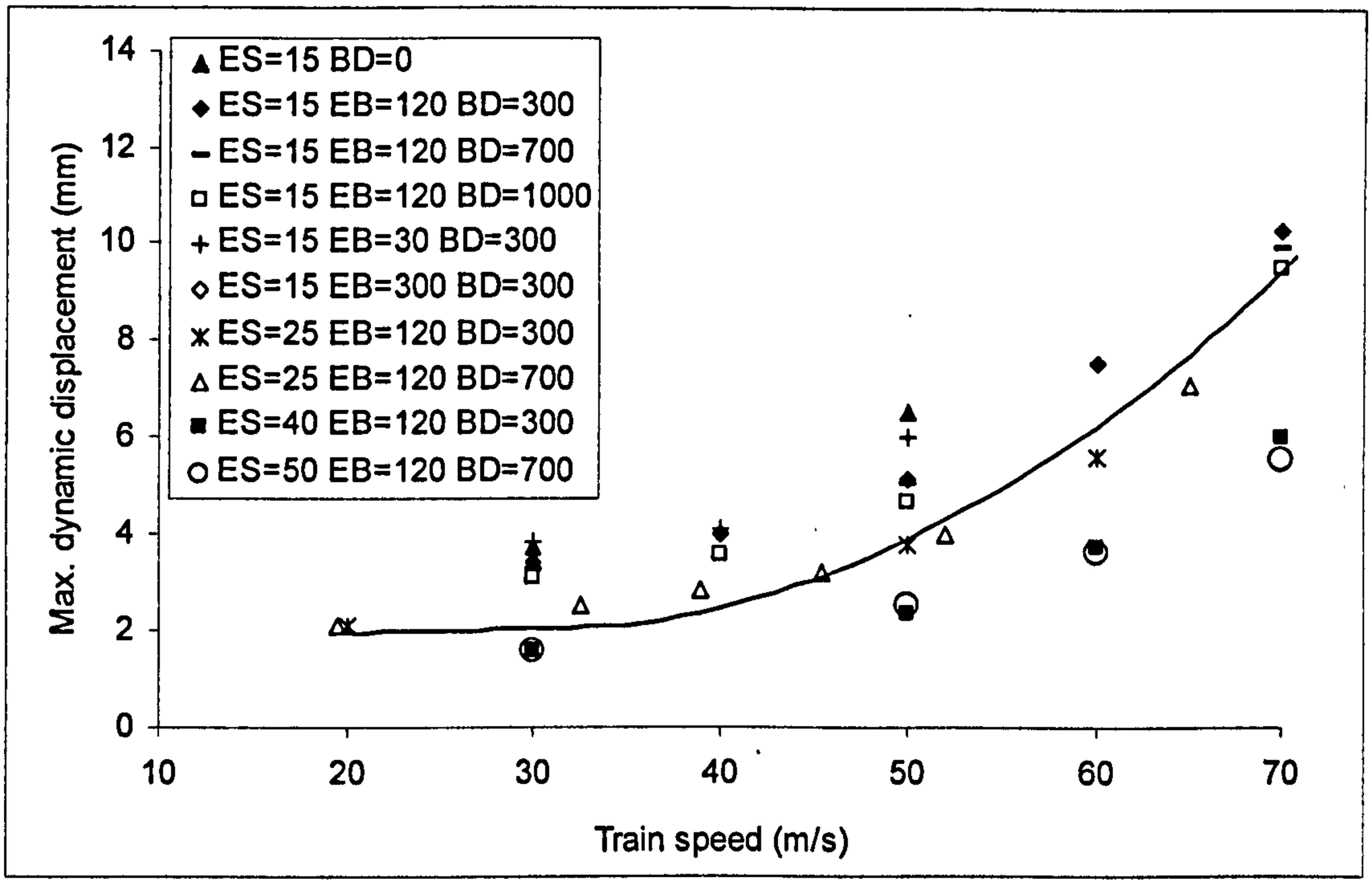

Figure 4.20. Maximum computed dynamic displacement versus train speed

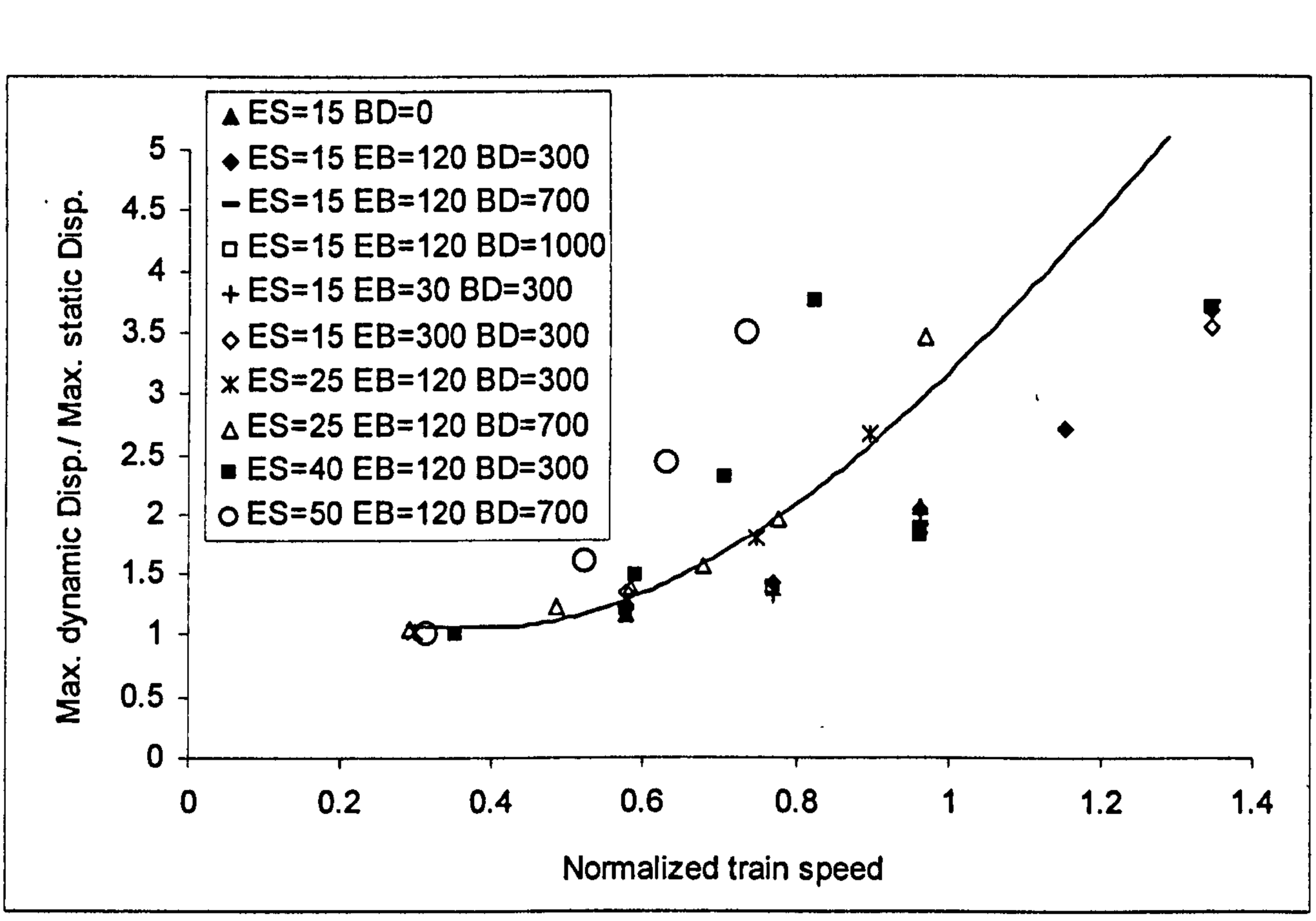

Figure 4.21. Maximum computed normalized displacement versus normalized train speed

one half of V_{cr}. Similar trends were observed in soft soil site measurements in the UK, Netherlands and Sweden, as shown in Figure (4.6).

Although the current model configuration predicts the essential features of critical/super-critical track response, namel y high levels of track displacement and train movements ahead of the displacement field (trains running faster than the surface ground wave velocity), it should be noted that finer meshing and considerably bigger domains will be required to study detailed track response under critical or super-critical regimes. Therefore, a finite element analysis will be computationally expensive in terms of run times using conversional computers; it is a subject of further research to employ parallel computing technology to study track response at very high line speeds.

4.6 Effect of Train Speed on the Track Maintenance

The experience of operating high line speeds on conventional ballasted track has clearly shown a considerable increase in the maintenance level required to ensure track geometry. In the case of relatively old tracks, the subgrade shows mainly elastic resilient behaviour and the loss of track geometry has been, to a larger extent, attributed to settlement in the ballast layer caused by dynamic loading (Figure 4.22).

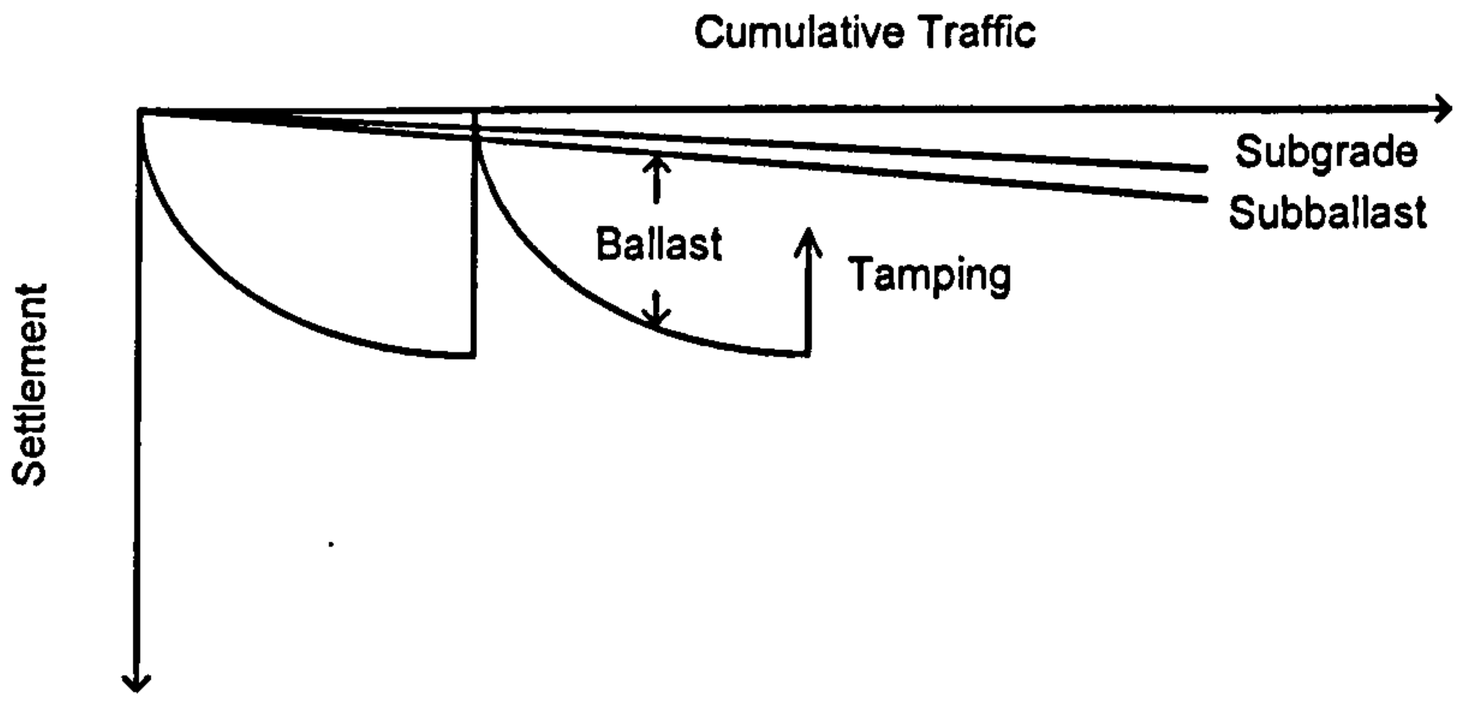

Figure 4.22. Substructure contribution to track settlement (Water and Selig, 1994)

Dahlberg (2001) has presented a review of several empirical models developed mainly on track loading levels and the number of load cycles or train passages. The vibration level in the ballast layer has also been considered as an important factor in the ballast deterioration process. Citing from Pita *et al.*(2004), Prud'Homme (1978) reported substantial increases in ballast acceleration with increasing train speed. He pointed out that high accelerations could cause increases in the attrition rate of ballast particles. Eisenmann and Rump (1997) suggested that the ballast particle velocity should not exceed 15-18 mm/s in order to prevent excessive deterioration of the ballast and subsequently the track geometry. The decompaction of granular soils under high accelerations has also been observed in experiments (Pita *et al.*, 2004).

The effect of vibration level and stress level in the ballast settlement was also highlighted in Sato (1977), giving the empirical relationship for ballast settlement:

$$\delta = \beta \sigma_b \gamma \tag{4.17}$$

where δ is the ballast settlement, σ_b the stress acting on ballast surface and γ is induced acceleration in the ballast. β is an empirical constant.

Figures (4.23) and (4.24) present the maximum vertical ballast particle velocity obtained from the numerical model for different track conditions against train speed and normalised train speed respectively. A continuous rise in the ballast particle velocity with train speed is observed. According to Eisenmann and Rump (1997), criteria based on ballast particle velocity can be considered as a guide to track maintenance classification. As seen in Figure (4.24), as long as the train speeds are lower than 50% of the track critical velocity, the track maintenance levels are seen to remain low (ballast particle velocity is lower than 20 mm/s).

As the train speed increases further, frequent higher levels of track maintenance may be required to retain the track geometry. When the train speed exceeds 70%-80% of the critical track velocity, high levels of vibration (Figure 4.24) and displacement (Figure 4.21) are observed, which would cause rapid deterioration of the track geometry and potentially lead to train derailment. Therefore the track maintenance can be categorized into three

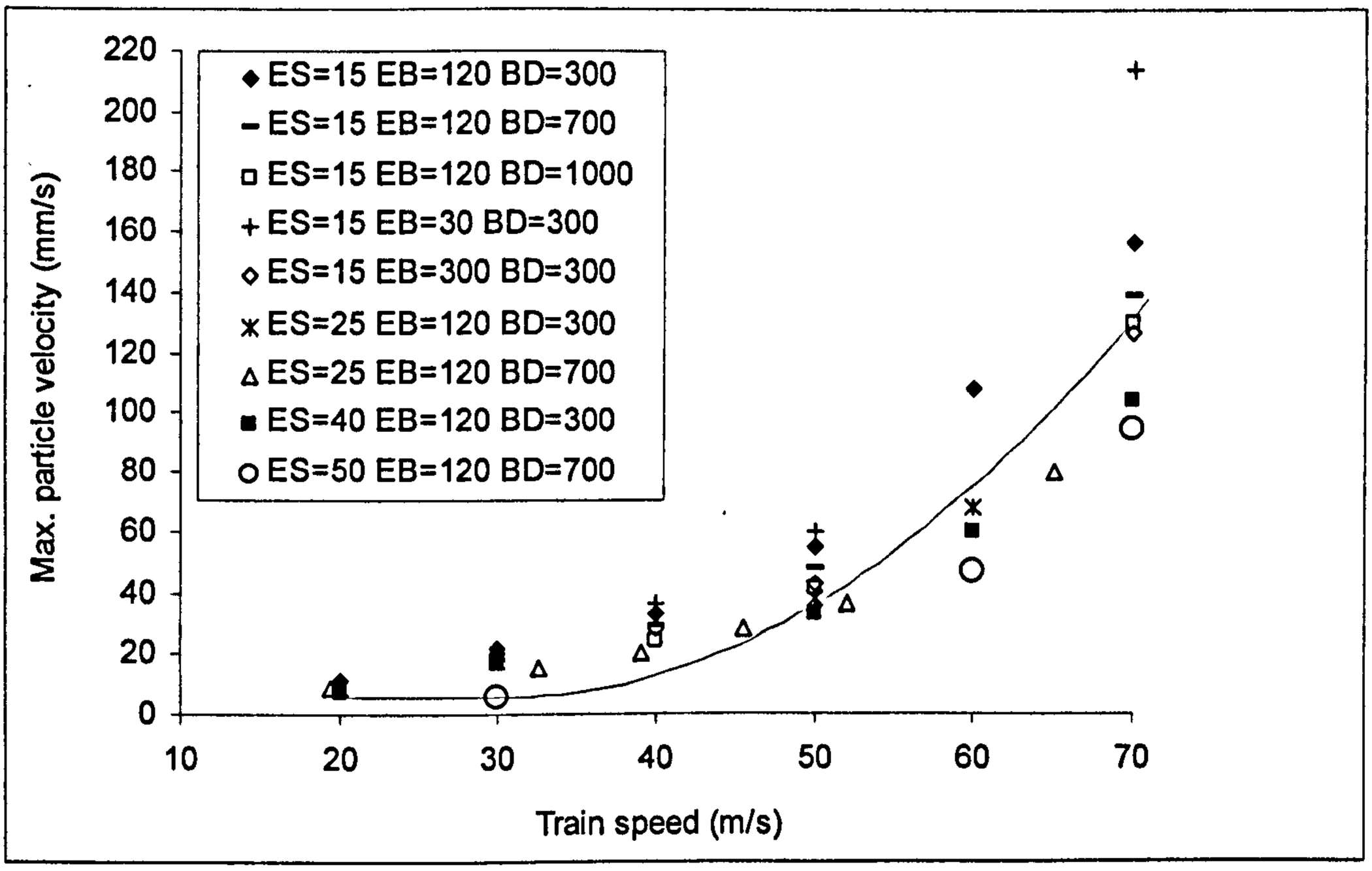

Figure 4.23. Maximum ballast vertical particle velocity versus train speed

Figure 4.24. Maximum ballast vertical particle velocity versus normalized train speed used to classify the maintenance requirement (H.M.: High Maintenance; L.M.: Low Maintenance; S.D.: Sever Deterioration)

different classes with respect to train speed: low maintenance ($V<0.50\ V_r$), high maintenance ($0.50\ V_r < V < 0.70\ V_r$), and severe deterioration ($V > 0.70\ V_r$) regions. These three classes of maintenance levels are denoted by L.M., H.M. and S.D. respectively in Figure (4.24). In terms of track stabilization, if the operational speed is higher than 70% of the critical track velocity, which is mainly affected by subgrade stiffness, ballast layer improvement for conventional ballast structures would probably not be enough. In these situations subgrade treatment is probably a necessity to ensure a safe and reliable track. Potentially the most economical solution would be a combination of both subgrade and ballast treatments. However, for speeds less than 70% of the critical track velocity, ballast treatments would probably fix the potential track geometry problem.

At a specific train speed, the ballast placed over the softer subgrade experiences (generally) higher levels of vibration than ballast over stiffer subgrades, as demonstrated in Figure (4.25). In terms of track dynamics, this suggests a negative effect of subgrade softness on track maintenance requirements. Moreover, according to Figures (4.26) and (4.27), increasing the depth and stiffness of ballast layer in conventional ballasted tracks can reduce the vibration level (in terms of ballast particle velocity). The effect of ballast depth and stiffness on ballast particle velocity seems to be more prominent as the train speed increases.

In terms of stress in the ballast, the deviatoric stress changes in the ballast are presented for different train speeds and track bed conditions in Figures (4.28) and (4.29). As expected, the stress level in the ballast dramatically increases as the train speed approaches the track critical velocity. According to Figure (4.28), the softer the subgrade, the higher the deviatoric stress in the ballast layer for a given train speed. From Figure (4.29), it is also seen that, while the deviatoric stress at a train speed lower than 50% of track critical velocity is about the static value; a considerable rise is observed when the train speed exceeds 70% of the critical velocity. These observations conform well to the classification of track maintenance levels which was made based on maximum ballast particle velocity.

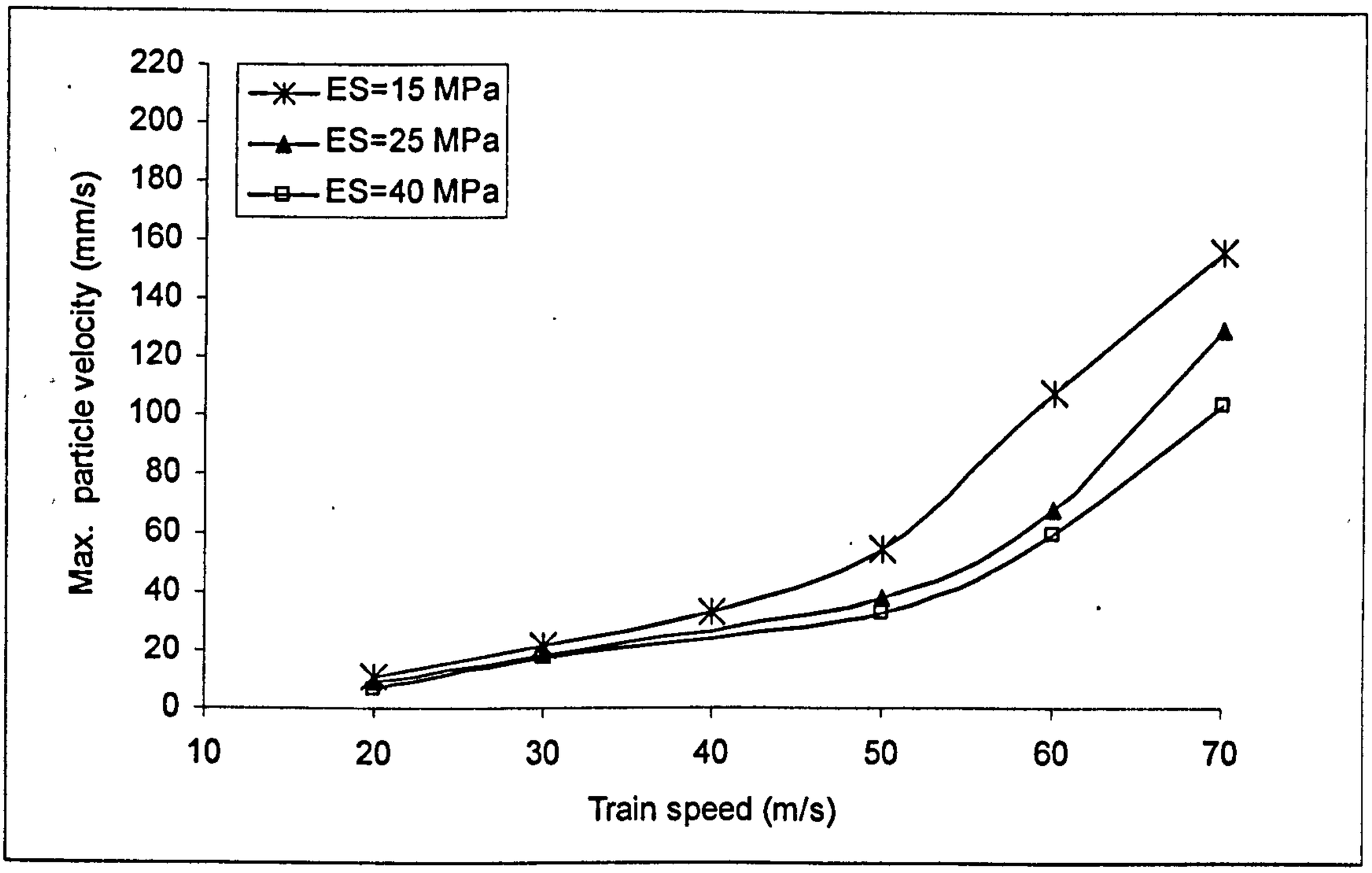

Figure 4.25. Effect of subgrade stiffness on ballast particle velocity (EB=120 MPa, BD=300 mm)

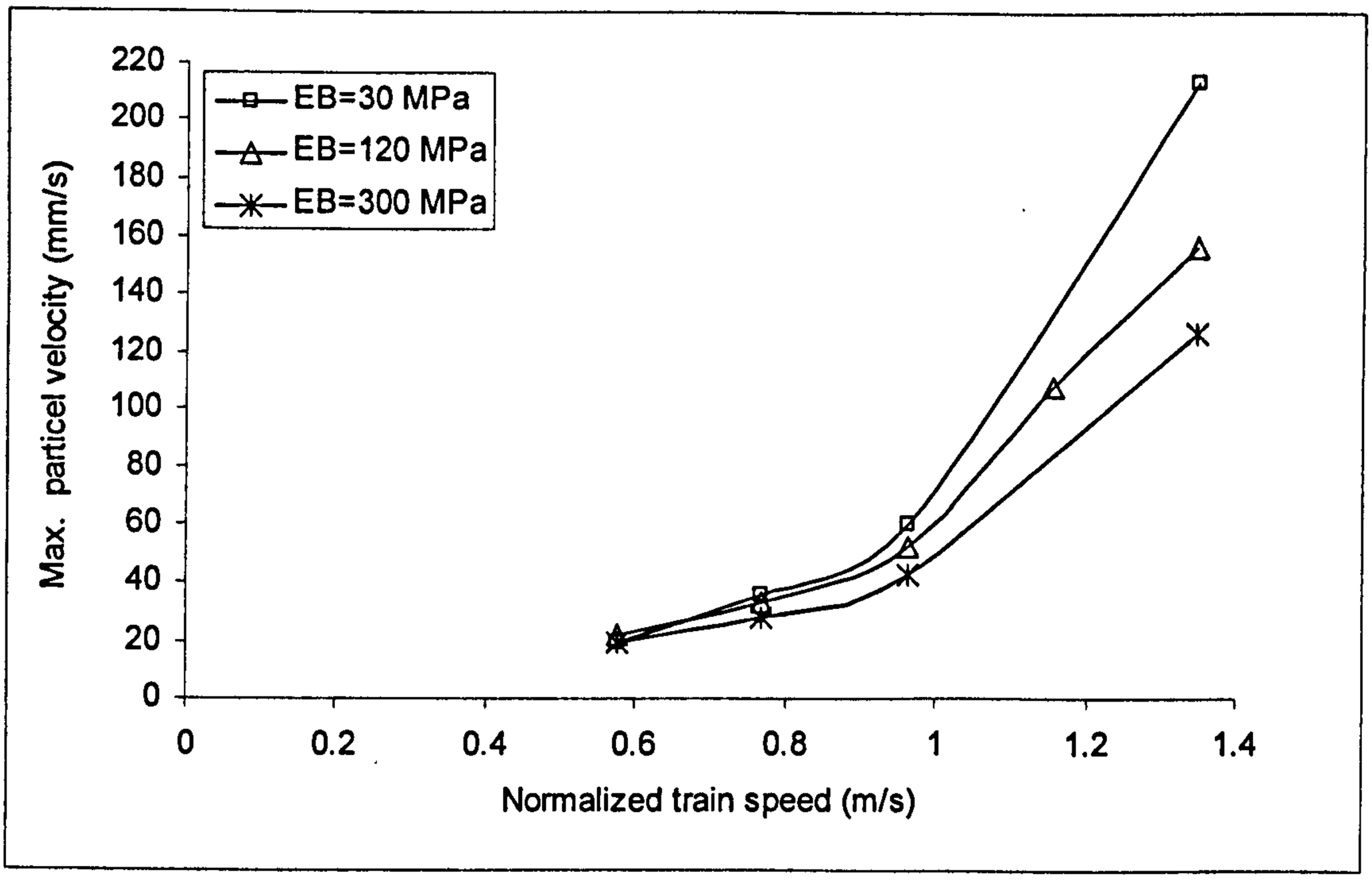

Figure 4.26. Effect of ballast stiffness on ballast particle velocity (ES=15 MPa, BD=300 mm)

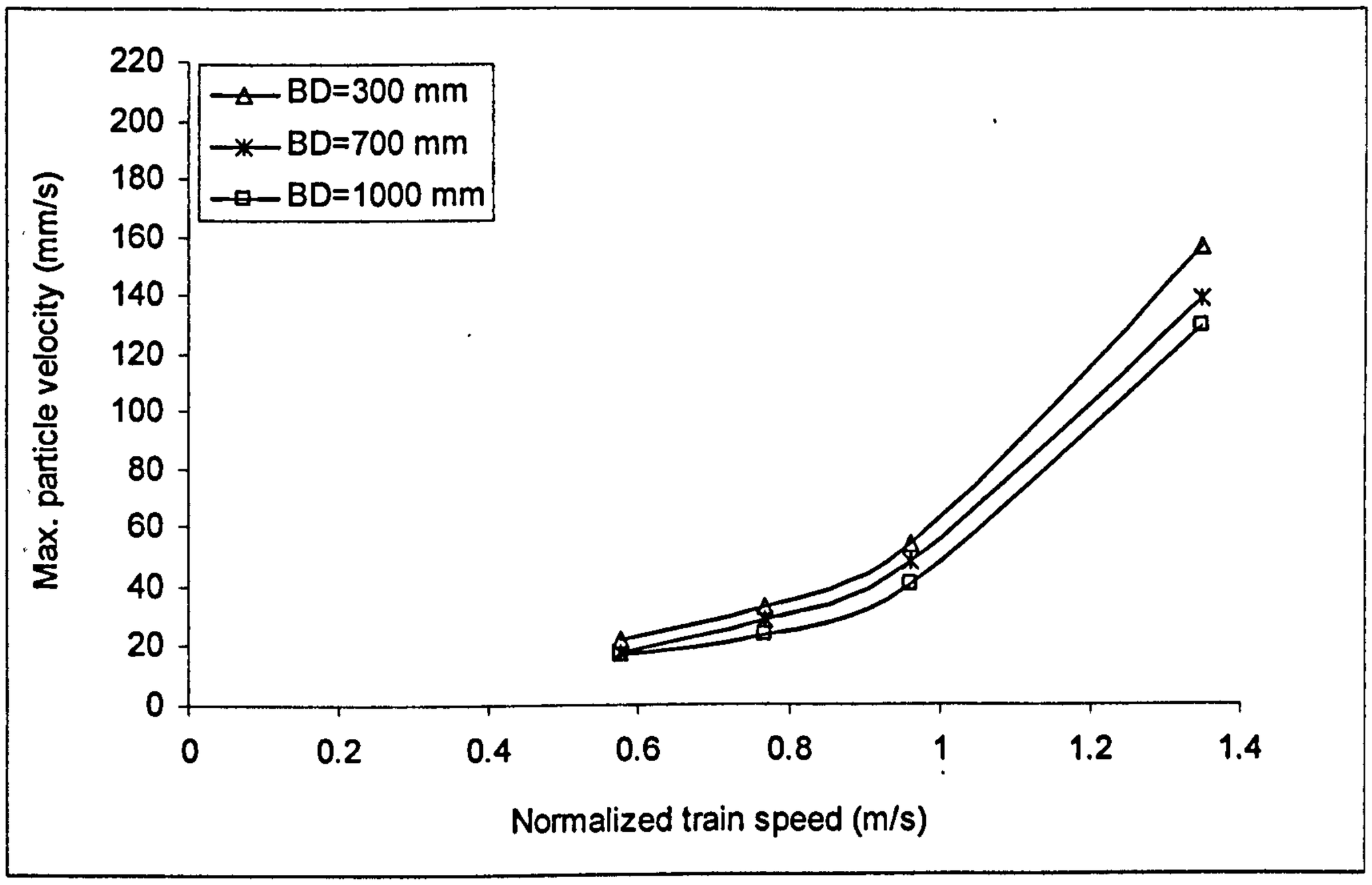

Figure 4.27. Effect of ballast depth on ballast particle velocity (ES=15 MPa, EB=120 MPa)

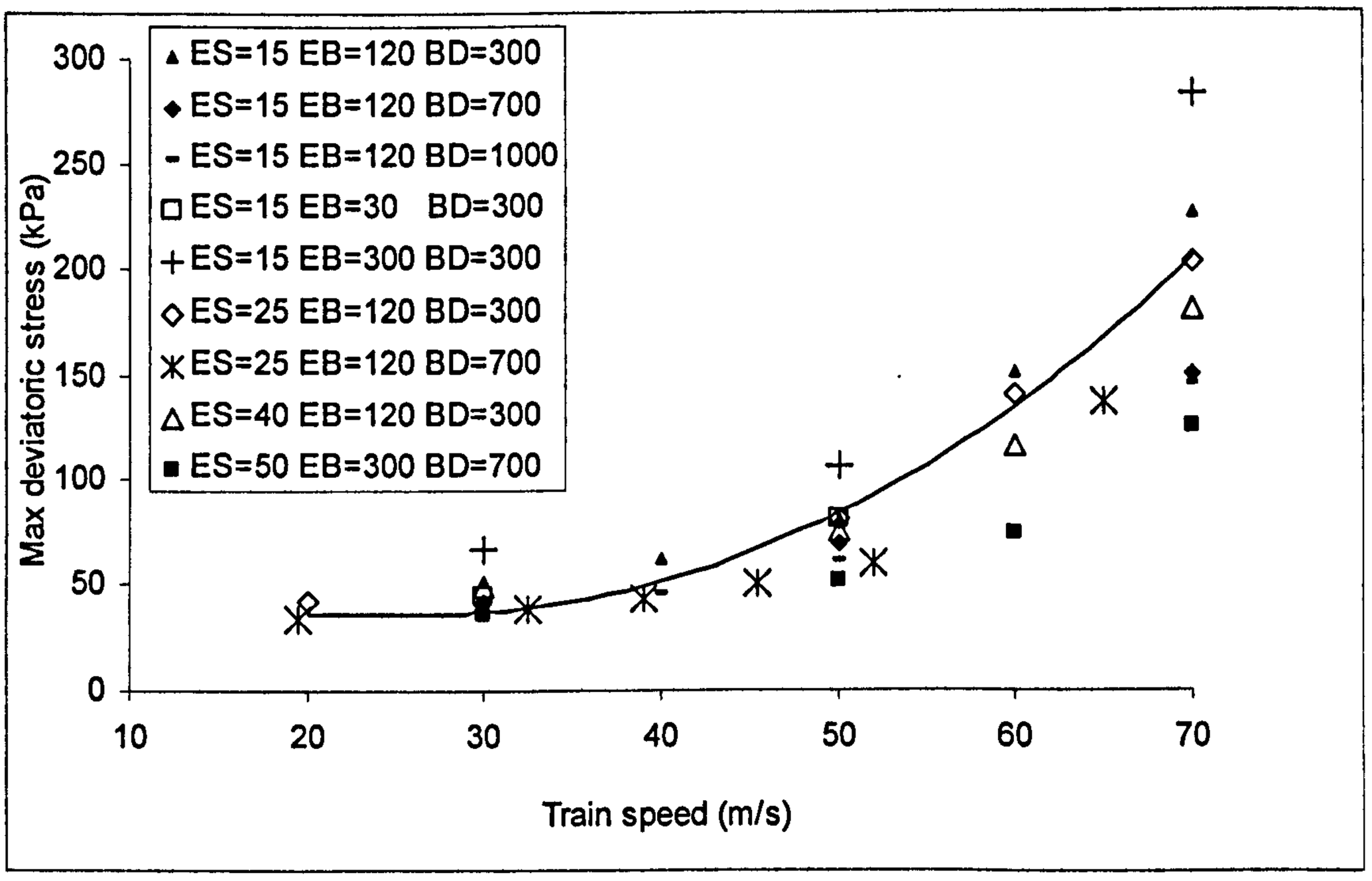

Figure 4.28. Maximum deviatoric stress on top of ballast layer versus train speed

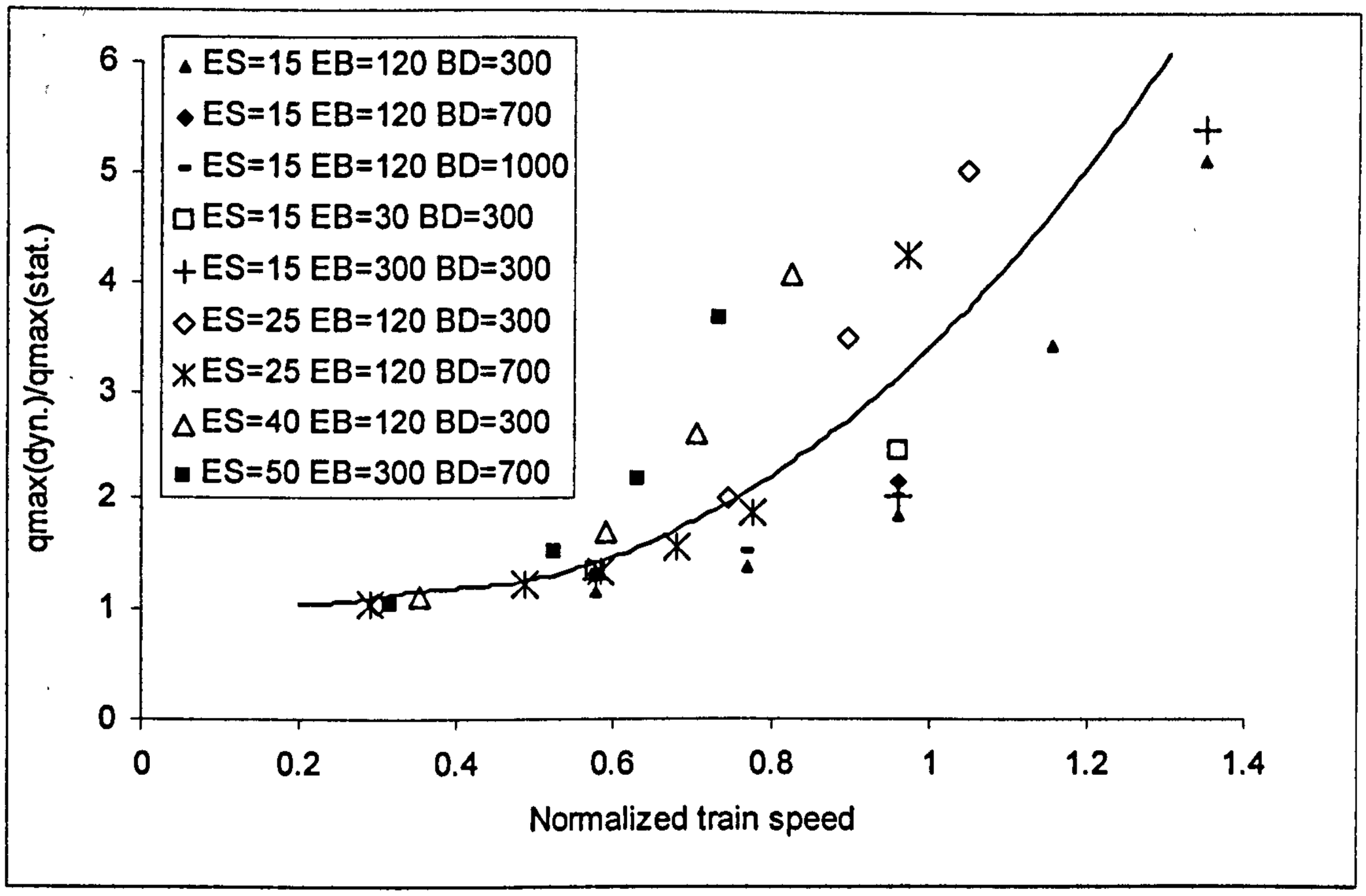

Figure 4.29. Normalized maximum deviatoric stress on top of ballast layer versus normalized train speed

It is well understood that the closer the stress state is to static yield/failure surface in the soil, the higher the permanent deformation generated and subsequently a higher level of maintenance is needed. As the strength of ballast depends significantly on mean (confining) pressure level, the stress ratio (i.e. the ratio of the deviatoric stress to the mean stress) is compared with the Mohr-coulomb criterion, given as the stress ratio for cohesionless granular ballast, to investigate the susceptibility of the ballast layer to permanent settlement. The Mohr-coulomb criterion is given as follows (Smith and Griffith, 1997):

$$\left(\frac{q}{p}\right)_{Mohr-Coulomb} = \frac{3Sin(\phi)}{\sqrt{3}Cos\theta - Sin\theta Sin\phi} \qquad (4.20)$$

where θ and ϕ are Lode and friction angles respectively. The Lode angle is defined as below:

$$\theta = \frac{1}{3} Arc\sin(\frac{-27J_3}{2q^3}) \tag{4.21}$$

where

$$J_3 = S_1 S_2 S_3 \tag{4.22}$$

$$S_i = \sigma_i - p \tag{4.23}$$

$$p = \frac{\sigma_1 + \sigma_2 + \sigma_3}{3} \tag{4.24}$$

$$q = \frac{1}{\sqrt{2}}\left[(\sigma_1 - \sigma_2)^2 + (\sigma_1 - \sigma_3)^2 + (\sigma_2 - \sigma_3)^2\right]^{0.5} \tag{4.25}$$

where σ_{1-3} are principal stress components. p and q are mean and deviatoric stresses respectively. These invariants are defined in such a way as to resemble their counterparts in conventional triaxial conditions. The ratio of induced stress ratio to the stress ratio at plastic yielding, termed here as plastic ratio $(\frac{q}{p}/(\frac{q}{p})_{MC})$ in the ballast layer, can be considered as an indictor of susceptibility of the ballast layer to permanent deformation.

Figure (4.30) presents the plastic ratio distribution in the ballast layer under the coach. As plastic ratio approaches one, i.e. the stress state approaches the yield surface, more plastic deformation is generated and hence more frequent maintenance is required. As clearly seen, the plastic ratio generally increases with train speed. Moreover, the softer the ground is, the higher the level of induced plasticity in the ballast. In other words, an increase in train speed, along with having softer ground, contributes significantly to the permanent settlement in the ballast layer and thus loss of track geometry.

As mentioned before, in a relatively old track, the subgrade exhibits essentially a resilient behaviour. However, if the applied stress is to be changed and approaches the failure

surface, owing to high speed traffic or introducing freight trains (heavy axle trains), plastic deformation may be generated in the subgrade which would affect the track maintenance requirements. As discussed in Chapter 2, the permanent settlement in a clayey subgrade is primarily a function of deviatoric stress and does not significantly depend on mean stress. In addition, according to Li and Selig (1996), if the deviatoric stress (deviator stress in triaxial space) in a clayey subgrade approaches the static strength of the soil, the rate of plastic strain generation would increase dramatically and so would permanent deformation of the track.

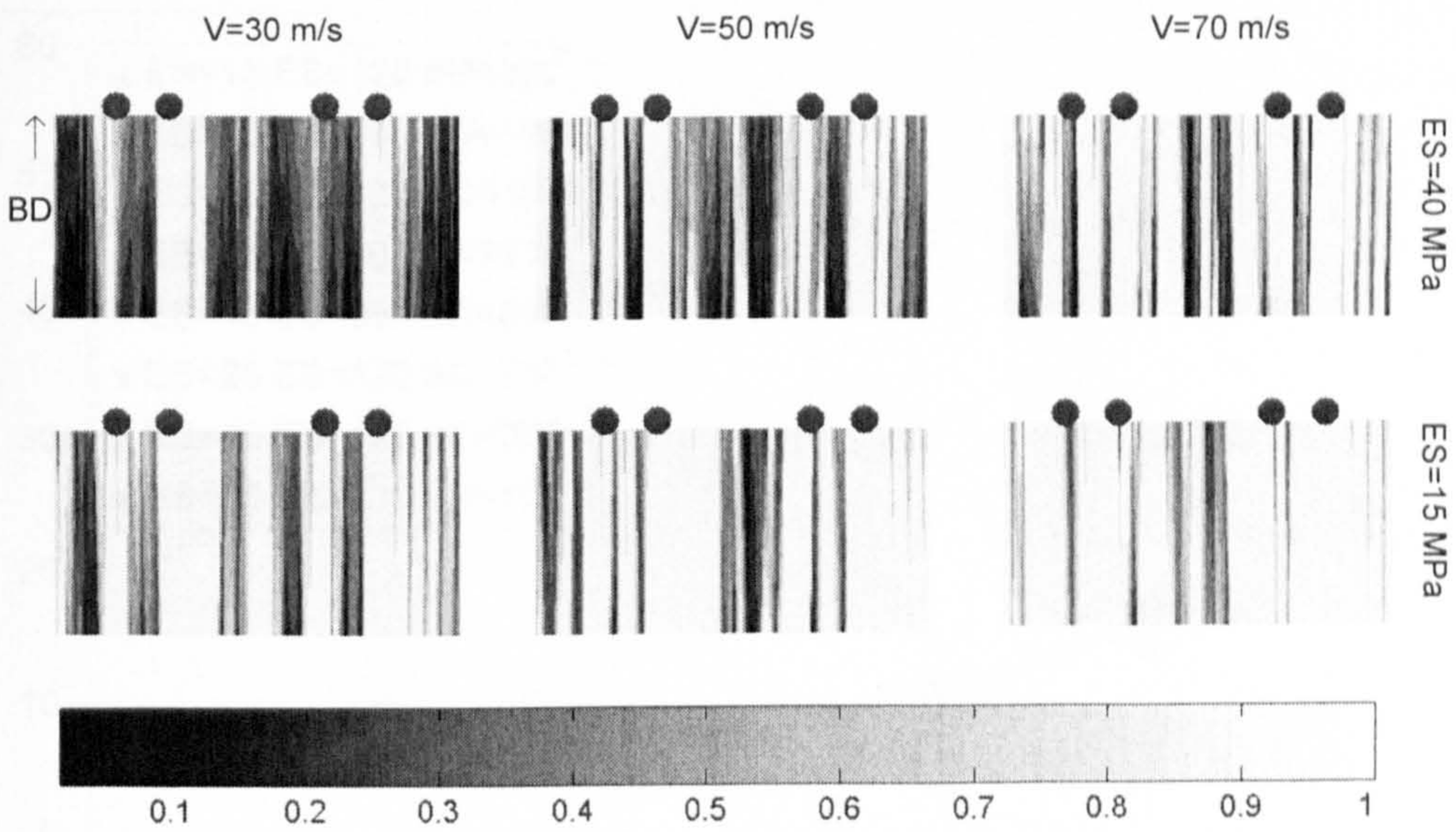

Figure 4.30. Plastic ratio distribution in the ballast layer (BD= 300 mm) under the coach wheels (V=30, 50, 70 m/s) on subgrades with two different stiffness (ES=40 , 15 MPa)

As seen in Figure (4.31), under a high speed regime (V=70 m/s), subgrades under softer ballast (EB=30 MPa, ES=15 MPa, BD=300 mm) experience considerably higher stresses when compared with subgrades under stiff ballast (EB=300 MPa, ES=15 MPa, BD=300 mm). Figures (4.31) and (4.32) also show that increasing the train speed, approaching the track critical velocity, would cause a noticeable increase in the stress level in subgrade, which would generate considerable plasticity in the subgrade over the passage of several trains. It can therfore be concluded that the subgrade of an old track, which has mainly resilient behaviour under low to medium train speed regimes, can start to show

considerable plasticity (and contribute significantly to geometry loss of the track) if the train speed is raised or axle weight is increased. The general trend between deviatoric stress in the subgrade and normalised train speed (Figure 4.32) fits well with the concept of track maintenance classification. The stress is about the static value for V<Vcr (low maintenance region) and dynamic effect starts to appear when the train speed exceeds $0.50V_{cr}$. A considerable rise in the stress occurs when the train speed passes 70% of track critical velocity, which may cause high levels of settlement in the subgrade, contributing to the frequent loss of track geometry (severe deterioration region).

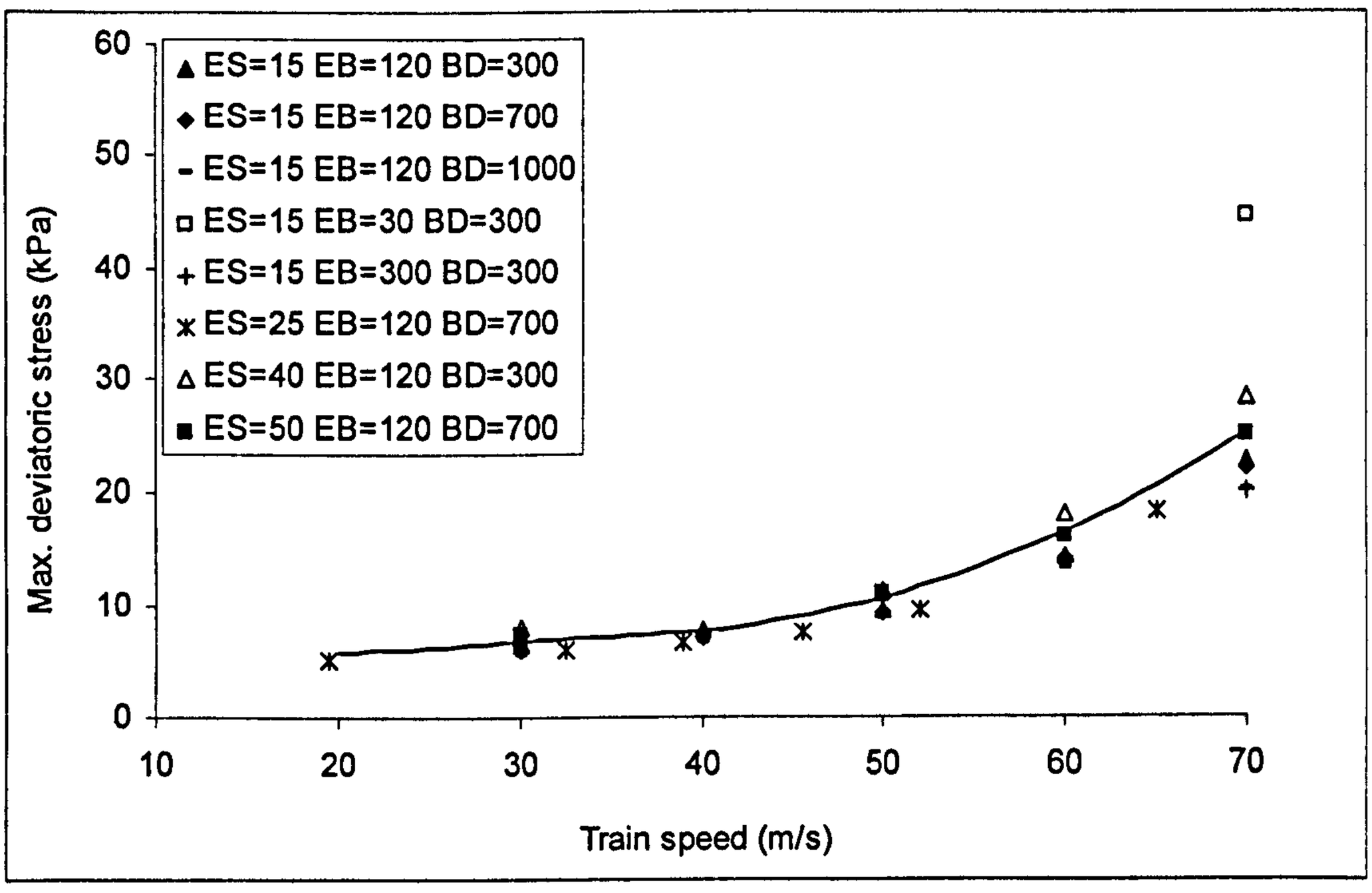

Figure 4.31. Maximum deviatoric stress applied to subgrade versus train speed (Depth=1.8 m)

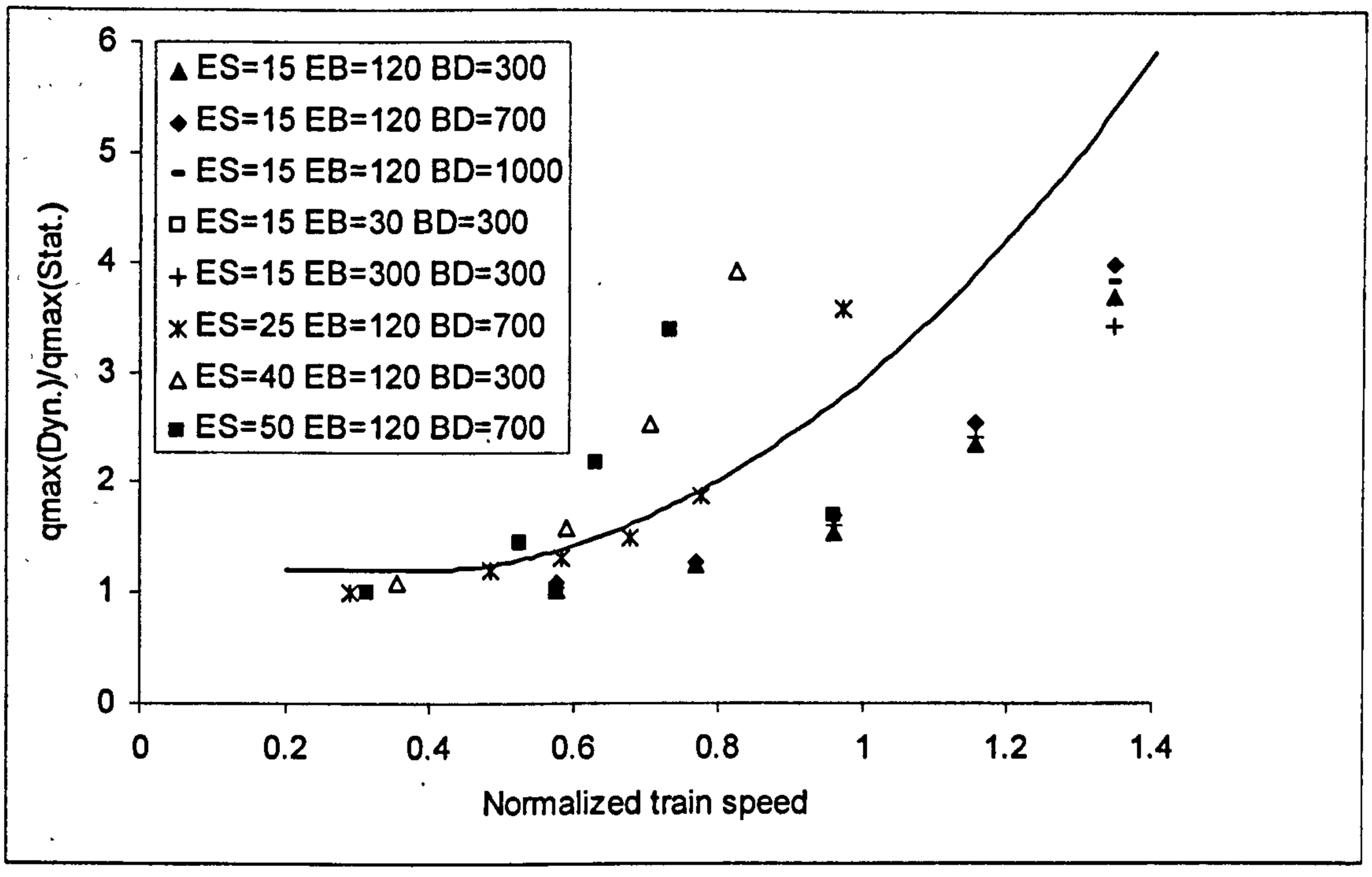

Figure 4.32. Normalized maximum deviatoric stress applied to subgrade versus normalized train speed (Depth=1.8 m)

4.7 Design Implications

The design of railway tracks has been generally empirical/ semi-empirical and has followed different guidelines in different countries. The main objective of such design methods is to protect the subgrade from deterioration (Burrow *et al.*, 2007). The primary modes of traffic-induced deterioration in the subgrade were classified in Chapter 2. Among these, subgrade erosion may be prevented by using appropriately thick sub-ballast layers, and massive shear failure occurs at stresses well above that causing progressive shear failure. Thus the track foundation design methods have been explicitly established on preventing excessive plastic deformation and progressive shear failure in the subgrade (Burrow *et al.*, 2007). Based on this concept, several design procedures have been proposed; some of these have been compared and discussed by Burrow *et al.* (2007). The American Railway Engineering Association (AREA, 1996) recommends several empirical equations to estimate the depth of track bed considering the allowable bearing capacity of subgrade and

vertical stress applied on the ballast surface. It suggests a universal allowable bearing pressure of 138 kPa to be considered for subgrades. These types of equations are, however, oversimplified, not reflecting the varying subgrade conditions, repeated dynamic loading, traffic type and train speed. According to the design procedures proposed by Raymond (1985), instead of using universal safe bearing pressure as recommended by AREA, the Casagrande soil classification system was used to estimate safe bearing pressures for various subgrade conditions. However, the stress in the subgrade was calculated from a homogenous elastic model and the multi-layered nature of railway tracks was not considered in this design approach.

The International Union for Railways (UIC 719 R, 1994) gives a set of recommendations for the design of railway tracks. Track bed layer thickness is determined based on the descriptive quality of subgrade, traffic characteristics and the thickness of the treated subgrade. The British rail method (Heath *et al.*, 1972) was developed to protect excessive plastic deformation in the ballast by limiting the stress level in the subgrade to a threshold value. A single layer homogenous elastic model is used to calculate the stress level in the subgrade. West Japan Railway Standards (WJRC, 2000a and b) determine the required depth of the track bed on the basis of annual tonnage and track types, namely high speed passenger (Shinkansen) and mixed traffic commuter lines. Li and Selig (1998a and b) developed an analytical approach and employed a static multi-layered elastic model, GEOTRACK (Chang *et al.*, 1980), to estimate the stress level in the subgrade, and consequently to estimate the accumulated plastic strain limit and total permanent deformation in the subgrade using an empirical equation. For design purposes, Li *et al.* (1996) suggested that plastic strain and displacement should be limited to 2% and/or 25 mm in the design period respectively. The effect of train speed was considered through an empirical amplification factor which is a function of train speed and wheel diameter (see Section 2.4).

The Network Rail code of practice, NR/SB/TRK/9039 'Formation treatment' (2005) assigns three different levels of dynamic sleeper support stiffness based on track configuration and train speed. The thickness of track bed layers against undrained subgrade modulus is then charted for the stiffness of these three different dynamic sleeper supports. Although not many technical details are given of how the procedure has been developed,

the effect of high train speed (higher than 100 mph) and softness of subgrade has been intuitively accounted for by increasing the minimum dynamic stiffness of track and minimum depth of track bed. Some of these models were discussed and compared by Burrow *et al.* (2007), as given in Table (4.1).

In conventional low-to-medium speed track, the track maintenance level is not typically high for local passenger trains, as discussed in the previous section. On this basis current track bed design procedures concentrate mainly on reducing the stress level and consequently plastic deformation in the subgrade as discussed before. According to the result presented in the previous section, as the train speed increases and approaches the track critical velocity, the level of required maintenance increases considerably, and frequent maintenance of the ballast layer will be needed. In this case, the maintenance level of the ballast should be taken into account in the design procedure. In addition, the speed effect has not been properly addressed in most design procedures; some empirical equations are used to estimate the dynamic load (e.g. Li and Selig, 1998a and b) or some crude recommendations on the minimum dynamic stiffness of railway tracks based on the expected train speed and track type (e.g. NR Code 039). By employing a three dimensional multi-layered track model, it is possible to estimate the stress level and its change with train speed to a reasonable degree of accuracy.

It is also possible to perform parametric studies on the effect of different track configurations on the ballast maintenance level, by considering the vibration and stress level in the ballast, as discussed in detail in the previous sections. As far as the train speed effect is concerned, a quantitative criterion is rarely given, i.e. whether the subgrade itself needs to be treated or not. According to WJRC (2000a and b), if the bearing capacity of subgrade is lower than 288 kPa, ground improvement is required.

NR Code 039 indicates that for train speeds higher than 100 mph, the minimum dynamic sleeper support stiffness (measured by a falling weight deflectometer) needs to be 100 kN/mm/sleeper end. It also reveals that "while it may be possible to make a slight increase in critical velocity by improving the track bed, a significant improvement can be made only by deep ground treatment". It is another area in which a dynamic model can be of great use. As discussed in the previous section, 70% of track critical velocity can be treated as the

speed limit; if the speed needs to be increased further, the subgrade needs to be improved. In this case, improvement of both subgrade and ballast layers may provide an economical option.

Factors	Li and Selig (1998a & b)	UIC 719 R	British Rail	NR code 039	WJRC
Static axle load	Via GEOTRACK	Yes	From an elastic model	N0-but 25.4 T axle load limit on UK network	No
Sleeper type, length and spacing	Via GEOTRACK	Yes	No difference in stresses found for sleeper spacings of 630-790 mm	No	No
Rail section	Via GEOTRACK	No	No	. No	No
Train speed	By using DAF	Yes	No	Via minimum requirement for the dynamic sleeper support stiffness	Crude variation, Shinkansen has greater depth than commuter lines
Annual tonnage	Yes	Yes	Could be incorporated using DAF	No	For commuter lines only
Cumulative tonnage	From annual tonnage multiplied by the design life	No	No	No	No
Subgrade condition	Charts are provided for different subgrade type in terms of the resilient modulus and soil strength	Yes	Using a threshold stress for the material in question	Undrained sub grade modulus or undrained shear strength	Bearing capacity of subgrade assumed to be 288 kPa otherwise ground improvement must be carried out

Table 4.1 Comparison of different available track design procedure (modified from Burrow *et al.*, 2007)

Figure (4.33) proposes a procedure for the design of railway tracks using three dimensional dynamic multi-layered models. The procedure fulfils two main objectives: protecting the subgrade from deterioration and decreasing the level of ballast maintenance.

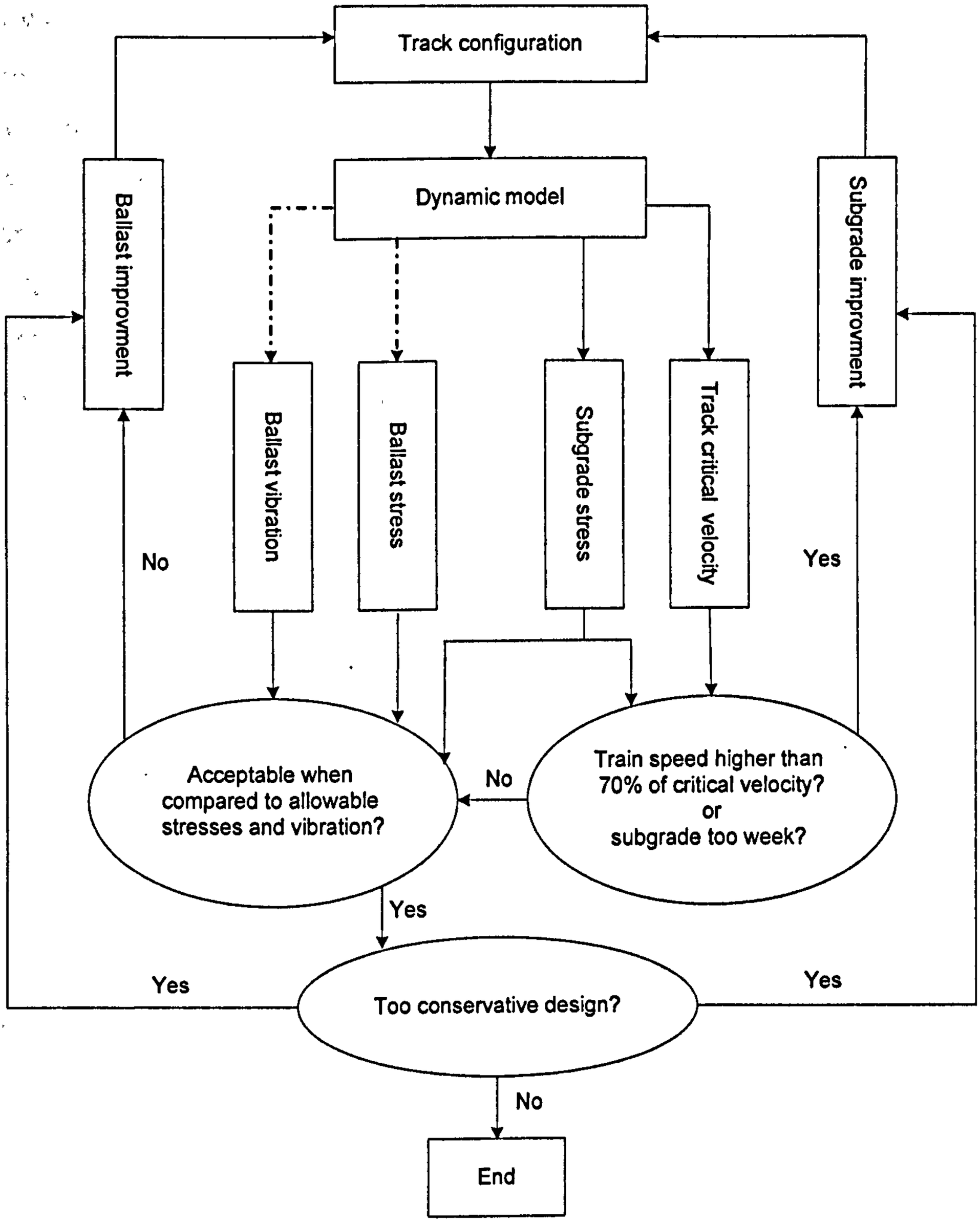

Figure 4.33. Proposed design procedure of a high speed railway track based on the three dimensional finite element model

The first objective can be achieved by limiting the stress in the subgrade to a threshold which is proportional to the failure stress, or limiting the plastic strain or deformation as suggested by Li and Selig (1998a and b); see Chapter 2 for further details.

In order to achieve the second objective, the stress level in the ballast layer may be limited to a threshold to avoid generation of excessive plasticity and consequently rapid loss of geometry which results in high levels of track maintenance. The threshold can be based on the deviatoric stress in the ballast (see chapter 2) or more rigorously based on a plasticity ratio (see Section 4.6). An approach can also be based on limiting the granular layer deformation or strain, both of which are calculated using empirical relationships (see Chapter 2). A rigorous constitutive relationship can also be used to estimate the plastic deformation in the ballast (and subgrade) under repeated dynamic loading caused by traffic. It is the subject of Chapter 7 to explore the application of such an advanced constitutive model.

In addition to stress levels in the ballast, it was identified that the track vibration level in the ballast (in terms of ballast particle velocity) can be used to classify the track maintenance level. Therefore for a properly designed track substructure, the ballast vibration should fall into an acceptable range (e.g. as given before for the ballast particle velocity).

The design procedure presented in Figure (4.33) can be outlined briefly as follows. The track critical velocity is estimated for the present configuration of the track in the first step. The subgrade will need to be improved if either the train speed is higher than 70% of track critical velocity or the subgrade is too weak. The weakness of the subgrade can be judged on the basis of stress or deformation level under the static train load (or low speed). Once the subgrade stiffness is considered to be sufficient, improvement of the ballast layer is designed to limit the stress levels in the ballast & subgrade, and vibration level in the ballast, to an acceptable level. The dynamic model can be used to perform parametric studies on the depth of the subgrade improvement, ballast depth and stiffness (and damping) improvement to offer an optimized design in terms of life-long performance and cost of track.

While for low speed cases ($V<0.50V_{cr}$) the static or pseudo dynamic procedure may be enough, for higher speeds it is necessary to adopt the dynamic design procedure, as outlined above. In a dynamic design procedure, nonlinearity of the subgrade & ballast response and train-track interaction also need to be taken into account. The train–track interaction is especially important, from a geotechnical point of view, in the presence of geometrical irregularities (e.g. welded joint) or structural irregularities (e.g. tracks in the vicinity of bridges and tunnels). Material nonlinearity and train-track interaction will be discussed in the following chapters.

4.8 Conclusion

In this chapter, train speed effects on railway track response were studied using the developed three-dimensional finite element models. The presence of track critical velocity was confirmed and was shown to be around the Rayleigh wave velocity of the subgrade for conventional tracks. The effect of stiffness and depth of the ballast layer on the track response was studied, and an improvement in the track response was indicated, especially as the train speed approaches and passes the track critical velocity. Owing to the degradation of ballast stiffness and the tensionless nature of the ballast, it was argued that the improvement coming from the ballast layer in the high speed range may not be as high as expected.

It was seen that the track response under trains running at a speed lower than 50% of the track critical velocity is essentially static, while as the speed passes 70% of track critical velocity, high levels of vibration and high displacements are observed in the track. 70% of track critical velocity was considered to be an appropriate train speed limit. The trend obtained from the simulations conforms well to the experimental and analytical observations. The effect of train speed on the track maintenance level was studied in terms of the stress level in the subgrade and ballast, and the vibration level in the ballast. Depending on the vibration and stress levels, the required maintenance level was categorized into three regions, namely low maintenance, high maintenance and severe deterioration region. It was found that in the high maintenance zone the treatment of ballast

would probably be enough, whereas in the severe deterioration zone the subgrade also needs to be treated. Based on the present study, a design procedure for high speed track was proposed to limit the subgrade deterioration and maintenance requirement of the ballast layer. The track critical velocity, stress in subgrade and ballast, and the vibration level in the ballast, are assessed to ensure an optimal treatment design for both ballast and subgrade in terms of life-long track performance (longevity) and maintenance cost.

CHAPTER 5

NONLINEARITY IN SUBSTRUCTURE

5.1 Introduction

Railway substructures usually consist of ballast/subballast layers placed on a layered subgrade which is often clay in the UK. Passage of trains will subject the ballast, subballast and subgrade layers to cyclic loading. Under a cyclic loading regime, the deformation behaviour of a soil medium is usually simplified into two separate categories, namely resilient and permanent deformations (Figure 5.1). Resilient response is responsible for instantaneous behaviour of the system to the moving vehicle or train, whereas permanent deformation will affect the long-term performance of the railway track. It is well known that, under typical traffic loading, after a number of load cycles have been applied, the plastic deformation accumulation rate decreases and the soil will start to show mostly resilient behaviour (Figure 5.2). Resilient behaviour is represented by the resilient modulus, which is defined as the repeated deviator stress divided by the recoverable (resilient) axial strain during unloading in the triaxial test (Seed *et al.*, 1962). In track system analyses, resilient behaviour is usually assumed to be linear. However, extensive researches in recent decades have proven nonlinearity in the resilient behaviour and have shown that the resilient modulus of soil (either coarse or fine grained) is significantly affected by several parameters, such as stress/strain state, density and moisture content.

In the present chapter, the factors affecting the resilient behaviour of ballast/subballast and clayey subgrade are reviewed. Several constitutive relationships are presented to capture the resilient nonlinearity, and their implementations in the dynamic finite element model are discussed . The finite element model, with incorporated substructure nonlinearity, is then used to investigate the effect of nonlinearity of the ballast and subgrade on the response of the track and the track maintenance level.

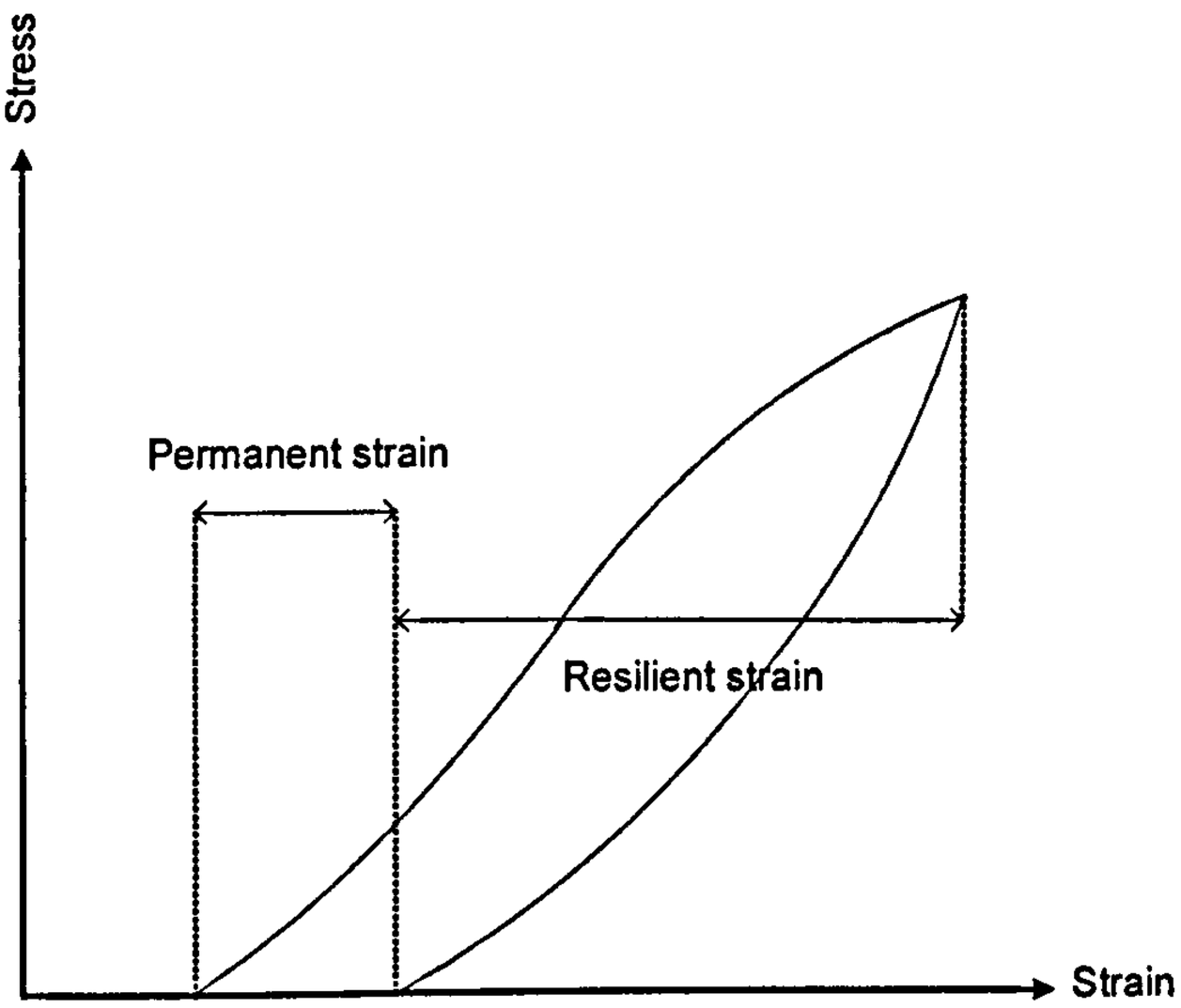

Figure 5.1. Strain in granular soil under cyclic loading (Lekarp *et al.*, 2000a)

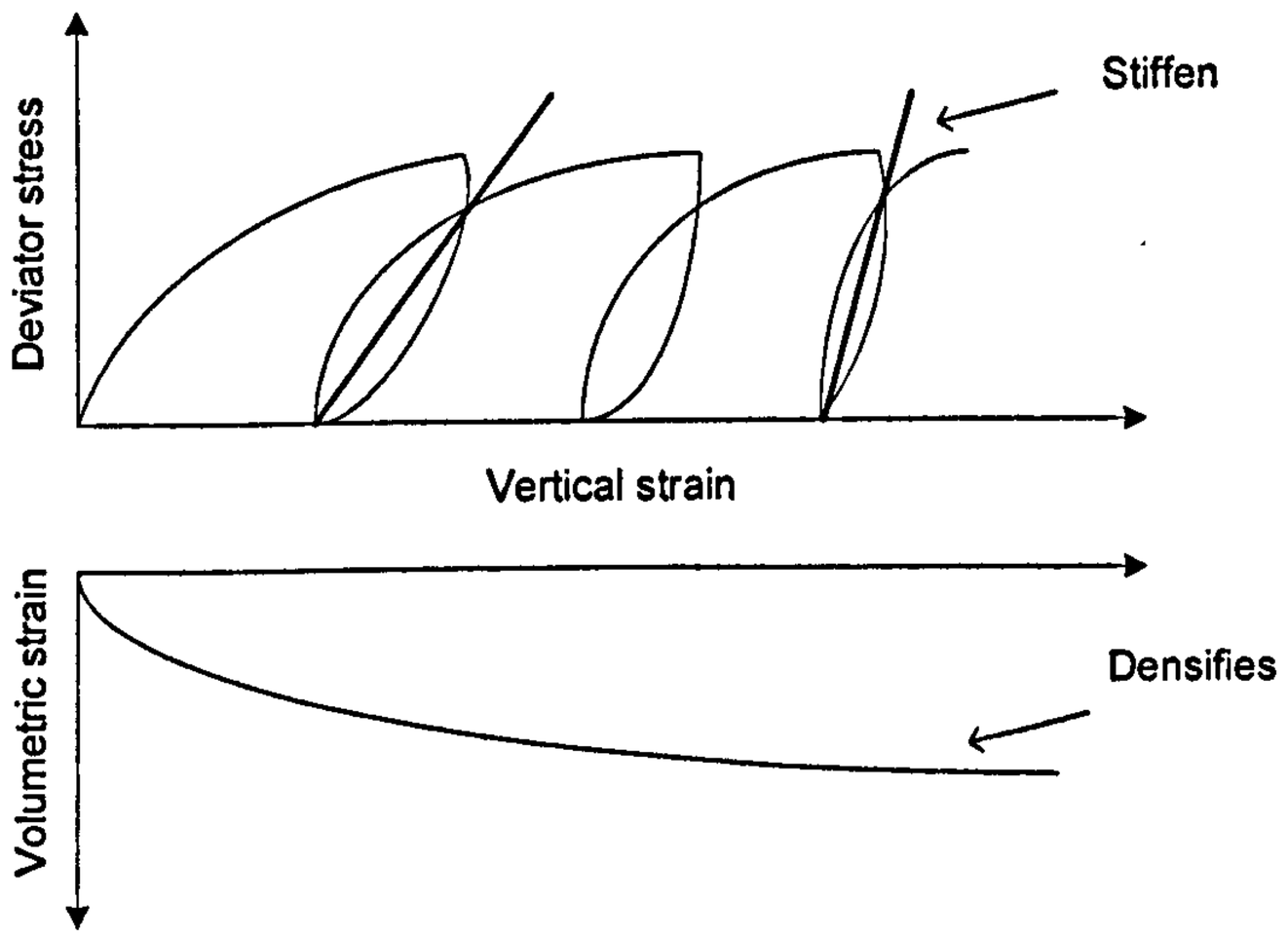

Figure 5.2. Typical behaviour of soil under cyclic loading (Selig and Waters, 1994)

5.2 Nonlinearity in Ballast/Subballast

Granular soils (ballast/subballast) in a well compacted state can properly carry the traffic load and distribute it over underlying layers. The mechanical behaviour of such a soil under repeated traffic loading is very complicated and has been the subject of research for several decades. The nonlinearity in the resilient behaviour of granular soils has also been recognised by researchers and many attempts have been made to develop nonlinear models which reflect the effect of different influencing parameters. The stress-strain state has been recognised as being one of the most influential parameters as far as the resilient behaviour of unbound granular soil is concerned. Many studies suggest a significant dependency of resilient modulus on confining pressure or mean stress (Mitry, 1964; Monismith *et al.*, 1967; Hicks, 1970; Knutson and Thompson, 1977; Uzan, 1985; Sweere, 1990). A typical increase in resilient modulus, with an increase in bulk stress (sum of effective principal stresses), is shown in Figure (5.3).

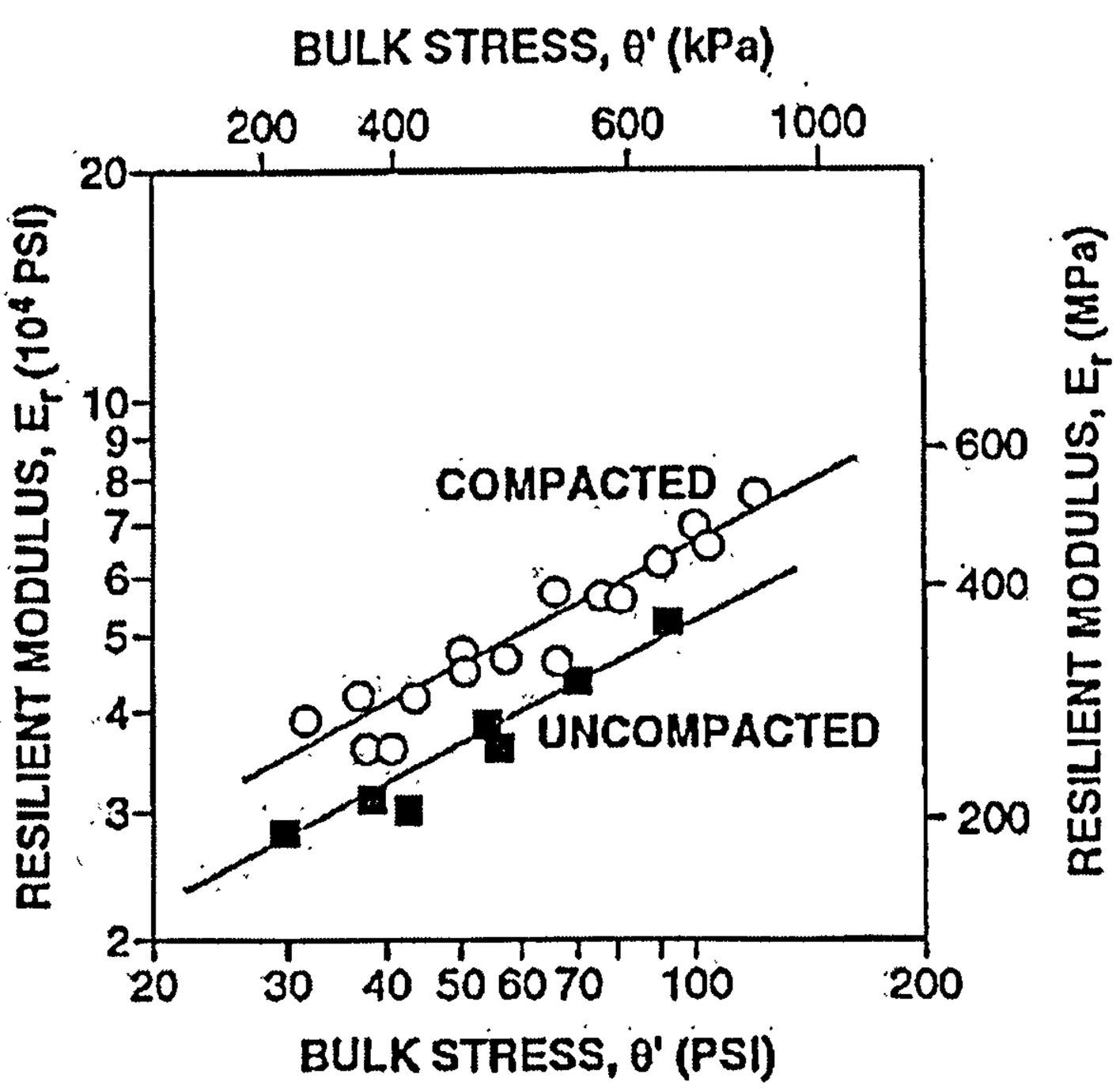

Figure 5.3. Dependence of the resilient modulus of a granular soil on bulk stress (Alva-Hurtado, 1980)

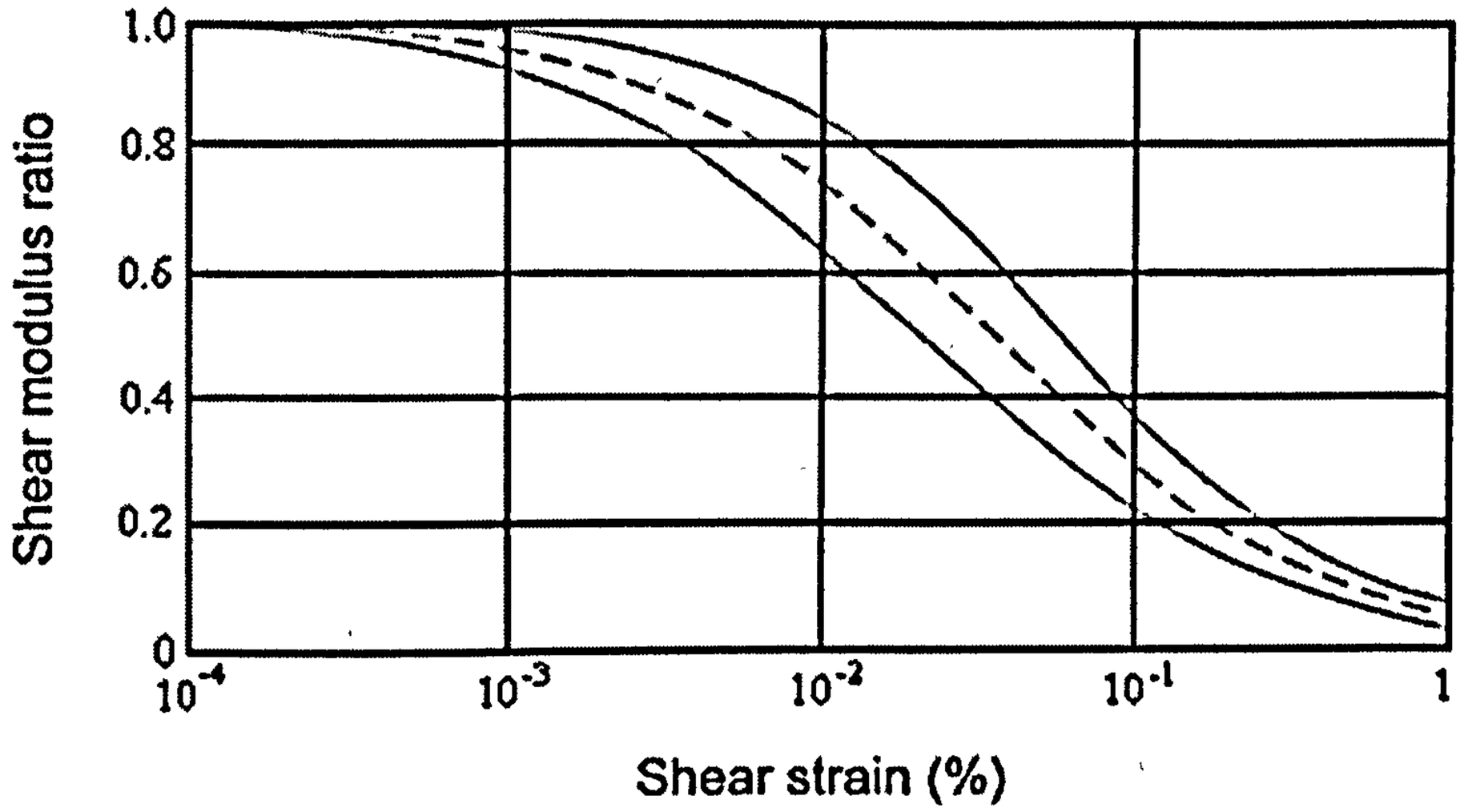

Figure 5.4. Typical reduction in shear modulus with increasing shear strain (Seed and Idriss, 1970)

Strain level is also considered to be an important factor for the stiffness modulus of the soil. It is well known that with increase in the shear strain, or shear stress, the equivalent secant modulus decreases (Figure 5.4) (see equations (5.25-5.27) for shear strain and stress definitions). Two contradictory phenomena may however occur at the same time within the soil, subjected to cyclic loading, namely an increase in the secant bulk modulus with bulk stress and a decrease in the secant modulus with deviatoric stress. Therefore the resilient behaviour of granular soils is governed by the interaction of both mechanisms. Increases in shear (deviatoric) stress or strain do not always imply decreases in the resilient stiffness. Hicks and Monismith (1971), Uzan (1985) and Sweere (1990) reported a slight increase in the resilient modulus with increasing deviatoric stress as long as shear failure is not approached. Brecciaroli and Kolisoja (2006) explained that at a low level of stress, the stiffness of the material increases as the stress increases; the particles are forced into new interlocked positions and the compacted material becomes more closely packed and harder to move. Strain softening is, however, observed as the stress level approaches the failure state (Figure 5.5). Whether strain hardening or softening mechanisms are dominant depends mainly on the level of shear strain/stress to which the granular soil is subjected.

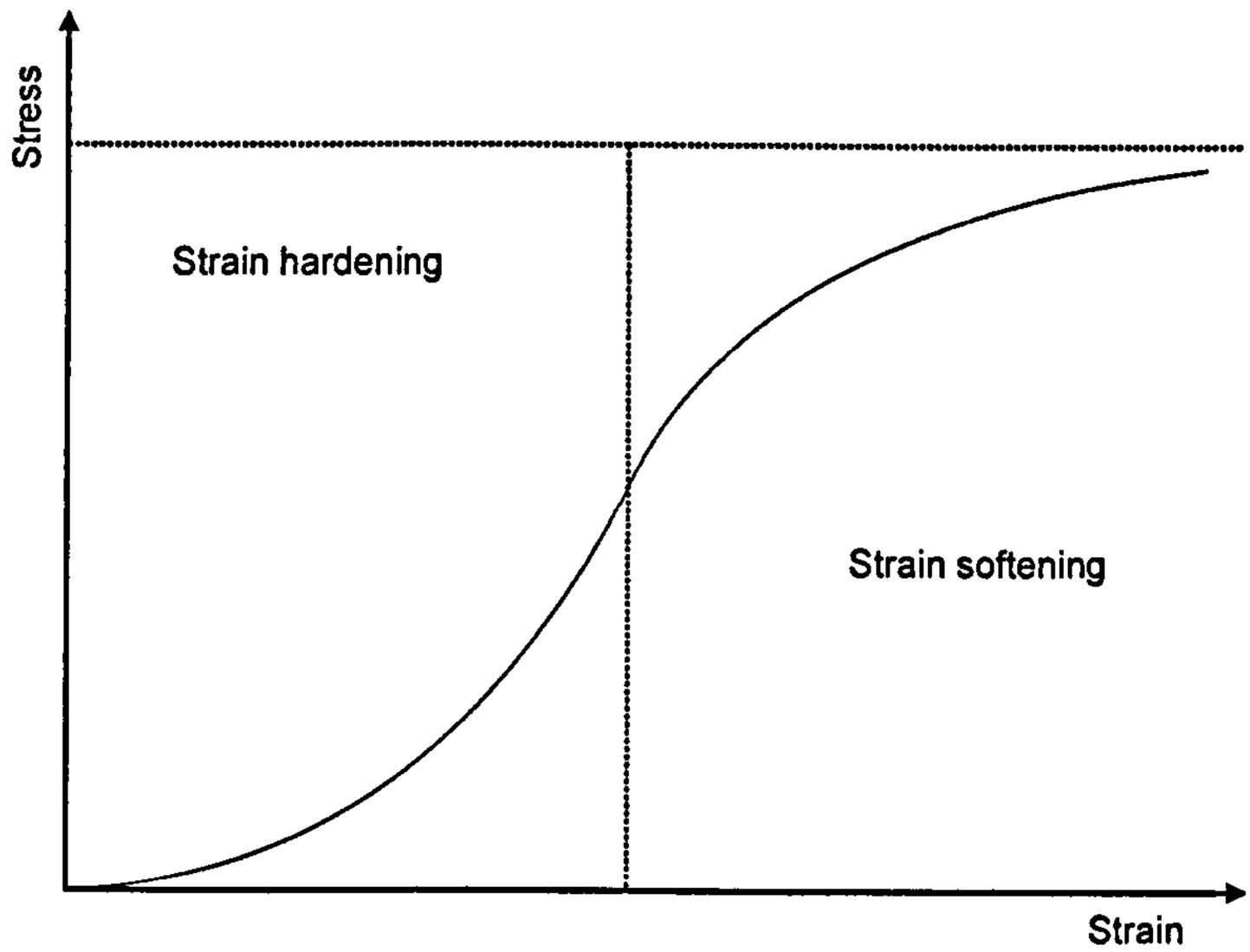

Figure 5.5. Stress-strain behaviour of unbound granular soil (Werkmeister, 2003)

Brecciaroli and Kolisoja (2006) discussed how the loads typically applied to railway embankments have a tendency to locate stress-strain in a region where the modulus increases with bulk stress is more pronounced than a decrease in the modulus value, owing to the increase in shear strain. Note, this might not be the case for ballast/subballast under high speed and/or heavy axle trains, which could experience high deviatoric stresses. In other words, a decrease in resilient modulus with increasing deviatoric stress might be dominant for the cases of high speed or heavy axle loads (depending also on the subgrade).

Kolisoja (1997) described the resilient behaviour of granular soil based on cyclic triaxial tests performed on dense coarse grained aggregate at different axial strain levels (Figure 5.6). After a slight initial decrease in resilient modulus with axial strain, a sharp increase in resilient modulus was observed, followed by a sharp reduction in the value of resilient modulus. The increase in resilient modulus with strain can be explained physically by the dilation concept. In dense granular media, the granular aggregates are densely packed and an increase in shear strain (parallel to an increase in axial strain) makes the aggregates "climb" over each other, which tends to increase the material volume. Such a particle rearrangement in a restrained area can cause an increase in resilient modulus (Uzan, 1985).

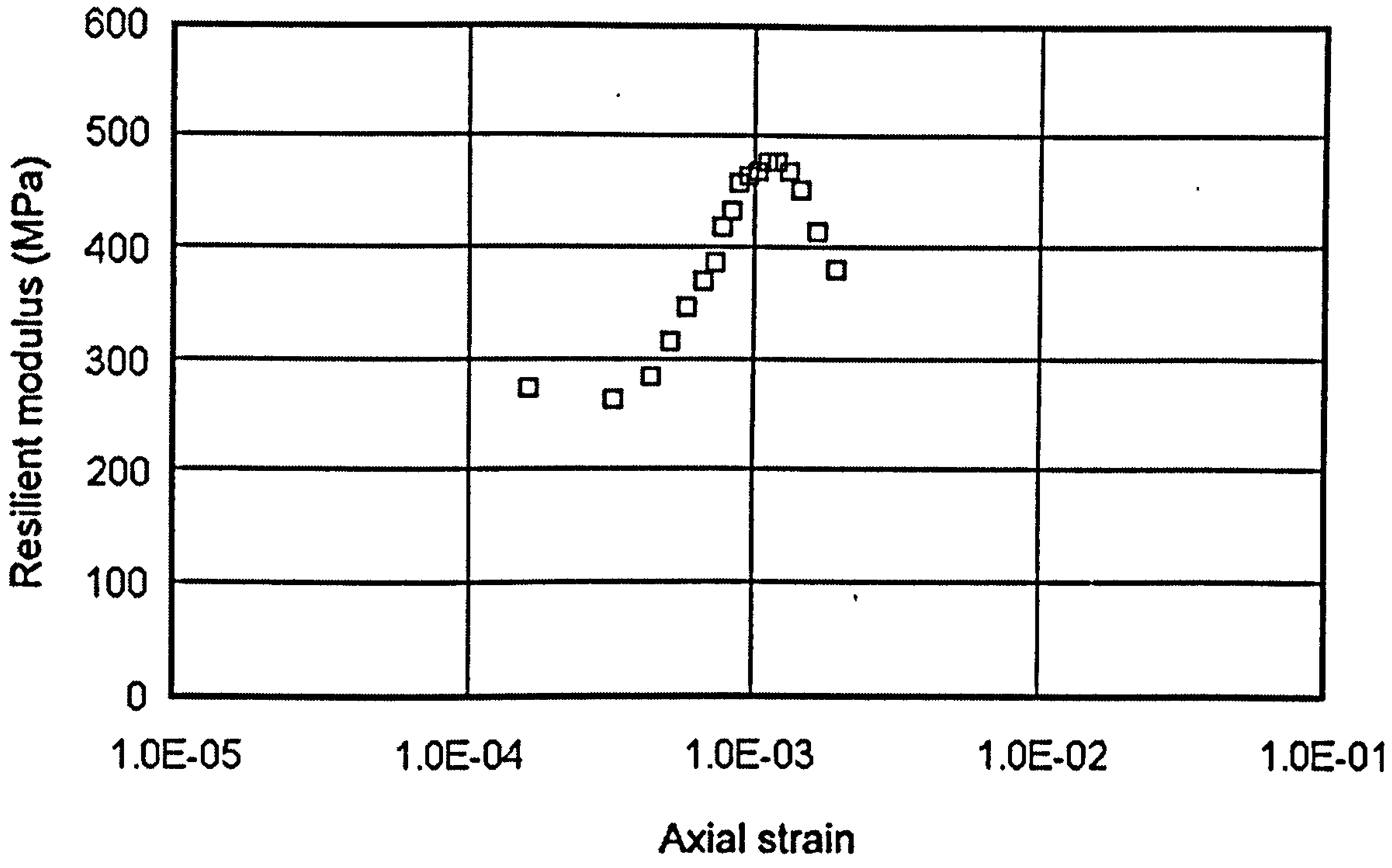

Figure 5.6. Dependence of resilient modulus of a dense coarse granular aggregate on strain level (Kolisoja, 1997)

Furthermore, researches have revealed that the stress history does not have an important effect on resilient response of unbound granular soil as long as the applied stresses are kept sufficiently low to avoid substantial permanent deformation (Hicks, 1970; Allen, 1973; Brown and Hyde, 1975; Mayhew, 1983). It is also accepted that the resilient response of dry and partially saturated granular soils is similar (Lekarp *et al.*, 2000a). However as complete saturation is approached, the resilient behaviour of granular soil may be affected significantly.

It has generally been observed that the resilient modulus decreases with an increase in moisture content (Haynes and Yoder, 1963). Moor *et al.*(1970) observed an increase in resilient modulus with the number of load cycles which was partly attributed to a decrease in the moisture content. However, more detailed research showed that after applying 50 or 100 load cycles, the resilient property of the soil was more or less the same (Hicks, 1970; Allen and Thompson, 1974).

Density is also expected to have a substantial effect on the resilient properties of granular soils. While it is widely agreed that increasing the density improves the stiffness of the granular soil in static loading, there is not such an agreement on the effect of density on the resilient modulus. Some investigations have considered the effect of density as relatively insignificant (Thom, 1988; Thom and Brown; 1988, Brown and Selig; 1991) while others have suggested that the dependency of resilient modulus on density is related to material type. On the other hand, many researchers (e.g. Hicks, 1970; Hicks and Monismith 1971;. Allen and Thompson, 1974; Rada and Witczak, 1981; Kolisoja 1997) observed that the resilient modulus generally increases with increasing density, as given in Figure (5.7). In Figure (5.7) Rc represents relative compaction which is the ratio of sample density to the maximum density as determined by standard compaction. Hicks and Monismith (1971) found the effect of density to be greater for partially crushed than for fully crushed aggregates. They further reported that the effect of density decreased as the fine content of the granular material increased. Vuong (1992) mentioned that at densities above the optimum value, the resilient modulus is not very sensitive to density changes. Kolisoja (1997) explained the increase in resilient modulus with density as follows: the number of particle contacts per particle increases greatly with increased density resulting from additional compaction of the particle system. This, in turn, decreases the average contact stress corresponding to a certain external load. Hence, the deformation in particle contacts decreases and the resilient modulus increases.

Poisson's ratio may also be affected by the soil physical and stress state. Hicks (1970) and Hicks and Monismith (1971) reported slight reductions in Poisson's ratio with an increase in moisture content. The level of density also seems to have some effect on Poisson's ratio. While some researchers have reported a slight decrease in Poisson' ratio with increases in density (Hicks and Monismith, 1971; Kolisoja, 1997) , others (e.g. Allen and Thompson, 1974) have considered the density effect on Poisson's ratio negligible. Conducting cyclic triaxial tests on alluvial sandy soils, Yokota and Konno (1980) demonstrated that the Poisson's ratios of these soils are in a range between 0.2 and 0.4. They also showed that Poisson's ratio tends to increase slightly with increasing magnitudes of shear strain, whereas the effect of confining pressure was found to be negligible. Lade and Nelson (1987) cited a series of cyclic triaxial tests on dry Hostun sand conducted by El Horsi (1984). According to El Horsi (1984) Poisson's ratio was found between 0.18 and 0.23, and

Poisson's ratio was constant under a low strain cyclic regime. Reviewing available experimental studies, Lade and Nelson (1987) concluded that Poisson's ratio can be assumed to be constant in modelling the elastic (resilient) behaviour of a given soil.

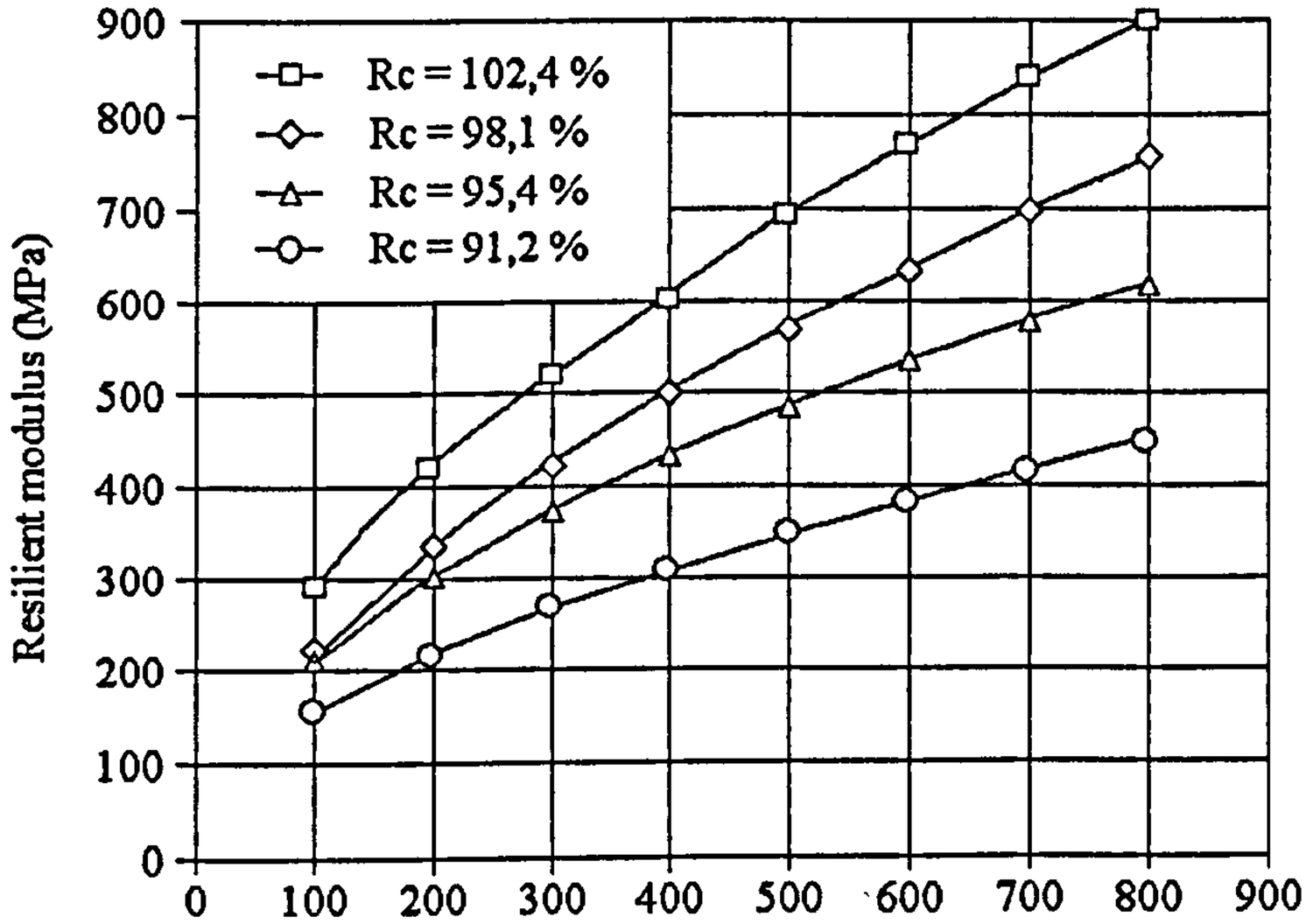

Figure 5.7. Resilient modulus of granular soil for different levels of compaction (Kolisoja, 1994)

At a given physical state (grading-density and moisture content and assuming they remained unchanged), the nonlinear resilient behaviour of granular soil can be formulated based solely on stress or strain parameters. Two different approaches are employed for computational modelling of the resilient behaviour of granular soils (Lekarp *et al.*, 2000a): In the first approach, the stress-strain relationship is formulated through a stress/strain dependent resilient modulus and a constant/varying stress/strain dependent Poisson's ratio. These types of models, which are widely used in pavement engineering, have been basically curve-fitted to experimental data. The second approach has a more theoretical base and characterised the resilient behaviour by decomposing both stresses and strains into volumetric and shear components. Instead of directly defining the resilient modulus and Poisson's ratio, the material behaviour is initially characterized by shear and bulk modulus. The application of the volumetric-shear approach is advantageous from the theoretical point

of view, and has more physical meaning than the resilient modulus and Poisson's ratio (Lekarp *et al.*, 2000a). These kinds of models are usually more complex in nature and possess more parameters which inhibit their use (considering the often limited available experimental data).

Before reviewing some of available nonlinear models, the strain-stress invariants are defined first (Equations 5.1 and 5.2 are replicated from Equations 4.24 and 4.25 respectively):

$$p = \frac{\sigma_1 + \sigma_2 + \sigma_3}{3} \tag{5.1}$$

$$q = \frac{1}{\sqrt{2}}\left[(\sigma_1 - \sigma_2)^2 + (\sigma_1 - \sigma_3)^2 + (\sigma_2 - \sigma_3)^2\right]^{0.5} \tag{5.2}$$

$$\varepsilon_v = \varepsilon_1 + \varepsilon_2 + \varepsilon_3 \tag{5.3}$$

$$\varepsilon_q = \frac{\sqrt{2}}{3}\left[(\varepsilon_1 - \varepsilon_2)^2 + (\varepsilon_1 - \varepsilon_3)^2 + (\varepsilon_2 - \varepsilon_3)^2\right]^{0.5} \tag{5.4}$$

where p and q are the mean and deviatoric stresses respectively. ε_v and ε_q are the volumetric and deviatoric strains respectively. σ_{1-3} and ε_{1-3} are the principal stress and strain components. These invariants are defined such that they resemble their counterparts in conventional triaxial conditions. Bulk and shear modulus are then defined as below:

$$K = \frac{p}{\varepsilon_v} \tag{5.5}$$

$$G = \frac{q}{3\varepsilon_q} \tag{5.6}$$

The oldest and most popular model relate the resilient modulus to bulk modulus through a power relationship, known as the $K-\theta$ model (Seed *et al.*, 1967; Brown and Pell, 1967; Hicks and Monismith, 1971):

$$E_r = k_1 p_{atm} \left(\frac{3p}{p_{atm}} \right)^{k_2} \tag{5.7}$$

k_1 and k_2 are material parameters. p_{atm} is atmospheric pressure (100 kPa). This equation has been extensively used and implemented in the computational analysis and design of pavements. In spite of that, Uzan (1985,1992) pointed out that the application of $K-\theta$ model is limited as this model neglects the effect of shear stress. He introduced a generalized relationship which considers the shear stress level and the mean stress level on the resilient behaviour simultaneously, which is named a universal model:

$$E_r = k_1 p_{atm} \left(\frac{3p}{p_{atm}} \right)^{k_2} \left(\frac{q}{p_{atm}} \right)^{k_3} \tag{5.8}$$

where k_1, k_2 and k_3 are the model parameters. Assigning a negative or positive value to k_3 can model the softening or hardening effect of shear stress on the resilient modulus. It is considered an appropriate model in modelling granular material behaviour and has been shown to be superior to the $K-\theta$ model in several studies (Witczak and Uzan 1988; Kolisoja, 1997). Although these types of models exhibit different degrees of success in experimental and numerical work, they do not satisfy the basic elasticity assumption; they are not conservative; i.e. the dissipated energy during a complete load cycle is not zero. In other words, the loading stress-strain path does not necessarily coincide with the unloading path and therefore hysteretic damping is present (see Figure 3.12). In order to have a conservative elastic model, the theorem of reciprocity must be satisfied (Boyce, 1980), i.e.

$$\frac{\partial \varepsilon_v}{\partial q} = \frac{\partial \varepsilon_q}{\partial p} \tag{5.9}$$

Based on this theorem, Boyce (1980) proposed a non-linear elastic model and decomposed the granular soil response into volumetric and deviatoric parts. According to Boyce (1980), the bulk modulus (K) and the shear modulus (G) are given as follows:

$$K_r = \frac{p_a}{\frac{1}{k_a} - \frac{\beta}{k_a}(\frac{q}{p})^2} (\frac{p}{p})^{1-n} \tag{5.10}$$

$$G_r = G_a(\frac{p}{p_a})^{1-n} \tag{5.11}$$

k_a, G_a and n are the model parameters and β is defined as below:

$$\beta = \frac{(1-n)k_a}{6G_a} \tag{5.12}$$

Volumetric and deviatoric strains are therefore expressed as below:

$$\varepsilon_v = \frac{1}{k_a} p_{atm}^{1-n} p^n \left[1 - \beta(\frac{q}{p})^2\right] \tag{5.13}$$

$$\varepsilon_q = \frac{1}{3G_a} p_{atm}^{1-n} p^n (\frac{q}{p}) \tag{5.14}$$

The Boyce model can also be expressed by Young's modulus E and Poisson's ratio ν (Correia, 2004):

$$E_r = \frac{9G_a(\frac{p}{p_a})^{1-n}}{3 + (\frac{G_a}{k_a})\left[1 - \beta(\frac{q}{p})^2\right]} \tag{5.15}$$

$$\nu = \frac{\frac{3}{2} - \left(\frac{G_a}{k_a}\right)\left[1 - \beta(\frac{q}{p})^2\right]}{3 + (\frac{G_a}{k_a})\left[1 - \beta(\frac{q}{p})^2\right]} \tag{5.16}$$

The Boyce model imposes a certain relationship between the deviatoric and volumetric response (based on reciprocity theory) which limits the number of model parameters to three. Correia (2004) discussed the application of Boyce's elastic constitutive relationships and suggested that the basic Boyce model gives reasonably good predictions for isotropic materials, while the anisotropic version as proposed by Hornych *et al.*(1998) appear to perform better in general cases. Reviewing a number of nonlinear resilient models for granular soils, Lekarp *et al.* (2000a) argued that the elasticity of the Boyce model is an important disadvantage. When a granular soil is subjected to cyclic loading , assuming the stress-strain behaviour is resilient, the loading and unloading part of the stress-strain curve do not coincide and therefore energy is dissipated (hysteretic dissipation). This is by definition an inelastic response. Sweere (1990) stated that the solution to the problem lies in removing the coupling of volumetric and deviatoric strains by the theorem of reciprocity (Equation 5.9).

Pappin and Brown (1980) developed the contour model decomposing volumetric and deviatoric responses. Based on the contour model, the volumetric strain depends on the maximum values of stress, while the deviatoric strain depends on the stress path length (in addition). Assigning two separate sets of parameters to volumetric and deviatoric relationships assured the inelasticity of response while giving more flexibility to curve-fitting the experimental data. Mayhew (1983) applied a similar approach and showed that stress path dependence has no major impact on deviatoric response. By removing the stress path dependence, the equations of the contour model turn into an inelastic modified version of the Boyce model, as suggested by Sweere (1990):

$$\varepsilon_v = \frac{1}{k_a} p_{atm}^{1-n} p^n \left[1 - \beta(\frac{q}{p})^2\right] \tag{5.17}$$

$$\varepsilon_q = \frac{1}{3G_a} p_{atm}^{1-m} p^m (\frac{q}{p}) \tag{5.18}$$

where n, m, k_a, G_a and β are the model constants. Volumetric and shear modulus can then be expressed as below:

$$K_r = \frac{(\frac{p}{p_a})^{1-n}}{\frac{1}{k_a} - \frac{\beta}{k_a}(\frac{q}{p})^2} \tag{5.19}$$

$$G_r = G_a (\frac{p}{p_a})^{1-m} \tag{5.20}$$

Sweere (1990) reported quite satisfactory predictions of both shear and volumetric strains based on the proposed approach.

5.3 Nonlinearity in Clayey Subgrade

It is well-known that the resilient behaviour of subgrade soil changes under different loading and environmental conditions. Li and Selig (1994) and Lee *et al.* (1997) classified the factors influencing the resilient modulus into three different categories: (1) Loading condition or stress state; (2) soil type and its structure, which primarily depends on the compaction method and effort; (3) soil physical state which is defined by water content and dry density. Elfino and Davidson (1989) studied the effect of water content variation on resilient modulus of clayey soil. They reported an increase in the resilient modulus with a decrease in water content which was mainly attributed to an increase in matric suction as the water content decreased. A detailed study of experimental results by Li and Selig (1994) also indicated that increasing moisture content leads to a significant decrease in soil stiffness. Thompson and Robnett (1979) related the resilient modulus of clayey subgrades to unconfined compressive strength, revealing an increase in the resilient modulus with increasing unconfined compressive strength. They also demonstrated that the degree of

saturation has a significant effect on the resilient modulus of clayey subgrade; at a given density an increase in the degree of saturation considerably decreased the resilient modulus. According to their experimental studies, an increase in relative density was also found to increase the resilient modulus (Thompson and Robnett, 1979). Gudishala (2000) conducted a series of cyclic triaxal tests on the clay sample under different moisture contents and dry density. He demonstrated that the curve representing the resilient modulus mimics the compaction test curve. For a given soil as the moisture content increased towards the optimum moisture content, followed by an increase in dry density, the resilient modulus increased. It decreased as the moisture content increased further and passed the optimum moisture content (which was followed by a decrease in the dry density).

Sneddon (1988) conducted resilient modulus tests for sand and fine-grained soils. While the resilient modulus of sand is a function of confining and deviatoric stress, the resilient modulus of fine-grained soil is mainly a function of the applied deviatoric stress. Several studies (e.g. Seed *et al.* 1962; Sneddon, 1988; Li and Selig, 1994; Frost *et al.*, 2004) show that the resilient modulus of clay decreases with deviatoric stress and a low asymptotic value is observed at higher deviator stress (Frost *et al.*, 2004), see Figure (5.8). S1-9 in Figure (5.8) denotes the clay sample with different moisture contents as was given in Figure (2.7). The number of load cycles has some minor effect but, similar to granular soil, the resilient model tends to become constant with the increasing number of cycles; it densifies to a resilient state. Therefore, constitutive relationships are primarily established between the resilient modulus and deviatoric stress. Thompson and Robnett (1979) proposed a "bilinear model":

$$E_r = K_1 p_a + K_2 q \qquad q < q_i \tag{5.21}$$

$$E_r = K_1 p_a + K_2 q \qquad q > q_i \tag{5.22}$$

where q is the deviatoric stress and p_a is atmosphesic pressure. K_{1-4} are model constants and q_i is the deviatoric stress at which the slope of E_r versus q changes.

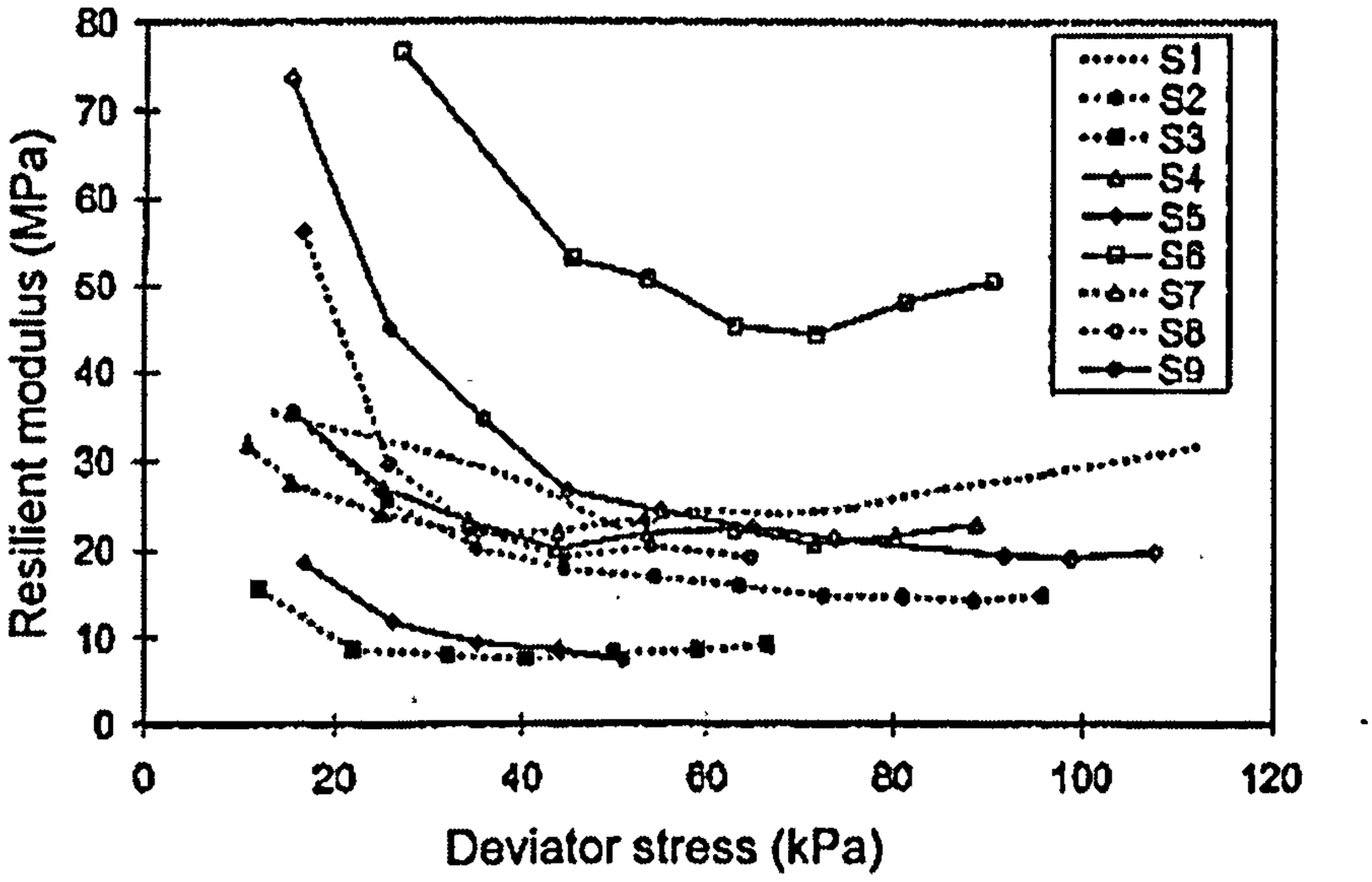

Figure 5.8. Resilient modulus variation with deviator stress (Frost *et al.*, 2004)

The resilient modulus has also been related to deviatoric stress through a power model:

$$E_r = K_1 P_a \left(\frac{q}{P_a}\right)^{K_3} \tag{5.23}$$

Mossazadeh and Witczak (1981) reported successful applications of this model to fine-grained soils. Brown *et al.* (1975) and Brown (1979) proposed a similar model but with the consideration of effective confining stress (σ_3') for saturated overconsolidated soils:

$$E_r = K_1 p_a \left(\frac{q}{\sigma_3'}\right)^{K_2} \tag{5.24}$$

Li and Selig (1994) found that while a bilinear model with five parameters gives the best fit to the available experimental data, the power model with, only two parameters, fits the data with reasonable accuracy. It was therefore concluded that the power model constitutes an appropriate nonlinear model for fine-grained soil in engineering practice; especially given the limited number of parameters that are needed to be calibrated.

Other forms of relationships between deviatoric stress and resilient modulus have also been proposed (see, e.g. Drum *et al.*, 1991; Li and Selig, 1994; Santha, 1994); however,

according to Li and Selig (1994), these models do not show any advantages over the above models.

Stiffness degradation of fine-grained soil can also be correlated to shear strain. An example of such a relationship was given in Figure (5.4) which presents the relationship between shear modulus ratio ($\frac{G_{sec}}{G_{max}}$) and shear strain (engineering) level. G_{max} is the maximum (secant) shear modulus measured at very low shear strain level (e.g. $\gamma = 10^{-4}\%$). The widely used devices to measure shear modulus of the soil are cyclic triaxial tests. Based on stress and strain measurements in a triaxial test, a secant shear modulus (G_{sec}) is obtained as follows:

$$G_{sec} = \frac{\tau}{\gamma} \tag{5.25}$$

where τ and γ are shear stress and shear strain(engineering):

$$\tau = \frac{\sigma_1 - \sigma_3}{2} \tag{5.26}$$

$$\gamma = \varepsilon_1 - \varepsilon_3 \tag{5.27}$$

σ_1 and σ_3 are major and minor principal stresses respectively. ε_1 and ε_3 are major and minor principal strains respectively.

A number of factors can influence the relationship between the shear modulus ratio and shear strain. Dobry and Vucetic (1987) listed the main factors affecting the maximum shear modulus and modulus ratio, of normally consolidated and moderately overconsolidated clays (Table. 5.1).

One of the most important factors is soil plasticity. It was noted that highly plastic soils are not as sensitive to large strains as soils of low plasticity. A typical effect of a plasticity

index on a reduction curve is shown in Figure (5.9). Ishibashi and Zhang (1993) stated that the relationship between shear modulus ratio and shear stress also depends on mean effective pressure: the higher the plasticity index the lower the reduction curve dependency (Figures 5.10 and 5.11). The following relationship was then proposed between shear modulus ratio, plasticity index and mean effective pressure:

$$\frac{G}{G_{\max}} = K(\gamma, PI)(\sigma_m')^{m(\gamma,PI)} \tag{5.28}$$

Increasing factor	G_{max}	G/G_{max}
Effective mean pressure, σ_m'	Increases with σ_m'	Increases with σ_m'; effect decreases with increasing *PI*
Void ratio, *e*	Decreases with *e*	Increases with *e*
Geologic age, t_g	Increases with t_g	May increase with t_g
Cementation, *c*	Increases with *c*	May increase with *c*
Overconsolidation ratio, *OCR*	Increases with *OCR*	Not affected
Plasticity Index, *PI*	Increases with *PI if OCR>1; remains approximately about constant if OCR=1*	Increases with *PI*
Cyclic strain, γ_c	-	Decreases with γ_c
Strain rate (frequency of cyclic loading)	No effect for non-plastic soils; increases with strain rate for plastic soils	Not affected

Table 5.1. Effect of environmental and loading conditions on the maximum shear modulus and moderately over consolidated clay (Dorby and Vucetic, 1987; Kramer, 1996)

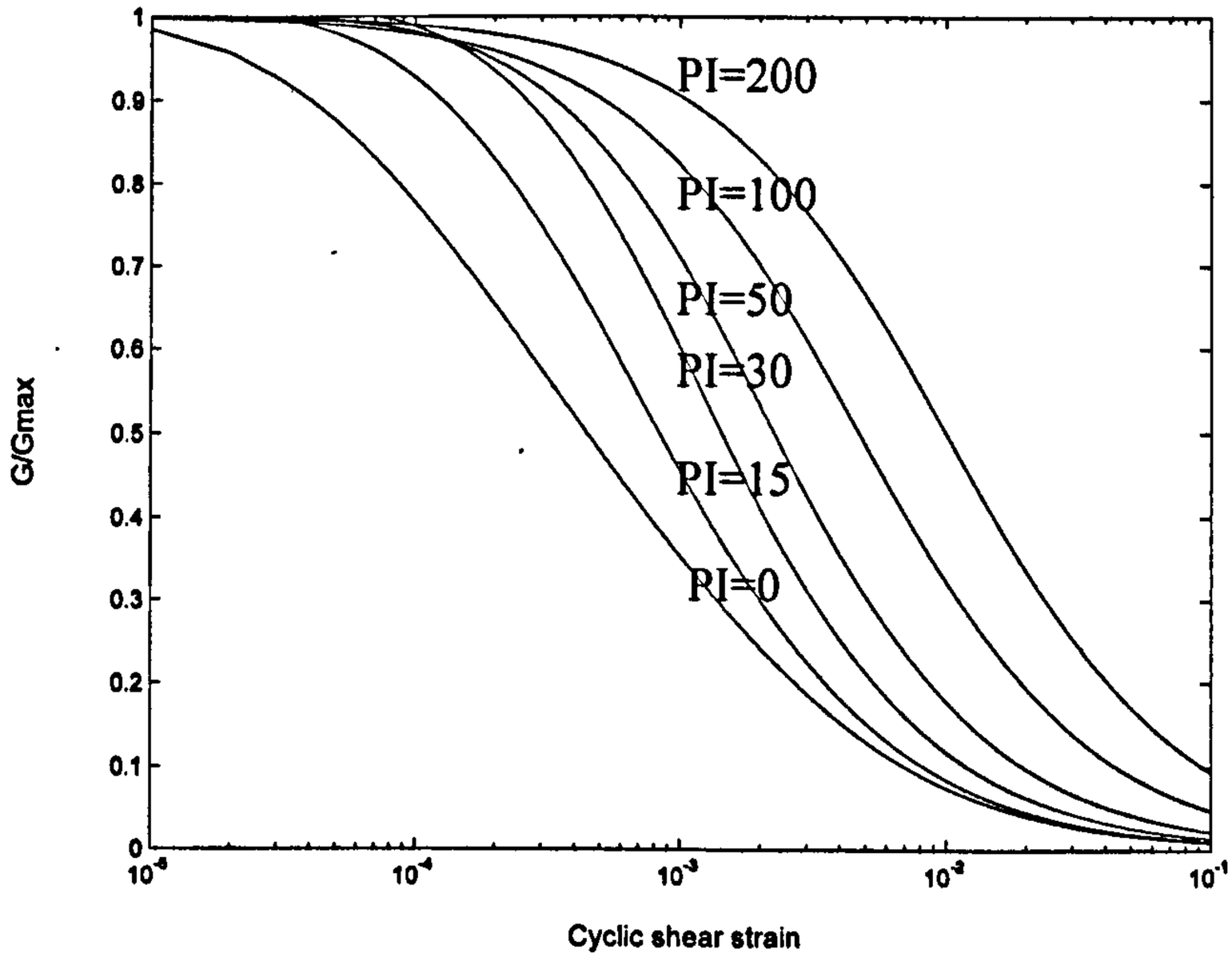

Figure 5.9. Shear modulus reduction curves for fine-grained soils of different plasticity index according to Equation 5.28 (σ_m'= 50 kPa)

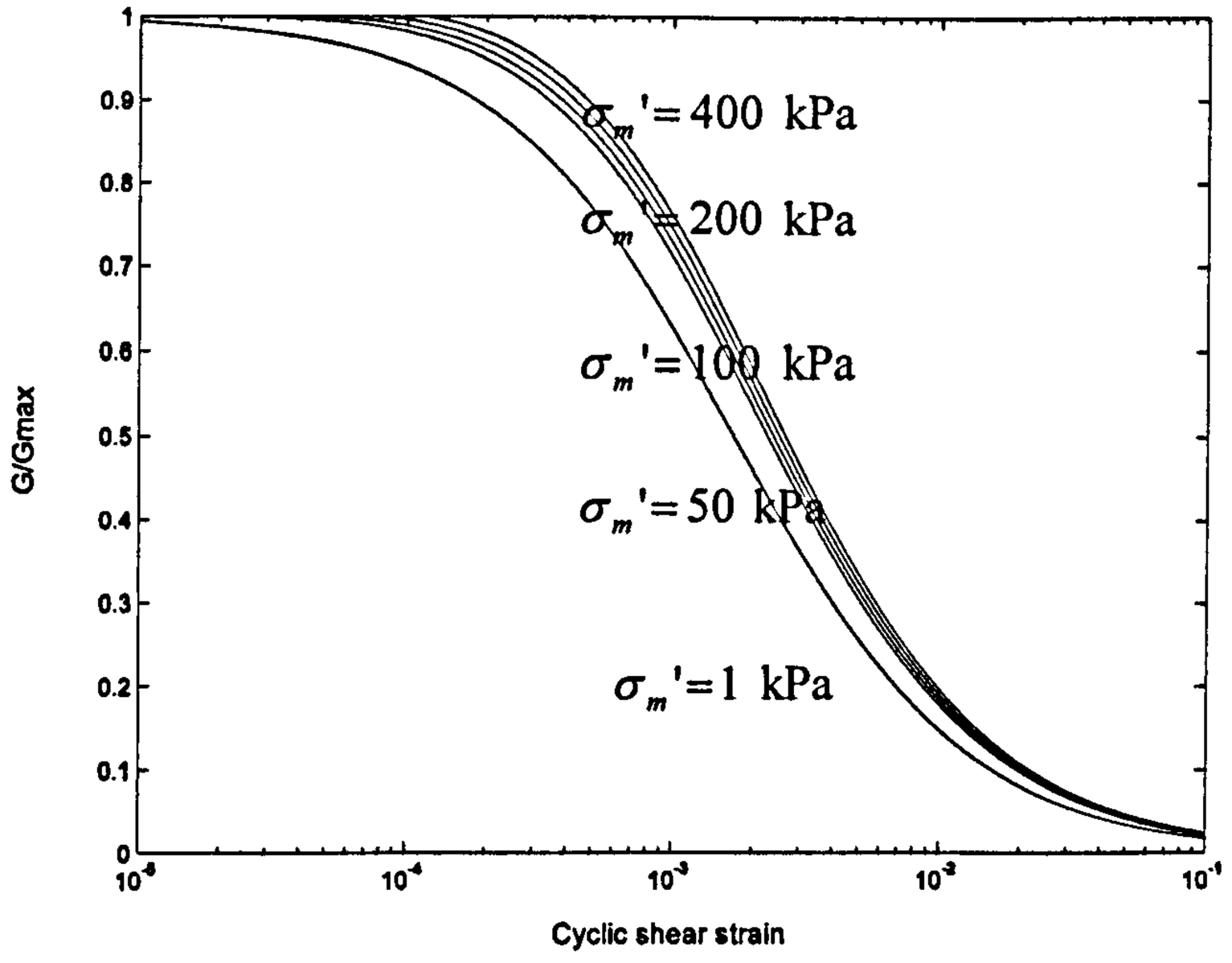

Figure 5.10. Influence of mean effective stress on shear modulus reduction curves for plastic soil according to Equation 5.28 (PI=50)

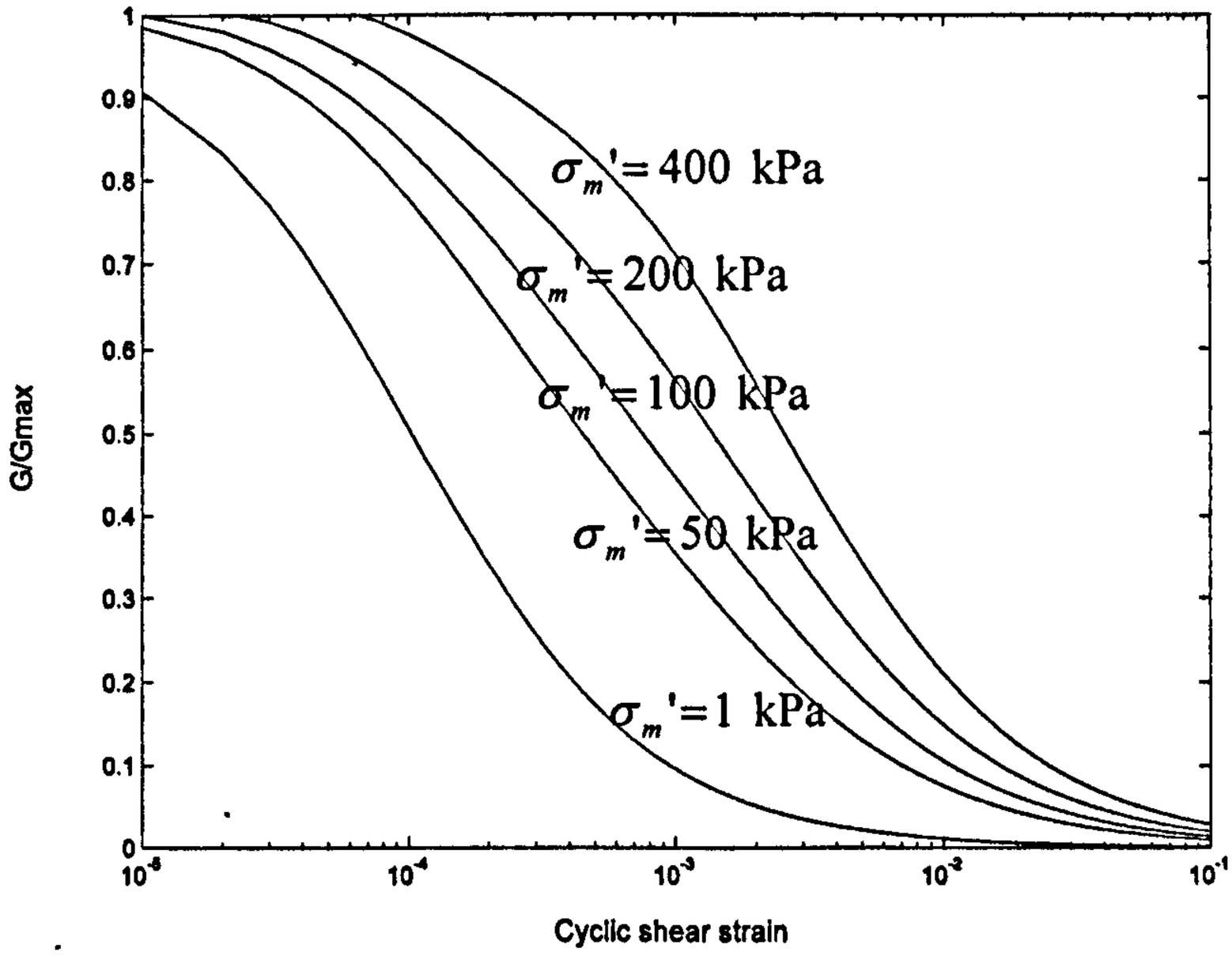

Figure 5.11. Influence of mean effective stress on shear modulus reduction curves for non-plastic soil according to Equation 5.28 (PI=0)

where

$$K(\gamma, PI) = 0.5\left\{1 + \tanh\left[\ln\left(\frac{0.000102 + n(PI)}{\gamma}\right)^{0.492}\right]\right\} \tag{5.29}$$

$$m(\gamma, PI) = 0.272\left\{1 - \tanh\left[\ln\left(\frac{0.000556}{\gamma}\right)^{0.4}\right]\right\}\exp(-0.0145PI^{1.3}) \tag{5.30}$$

For $PI = 0$, $n(PI) = 0$ For $0 < PI \le 15$, $n(PI) = 0$

For $15 < PI \le 70$, $n(PI) = 0$ For $PI > 70$, $n(PI) = 0$

where σ_m' , γ and PI are the mean effective stress, the shear stress and the plasticity index respectively.

5.4 Finite Element Implementation

The presented nonlinear relationships are in secant forms, i.e. they relate total stresses and total strains:

$$\sigma_{ij} = D^{S}_{ijkl}\varepsilon_{kl} \quad \text{or} \quad \varepsilon_{ij} = C^{S}_{ijkl}\sigma_{kl} \tag{5.31}$$

where $\sigma_{ij}, \varepsilon_{kl}, D^{S}_{ijkl}$ and C^{S}_{ijkl} are components of stress, strain and secant stiffness and compliance tensors (the inverse of stiffness tensor) respectively.

Assuming isotropic behaviour, the stiffness and compliance tensors are:

$$D^{S}_{ijkl} = \frac{E_r}{(1+v)} I_{ijkl} + \frac{vE_r}{(1+v)(1-2v)} \delta_{ij}\delta_{kl} \tag{5.32}$$

$$C^{S}_{ijkl} = \frac{1+v}{E} I_{ijkl} - \frac{v}{E} \delta_{ij}\delta_{kl} \tag{5.33}$$

where $I_{ijkl} = \frac{1}{2}(\delta_{ik}\delta_{jl} + \delta_{il}\delta_{jk})$ is a fourth order identity tensor. δ_{ij} is Kronecker's delta ($\delta_{ij} = 1, i = j$ and $\delta_{ij} = 0, i \neq j$).

The stress-strain can also be related through the tangent stiffness-compliance relationships:

$$d\sigma_{ij} = D^{T}_{ijkl} d\varepsilon_{kl} \quad \text{or} \quad d\varepsilon_{ij} = C^{T}_{ijkl} d\sigma_{kl} \tag{5.34}$$

where $d\sigma_{ij}$, $d\varepsilon_{kl}$, C^{T}_{ijkl} and D^{T}_{ijkl} are components of incremental stress, incremental strain and tangent stiffness and compliance tensors respectively:

$$d\varepsilon_{ij} = \frac{\partial(C^S_{ijkl}\sigma_{kl})}{\partial\sigma_{mn}} d\sigma_{mn} = \overbrace{(C^S_{ijmn} + \frac{\partial C^S_{ijkl}}{\partial\sigma_{mn}}\sigma_{kl})}^{C^T_{ijmn}} d\sigma_{mn} \tag{5.35}$$

$$d\sigma_{ij} = \frac{\partial(D^S_{ijkl}\varepsilon_{kl})}{\partial\varepsilon_{mn}} d\varepsilon_{mn} = \overbrace{(D^S_{ijmn} + \frac{\partial D^S_{ijkl}}{\partial\varepsilon_{mn}}\varepsilon_{kl})}^{D^T_{ijmn}} d\varepsilon_{mn} \tag{5.36}$$

As the standard nonlinear finite elements are often cast as strain-driven, the stiffness tensor is then employed in the implementation of the material models. Tangent and/or secant stiffness tensors can be considered in the implementation procedure. As is usually the case with explicit time integration, the time step is very small; the stiffness property can be found based on the stress level obtained in the previous time increment. In this way, it can be assumed that the stress change between subsequent time steps is small and its effect on stiffness change is therefore negligible. However, if the time step size is relatively big, this assumption cannot be made and an iterative procedure must be adopted to find the correct stress level and stiffness properties. A direct substitution iterative approach can be employed in every time step to update stress and then stiffness at each Gauss point. At a given time step, the internal stresses is initially calculated based on the stiffness at the previous time step. The new stiffness matrix is then obtained using the new stresses, and the new stress level is used to form the new stiffness matrix. This loop is continued until the convergence criterion is met. As the constitutive equations presented above are based on deviatoric or mean stresses, the convergence criterion has been written based on them:

$$\frac{q^{t+1}_{j+1} - q^{t+1}_{j}}{q^{t}} < 0.001 \tag{5.37}$$

$$\frac{p^{t+1}_{j+1} - p^{t+1}_{j}}{p^{t}} < 0.001 \tag{5.38}$$

where q^t_j, p^t_j are deviatoric and mean stresses at time step t for the iteration j. Depending on whether both or one of these two stress invariants are incorporated in the

resilient model, one or both convergence criteria are considered. This implementation is based on the secant form of constitutive, stress and strain tensors. A standard/modified Newton Raphson approach can also be incorporated with a tangent stiffness constitutive tensor. In the case of the standard Newton-Raphson approach, as the displacement is known at the start of the time step, so the strain tensor (ε^{t+1}) is also known at gauss point level. The following calculations are performed until the convergence is achieved:

$$\Delta\sigma_{j+1}^{t+1} = D^T(\sigma_j^{t+1})(\varepsilon^{t+1} - \varepsilon_j^{t+1}) \tag{5.39}$$

$$\sigma_{j+1}^{t+1} = \sigma_j^{t+1} + \Delta\sigma_{j+1}^{t+1} \tag{5.40}$$

$$\varepsilon_{j+1}^{t+1} = (D^S(\sigma_{j+1}^{t+1}))^{-1}\sigma_{j+1}^{t+1} \tag{5.41}$$

The starting point of the loop is considered to be the stress and strain tensors at the previous time step. The secant stiffness is used in Equation (5.41) to obtain the strain level associated with a given stress. The modified Newton-Raphson method differs from the standard Newton-Raphson method in that the tangent constitutive tensor is not updated, or is updated infrequently (in Equation 5.39). This avoids the expensive repetition of forming a large size tangent matrix. However, more iterations are needed in order to reach convergence. Since the prescribed nonlinear equation for the nonlinear resilient models is solved at the Gauss point level, the size of the tangent matrix is small and therefore it is relatively fast to update at every time step. It should be noted that the constitutive relationships are implemented using Equations (5.39-5.41); an equation needs to be solved at each iteration (Equation 5.41), whereas in the direct substitution approach no equation is solved. The direct substitution approach may therefore lead to faster convergence in some cases.

The displacement and consequently strain are known at the start of the time step in explicit time integration, according to Equations (3.17) and (3.20). The implementation of strain-based constitutive relationships like the shear modulus related to shear strain level in the dynamic finite element code, is therefore straightforward; the stiffness is updated based on the strain level in the corresponding time step, and no iteration is needed. It is therefore of

interest to write the given constitutive relationships based on strain invariants. Considering the relationships between volumetric stress and strain (Equation 5.5), deviatoric stress and strain (Equation 5.6), and also relationships involving bulk modulus, shear modulus, Young's modulus and Poisson's ratio, the universal models can be written in terms of volumetric and deviatoric strains:

$$E_r = k_1^* P_{atm} \varepsilon_v^{k_2^*} \varepsilon_q^{k_3^*} \tag{5.42}$$

$$k_1^* = k_1^{\frac{1}{1-k_2-k_3}} \left(\frac{1}{1-2v}\right)^{k_2^*} \left(\frac{3}{2(1+v)}\right)^{k_3^*} \tag{5.43}$$

$$k_2^* = \frac{k_2}{1-k_2-k_3} \tag{5.44}$$

$$k_3^* = \frac{k_3}{1-k_2-k_3} \tag{5.45}$$

For the definition of parameters, see Equation (5.8). As $K-\theta$ and power models are specific forms of the universal model given by Equation (5.8), i.e. $k_3 = 0$ for $K-\theta$ model and $k_2 = 0$ for power model, they can also be represented by Equation (5.42). Such a strain-based model cannot however be achieved for more complicated models such as those of Boyce (1980) and Sweere (1990).

For the present study, the universal, power, $K-\theta$ and Boyce models are implemented in the finite element code. The strain-based relationship (Equation 5.42) is employed to represent the universal, power and $K-\theta$ models, whereas the Boyce model is implemented using the stress-based relationship (Equations 5.15 and 5.16). At a given time step, the stiffness property in the Boyce model is found based on the deviatoric and mean stress level at the end of the previous time step. As discussed before, this approach is considered to be viable as the time increment used is small (15*E-6 s).

5.5 The Effect of Subgrade Nonlinearity on Track Response

As discussed by Li and Selig (1994), the power model can constitute an appropriate nonlinear representation of clay soil behaviour and it is therefore considered in the present study. The model has been calibrated (k_1=120.24 and k_3=-0.46) using conventional cyclic triaxial test results on clay (Li and Selig, 1994), as shown in Figure (5.12). Several nonlinear simulations, with nonlinear subgrade and linear ballast, are performed at different train speeds and compared against linear simulations: one with an initial (upper bound) elastic modulus of ES=40 MPa and the other with a lower bound elastic modulus of ES=15 MPa. A typical track with 300 millimetres of ballast is considered. The ballast behaviour is assumed to be linear (EB=120 MPa) in this section. A passenger coach, with an axle load of 17.4 T, is considered as before. For model configurations, see Section 3.3.1.

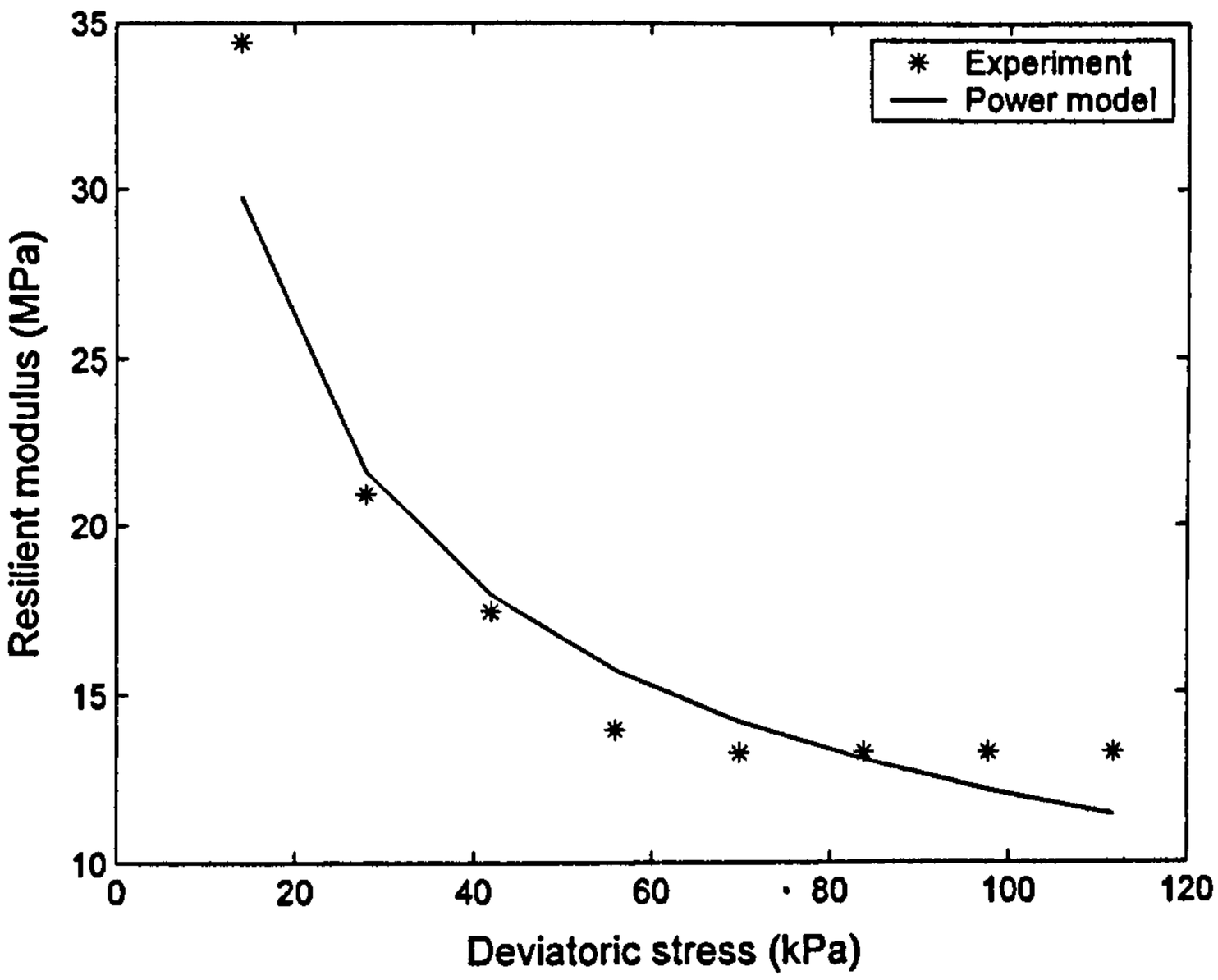

Figure 5.12. Calibrated power model against experiments on clay (under conventional triaxial condition)

The resilient modulus of the subgrade, under the passage of a train coach, are depicted in Figures (5.13a) and (5.13b) for two different train speeds: V=30 m/s and V=70 m/s. In

both cases, the resilient modulus degrades while the train is passing the point of interest (where the response is presented). While degradation of subgrade stiffness is limited for low speed cases (Figure, 5.13a), a significant decrease in subgrade stiffness is observed as the train speed increases to 70 m/s (Figure 5.13b).

A typical response of a railway track with a nonlinear subgrade is compared with the responses of linear track (linear subgrade and ballast), at different train speeds, in Figures (5.14-5.24). At a low train speed (V=30 m/s), both linear and nonlinear simulations give similar responses in terms of sleeper displacement (Figures 5.14a and 5.14b), ballast particle velocity (Figures 5.15a and 5.15b), ballast vertical acceleration (Figures 5.16a and 5.16b) and vertical stresses in the subgrade (Figures 5.17a and 5.17b) and the ballast (Figures 5.18a and 5.18b). This is expected due to the low deviatoric stress in the subgrade and consequently limited degradation of subgrade stiffness (Figure 5.13a). At a train speed of 70 m/s, the nonlinear track response differs from the linear one. In particular, the nonlinear simulation results in higher displacements when compared with displacements from the linear simulation; compare Figure (5.19a) to Figure (5.19b). The ballast vibration (Figures 5.20 and 5.21) and the vertical stress in the ballast (Figure 5.22) and subgrade (Figure 5.23), obtained from nonlinear simulation, are slightly different from their counterparts in linear simulations.

Figure (5.24) presents the displacement field on the surface of the ground for a train speed of 30 m/s for nonlinear and linear simulations. As expected, both nonlinear and upper bound linear (ES=40 MPa) simulations give effectively the same displacement pattern and amplitude. For a train speed of 70 m/s however this is not the case. Comparing the linear (ES=40 MPa) and the nonlinear simulations in Figure (5.25) clearly shows the increase in asymmetry in the displacement pattern and displacement amplitude when nonlinearity is taken into account. This suggests that the critical track velocity may be affected by nonlinearity of the subgrade. In other words, the linear solution (ES=40 MPa) can under-predict the ground displacements and over-predict the critical track velocity when compared with the nonlinear solution. Such a trend is also shown in Figure (5.26), which presents maximum displacements for the upper bound linear elastic (ES=40 MPa), lower bound linear elastic (ES=15 MPa) and the nonlinear simulations. Similar trends are observed for vibration levels in the ballast in terms of ballast particle velocity (Figure 5.27),

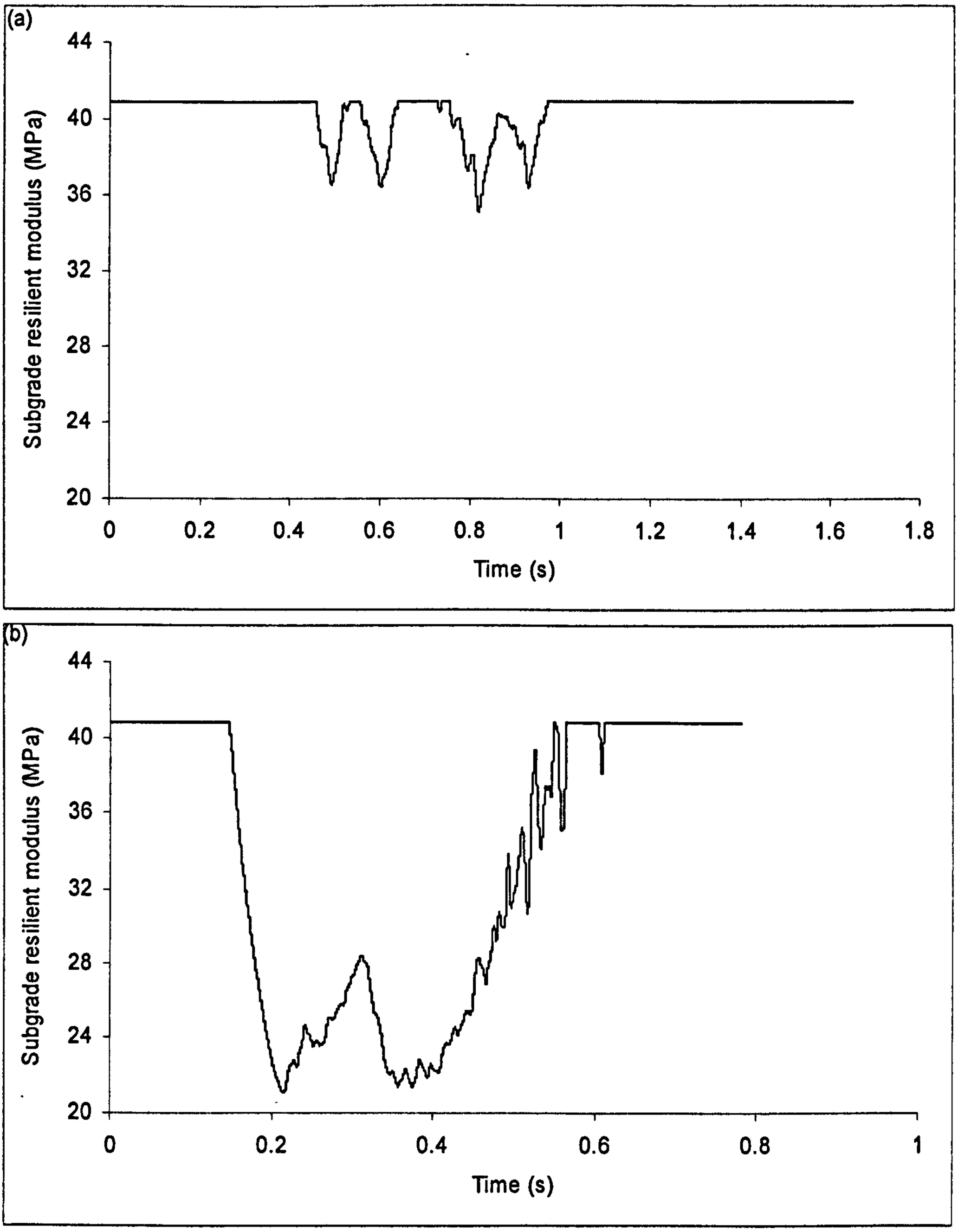

Figure 5.13. Resilient modulus change in subgrade (depth=1.8 m) from nonlinear simulations (nonlinear subgrade, EB=120 MPa, BD=300 mm) at (a) V=30 m/s (b) V=70 m/s

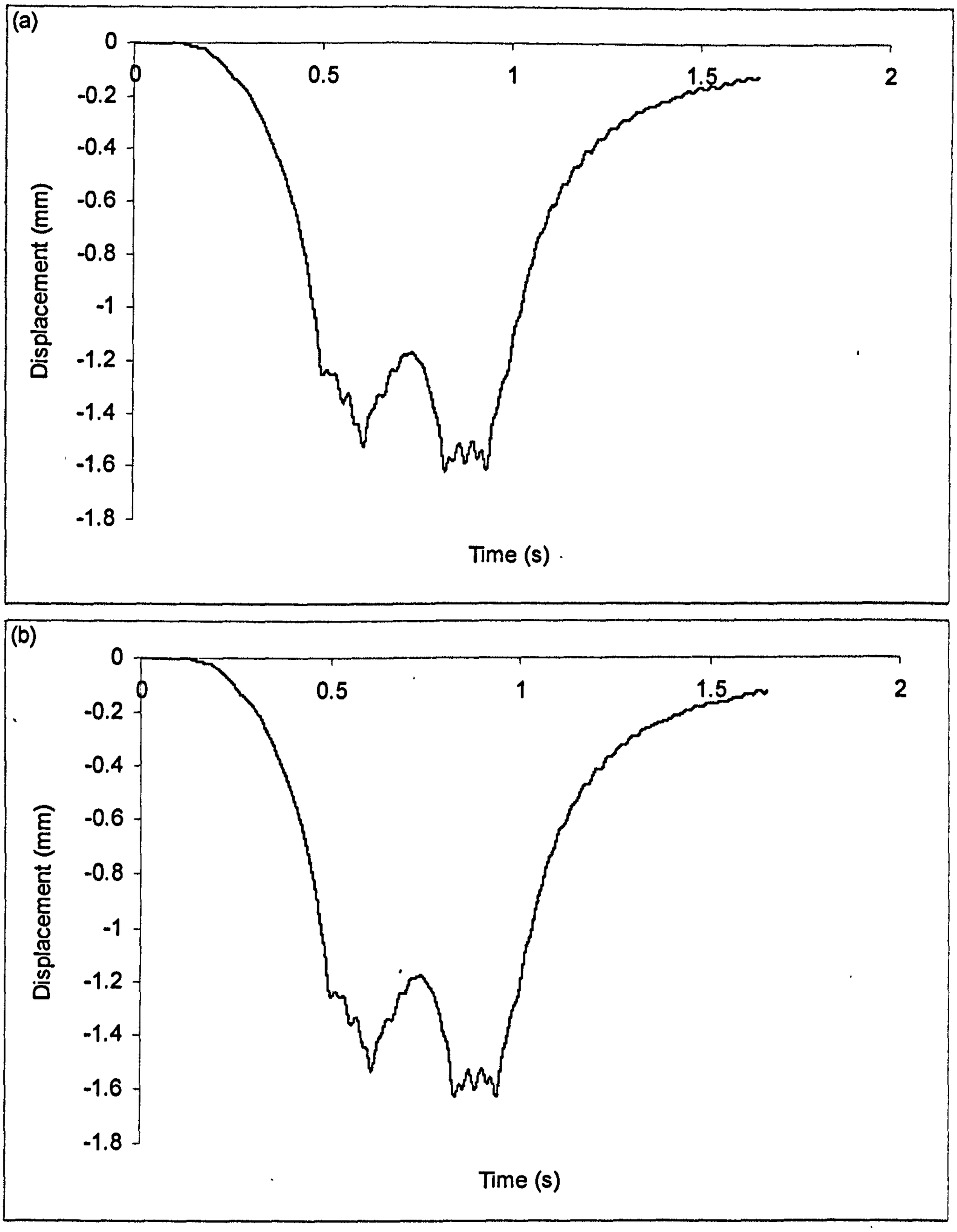

Figure 5.14. Sleeper displacement under a train coach (EB=120 MPa, BD=300 mm) at V=30 m/s (a) nonlinear subgrade (b) linear subgrade (ES=40 MPa)

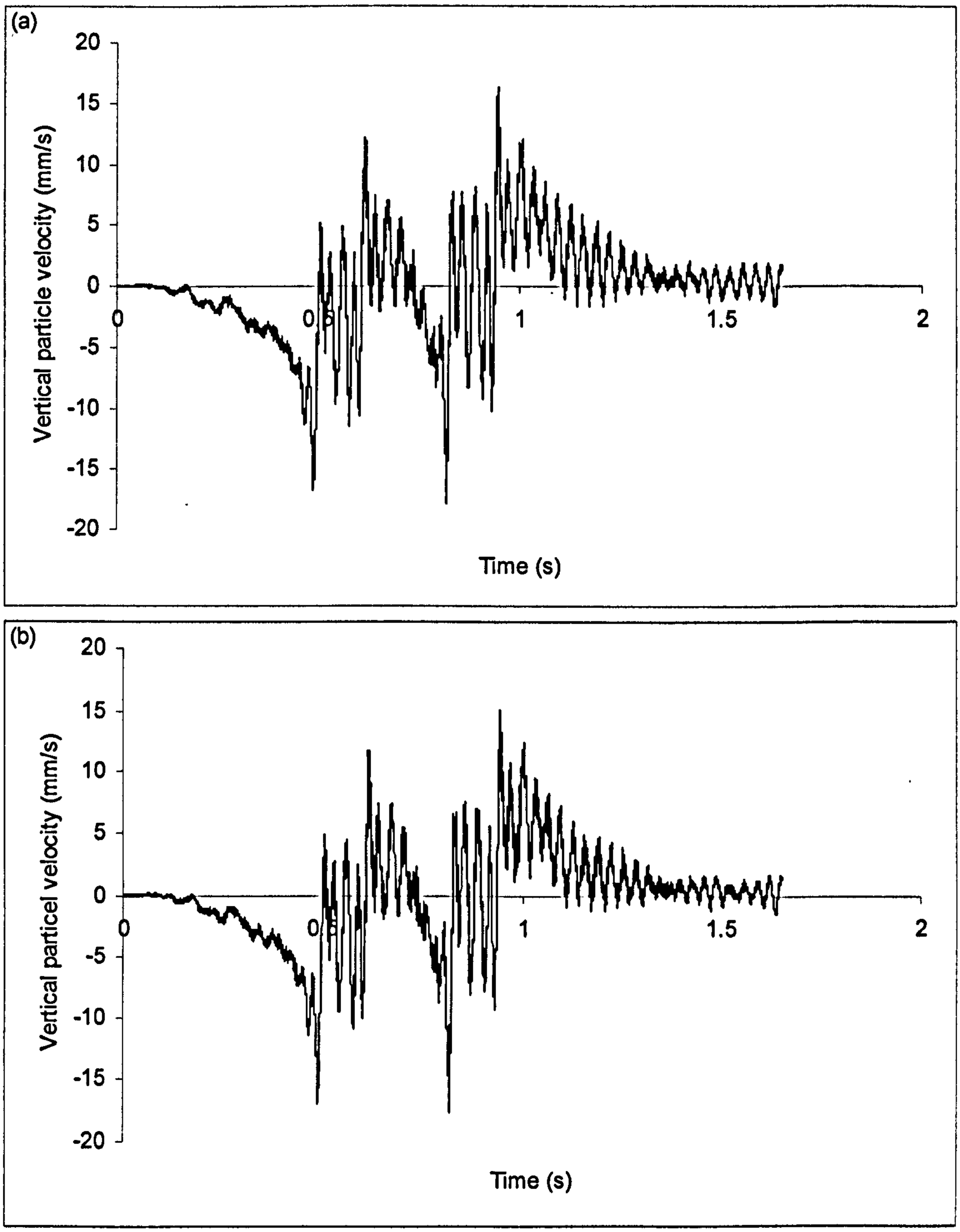

Figure 5.15. Ballast particle velocity under passage of a train coach at V=30 m/s (EB=120 MPa, BD=300 mm) (a) nonlinear subgrade (b) linear subgrade (ES=40 MPa)

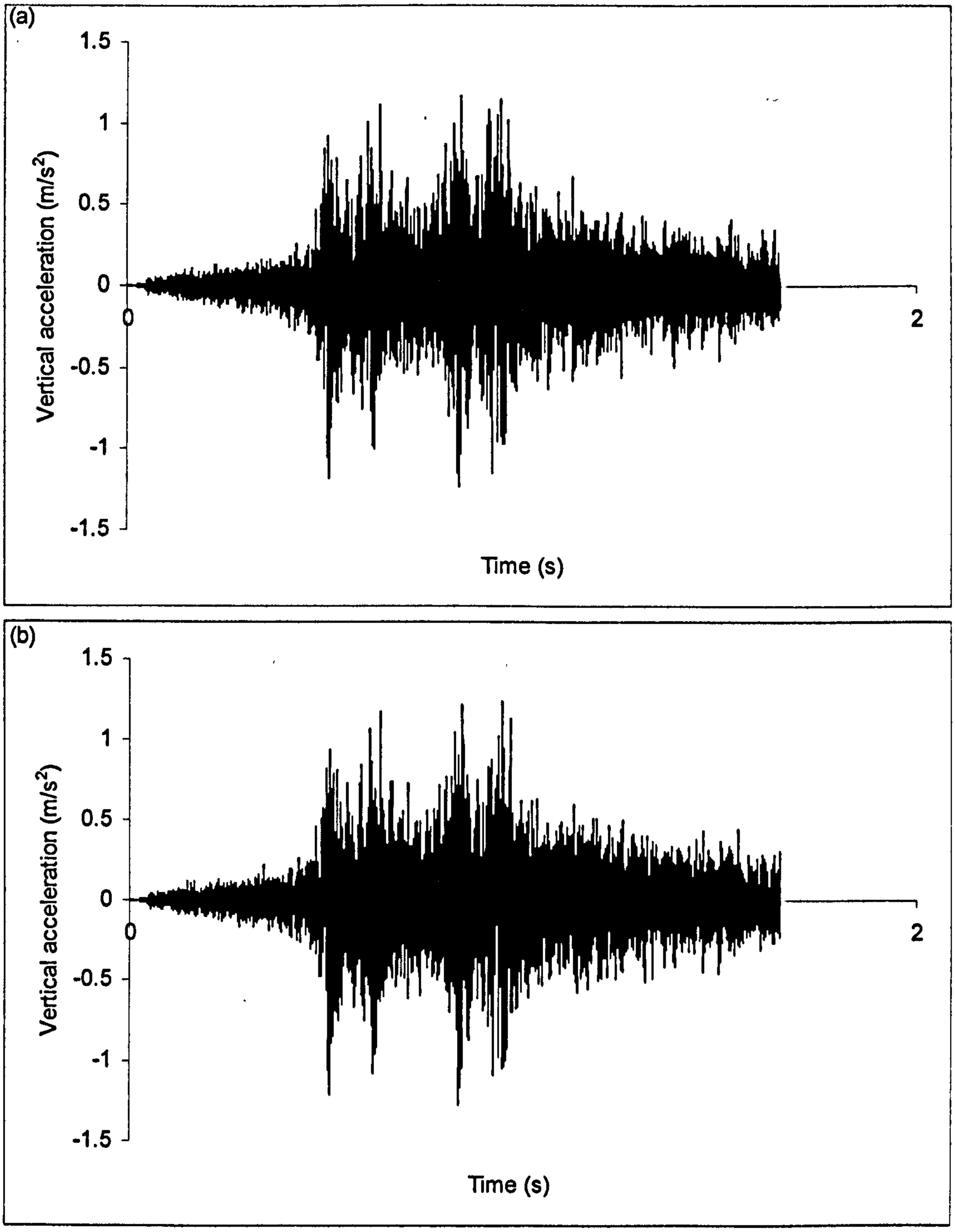

Figure 5.16. Ballast particle acceleration under passage of a train coach at V=30 m/s (ES=15 MPa, EB=120 MPa, BD=300 mm) (a) nonlinear subgrade (b) linear subgrade (ES=40 MPa)

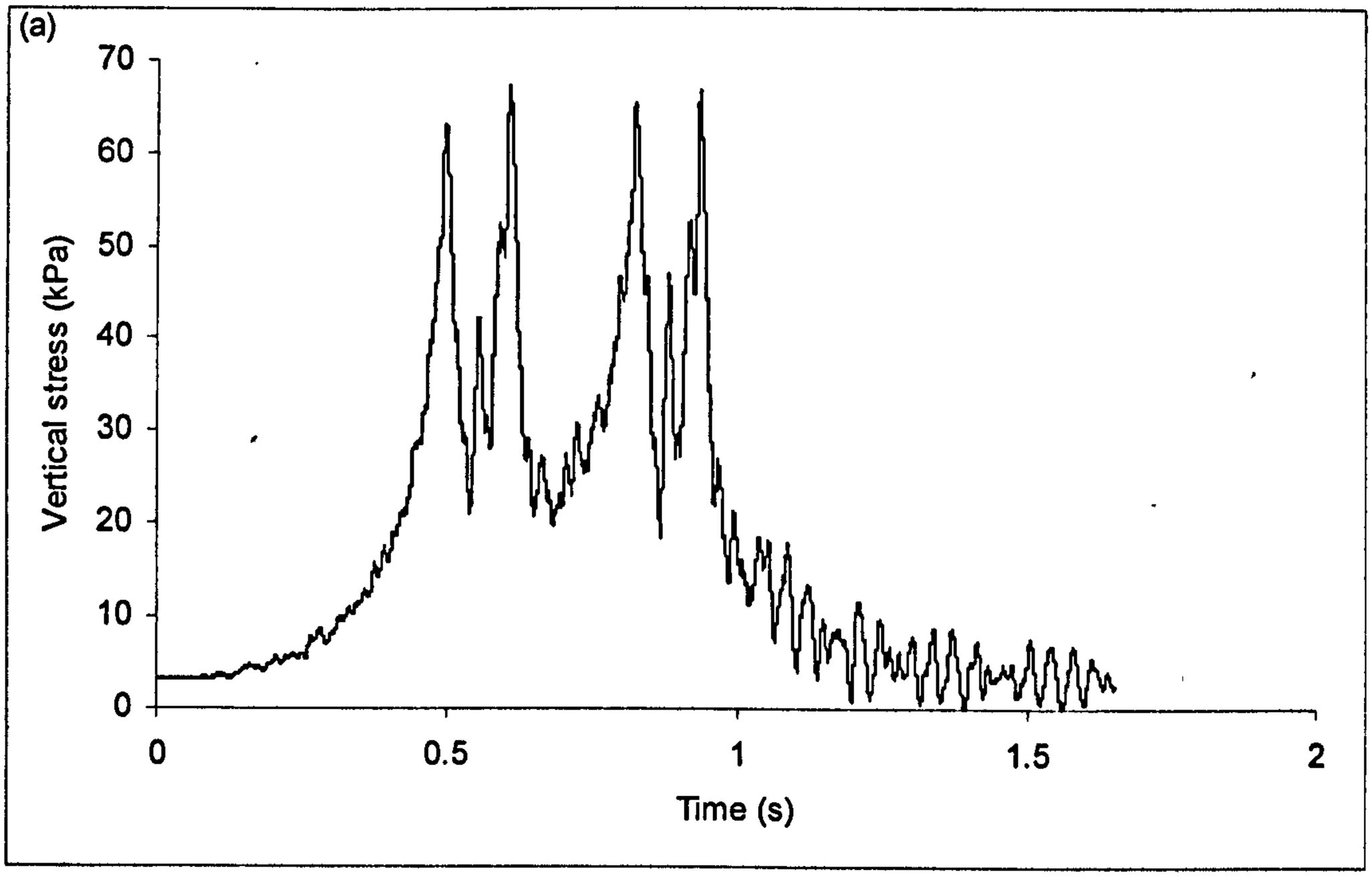

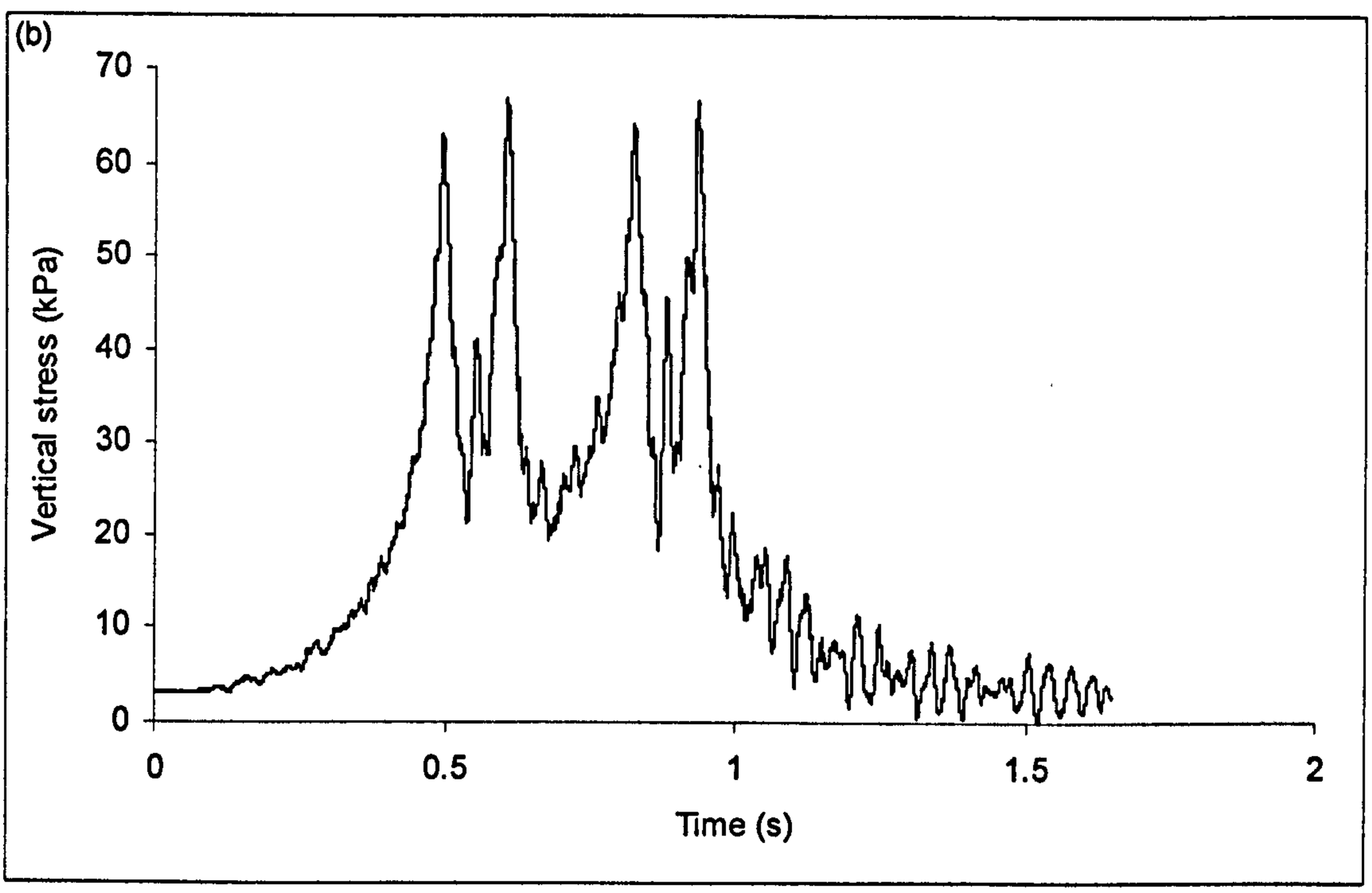

Figure 5.17. Vertical stress on top of ballast layer under passage of a train coach at V= 30 m/s (EB=120 MPa, BD=300 mm) (a) nonlinear subgrade (b) linear subgrade (ES=40 MPa)

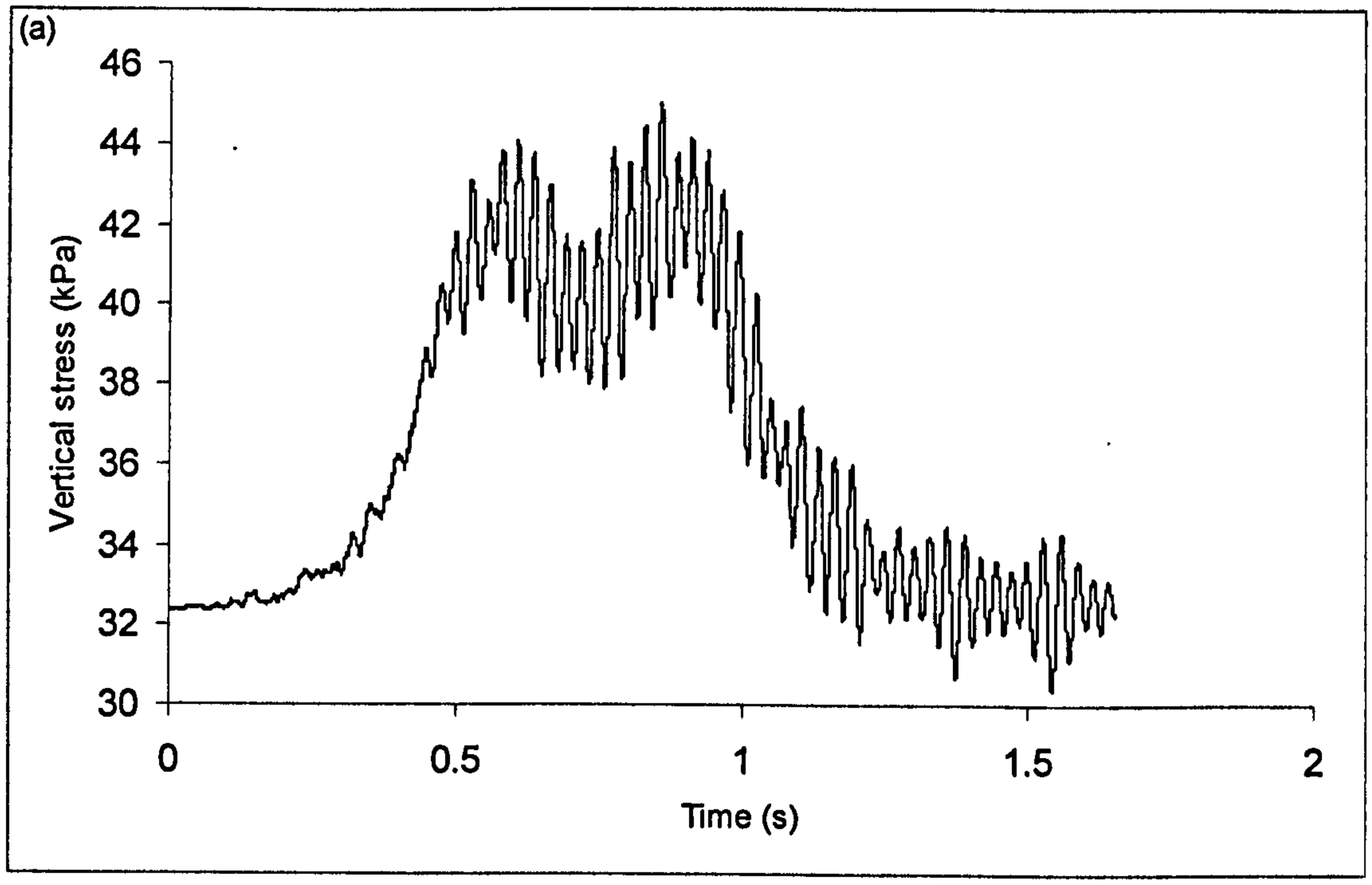

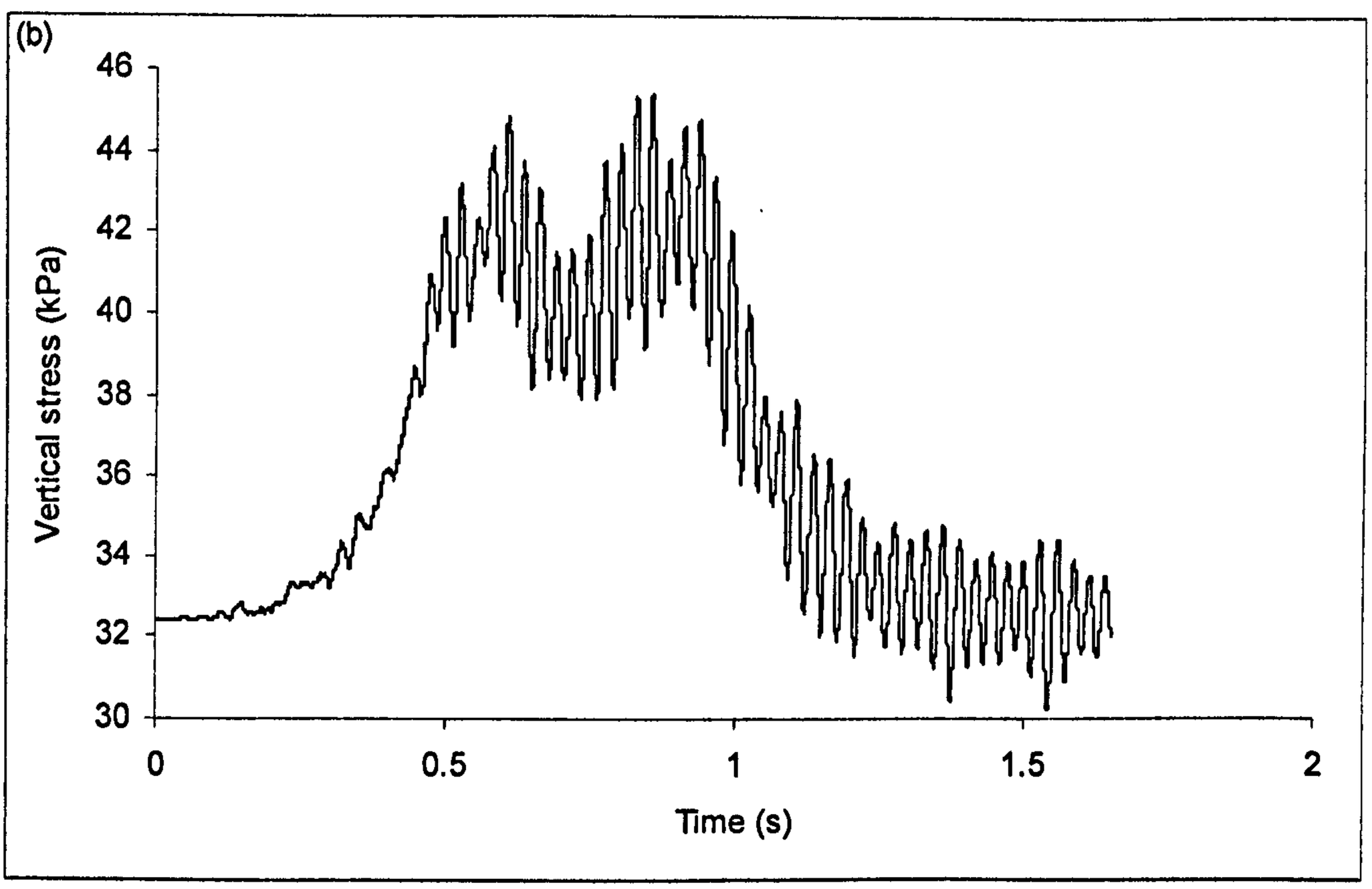

Figure 5.18. Vertical stress in the subgrade (At depth=1.8 m) under passage of a train coach at V=30 m/s (EB=120 MPa, BD=300 mm) (a) nonlinear subgrade (b) linear subgrade (ES=40 MPa)

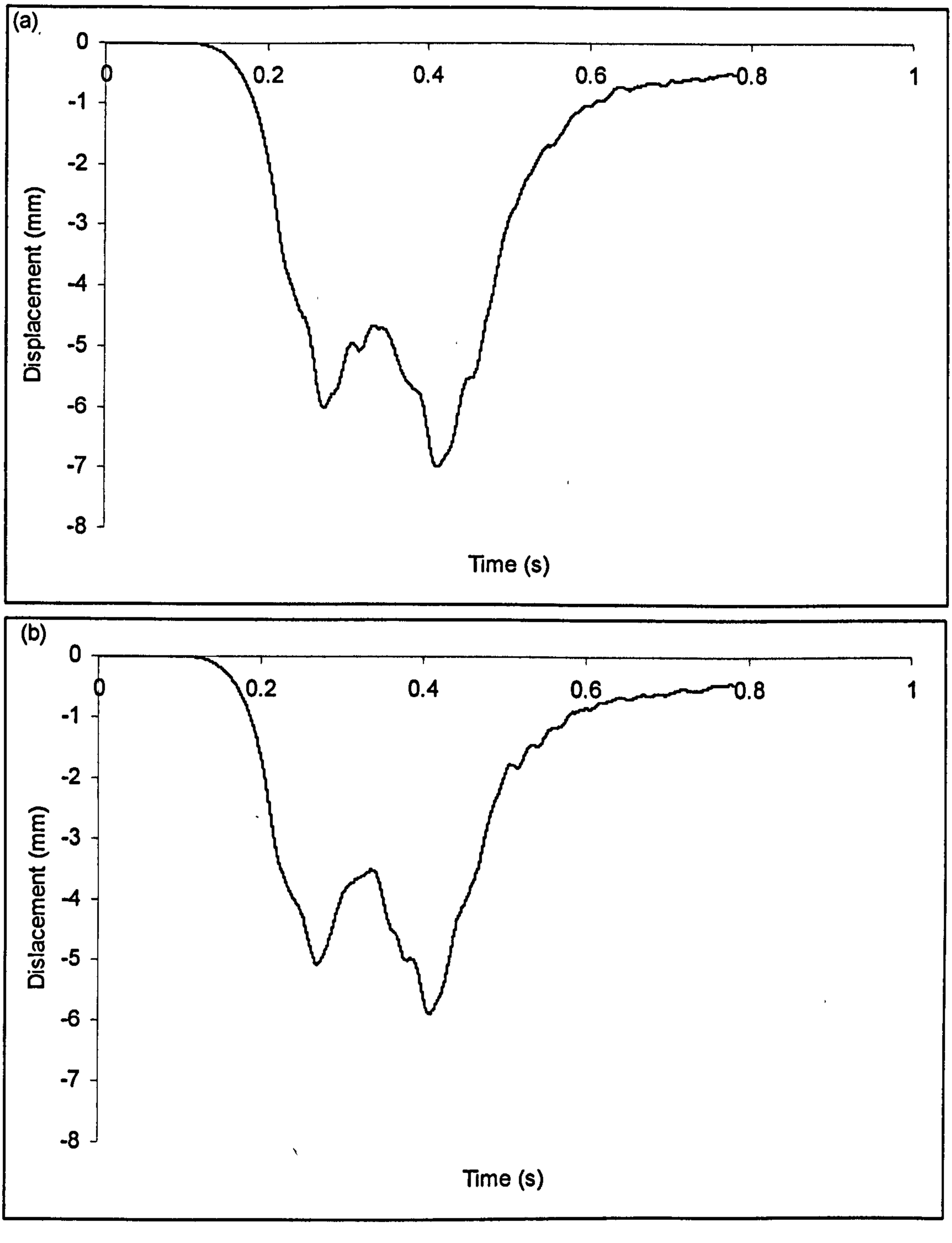

Figure 5.19. Sleeper displacement under a train coach (EB=120 MPa, BD=300 mm) at V=70 m/s (a) nonlinear subgrade (b) linear subgrade (ES=40 MPa)

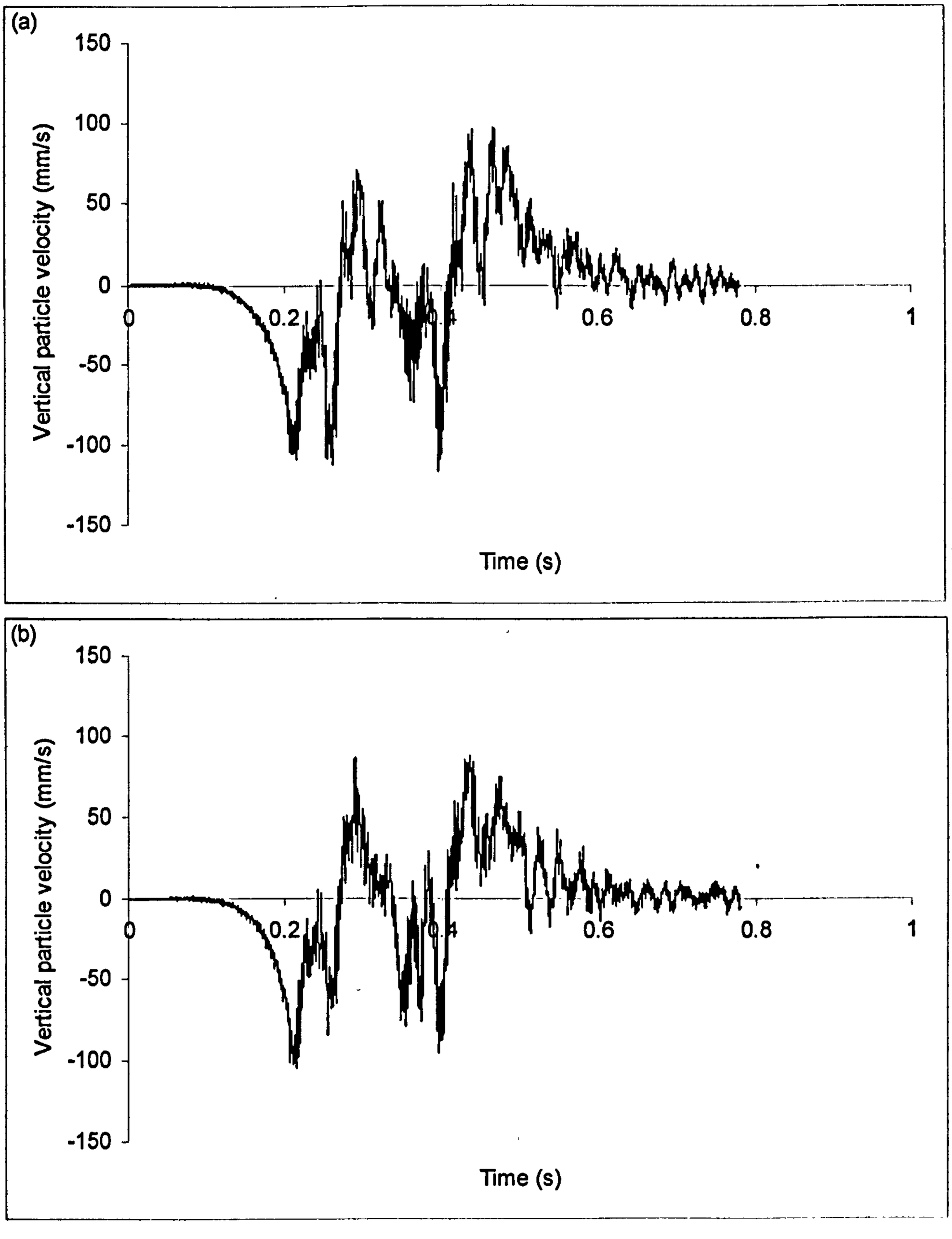

Figure 5.20. Ballast particle velocity under passage of a train coach at V=70 m/s (EB=120 MPa, BD=300 mm) (a) nonlinear subgrade (b) linear subgrade (ES=40 MPa)

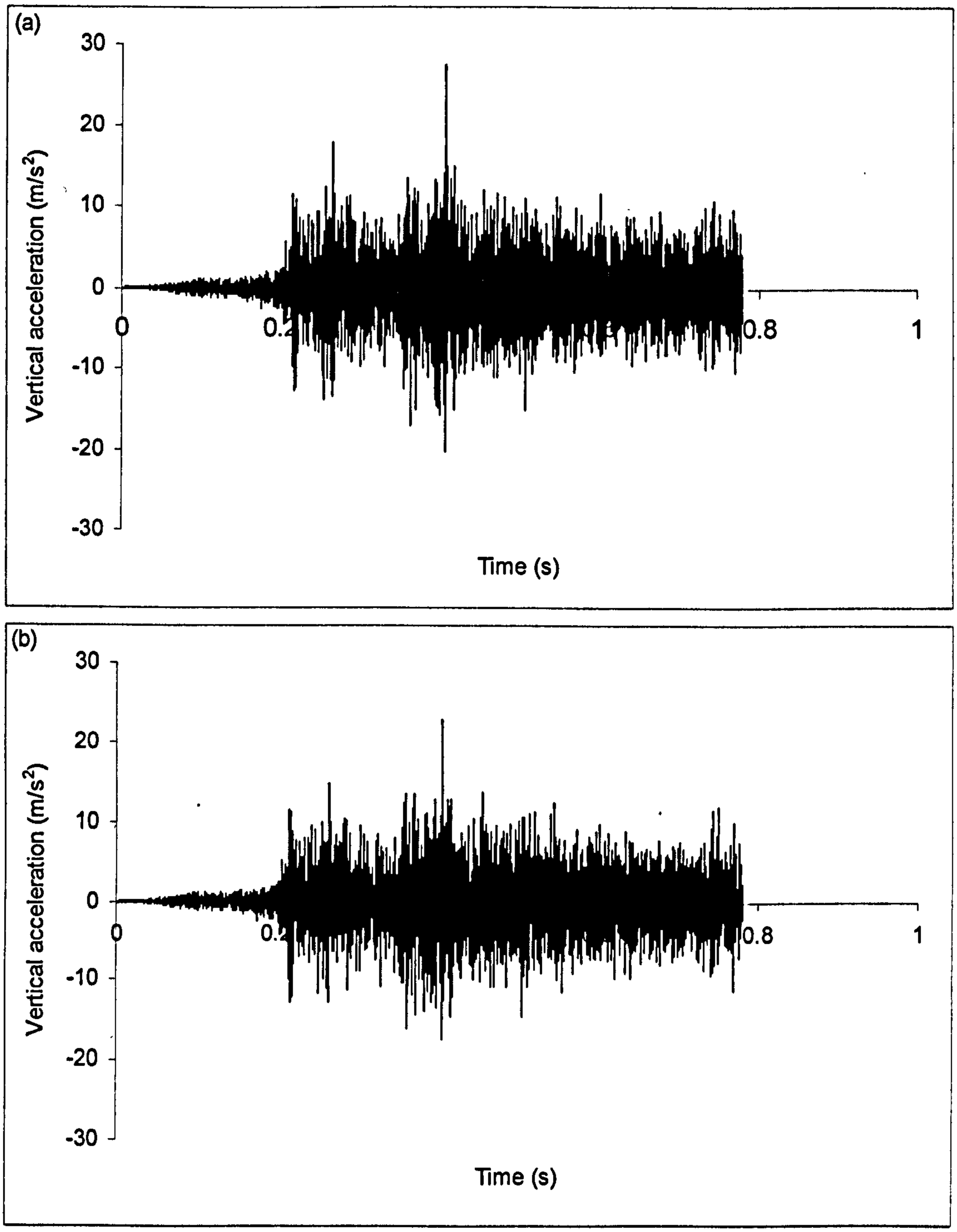

Figure 5.21. Ballast particle acceleration under passage of a train coach at V=70 m/s (EB=120 MPa, BD=300 mm) (a) nonlinear subgrade (b) linear subgrade (ES=40 MPa)

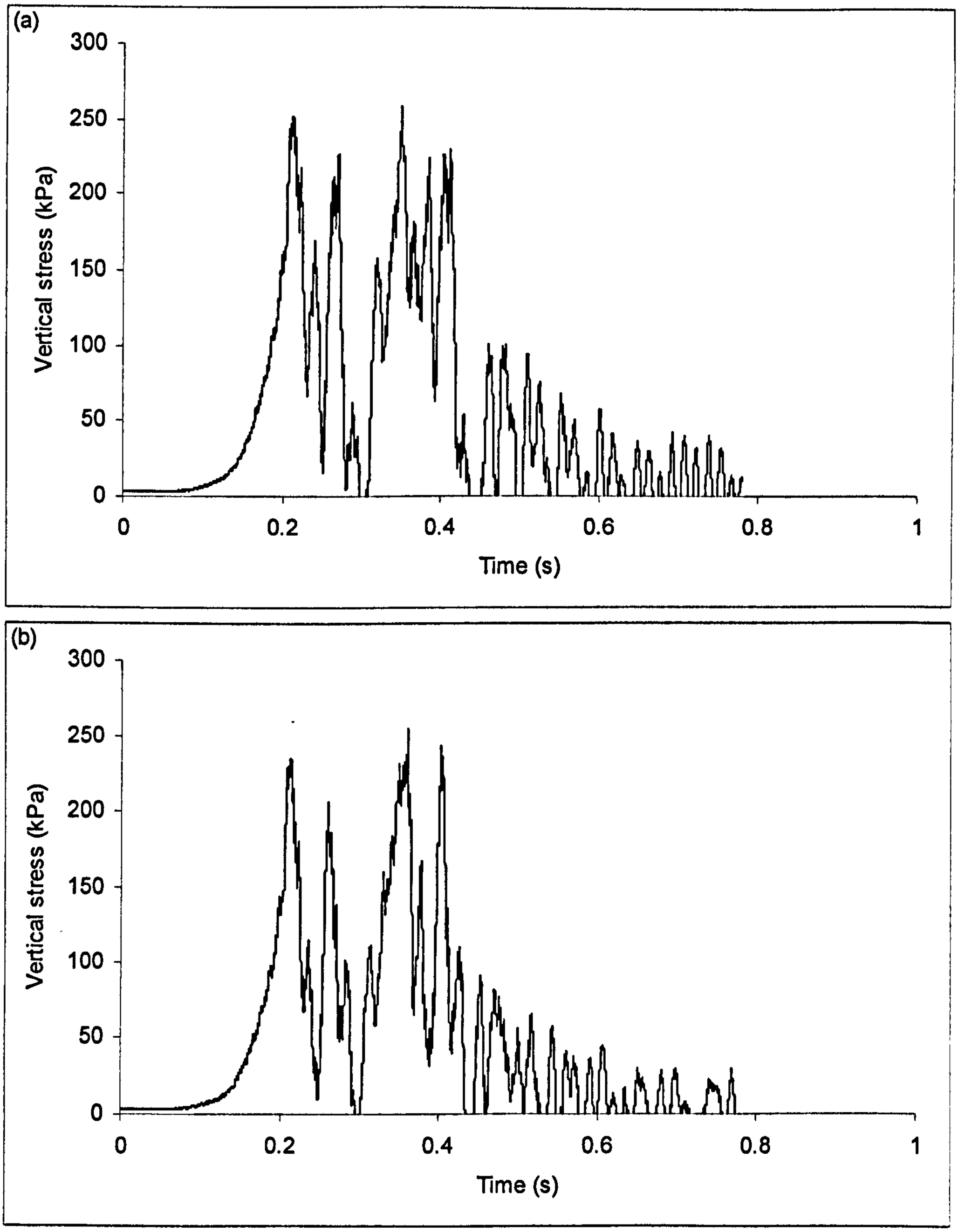

Figure 5.22. Vertical stress on top of ballast layer under passage of a train coach at V= 70 m/s (EB=120 MPa, BD=300 mm) (a) nonlinear subgrade (b) linear subgrade (ES=40 MPa)

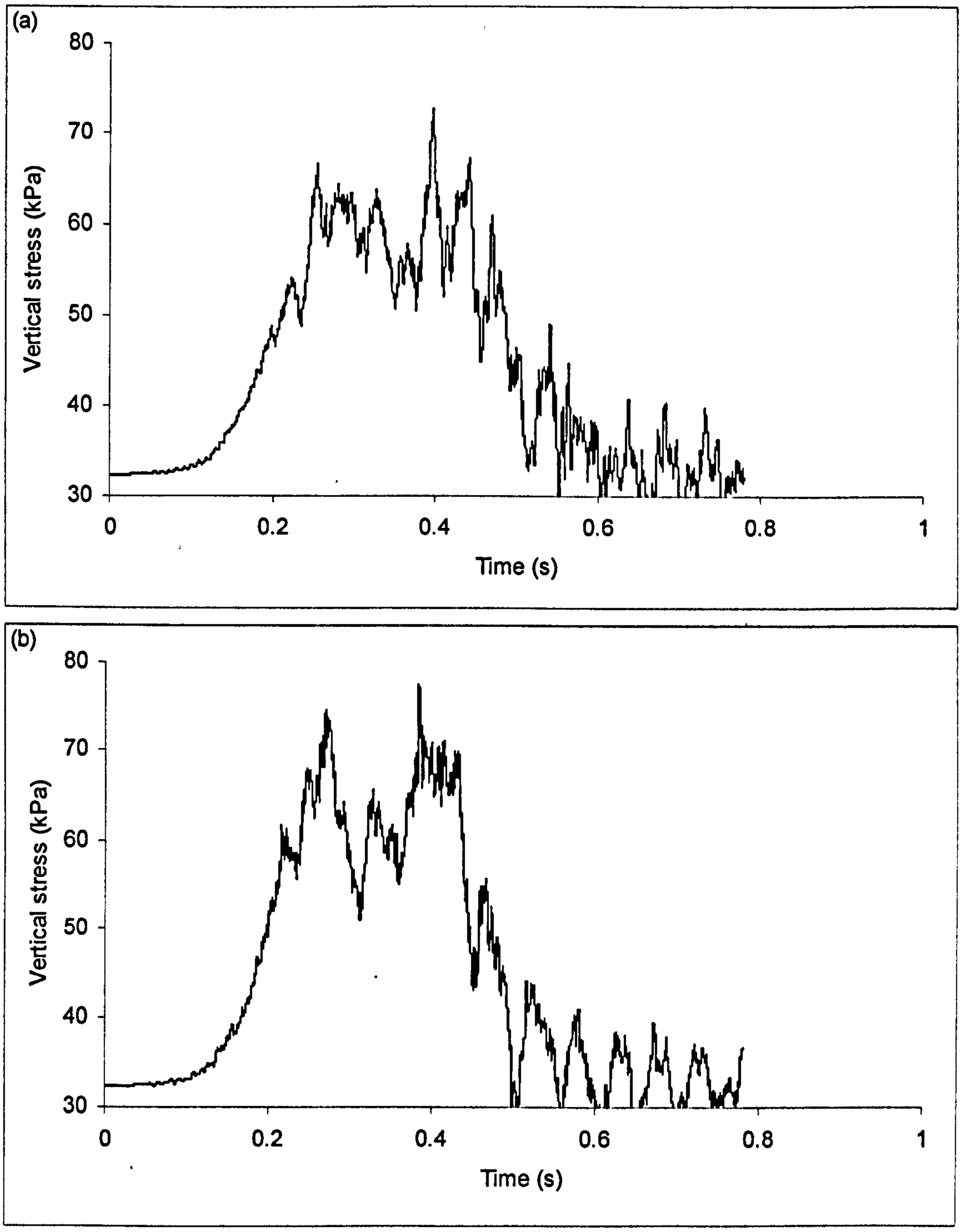

Figure 5.23. Vertical stress in the subgrade (At depth=1.8 m) under passage of a train coach at V=70 m/s (EB=120 MPa, BD=300 mm) (a) nonlinear subgrade (b) linear subgrade (ES=40 MPa)

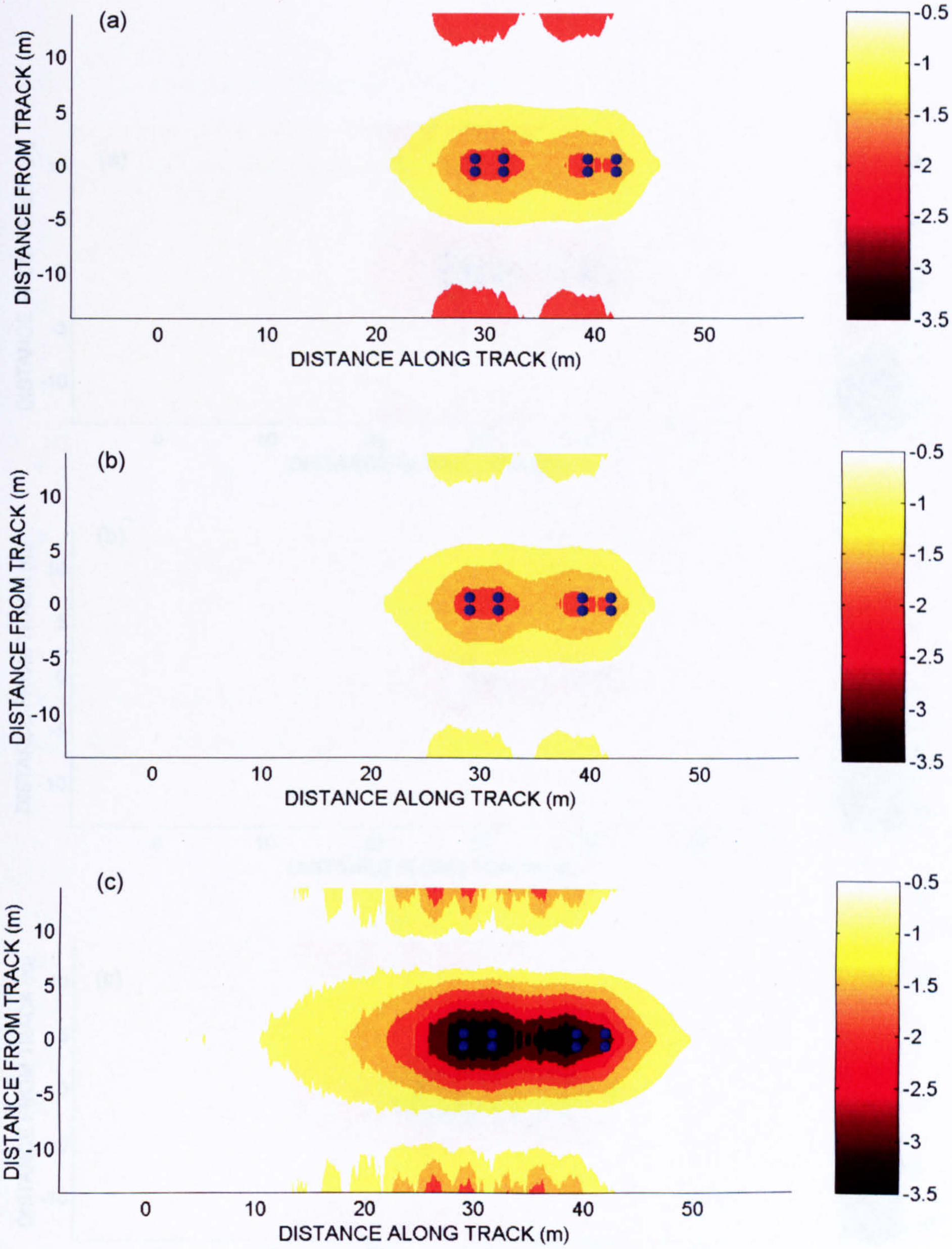

Figure 5.24. Plan view of displacement field for (a) nonlinear simulation (nonlinear subgrade) (b) linear simulation (ES=40 MPa), (c) linear simulation (ES=15 MPa) at a speed of 30 m/s (EB=120 MPa, BD=300 mm)

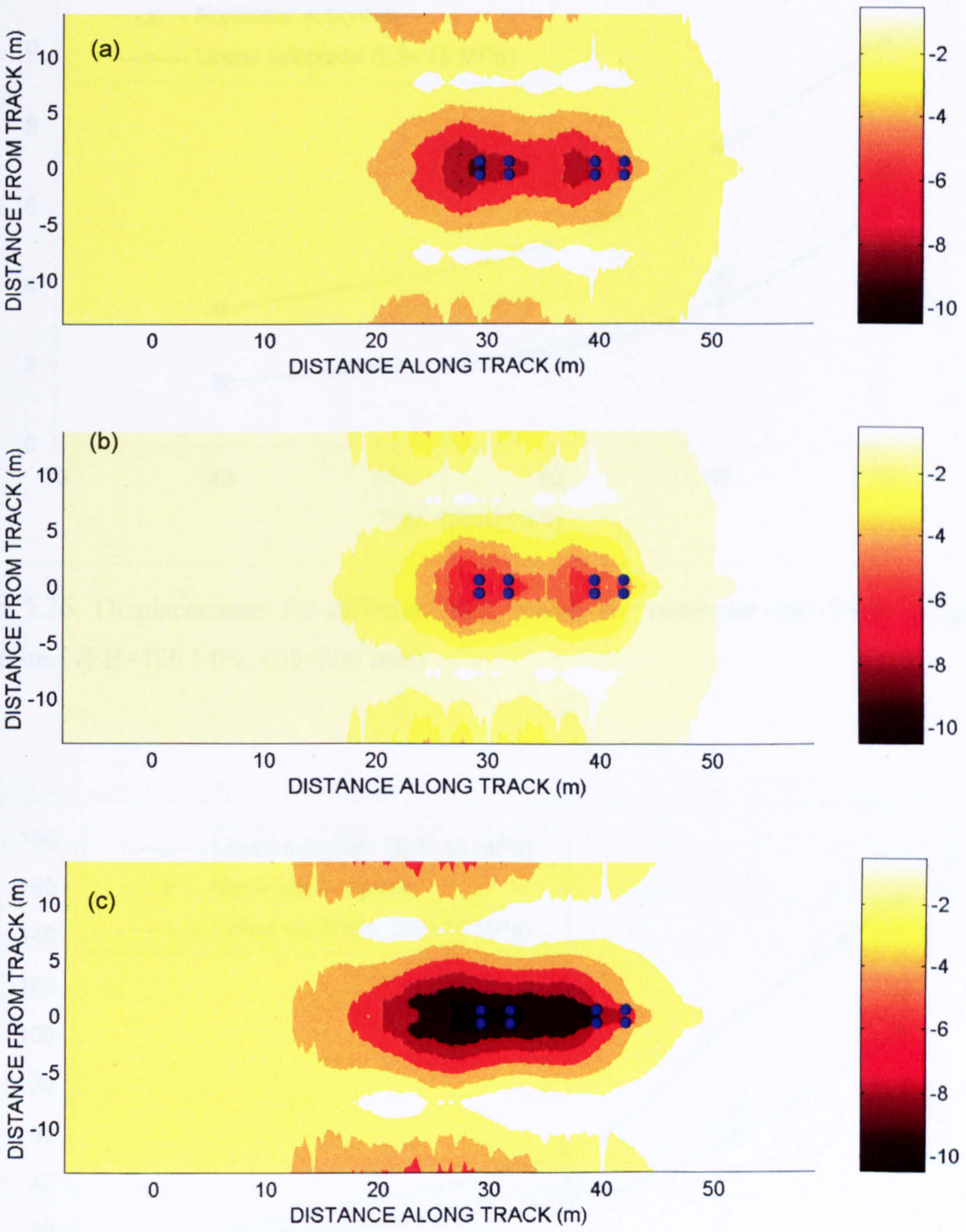

Figure 5.25. Plan view of displacement field for (a) nonlinear simulation (nonlinear subgrade) (b) linear simulation (ES=40 MPa) (c) linear simulation (ES=15 MPa) at a speed of 70 m/s (EB=120 MPa, BD=300 mm)

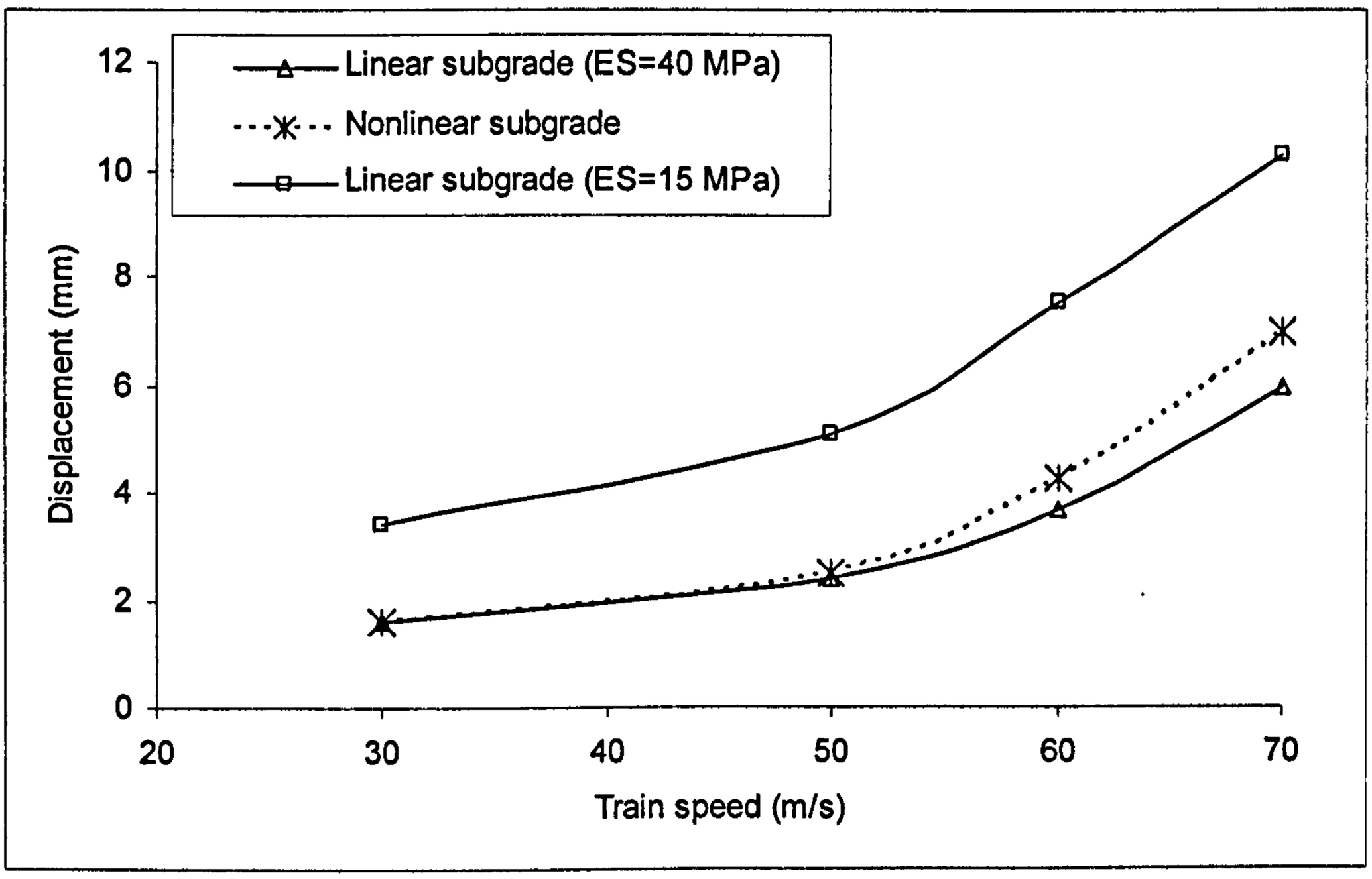

Figure 5.26. Displacements for different train speeds for nonlinear and linear subgrade simulations (EB=120 MPa, BD=300 mm)

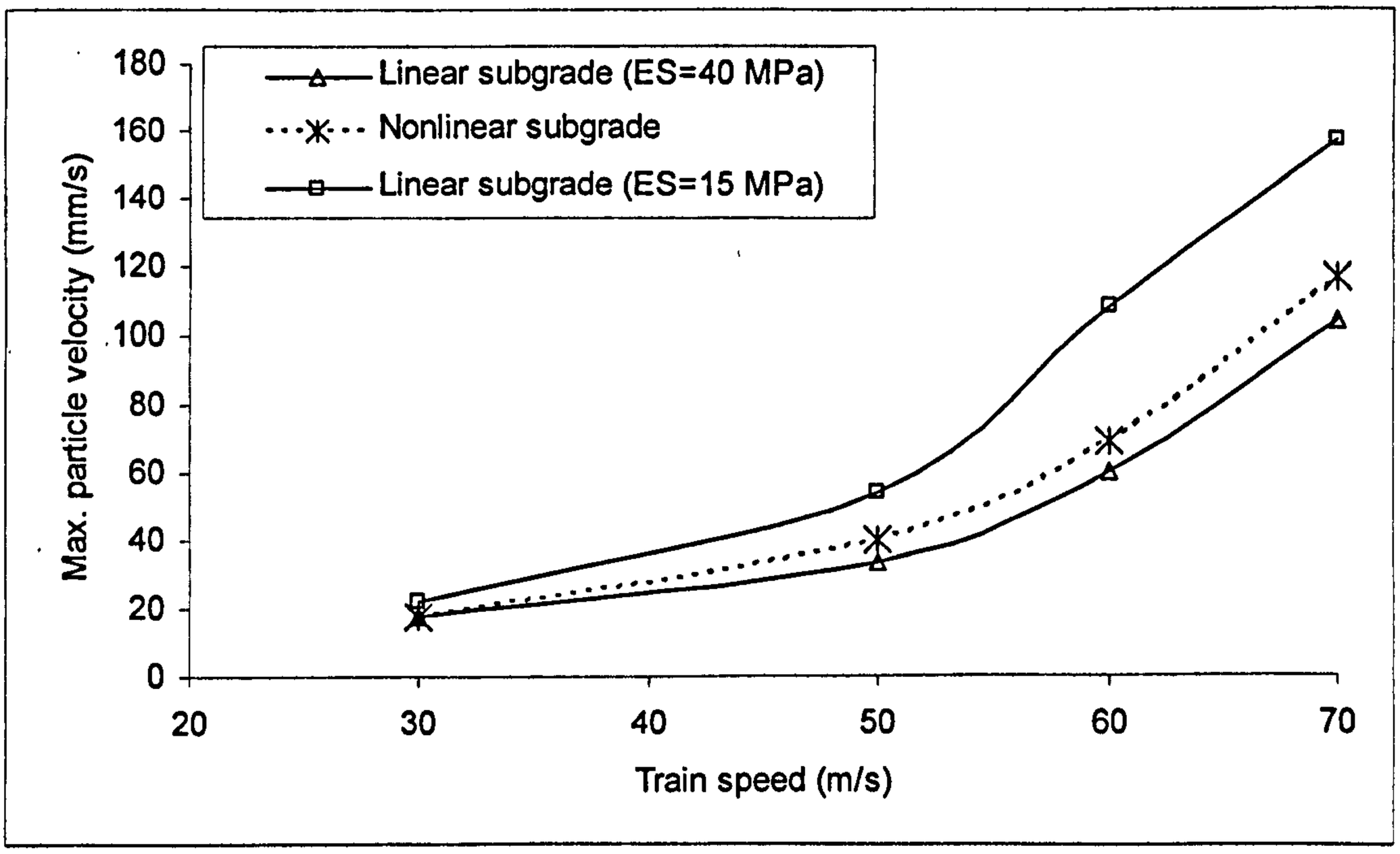

Figure 5.27. Maximum ballast particle velocity for different train speeds for nonlinear, and linear subgrade simulations (EB=120 MPa, BD=300 mm)

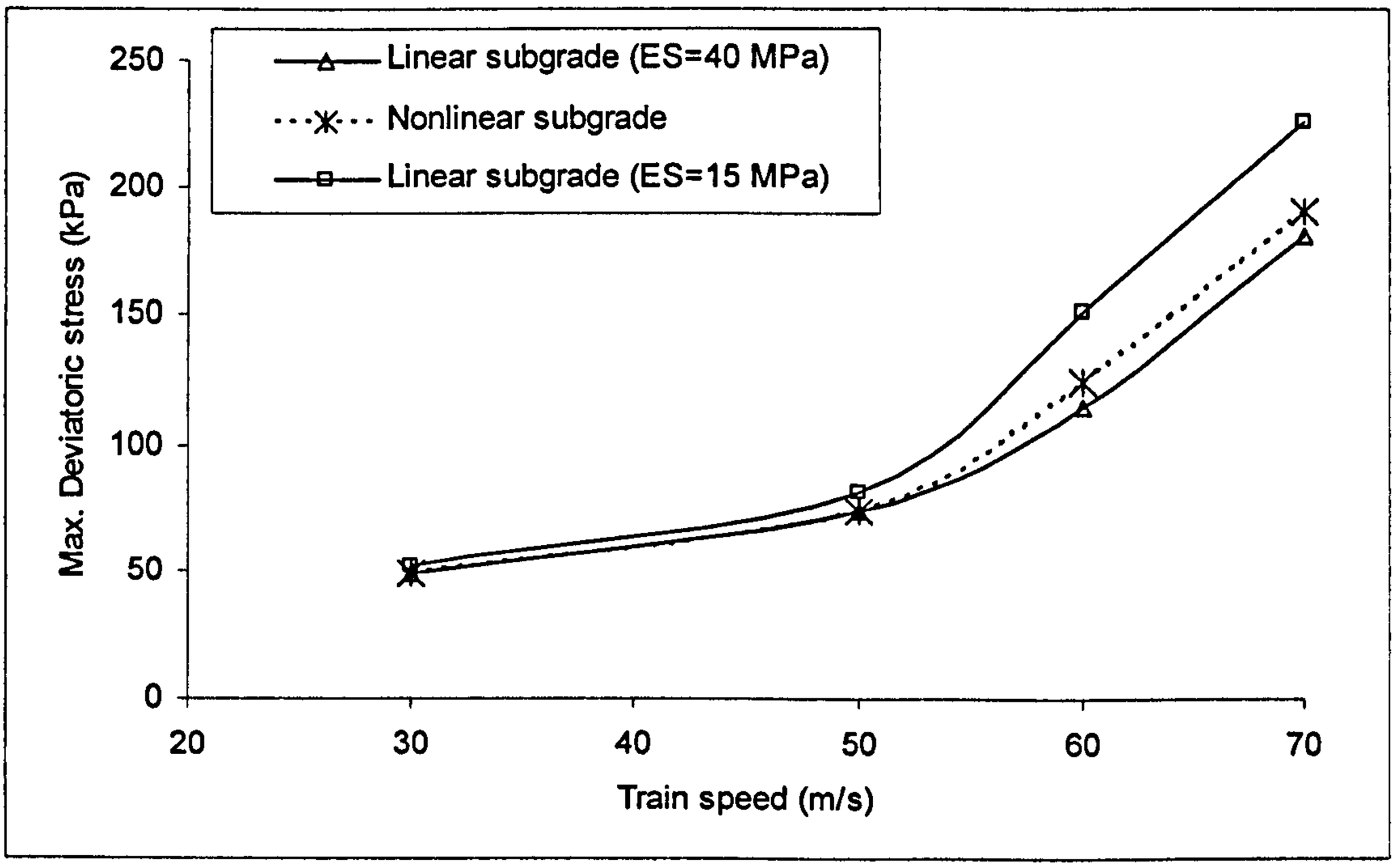

Figure 5.28. Simulated deviatoric stress in the ballast on linear (E=40 MPa) and nonlinear subgrade (EB=120 MPa, BD=300 mm)

suggesting that the assumption of upper bound linearity could effectively underestimate the ballast vibration level (ballast particle velocity) and consequently the track maintenance level, as discussed in Chapter 4. Moreover, the nonlinear simulation predicts higher deviatoric stress, when compared with to the upper-bound linear simulation (ES=40 MPa) in the ballast for high speed cases, as shown in Figure (5.28).

As discussed in Chapter 4, the closer the stress state is to the static yield/failure surface in the soil, the more permanent deformation generated, and subsequently a higher level of maintenance is required. On this basis, the ratio of induced stress ratio to the stress ratio at plastic yielding (based on Mohr-Coulomb yield criterion), termed as the plastic ratio $(\frac{q}{p}/(\frac{q}{p})_{MC})$ in the ballast layer, was considered in Chapter 4 as an indictor of susceptibility to permanent deformation in the ballast (see Section 4.6).

As the plastic ratio approaches one, i.e the stress state approaches the yield surface, more plastic deformation is generated and more frequent maintenance is needed. Figure (5.29) shows the plasticity ratio distribution in the ballast layer obtained from track analyses with linear and nonlinear subgrade models. Plastic ratio distribution from nonlinear simulation is, to a large degree, similar to the plastic ratio from the linear simulation (ES=40 MPa) for train speeds of 30 m/s and 50 m/s. However, at a train speed of 70 m/s, the plastic ratio, obtained from nonlinear simulations, seems to be generally higher and the zones with high plastic ratio seem to have extended when compared with the linear simulation. According to this observation, it is confirmed that the maintenance level in the ballast can be adversely affected by subgrade nonlinearity. Therefore, it is important that subgrade nonlinearity be incorporated into the model to enable a correct prediction of maintenance level in the track, especially at higher speeds.

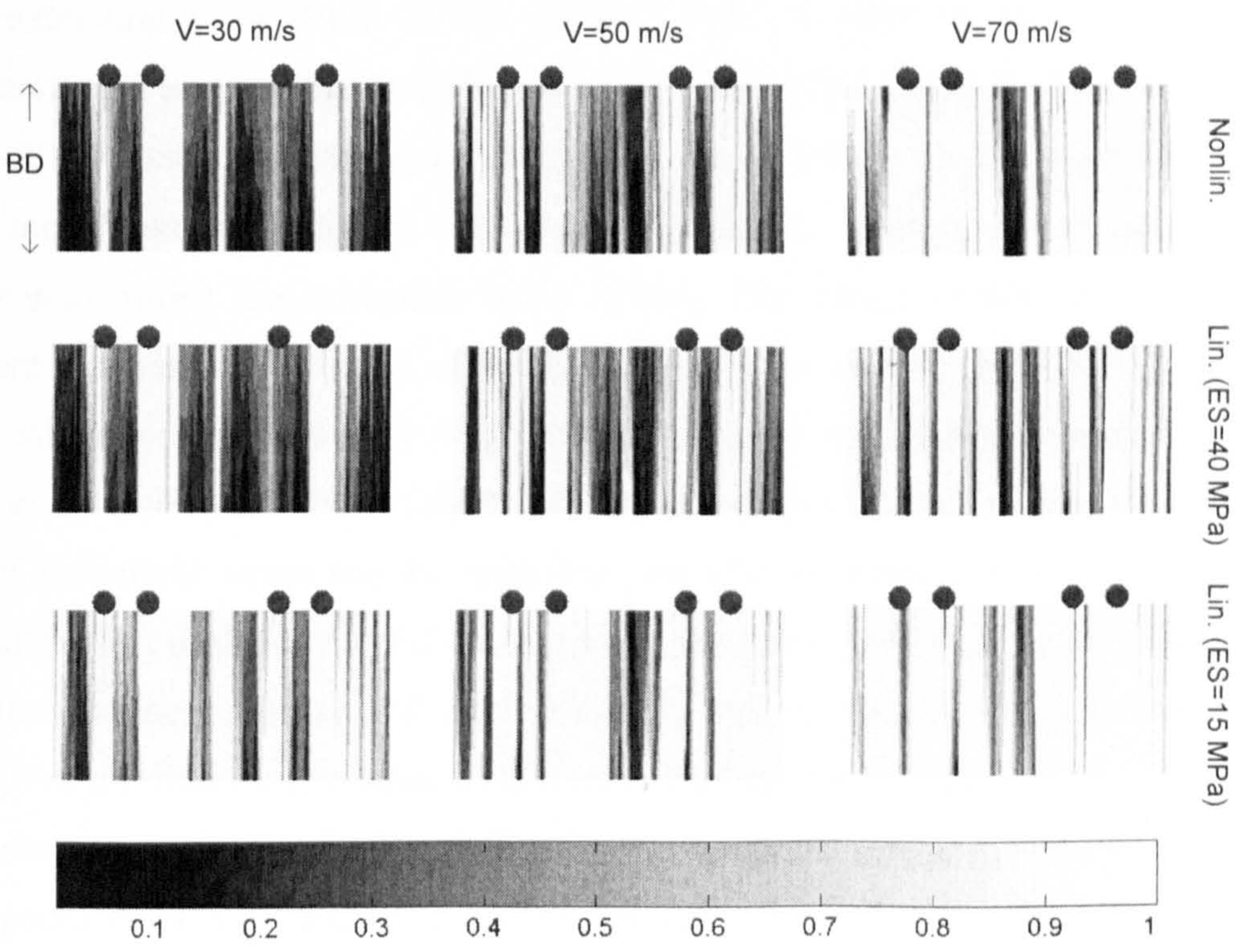

Figure 5.29. Plastic ratio distribution in the ballast layer under the coach wheels for simulations with linear and nonlinear subgrades (EB=120 MPa, BD=300 mm)

This section studied the effect of subgrade nonlinearity on track response under the passage of a passenger train (axle load of 17.4 T) at different train speeds. It should be noted that the effect of subgrade nonlinearity is also related to train axle load as well as train speed. Under a freight train, with a heavy axle load, high deviatoric stresses may be induced in the subgrade which may trigger a higher level of stiffness degradation, even in a low speed regime. Therefore for heavy axle trains, nonlinearity of subgrade may need to be addressed even at lower speeds.

5.6 The Effect of Ballast Nonlinearity on Track Response

A railway track with a ballast depth of 300 mm resting on 7 metres of linear soft subgrade (ES=15 MPa) is considered. The soft subgrade is placed on a relatively stiff layer (ES=50 MPa) extending to a depth of 35 metres, where it rests on bed rock. The model configuration is as given before in Section 3.3.1. Ballast behaviour has been represented by linear, $K-\theta$, universal and Boyce constitutive relationships. As discussed previously, the $K-\theta$ model takes into account only mean stress effects, whereas the universal and Boyce models also reflect the deviatoric stress effects. The model parameters are adjusted to represent the reasonable change of ballast stiffness with induced stress level. The range of ballast stiffness compares well with those considered by different researchers, such as Shahu *et al.* (1999) and Hall (2000). At low to medium speeds, as discussed before, the level of deviatoric stress can be relatively low (for passenger trains) and therefore the hardening effect of the deviatoric stress maybe dominant. For higher speed cases, however, the ballast stiffness reduces with high deviatoric stresses, which would be induced in the ballast. For a railway track under freight train loading (heavy axle loading), the softening mechanism (reduction of ballast stiffness with deviatoric stress) may be dominant for all train speeds since the induced deviatoric stress in the ballast can be high, even at low speeds. By assigning negative and positive values to k_3 in the universal model, the softening or hardening effect of deviatoric stress can be respectively simulated. The models' parameters are given in Table (5.2). Figures (5.30) and (5.31) present the resilient modulus change with mean stress and stress ratio in a conventional compression triaxial test (constant confining pressure) for different models; these are used for simulations of

track response under low to medium train speeds (V=30 and 50 m/s). Figure (5.32) depicts the variation of the ballast resilient modulus with deviatoric stress under triaxial conditions for a universal (softening) model representing the ballast resilient behaviour under a high speed regime. An initial increase of resilient stiffness along with increases in deviatoric (deviator) stress, caused by the dominant effect of the mean stress, is followed by reduction of resilient stiffness with a further increase in deviatoric stress.

All nonlinear simulations are completed successfully, apart from the one with the Boyce model. The simulation with the Boyce model starts to diverge when the train is about 20 m into the mesh. The numerical divergence problem may be the result of a rapid change of resilient stiffness from one time step to another one. It would introduce a rapid change in internal forces and consequently in accelerations which are probably causing the convergence problem. The simultaneous change of Poisson's ratio may also contribute to the convergence problem. To overcome this problem, the Boyce model may need to be implemented differently, for example along with an implicit time integration scheme. This problem is not investigated further here, and the effects of ballast nonlinearity are studied in this section using other successful simulations with the universal and $K-\theta$ constitutive relationships. In spite of the convergence problem, initial results, in the form of a displacement field (Figure 5.33), obtained from a nonlinear simulation with the Boyce model at a train speed of 50 m/s, suggests that the corresponding track response is remarkably similar to those obtained from other nonlinear and linear simulations at the same train speed.

Ballast Models	Parameters
$K-\theta$	k_1=1000 k_2=0.33
Boyce	k_a=55E6 G_a=80E6 n=0.626
Universal (hardening)	k_1=1000 k_2=0.33 k_3=0.05
Universal (softening)	k_1=1000 k_2=0.40 k_3=-0.65

Table 5.2. Parameters of different ballast models

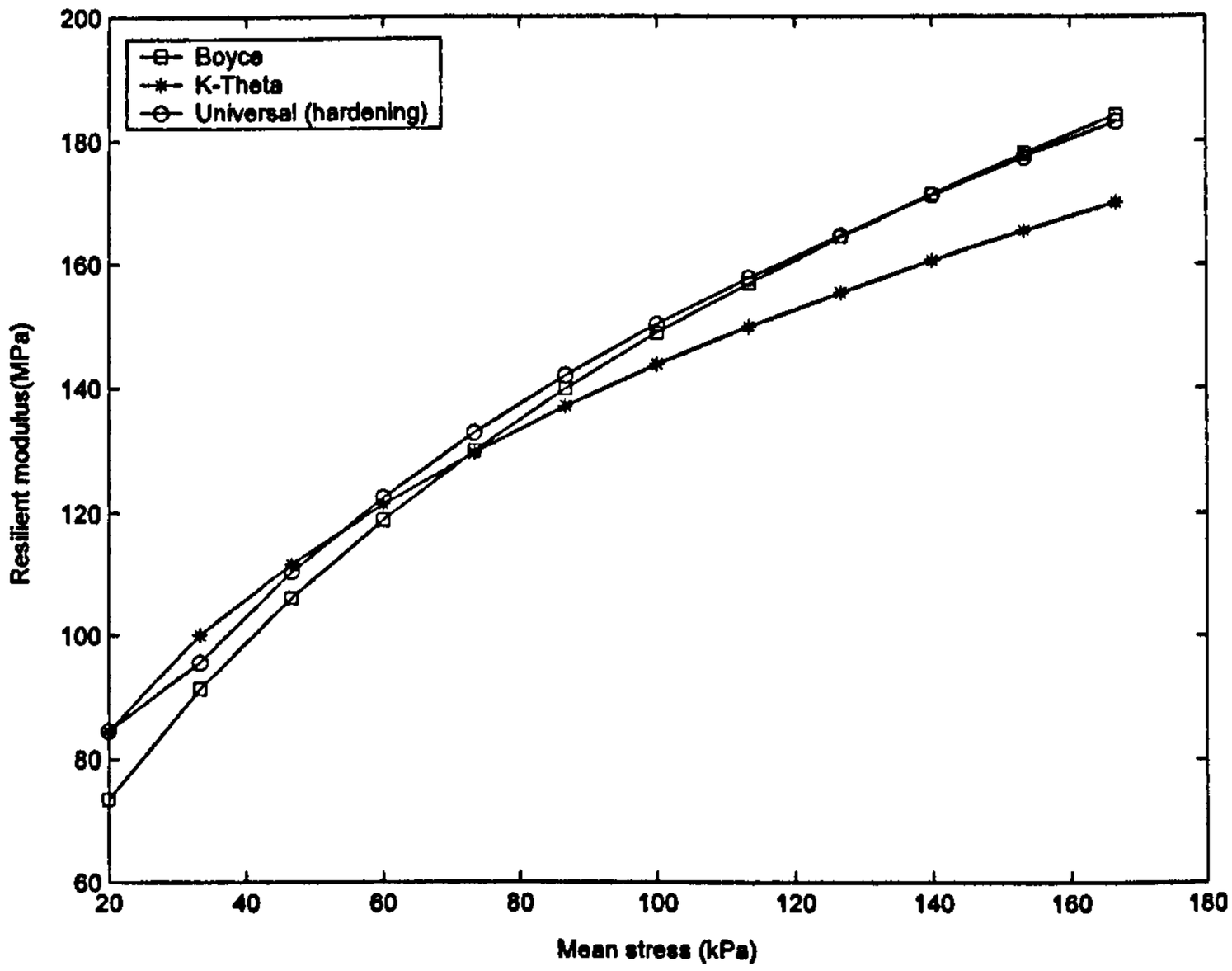

Figure 5.30. Resilient modulus variation with mean stress for different calibrated ballast models in conventional triaxial condition ($\sigma_3 = 20$ kPa)

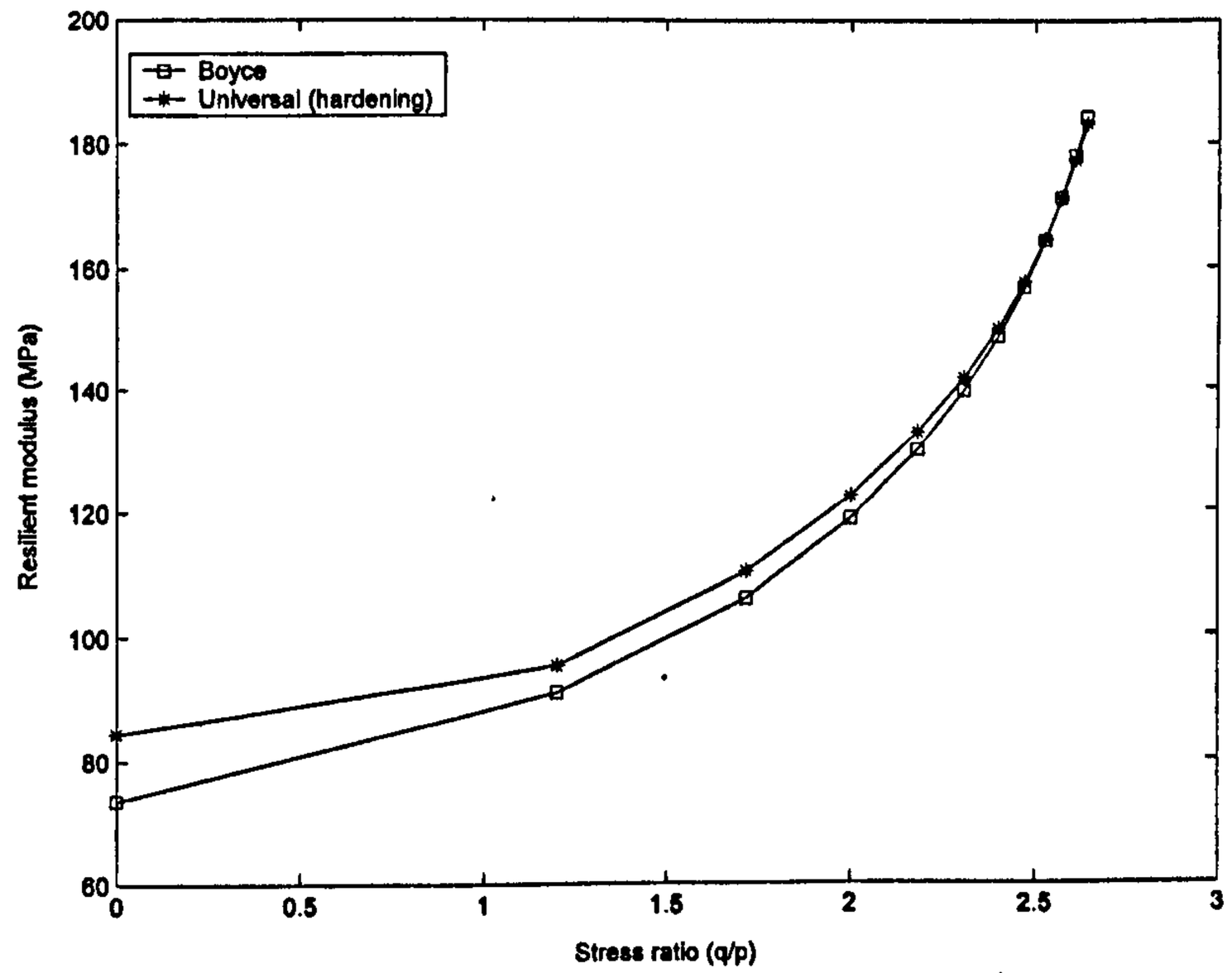

Figure 5.31. Resilient modulus variation with stress ratio for different calibrated ballast models in conventional triaxial conditions ($\sigma_3 = 20$ kPa)

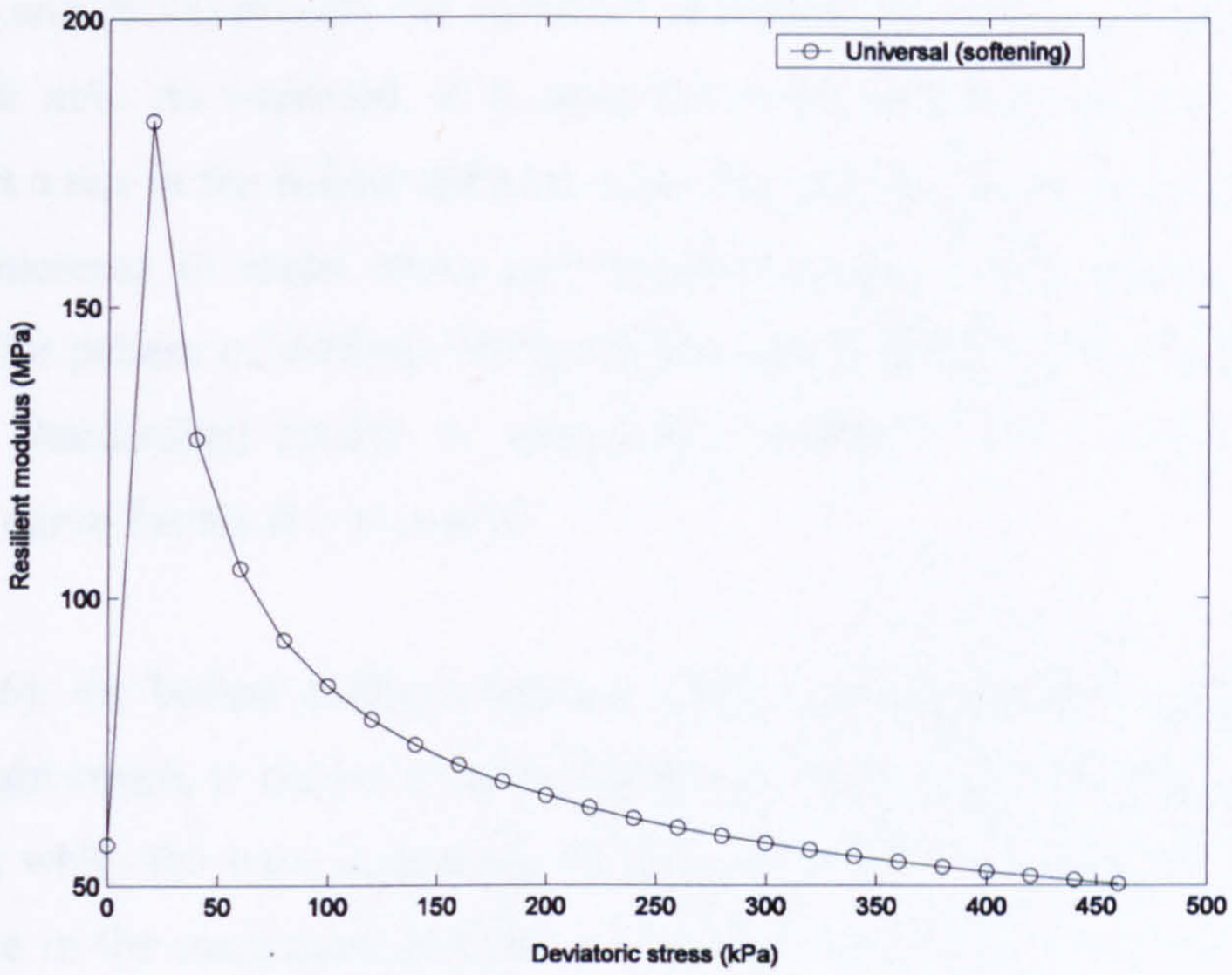

Figure 5.32. Resilient modulus variation with deviatoric stress for the universal (softening) model in conventional triaxial conditions ($\sigma_3 = 20$ kPa)

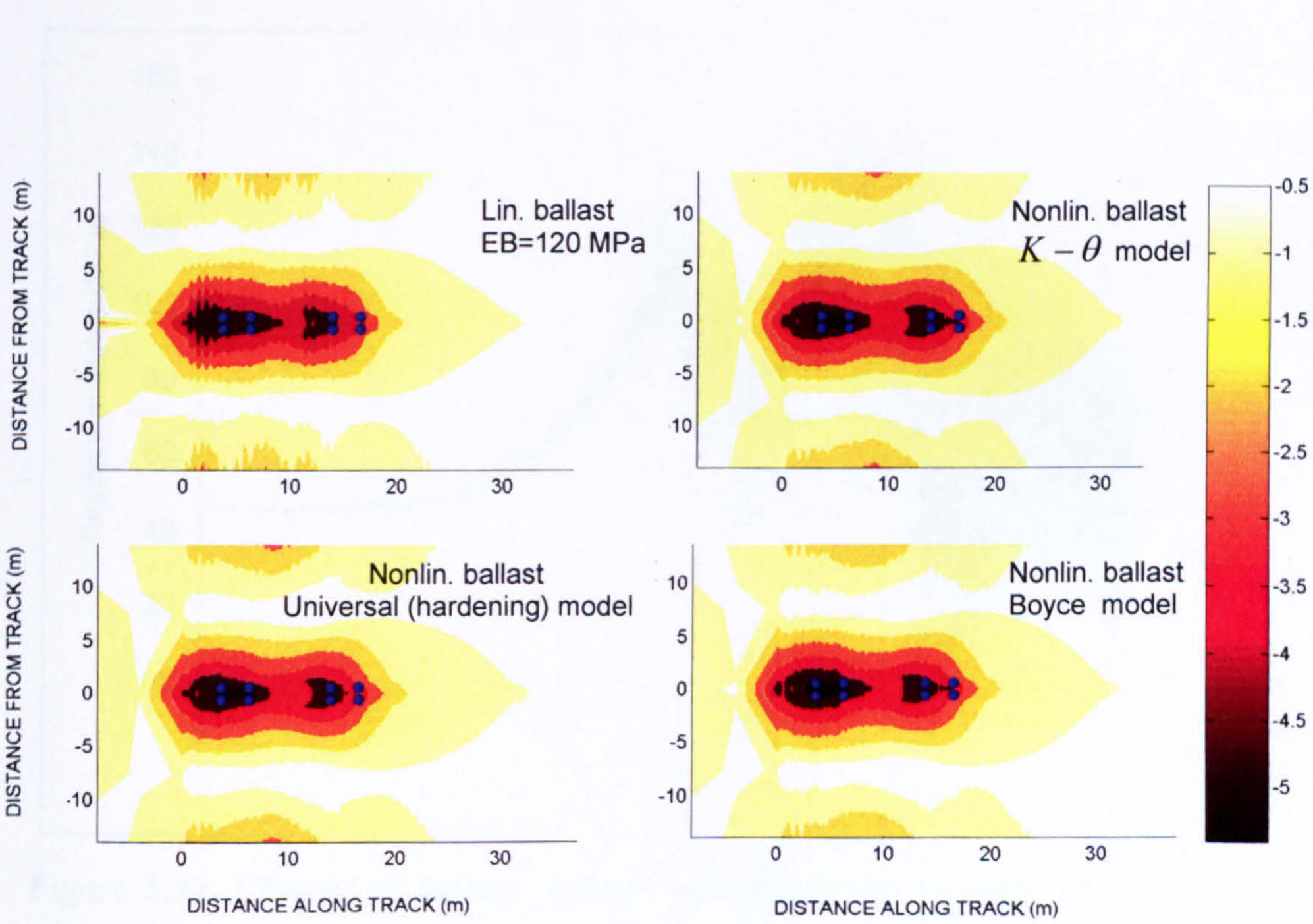

Figure 5.33. Plan view of displacement field for (a) linear simulation (E_b=120) , (b) $K-\theta$ model (c) universal (hardening) (d) Boyce model at a train speed of 50 m/s (ES=15 MPa, BD=300 mm)

Figures (5.34) and (5.35) present the variation of ballast stiffness under passage of a train coach at V=50 m/s. As expected, it is seen that both models (universal-hardening and $K-\theta$) predict a rise in the ballast stiffness when the train passes the point of interest, as a result of the increase in mean stress and deviatoric stress in the ballast. Both models produce a similar pattern of stiffness change in the ballast. However, the stiffness curve for the universal (hardening) model is remarkably smoother when compared with the corresponding curve for the $K-\theta$ model.

In Figure (5.36), the ballast stiffness change, using a universal (softening) model under passage of a train coach, is shown for a train speed of 70 m/s. The stiffness of the ballast is still increasing while the train is passing the point at which the response is simulated. A limited increase in the maximum stiffness is observed however, when compared with the nonlinear simulation at V=50 m/s (Figures 5.34 and 5.35). Considering the remarkable

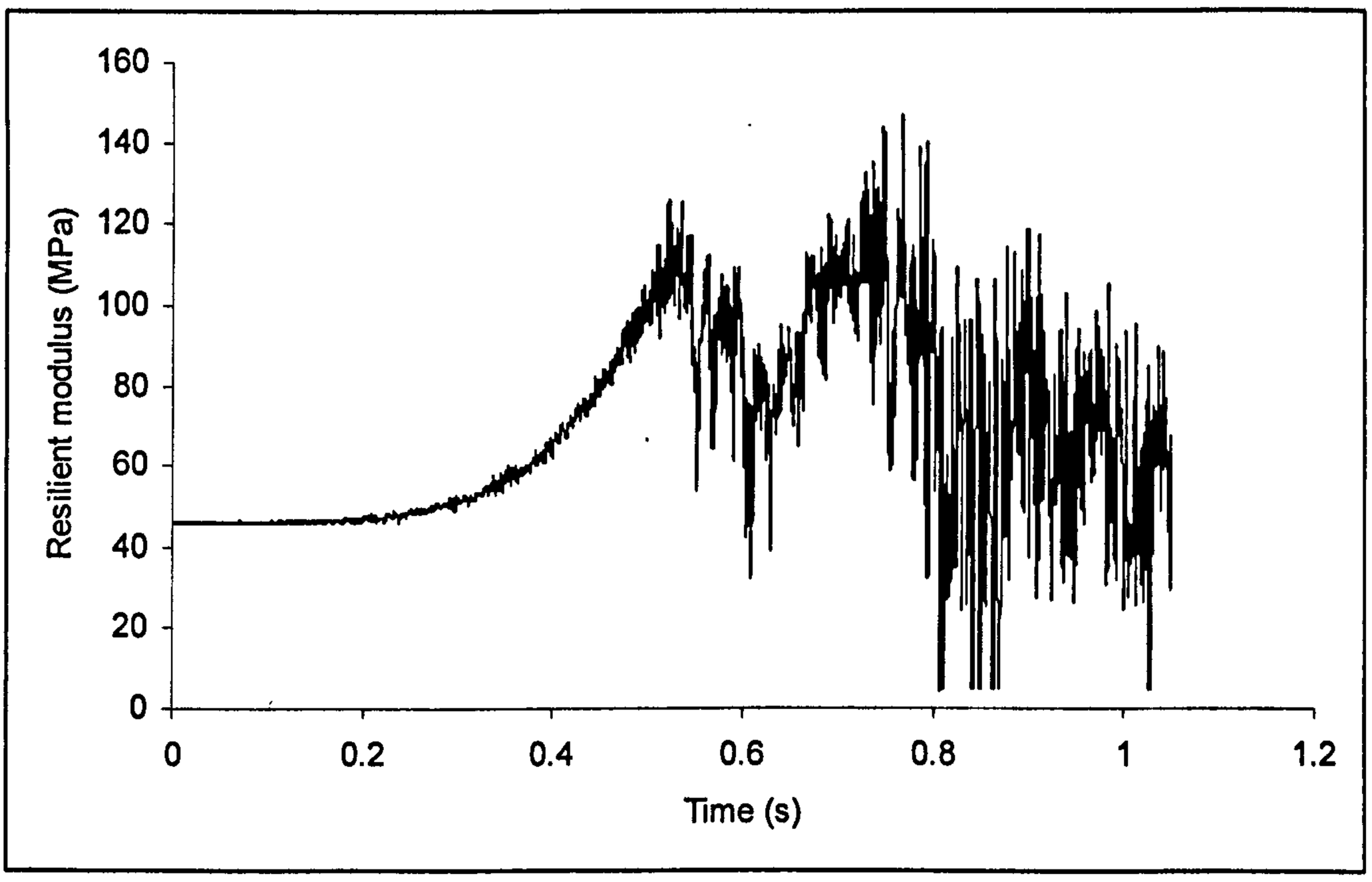

Figure 5.34. Change of ballast resilient modulus under passage of a train coach from nonlinear simulation with $K-\theta$ model (ES=15 MPa, BD=300 mm, V=50 m/s)

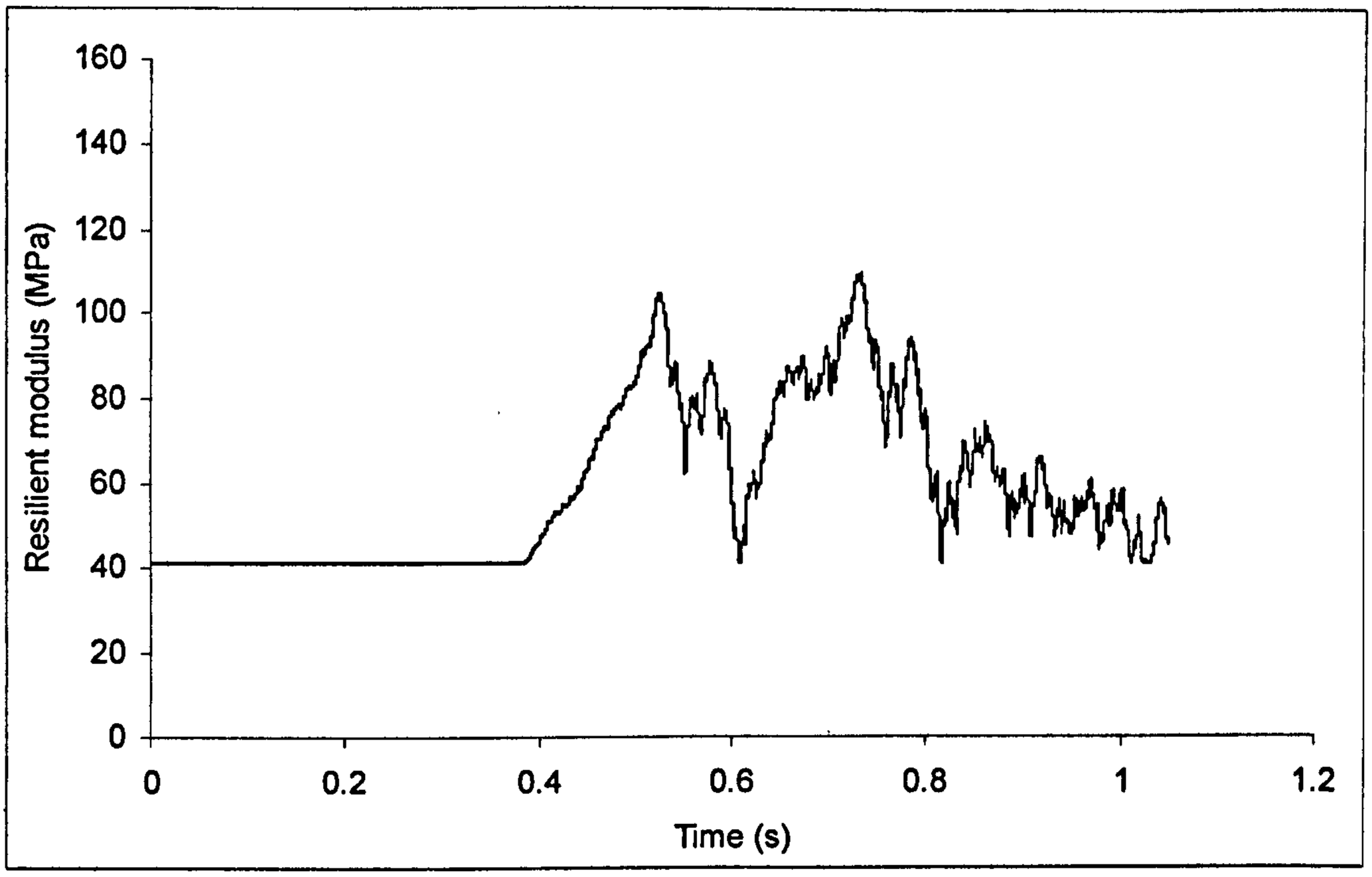

Figure 5.35. Change of ballast resilient modulus under passage of a train coach from nonlinear simulation with universal model-hardening (ES=15 MPa, BD=300 mm, V=50 m/s)

Figure 5.36. Change of ballast resilient modulus under passage of a train coach from the nonlinear simulation with universal model-softening (ES=15 MPa, BD=300 mm, V=70 m/s)

increase in the ballast stress level from V=50 m/s to V=70 m/s, as presented in Chapter 4 (Figure 4.28), this limited increase in the stiffness can be attributed to the softening effect of the deviatoric stress as represented by a negative k_3 in the universal model. According to the softening universal model, the increase in resilient modulus, which is linked to the increase in mean stress, is counteracted by the decrease in the resilient modulus with deviatoric stress.

Figures (5.37-5.46) depict the response of the track for nonlinear and linear simulations at train speeds of 50 m/s and 70 m/s. At a train speed of 50 m/s, the nonlinear and linear models give similar displacement responses (Figure 5.37). The nonlinear simulation with the universal (hardening) model gives a remarkably similar response in terms of vibration and stress level when compared with the linear simulation (EB=120 MPa), as seen in Figures (5.38-5.42). Owing to the oscillatory nature (rapid change) of ballast stiffness in the nonlinear simulation with the $K-\theta$ model (Figure 5.34), considerably higher accelerations are predicted in the ballast when compared with the nonlinear simulations with the universal (hardening) and linear simulations. In comparison with simulations with the universal (hardening) model, more oscillations are also observed in the stress and velocity responses simulated based on the $K-\theta$ model. For the case studied, it can be said that the track responses are, in general, similar for linear and nonlinear simulations at a train speed of 50 m/s, as shown in Figures (5.37-5.41).

At a train speed of 70 m/s, the nonlinearity in the ballast stiffness has significant effects. The displacements from the nonlinear simulation (with universal-softening model) results in considerably higher displacement in comparison with those displacements from the linear simulations (Figures 5.42a and 5.42b). In addition, the nonlinear simulations predict considerably higher vibration in the ballast in terms of the ballast particle velocity and acceleration (Figures 5.43 and 5.44). As a result of the change in the ballast stiffness and corresponding changes in displacements, the vertical stress level in the ballast is seen to be significantly influenced by ballast nonlinearity (Figures 5.45a and 5.45b). According to Figures (5.46a) and (5.46b), the vertical stress pattern in the subgrade is also affected by nonlinearity in the ballast. Despite that, it is seen that the maximum vertical stress in the subgrade does not change significantly with nonlinearity in the ballast, even under a high

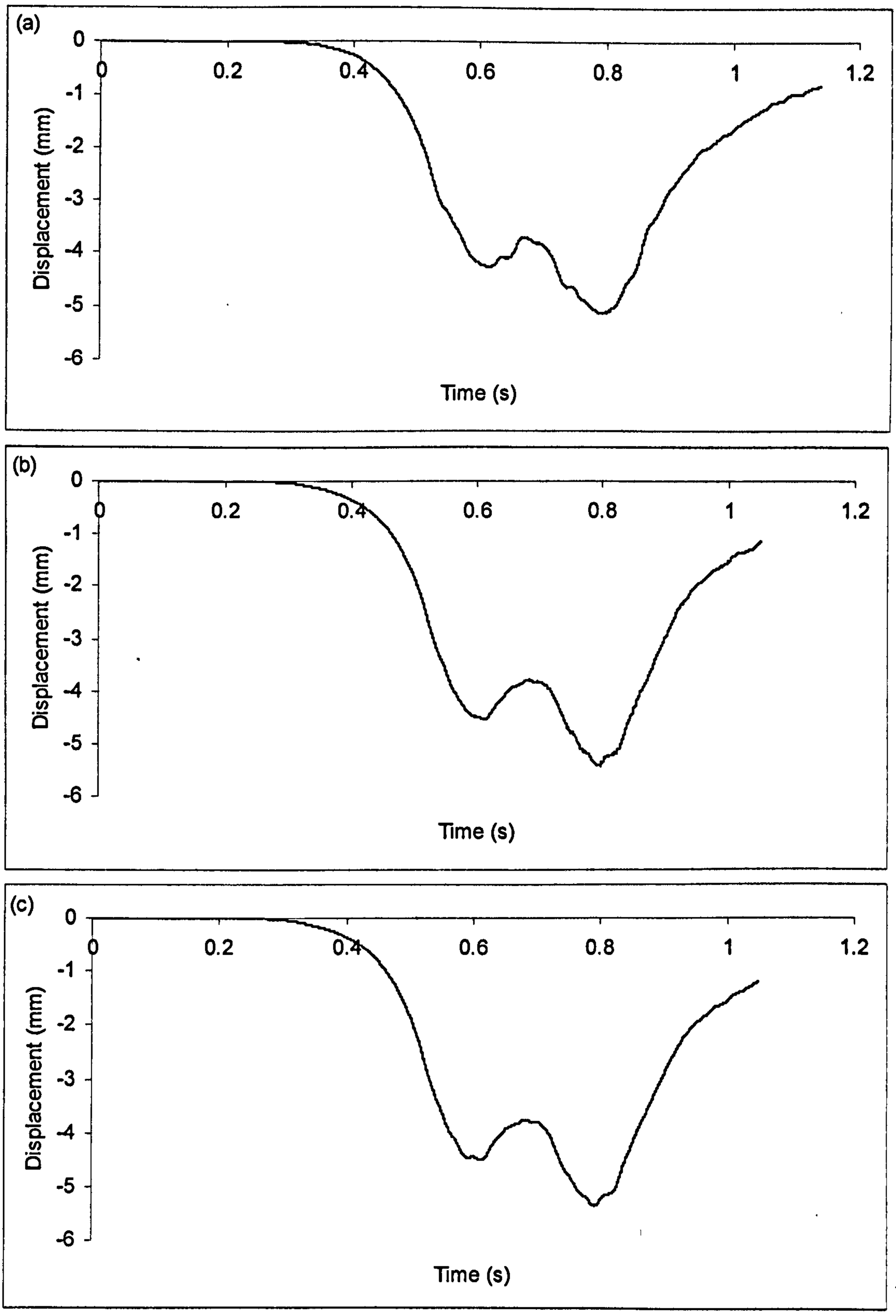

Figure 5.37. Sleeper displacement under a train coach (EB=120 MPa, BD=300 mm) at V=50 m/s -(a) linear ballast (EB=120 MPa) (b) nonlinear ballast ($K-\theta$ model) (c) nonlinear ballast (universal-hardening model)

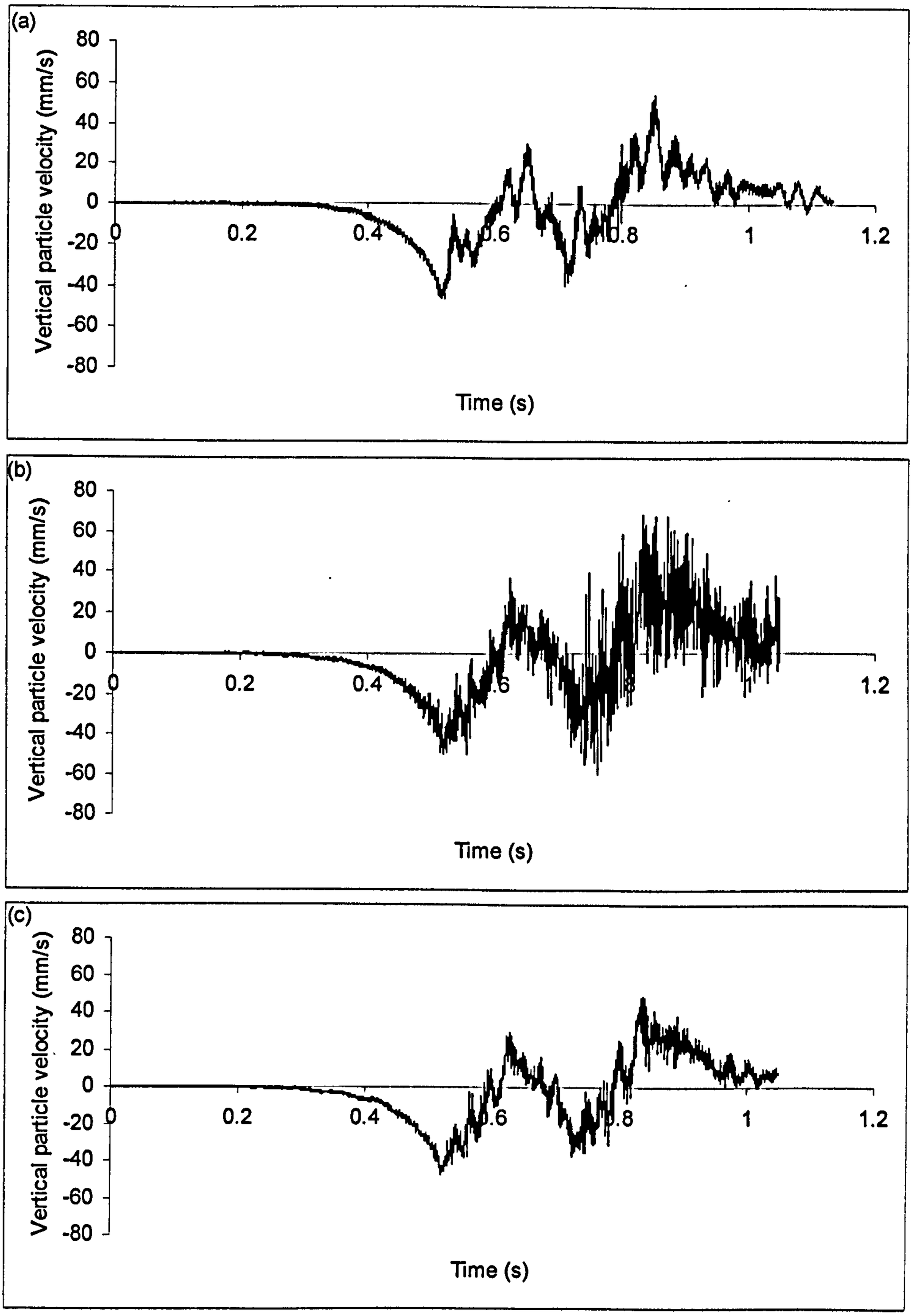

Figure 5.38. Ballast vertical particle velocity under a train coach (EB=120 MPa, BD=300 mm) at V=50 m/s -(a) linear ballast (EB=120 MPa) (b) nonlinear ballast ($K-\theta$ model) (c) nonlinear ballast (universal-hardening model)

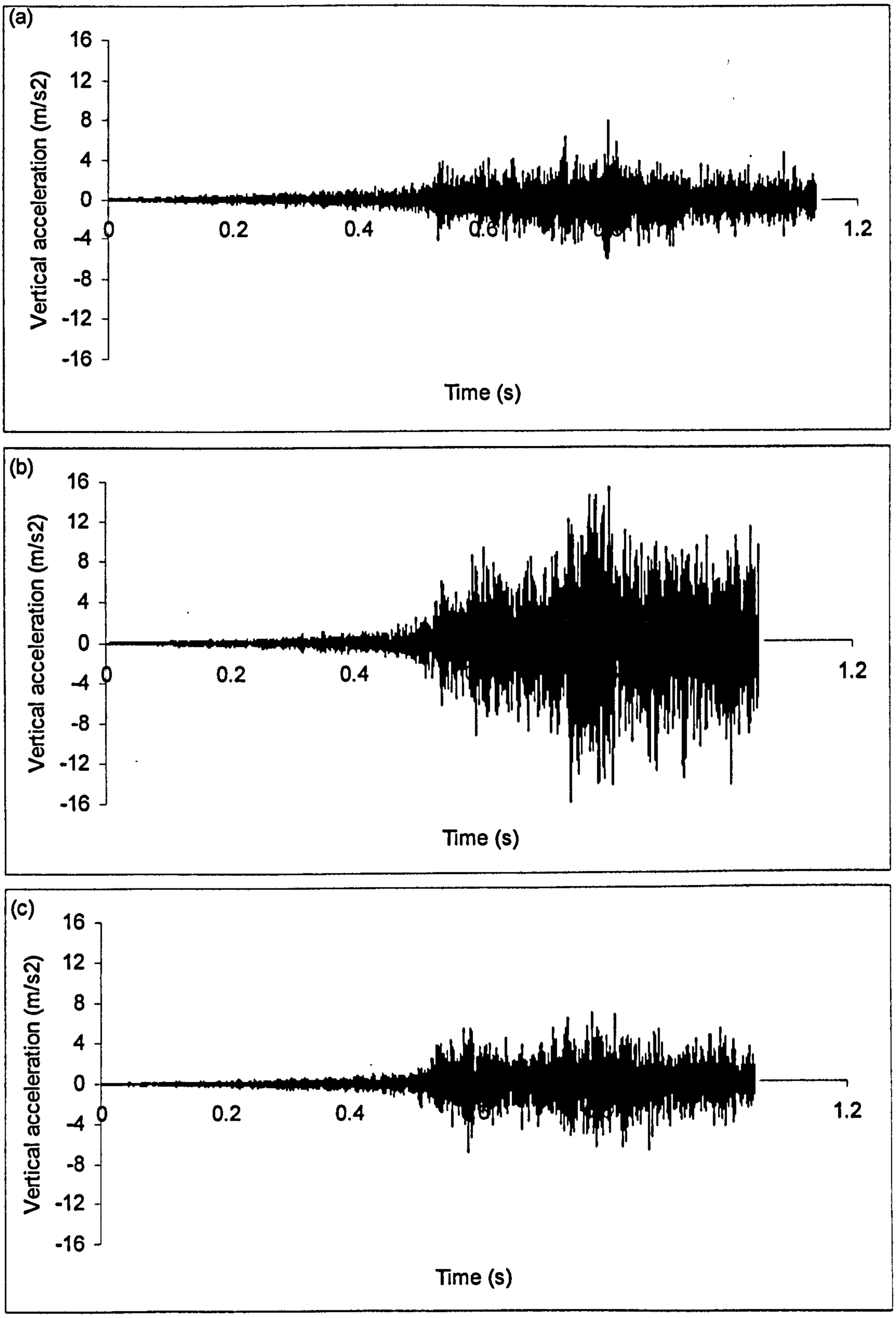

Figure 5.39. Ballast vertical particle acceleration under a train coach (EB=120 MPa, BD=300 mm) at V=50 m/s -(a) linear ballast (EB=120 MPa) (b) nonlinear ballast ($K-\theta$ model) (c) nonlinear ballast (universal-hardening model)

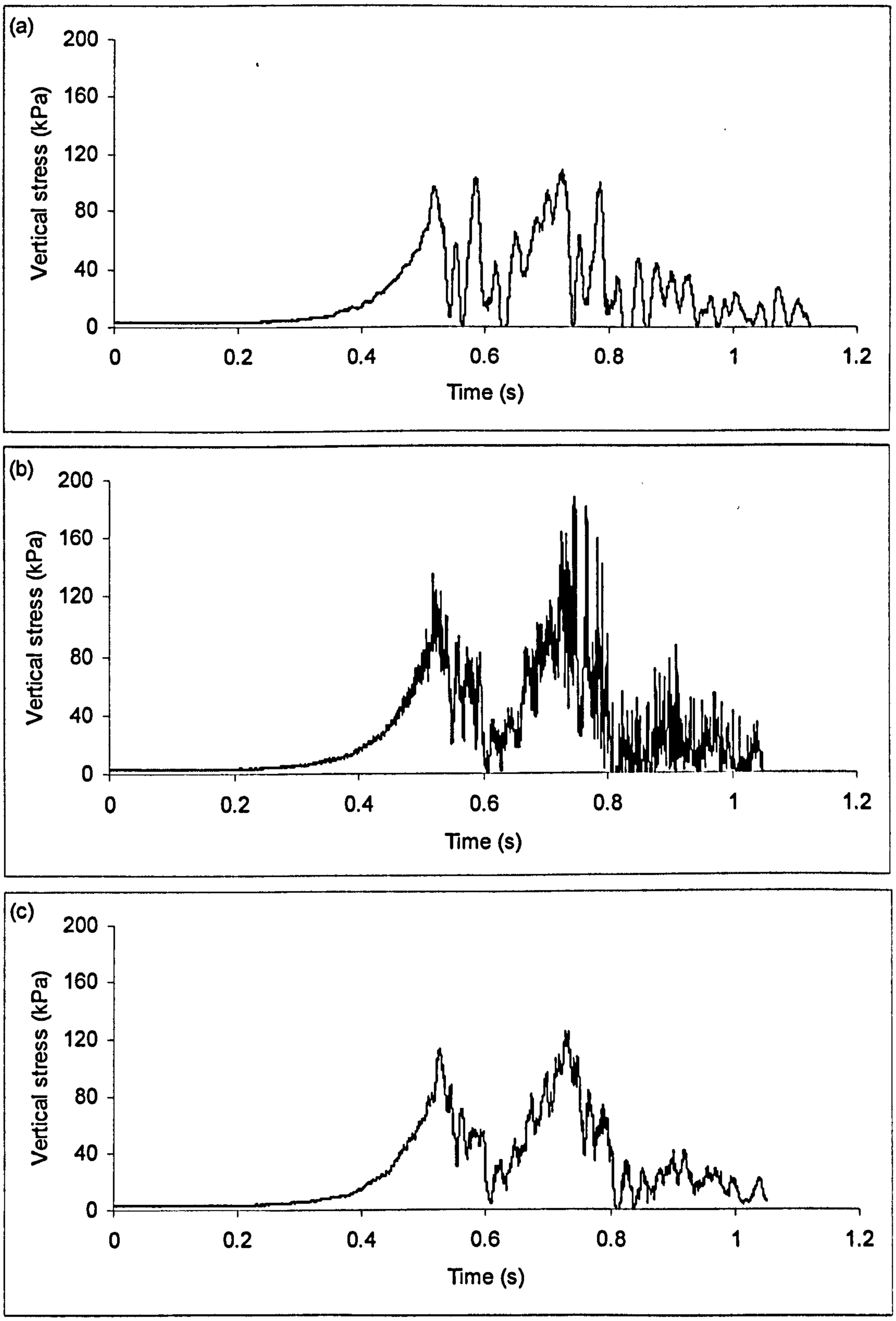

Figure 5.40. Vertical stress on top of ballast under a train coach (EB=120 MPa, BD=300 mm) at V=50 m/s -(a) linear ballast (EB=120 MPa) (b) nonlinear ballast ($K-\theta$ model) (c) nonlinear ballast (universal-hardening model)

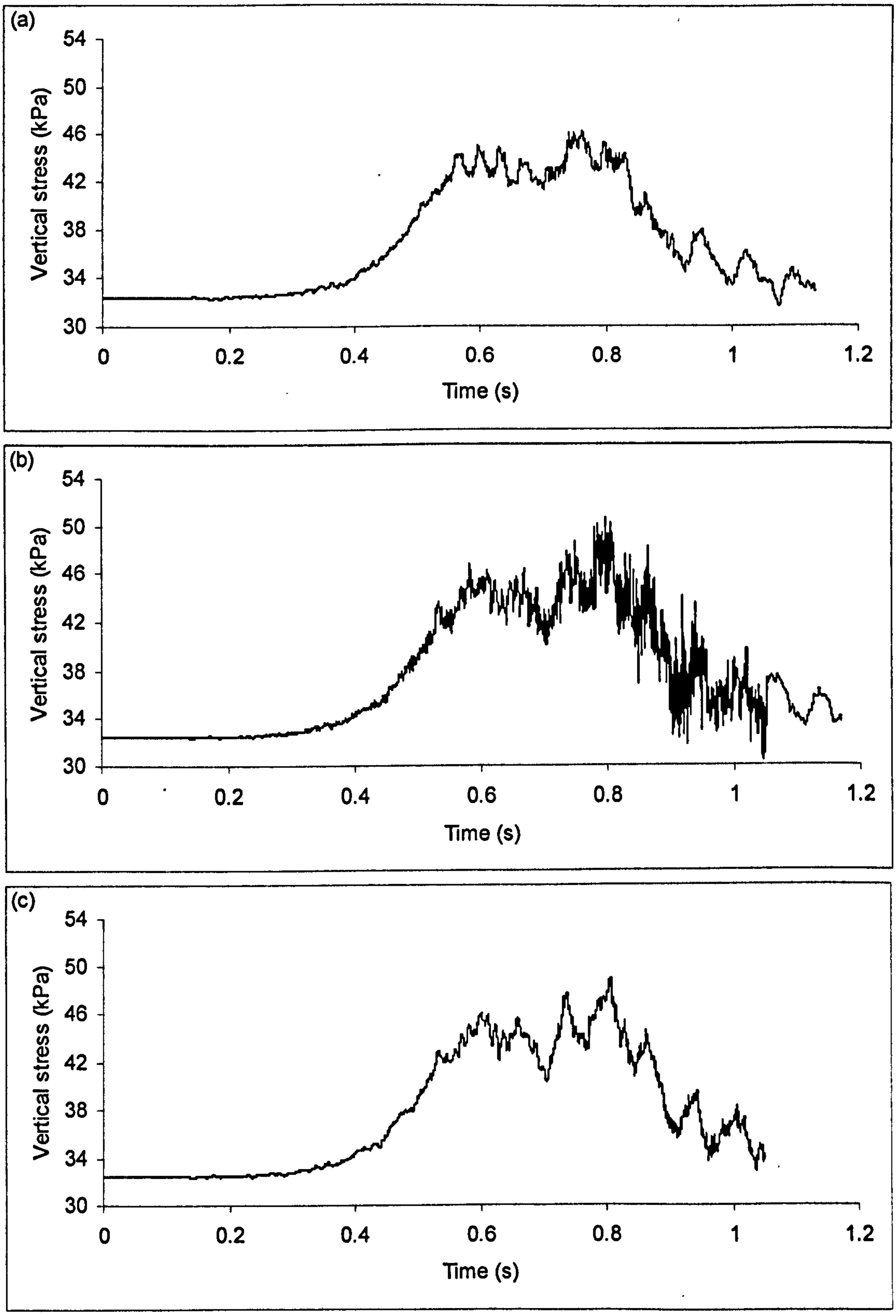

Figure 5.41. Vertical stress in subgrade (depth=1.8m) under a train coach (EB=120 MPa, BD=300 mm) at V=50 m/s -(a) linear ballast (EB=120 MPa) (b) nonlinear ballast ($K-\theta$ model) (c) nonlinear ballast (universal-hardening model)

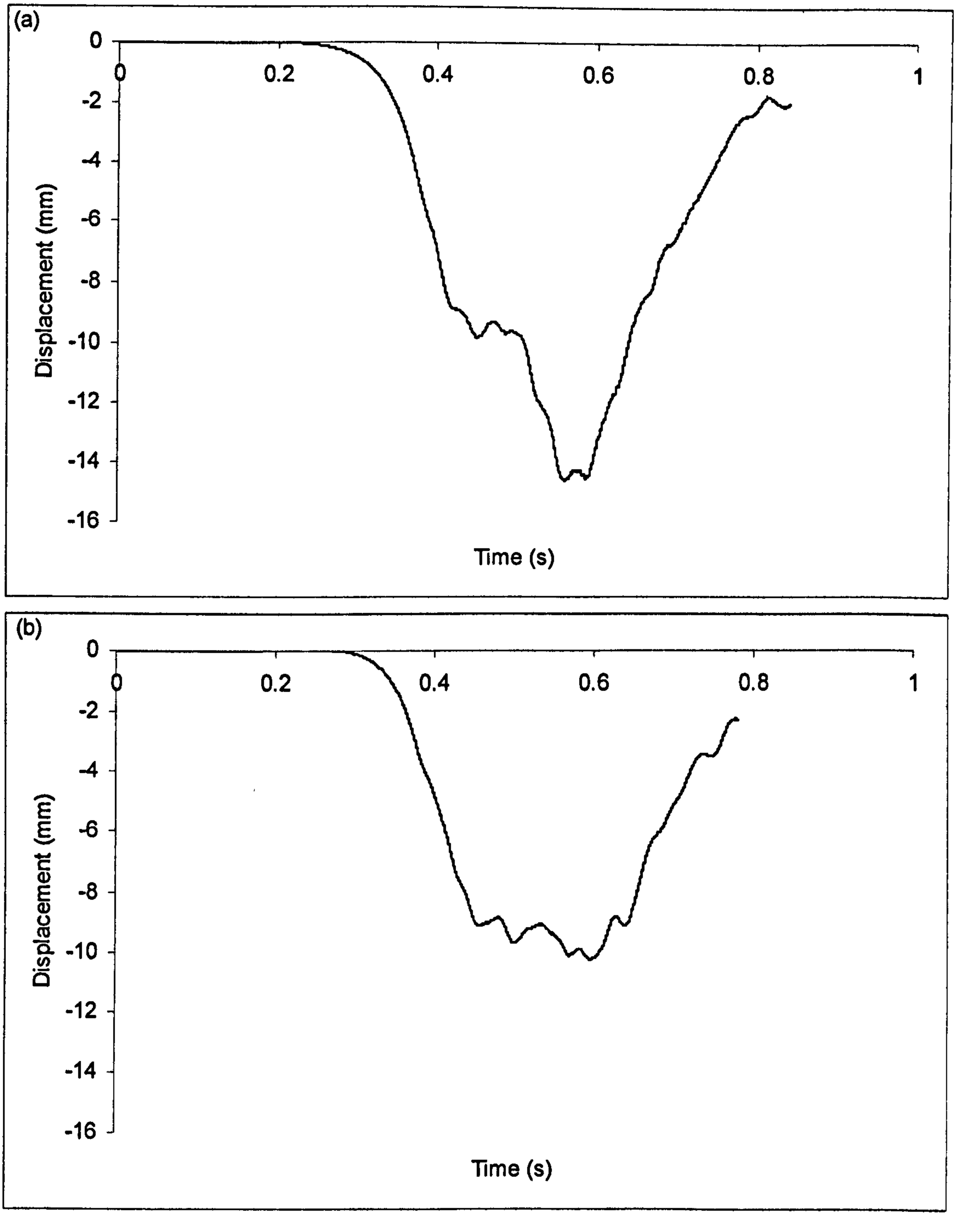

Figure 5.42. Ballast vertical displacements under a train coach (ES=15 MPa, BD=300 mm) at V=70 m/s (a) nonlinear ballast (universal-softening model) (b) linear ballast (EB=120 MPa)

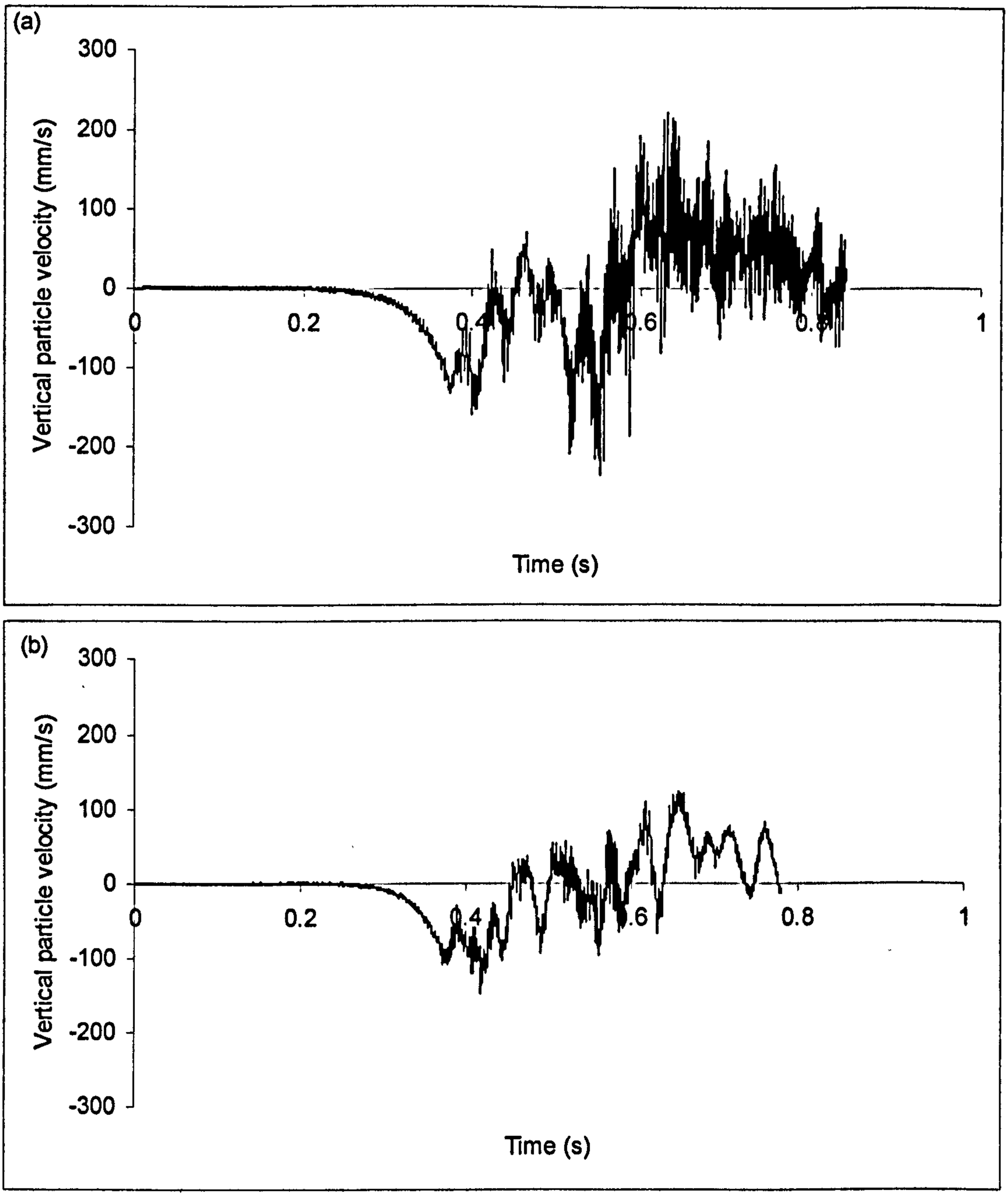

Figure 5.43. Ballast vertical particle velocity under a train coach (ES=15 MPa, BD=300 mm) at V=70 m/s (a) nonlinear ballast (universal-softening model) (b) linear ballast (EB=120 MPa)

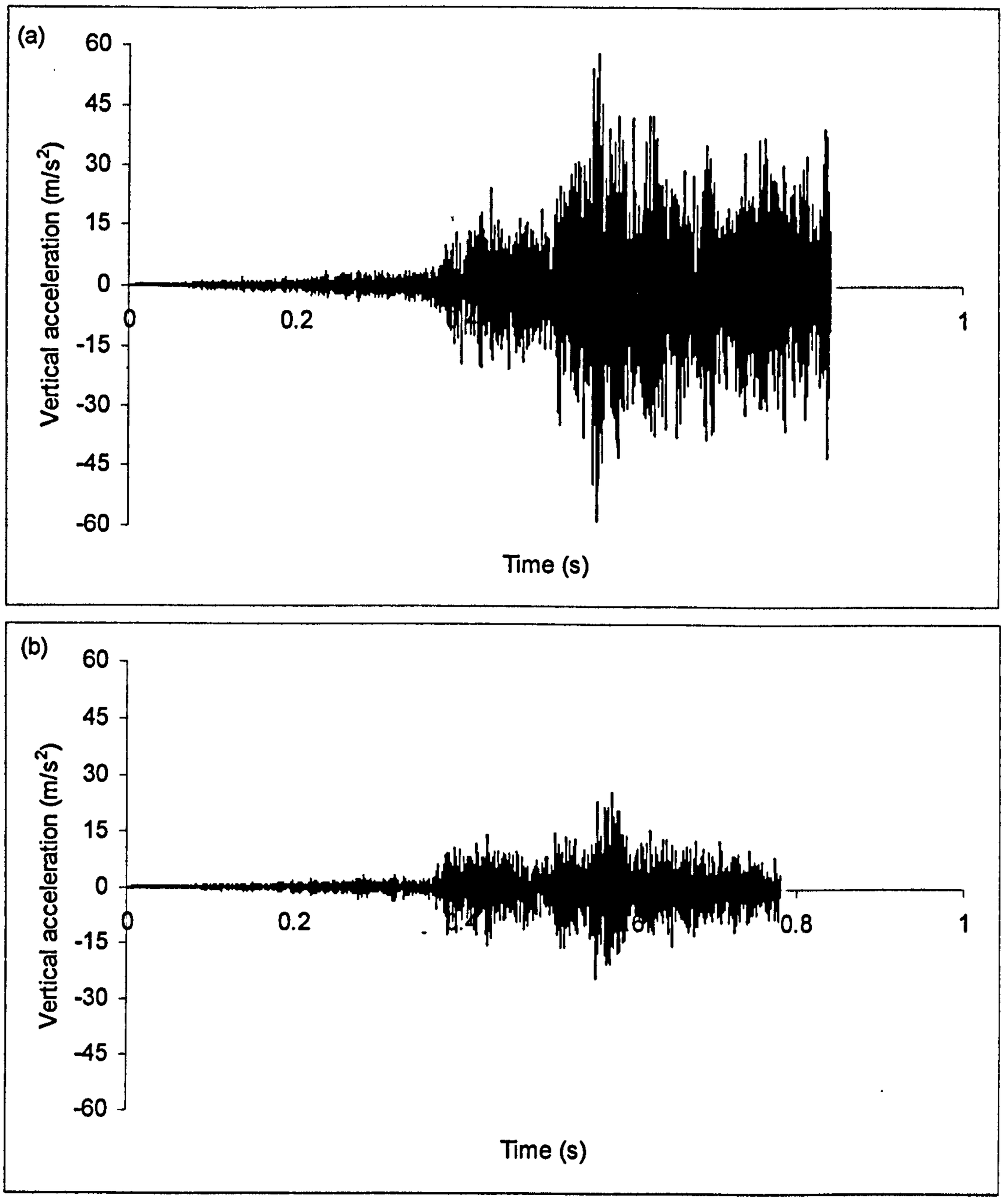

Figure 5.44. Ballast vertical acceleration under a train coach (ES=15 MPa, BD=300 mm) at V=70 m/s (a) nonlinear ballast (universal-softening model) (b) linear ballast (EB=120 MPa)

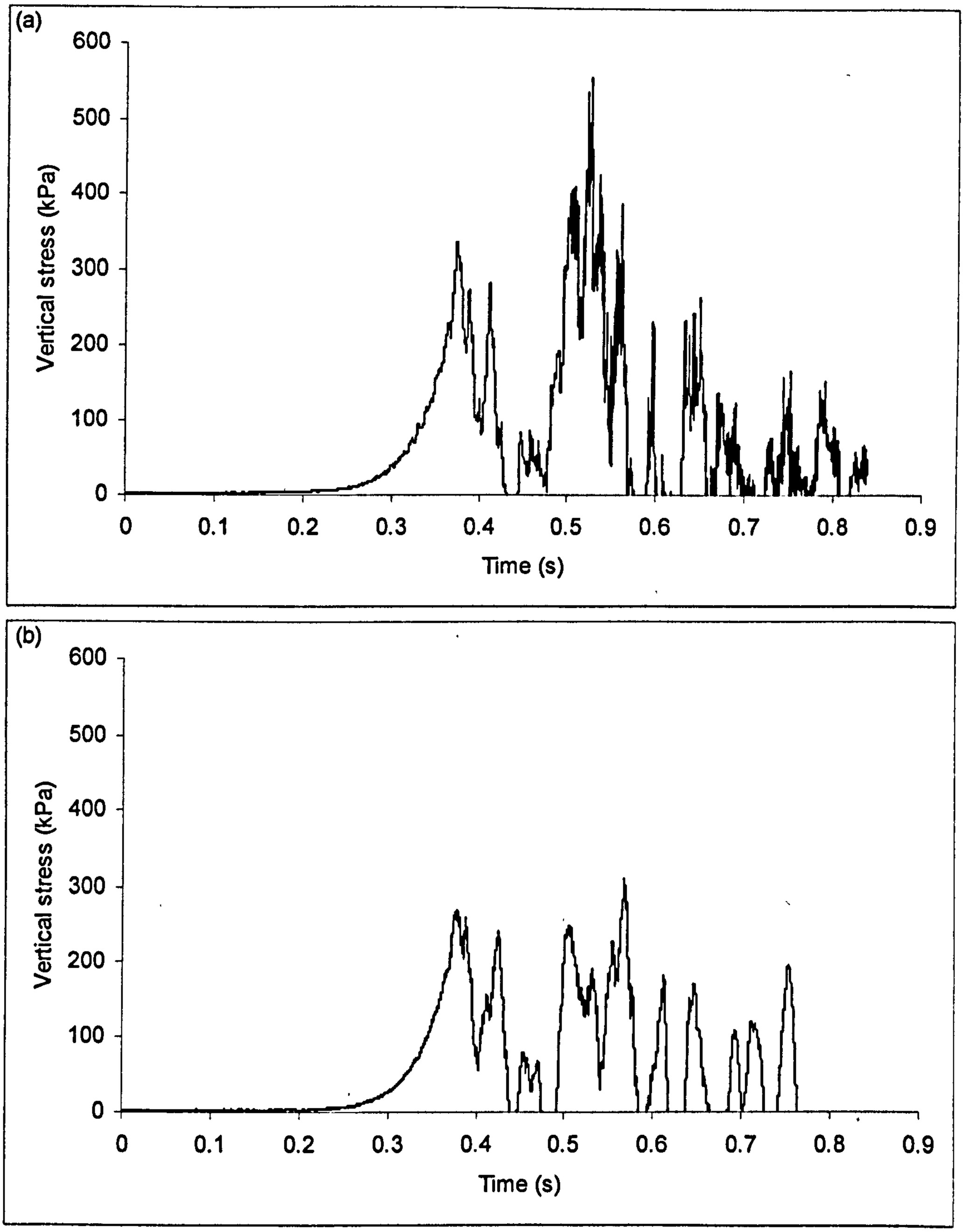

Figure 5.45. Vertical stress on the ballast under a train coach (ES=15 MPa, BD=300 mm) at V=70 m/s (a) nonlinear ballast (universal-softening model) (b) linear ballast (EB=120 MPa)

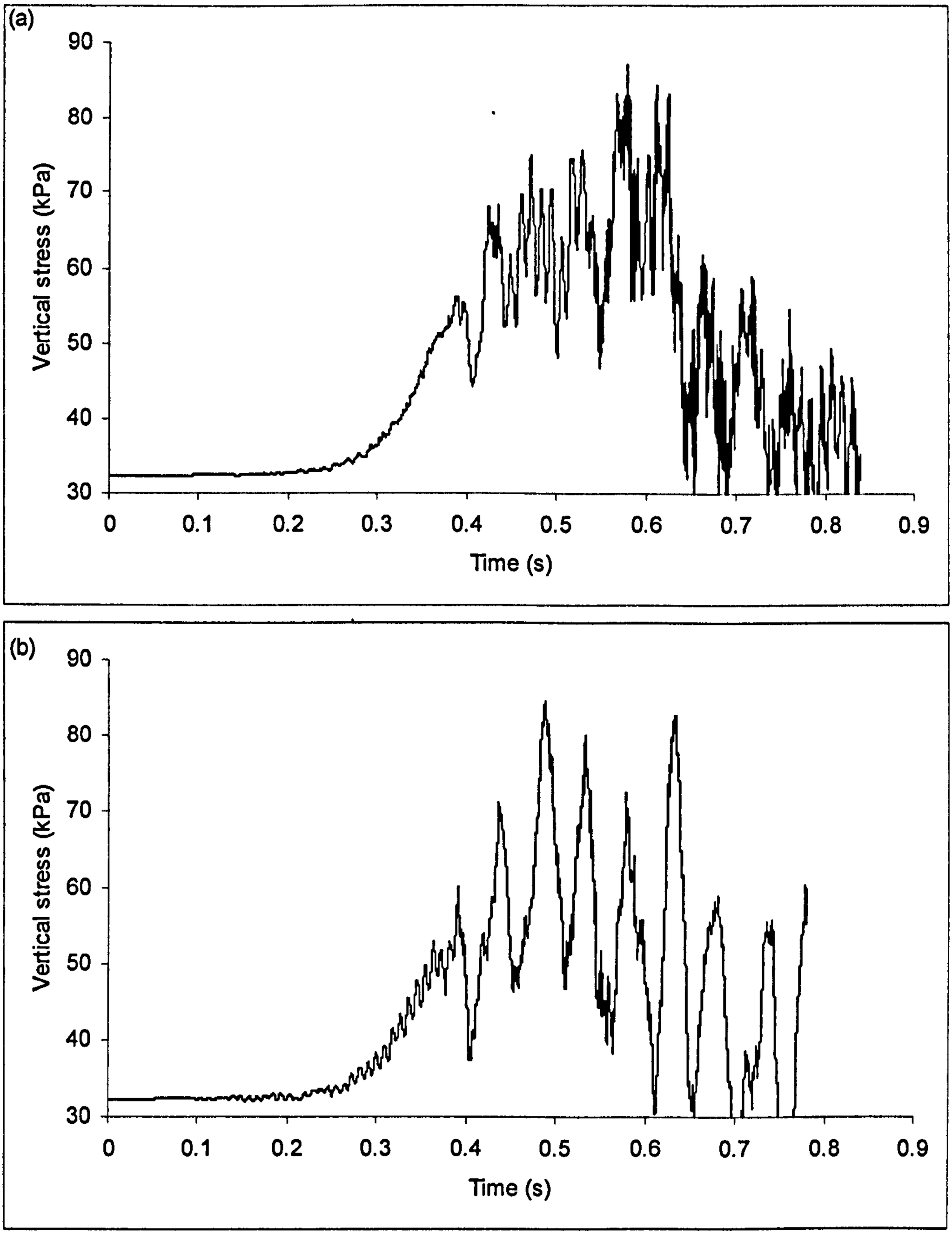

Figure 5.46. Vertical stress in the subgrade (depth=1.8 m) under a train coach (ES=15 MPa, BD=300 mm) at V=70 m/s (a) nonlinear ballast (universal-softening model) (b) linear ballast (EB=120 MPa)

speed regime. With respect to permanent deformation in the subgrade, as discussed before, the main stress parameter is the deviatoric stress, not the vertical stress alone. As will be shown later in this section, this observed similarity in the vertical stress level does not necessarily mean that ballast nonlinearity does not affect the deviatoric stress in the subgrade.

Plan views of the track displacement under a train coach, at a speed of 70 m/s, is presented for simulations with the nonlinear ballast (universal-softening) and linear ballast (EB=120 MPa) models in Figures (5.47a) and (5.47b). Figure (5.47) reveals that the simulation with the nonlinear ballast model (universal-softening) results in considerably higher displacement, and the displacement is considerably more asymmetrical when compared with that in the linear simulation. It implies that the critical track velocity, if defined based on interaction between the ballast and subgrade, can be lower relative to the estimated critical velocity from a linear ballast analysis. In addition, if the nonlinearity of the subgrade is also taken into account, higher deviatoric stresses would be induced in the ballast. The ballast stiffness would therefore further decrease which adversely affects the track response by generating higher displacement amplitudes and increasing the asymmetry of the displacement field. Stiffness variation of the ballast (e.g from nonlinearity, mud pumping) suggests that the improvement in the critical track velocity, coming from the stiffness of a thin ballast layer, may not be as high as expected from a linear analysis. Therefore, it is again confirmed that Rayleigh's wave velocity of the subgrade should be practically taken as the critical track velocity for conventional railway tracks.

The effect of ballast nonlinearity on the maximum deviatoric stress induced in the subgrade is investigated in Figure (5.48). The deviatoric stresses in the subgrade obtained from the nonlinear simulation (nonlinear ballast) is generally higher than those obtained from the linear simulation with upper bound stiffness (EB=120 MPa) and lower than those of lower bound stiffness (EB=30 MPa). It is also seen that the effect of ballast nonlinearity is more pronounced at higher speed, as a substantial increase in the deviatoric stress in the subgrade is observed when compared with linear simulations (EB=120 MPa). It shows that a finite element simulation with a linear ballast model can significantly underestimate the deviatoric stress level in the subgrade. As a consequence, the permanent settlement predicted from a nonlinear simulation (nonlinear ballast) can be considerably higher than

that of linear simulations, especially at higher train speeds. Moreover higher deviatoric stresses as predicted from nonlinear simulations (nonlinear ballast) causes a larger degradation in the resilient stiffness of the subgrade (e.g. according to power model, Equation, 5.23). In the presence of ballast nonlinearity, a higher impact of subgrade nonlinearity may therefore be expected.

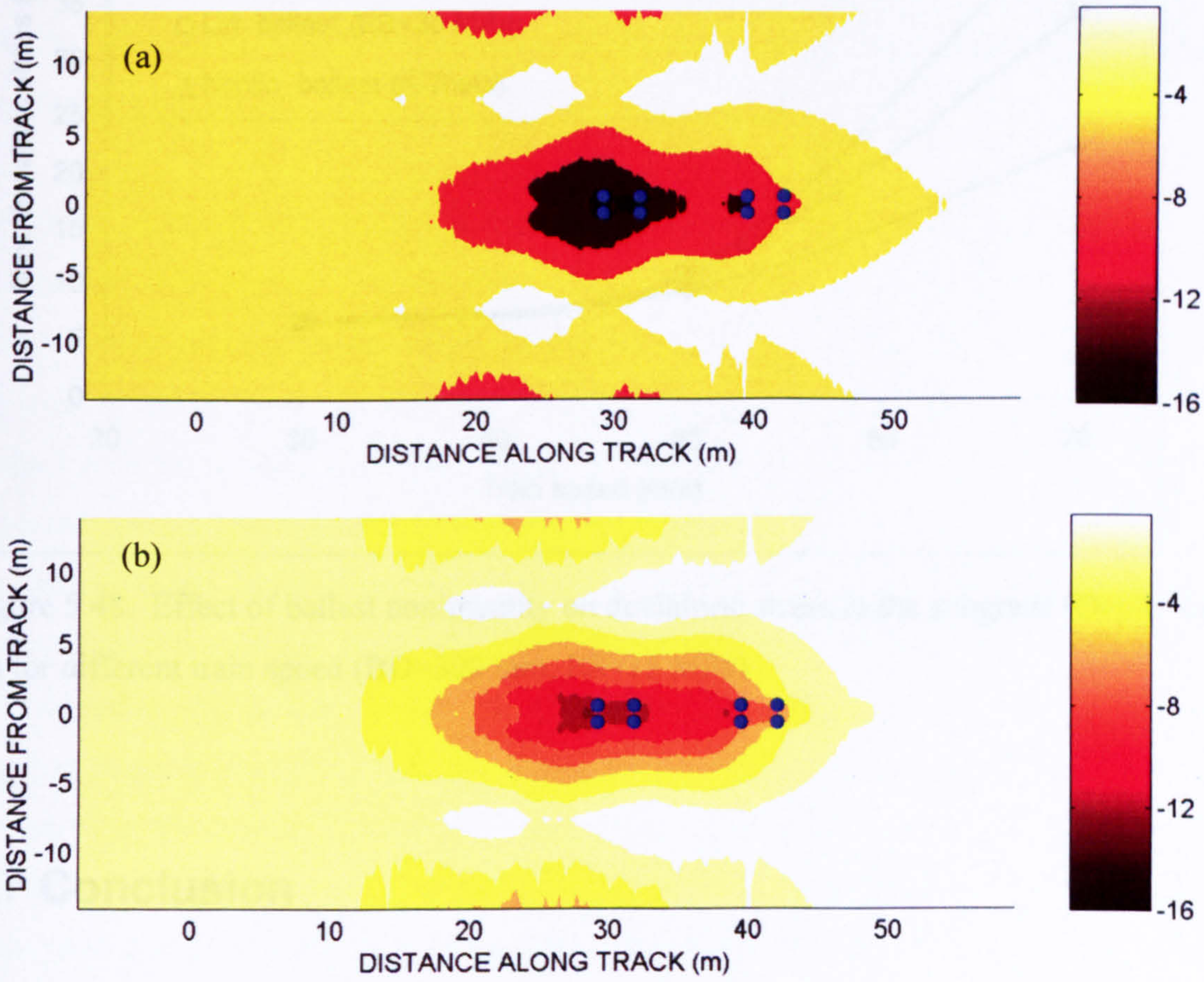

Figure 5.47. Plan views of displacements field for (a) nonlinear simulation (universal – softening model for ballast) and (b) linear simulation (EB=120 MPa) –(ES=15 MPa, BD=300 mm)

As mentioned before, nonlinearity of subgrade would also affect the stress state in the ballast and therefore boost the effect of ballast nonlinearity. It is worth reiterating here that the effect of ballast and subgrade nonlinearity may be considerable, even at low speeds, for

freight trains owing to their heavy axles and consequently higher induced stresses in the ballast and subgrade.

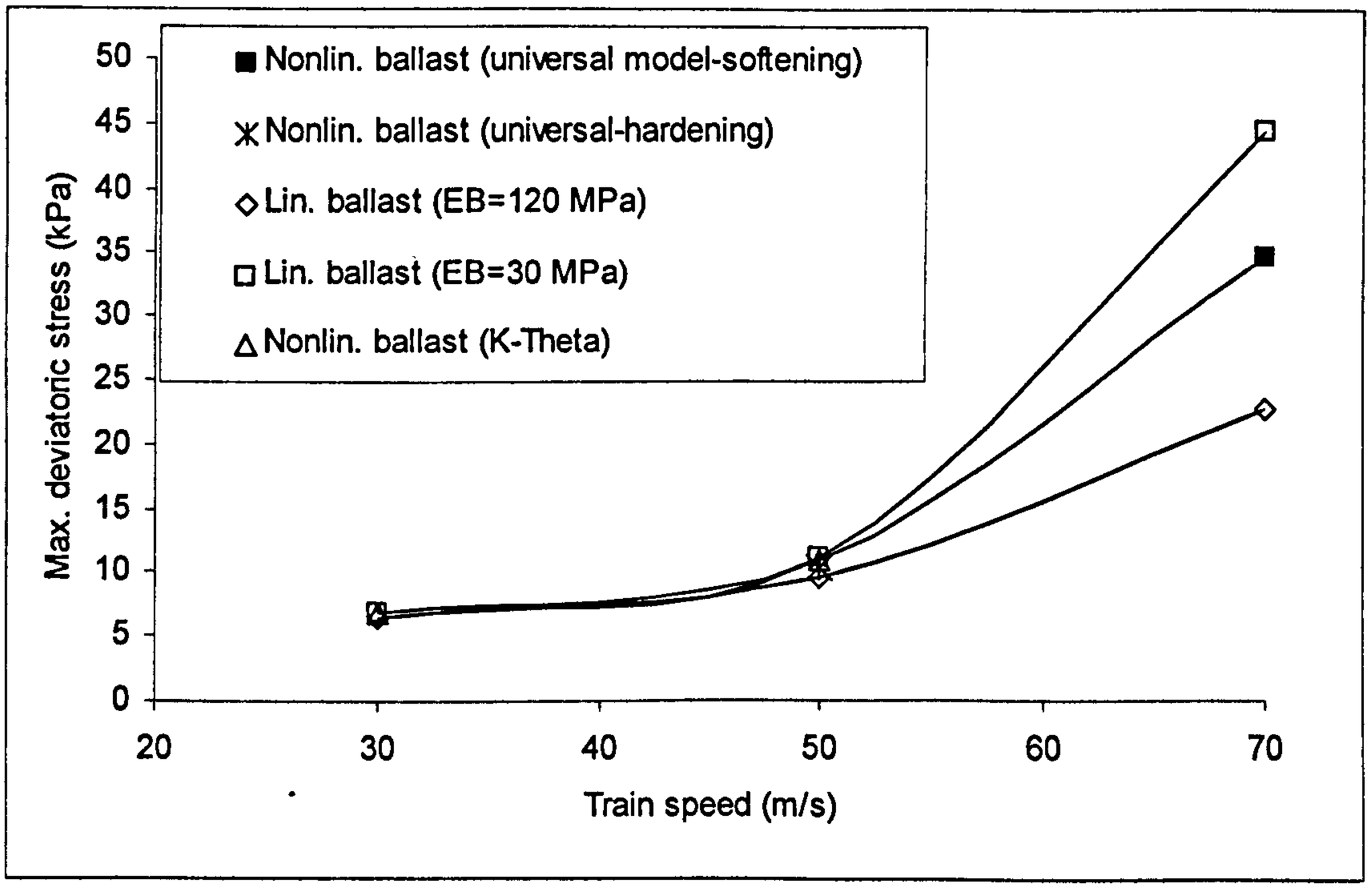

Figure 5.48. Effect of ballast nonlinearity on deviatoric stress in the subgrade (Depth=1.8 m) for different train speed (BD=300 mm, ES=15 MPa)

5.7 Conclusion

Nonlinearity of ballast and subgrade was discussed in this chapter. The nonlinear resilient models for the ballast and clayey subgrade were reviewed and their implementations in a dynamic finite element model were presented. Strain-based nonlinear constitutive relationships were derived to facilitate the implementation of constitutive relationships in the explicit finite element code. It was discussed that the nonlinear resilient model for the subgrade should reflect the decrease in the stiffness with deviatoric stress/strain. It was also discussed that ballast stiffness would increase with mean stress and slightly increase with deviatoric stress for low train speeds, due to relatively low stresses induced in the ballast

(for a passenger train). Ballast stiffness degradation with deviatoric stress/strain appears to be dominant at higher speeds for typical tracks. Nonlinear models were calibrated to reflect the hardening and softening effects of the deviatoric stress on the ballast stiffness. Several nonlinear simulations were conducted incorporating nonlinear resilient constitutive relationships for the ballast and subgrade. It was shown that the effect of subgrade nonlinearity is increased with the increase in train speed, and the simulations with a linear subgrade model may underestimate the track critical velocity. The track displacement and maintenance level (in terms of stress level, related to induced plasticity, and ballast particle velocity) may also be underestimated based on linear simulations (with linear subgrade), especially at higher train speeds.

For low to medium train speeds, the ballast nonlinearity was seen to have minimal effect (for ballast with limited depth) while a significant increase in track displacement and vibration level and asymmetry of the displacement response in the ballast were observed as the train speed increased further. It was then suggested that the improvement of the track critical velocity coming from the stiffness of the ballast layer may be less than what is expected from a linear model. It was confirmed that the track critical velocity should be practically taken approximately equal to the Rayleigh wave velocity of subgrade, irrespective of the ballast stiffness. However, if a considerably deep ballast is placed on a soft subgrade, the ballast nonlinearity can affect the response of the track in a low to medium range of train speed and also shift the track critical velocity to a higher value when compared to the critical velocity of the track with a thin layer of ballast. However, in order to estimate the critical velocity of such a track, stiffness degradation of the ballast under a higher speed regime needs to be considered. Deviatoric stress level in the subgrade, which can be correlated to permanent settlement in the subgrade, was also significantly affected by the ballast nonlinearity. The simulations with nonlinear ballast models may predict considerably higher deviatoric stresses applied to the subgrade, when compared with the stresses predicted from a linear simulation. The effect of the ballast nonlinearity on the subgrade stress is more pronounced for higher train speeds. However, it was discussed that for heaver trains (i.e. heavier than the passenger train studied in this section) nonlinearity of the subgrade and ballast may have a significant effect on the track response, even at lower train speeds.

CHAPTER 6

TRAIN-TRACK INTERACTION: MECHANICS OF STIFFNESS TRANSITIONS

6.1 Introduction

Track irregularities arise from different sources, such as the non-homogenous properties of the subsoil & ballast, rail defects, joints, welds and transition zones near bridges and tunnels. These irregularities induce a dynamically oscillating wheel/rail contact force. Dynamic changes of the contact force are responsible to a large extent for deterioration of the track components. The train-track interaction must therefore be taken into account if a reasonable prediction of track behaviour is to be made in the presence of irregularities. In other words, it may not be viable to model the train by a constant moving load where track irregularities exist.

In the present chapter, the train-track interaction problem is investigated. Different train models are studied and formulated into a finite element framework. The train models are then coupled with the three-dimensional track models through a nonlinear contact theory. The interaction problem between the track and train is solved in the time domain using explicit time integration schemes; the performance of which compares favourably against an analytical solution to a benchmark problem. Different types of irregularities are discussed in detail and their representations in the coupled train-track models are presented.

A type of geotechnical irregularity, i.e. the stiffness transition between plain track and a bridge abutment/tunnel base, is studied. Using the three-dimensional finite element models, the effect of the stiffness change in the transition zone and the presence of a fault are investigated in terms of the rail/wheel interaction force, the stress in the ballast and subgrade, and the train body acceleration; which is considered to be a passenger comfort

index. In this chapter, a simple train-irregularity model is also developed which computes the train response to any given irregularity, such as the deflection difference induced in a transition zone caused by a stiffness change. Using this train-irregularity model, the effects of the transition length, the train speed on the wheel/rail interaction force and the passenger comfort in the transition zone, are studied. Furthermore, a strong linear relationship between the second spatial derivative of the transition curve, which represents the change in the deflection between soft and stiff sides of the transition, and the maximum dynamic force in the transition zone is determined. It is proposed that the second spatial derivative of the transition curve can be used to assess (design) transitions geometrically. Finally, the design principles for transition zones and available site observations are critically studied against the outcome of the transition studies conducted in this chapter, and modifications are suggested towards the sustainable design of transitions.

6.2 Train-Track Interaction

Despite the traditional approach in treating the train vehicle and the railway track separately, in reality the train-track is dynamically coupled as an integral entity at the rail/wheel contact where the common source of excitation for both systems occurs. Severe dynamic disturbances at the wheel/rail interface may occur as a result of geometrical irregularities, either along the rail head surface-such as rail joints, imperfect rail welds and rail corrugations, or around the wheel circumference - such as wheel shells, flat spots, or a completely out of round wheel. The consequence of irregular wheel/rail interaction is the product of large wheel/rail impact forces, which are one of the main causes of damage to the wheels, rails, the track foundation and other vehicle and track components. The formation and development of wheel/rail irregularities and the intensity of dynamic wheel/rail interaction are mutually related, each being the cause of the other. The existence of a defective spot increases the wheel impact force on the rail, which in turn causes the existing defect to grow and may initiate other types of irregularities on the wheel or rail surface - resulting in a 'vicious circle'.

Zhai *et al.* (2001) described four major dynamic problems regarding the train-track interaction for high speed tracks. First, increased speed brings about impacts and vibrations on turnout structures. Because of the existence of a rail discontinuity in fixed noses (often called frogs in the US), the impact between wheels and noses becomes more severe when a train passes through a fixed frog at higher speed, which may shorten the life of the turnout. Secondly, welded rail joints are another source of interaction problem on the speed-raised lines, because the short-wavelength irregularities on the welded rail joints may lead to intense wheel-rail dynamic effects at higher speeds. The third problem lies in the bridge/tunnel-plain track transition sections (a form of structural irregularity). When a train passes through these sections at high speeds, the dynamic load will fluctuate and the vehicle will vibrate strongly, influencing the ride comfort and deterioration rate of track geometry and structure. The fourth prominent problem relates to the presence of a wheel flat. Periodic impact load induced by wheel flats will adversely affect the geometry and maintenance of the railway track. Short and long wave length irregularities presented on the track surface can also cause dynamic train/track interaction force oscillations leading to so-called "cyclic top" problems on the ballast surface and train vibrations.

Further to apparent geometrical and structural irregularities on the track surface, even if the track is initially straight, stiffness variations throughout the track can be a source of train excitation and consequently interaction force oscillation. These stiffness variations can be caused by the discrete support of sleepers (see Section 6.3.1 for further details) and/or variations in substructure stiffness. A common source of stiffness variation along the track may be ballast depth variations and localised "dirty" ballast as a result of ballast particle abrasions and/or mud pumping. When fines (dirt) block the ballast voids, excess pore water pressure can be generated which will reduce the stiffness and strength of ballast, forming a "wet spot". Such variations in stiffness and strength of ballast (or generally substructure) will increase the dynamic train load oscillations on the track considerably, and will eventually cause differential settlements in the track which adversely influence the train-track interaction, inducing even further geometrical irregularities (cyclic-top). Clark *et al.* (2002) noted that these strength/stiffness differences will initially reduce the operational efficiency in terms of ride comfort; however if it is left untreated, there might be a danger of train derailments at higher speeds. It should be noted that these kinds of irregularities may not be fully inspected visually, and traditional field tests (e.g. trial holes, cone

penetration tests) are required, enabling the condition of substructure to be assessed (e.g. Brough *et al.*, 2003). As an alternative, geophysical investigations can also be employed which offer a considerably faster approach towards track bed assessment along the track when compared with traditional methods (see e.g. Gallagher *et al.*, 1999; Hugenschmidt, 2000; Clark *et al.*, 2004).

If the railway track design is of primary concern, two main phenomena, in relation to train-track interaction, need to be taken into account, namely how the track-train interaction force changes regarding the train-track geometrical and mechanical properties, and how the track design will affect train safety and passenger comfort. Simplified models of the train consisting of rigid masses, springs and dampers are considered to be representative of these phenomena and have gained extensive use in railway track engineering (e.g. Nielsen and Igeland, 1995, Zhai and Cai, 1997, Zhai *et al.* 2001, Liang *et al.*, 2001, Wu and Thompson, 2003). Most of these train models have however, been coupled with beam models which have serious drawbacks in the simulation of the track behaviour, as discussed in previous chapters.

The train consists of coaches (or locomotive(s)), bogies and wheels. Primary and secondary suspension systems connect wheel-bogie and bogie-coach respectively, as shown in Figure (6.1). Unsprung masses of the wheel and axle are responsible for dynamic loads with higher frequencies, while pitching and bouncing of bogies and coach (sprung mass) are responsible for the lower frequency dynamic loads. Mathematical models of varying complexity can therefore be used to represent a train, depending on the modelling objectives. To pick up the high frequency change of the force (up to 5000 Hz in case of wheel/rail noise), Grassie *et al.* (1982) suggested using a linear model involving wheel unsprung mass and a linear contact spring. These types of models have gained wide applications in modelling high frequency train-track interaction problems, such as noise generation caused by wheel flat (Wu and Thompson, 2002) and rail joint (Wu and Thompson, 2003). Such models may not, however, be appropriate if the track substructure response is to be investigated, as they do not represent the lower frequency interaction load. Moreover, passenger comfort is usually correlated to the acceleration level in the coach which is not present in the "wheel models". Accordingly, the train models in the present

research incorporate all the components, including the coach, bogies, wheels and suspension systems.

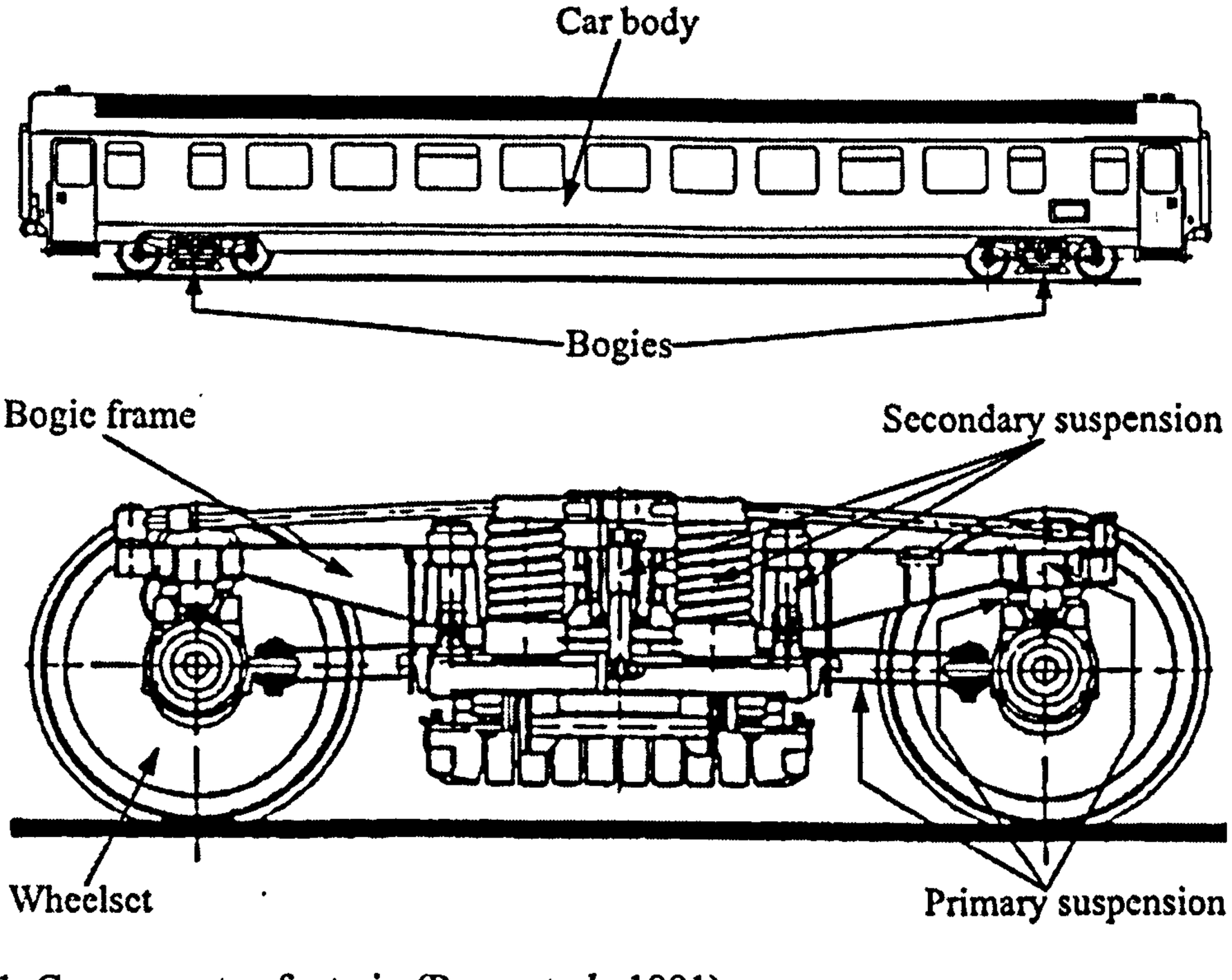

Figure 6.1. Components of a train (Popp *et al.*, 1991)

In the present research, only the vibrations in the vertical plane are studied. The loading is assumed to be symmetrically distributed on the two rails, so half of the train is considered sufficient in forming the train model. The yawing and rolling movement of the train is not considered in the present research. In order to study the effect of the different train components, two different models have been considered, namely quarter and pseudo full train models. A quarter train model incorporates primary and secondary suspension systems, bogie and coach masses. However, only the bouncing of the bogie and coach is taken into account in a quarter train model. The pseudo full train model includes all elements and incorporates both the pitching and bouncing of the train components in the vertical plain.

6.2.1 Quarter Train Model

A sketch of the model is shown in Figure (6.2a). The model comprises a quarter of a coach, half of a bogie and a wheel, which are interconnected through the suspension systems represented by dampers and springs. The symmetry of the train around the central track line is considered, and the model is formulated on this. The system has three degrees of freedom, namely the wheel, the bogie and the coach vertical displacements. Considering the dynamic equilibrium, the motion equations for the wheel, bogie and coach are formulated as follows.

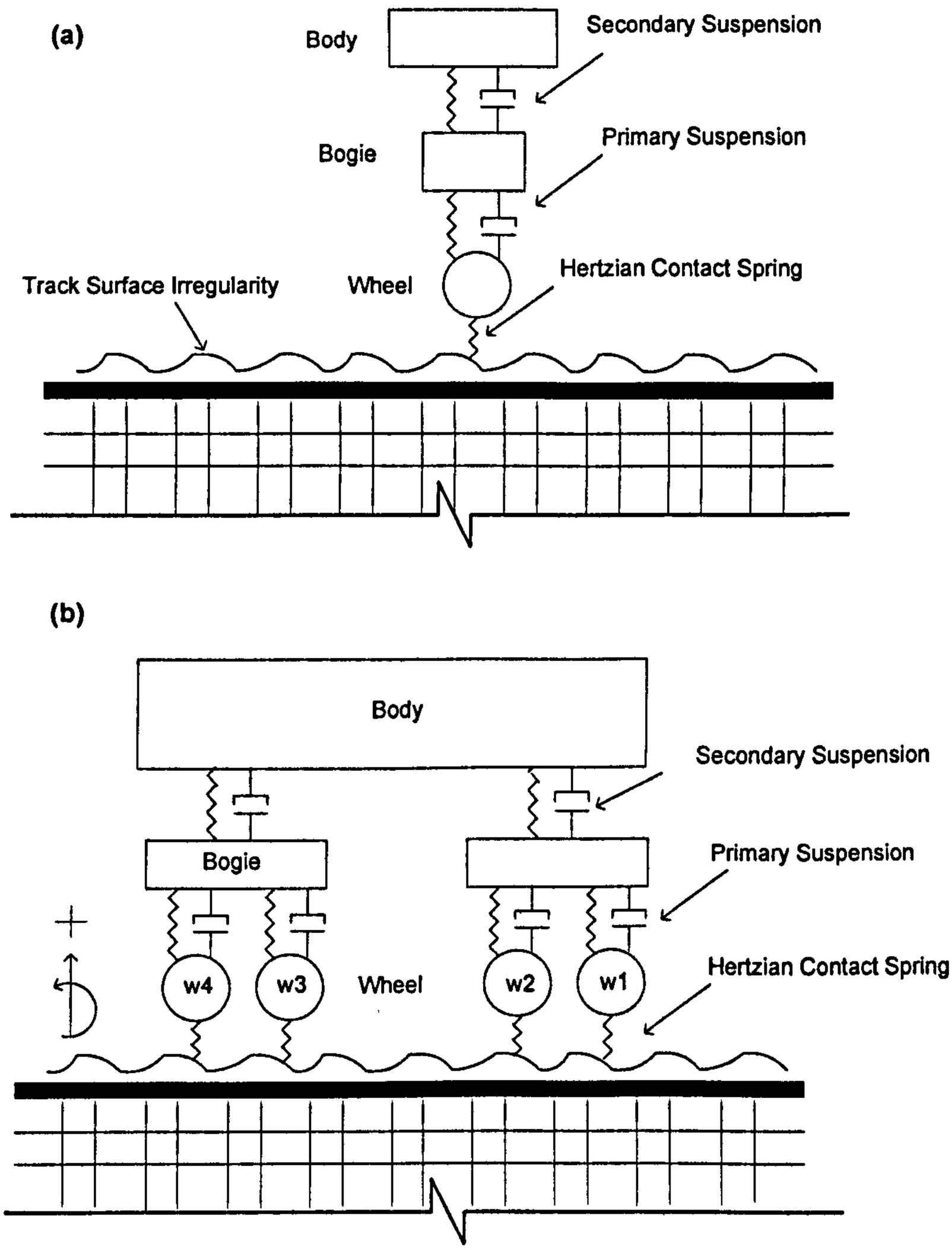

Figure 6.2. Sketches of the quarter (a) and pseudo full (b) train models

Coach body bounce:

$$k_c(u_c - u_b) + c_c(\dot{u}_c - \dot{u}_b) + \frac{m_c}{8}g + \frac{m_c}{8}\ddot{u}_c = 0 \tag{6.1}$$

Bogie bounce:

$$k_b(u_b - u_w) + c_b(\dot{u}_b - \dot{u}_w) - k_c(u_c - u_b) - c_c(\dot{u}_c - \dot{u}_b) + \frac{m_b}{4}g + \frac{m_b}{4}\ddot{u}_b = 0 \tag{6.2}$$

Wheel bounce:

$$-F_{wr} - k_b(u_b - u_w) - c_b(\dot{u}_b - \dot{u}_w) + \frac{m_b}{4}g + m_w\ddot{u}_w = 0 \tag{6.3}$$

u_w, u_b and u_c are the vertical displacements of the wheel, bogie and coach. $\dot{u}$ and $\ddot{u}$ stand for the vertical velocity and acceleration of the train components respectively. m_w, m_b and m_c are the wheel, bogie and coach masses respectively. k_b and k_c are the primary stiffness and secondary stiffness coefficients respectively. Similarly c_b and c_c are the primary stiffness and secondary damping coefficients respectively. F_{wr} is rail/wheel interaction force.

These equations can be summarized in conventional finite element format:

$$M\ddot{U} + C\dot{U} + KU = F_{ext} \tag{6.4}$$

$$U = \begin{bmatrix} u_w & u_b & u_c \end{bmatrix} \qquad \dot{U} = \begin{bmatrix} \dot{u}_w & \dot{u}_b & \dot{u}_c \end{bmatrix} \; \ddot{U} = \begin{bmatrix} \ddot{u}_w & \ddot{u}_b & \ddot{u}_c \end{bmatrix} \tag{6.5}$$

$$M = diag\begin{bmatrix} m_w & \frac{m_b}{4} & \frac{m_c}{8} \end{bmatrix} \tag{6.6}$$

$$C = \begin{bmatrix} c_b & -c_b & 0 \\ Sym. & c_b + c_c & -c_c \\ & & c_c \end{bmatrix} \tag{6.7}$$

$$K = \begin{bmatrix} k_b & -k_b & 0 \\ Sym. & k_b + k_c & -k_c \\ & & k_c \end{bmatrix} \tag{6.8}$$

$$F_{ext} = \begin{bmatrix} -m_w g + F_{wr} \\ -\frac{m_b}{4} g \\ -\frac{m_c}{8} g \end{bmatrix} \tag{6.9}$$

6.2.2 Pseudo Full Train Model

The pseudo full train model (Figure 6.2b) has 10 degrees of freedom. The model incorporates pitching of the coach and bogies as well as their bouncing movements. The motions of the coach, bogies and wheels are formulated as below:

Coach body bounce:

$$\begin{aligned} &k_c(u_c + \alpha_c L_c - u_{bf}) + k_c(u_c - \alpha_c L_c - u_{br}) + c_c(\dot{u}_c + \dot{\alpha}_c L_c - \dot{u}_{bf}) + \\ &c_c(\dot{u}_c - \dot{\alpha}_c L_c - \dot{u}_{br}) + \frac{m_c}{2}\ddot{u}_c + \frac{m_c}{2} g = 0 \end{aligned} \tag{6.10}$$

Coach body pitching:

$$\begin{aligned} &k_c(u_c + \alpha_c L_c - u_{bf}) L_c - k_c(u_c - \alpha_c L_c - u_{br}) L_c + c_c(\dot{u}_c + \dot{\alpha}_c L_c - \dot{u}_{bf}) L_c - \\ &c_c(\dot{u}_c - \dot{\alpha}_c L_c - \dot{u}_{br}) L_c + \frac{J_c}{2}\ddot{\alpha}_c = 0 \end{aligned} \tag{6.11}$$

Front bogie bounce:

$$k_b(u_{bf}-\alpha_{bf}L_b-u_{w2})+k_b(u_{bf}+\alpha_{bf}L_b-u_{w1})-k_c(u_c+\alpha_cL_c-u_{bf})+$$
$$c_b(\dot{u}_{bf}-\dot{\alpha}_{bf}L_b-\dot{u}_{w2})+c_b(\dot{u}_{bf}+\dot{\alpha}_{bf}L_b-\dot{u}_{w1})-k_c(\dot{u}_c+\dot{\alpha}_cL_c-\dot{u}_{bf})+ \quad (6.12)$$
$$\frac{m_b}{2}g+\frac{m_b}{2}\ddot{u}_{bf}=0$$

Front bogie pitching

$$k_b(u_{bf}+\alpha_{bf}L_b-u_{w1})L_b-k_b(u_{bf}-\alpha_{bf}L_b-u_{w2})L_b-$$
$$c_b(\dot{u}_{bf}-\dot{\alpha}_{bf}L_b-\dot{u}_{w2})L_b+c_b(\dot{u}_{bf}+\dot{\alpha}_{bf}L_b-\dot{u}_{w1})L_b+\frac{m_b}{2}\ddot{\alpha}_{bf}=0 \quad (6.13)$$

Rear bogie bounce:

$$k_b(u_{br}-\alpha_{br}L_b-u_{w4})+k_b(u_{br}+\alpha_{br}L_b-u_{w3})-k_c(u_c-\alpha_cL_c-u_{br})+$$
$$c_b(\dot{u}_{br}-\dot{\alpha}_{br}L_b-\dot{u}_{w4})+c_b(\dot{u}_{br}+\dot{\alpha}_{br}L_b-\dot{u}_{w3})-c_c(\dot{u}_c-\dot{\alpha}_cL_c-\dot{u}_{br})+ \quad (6.14)$$
$$\frac{m_b}{2}\ddot{u}_{br}=0$$

Rear bogie pitching:

$$-k_b(u_{br}-\alpha_{br}L_b-u_{w4})L_b+k_b(u_{br}+\alpha_{br}L_b-u_{w3})L_b-c_b(\dot{u}_{bf}-\dot{\alpha}_{br}L_b-\dot{u}_{w4})+$$
$$c_b(\dot{u}_{br}+\dot{\alpha}_{br}L_b-\dot{u}_{w3})+\frac{J_b}{2}\ddot{\alpha}_{br}=0 \quad (6.15)$$

Wheels' bounce:

$$-F_{w4}-k_b(u_{br}-\alpha_{br}L_b-u_{w4})-c_b(\dot{u}_{br}-\dot{\alpha}_{br}L_b-\dot{u}_{w4})+m_w\ddot{u}_{w4}=0 \quad (6.16)$$

$$-F_{w3}-k_b(u_{br}+\alpha_{br}L_b-u_{w3})-c_b(\dot{u}_{br}+\dot{\alpha}_{br}L_b-\dot{u}_{w3})+m_w\ddot{u}_{w3}=0 \quad (6.17)$$

$$-F_{w4}-k_b(u_{bf}-\alpha_{bf}L_b-u_{w2})-c_b(\dot{u}_{bf}-\dot{\alpha}_{bf}L_b-\dot{u}_{w2})+m_w\ddot{u}_{w2}=0 \quad (6.18)$$

$$-F_{w1}-k_b(u_{bf}+\alpha_{bf}L_b-u_{w1})-c_b(\dot{u}_{bf}+\dot{\alpha}_{bf}L_b-\dot{u}_{w1})+m_w\ddot{u}_{w1}=0 \qquad (6.19)$$

$2L_b$ and $2L_c$ are the distance between the centres of wheels connected to a bogie and distance between the centreline of two bogies of the same coach. J_b and J_c are the rolling moment of inertia for the bogie and coach respectively. u_{bf} and α_{bf} are displacement and rotation of front bogie respectively. u_{br} and α_{br} are the displacement and rotation of rear bogie respectively. m_w, m_b and m_c are as previously defined.

These equations lead to the following displacement, stiffness and damping matrices which are used to form Equation (6.4):

$$K=\begin{bmatrix}
k_b & 0 & 0 & 0 & 0 & 0 & -k_b & -k_bL_b & 0 & 0\\
 & k_b & 0 & 0 & 0 & 0 & -k_b & k_bL_b & 0 & 0\\
 & & k_b & 0 & -k_b & -k_bL_b & 0 & 0 & 0 & 0\\
 & & & k_b & k_b & k_bL_b & 0 & 0 & 0 & 0\\
 & & & & k_c+2k_b & 0 & 0 & 0 & -k_c & k_cL_c\\
 & & & & & 2k_bL_b^2 & 0 & 0 & 0 & 0\\
 & & Sym. & & & & k_c+2k_b & 0 & -k_c & -k_cL_c\\
 & & & & & & & 2k_bL_b^2 & 0 & 0\\
 & & & & & & & & 2k_c & 0\\
 & & & & & & & & & 2k_cL_c^2
\end{bmatrix} \qquad (6.20)$$

$$C=\begin{bmatrix}
c_b & 0 & 0 & 0 & 0 & 0 & -c_b & -c_bL_b & 0 & 0\\
 & c_b & 0 & 0 & 0 & 0 & -c_b & c_bL_b & 0 & 0\\
 & & c_b & 0 & -c_b & -c_bL_b & 0 & 0 & 0 & 0\\
 & & & c_b & c_b & c_bL_b & 0 & 0 & 0 & 0\\
 & & & & c_c+2c_b & 0 & 0 & 0 & -c_c & c_cL_c\\
 & & & & & 2c_bL_b^2 & 0 & 0 & 0 & 0\\
 & & Sym. & & & & c_c+2c_b & 0 & -c_c & -c_cL_c\\
 & & & & & & & 2c_bL_b^2 & 0 & 0\\
 & & & & & & & & 2c_c & 0\\
 & & & & & & & & & 2c_cL_c^2
\end{bmatrix} \qquad (6.21)$$

$$M = diag\left[m_w \quad m_w \quad m_w \quad m_w \quad \frac{m_b}{2} \quad \frac{J_b}{2} \quad \frac{m_b}{2} \quad \frac{J_b}{2} \quad \frac{m_c}{2} \quad \frac{J_c}{2} \right] \tag{6.22}$$

$$U = \left[u_{w1} \quad u_{w2} \quad u_{w3} \quad u_{w4} \quad u_{br} \quad \alpha_{br} \quad u_{bf} \quad \alpha_{bf} \quad u_c \quad \alpha_{bc} \right]^T \tag{6.23}$$

$$F_{ext} = \left[p_1 \quad p_2 \quad p_3 \quad p_4 \quad -m_b g \quad 0 \quad -m_b g \quad 0 \quad -m_c g \quad 0 \right] \tag{6.24}$$

$$p_1 = -m_w g + F_{wr1} \tag{6.25}$$

$$p_2 = -m_w g + F_{wr2} \tag{6.26}$$

$$p_3 = -m_w g + F_{wr3} \tag{6.27}$$

$$p_4 = -m_w g + F_{wr4} \tag{6.28}$$

The specification of the train adopted in this chapter is given in Table (6.1). The train suspension properties are according to Lei and Noda (2002).

Parameter	Value	Parameter	Value
Axle load (tons)	17.4	L_c (m)	5.15
M_w (tons)	1	K_b (kN/m)	3.28E3
M_b (tons)	3.26	K_c (kN/m)	1.31E3
M_c (tons)	55.08	C_b (kNs/m)	90
L_b (m)	1.3	C_c (kNs/m)	30
K_{WT} (GN/ $m^{1.5}$)	93.7	J_b (tons.m^2)	2.07
-	-	J_c (tons.m^2)	1409.98

Table 6.1. Specification of train used in the present chapter

6.2.3 Wheel/Rail Interaction Force

In order to model the rail wheel interaction, different types of models have been employed in the studies in the literature with different levels of complexity and applications. The complexity of such models arises from the nature of the contact forces (e.g. normal, frictional) or the contact mechanism. Steenbergen (2006) reviewed one contact and two contact interaction models which may occur if the curvature of the irregularity is higher than that of the wheel circumference, as shown schematically in Figure (6.3). He compared the two contact mechanisms and concluded that using a single point contact model may not estimate the contact force correctly, for irregularities with a two contact point mechanism such as a dipped joint. Sun and Dhanasekar (2002) mentioned that if the wavelength of the irregularity is larger than a characteristic length, $L_d = 2\sqrt{2ra - a^2}$, where L_d is the wavelength of the irregularity, r is rolling radius of the wheel and a is the wave depth of the irregularity, the contact will be continuous (Figure 6.3a). Otherwise, the wheel and the rail would not be in contact continuously (Figure 6.3b) and therefore a complicated contact theory is required to represent the mechanism. Irregularities with such short wave length irregularities would generate high frequency excitation, which is not a main concern as far as the response of track support layers and corresponding substructure track deterioration is concerned. A single continuous contact model is therefore considered to be appropriate for the present research which is focused mainly on the track substructure response and design. The model can be extended to incorporate more complicated contact mechanisms to study track/train deterioration or noise emissions, which is beyond the scope of present research.

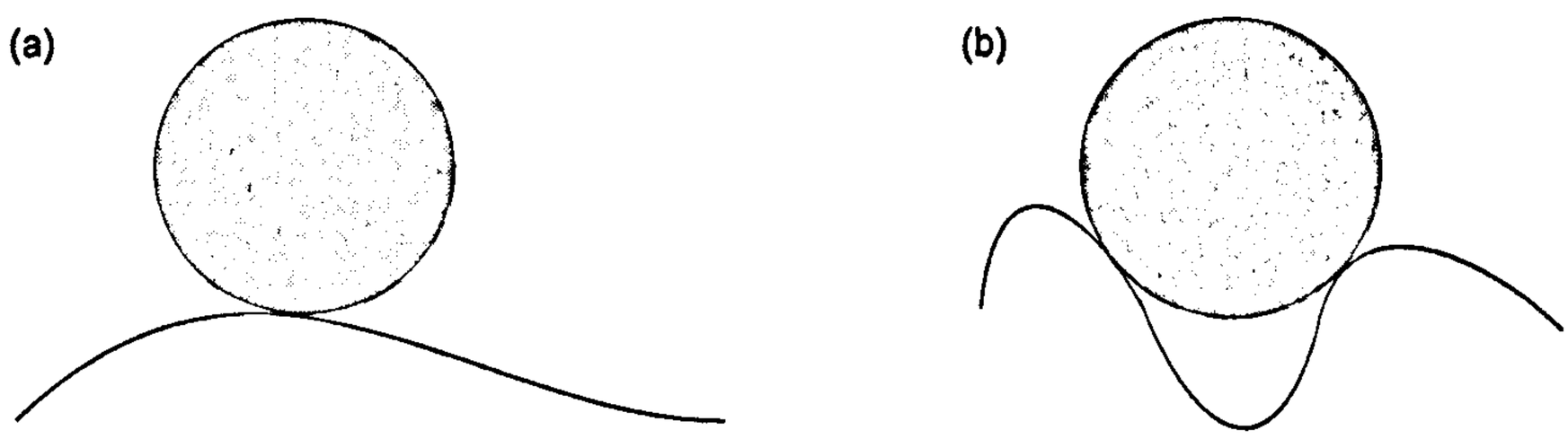

Figure 6.3. Different types of wheel-rail contact; (a) continuous single-point contact, (b) transient double-point contact

In the present research a continuous single point contact is assumed. Normal force between the wheel and rail is considered and the frictional forces are not accounted for. A nonlinear Hertzian spring is considered which permits the separation of the wheel and rail. According to nonlinear Hertzian theory, the interaction force between the rail and wheel is obtained as follows:

$$\begin{cases} F_{wr} = K_{wr}(u_w - u_r - r)^{3/2} & u_w < u_r + r \\ F_{wr} = 0 & u_w \geq u_r + r \end{cases} \tag{6.29}$$

where, F_{wr} is the interaction force between the rail and the wheel, K_{wr} is the Hertzian constant, u_w is the wheel displacement, u_r is the rail displacement and r is the rail surface irregularity. Geometrical representations of some irregularities are given in Table (6.2). K_{wr} can be deduced as follows (Johnson, 1985):

$$K_{wr} = \frac{4G_{wr}\sqrt{R_e}}{3(1-v_{wr})} \tag{6.30}$$

$$R_e = \sqrt{r_w R} \tag{6.31}$$

$$R = \rho_w R_t / (\rho_w - r_w) \tag{6.32}$$

in which G_{wr} and v_{wr} are the shear modulus and Poisson's ratio respectively. r is the rolling radius of the wheel. ρ_w and R_t are wheel profile radius and rail profile radius respectively.

Irregularity	Geometrical Presentation	Definition of Parameters	References
Switch	$r=\frac{1}{2}a(1-\cos(\frac{2\pi x}{L}))$	L: Wavelength of irregularity A: Depth of irregularity C: Distance along track	Zhai et al. (2001)
Wheel Flat	$r=\frac{1}{2}D_f(1-\cos(\frac{2\pi x}{L}))$	$D_f=\frac{L^2}{16R}$ D_f : Effective flat depth R: Wheel radius	Lyon (1972)
Frogs	$r=\begin{cases} h_0\sin(\frac{2\pi x}{L_0}) & (0\le x\le x_1) \\ h_d\frac{(x-x_0)}{(x_2-x_1)} & (x_1<x\le x_2) \\ h_d\frac{(x_3-x)}{(x_3-x_2)} & (x_2<x\le x_3) \\ 0 & (x>x_3) \end{cases}$	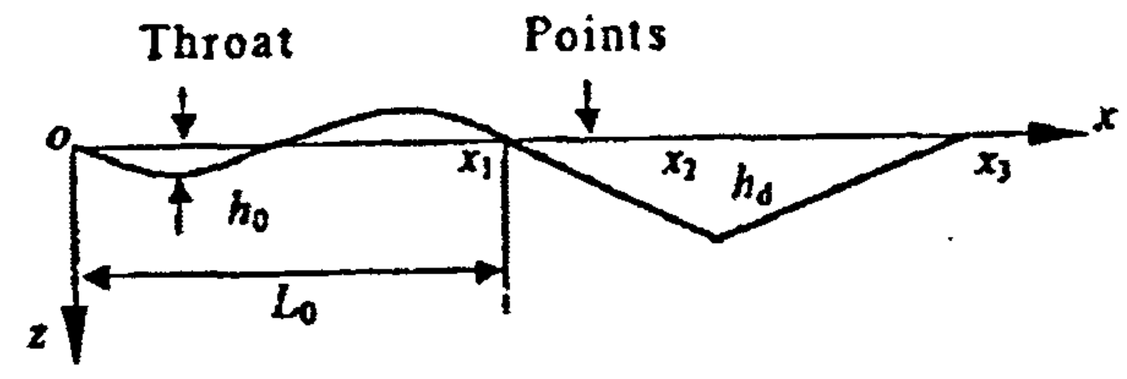	Zhai et al. (2001)
Corrugation	$r=-\alpha(1-\exp(-x^3))\sin(\frac{2\pi x}{L})$ $r(x)=\alpha\left[1-\cos(\frac{2\pi x}{L})\right]$	α : Amplitude of the corrugation L: wave length of the corrugation	Nielsen & Abrahamsson (1992) Eslveld (2001)

Table 6.2. Geometrical representation of some rail and wheel imperfections

6.2.4 Coupling The Track-Train Models-Time Integration of The System

The coupled train-track model can be solved in the frequency or time domains. Train-track interaction is of a transient nature in many cases owing to the presence of isolated or random track irregularities and non-homogeneity of the support stiffness. As the frequency domain solution is mainly limited to linear and steady state systems, time domain integration is employed in the present research to solve the train-track interaction problem. Two explicit integration methods, namely classical explicit scheme and Zhai's Method (Zhai, 1996) as described in Chapter 3, similar to those used for the track model, are implemented. These models are validated against a benchmark problem as follows.

A wheel system passing a periodic irregularity is considered, as shown in Figure (6.4). The irregularity is in the following form:

$$r(x) = A\sin(\omega_r x) \tag{6.33}$$

where x is distance, A is irregularity amplitude and ω_s is the circular spatial frequency the of irregularity defined as:

$$\omega_s = \frac{\omega}{v} = \frac{2\pi}{L} \tag{6.34}$$

In which ω, v and L are the circular frequency of irregularity, wheel speed and irregularity wave length respectively.

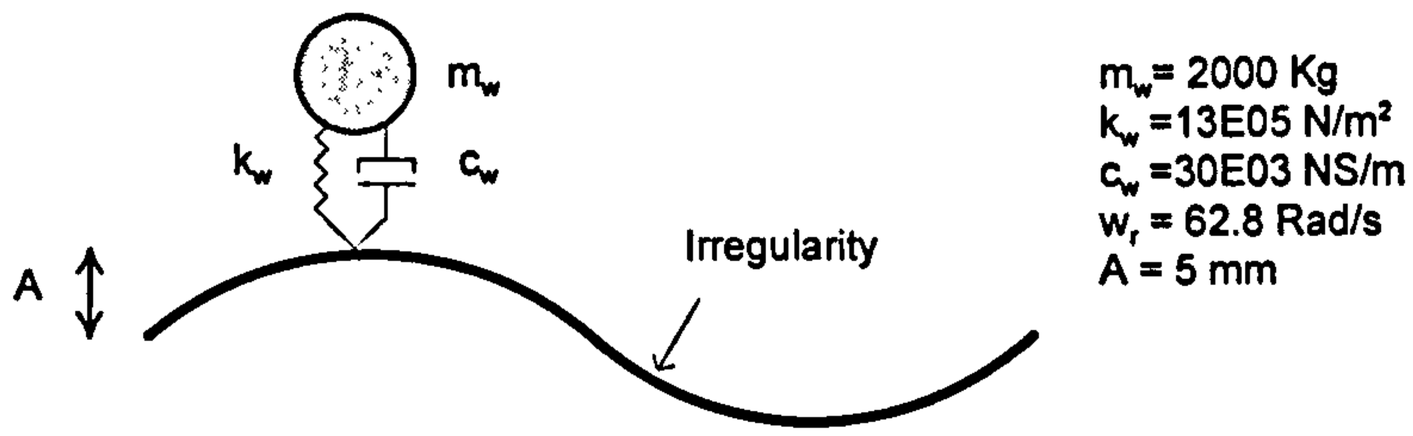

Figure 6.4. A wheel model passing a periodic irregularity with a given specification

The wheel displacement can be presented analytically in the following form:

$$u_w = B + C\sin(\omega_s x) + D\cos(\omega_s x) \tag{6.35}$$

$$B = \frac{m_w g}{k_w} \tag{6.36}$$

C and D are obtained from solving the following equations:

$$\begin{cases} (-m_w\omega^2 + k_w)C - c_w\omega D = k_w A \\ c_w\omega C + (-m_w\omega^2 + k_w)D = c_w\omega A \end{cases} \tag{6.37}$$

The analytical solution is compared with the numerical solutions obtained from the classical explicit scheme and Zhai's method for a specific irregularity input and wheel properties, as given in Figure 6.4. As can be seen in Figure 6.5, Zhai's integration method performs better than the classical explicit scheme in this case. Zhai's method is therefore chosen for the time integration of the wheel-rail interaction problem, especially if a relatively large time step is considered.

In explicit time integration methods used in the present model, the nodal displacements of the train-track system are estimated at the start of time step (see Chapter 3). The displacements of the wheels and rail are then known; the wheel/rail interaction force can then be calculated using Equation (6.29). In the next step, the velocities and accelerations associated with the train and track components are estimated for the given time step.

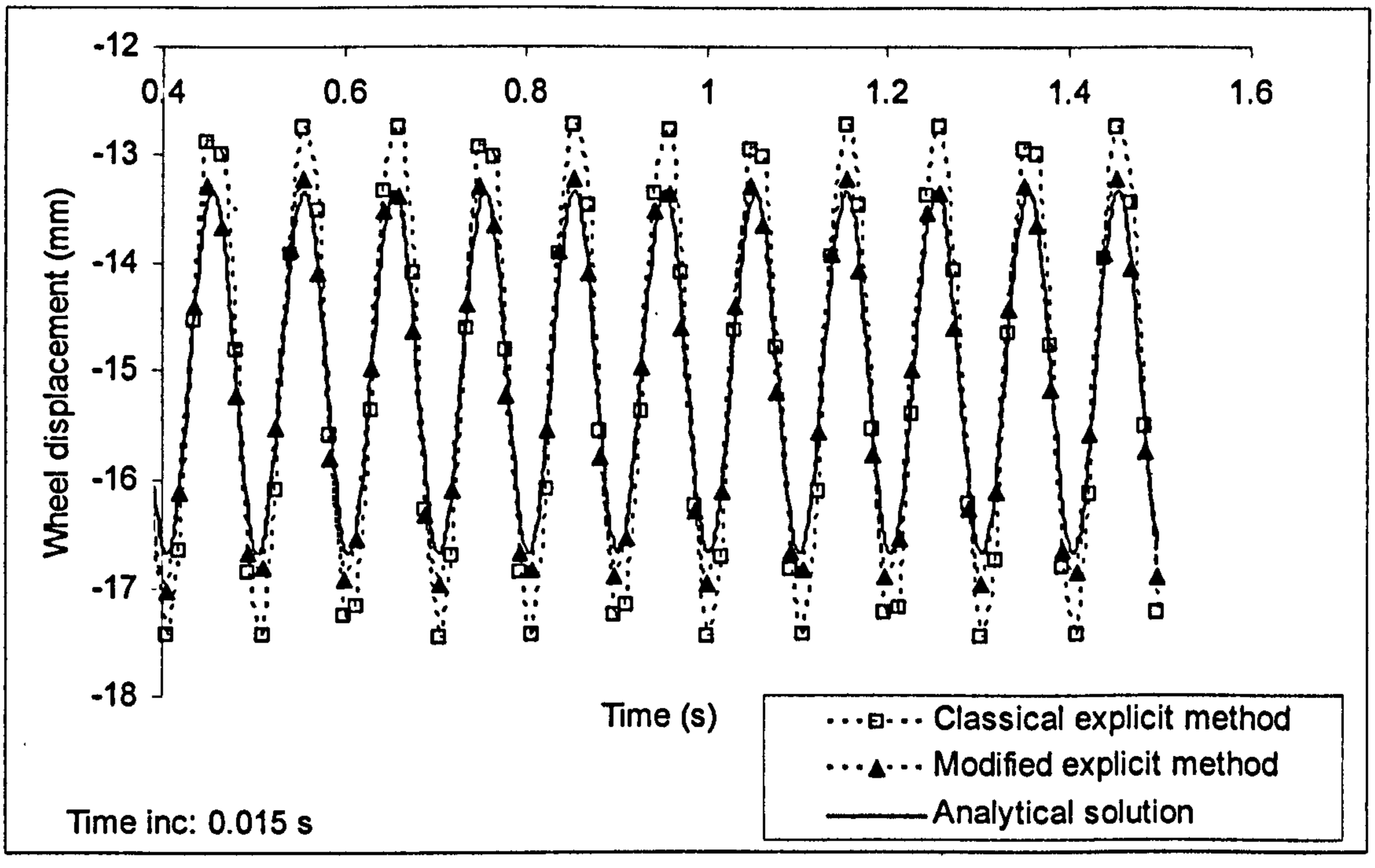

Figure 6.5. Analytical solution compared with the numerical solution for "wheel-periodic irregularity" problem

6.3 Stiffness Transitions

In practice, railway tracks near bridge abutments or tunnels (Figure 6.6), where railway track stiffness changes abruptly, often require frequent maintenance in order to ensure track geometry. The observed problems in the transition zone can include ballast penetration into the subgrade, hanging sleepers (i.e. voids forming underneath the sleepers), permanent rail deformation (Figure 6.7), worn track components, cracking of the concrete sleepers and/or slab-track, and loss of gauge (Kerr and Moroney, 1993; Thompson and Woodward, 2004; Li and Davis, 2005; Woodward *et al.*, 2007a and 2007b). Railway track transition mechanics can be explained as follows: at transition points the train wheels will experience rapid changes in elevation (either up or down) caused by abrupt changes in track stiffness. This change in elevation will excite the train components, i.e. the wheels, bogies and coach, which in turn will lead to vertical train-track interaction forces that are dynamically amplified in the transition zone. The level of dynamic excitation of the train and subsequent increased dynamic forces, depends on the elevation change (related to stiffness change),

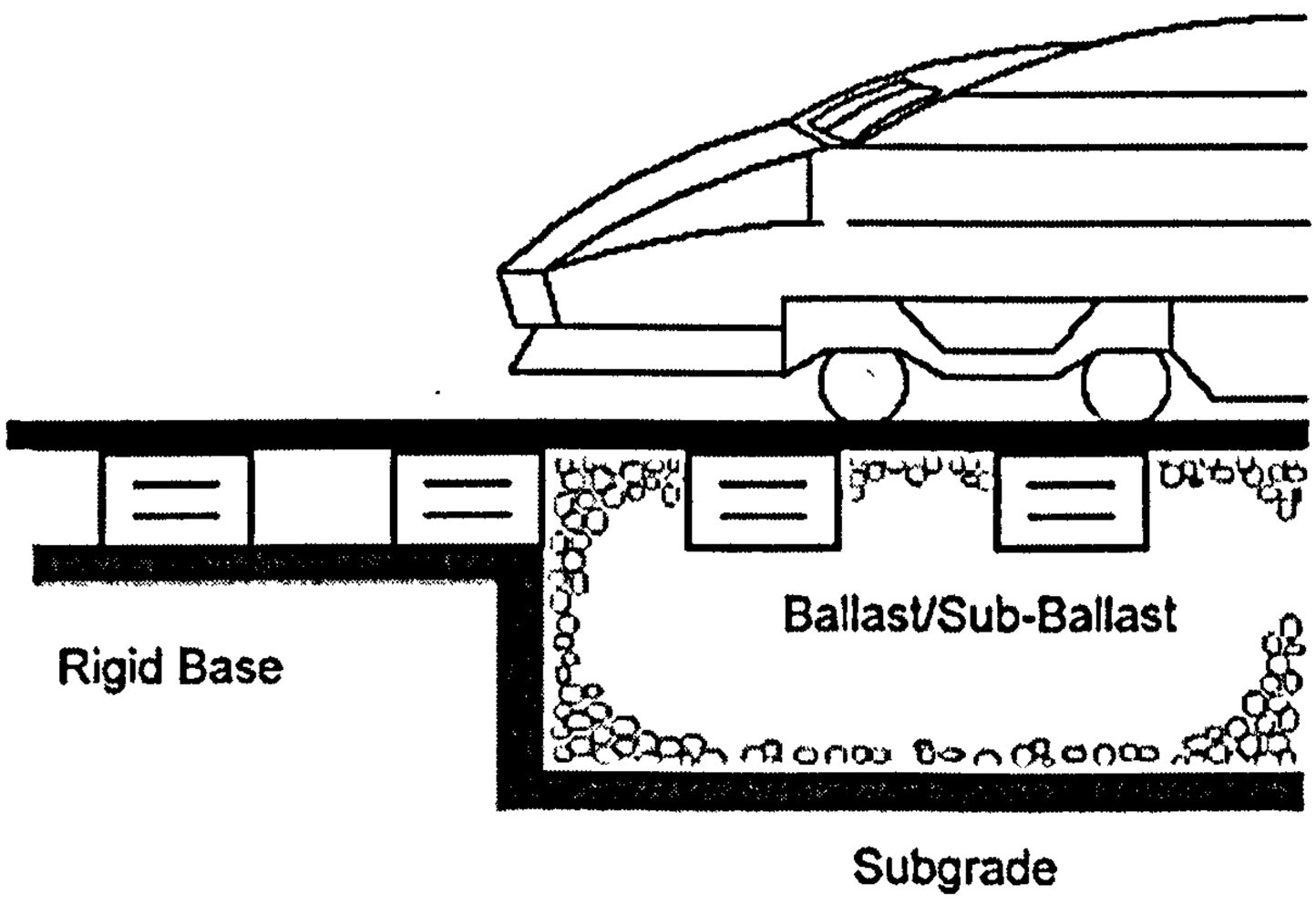

Figure 6.6. A schematic layout of railway track stiffness transitions (Banimahd and Woodward, 2007)

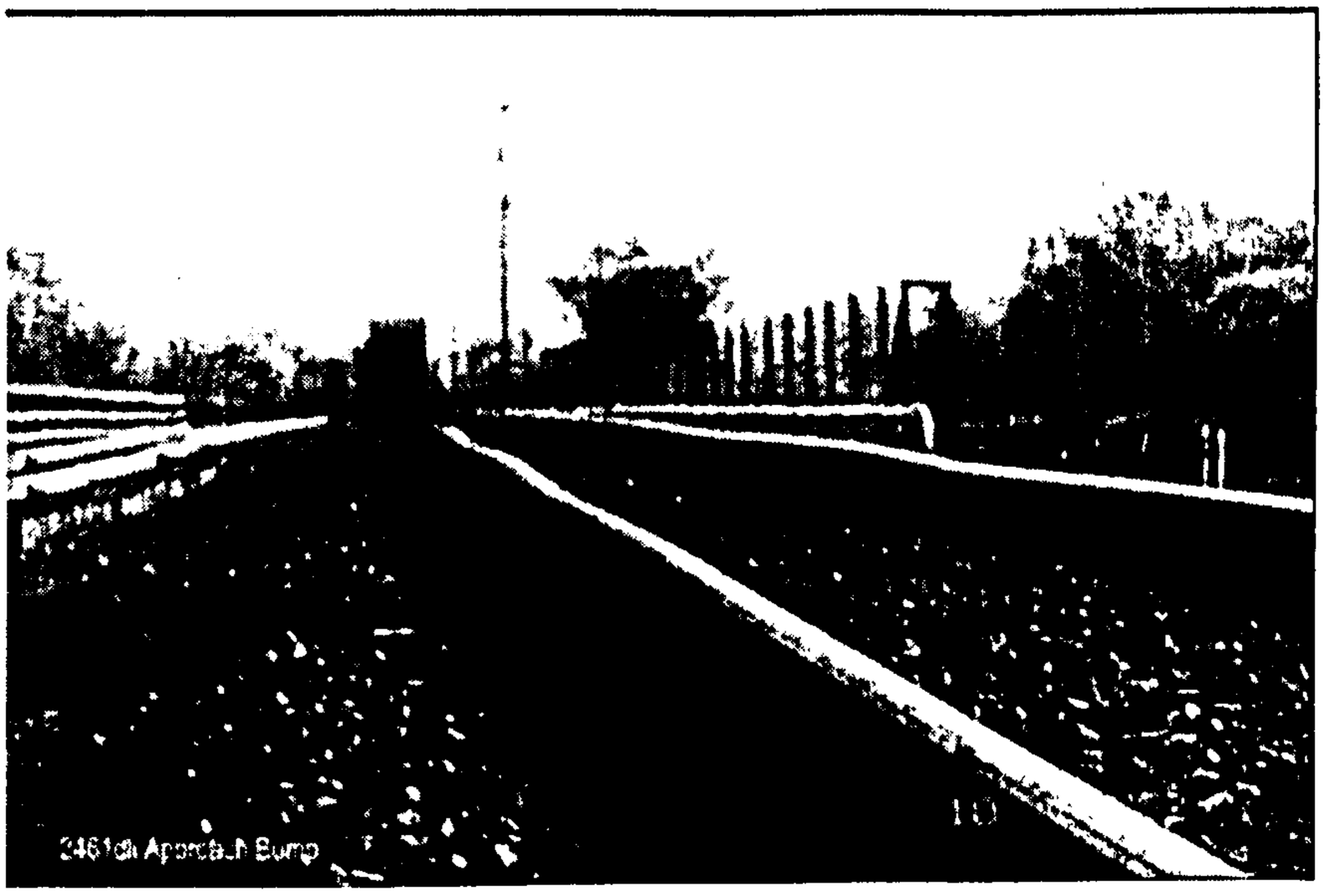

Figure 6.7. Permanent irregularities developed in a bridge approach (Li and Davis, 2005)

train speed and the mass and suspension characteristics of the train. Even in cases of no significant dynamic load change in the transition zone, the ballasted track may inherently settle more than the track on the bridge abutment or tunnel base, creating dips in the track running surface and voided sleepers. The settlement in the vicinity of a transition zone can be significantly accelerated in the presence of soft subgrade soils and/or poor drainage.

Because of the relationship between the dynamic train load and the track deflection, the railway track geometry in the transition zone can deteriorate at an accelerating rate through a self-perpetuating mechanism; as the dynamic load increases so does the track differential settlement which in turn leads to even higher dynamic forces and so on.

In order to arrive at an appropriate mitigation strategy and design, the transition zone needs to be correctly modelled. These models need to address all track components, the multi-layered nature of the substructure, track geometrical irregularities and track-train interactions. Most of such models applied to transition zones (up to the present day) have been based on spring-beam type or two dimensional finite element models. Suiker and Esveld (1997) employed a two-dimensional plain-stress finite element model to study the transition between a soft and stiff half space under a moving load, and reported amplification of the stress level near the transition zone for different levels of stiffness changes and load speed. In Suiker and Esveld (1997), rail and ballast layers were not incorporated in the models. As the train was represented by constant load, the dynamic amplification of the load in the vicinity of transition was not presented and the amplification of stress, in Suiker and Esveld (1997), is therefore associated mainly with the load speed effect, as discussed in Chapter 4. Zhai and True (1999) employed a beam type model coupled with a train model; they studied the effect of a ramp approaching a bridge and reported a direct relationship between the ramp gradient and the dynamic response of the train. They concluded that the ramp gradient is the most important factor as far as train dynamic excitation is concerned. They also showed that the effect of ramp gradient increased with train speed. By considering a coupled beam-train model, Lei and Mao (2004) studied changes in the train body acceleration and the rail-wheel interaction forces in the transition zone. They observed considerable dynamic amplifications caused by differential settlements between the plain line track and the track on the bridge abutment. According to their simulation, the abrupt change of vertical stiffness itself does not cause a significant increase in the rail/wheel interaction force.

In the present section, the transition mechanism is investigated using the developed dynamic train-track coupled finite element model. It is followed by parametric studies on the stiffness transition problem using a train-irregularity model. Finally, some suggestions are given for the transition design, based on the findings in this chapter.

6.3.1 3D Finite Element Coupled Train-Track Model

6.3.1.1 Plain Track

Plain tracks, on subgrade with different stiffness, are simulated here using the three-dimensional coupled train-track model. The track meshing layout is similar to that used in previous chapters (Figure 3.5). The model configuration is according to Section 3.3.1. A quarter train model is employed with the specifications according to Table (6.1). The sleeper spacing is 0.77 as given in Table (3.1). Different subgrade stiffness is considered while the depth and stiffness of the ballast are kept unchanged (EB=120 MPa, BD=300 mm).

Figures (6.8) and (6.9) depict the interaction force oscillations on plain track laid on subgrade with different stiffness for train speeds of 50 and 70 m/s. According to Figure (6.8) and (6.9), the discrete supports of the sleepers cause oscillations in the rail/wheel interaction force, the extent of which is related to train speed and track stiffness (here subgrade stiffness). For a given ballast depth and stiffness, the softer the subgrade, the greater the extent of oscillation in the interaction force (difference between maximum and minimum interaction forces). A greater extent of interaction force is also seen as the train speed increases. The FFT analysis of interaction forces signal gives the frequency associated with the discrete support of sleepers as shown in Figure (6.10) for different train speeds. The frequency associated with the discrete support excitation increases with train speed, as expected.

With respect to the excitation of discrete sleeper supports, it is observed in Figure (6.11) that the maximum dynamic interaction force is adversely affected by subgrade stiffness (for a given ballast depth and stiffness), the effect of which is more pronounced with train speed. This result is analogous with trends reflected by empirical relationships suggested for the dynamic amplification factor, according to Equations (2.9) and (2.10).

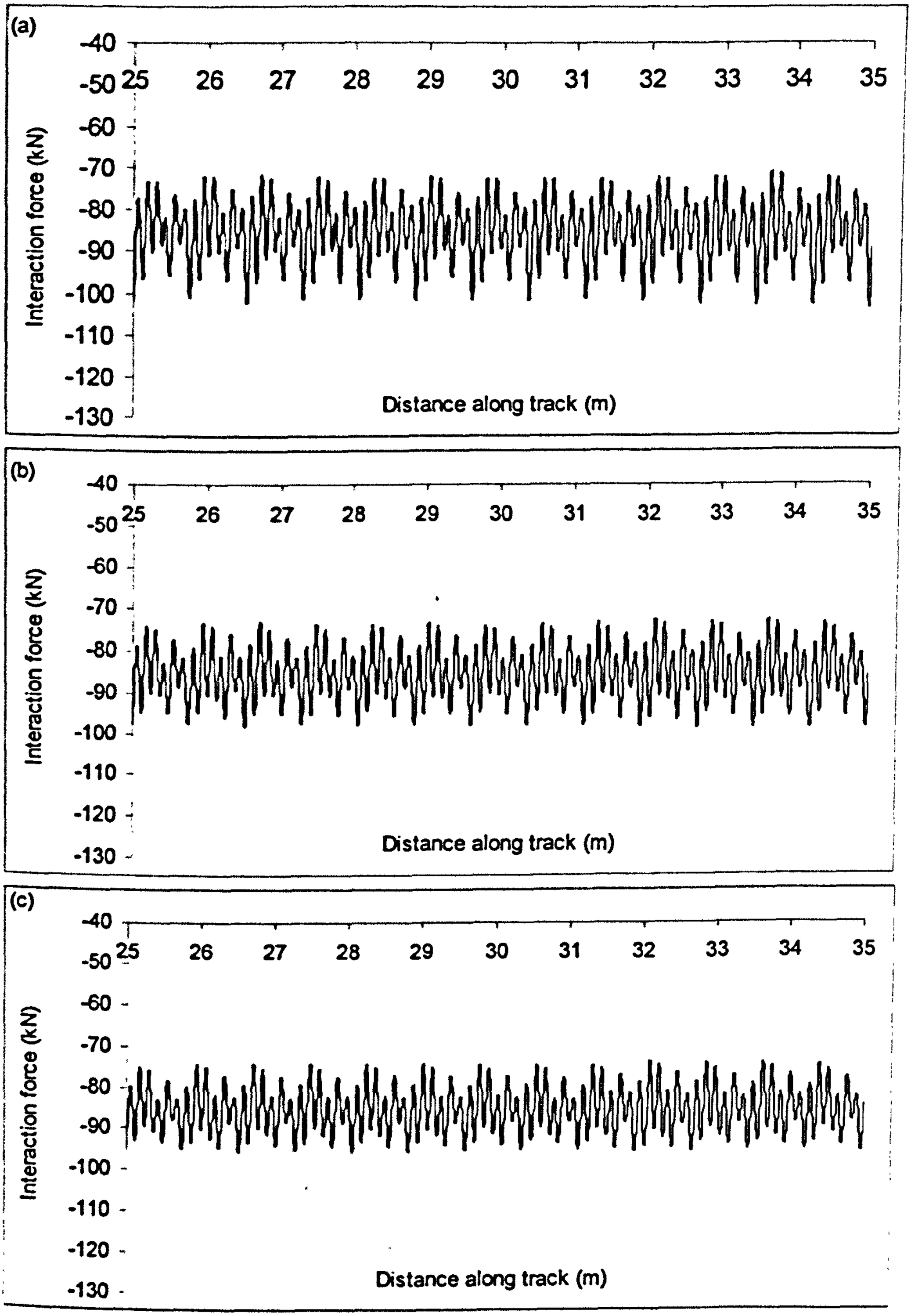

Figure 6.8. Rail/wheel interaction force caused by discrete support (sleeper) excitation for different subgrade conditions (EB=120 MPa, BD=300 mm, V=50 m/s): (a) ES=25 MPa (b) ES =40 MPa (c) ES =100 MPa

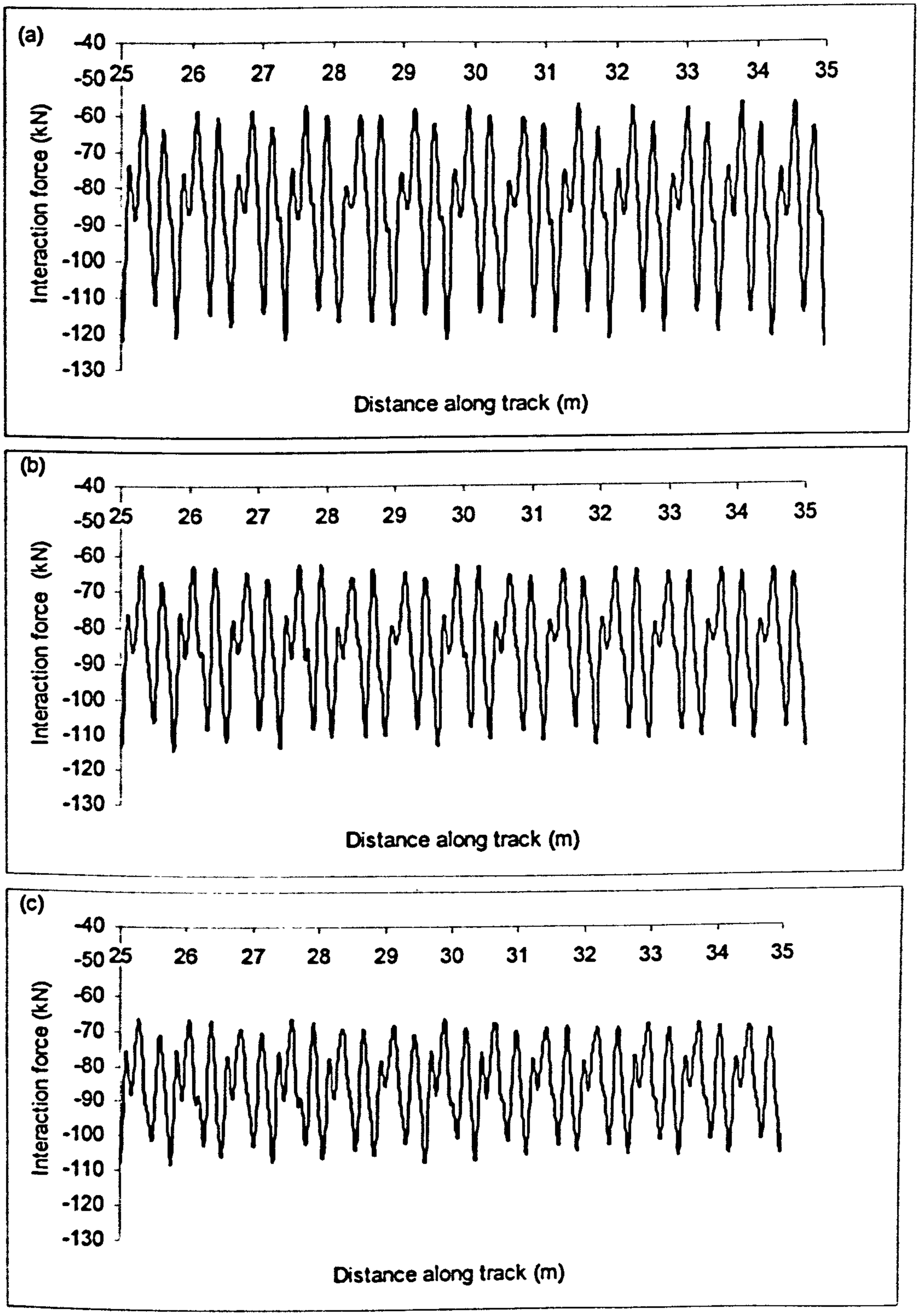

Figure 6.9. Rail/wheel interaction force caused by discrete support (sleeper) excitation for different subgrade conditions (EB=120 MPa, BD=300 mm, V=70 m/s): (a) ES=25 MPa (b) ES =40 MPa (c) ES =100 MPa

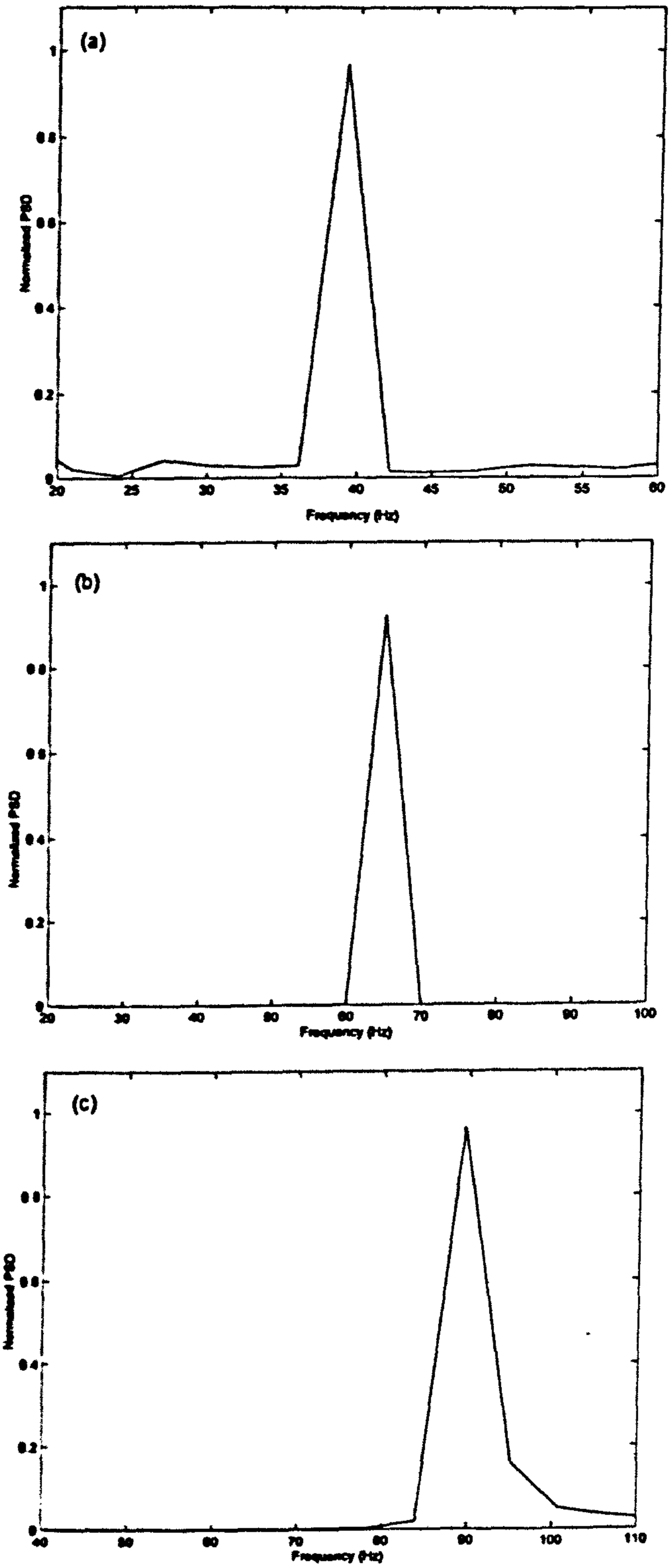

Figure 6.10. Frequency content of interaction force representing discrete sleeper excitation for different train speeds (EB=120 MPa, BD=300 mm, ES=15 MPa): (a) V=30 m/s (b)V=50 m/s (c)V=70 m/s

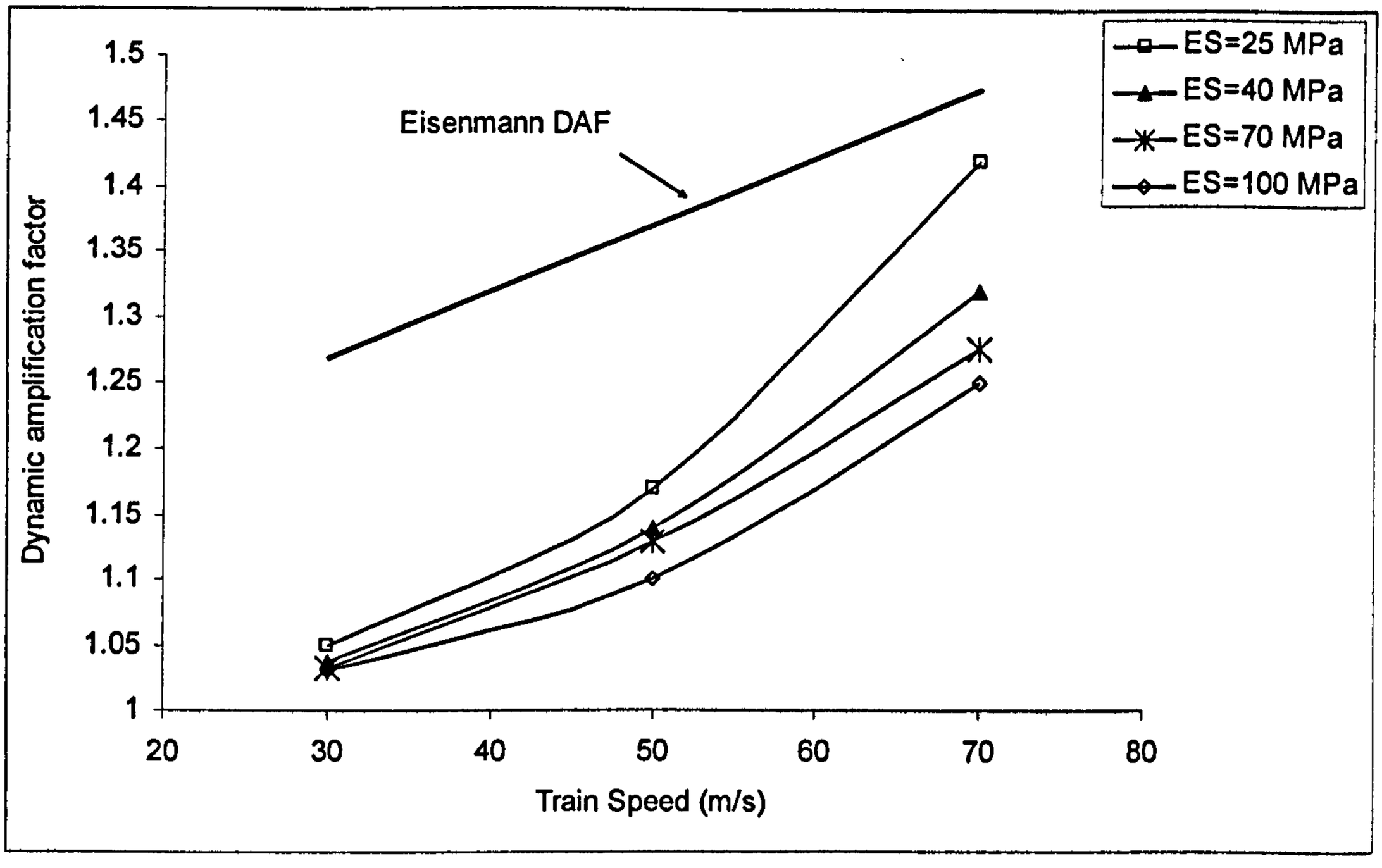

Figure 6.11. Dynamic amplification of wheel/rail interaction force caused by discrete sleeper support excitation (BD=300, EB=120 MPa)

The empirical Eisenmann dynamic amplification factor is also depicted in Figure (6.11). The Eisenmann factor is calculated assuming the track is in good condition (minimum geometrical irregularity). In cases where there is only a minimum irregularity (good track), it is seen that Eisenman's empirical relationship is relatively conservative, especially in the lower speed cases, if just the sleeper-space effect is taken into account.

6.3.1.2 Non-Faulted Transition

The developed coupled train-track finite element model is employed here to study the effects of stiffness change in the transition zone. For this section, it is assumed that no voided sleepers or geometrical irregularities are present in the transition zone. The stiffness transition between track placed on soil (with different subgrade stiffnesses) and that placed on a rigid base (representing a tunnel concrete slab track or bridge abutment) are considered as shown in Figure (6.12). No designed transition, e.g. gradual increase of stiffness, is

considered here. The track configuration is as given in Section 3.3. The rigid base is represented by a linear elastic material with resilient modulus of 20 GPa, and Poisson's ratio of 0.3. Ballast and subgrade are both represented by linear constitutive relationships. Ballast stiffness and depth are kept constant for all transition simulations (EB=120 MPa, BD=300 mm). A quarter train model is employed, in this section, for the finite element modelling of a coupled train-track system in the vicinity of the transition zone. The train property is given in Table (6.1).

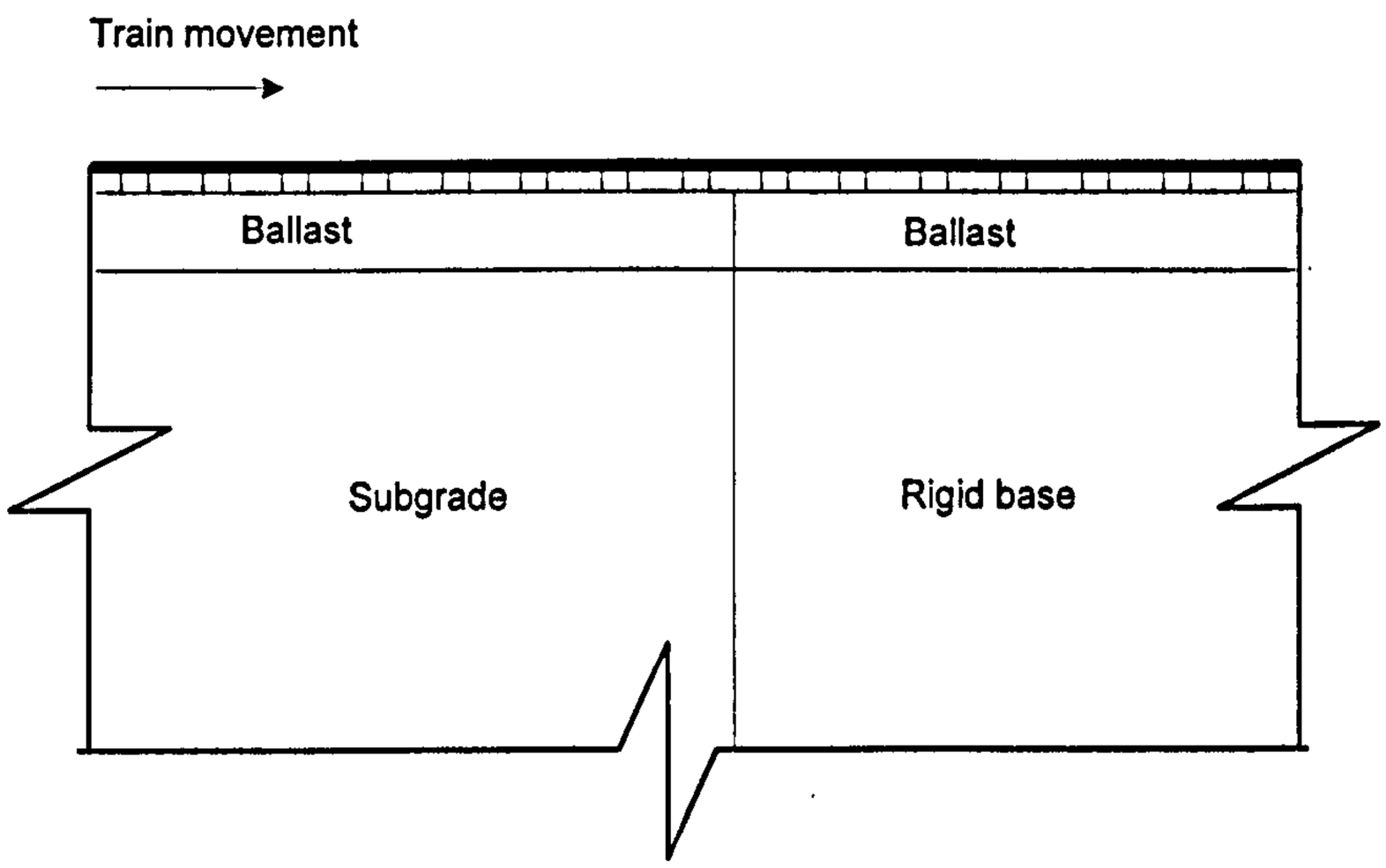

Figure (6.12). Schematic representation of the stiffness transition problem studied in present research

Typical displacement of the track in the vicinity of a transition zone (soil to rigid base) is shown in Figures (6.13) and (6.14). Owing to considerable differences between the stiffness of subgrade and rigid base, the displacement induced in the soil and rigid base are very different as expected. According to Figures (6.13) and (6.14), the difference between the displacement in the soil and rigid base, is seen to increase for softer soils and higher train speeds.

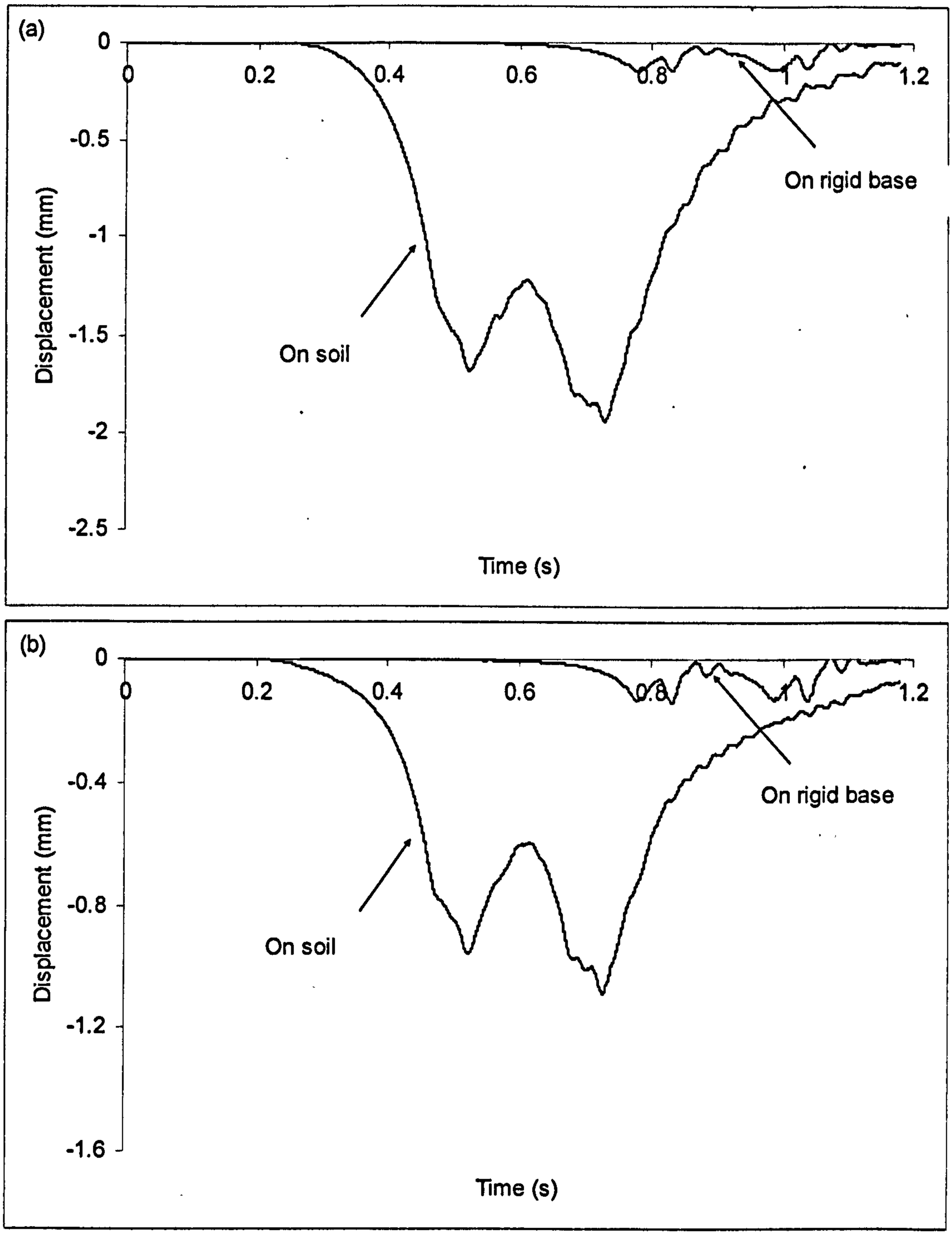

Figure 6.13. Displacements of railway track under the coach on soft and rigid sides of the transition at V=50 m/s (EB=120 MPa, BD=300 mm) (a) ES=40 MPa (b) ES=100 MPa

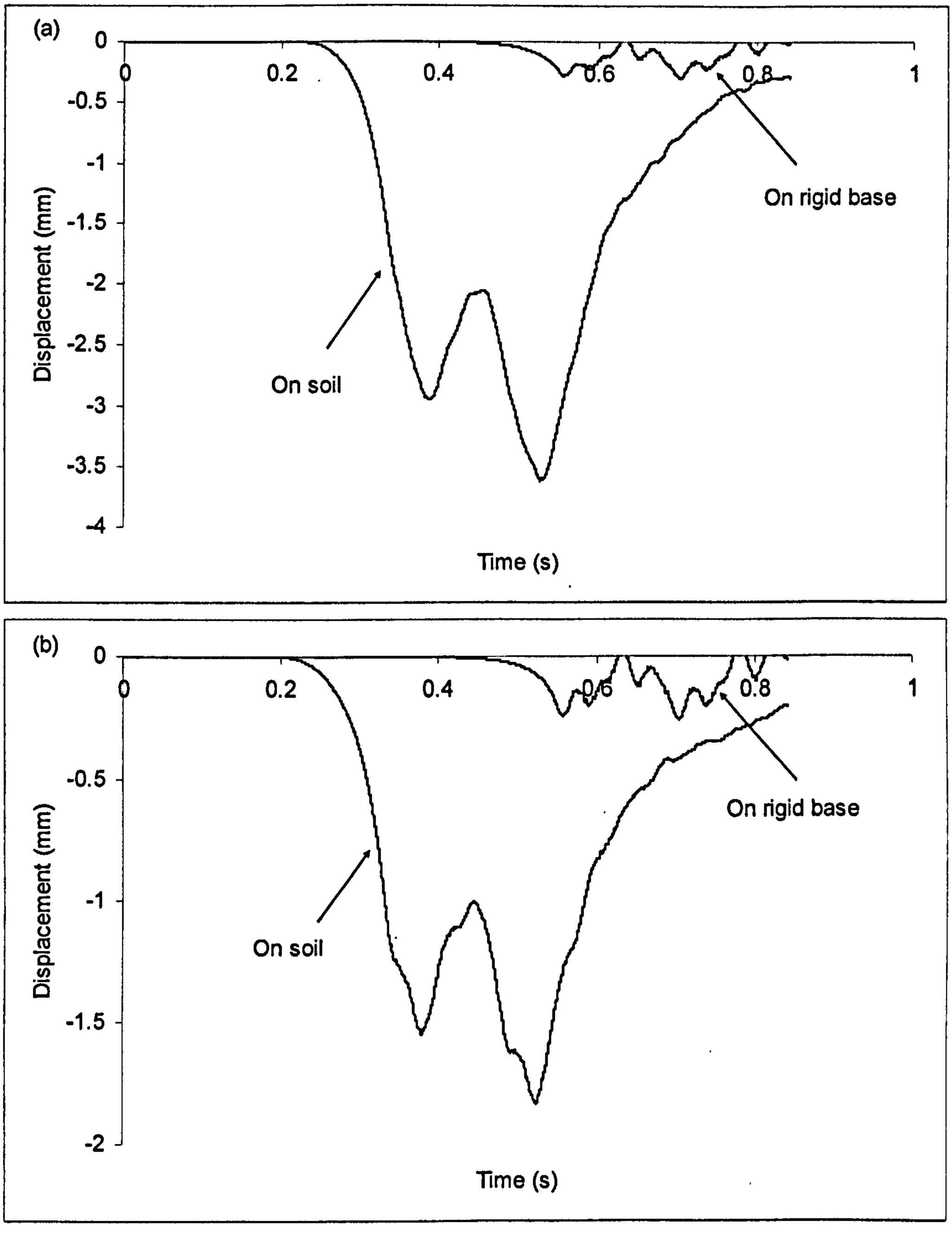

Figure 6.14. Displacements of railway track under the coach on soft and rigid sides of the transition at V=70 m/s (EB=120 MPa, BD=300 mm) (a) ES=40 MPa (b) ES=100 MPa

The mechanism of amplification of the wheel-rail interaction force and excitation of the train are illustrated in Figures (6.15-6.18). Figures (6.15a-6.18a) give the track displacements under a wheel in the transition zone obtained from the developed finite element model. A typical induced displacement field in the vicinity of a non-faulted transition zone is depicted in Figure (6.19). It is clearly observed that the displacement change starts at a distance from the rigid base (e.g. tunnel base) mainly because of the flexural stiffness of the rail (it can also be the result of a designed transition, e.g. a gradual change in the stiffness when approaching the rigid base). Rail/wheel interaction forces between the wheel and the train body accelerations in the same soil-rigid base transition are given in Figures (6.15b-6.18b) and Figures (6.15c-6.18c) respectively. As the displacement starts to change, the train components begin to get excited owing to the approaching stiff base, and therefore dynamic forces between the rail and wheel are amplified.

Increases in the acceleration level of the train coach, as indicated in Figure (6.15c-6.18c) when approaching the rigid base, explains why a passenger feels the train passing over a stiffness transition. It is also noted that if a softer subgrade exists in the vicinity of the transition, then a higher deflection difference between the soft and rigid sides of transition would exist which adversly affects the interaction force and train body acceleration, as shown in Figures (6.15b-6.18b) and Figures (6.15c-6.18c). In other words, the amplification of dynamic interaction force and train excitation in the transition zone is directly linked to the deflection differences between the soft and rigid sides of the transition zone.

The effects of subgrade stiffness (for a given ballast stiffness and depth) on the maximum interaction force and train body acceleration are summarized in Figures (6.20) and (6.21) respectively. The adverse effect of subgrade stiffness on the train excitation, in terms of interaction force and train body acceleration, gets bigger as the train speed increases. In addition, the train speed is also seen to have an important impact on the rail/wheel interaction force in the transition zone as the increase in both interaction force and train body acceleration are observed with train speed.

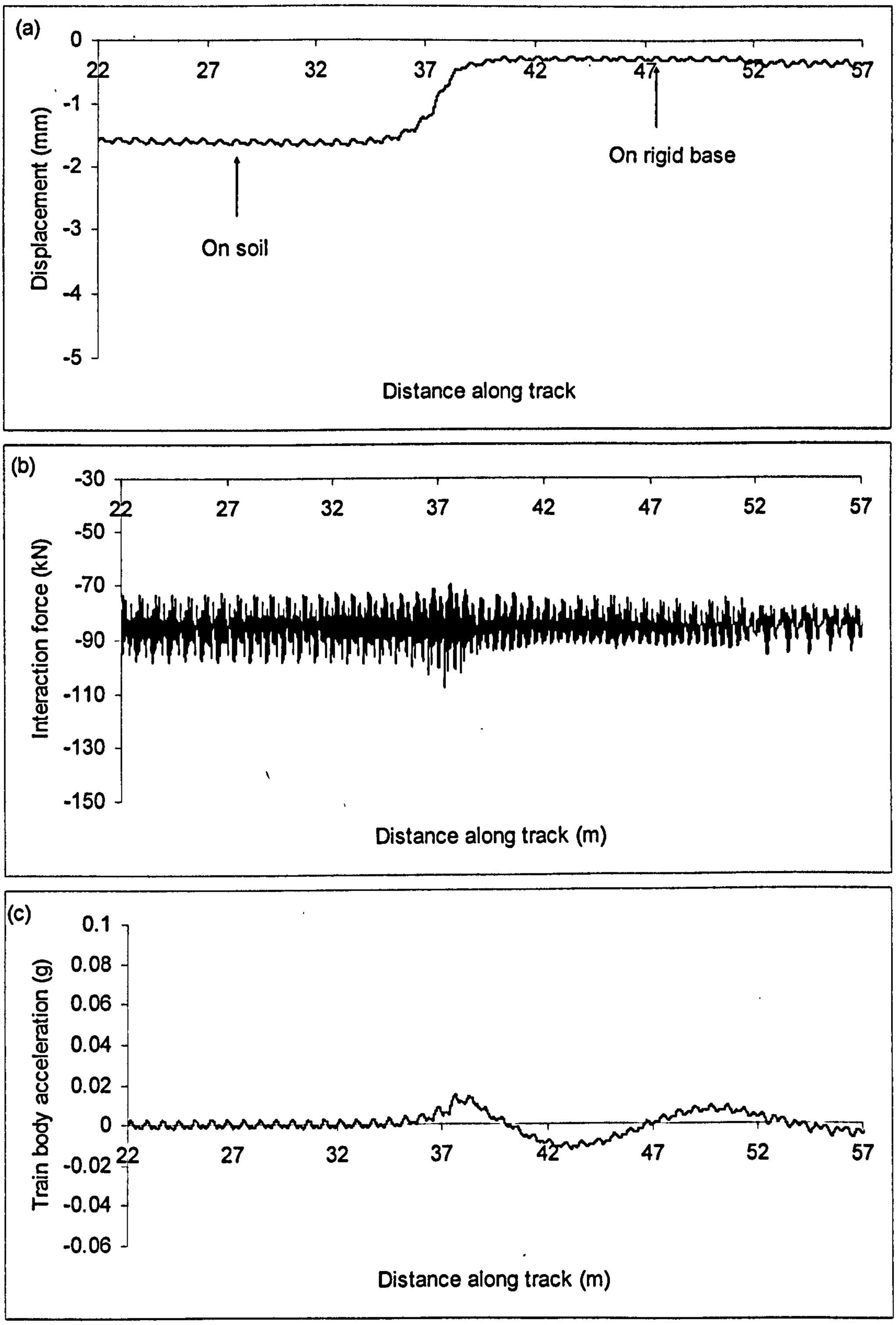

Figure 6.15. Track displacement (a), interaction force (b) and train body acceleration (c) in the vicinity of a non-faulted transition (ES=40 MPa, V=50 m/s)

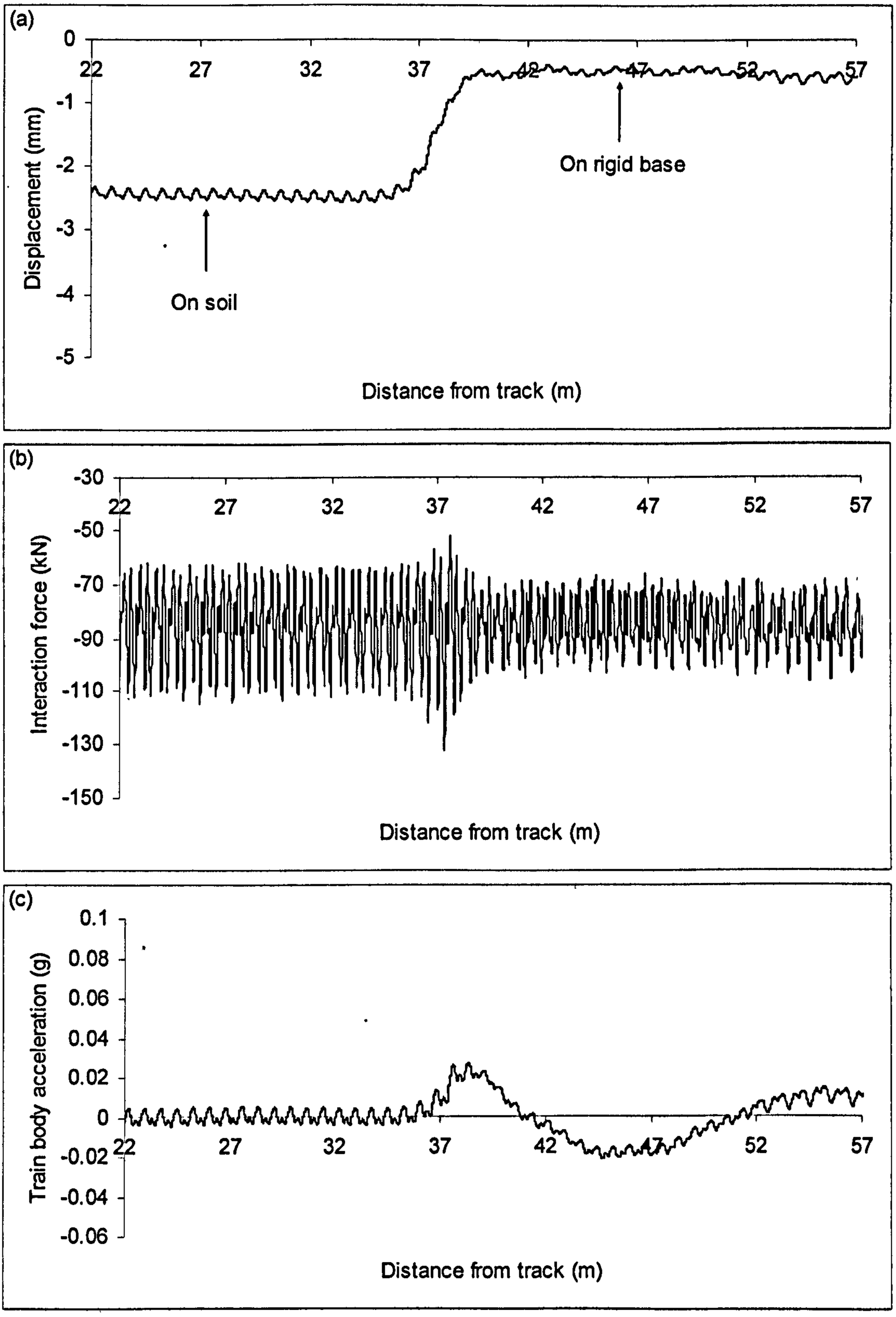

Figure 6.16. Track displacement (a), interaction force (b) and train body acceleration (c) in the vicinity of a non-faulted transition (ES=40 MPa, V=70 m/s)

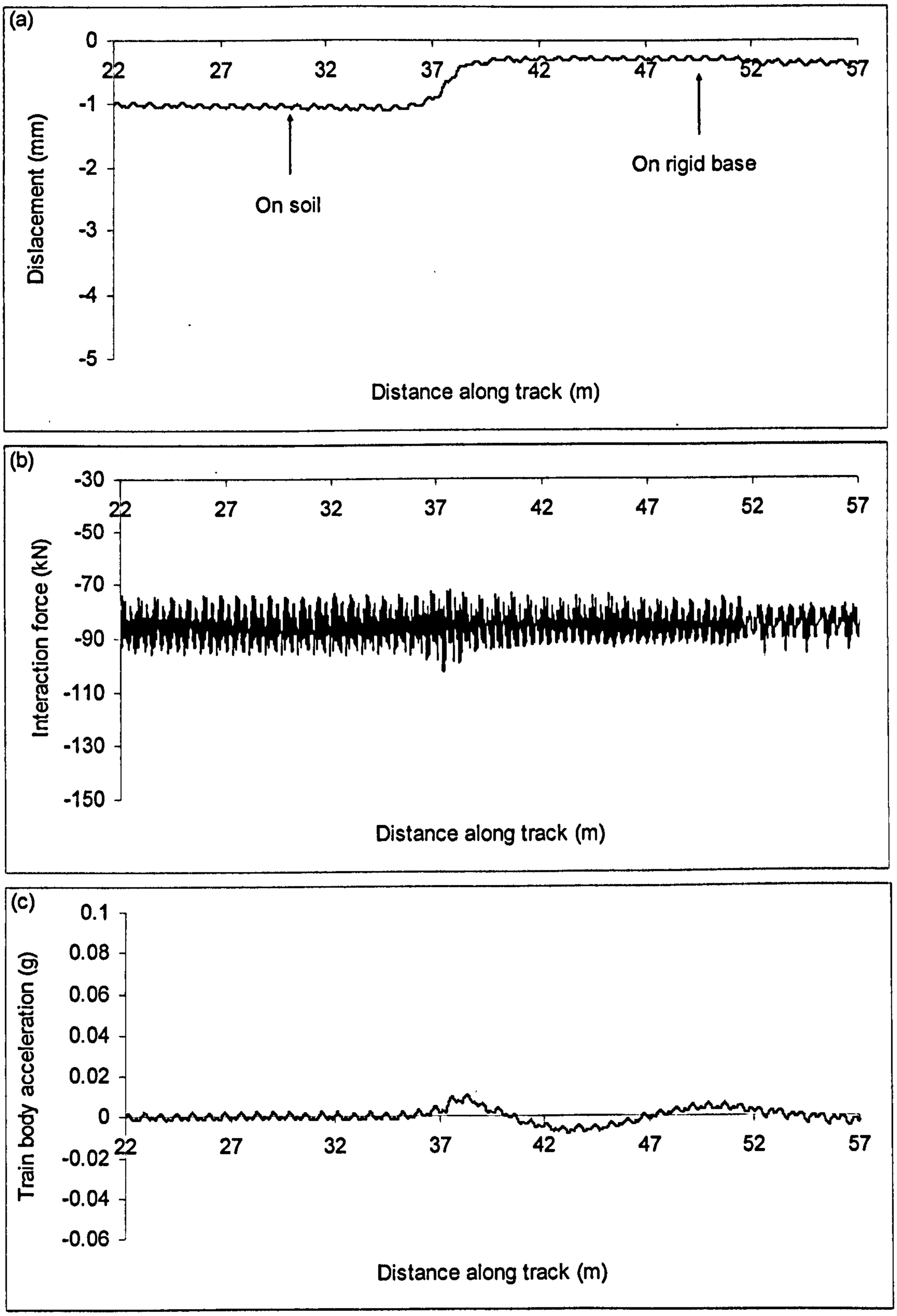

Figure 6.17. Track displacement (a), interaction force (b) and train body acceleration (c) in the vicinity of a non-faulted transition (ES=100 MPa, V=50 m/s)

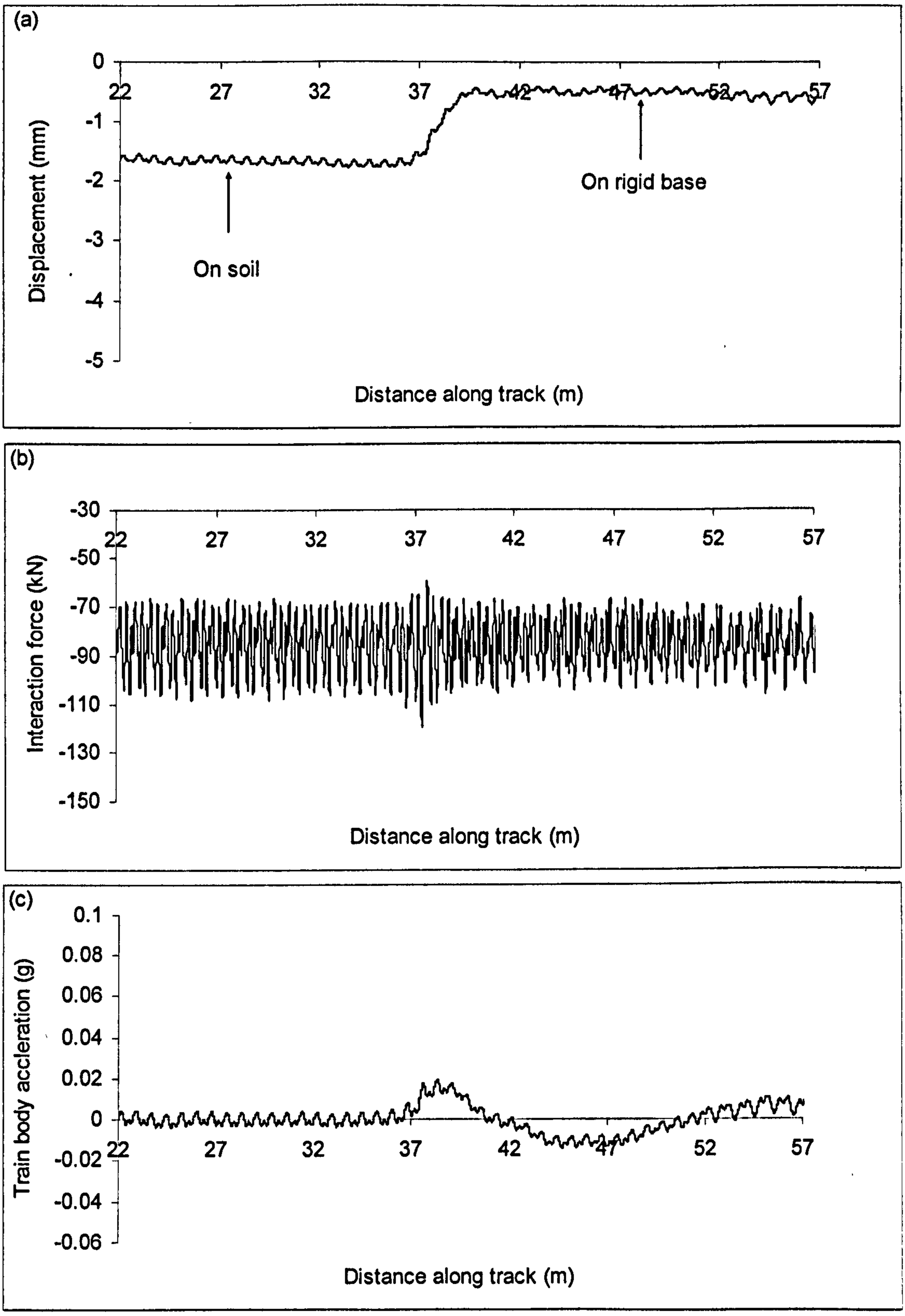

Figure 6.18. Track displacement (a), interaction force (b) and train body acceleration (c) in the vicinity of a non-faulted transition (ES=100 MPa, V=70 m/s)

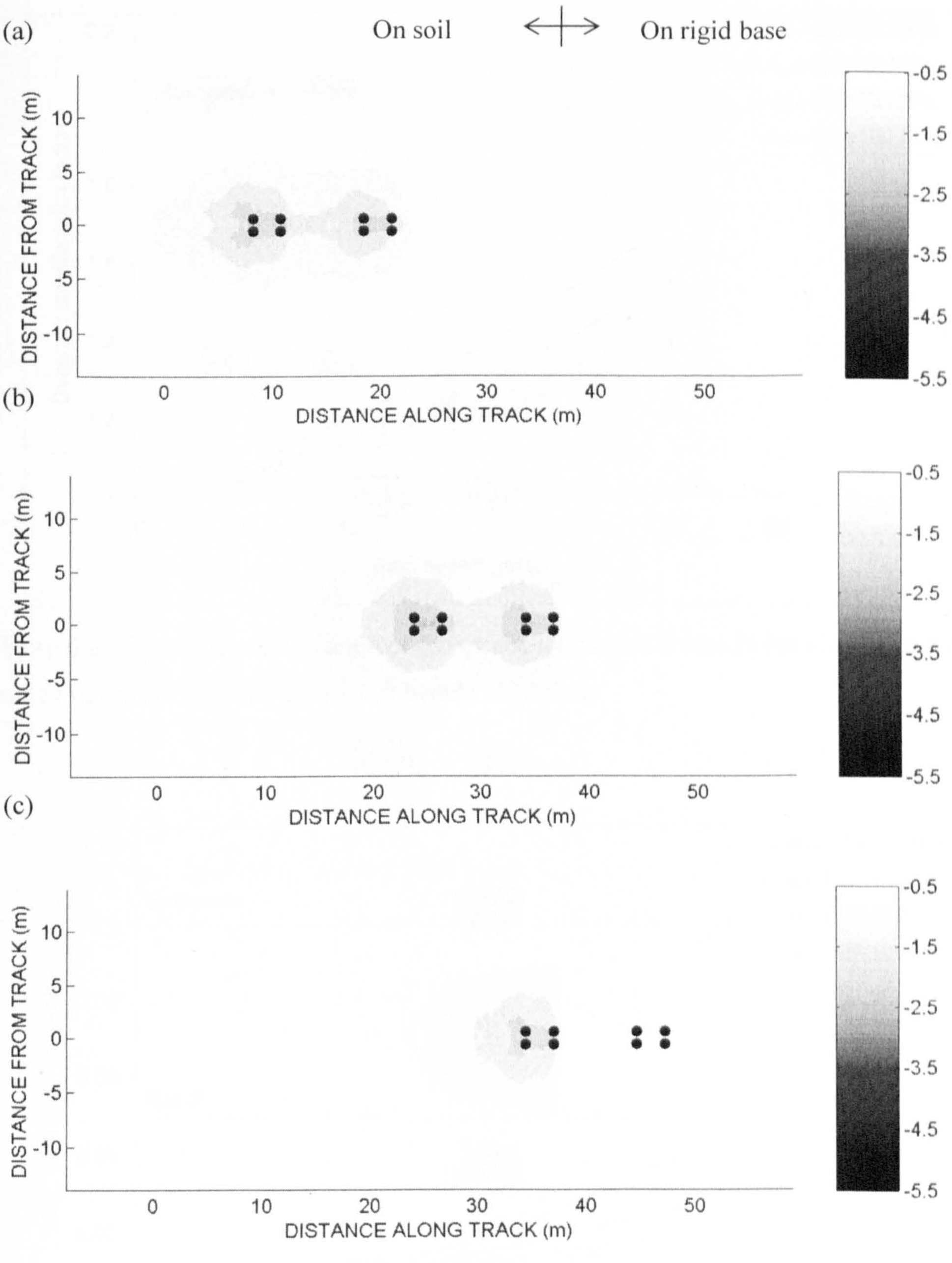

Figure 6.19. Induced displacement contours under a train coach passing a non-faulted transition zone (ES=100 MPa, EB=120 MPa, BD=300 mm)

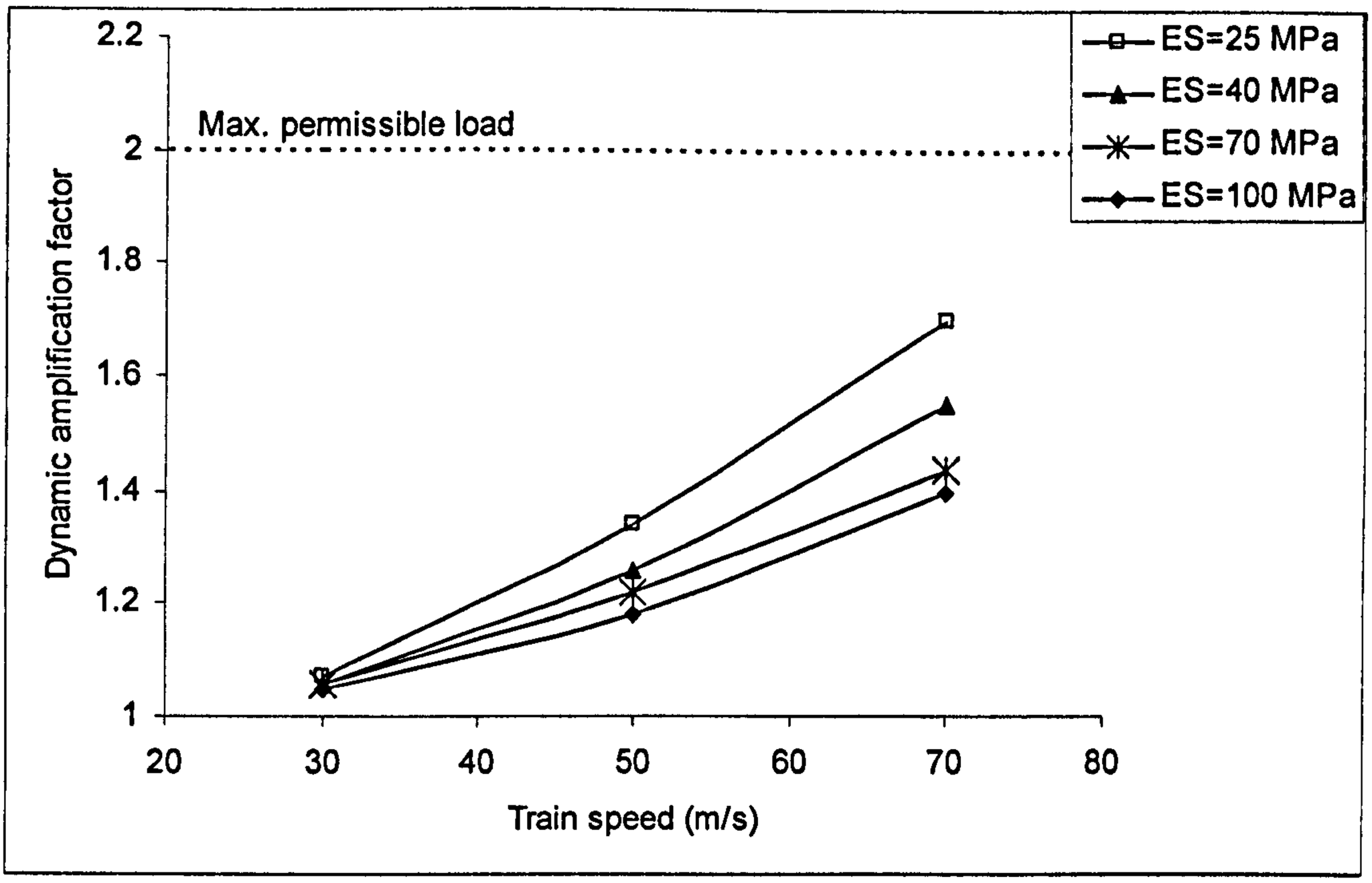

Figure 6.20. Dynamic amplification of train/track interaction forces in the vicinity of a non-faulted transition zone for different subgrade conditions

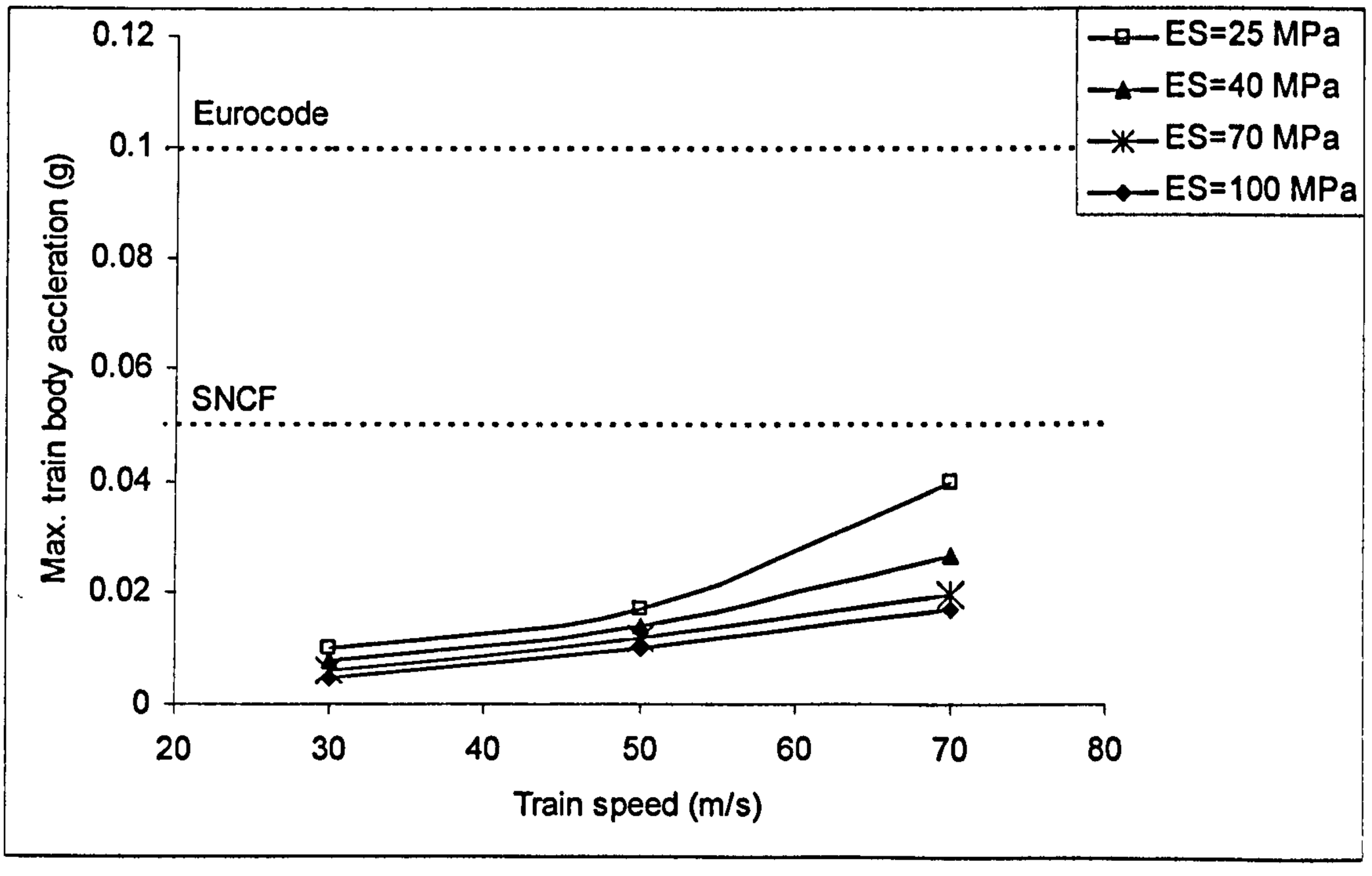

Figure 6.21. Train body accelerations in the vicinity of a non-faulted transition zone for different subgrade conditions

Regarding the dynamic load applied on the track in the transition zone, a maximum permissible load may be assigned, based on experimental and site observations. In the present research, the maximum permissible wheel load of 170 kN (Esveld, 2001) is employed. Considering the static load of the train (axle load =17.4 T, wheel load =8.2 T), then a maximum dynamic amplification of 2 is believed to be the maximum permissible level of DAF on the track in the transition zone for the cases studied. According to Figure (6.20), it is seen that the dynamic interaction force in the presence of a transition (as a result of the resilient deflection difference) remains under the permissible level for all cases with different subgrade stiffnesses and train speeds.

In terms of the maximum permissible vertical train body acceleration, which is considered to be representative of the passenger comfort level, different values have been suggested. While Eurocode (European Committee for standardization, 1995) suggests a maximum value of $1 m/s^2$ (0.1g), Zhai *et al.* (2001) recommend a maximum of 1.25 m/s^2 (0.12g) . Lei and Mao (2004) recommend 0.2g as a riding quality criterion based on Chinese railway practice. SNCF (the national railway of France) put a very restrictive value of 0.05 g as the maximum permissible vertical acceleration (Grandil and Ramodence, 1990). According to Figure (6.21), while the maximum vertical train body acceleration increases with softness of the subgrade and train speed, they remain under the most restrictive limit (0.05g) for all cases.

From the results obtained in this section, it can generally be said that the stiffness change and its consequent resilient displacement difference between soft and rigid sides does not cause, on its own, any significant change in the dynamic load and passenger comfort level, when compared to the permissible load and train body acceleration level. That is in agreement with the findings of Lei and Mao (2004). They used a beam type model and studied the effect of an abrupt stiffness change in the track (from stiffness k to 100k), where they concluded that an abrupt change of track stiffness does not cause a significant increase in the dynamic interaction force.

It should be noted that the results presented above are based on the observation that the rail accommodates a short transition length which bridges "smoothly" the displacement between soft and stiff sides (Figures 6.15a-6.18a). This transition length, which is caused mainly by the flexural stiffness of rail, is termed here as the "natural transition length". It is suggested that the natural transition length be supported by a designed transition (gradual change of substructure stiffness) to reduce the tension forces acting in the rail, the fastenings and a few sleepers at the start of the rigid base, which can prevent excessive deterioration of the superstructure in this zone.

In the transition simulations, as the rails are assumed to be fixed on the sleepers in the three-dimensional finite element model, the results from the transition simulations represent the cases with a high degree of fixity. Even for a high fixity track after a number of train passages, owing to deterioration of the fastenings and sleepers on the stiff side (bridge abutment, slab track), the flexural stiffness of railway would reduce and consequently the natural transition length might reduce. In addition, slip of the sleeper on the ballast and separation of sleeper (from ballast or slab track) on the rigid base, which are not considered in the present finite element simulations, may also decrease the flexural stiffness of rail and reduce the natural transition length as a consequence. The decrease in flexural stiffness could result in larger resilient displacements in the softer side as well. A larger displacement difference between the soft and stiff sides of the transition zone, along with the possible decrease in natural transition length, can result in higher interaction forces and possible deterioration in the transition zone.

The natural transition length is also affected by the interface mechanism between the rigid side wall and the soil on the other side. To accommodate the relative displacement in the interface (Rigid base/subgrade), an extremely soft and thin layer of elements was placed between the rigid base and subgrade in the transition simulations. Nonlinearity of the resilient behaviour of subgrade and ballast would also affect the resilient displacement of track; especially at higher speeds (see Chapter 5). Therefore the transition simulations based on nonlinear constitute relationships for the ballast and subgrade might result in a higher interaction force and train body acceleration when compared with the values obtained from linear simulations, as presented in this section.

It should be mentioned that, although the interaction force developed solely as a result of the resilient displacement difference between the soft and rigid sides of the transition (caused by stiffness difference) is relatively modest, the track may still be prone to permanent settlement, voided sleepers or track faults, after a number of train passages. This will occur if proper measures are not taken into account (mainly because the softer/weaker side will inherently settle more than the stiffer/stronger side). The effects of track faults and permanent settlement will be discussed in more detail in subsequent sections.

6.3.1.3 Faulted Transitions

In reality, owing to the transition mechanism discussed earlier, most ballasted track transitions near bridges or tunnels are voided. The elimination of the void through maintenance in the vicinity of the bridge abutment or tunnel base in ballasted track has proved difficult because of problems of tamping the track in this zone (as a result of the adjacent track fixity condition) as noted by Thompson and Woodward (2004). For this reason, the track transition area can remain voided under operational conditions. Wet spots in this zone can also provide weak points. In addition, worn track components can also give surface geometrical irregularities in the transition zone as a result of overstressing or rail corrugation effects. In an accurate transition analysis, the existence of many different kinds of faults should be considered.

The results of two simulations which incorporate a track fault are presented here. In a three-dimensional finite element model, a track fault is represented by a series of ballast elements with very low stiffness (EB=5 MPa) representing a weak zone (e.g. wet spot) near the rigid side. The track-train model configuration remains similar to the configuration used in the previous section for non-faulted transitions.

Figure (6.22) shows the displacement fields on the surface of railway track when a train is approaching and passing over a long faulted transition zone. A change in the displacement pattern as the coach approaches and passes over the voided area is clearly seen. Higher

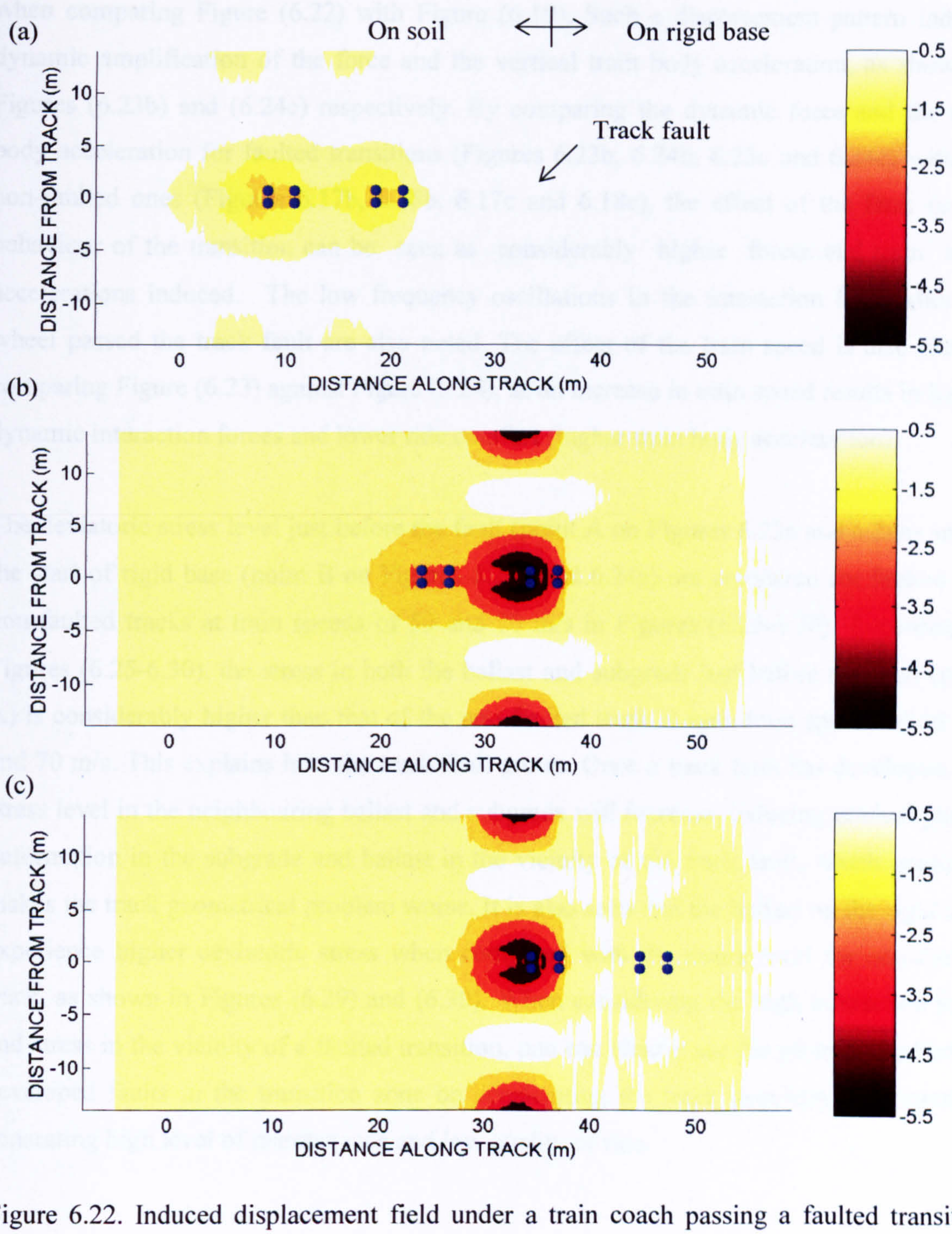

Figure 6.22. Induced displacement field under a train coach passing a faulted transition zone (ES=100 MPa, V=70 m/s)

track deflections and displacement concentrations around the faulted area are observed, when comparing Figure (6.22) with Figure (6.19). Such a displacement pattern induces dynamic amplification of the force and the vertical train body acceleration, as shown in Figures (6.23b) and (6.24c) respectively. By comparing the dynamic force and the train body acceleration for faulted transitions (Figures 6.23b, 6.24b, 6.23c and 6.24c) with the non-faulted ones (Figures 6.17b, 6.18b, 6.17c and 6.18c), the effect of the fault on the behaviour of the transition can be seen as considerably higher forces and train body accelerations induced. The low frequency oscillations in the interaction force after the wheel passed the track fault are also noted. The effect of the train speed is also shown, comparing Figure (6.23) against Figure (6.24), as an increase in train speed results in higher dynamic interaction forces and lower ride comfort (higher train body acceleration).

The deviatoric stress level just before the fault (point A on Figures 6.23a and 6.24a) and at the start of rigid base (point B on Figures 6.23a and 6.24a) are compared for faulted and non-faulted tracks at train speeds of 50 and 70 m/s in Figures (6.25-6.30). According to Figures (6.25-6.30), the stress in both the ballast and subgrade just before the fault (point A) is considerably higher than that of the non-faulted track at both train speeds of 50 m/s and 70 m/s. This explains how the track fault grows. Once a track fault has developed, the stress level in the neighbouring ballast and subgrade will increase, inducing gradual plastic deformation in the subgrade and ballast in the vicinity of the track fault, which gradually makes the track geometrical problem worse. It is also seen that the ballast on the rigid base experience higher deviatoric stress when compared with the stress level for non-faulted track, as shown in Figures (6.29) and (6.30). When considering the high interaction force and stress in the vicinity of a faulted transition, one can clearly see the prominent effect of developed faults in the transition zone on accelerating the track geometry deterioration, generating high level of maintenance and low quality of ride.

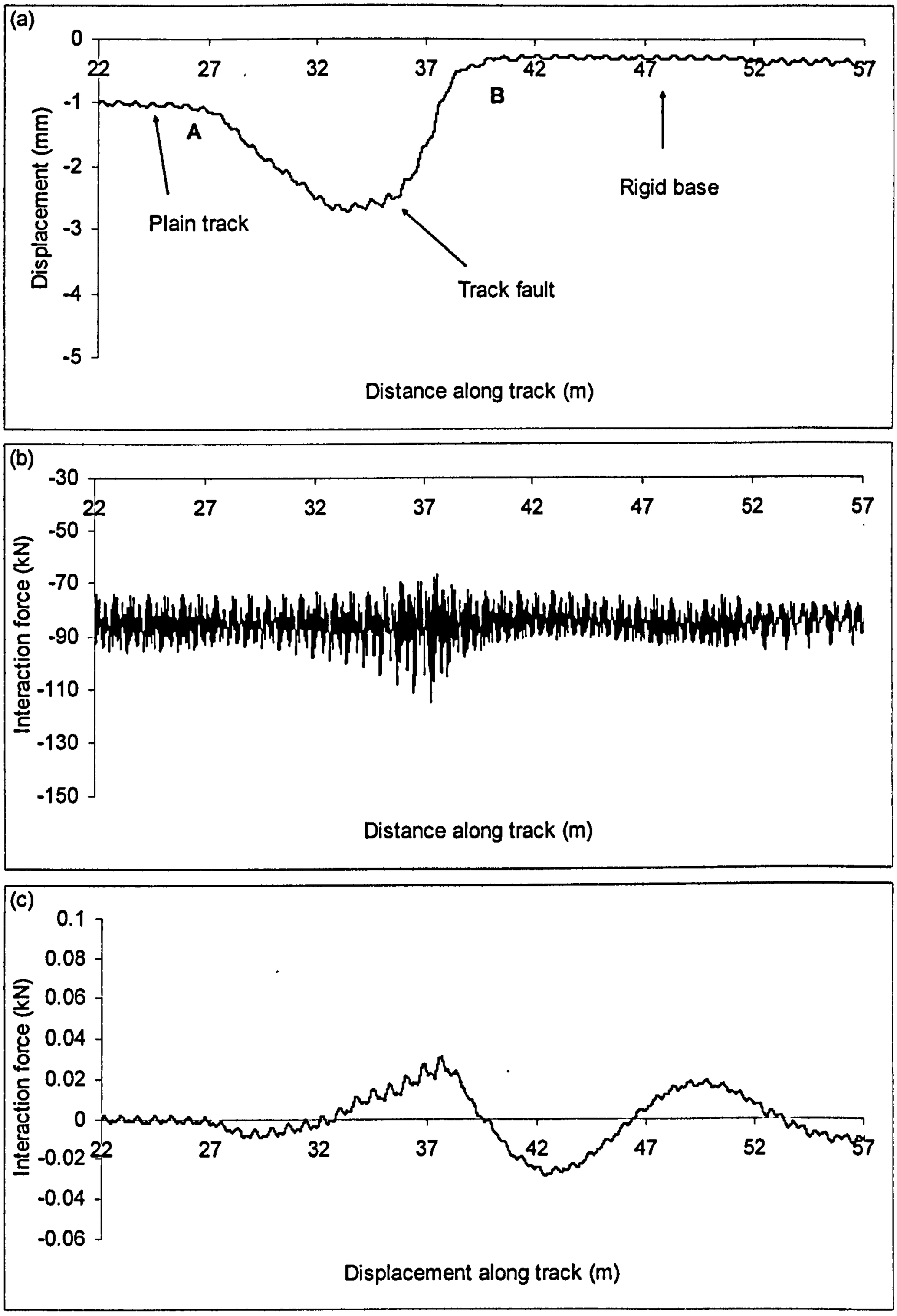

Figure 6.23. Track displacement (a), interaction force (b) and train body acceleration (c) in the vicinity of a faulted transition (ES=100 MPa, V=50 m/s)

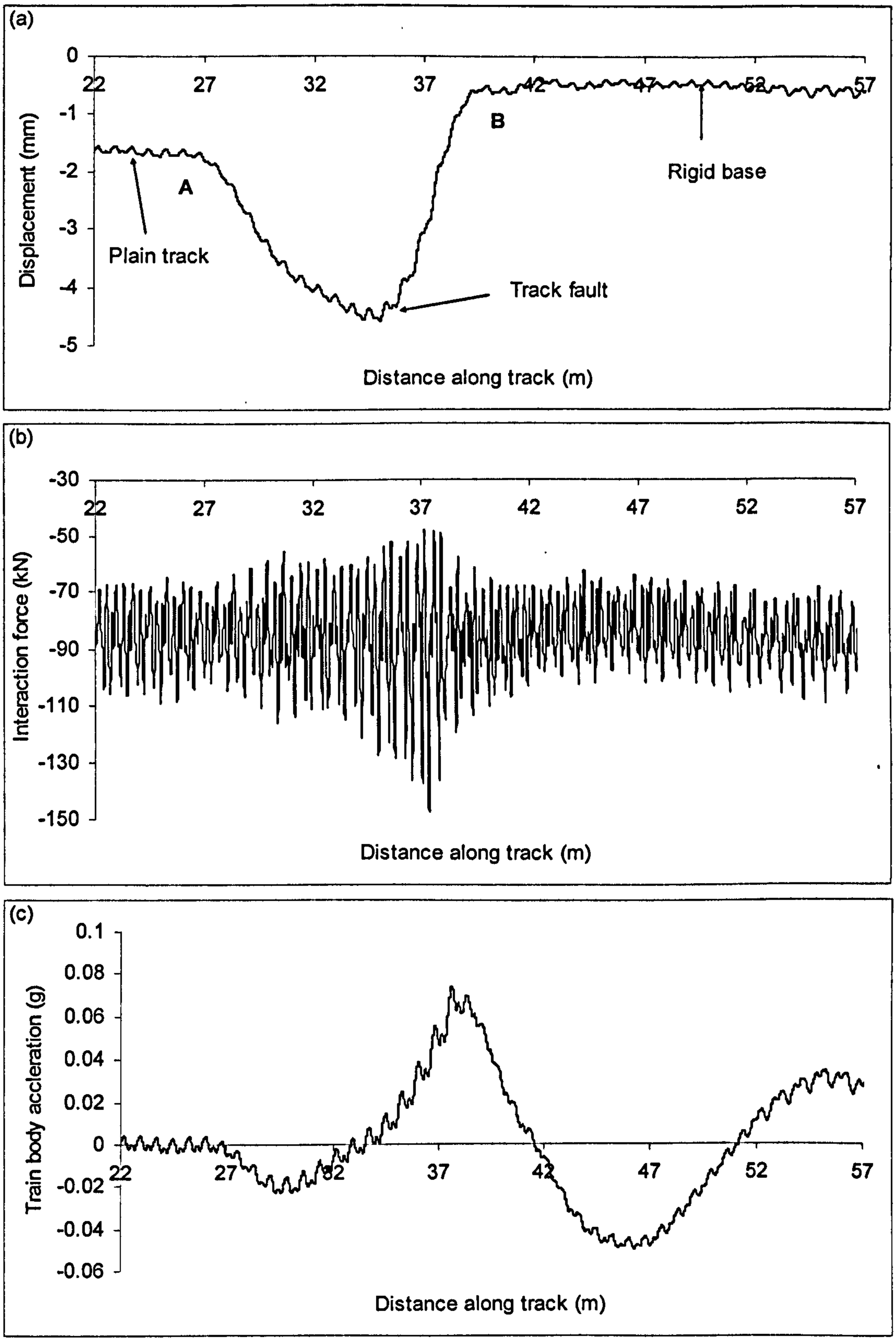

Figure 6.24. Track displacement (a) interaction force (b) and train body acceleration (c) in the vicinity of a faulted transition (ES=100 MPa, V=70 m/s)

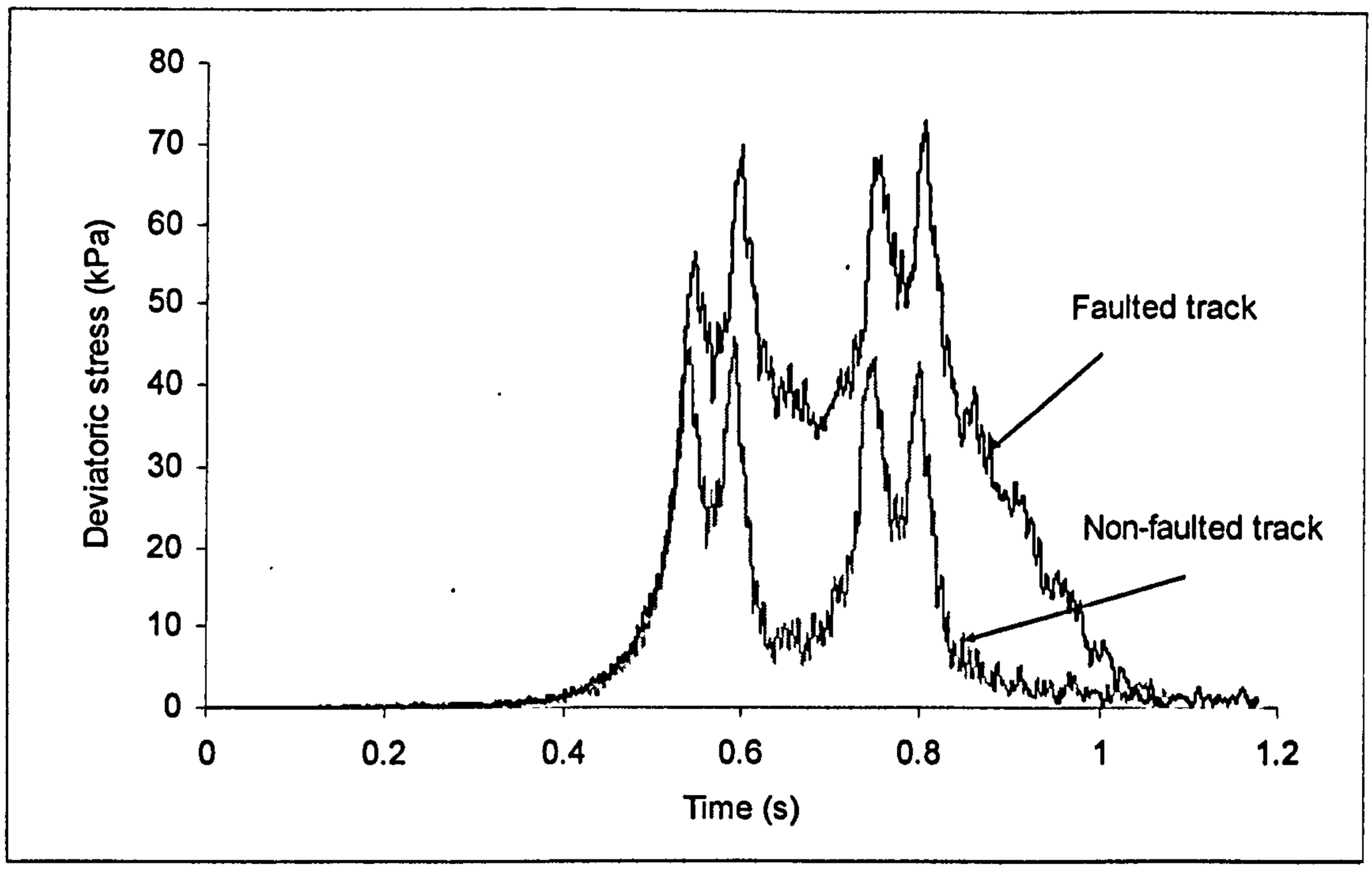

Figure 6.25. Deviatoric stress on top of ballast layer near the faulted zone (Point A) against deviatoric stress in the same position in non-faulted transition at V=50 m/s

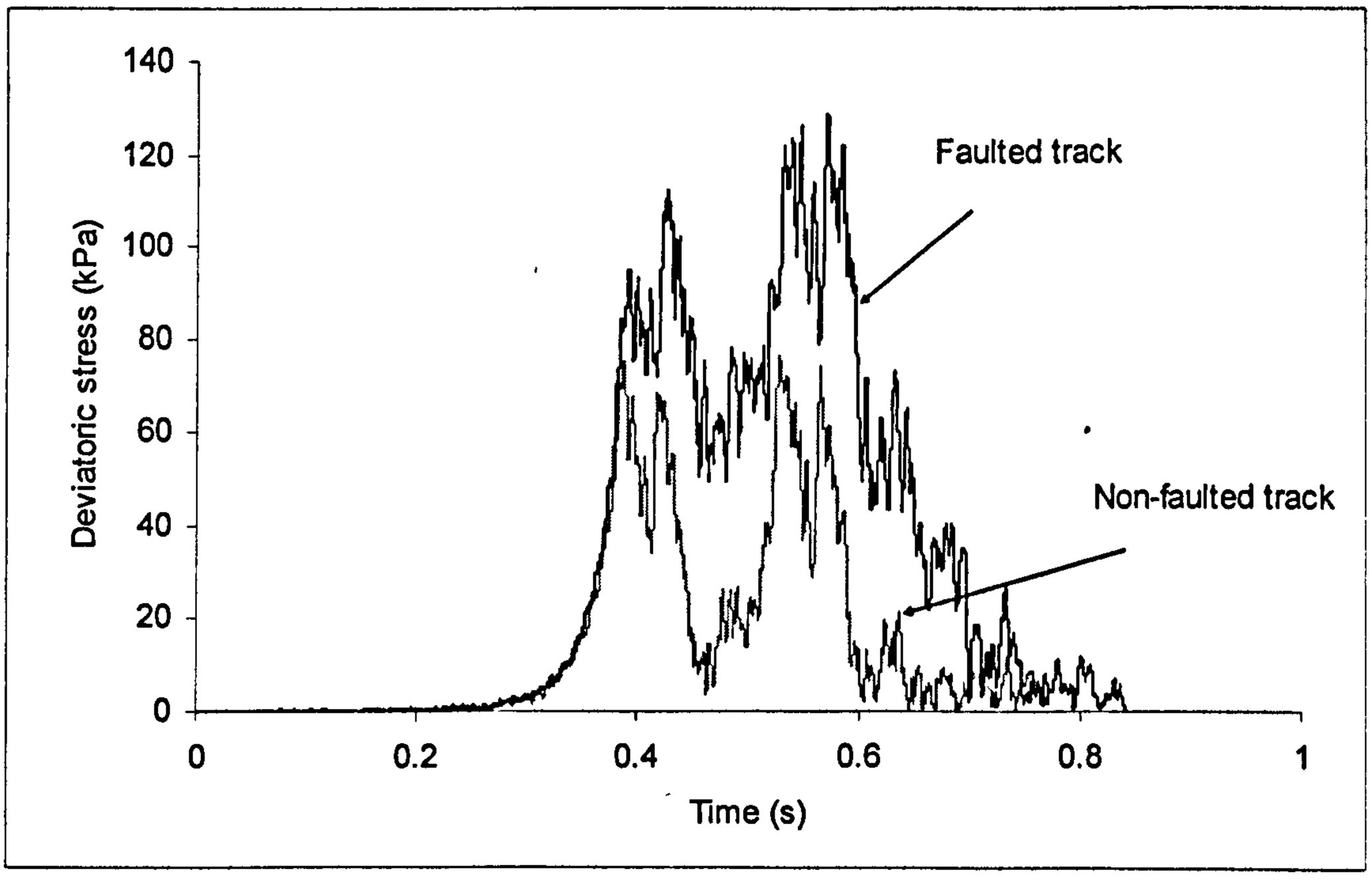

Figure 6.26. Deviatoric stress on top of ballast layer near the faulted zone against deviatoric stress (Point A) in the same position in non-faulted transition at V=70 m/s

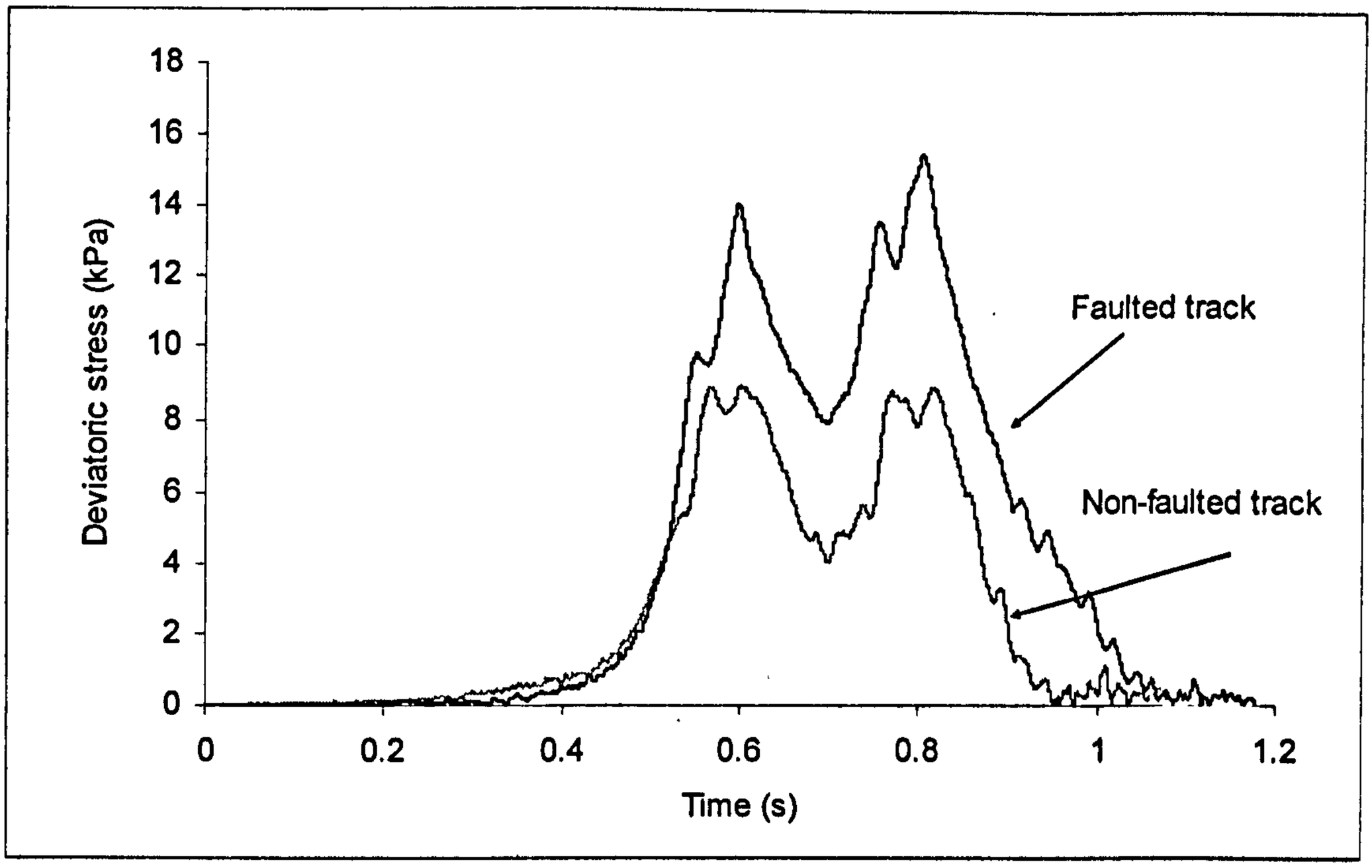

Figure 6.27. Deviatoric stress in the subgrade (depth=1.8 m) near the faulted zone (Point A) against deviatoric stress in the same position in non-faulted transition at V=50 m/s

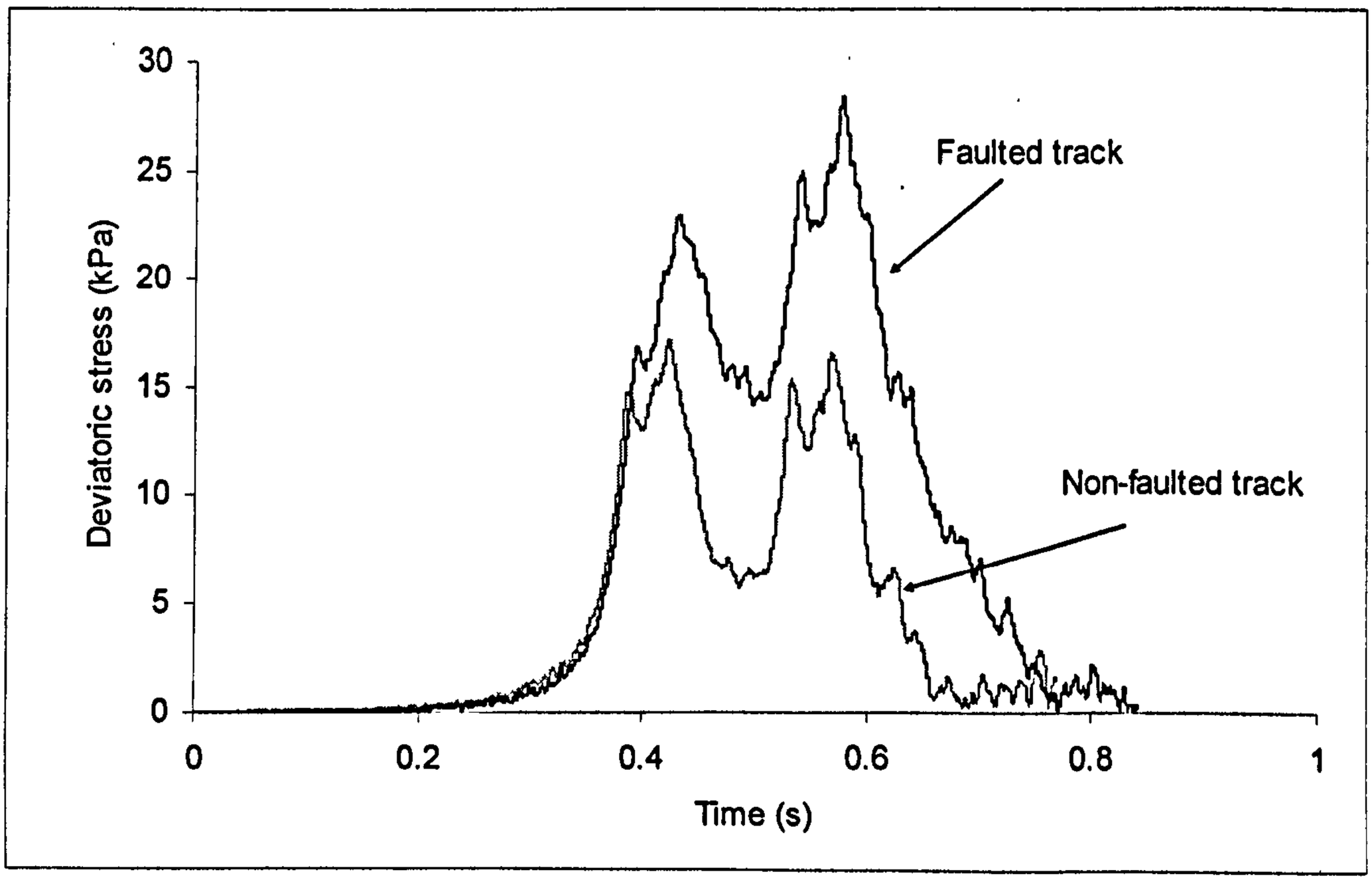

Figure 6.28. Deviatoric stress in the subgrade (depth=1.8 m) near the faulted zone against deviatoric stress (Point A) in the same position in non-faulted transition at V=70 m/s

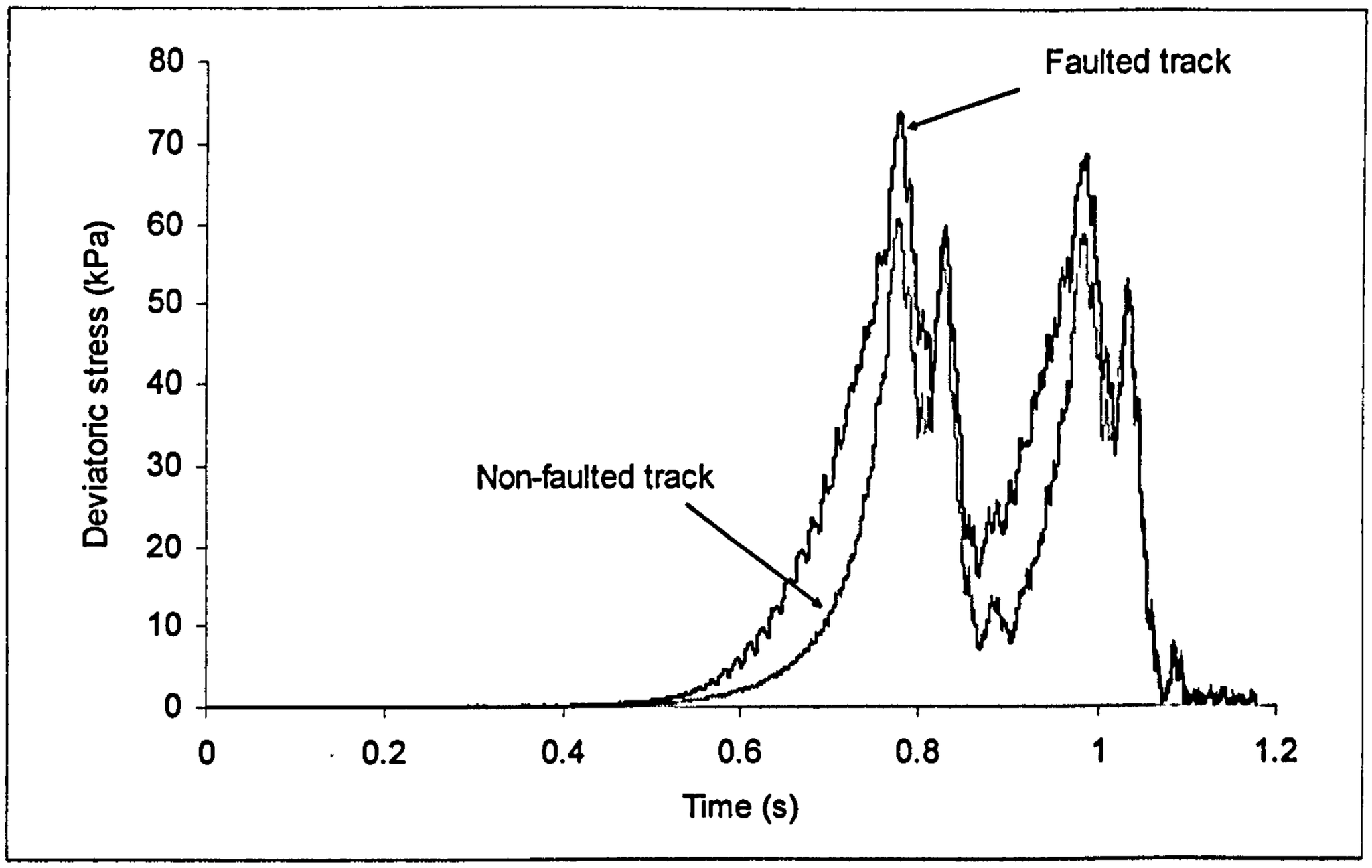

Figure 6.29. Deviatoric stress on top of ballast layer near the faulted zone (Point B) against deviatoric stress in the same position in non-faulted transition at V=50 m/s

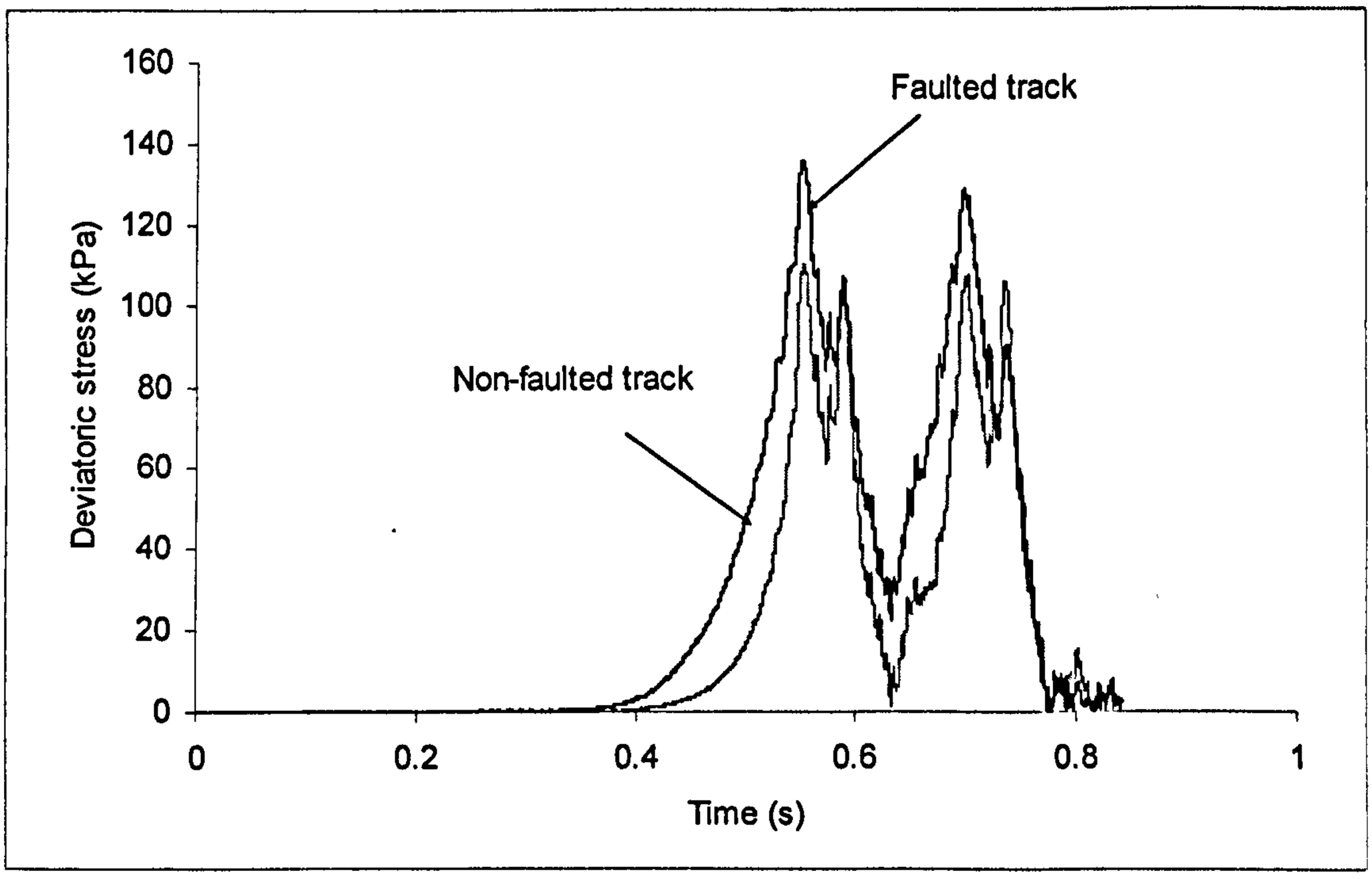

Figure 6.30. Deviatoric stress on top of ballast layer near the faulted zone against deviatoric stress (Point B) in the same position in non-faulted transition at V=70 m/s

6.3.2 Train-Irregularity Model

As discussed in previous sections, finite element simulations suggest that the dynamic excitation of a train in the transition zone (non-faulted) is mainly the result of the displacement difference on the soft and rigid sides. In addition, it was seen that the train would be excited through a similar mechanism in the presence of (relatively long) faults which introduce uneven displacement patterns. On these bases, if the displacement pattern in the transition zone is assumed to be known, it should be possible to estimate the interaction force and train body acceleration by simulating the train running over an irregularity representing the deflection pattern in the transition (termed here 'transition curve'). To validate the application of such a model, namely the "train-irregularity model" for the transition studies, the track-train interaction mechanism is further investigated in this section.

The effective masses of the track substructure, the superstructure and train wheels play very important roles in train-track interaction, as shown schematically in Figure (6.31a). The way in which these masses react to the dynamic excitation dictates the train-track interaction mechanism. To illustrate their effect, the classical problem of a dipped joint is investigated.

As discussed in Chapter 2, the interaction force when the train passes a dipped joint and can be represented by two classes of forces, namely P_1 and P_2 forces (see Figure 2.3), according to Jenkins *et al.* (1974). The first pick, called P_1, is of high frequency nature and therefore is just responded to by the superstructure, including rail, pad and sleepers. Since the effective mass of the wheel is usually higher than that of the superstructure, such an instantaneous force originates mainly from the reaction of the superstructure, and hence the wheel mass can be assumed to be fixed, as described by Figure (6.31b). This assumption was also utilized by Steenbergen and Esveld (2006) to relate the geometrical properties of rail welds to the corresponding maximum dynamic load exerted on the track.

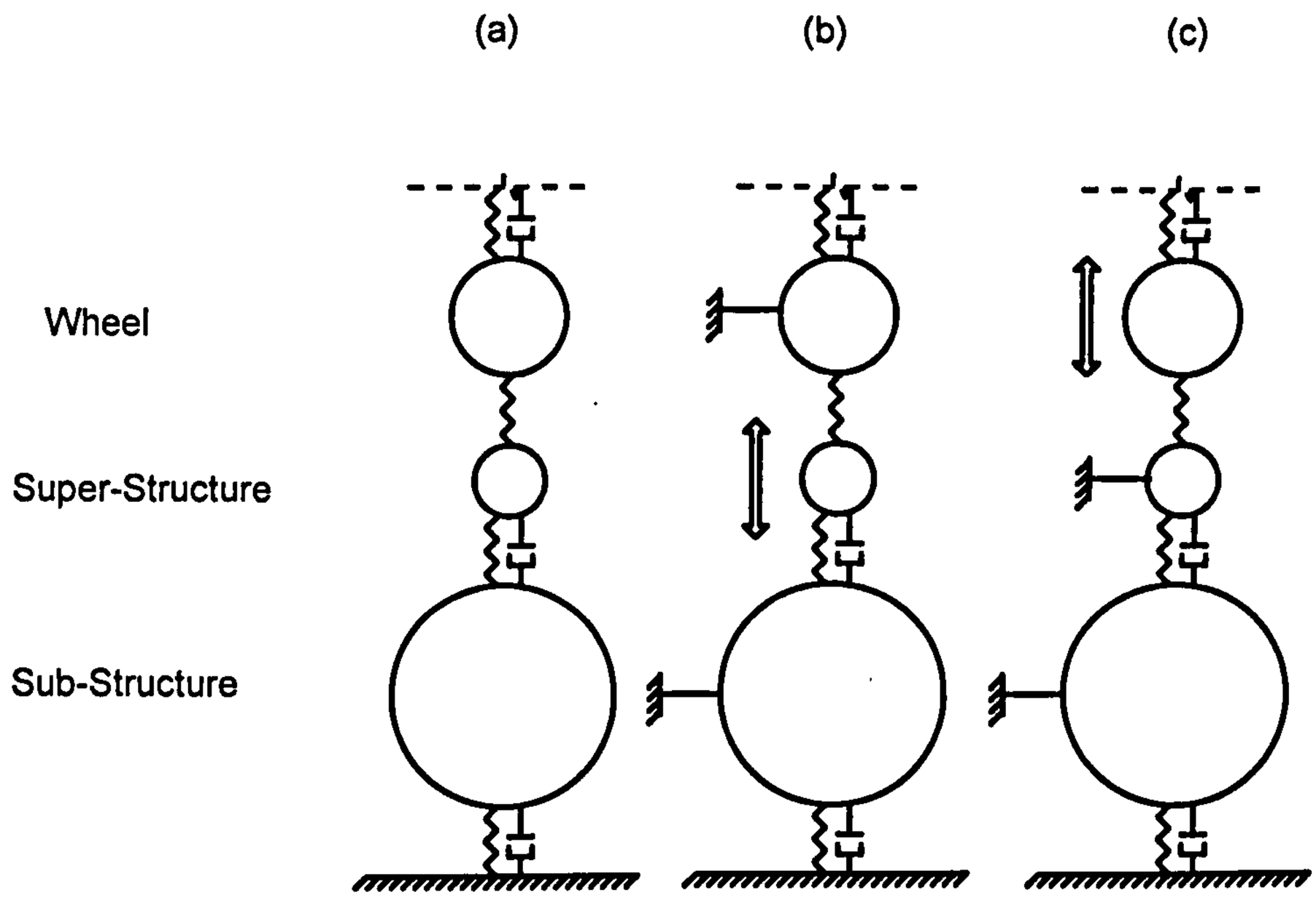

Figure 6.31. (a) Train and track mass contribution in train-track interaction (b) P_1 interaction mechanism (c) P_2 interaction mechanism

Unlike the P_1 force, the P_2 force is of lower frequency nature and results from wheel mass reaction to the excitation. The P_2 force is transmitted to substructure, and consequently the effective mass of substructure and superstructure acts together against the P_2 force. As the effective mass of the substructure and superstructure is considerably higher than that of the wheel, the track mass (total mass of the track including the super and substructure) can be assumed to be fixed when representing the interaction mechanism for the P_2 force (Figure 6.31c).

The dynamic excitation in the transition zone is essentially similar to the P_2 excitation, i.e. it is caused by the excitation of the train mass (mainly those of the wheels) as a result of irregularities e.g. the difference in the deflection in the softer and harder sides of a transition. To simplify the interaction issue, a typical transition problem can therefore be represented as a train passing an irregularity representing a transition curve (train-irregularity model). The train is represented as before and the transition curve is presented

by a mathematical relationship. The Hertizian contact theory is implemented and the interaction problem is solved by an explicit time integration (Zhai, 1996).

It should be noted that the train-irregularity model is a simplification of the problem, and does not replace the three-dimensional train-track model for all cases, especially when the interaction of the train and the mass and stiffness of the track component play an important role in the interaction mechanism. An example of this can be a voided sleeper where the mass of sleeper and rail act against the dynamic train/track interaction initially, followed by the reaction of the train to the geometrical/stiffness irregularity, caused by the voided sleeper. The stiffness and mass of the track components, especially in the voided area, should therefore be taken into account thorough the coupled train-track finite element model, with fine meshing around the voided sleeper. In this case, as the length of the voided area is short, one point contact theory may not be representative of the rail-wheel contact and more complicated theories, such as two point rail/wheel contacts, may be needed, as discussed in Section 6.2.3. Contact elements may also need to be utilized to represent contact and separation of the sleeper and ballast surface. In spite of that, given that the short length geometrical/stiffness faults are not present in the transition zone, the simple irregularity-train models can simulate the train responses in terms of the interaction force and train body acceleration, which are considered to be main factors in designing transition zones. This simple model is computationally very fast and is therefore used in the next sections to conduct extensive parametric studies on the length which is needed to accommodate the difference in deflections between the soft and rigid sides of a transition, termed here as "deflection spanning length", for different train speeds and deflection levels.

6.3.2.1 Parametric Study of Stiffness Transition

The deflection levels between the displaced/settled plain line track and the rigid base, the length in which this difference is traversed (deflection spanning length) and the train speed are the factors which are studied here, using a train-irregularity model. The transition curve from the soft to the stiff base is produced using the following equations (Schooleman, 1996), as shown in Figure (6.32):

$$\begin{cases} z(y) = R_{vert}\left\{1-\sin(\arccos(\dfrac{y}{R_{vert}}))\right\} & y \le L/2 \\ z(y) = \dfrac{L^2}{4R_{vert}} - R_{vert}\left\{1-\sin(\arccos(\dfrac{L-y}{R_{vert}}))\right\} & y > L/2 \end{cases} \tag{6.39}$$

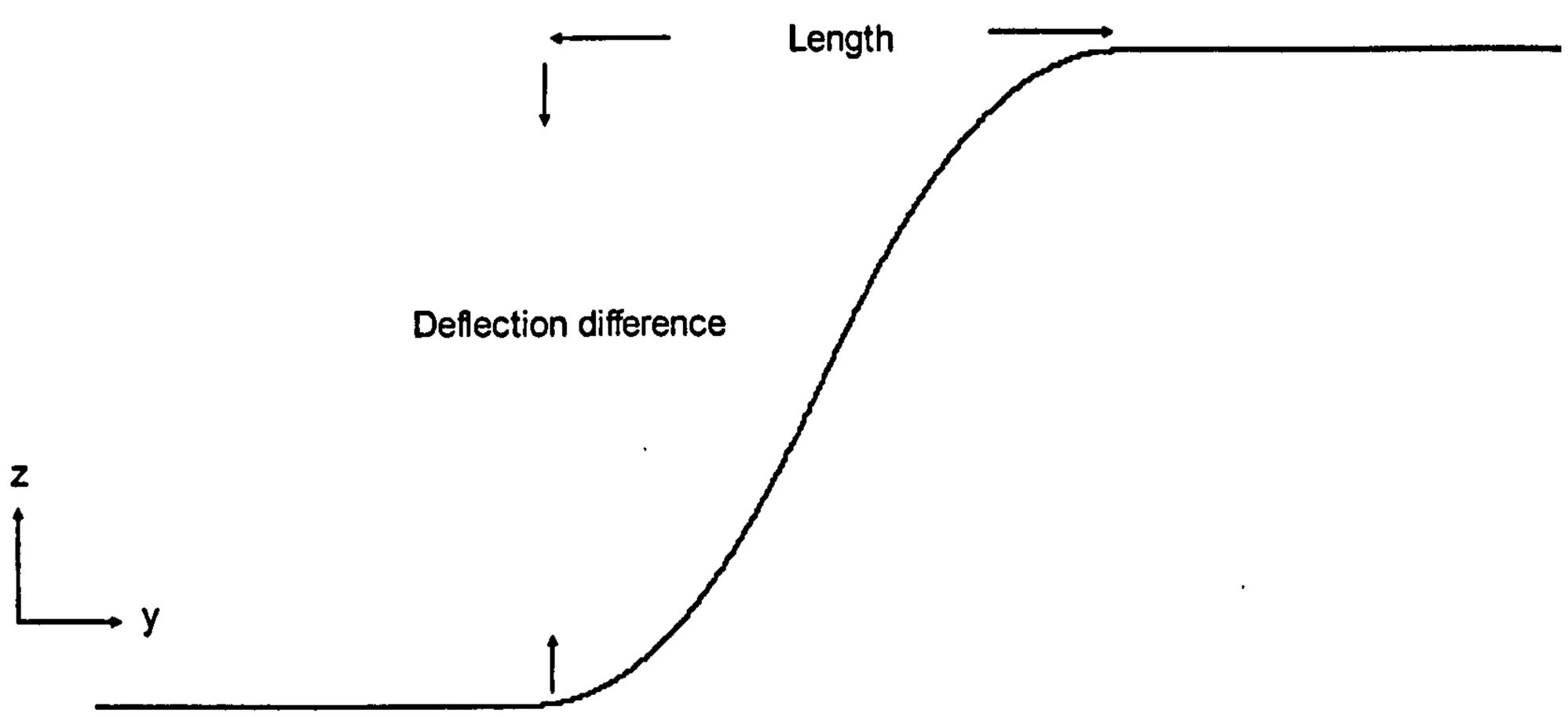

Figure 6.32. Stiffness transition representation as an irregularity

where y is the distance along track in the transition zone, L is deflection spanning length and R_{vert} is vertical radius calculated from the following relationship:

$$R_{vert} = \frac{L^2}{4\Delta h} \tag{6.40}$$

where Δh is deflection difference between the track on the soft and stiff sides. Both pseudo full and half train models are considered, specifications of which are given in Table 6.1.

Figures (6.33 and 6.34) compare the interaction forces and the train body accelerations induced when a pseudo full train or quarter train passes a typical transition. While the interaction force is almost the same, the vertical train body acceleration generated in the full train model is considerably lower than the acceleration generated in a quarter train model. Such differences in responses can be explained through the mechanism governing these two different variables. The interaction force is, to a large extent, governed by the unsprung mass of the wheel. On this basis, the interaction force response of a quarter and pseudo full train models was expected to be similar. Regarding the vertical acceleration of the train body, the suspension system (dampers and springs in the train models), and masses of the car body and pitching of the train are the major players, which are differently represented in the pseudo full and quarter train models. In the pseudo full train model, all dampers connected to the coach and bogies participate, to a different degree, to dissipate the wheel excitation. Accordingly, the level of damping associated with the coach is considerably higher in the pseudo full train model than the quarter train model, which clearly explains why the body acceleration of the pseudo full train model is substantially lower than that of the quarter train model. Comparing the interaction force for the second (fourth) and first (third) wheel (Figure 6.33), it is clearly seen that when the first (third) wheel starts to climb the transition, the interaction force in the second (fourth) wheel will be also affected through pitching and displacement of the bogie (it is circled in Figure 6.33b). Although this effect is fairly small, after thousands of train passages, it can gradually induce permanent deformation and geometrical irregularities in the area near the transition zone. As described earlier, such an irregularity increases the train-track dynamic load which eventually worsens the geometry of the track and extends the problem to a larger area. In addition, when the whole train passes the transition zone, the interaction force is still bouncing until the excitation is completely damped.

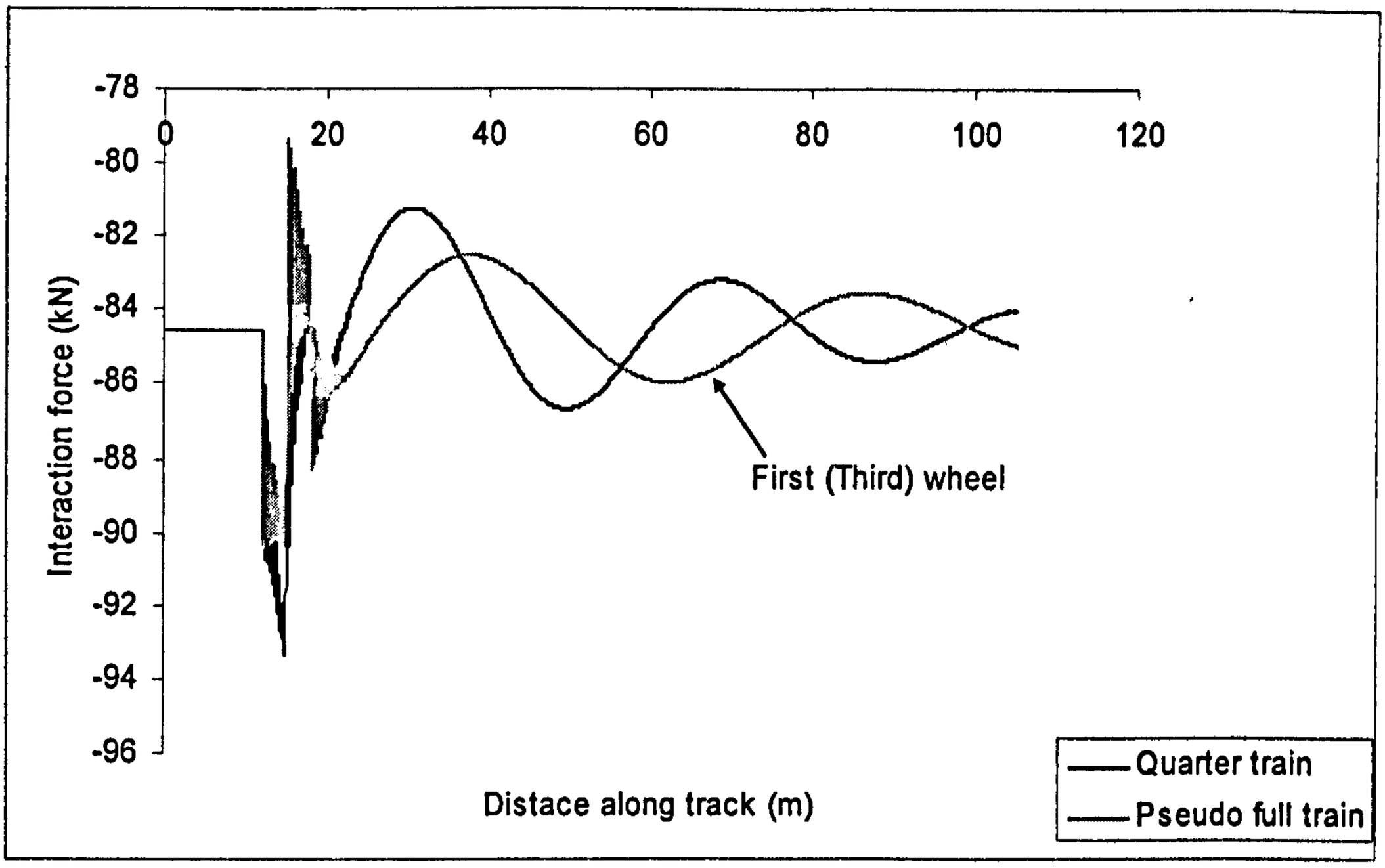

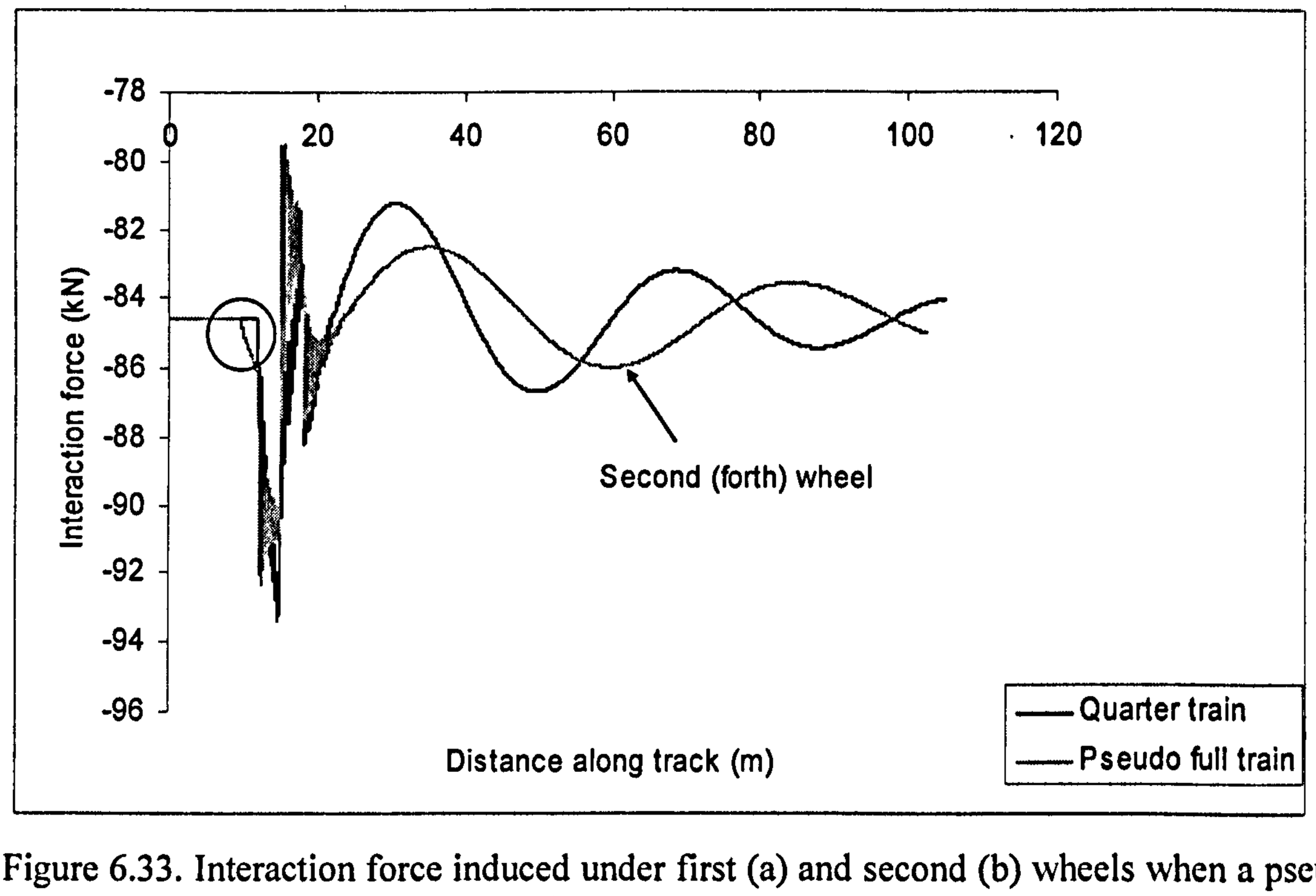

Figure 6.33. Interaction force induced under first (a) and second (b) wheels when a pseudo full/quarter train passes a typical transition (L=6 m, Δh=5 mm, V=70 m/s)

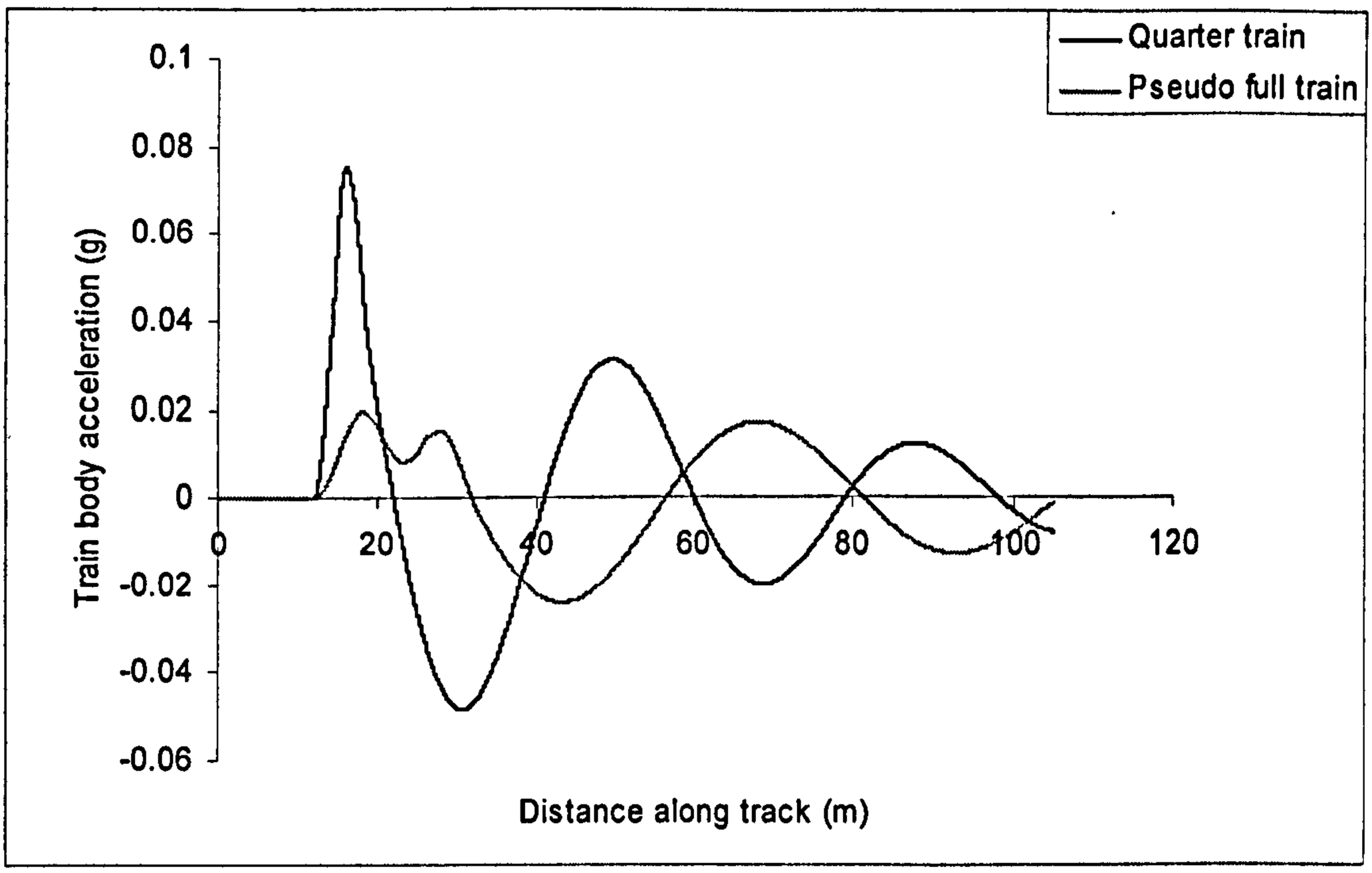

Figure 6.34. Train body vertical acceleration induced when a pseudo full or quarter train passes a typical transition (L=6 m, Δh=5 mm, V=70 m/s)

Such a bouncing dynamic load may also affect the geometry of the track in the long term. The length of track affected after the transition zone is determined based on the natural frequencies of the train bogie and car body, and can be relatively long, as shown in Figure (6.33). In an appropriate transition design, proper care should therefore be taken to minimize the generation of permanent deformation in the ballasted area near the transition zone.

The dynamic amplification factor and train body acceleration resulting from a quarter train and pseudo full train model passing the transition is presented in Figures (6.35) and (6.36). Comparing Figures (6.35) and (6.36), it is confirmed that the quarter and pseudo full train models predict similar dynamic interaction forces for transition problems at the train speeds considered. It can be clearly observed that an increase in the deflection spanning length results in a decrease in the transition dynamic amplification factor for a given deflection difference and train speed. As expected, with the increase in train speed and deflection difference, the dynamic amplification factor increases considerably for a given

spanning length. It is also observed that the rate of decrease in the interaction forces is highest when the deflection spanning length increases from 2m to 4m, compared with the interaction force change caused by further increases in the spanning length. Hence, for the cases considered, the transition length of 4m can be theoretically considered as the minimum required deflection spanning length according to the present parametric study.

As before, the maximum permissible dynamic wheel load is assigned to be 170 kN or a dynamic amplification of 2 (see Section 6.3.1.2). Provided there is no other irregularity, this permissible dynamic load level is associated with two excitation sources, namely discrete sleeper support and the deflection difference induced in the transition zone. It does not therefore define the limit for load excitation that is solely related to the presence of transition, as simulated by the train-irregularity model. To find a maximum permissible dynamic amplification factor exclusively related to the presence of a stiffness transition, it is assumed that the maximum permissible dynamic amplification factor can be decoupled in the following way:

$$DAF_{max}=DAF \text{ (caused by sleeper discrete support)} * DAF_{max}\text{(caused by transition)} \quad (6.41)$$

Accordingly, if a conservative constant value of 1.3 is assumed for the dynamic amplification factor related to the sleeper discrete support (see Figure 6.11), then the permissible DAF, exclusively related to a stiffness transition is calculated to be 1.55, as depicted in Figures (6.35 and 6.36).

For a given deflection difference, it is observed that longer spanning lengths are needed as the train speed increases. Studies in Chapter 4 revealed that as long as the train speed is lower than the track speed limit (70% of track critical velocity), the track resilient displacement would not be higher than 10 mm for conventional tracks. For deflection differences of less than 10 mm, it is seen that the spanning length of 4 m is enough to keep the interaction force lower than the permissible level for all speed levels. For conventional track stiffness transitions, with deflection differences of a few millimetres, provided there is no track fault in this zone, e.g. voided sleepers or wet spots, only small amplifications of the rail-wheel interaction force may occur for low to medium train speeds, as shown in Figures (6.35 and 6.36). However a significant rise in the train speed can significantly

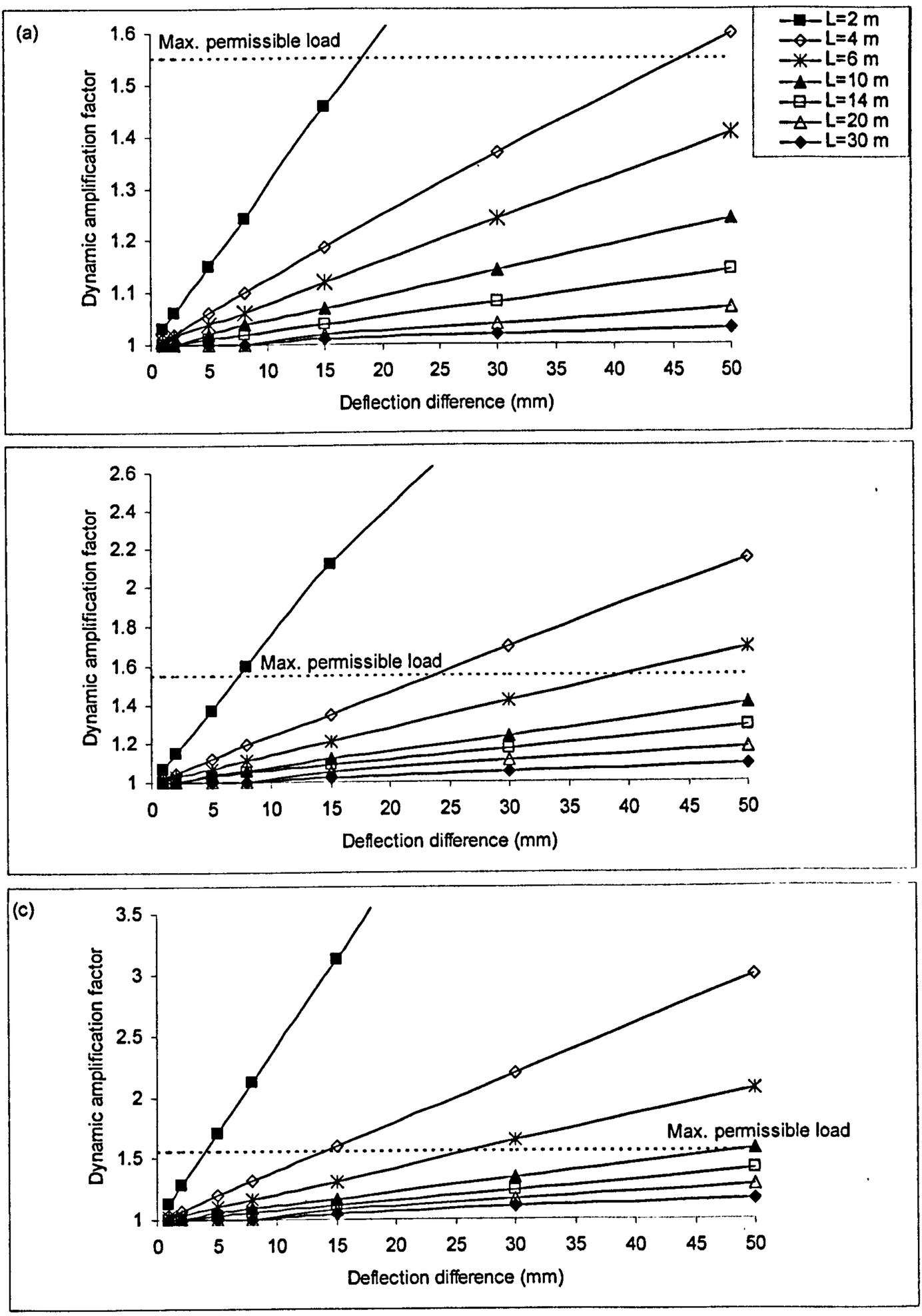

Figure 6.35. Effect of transition length and train speed on rail-wheel interaction force using the quarter train model, a) V=30 m/s, b) V=50 m/s, c) V=70 m/s

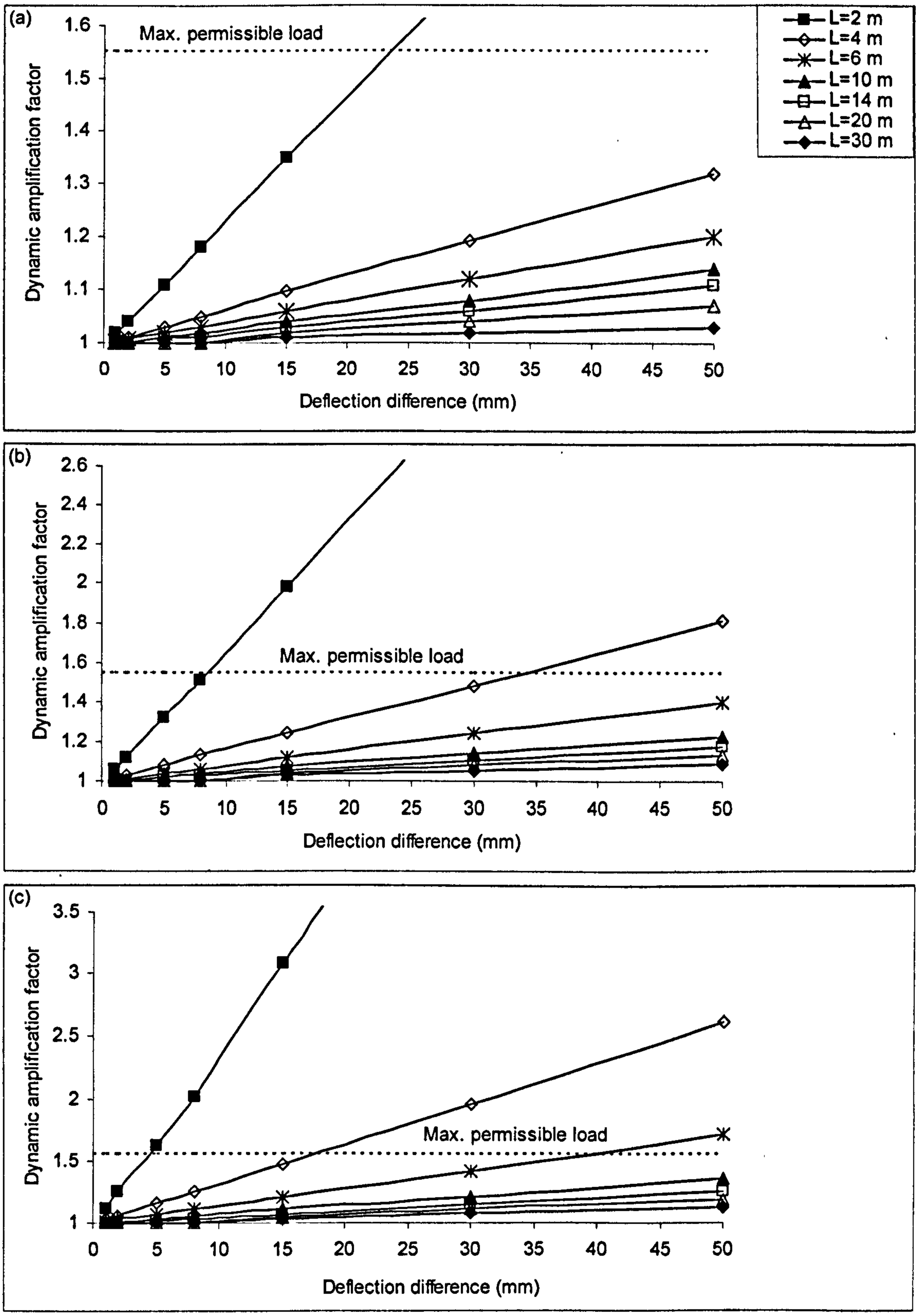

Figure 6.36. Effect of transition length and train speed on rail-wheel interaction forces using the full train model, a) V=30 m/s, b) V=50 m/s, c) V=70 m/s

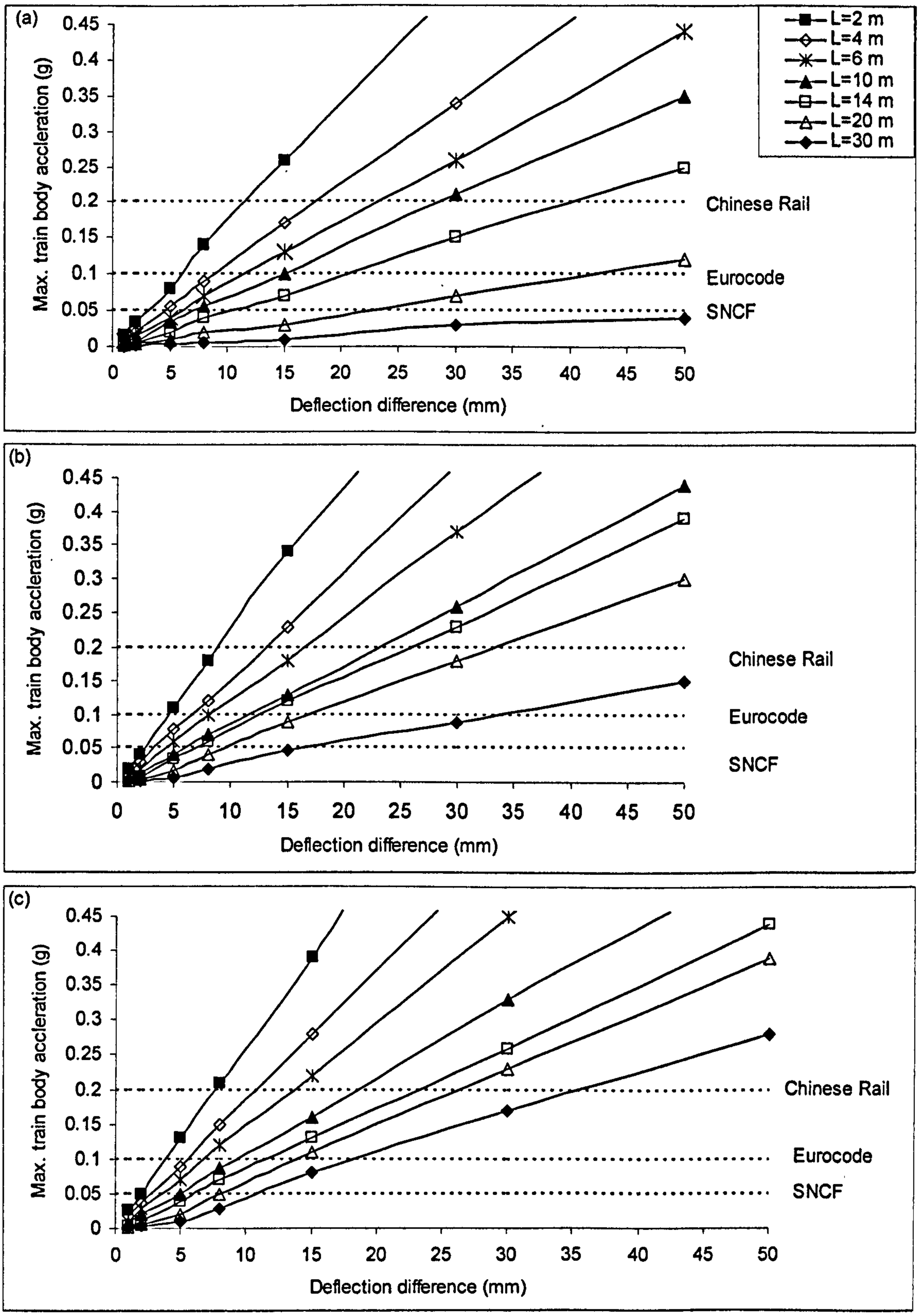

Figure 6.37. Effect of transition length and train speed on train body acceleration using the quarter train model, a) V=30 m/s, b) V=50 m/s, c) V=70 m/s

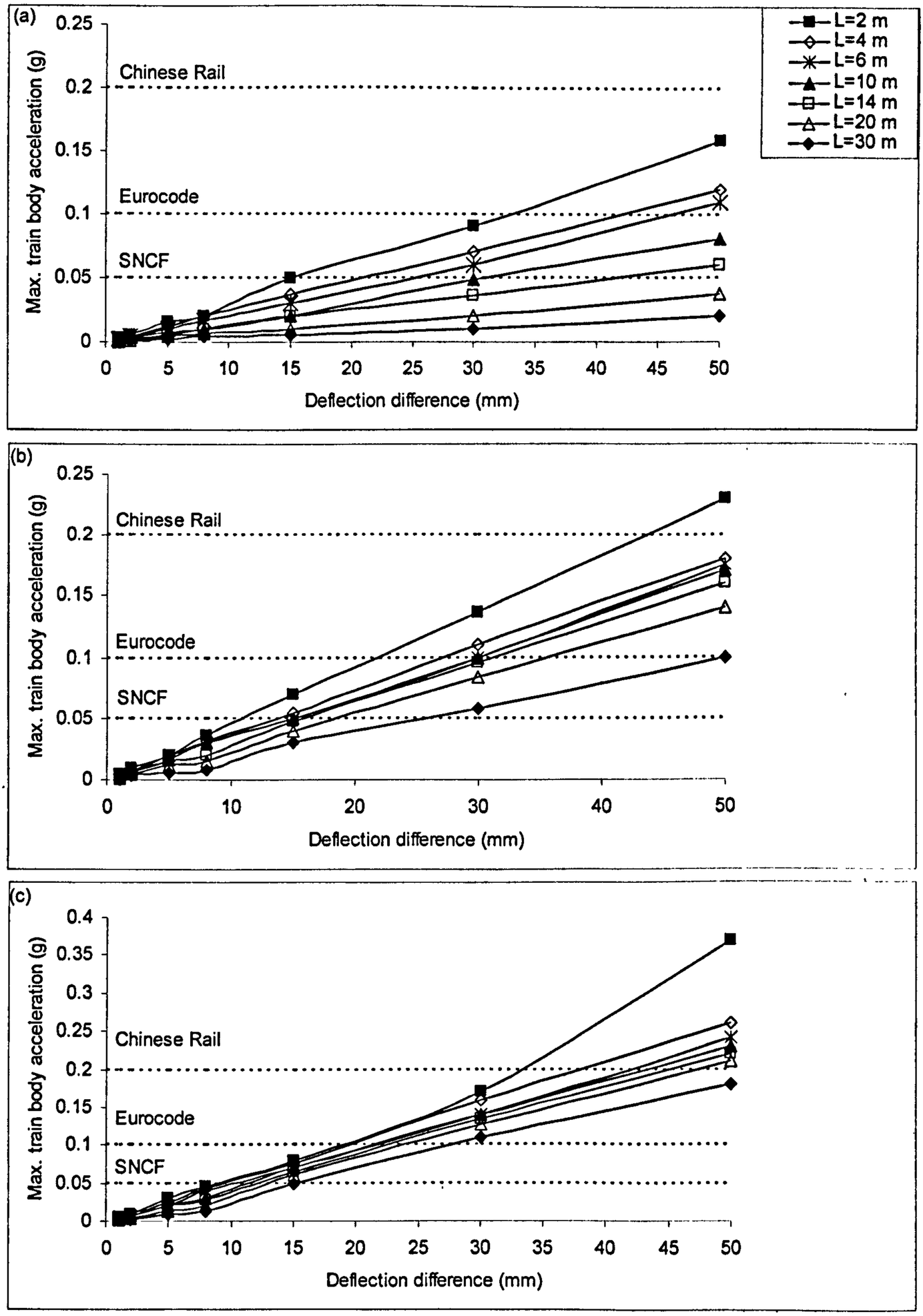

Figure 6.38. Effect of transition length and train speed on train body acceleration using the quarter train model, a) V=30 m/s, b) V=50 m/s, c) V=70 m/s

increase the dynamic amplification factor if no transition, or only a very short transition, is provided. For example, for a 5mm elevation difference and if a 2m spanning length is assumed, the DAF increases from approximately 1.12 at V=30 m/s to approximately 1.7 at V =70 m/s. The effect of speed is, however, minimized when the transition is longer than 4m (Figure 6.36).

It is, however, important to note that the deflection difference can come from both the instantaneous resilient displacement of the track and long-term settlement of the track owing to plasticity generated within the ballast, sub-ballast and subgrade (e.g. embankment consolidation and ballast settlement). According to Figure (6.36), as plastic settlement is developed in the plain track and hence deflection difference increases into the range of centimetres, the dynamic load would increase considerably, especially if the spanning length is not long enough. In other words, a high level of deflection difference on a short spanning length (which can also represent voids or faults in a transition) would considerably increase the dynamic force on the track, which in itself is a source of even more track deterioration and induced plasticity in the track substructure. In the cases of a high level of settlement in the track, a 10 metres length of transition, for a high speed of V=70 m/s, is needed to span such a deflection difference, according to Figure (6.36). A further increase of spanning length, however, is seen to have minimal effects on the dynamic load level.

Figures (6.37) and (6.38) depict the maximum train body acceleration for different train speeds, deflection differences and spanning length. The maximum train body acceleration obtained from the quarter train model is considerably higher than that of the pseudo full train model which is attributed to different damping representation in the models, as discussed previously. Accordingly, if passenger comfort is concerned, the pseudo full train model should be employed in studying the passenger comfort as the quarter train model tends to overestimate the train body acceleration, especially for cases with significant deflection difference and high train speed. According to Figure (6.38), an increase in train body acceleration is observed as the train speed increases and spanning length decreases for a given deflection difference. The prominent effect of the deflection difference is also observed on passenger comfort; as the deflection increases, there is a significant increase in train body acceleration and consequently deterioration in passenger comfort is experienced.

The accumulation of permanent deformation in the transition zone, which is the cause of high deflection differences, should be prevented (or limited) in a high speed track in order to ensure a comfortable ride. According to Figure (6.38), 4 m of spanning length, as suggested based on the dynamic amplification factor for resilient deflection differences (less than 10 mm), is sufficient to provide a comfortable ride even if the most restrictive criterion is considered (0.05g). For higher deflection differences (coming from plastic settlement in the substructure), the spanning length should be much longer to satisfy even the least restrictive criterion (0.2g). It also seems that passenger comfort criteria are more difficult to fulfil than the interaction load criteria, especially for high speed cases. For example, considering the pseudo full train model, in the case of 50 mm elevation difference, a transition length of 10 m easily satisfies the load criteria (Figure 6.36), at a train speed of 70 m/s. A minimum 30 metres of transition is however needed to fulfil the least restrictive criterion of the maximum train body acceleration (Figure 6.38). These findings imply that it is partially down to high speed train design to provide an enhanced suspension system to improve passenger comfort at high speed operations. As is the case in practice, high speed trains are specifically designed to give a high quality ride under their operational conditions (they tend to have stiff bogies and good suspension characteristics).

6.3.2.3 Deformation-Geometry Based Assessment of Stiffness Transition

As shown in the previous section, the deformation/geometry pattern representing the railway stiffness transition, i.e. the transition curve, has a direct relationship with the magnitude of the dynamic train-track interaction force. Conventionally, dynamic force is related to elevation difference/transition length, as given in the previous section. A similar relationship can be given simply based on the ratio of elevation difference to transition length, which effectively represents the first spatial derivative of the transition curve (e.g. see Lei and Mao, 2004). Steenbergen and Esveld (2006) studied the rail weld irregularity problem and developed an assessment concept based on the geometrical properties of the rail weld. They indicated that a P_1-like dynamic force generated on a rail weld can be correlated to the effective mass of the track and second spatial derivative of the geometry.

Such a concept can also be extended to a P_2-like dynamic force generated in the transition zone. A wheel passing the transition curve is depicted in Figure (6.39). Considering that the magnitudes of a P_2-like interaction force (F_{wr}) are governed mainly by the unsprung mass of the wheel (m_w) according to the equation of motion in the vertical direction:

$$F_{wr} \approx F_{Stat} + m_w \ddot{z}_w \tag{6.42}$$

where $\ddot{z}_w$ is the vertical wheel acceleration. In a quasi static case, it is assumed that the wheel follows the transition curve ($z_w = z_r$) as shown in Figure (6.39). Using the chain rule $\ddot{z}_w$ can then be written as below:

$$\ddot{z}_w = \frac{d}{dt}\left(\frac{dz_r}{dx}\dot{x}\right) \qquad (\dot{x} = V) \tag{6.43}$$

or

$$\ddot{z}_w = V^2\left(\frac{d^2 z_r}{dx^2}\right) \tag{6.44}$$

where V is the wheel speed. Using Equation (6.44), Equation (6.41) can be re-written as follows:

$$F_{wr} \approx F_{Stat} + M_w V^2\left(\frac{d^2 z_r}{dx^2}\right) \tag{6.45}$$

Although the quasi-static assumption does not hold for all cases, such a relationship suggests a possible logical link between the dynamic interaction force, train speed and second spatial derivative of the transition curve.

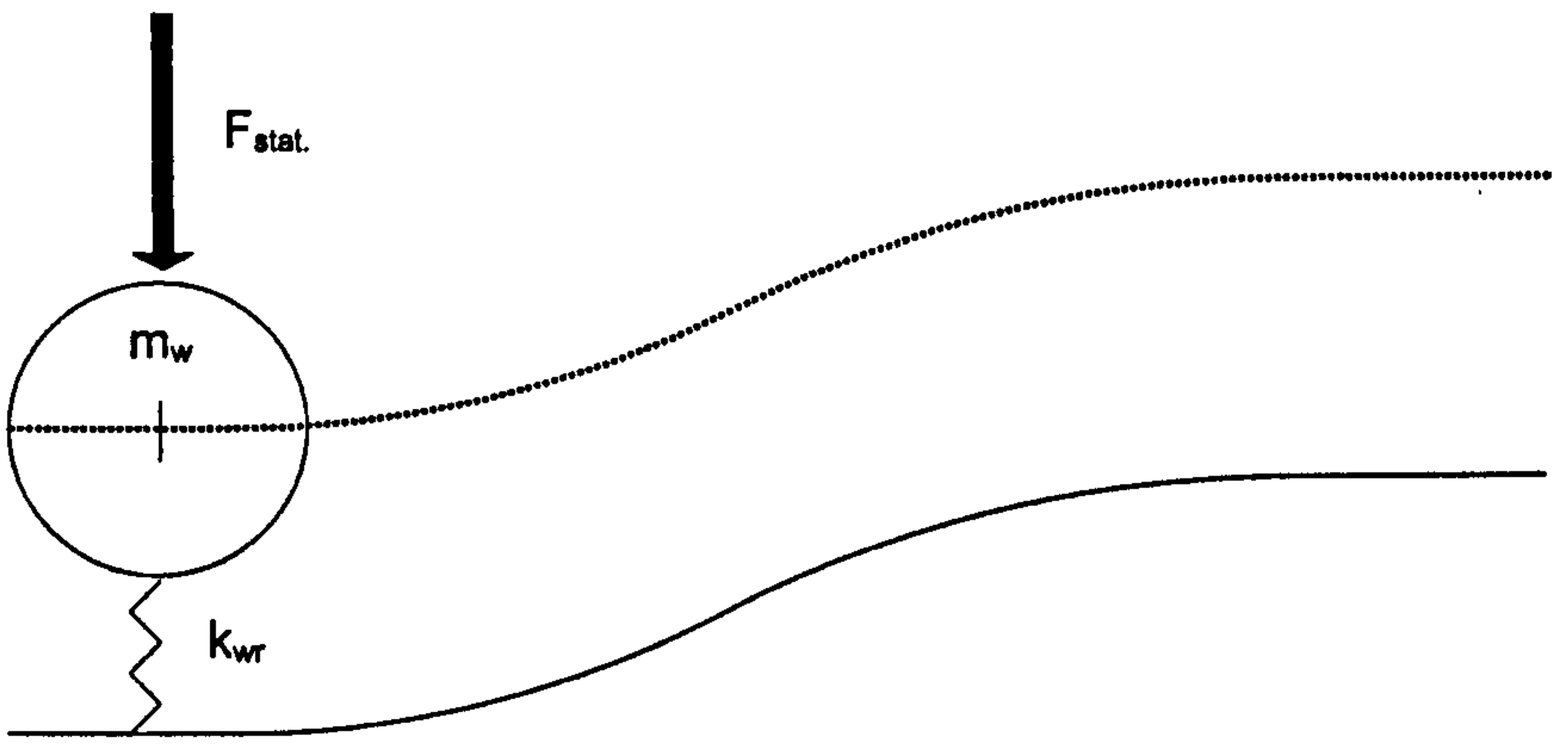

Figure 6.39. A wheel model following a transition curve quasi-statically

When running a train model over a simple representation of a transition curve (using the train irregularity model), such a link can be observed (Figure 6.40). It is seen that the train is dynamically excited when the gradient of transition curve is changed. In Figure 6.40, a one-to-one relationship is observed between the location where the maximum change in gradient occures and the maximum dynamic load. However, such a relationship is not observed between the gradient of the curve and maximum interaction force. It suggests that the second spatial derivative of the transition curve could be a better indication for the assessment of transitions, compared with traditional approaches.

For all cases considered in the parameteric study, when using a geometrical irregularity-train model (Section 6.3.2.3), the maximum first and second spatial derivatives are calculated analytically from Equation 6.39 and depicted against the maximum transition dynamic amplification factor for different train speeds, as given in Figures (6.41) and (6.42). The relationship between the maximum dynamic force and the maximum first derivative and second derivative appears to be represented by linear relationships. As expected, increases in the maximum first and second derivative of the transition curve generally result in a higher interaction force, according to Figures (6.41) and (6.42). At train speed of 30 m/s, according to the correlation coefficients given, a slightly better correlation is observed between the maximum first spatial derivative and the maximum dynamic force (Figure 6.41a), compared with the correlation between the second spatial derivative and the dynamic force (Figure 6.42a). For higher speeds, the correlation between

the first derivative and the dynamic force deteriorates (6.41b and 6.41c), while the second derivative satisfactory correlates to the maximum dynamic force (6.42b and 6.42c). It is also observed that with the increase in the train speed, the gradients of lines representing the relationships between the first and second gradients of transition curve and interaction force also increase (Figures 6.41 and 6.42), confirming the profound effect of train speed on the dynamic force applied in the transition zone. Considering the design criteria for the maximum admissible force, the maximum magnitude of the first and second derivatives for a given train speed can be defined as shown in Figures 6.41 and 6.42. For a given transition zone, based on the proposed relationships, the maximum dynamic load can be defined which can be used in a static/cyclic model to predict the short-term and long-term performance of a railway track.

it should be noted that, in order to obtain the spatial first/second derivative of geometry in practice (e.g. from TRV recordings), a numerical approach should be taken. The derivatives need to be calculated at sampling points. The sampling points should be chosen in such a way as to filter out the short wave frequencies and hence represent the transition curve. At sampling point n, the derivative can be calculated as follows:

$$\frac{dz_n}{dx} = \left(\frac{z_{n+1} - z_{n-1}}{2d}\right) \tag{6.46}$$

$$\frac{d^2 z_n}{dx^2} = \left(\frac{z_{n+2} - 2z_n + z_{n-2}}{4d^2}\right) \tag{6.47}$$

z_n is the elevation at point n (from TRV recordings), d is the distance between the two sampling points.

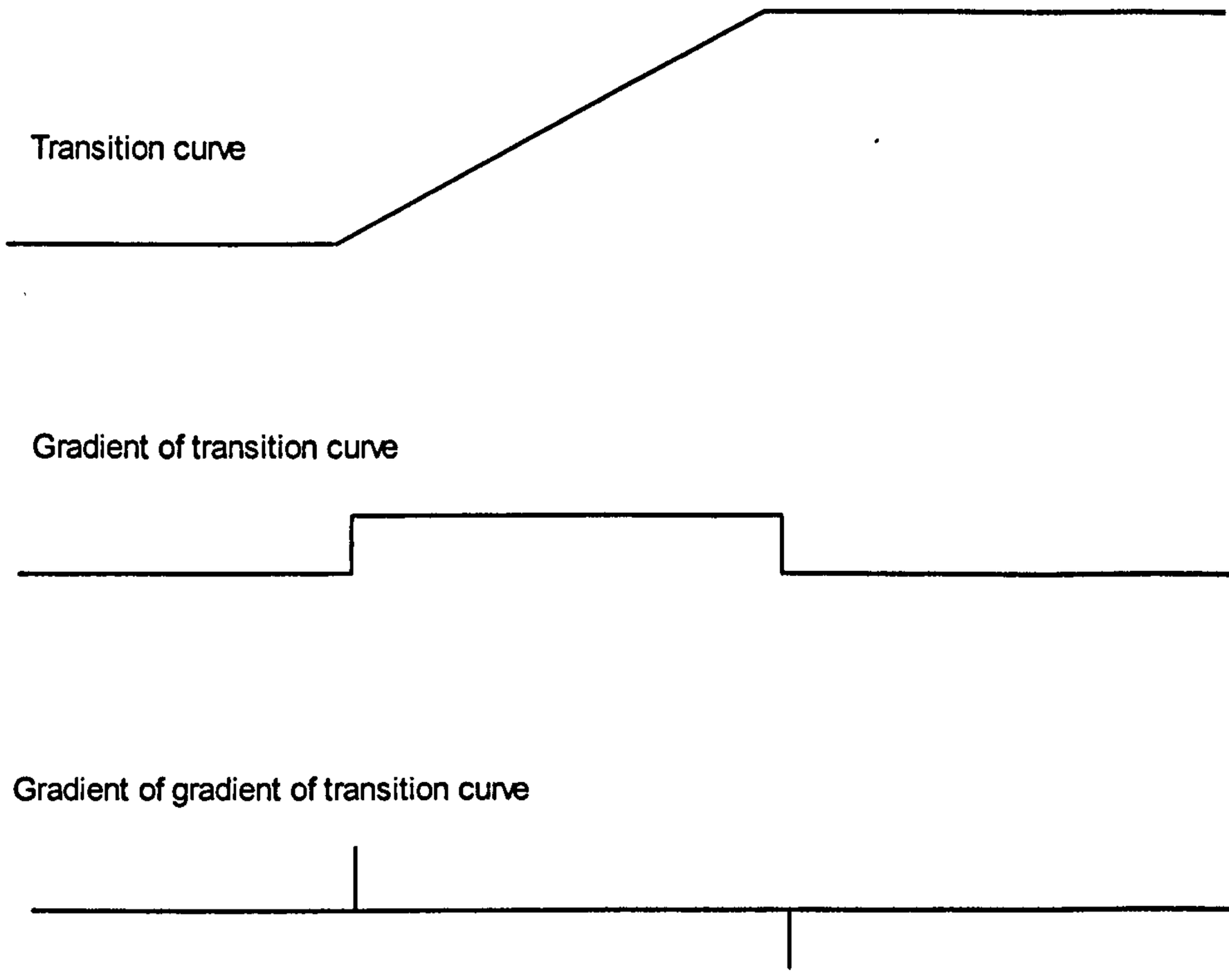

Figure 6.40. Relationship between geometrical parameters and interaction force in a typical transition

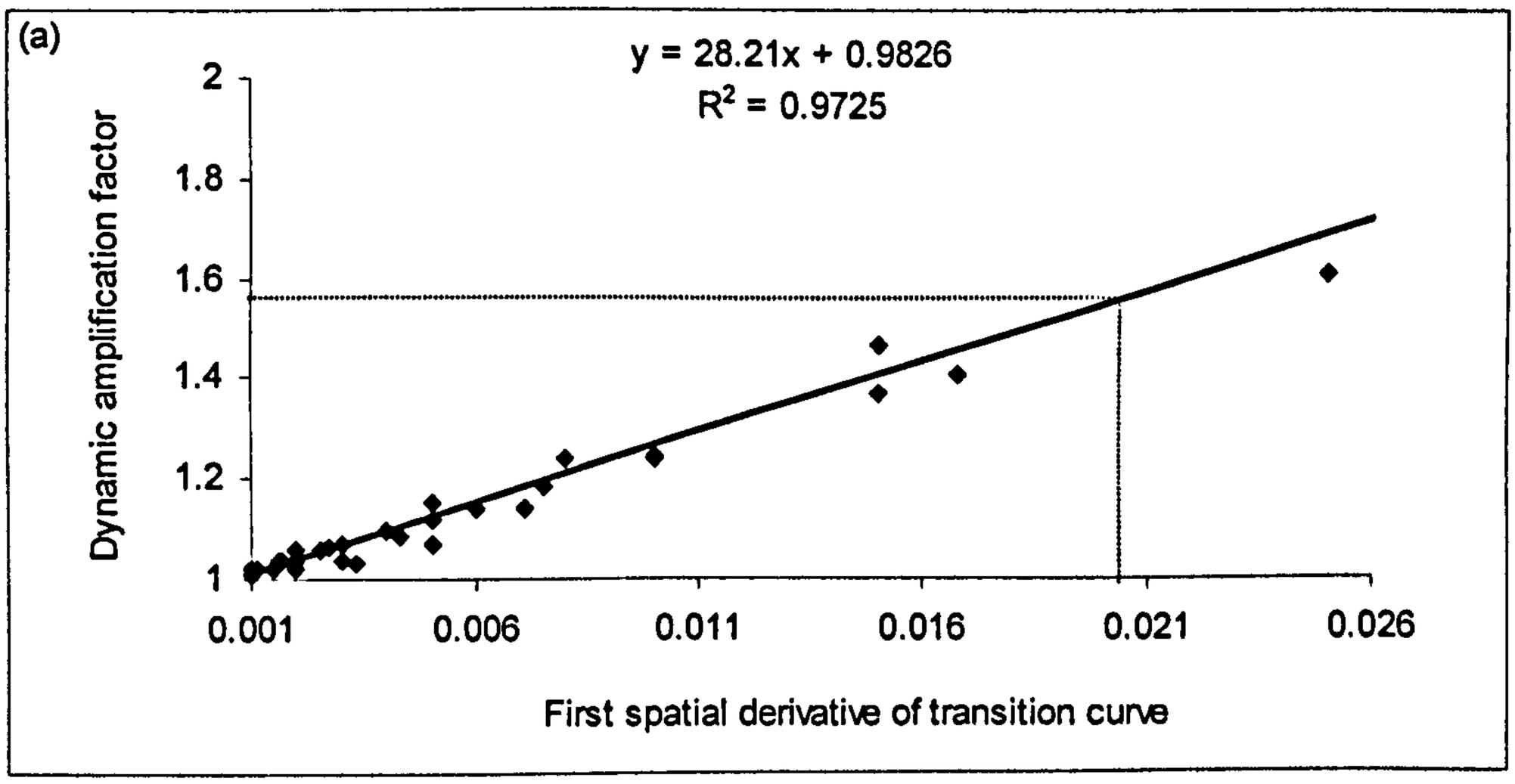

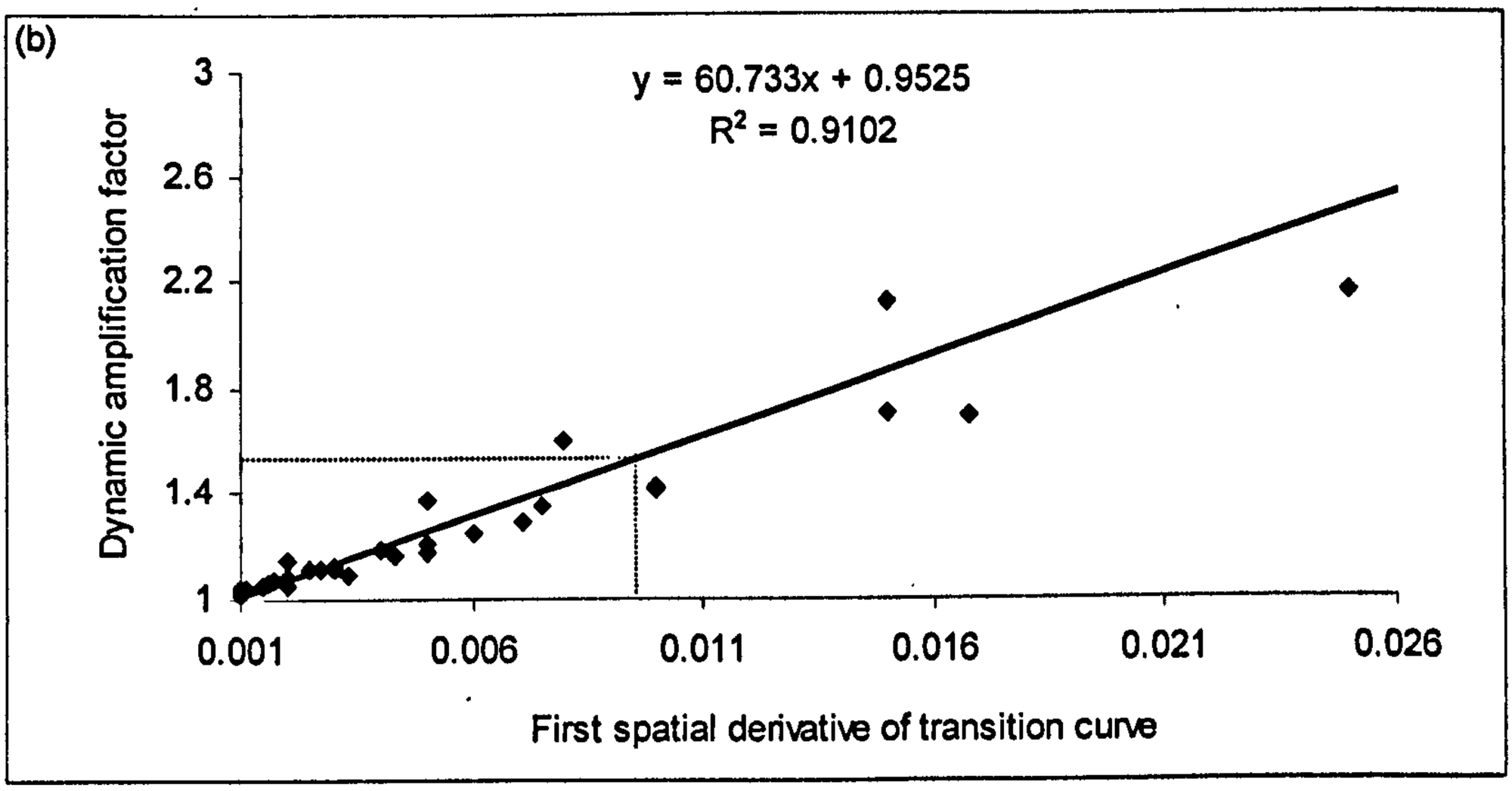

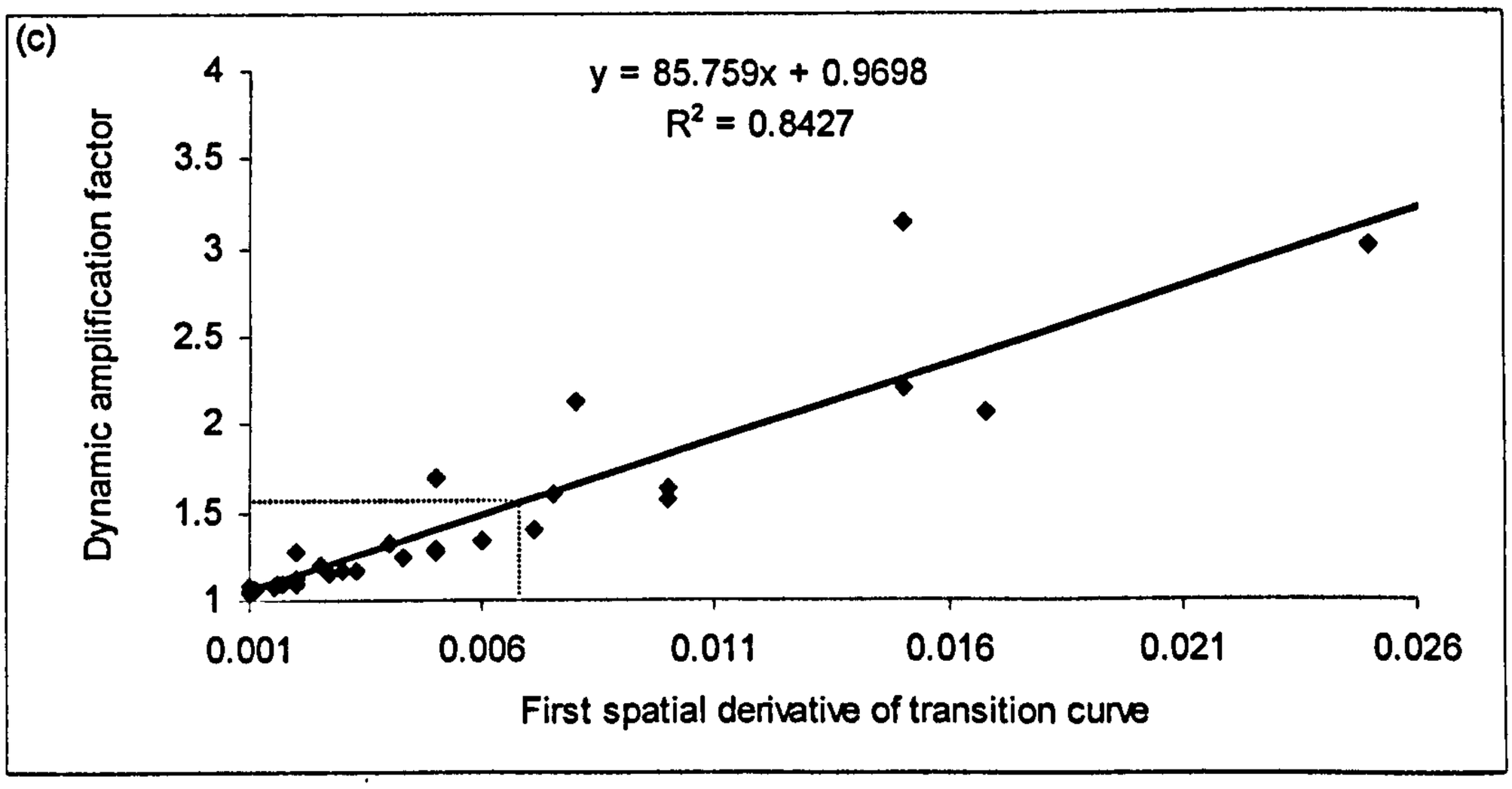

Figure 6.41. Relationship between dynamic amplification of interaction force and first derivative of transition curve

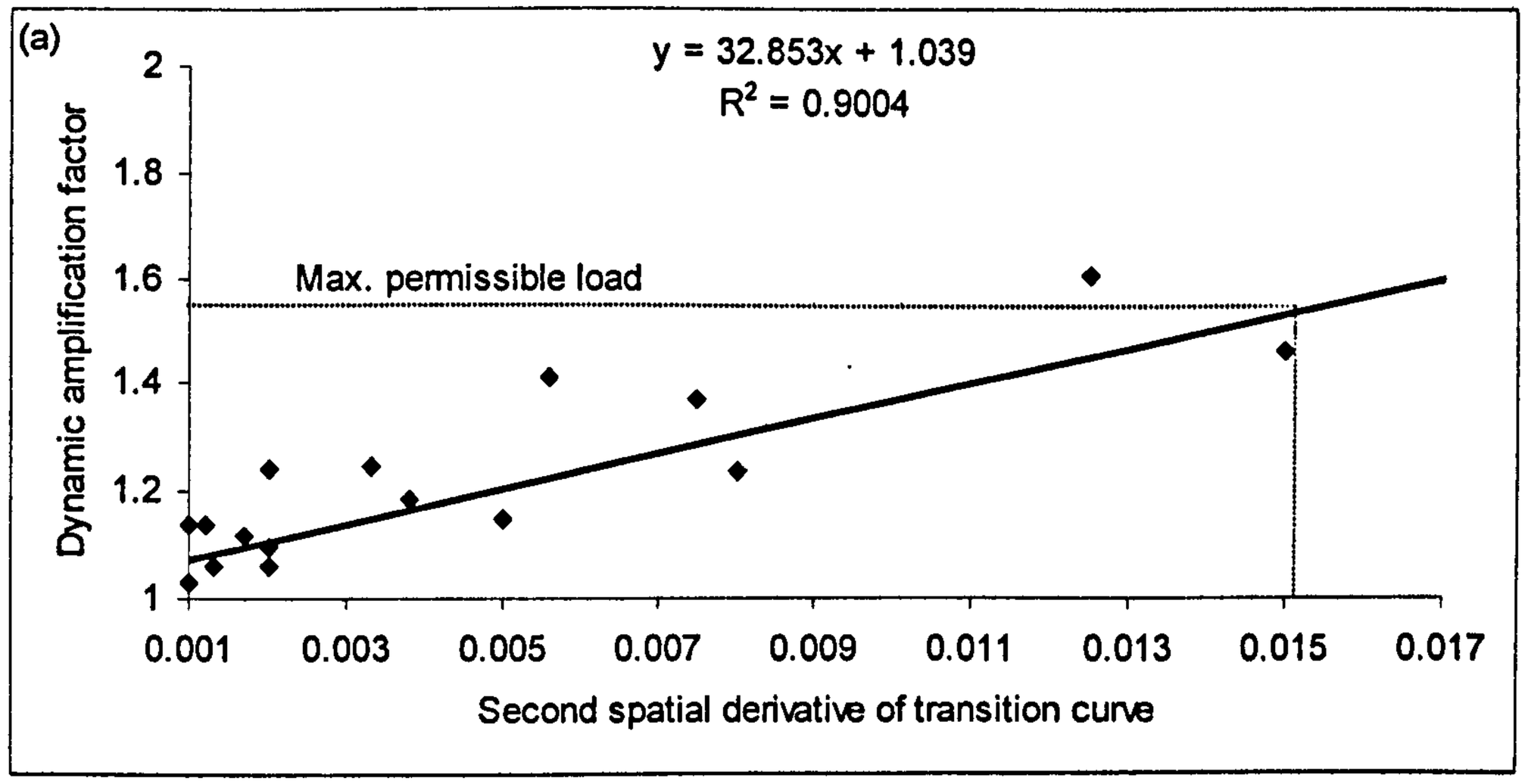

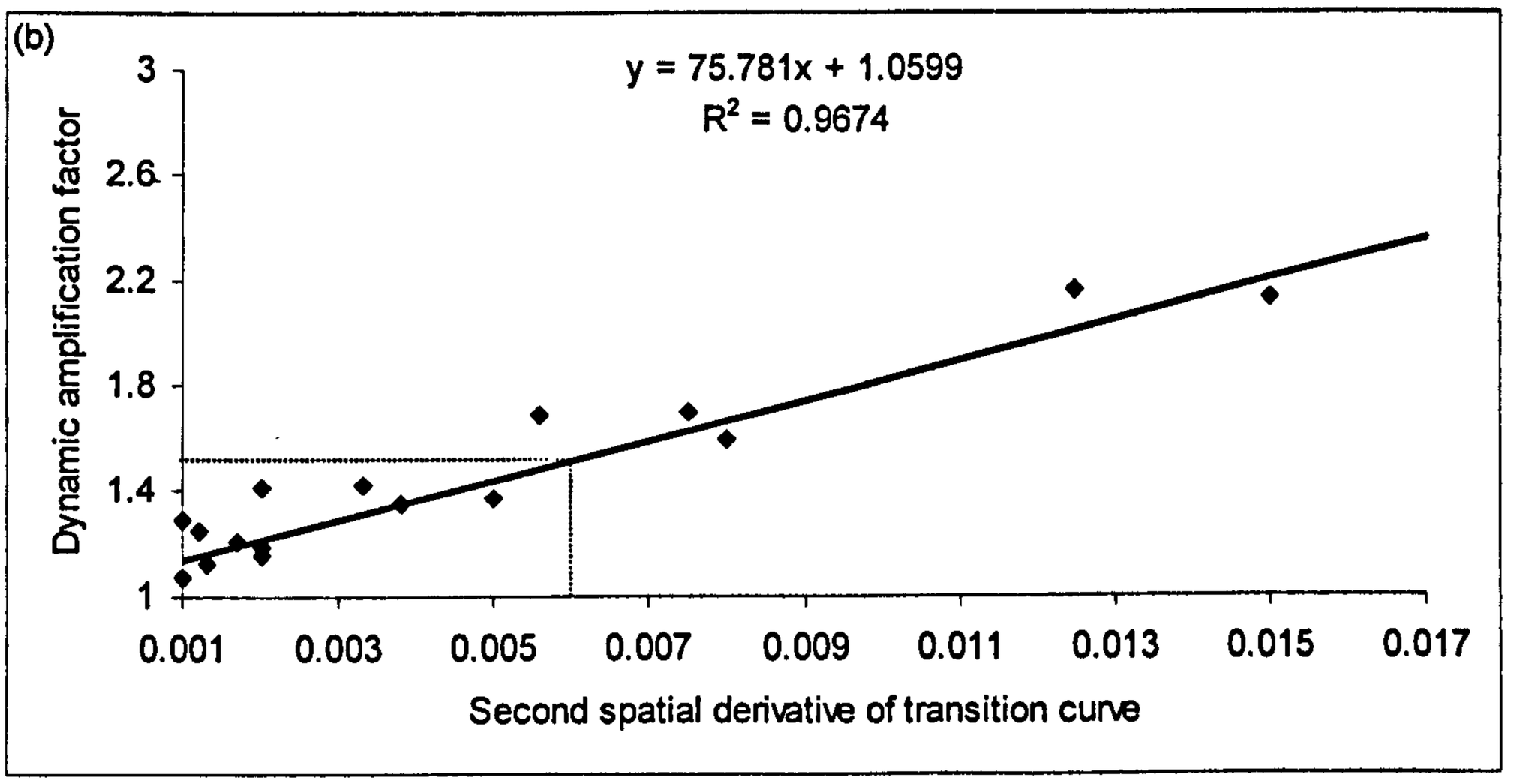

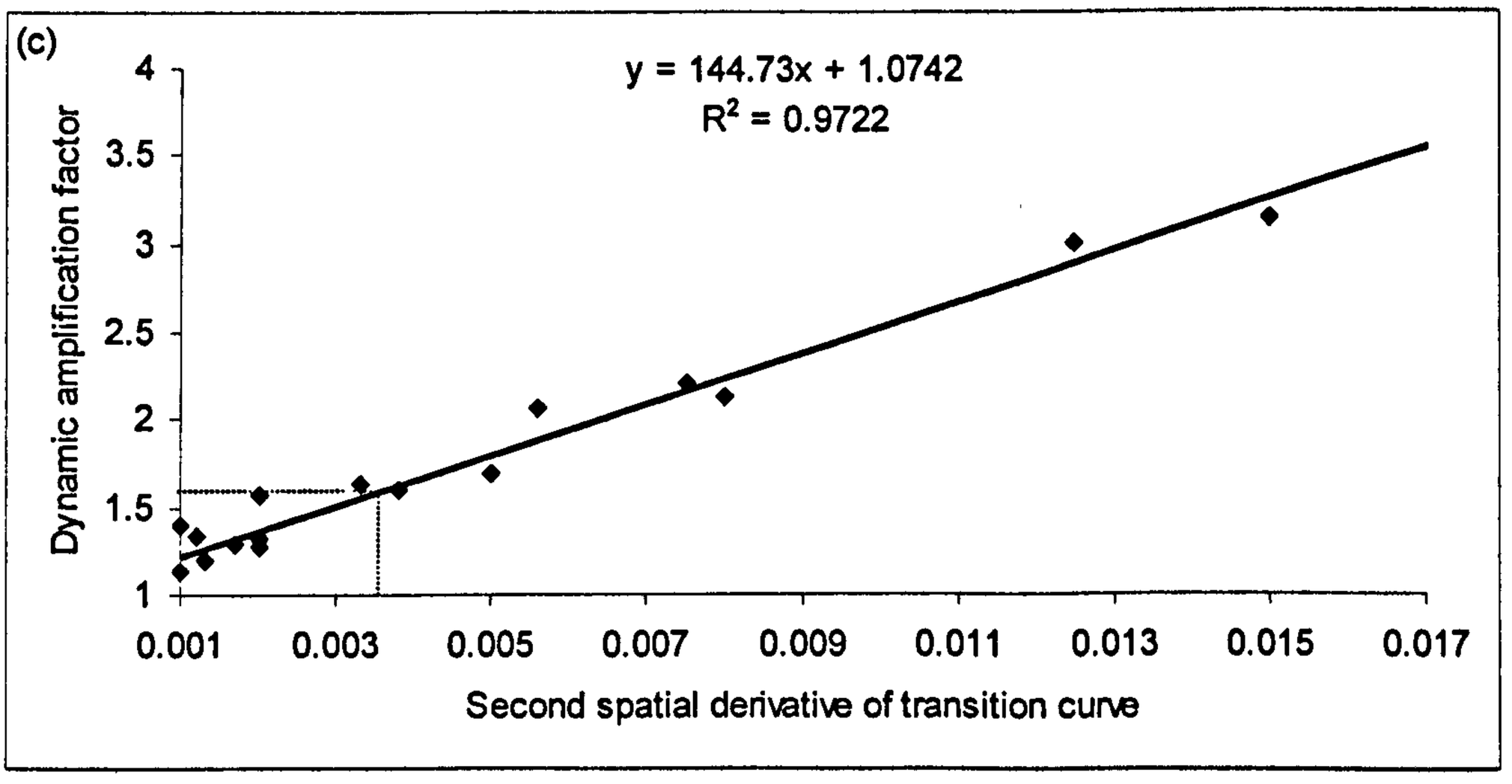

Figure 6.42. Relationship between dynamic amplification of interaction force and second derivative of transition curve

6.4 Design Implications

Different methods have been applied to mitigate track transition problems which are traditionally based on two approaches; increasing the stiffness of the railway track in the vicinity of the bridge abutment or tunnel base and/or reducing the track stiffness on the stiffer side. Kerr and Moroney (1993) suggest that the main principle to be observed in the design of a transition zone is ideally to ensure that the tracks on the soft and stiff sides give the same vertical deflection, or at least the vertical deflections should not undergo rapid changes. Oversized sleepers in the softer side of the transition zone have been used to engage a larger section of ballast to produce a stiffer track near the bridge abutment and concrete slab tracks. Another category of remedies, geotextiles or hot mixed asphalt (HMA), has been employed between the ballast and subgrade layer to create a smoother stiffness change in the transition zone. Cantilevered or floating transition slabs, horizontal or angled with varying thickness throughout the transition length, have also been used, especially in the UK, to improve the stiffness of track in the bridge approach (e.g. Woodward *et al.*, 2005). Another method based on increasing the bending stiffness of the rail by placing extra rails attached to the sleepers has also been developed by the German federal railway for ICE high speed lines. To soften the stiffer side, elastic pads have also been placed, in some cases, between the sleepers and the rail on the stiffer side to reduce the dynamic load exerted on the track in this area. As mentioned before, these methods, which were reviewed by Kerr and Moroney (1993), are based on providing a smooth transition change between the softer and stiffer sides. However, it was shown in this study that stiffness change on its own does not increase the dynamic load significantly, provided a short transition (deflection spanning length) is used. In the case of a relatively small deflection difference caused by the resilient behaviour of the railway track components, 4 metres of spanning length was seen to be enough to span the deflection between the stiff and soft sides (note that 4 metres is usually higher than the natural transition length which is provided by fastened rails, see Section 6.3.1.2). Considerably higher dynamic forces on the track start to appear, however, when a higher deflection difference caused by plasticity in the substructure and/or track faults is developed. In addition, it was shown that in the vicinity of the fault, that the stress levels in the ballast and subgrade are considerably higher than those of the non-faulted track, leading to the development of a progressive fault in the

track according to Section 6.3.1.2. Lundqvist and Dahlberg (2005) studied the problem of voided sleepers and presented similar findings. They found that a hanging (voided) sleeper with just a 1 mm gap can cause the contact ballast/sleeper force at the sleeper adjacent to the hanging one to increase by 70 %.

Thompson and Woodward (2004) emphasized the importance of limiting sleeper voiding and other track faults in the transition zone. They reported several site observations in the UK with persistent poor vertical geometry in the bridge or slab track approach. Specifically, at Hop Garden Bridge, just south of Worplesdon station on the Woking to Guildford line. Although there was no indication of weak formation, they pointed out that the track, on both the run-on and run-off sides of the bridge, had a persistent dip; the first few sleepers on either sides of the bridge were voided. This persistent voiding occurred despite the fact that the ballast was relatively new and that the track had been maintained regularly in this area. According to Thomson and Woodward (2004), there were two main different (but interrelated) problems associated with the transition zone, namely the abrupt change of stiffness and ballast voiding under the sleepers caused by a high dynamic interaction force in the transition zone. It was mentioned that ballast voiding is the main problem and should be stopped through a transition design which limits the plastic deformation in the ballast and sub-ballast.

Li and Davis (2005) reported the outcome of a case study on the performance of railway bridge approaches. For the approaches to four bridges, different transition foundation designs were considered: HMA layer under the ballast; geocell confined sub-ballast layer; 2m deep cement stabilized backfill under track bed (subgrade improvement); and a case with 500 mm of ballast placed on the subgrade surface. In the first three cases, track improvements in the transition zone were intended, whereas the fourth case was used as a control section for comparison purposes. They reported that none of three foundation strengthening methods improved track geometry performance significantly in comparison with the control section, as similarly high (permanent) settlement was observed and therefore maintenance requirements were similar for all four cases. They reported some improvement in the track modulus following the foundation treatments but mentioned that the change in stiffness between the track stiffness on the bridge and on the improved foundations was still high because of the high stiffness of track on the bridge. According to

their measurements, considerable subgrade settlement was not indicated. It was therefore found that track geometry degradation in the transition zone comes mainly from the ballast and sub-ballast layer, especially if the track is relatively old (i.e. the subgrade is well consolidated) or well compacted. That was also confirmed by the observation that although the track settlement on the cemented subgrade was slightly lower than the track settlement on the untreated subgrade (control case), the track with treated subgrade still experienced significant geometrical deteriorations (Li and Davis, 2005). Based on the studies conducted in this chapter, the ineffectiveness of the foundation strengthening method reported by Li and Davis (2005) can be explained. In none of the remedies was a measure taken to limit the development of settlement in the ballast, although stiffening the transition approach could decrease resilient settlement in the plain track and therefore slightly reduce the dynamic load. This reduction is limited because the rise in the dynamic force in the transition caused by the resilient deflection difference coming from the stiffness change is itself limited for conventional tracks, as discussed previously. Thus, as soon as uneven settlement is developed in the ballast (weaker side settles inherently more than the harder side), a higher dynamic interaction force is developed in the zone, which accelerates uneven settlement. Also, these settlements may form localised faults such as voided sleepers which will be a source of severe train excitation leading to even worse geometrical deteriorations. On this basis, the design of a transition zone should be based mainly on minimizing potential track faults and permanent deformation in these zones (mainly in the ballast and sub-ballast) rather than simply providing a smoother track stiffness change.

In terms of length of transition, according to the studies conducted in this chapter, a relatively short length providing a smooth stiffness change is required to span the resilient defection difference on the soft and stiff sides of the transition (L=4 m); however this length increases up to 10 m for high speed cases, if a large defection difference is induced by settlement on the softer side. Throughout the spanning length, a measure should be taken to minimise plastic deformation and track fault development from the start, as pointed out before. Further to that, a run-in and run-off length should be considered to limit the generation of plasticity and related track faults after and before the spanning length, which is associated with the oscillation of force in the back wheels when the front wheels are climbing the transition curve or low frequency oscillation of the dynamic wheel/rail interaction force after the wheel passes the transition curve (see Section 6.3.2.1). The

required run-in and run-off lengths are related to the suspension characteristics of the train. According to the cases studied, the run-off length is especially long, as the oscillation of the interaction force caused by the transition excitation continues to be significant, even at a distance of 20 metres (and possibly further) from the transition (note the oscillation of the interaction force after the train passed the transition zone in Figure 6.33). The run-off length is particularly important when a transition from stiff to soft side is concerned, because of the low frequency oscillations of the interaction force (as shown in Figure 6.33). This may cause long-wave geometrical irregularities on the plain track throughout a relatively long distance after the transition. In the run-in transition and run-off transition zone, the aim is essentially to stop the development of faults, not to provide a gradual stiffness change. Figure (6.43) schematically depicts the divisions on whole transition length.

It is worth emphasizing that poor drainage conditions can be responsible for geotechnical track problems, as was also discussed in Chapter 2. It is therefore vital to insure that any remedies applied to the transition zone will provide the necessary drainage.

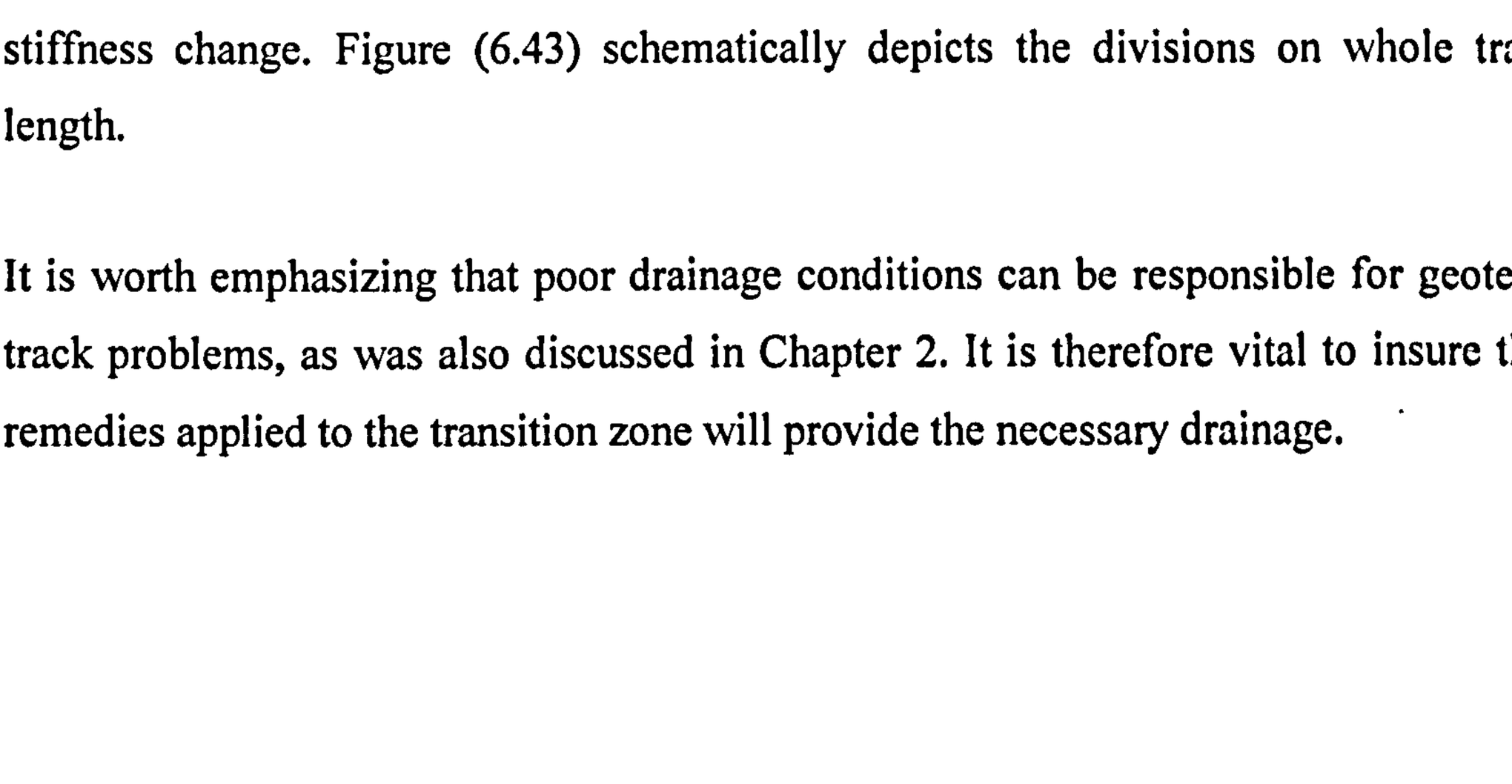

Figure 6.43. Schematic representation of divisions of transition length

6.4 Conclusion

In this chapter, the problem of train-track interaction is investigated. The stiffness transition mechanism was studied in detail. Two train models, namely a quarter and a pseudo full train model, were coupled with a three-dimensional finite element track model. Using the coupled model, it was shown that in the presence of no track faults, change of stiffness itself does not cause a major problem, especially in the low to medium speed cases. However, the presence of a void and/or another fault in the transition zone can accelerate deterioration of the railway track geometry as the result of a considerable increase in the dynamic wheel/rail interaction force and induced stress in the ballast layer. It was also observed that the increase in train speed, and having softer subgrade soil, can increase the interaction force and affect passenger comfort adversely.

It was also discussed that the train/track mechanism in the transition zone is mainly caused by the response of the train wheels to irregularities produced in the transition zone. Based on this concept, a train-irregularity model was developed which simulated the train excitation when passing a transition curve representing a deflection change in a transition zone. An extensive parametric study was conducted on the effect of deflection difference (between soft and rigid sides of the transition), deflection spanning length and train speed on the rail/wheel interaction force and maximum vertical train body acceleration. It was shown that pseudo full and quarter train models give approximately the same interaction force, whereas the quarter train model gives considerably higher train body acceleration when compared with the pseudo full train model. The higher the deflection difference, the higher the interaction force and train body accelerations are for a given train speed. A longer spanning length needs to be used to accommodate higher deflection differences at higher train speeds. It was also confirmed that elevation difference in the range of a few millimeters, coming from the resilient behaviour of a conventional track, would not increase the interaction force considerably; provided a short spanning length is present (4 metres). Permanent deflection of the track can, however, create an elevation difference in the range of centimetres, which can cause high dynamic load and progressive deterioration of the track geometry.

From a study of the dynamic force induced in the transition zone with respect to the first and second spatial derivatives of the transition curve, it was found that although for low speed (V=30 m/s), the dynamic amplification of the train load can be satisfactorily correlated to the first derivative of the transition curve (the curve gradient), for higher speed cases (V=50 and 70 m/s) such a correlation starts to deteriorate and a second spatial derivative seems to provide better correlation to the dynamic amplification factor. It is therefore proposed that the second spatial derivative of a transition curve be used for assessment of the transition zone in terms of the load exerted on a transition zone, especially for medium to high speed tracks.

The transition design principles were reviewed and it was suggested that the design of a transition zone should be based on minimizing potential track faults and permanent deformation in these zones, rather than simply providing a smoother track stiffness change. Regarding the length of transition, in addition to deflection spanning length, a run-in and run-off length (before and after the spanning length respectively) should be considered to limit the generation of plasticity and related track faults originating from excitation of train coach when it is on the transition (or past the transition). The run-off length was particularly important, as low frequency oscillations of the wheel/rail interaction force when the train coach passed a transition curve were noted to continue over a relatively long distance after the spanning length had finished.

CHAPTER 7

APPLICATION OF AN ADVANCED CONSTITUTIVE SOIL MODEL

7.1 Introduction

Traditionally, track resilient and plastic behaviours have been treated separately. The resilient behaviour can be investigated through the concept of the resilient modulus of substructure components (e.g. ballast, subballast and subgrade) using rigorous computational methods (e.g. three-dimensional dynamic finite element model presented in previous chapters). However the estimation of (plastic) settlement of the track has mostly remained empirical. Despite some insights provided by these empirical relationships, they do not consider the substructure soil behaviour appropriately. As mentioned in Chapter 2, Dahberg (2001) reviewed these empirical relationships and noted that many empirical models used to describe the long-term behaviour of a railroad track focus on the loading of the track (number of loading cycle and/or passed tonnage); the complicated mechanism of the stress-strain response of the substructure soil has not been taken into account appropriately. In addition, these empirical relationships are bounded to the conditions under which they have been developed and their applications to other cases, and different operational conditions, are limited. It is especially the case for tracks under high speed and heavy axle regimes in which the substructure is experiencing higher stresses and consequently faster deteriorations. Some railway tracks are also found under mixed freight–passenger traffic which exposes the track to a varying stress condition. Under such complicated stress regimes the substructure soil may experience considerable plasticity and may even fail in the worst cases (shear failures as discussed in Chapter 2), the mechanism of which can only be described by an advanced elastic-plastic soil constitutive model. These constitutive models should especially address the stress state dependent stiffness/strength, strain hardening and softening, the dilation mechanism and the progressive nature of failure, as occurs in natural soils.

In this chapter, an example of such an advanced constitutive model, namely ALTERNAT, is described as it can be used to simulate the monotonic and cyclic behaviour of granular systems such as ballast, sub-ballast and granular subgrade (it can also be used for fine grained soil). Calibration of ALTERNAT is also addressed and a procedure is developed based on an optimisation technique, called the micro genetic algorithm, to determine the model parameters based on experimental data. In order to develop a good understanding of how complex soil behaviour affects the response of a foundation system (such as railway track), the monotonic responses of shallow footings are extensively studied using a finite element code incorporating ALTERNAT. The footing problem was chosen to be studied for two main reasons. First, a surface footing can represent a railway track system under the train loading (monotonic loading). For example, sleepers on the ballast and slab tracks on subgrade can be simulated as surface footings. Hence studying the responses of surface footings, up to the failure point will give invaluable insights into the parameters affecting the monotonic response of footing like geo-systems, such as track foundations in terms of settlement and failure mechanisms. Second, as a classical problem, the surface footings have been investigated for several decades which offers a great deal of data in this area and which can then be utilised to evaluate the performance of ALTERNAT in simulating the monotonic response of a geotechnical system. A successful simulation of the monotonic response of surface footings is therefore seen as an important step towards application of the ALTERNAT model to the long-term monotonic and cyclic response of railway track. Following the footing studies, the cyclic response of a granular soil is briefly studied and it is shown that ALTERNAT can simulate the essential features of the cyclic behaviour of granular bodies such as ballast. Finally, an approach is proposed for future studies which can integrate the dynamic train-track coupled model and ALTERNAT to simulate life-long performance of railway tracks. According to the results in the present section, it can be said that ALTERNAT can be successfully used in modelling the monotonic and cyclic behaviour of railway track soil systems.

7.2 Constitutive Model, ALTERNAT

For an elastic-plastic soil, the relationship between the incremental stress and strain is related in the following form:

$$d\sigma = [D^{ep}]d\varepsilon \tag{7.1}$$

where D^{ep} is the elasto-plastic constitutive matrix:

$$[D^{ep}] = [D^{e}] - [D^{p}] \tag{7.2}$$

$[D^{e}]$ and $[D^{p}]$ are the elastic and plastic constitutive matrices. The constitutive model, ALTERNAT (Molenkamp, 1987; 1990), has been developed in the framework of incremental plasticity which assumes the decomposition of the total strain increment ($d\varepsilon$) into elastic ($d\varepsilon^{e}$) and plastic parts ($d\varepsilon^{p}$):

$$d\varepsilon = d\varepsilon^{e} + d\varepsilon^{p} \tag{7.3}$$

An updated Lagrangian description is used to calculate the plastic properties in such a way that a frame of reference rotates with the material during continued alternating loading (Figure 7.1); co-rotational pure deformation can be described (Molenkamp, 1987).

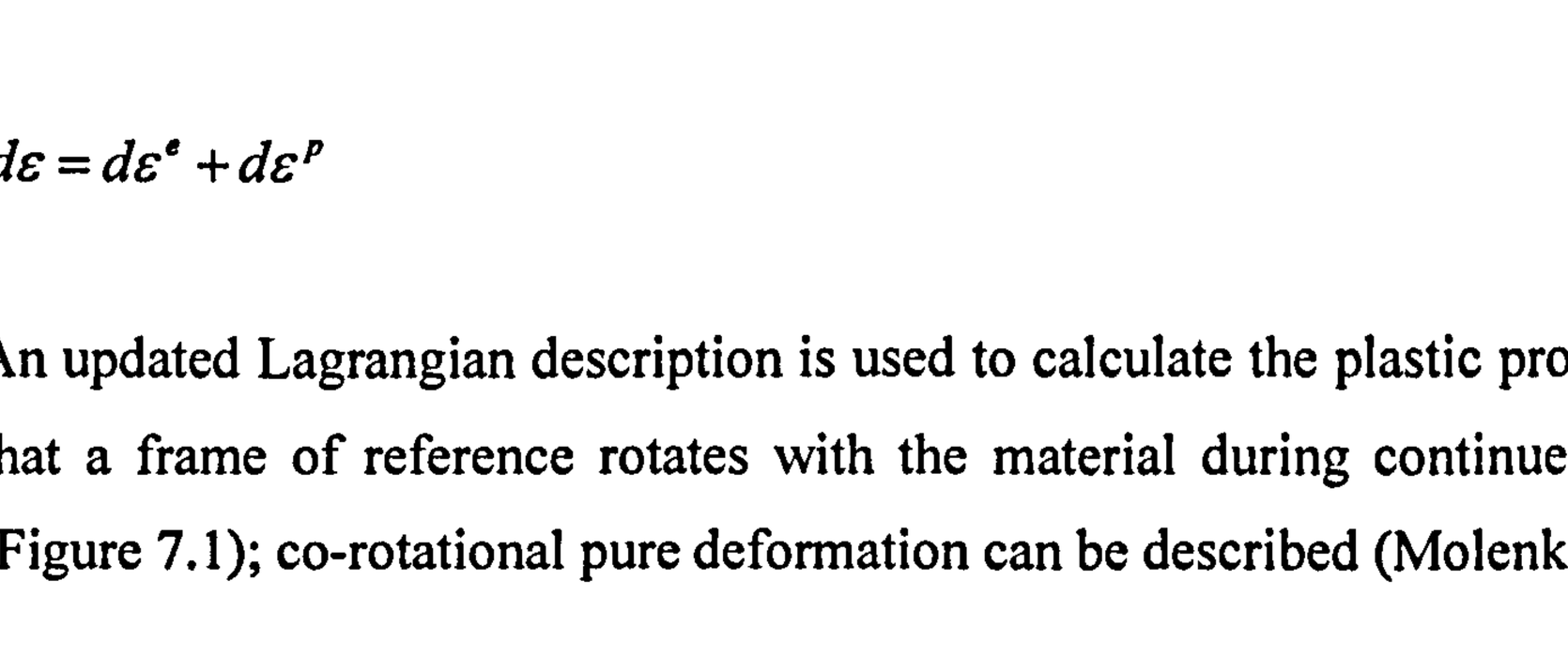

Figure 7.1. Illustration of co-rotational frame of reference

7.2.1 Non-Linear Elasticity

According to ALTERNAT, when the soil is loaded from the initial state its initial response is assumed to be elastic. Once the active stress crosses the initial yield surface, the surface will expand and the material will experience elastic-plastic behaviour. The nonlinear elastic behaviour in ALTERNAT is based on the following complementary potential function which insures that no loss of energy is permitted in elastic deformation (Molenkamp, 1988; 1992):

$$Q = A\frac{p_a}{(P+1)}\left(\frac{s}{p_a}\right)^{P+1}\left[1+\frac{3P(P+1)}{4R}\left(\frac{t}{s}\right)^2\right] \tag{7.4}$$

where, the scalars A, P and R are the elastic material parameters and P_a is atmospheric pressure. Deviatoric and isotropic stresses are denoted in equation (7.4) by t and s respectively. These are defined as:

$$s = \frac{1}{\sqrt{3}}\sigma_{ij}\delta_{ij} \tag{7.5}$$

$$t = \sqrt{(t_{ij}t_{ij})} \tag{7.6}$$

$$t_{ij} = \sigma_{ij} - \frac{1}{3}\sigma_{kl}\delta_{kl}\delta_{ij} \tag{7.7}$$

σ_{ij} and δ_{ij} are Cauchy stress and Kronecker delta respectively. The parameter R is defined as the ratio of shear modulus, G to the isotropic bulk modulus:

$$R = \frac{G}{K_{iso}} \tag{7.8}$$

$$G = \frac{RP_a}{3AP}\left(\frac{s}{P_a}\right)^{1-P} \tag{7.9}$$

$$K_{iso} = \frac{1}{3}\frac{P_a}{AP}\left(\frac{s}{P_a}\right)^{1-P} \qquad \text{For } \frac{t}{s} = 0 \text{ (isotropic loading)} \tag{7.10}$$

The inverse of the elastic tangent stiffness matrix D^{-1}_{ijkl} can then be obtained from:

$$D^{-1}_{ijkl} = \frac{\partial^2 Q}{\partial \sigma_{ij} \partial \sigma_{kl}} \tag{7.11}$$

7.2.2 Anisotropic Yield Surface

To simulate both inherent and stress-induced anisotropy, the yield surface is centred around a non-zero deviatoric stress state when viewed in the deviatoric plain. This stress state is defined by a non-dimensional deviatoric tensor of anisotropy. The yield surface is according to Lade and Duncan (1975) and Lade (1977):

$$F^d = F\left[I(T_{ij})\right] - f(\chi) = \frac{I_1^3}{I_3} - 27 - f(\chi) = 0 \tag{7.12}$$

where χ is the hardening parameter defining the rate at which the yield surface expands or contracts as a result of plastic straining. $f(\chi)$ is the size of the yield surface. I_1 and I_3 are the first and third invariants of the pseudo-stress respectively. The pseudo stress T_{ij} is a measure of the stress state from the centre of anisotropy (ξ) which represents the mobilised friction angle:

$$T_{ij} = \sigma_{ij} - \frac{1}{3}\sigma_{kk}\xi_{ij} \tag{7.13}$$

σ_{ij} is the active stress and ξ_{ij} is a non dimensional deviatoric tensor of anisotropy. During plastic yielding the stress state must remain on the yield surface (consistency condition), i.e. $dF^d = 0$:

$$\frac{\partial F}{\partial T_{kl}} dT_{kl} - \frac{df}{d\chi} d\chi = 0 \tag{7.14}$$

Therefore,

$$d\chi = \frac{1}{\dfrac{df}{d\chi}} \frac{\partial F}{\partial T_{kl}} dT_{kl} \tag{7.15}$$

In ALTERNAT, The increment in the hardening parameter ($d\chi$) is a function of plastic deviatoric strain incerement (de^p):

$$d\chi = de^p \frac{\left(\dfrac{n_i - n_d}{n_i - n_d - \Sigma_c \Delta\varepsilon^p_{vol,c}} \right)^{\kappa} \dfrac{\partial F}{\partial T_{kl}} dT_{kl}}{k(\chi,\theta)\left(\dfrac{s}{p_a}\right)^{L} \dfrac{\partial F}{\partial \sigma_{mn}} d\sigma_{mn}} \tag{7.16}$$

where n_i and n_d are the initial and minimum (after densification) porosities. $\Sigma_c \Delta\varepsilon^p_{vol,c}$ is the accumulated plastic volumetric strain caused by alternating loading and κ is the cyclic densification parameter. The term with the porosities simulates plastic densification as a result of cyclic loading, and ranges from unity at the initial isotropic state to infinity at the maximum densification. The effect of increasing the plastic densification parameter κ is presented in Figure (7.2). As κ increases, the deviatoric plastic strain increment decreases with increasing cycles, and hence an increase in shear stiffness caused by cyclic densification is simulated. S and L are also material constants.

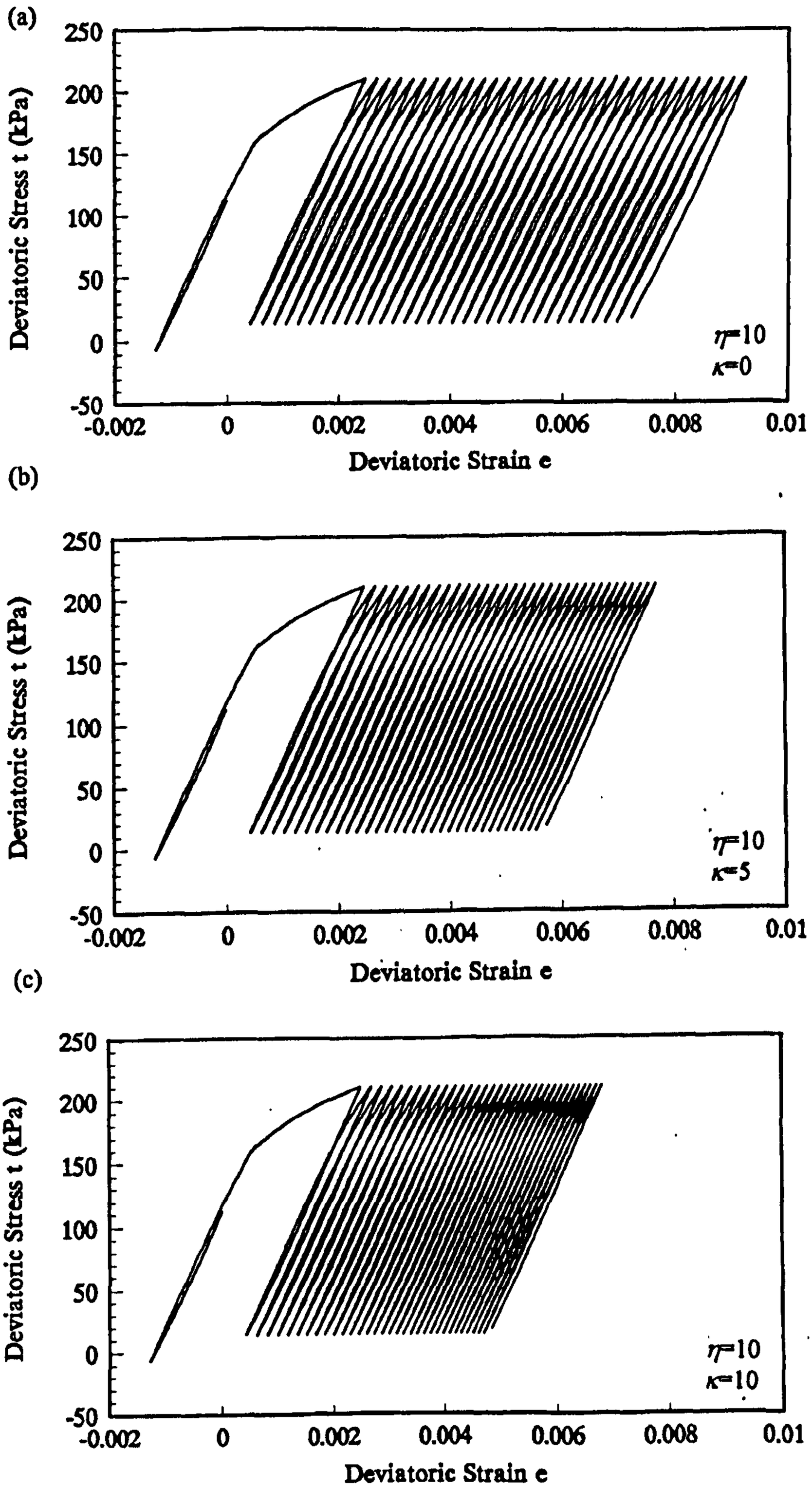

Figure 7.2. Effect of the material parameter κ on the simulation of plastic densification under cyclic loading (Woodward and Molenkamp, 1999)

The function $k(\chi,\theta)$ describes the distribution of the plastic stiffness around the circumference of the yield surface with hardening parameter χ and lode angle θ:

$$k(\chi,\theta)=-\left(1+S(1+\cos 6\theta)\frac{\dfrac{\partial I_3(T^c)}{\partial T_{kl}}T^{de}_{kl}}{\dfrac{\partial I_3(T^e)}{\partial T_{mn}}T^{de}_{mn}}\right) \tag{7.17}$$

Superscripts c and e refer to the third invariant of triaxial compression and extension pseudo-stresses respectively, and T^{de} is the deviatoric component of the pseudo-stress.

7.2.3 Non-Associative Flow Rule

The plastic flow rule is defined using a potential function which dictates the direction of the plastic strain increment caused by an increment of stress. As in ALTERNAT, when the potential surface is not the same as the yield surface, the flow rule is said to be non-associative. In ALTERNAT the flow rule is decomposed into isotropic and deviatoric components:

$$d\varepsilon^p_{ij}=\frac{\partial G^p}{\partial \sigma_{ij}}\lambda=\left(\alpha\delta_{ij}+\frac{\partial G^d}{\partial \sigma_{ij}}\right)\lambda \tag{7.18}$$

The deviatoric component of the potential function G^d uses the same expression as the yield function, except that a modified pseudo-stress T^* is used to make the deviatoric potential surface more circular in the deviatoric plane:

$$T^*=\frac{1}{3}\sigma_{kl}\delta_{kl}\delta_{ij}+R_p\left(T_{ij}-\frac{1}{3}\sigma_{kl}\delta_{kl}\delta_{ij}\right) \tag{7.19}$$

where R_p is a material parameter. $d\varepsilon_{ij}^p$ is the magnitude of the plastic strain increment, G^p is the plastic potential function (superscript d stands for deviatoric) and $\alpha\delta_{ij}$ is based on Rowe's stress dilatancy theory for granular soils (Jong, 1976):

$$\frac{dv^p}{de^p} = \alpha\sqrt{3} \tag{7.20}$$

In ALTERNAT, the dilatancy relationship is expressed for triaxial compression and extension, then generalised to other stress paths (for any value of Lode angle) by an interpolation. According to Molenkamp (1982), the stress-dilatency theory results in the following expression for plastic dilatancy ratio for loading in triaxial compression and extension respectively:

$$(\frac{dv^p}{de^p})_c = \alpha\sqrt{3} = \frac{-\sqrt{2}(1-k)-(2+k)\frac{t}{s}}{(1+2k)+\sqrt{2}(1-k)\frac{t}{s}} \tag{7.21}$$

$$(\frac{dv^p}{de^p})_e = \alpha\sqrt{3} = \frac{\sqrt{2}(1-k)-(1+2k)\frac{t}{s}}{(2+k)-\sqrt{2}(1-k)\frac{t}{s}} \tag{7.22}$$

where

$$k = Tan^2(\frac{\pi}{4}+\frac{\phi_u}{2}) \tag{7.23}$$

ϕ_u is the interparticle friction angle. The characteristic shear stress level $(\frac{t}{s})_{\mu c}$ at zero dilatancy is related to the interparticle friction angle which is assumed to depend on the void ratio, e_v and the isotropic stress:

$$(\frac{t}{s})_{\mu c} = \frac{2\sqrt{2}\sin\phi_{\mu}}{3-\sin\phi_{\mu}} = C\left[(1+\xi)-\xi\exp(-\theta_p(\frac{s}{P_a}))\right][1-\exp(-\varsigma e_v)] \qquad (7.24)$$

where C, ξ, ς and θ_p are material parameters. By assigning these material parmeters, the shear stress level, at which dilation starts and subsequent dilation in the soil with respect to density and isotropic stresses, can be controlled. Figure (7.3) shows the effect of C on the characterstic shear stress level at zero dilatancy. Decreasing C results in a reduction in the shear stress level after which dilation will occur, representing the increase in dilation with soil density. On the other hand, as the isotropic stress increases the $(\frac{t}{s})_{\mu c}$ will also increase, simulating the reduction in dilation with confining pressure. The dependence on isotropic stress significantly reduces at higher isotropic stress levels, i.e. the curves for $\frac{s}{P_a}$=10 and 100 approximately coincide.

λ is termed as the plastic multiplier defined as:

$$\lambda = \frac{\frac{\partial F}{\partial \sigma_{kl}} d\sigma_{kl}}{H_m} \qquad (7.25)$$

Multiplying both sides of Equation (7.25) by $\frac{\partial F}{\partial \sigma_{mn}} D_{mnij}$ and after some rearrangements:

$$\lambda = \frac{\frac{\partial F}{\partial \sigma_{mn}} D_{mnij} d\varepsilon_{ij}}{H_m + \frac{\partial F}{\partial \sigma_{mn}} D_{mnij} \frac{\partial G}{\partial \sigma_{ij}}} \qquad (7.26)$$

(a)

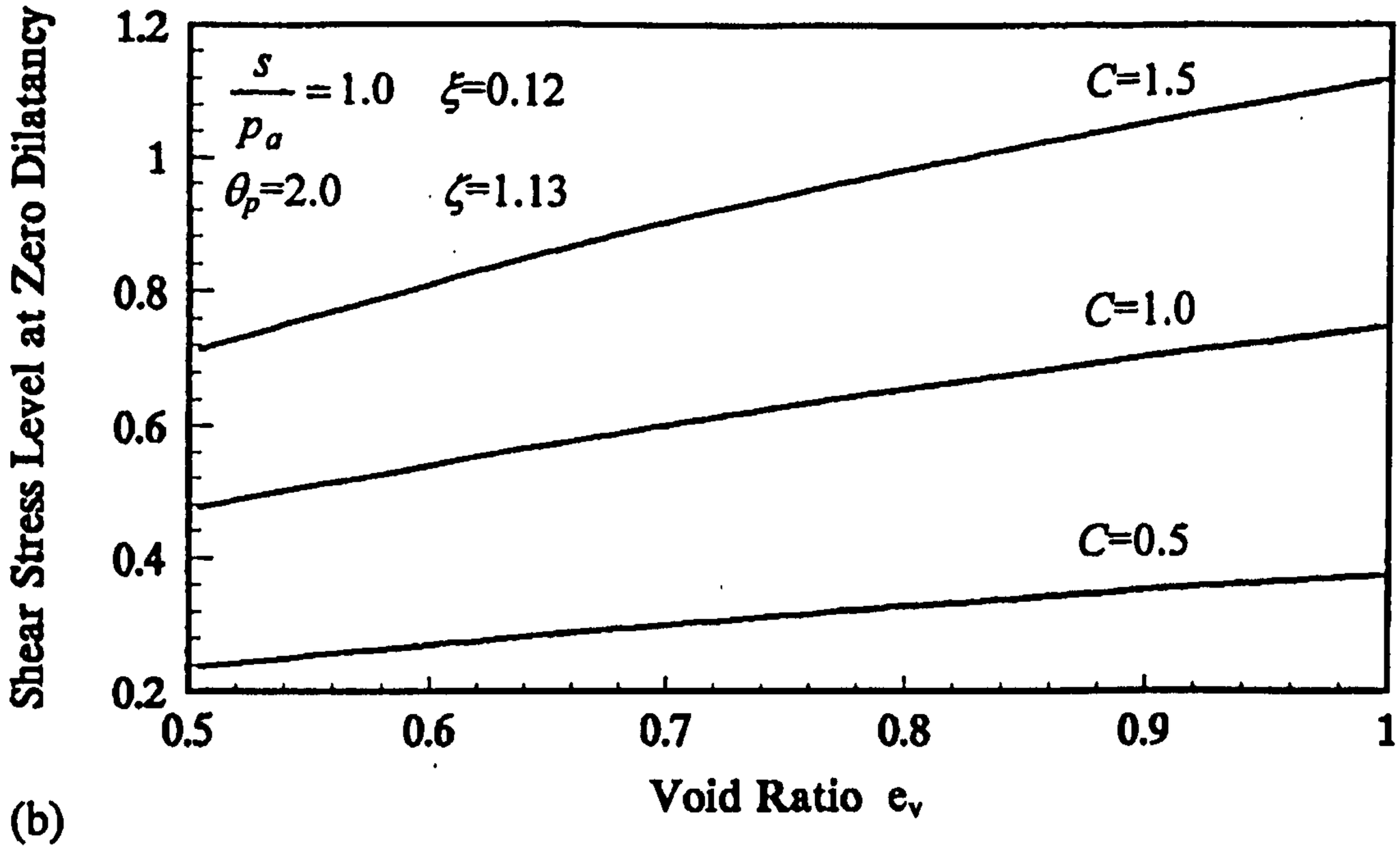

(b)

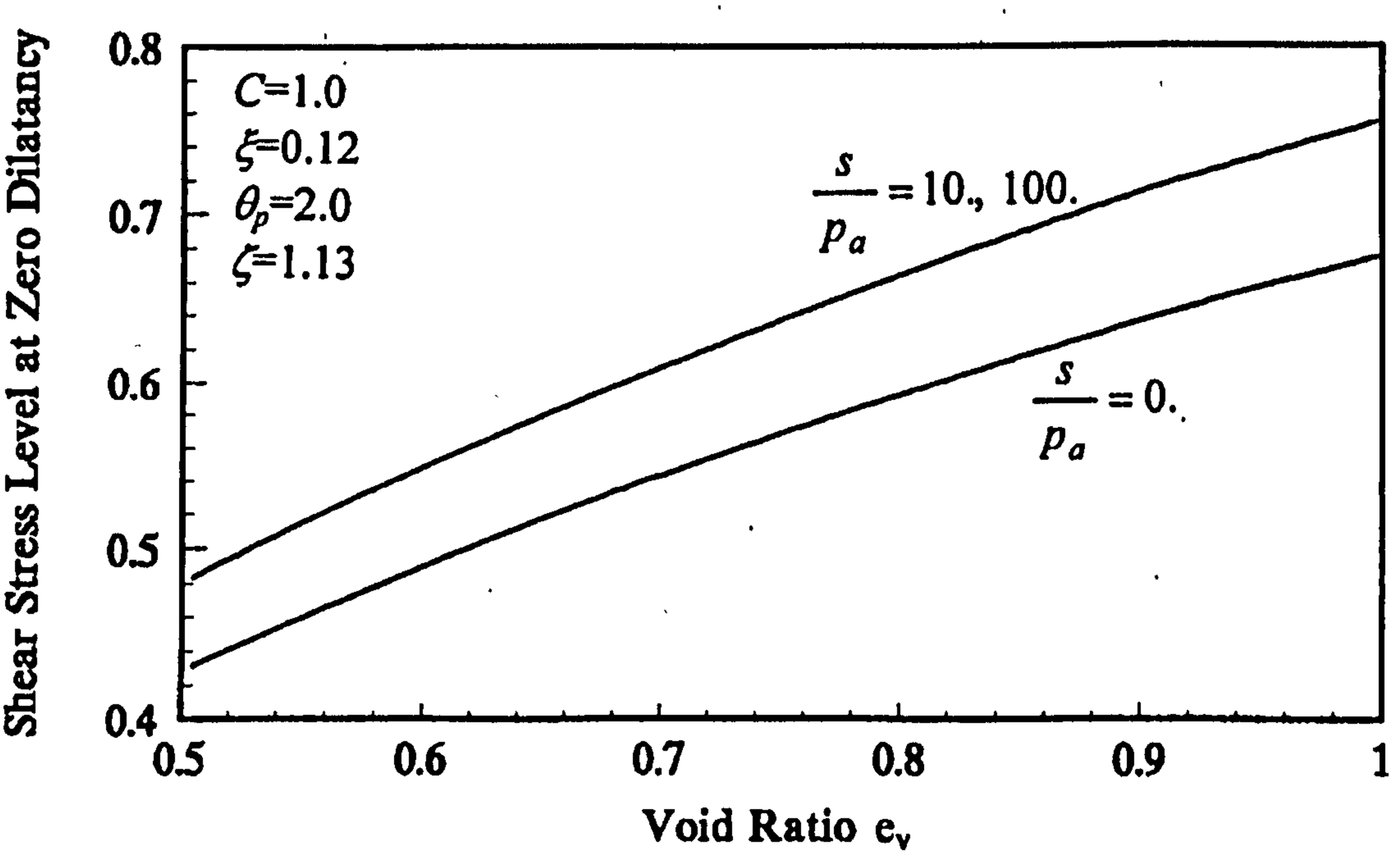

Figure 7.3. Effect of material parameter, C (a) and isotropic stress level, s/pa (b) on shear stress level at zero dialatancy $(t/s)_{\mu c}$ (Woodward and Molenkamp, 1999)

Substitution of (7.26) in (7.3) gives

$$D^p = \frac{D_{klrs}\dfrac{\partial G}{\partial \sigma_{rs}}\dfrac{\partial F}{\partial \sigma_{mn}}D_{mnij}\,d\varepsilon_{ij}}{H_m + \dfrac{\partial F}{\partial \sigma_{mn}}D_{mnij}\dfrac{\partial G}{\partial \sigma_{ij}}} \tag{7.27}$$

H_m is the modified hardening modulus. It is defined in the next section.

7.2.4 Kinematic Rule

In ALTERNAT, the yield surface may expand and translate (isotropic and deviatoric kinematic hardening). Kinematic hardening is considered by formulating a kinematic rule to account for changes in the deviatoric tensor of anisotropy ξ_{ij}. Two assumptions are made to develop an algorithm to compute the increment in the deviatoric tensor of anisotropy ξ_{ij}, $d\xi_{ij}$:

- After a stress reversal, all subsequent yield surfaces in the pi-plane pass through the reversal stress σ^r and remain tangent (Figure 7.4). A consequence of this is that the deviatoric components of partial derivatives of the yield surface must remain proportional to each other after the stress reversal. This assumption was introduced by Lade (1979) and supported by experimental evidence. Also, Molenkamp (1987) argued that it seemed a logical assumption, because the boundary of the elastic region near the stress reversal point is kept unchanged also after stress reversal.

- The reversal and active stresses remain on the same yield surface (Figure 7.4).

The deviatoric hardening modulus H is used to describe the plastic stiffness of the soil (i.e. it relates deviatoric strain increments to stress increments). It is dependent on the position of the yield surface in the principal stress space. In other word, the distribution of the yield

surface across the stress space defines the distribution of the kinematic hardening modulus across the stress space. H is found from the following equation:

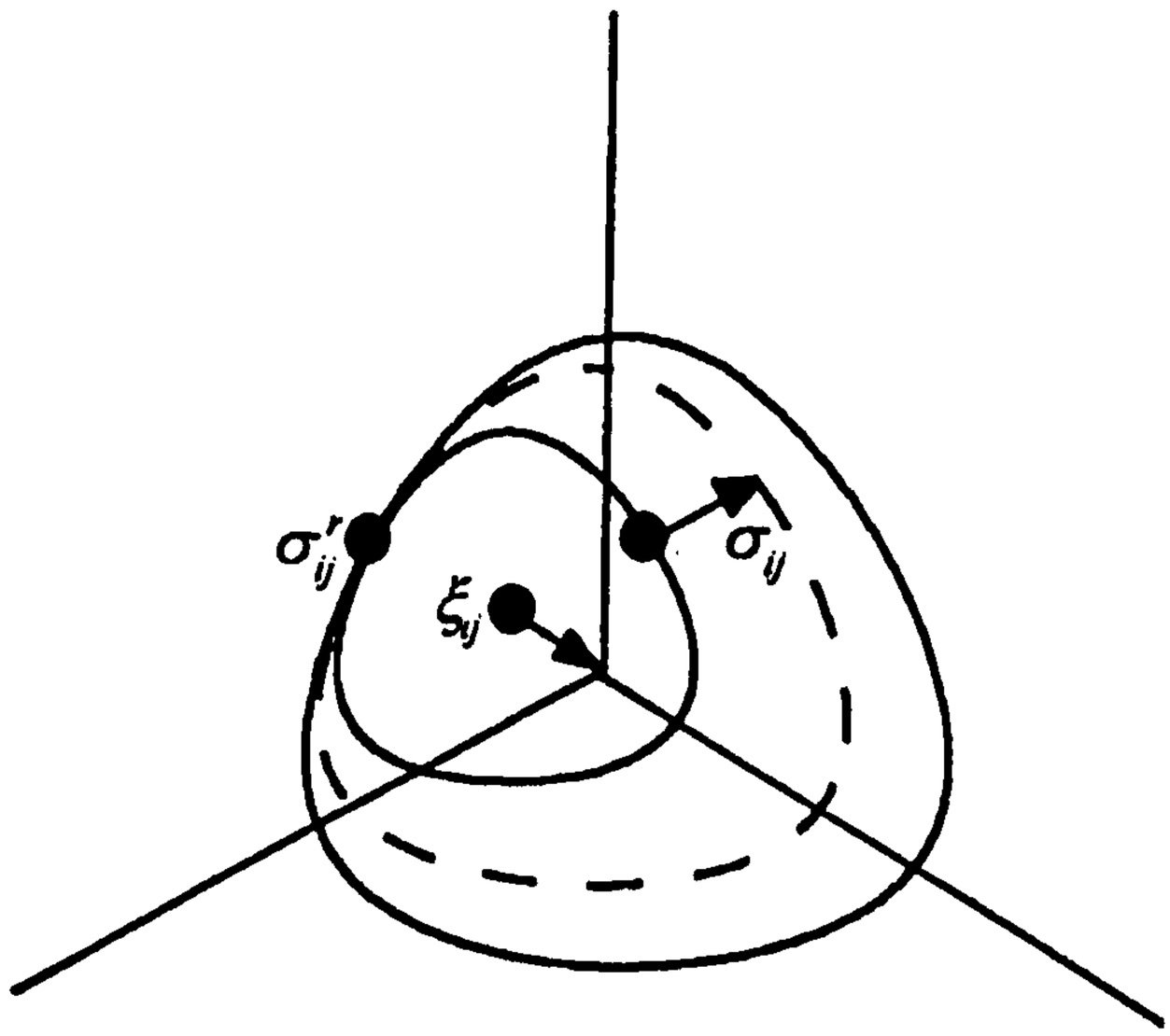

Figure 7.4. Illustration of kinematic rules in ALTERNAT (Woodward and Molenkamp, 1999)

$$H = \frac{df}{d\left(\frac{t}{s}\right)} \frac{d\left(\frac{t}{s}\right)}{d\chi} \frac{\left(\frac{n_i - n_d}{n_i - n_d - \Sigma_c \Delta\varepsilon^p_{vol,c}}\right)^{\kappa}}{\kappa(\chi,\theta)\left(\frac{s}{p_a}\right)^{L}} \tag{7.28}$$

$$\frac{df}{d(\frac{t}{s})} = 81 \frac{(\frac{t}{s})}{[1+\sqrt{2}(\frac{t}{s})]^2[1-(\frac{1}{\sqrt{2}})(\frac{t}{s})^3} \tag{7.29}$$

where, $\frac{t}{s}$ is the shear stress level for triaxial compression. Each kinematic yield surface has its own distribution of the hardening modulus, modelling the change of plastic stiffness during loading.

The kinematic rule defined before ensures that plastic deviatoric strains are developed during loading and unloading. However, under cyclic loading, it simulates a closed strain-stress loop, i.e. zero cyclic mobility. According to Molenkamp (1987), cyclic mobility here is defined as the change in deviatoric strains in consecutive cycles. To accommodate cyclic mobility, the hardening modulus is modified as follows:

$$H_m = H.X \tag{7.30}$$

X is a factor depending on the scalar measure ψ of direction of loading according to the expression:

$$X = \exp(-\eta\psi) \tag{7.31}$$

in which,

$$\psi = 3\xi_{ij}\left(\frac{\sigma_{ij}}{\sigma_{kl}\delta_{kl}} - \frac{\sigma^r_{ij}}{\sigma^r_{pq}\delta_{pq}}\right)\xi_{pq}\xi_{pq} \tag{7.32}$$

η is a material parameter. This modification of the hardening modulus permits absolute magnitude of the strain increments; this is because the loading phases of cyclic loading are larger than the magnitude of the opposite strain increments due to the unloading phases, therefore simulating cyclic mobility. Figure (7.5) shows the effect of the parameter, η, on the simulation of cyclic mobility at a given isotropic stress when the densification parameter is set to zero. When η=0, a closed form stress-strain loop is generated, whereas as η increases, a higher cyclic deviatoric strain is mobilised.

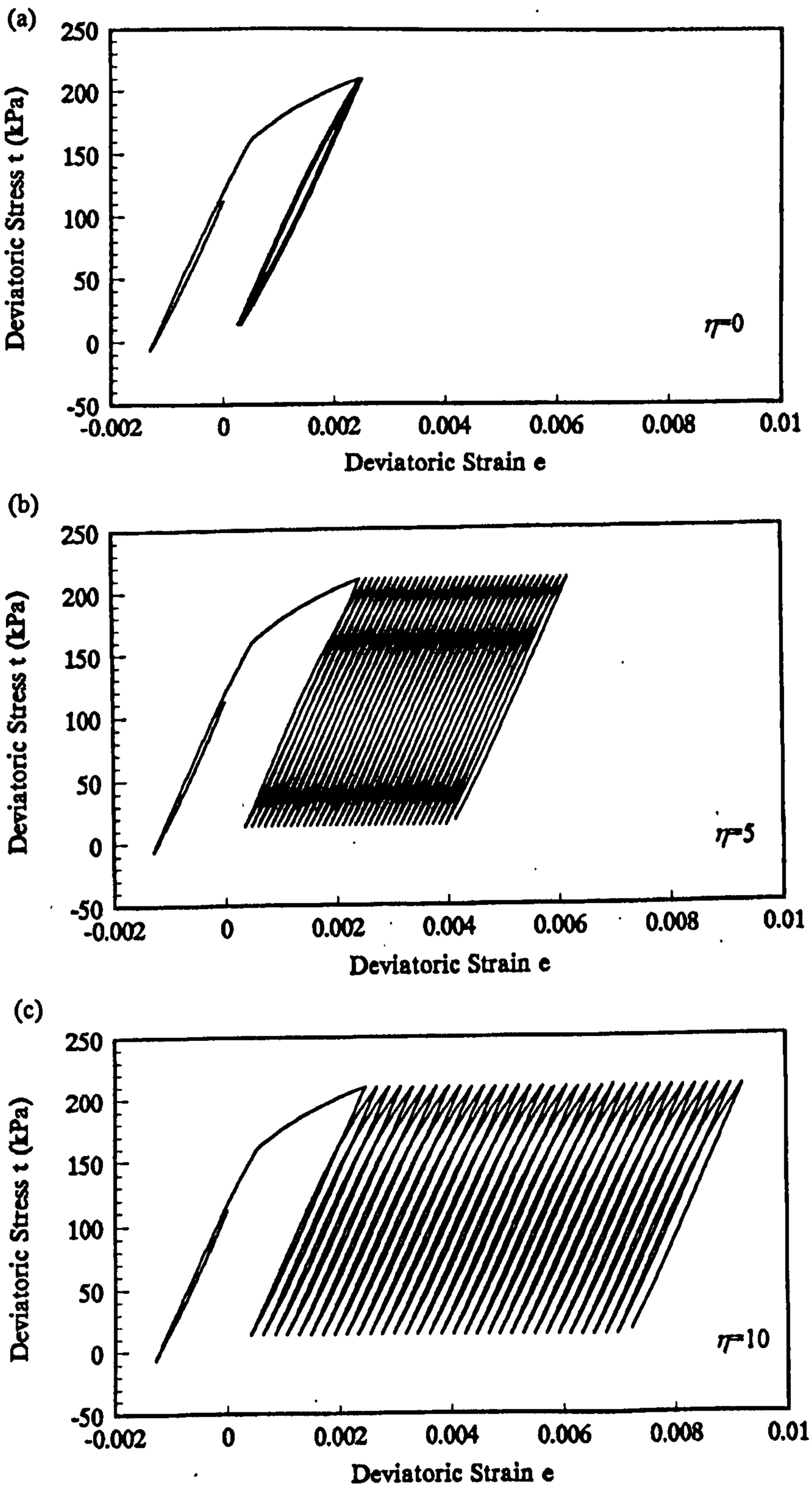

Figure 7.5. Effect of the material parameter η on the simulation of cyclic mobility at constant isotropic stress (Woodward and Molenkamp, 1999)

Typical movements of the yield surface can be seen in Figure (7.6). In its initial state, three yield surfaces are assumed. Two of them are anisotropic, centred around a non-zero deviatoric stress (k_0 state), and one is the smallest isotropic yield surface. The initial response is assumed to be nonlinear elastic until the current stress state touches the first yield surface. Then this first initial yield surface will expand and the soil will experience elasto-plastic behaviour. As the loading continues, this yield surface will expand and touch the next encompassing yield surface. If the soil experiences a stress reversal, a new yield surface is generated at the stress reversal point at a predefined size. The initial unloading behaviour is elastic when the stress state is inside the new yield surface. This is followed by elasto-plastic behaviour as this new yield surface is surpassed and the kinematic yield surface starts to expand. During the unloading and reloading sequence, the expansion, destruction and generation of different yield surfaces are shown in Figure (7.6).

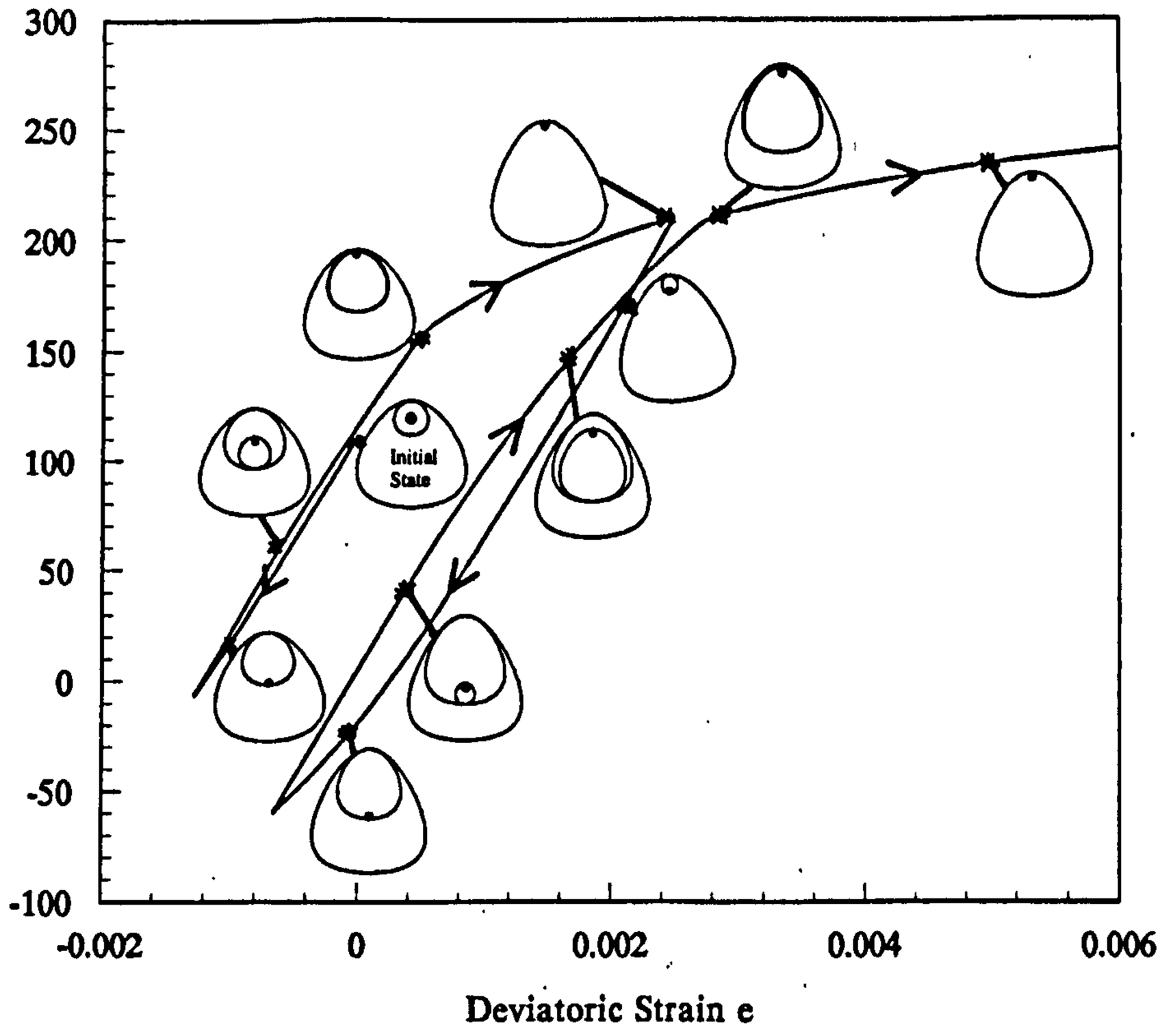

Figure 7.6. Illustration of typical yield surface movement for cyclic loading in π plane (Woodward and Molenkamp, 1999)

7.2.5 Strain Hardening and Softening Behaviour

A combined relationship (Equation 7.33) is used to describe the smooth transition from pre-peak strain hardening to post peak strain softening, in terms of the shear stress level in triaxial compression, as a function of the plastic deviatoric strain. If the pre-peak shear stress level is termed Y_1 and the post peak shear stress level Y_2, then:

$$\left(\frac{t}{s}\right)=\frac{Y_1 Y_2}{\left(Y_1^n+Y_2^n\right)^{\frac{1}{n}}} \tag{7.33}$$

Y_1 and Y_2 are obtained from the following:

$$Y_1=\left[\frac{e^p}{\left(\frac{s}{p_a}\right)^L \frac{(1+e_v)E}{(Q-e_v)^2}}\right]^{\frac{1}{D}} \tag{7.34}$$

$$Y_2=M\left\{(1-\upsilon)+\upsilon.\exp\left(-\psi\left(\frac{s}{p_a}\right)\right)\right\}\exp(-\beta e_v) \tag{7.35}$$

where, E, Q and D are the parameters for the pre-peak strain hardening range. M, υ, ψ and β are the parameters for the post-peak strain softening range and e_v denotes the void ratio. d(t/s)/d(x) is given as:

$$\frac{d(\frac{t}{s})}{d\chi}=\frac{1}{(Y_1^n+Y_2^n)^{(\frac{1}{n}+1)}}(Y_1^{n+1}\frac{dY_2}{d\chi}+Y_2^{n+1}\frac{dY_1}{d\chi}) \tag{7.36}$$

7.2.6 Critical State

The critical state concept has also been incorporated in ALTERNAT, by considering the fact that the friction angle corresponding to shearing at constant volume (ϕ_{cv}) should be equal to the true interparticle friction angle (ϕ_{μ}). The critical state component of the model is formed by equating the post peak shear stress level to the shear stress level at zero dilatancy:

$$\exp(-\beta e_v) = \begin{bmatrix} M\left\{(1-\upsilon)+\upsilon\exp\left(-\psi\left(\frac{s_c}{p_a}\right)\right)\right\}+ \\ C\left\{(1+\xi)-\xi\exp\left(-\theta_p\left(\frac{s_c}{p_a}\right)\right)\right\} \end{bmatrix}^{-1} \cdot C\left\{(1+\xi)-\xi\exp\left(-\theta_p\left(\frac{s_c}{p_a}\right)\right)\right\} \tag{7.37}$$

The void ratio at the critical state of the material is therefore a function of the isotropic stress level at the critical state $\left(\frac{s_c}{p_a}\right)$, the post-peak strain softening parameters and the true interparticle friction angle parameters.

7.2.7 Finite Element Implementation

ALTERNAT has been implemented into a finite element code called ALTICA (ALTernat Incremental Computer Algorithm) after Woodward and Molenkamp (1999). ALTICA uses 8 noded quadrilateral and isoparametric 20 noded brick elements for two dimensional and three dimensional analyses respectively. Reduced integration with a 2x2 and 2x2x2 integration rules are used for two and three-dimensional simulations. An initial stress algorithm (Smith and Griffiths, 1997) is applied to determine the next state of stress via either force or displacement increments. This particular algorithm uses a non-linear elastic stiffness matrix, which is symmetric, as a predictor. Although using the elastic component tends to lead to more iteration, it is more stable in strain softening, and storage requirements are significantly reduced. Over each loading increment, an equivalent elastic

solution is found (predictor) and if the stress violates the yield condition, an iterative correction procedure, based on the constitutive model, returns the stress to the failure surface. According to the initial stress method, the displacement is found as follows:

$$du_n^m = K_e^{-1} dF_n^{m-1} \tag{7.38}$$

du is the incremental displacement, dF is total incremental load. K_e^{-1} is the inverse of the global non-linear elastic stiffness matrix and subscript, n and superscript m refer to the increment and iteration number. The total incremental load(dF_n^{m-1}) is composed of the global incremental external load($\{dF^{ext}\}_n^0$), the error in the incremental body load from the previous increment ($\{dF^{err}\}_{n-1}^0$) and the incremental body load ($\{dF^{body}\}_n^{m-1}$)given by:

$$dF_n^{m-1} = \{dF^{ext}\}_n^0 + \{dF^{err}\}_{n-1}^0 + \{dF^{body}\}_n^{m-1} \tag{7.39}$$

$$\{dF^{body}\}_n^{m-1} = \sum_{elements}^{all} \int B^T D^p d\varepsilon_n^{m-1} dV \tag{7.40}$$

where D^p is plastic constitutive matrix, B is strain-displacement matrix relating strain and displacement. Convergence is assumed to be achieved if the normalized change in displacements in two subsequent increments is less than a predefined tolerance.

For a more detailed description of the model and its implementation the reader should refer to Molenkamp (1987, 1990) and Woodward and Molenkamp (1999).

7.2.8 Model Parameters

Table (7.1) gives the list of material parameters characterizing ALTERNAT along with their typical values. There are in total 24 parameters representing different features of granular soil behaviour, as summarized below (Woodward and Molenkamp, 1999):

- Nonlinear elasticity
- Pre peak hardening
- Post peak softening
- Dialatancy based on row's stress-dialatancy theory
- Critical state
- Cyclic mobility
- Cyclic densification
- Tensile strength

Parameter	Description	Typical Value
A	Non-linear elastic model	0.0009
P		1.0
R		0.6
E	Pre-peak strain hardening for triaxial compression	0.02
D		3.3
Q		2.5
N		3.0
L		0.3
M	Post-peak strain softening for triaxial compression	1.5
υ		0.1
ψ		0.2
β		1.13
C	Dilatancy and critical state	0.96
ξ		0.12
θ_p		2.0
ζ		1.13
η	Cyclic mobility	4.0
e_{vi}	Initial void ratio	0.675
e_{vd}	Void ratio at the maximum densification	0.52
k	Plastic densification parameter	1.0
R_p	Plastic potential in the π-plane	0.3
S	Hardening in the π-plane	0.0
σ_t / P_a	Normalized tensile strength	1.0E-5
c / P_a	Normalized cohesion	0.0

Table 7.1. ALTERNAT parameters with their typical values (Woodward and Molenkamp, 1999)

7.2.9 Model Calibration

In order to represent specific soil behaviour under different stress paths, the constitutive model should be calibrated; i.e. the model parameters should be determined. Proper calibration of constitutive model plays a crucial role in the success of finite element modelling of geo-structures. The calibration process is traditionally initiated by singling out the effects of every parameters or a small group of parameters. In other words, a certain well-defined mechanical state is found in which the material behaviour is controlled by one or only a couple of material parameters. The parameters are then determined considering the corresponding stress-strain state through a curve fitting approach. This process sometimes proves cumbersome, if not impossible. In many cases it may not be possible to find such a state owing to the complexity and interacting nature of the effects of the parameters. Furthermore, the developed process is usually problem dependent, i.e. each constitutive model has its own calibration method. In addition to theoretical difficulties, such methods often require an advanced set of experimental tests specially designed for the model calibration, which is rarely available in practice.

The calibration procedure can be alternatively treated as an optimization problem in which the model parameters are determined through minimizing a defined error function, representing the difference between simulated and measured responses for available experimental test sets. In other words, by using an optimization technique, a set of model parameters is found which is believed to approximate the experimental test with (almost) minimum discrepancies. While the quality of the calibration is still dependent on the quality and size of the experimental data, there is no need to have any specific set of experimental results which reflects solely the effect of certain parameters. The available data set may comprise several sets of experimental tests with interacting mechanisms, all of which can be used for calibration proposes, as will be explained below. Another major advantage of using the optimization technique is that the calibration procedure is totally independent of the model being calibrated, fundamentally different from classical calibration procedures.

In recent years, various engineering disciplines have used genetic algorithms (GA) to solve optimization problems. GA, which is loosely based on Darwin's theory of evolution, promotes the best sets of solutions, from a solution pool, to survive and produce individuals

that populate the next generation pool of solutions. Applying such a solution filtration scheme for a substantial number of generations may theoretically result in a fitter set of solution(s) to the optimization problem.

GAs are search algorithms, based on the mechanism of natural selection combining a "survival of the fittest" approach with some randomization and mutation techniques. A standard genetic algorithm (SGA) may be summarized as follows:

1. All variables are represented in a binary form and attached together in one block to form "individuals". A "population" is then produced from randomly generated individuals.

2. A "fitness (unfitness) function" is used to evaluate the performance of each individual.

3. The fittest individuals are allowed to "reproduce", resulting in a new "generation". This is done by a mating method called "crossover" which combines the characteristics from two sets of individuals from the current generation to produce those of the next generation. "Mutation" is also applied through random changes to a very small set of the population.

4. The above steps are repeated until the fitness criteria are fulfilled. This searching system theoretically improves the fitness of individuals over successive generations.

Every individual in a GA presents a possible solution for the given optimization problem. In every generation, the individual with higher fitness has a higher probability of survival and reproduction. Most fit individuals are mated to produce a new generation while the less fit individuals tend to "die off" as they are less likely to be chosen for reproduction. Mutation is also employed on a random basis to improve the diversity in the population, ensuring that the solution space is searched properly. This process continually enhances the fitness of the population over generations, eventually leading to an optimum or most fit solution.

A standard genetic algorithm usually operates with a relatively large population size. The usual choice of population size is based on the consensus that a bigger population results in better schema processing, a lesser chance of premature convergence, and better optimal results. As fitness functions have to be evaluated for every single individual, having a larger population size translates into a longer processing time. This issue is especially relevant to advanced constitutive model calibration. In the simplest case, the evaluation of constitutive model performance, against lab test results, may comprise (for example) the following steps:

1- Simulation of the lab test using a single finite element within which the constitutive model is implemented.

2- Comparing the simulation against experimental results in the form of error function (unfitness function)

In the case of an advanced constitutive model, it is obvious that the first step is considerably time consuming, making the optimisation procedure costly in terms of running time, if a large number of evaluations (i.e. number of population by number of generation), is supposed to be conducted. Numbers of evaluations should therefore be reduced while ensuring that the performance of the algorithm would not be adversely affected.

Krishnakumar (1989) introduced the concept of Micro Genetic Algorithm (MGA) for optimization purposes. It is essentially different from SGA in terms of the population size used, as a very small population size is employed in MGA (in most of cases, including 5 individuals). It is well known that SGA performs poorly with a very small population owing to insufficient information processing and early convergence to non-optimal results. A modified algorithm is therefore proposed for MGA (Krishnakumar, 1989):

1. A micro population of 5 individuals is generated randomly. If the fittest individual is known from previous generations, the other 4 individuals will be generated randomly.

2. The fitness of each individual is determined and the fittest individual is carried to the next generation (elitist strategy).

3. Using a selection strategy, four individuals are paired to produce four new individuals for the following generation, adopting the so-called crossover technique.

4. Convergence of the population is checked; if the population is converged, the procedure restarts from step 1 (start and restart strategy). Otherwise the optimization loop continues by going to step 2.

Unlike SGA which is prone to premature convergence, in the case of MGA, "the start and restart" strategy helps in avoiding the premature convergence, and consequently the algorithm is always looking for a better solution (Krishnakumar, 1989). It should be noted that mutation is not applied in the MGA algorithm, as enough diversity is already present in the algorithm. In a few reported applications, it has been shown that MGA can successfully find the optimum solution and outperform the SGA in terms of the number of function evaluations (e.g. Krishnakumar, 1989; Carroll, 1996). Krishnakumar (1989) particularly noted that a small population with a start and restart procedure performs better than a large population in reaching the near-optimal region. Detailed descriptions of SGA and MGA and their computational implementation are beyond the scope of this research and can be found (for example) in Goldberg (1988) and Krishnakumar (1989).

In order to calibrate constitutive models such as ALTERNAT, a Micro genetic alogorthim driver is developed. Figure (7.7) illustrates the calibration procedure using MGA. The MGA driver only evaluates the performance of every set of parameters based on their associated simulation error and reproduces the next generation of parameters. A single finite element, in which the constitutive model (here, ALTERNAT) is implemented, simulates the lab tests (e.g. triaxial compression) for every set of parameters. Simulation error is then determined comparing the simulated and measured response which is fed back into the MGA. Simulation error, which defines the magnitude of unfitness function for a certain set of material parameters, is used in the MGA process. The calibration procedure is continued until the difference between simulated and measured response is minimised. As

can be seen, the calibration methodology is totally independent of the constitutive model being calibrated.

Error or unfitness function is defined as below:

$$EF = \alpha \sum_{n} \left(\frac{T^s - T^e}{T^e} \right) + \beta \sum_{n} \left(\frac{E^s - E^e}{E^e} \right) \tag{7.41}$$

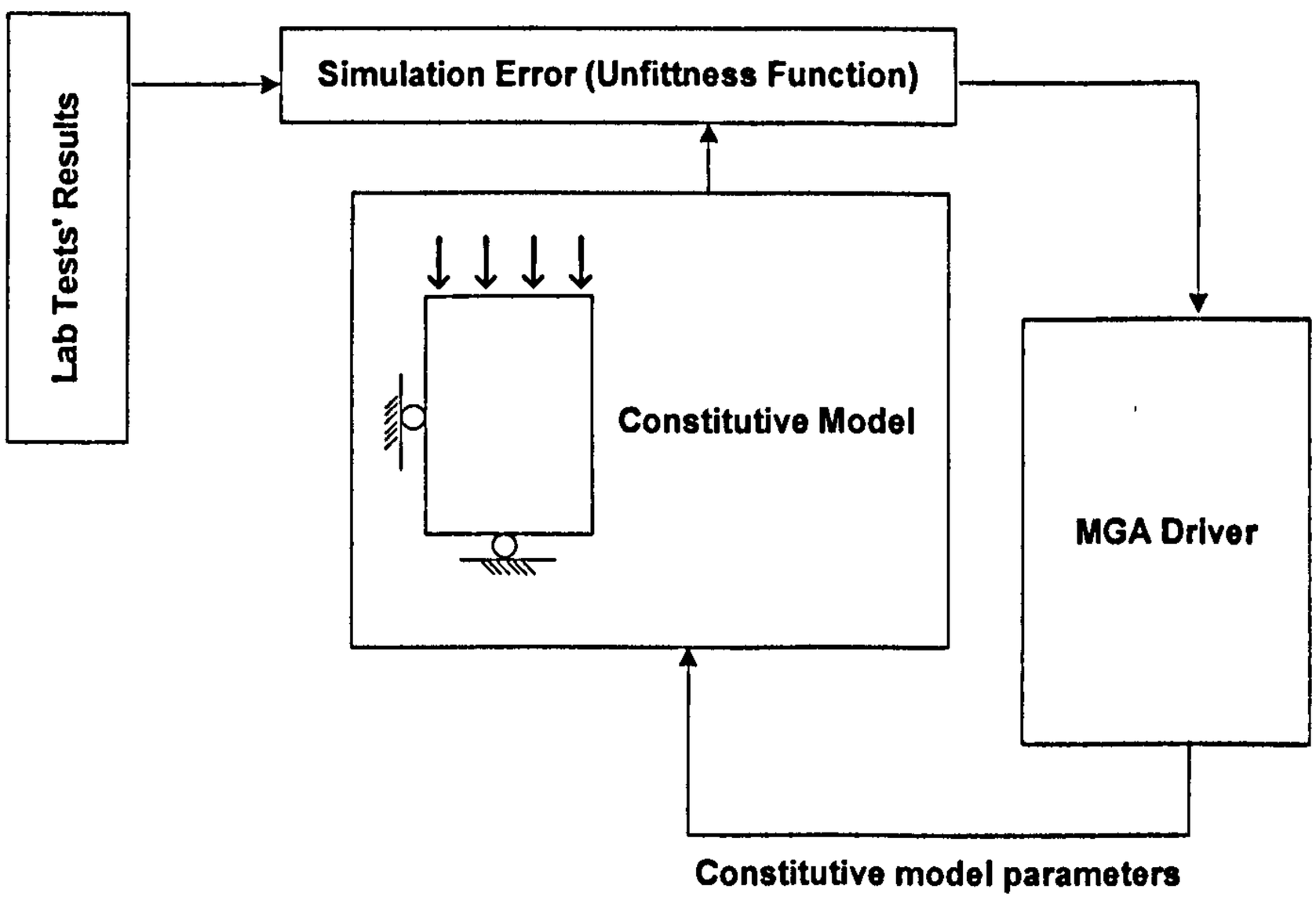

Figure (7.7). Calibration of a constitutive model using the Micro Genetic Algorithm

In which T and E denotes the stress and strain responses respectively. Superscripts s and e denote simulated and experimentally measured responses. n is number of lab tests available under different stress/strain conditions. α and β are the weighting coefficients (in present application, $\alpha = \beta = 0.5$). Such an error function takes into account both stress and strain responses in the optimisation process. In other words, if this error function is minimized, the calibrated constitutive model is believed to give the (near) best approximation of both strain and stress responses, compared with experiments.

To study different granular soils, ALTERNAT is calibrated to six cohesionless granular soils, namely Toyoura, Hostun, Nevada, Ersak sands and Tan and Mia-Liao silty sands at different relative density levels using currently available triaxial test data obtained from the literature (Meimon *et al.*, 1991; Arulmoli *et al.*, 1992; Briaud and Gibbens,1994; Huang *et al.*, 1999; Maeda and Miura, 1999a and b; Woodward and Nesnas, 2000). κ *and* η are related to cyclic response and therefore taken as constants for footing simulations under monotonic loading. Initial and final void ratios are also known from experiments. R_p, S, ξ and β are considered to be constant, as suggested by Woodward and Molenkamp (1999). However, other parameters need to be determined in the calibration procedure. The calibrated parameters are presented in Table (7.2). Calibration of ALTERNAT to Nevada, Hostun and Ersak are taken from Woodward and Molenkamp (1999) and Woodward and Nesnas (2000). It should be noted that Woodward and Molenkamp (1999) calibrated ALTERNAT against both undrained cyclic and drained monotonic responses of Nevada sand. The calibration to other granular soils was, however, performed by the author.

To demonstrate how the calibration procedure works, as an example, the calibration of ALTERNAT to drained triaxial test results on Toyoura sand of 70% relative density under three different confining pressures is described in detail. In this case volumetric strain and stress ratio are taken as the strain and stress measures to define the error function according to Equation (7.41). Figure (7.8) gives the normalised least error (pertaining to the best set of parameters in every generation) against number of generations. It can be seen that the simulation error is decreasing with the number of generations, if the best set of parameters in every generation is concerned. Although a number of potential local optimums are noted in the error function, it is clearly observed that the optimisation procedure is not trapped in local optimums and manages to find the (near) best solution, thanks to the "start and restart" strategy. Figure (7.9) depicts the average error (for the population in a given generation) with the number of generations. Although the general trend reveals that the average error is decreasing with the number of generations in an overall view, the trend is not smooth and the average error sometimes increases from one generation to the next. It clearly shows that the micro genetic algorithm does not guarantee that the average behaviour of the population will be improved from one generation to the next. This does not pose any problem because the sole aim of the optimisation is to find the optimum

solution as quickly as possible, not a population of solutions with optimum average behaviour. However, it implies that the performance measures for micro-genetic algorithms, should be based on the best-so-far solution, rather than on any average performance, also noted by Krishnakumar (1989).

Parameters	Ersak Sand	Toyoura Sand		Nevada Sand	Hostun Sand		Mia-Liao silty sand (MLS)	Tan silty sand
		D_r=50%	D_r=70%	D_r=40%	Loose	Medium	D_r=50%	Dr=55%
Non-linear elasticity								
A	0.0009	0.011	0.011	0.0012	0.011	0.011	0.011	0.0012
P	0.6	0.28	0.28	0.6	0.268	0.268	0.28	0.6
R	1	0.5	0.5	0.6	1	1	0.5	0.6
Pre-peak Hardening								
E	0.02	0.04	0.04	0.016	0.4	0.361	0.18	0.03
D	3.3	3.21	3.21	3.3	3.2	4.61	3	3.3
Q	2.5	2.6	2.6	2.5	2.6	2.6	2.5	2.5
N	3	7.19	7.19	3	7.19	7.2	3.75	3
L	0.3	0.1	0.1	0.3	0.1	0.1	0.4	0.3
Post-peak strain softening								
M	1.5	1.9	1.9	1.62	1.63	1.659	1.91	1.8
υ	0.1	0.1	0.1	0.1	0.1	0.1	0.1	0.1
ψ	0.2	0.25	0.25	0.2	0.25	0.25	0.25	0.2
β	1.13	1.13	1.13	1.13	1.13	1.13	1.13	1.13
Dilatancy and critical state								
C	0.96	0.9	0.8	0.93	0.97	0.93	1	1
ξ	0.08	0.12	0.12	0.12	0.12	0.12	0.12	0.12
θ_p	2	0.2	0.2	2	2	0.2	0.2	2
ζ	1.13	1.13	1.13	1.13	1.13	1.13	1.13	1.13
Cyclic Mobility								
η	4	4	4	4	4	4	4	4
Initial void ratio								
e_{vi}	0.675	0.808	0.737	0.73	0.73	0.64	0.81	0.77
Minimum void ratio (after densification)								
e_{vd}	0.525	0.625	0.625	0.567	0.567	0.567	0.57	0.64
plastic densification Parameter								
κ	1	1	1	10	1	1	1	1
Plastic potential and Hardening in the Л-plane								
R_p	0.3	0.8	0.8	0.3	0.3	0.3	0.3	0.3
S	0	0	0	0	0	0	0	0

Table 7.2. Calibrated parameters of ALTERNAT based on currently available data in the literature for different granular soils

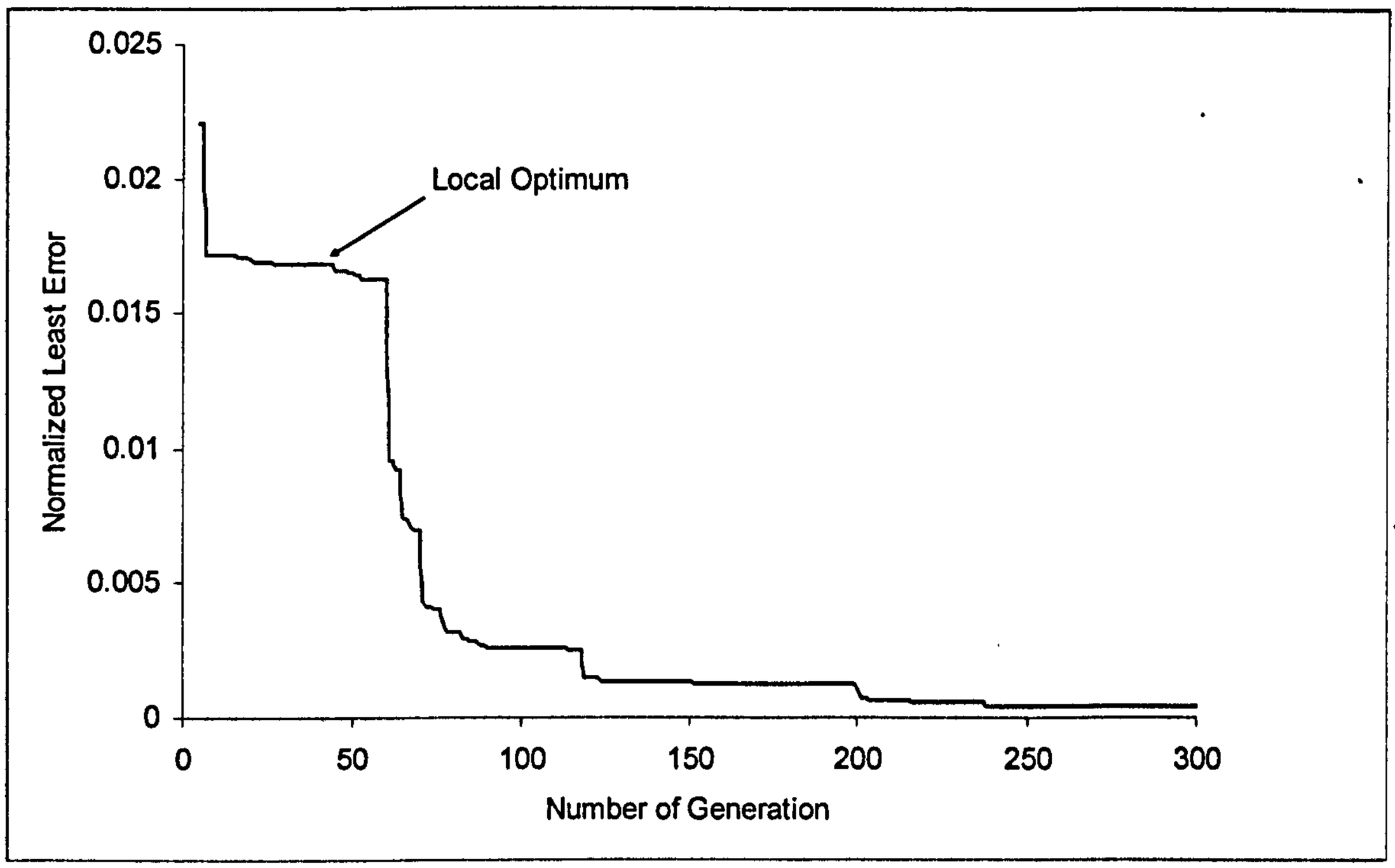

Figure 7.8. Least Error Evolution over generations for calibration of ALTERNAT to Toyoura sand at 70% relative density

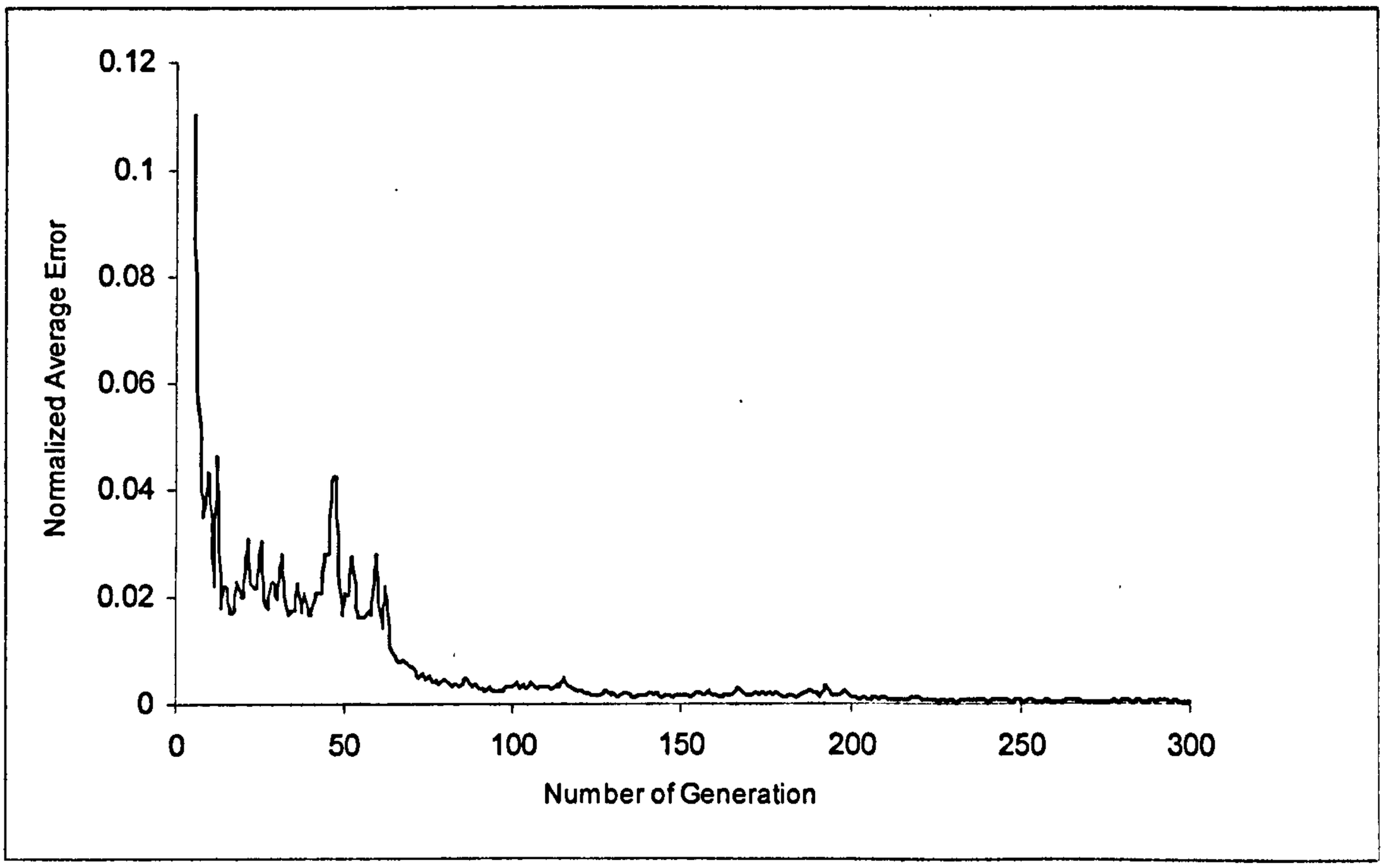

Figure 7.9. Mean Error Evolution over generations for calibration of ALTERNAT to Toyoura sand at 70% relative density

For generations 4 and 300, simulation capabilities of the model are compared against lab measurements under different confining pressures, as given in Figure (7.10). The improvement in the simulation capacity of the constitutive model, over generations, is clearly shown. While the best set of parameters in generation 4 is unable to simulate any of stress-strain curves, the best set of parameters in generation 300 simulate both stress and strain responses satisfactorily.

7.3 Footing Problem

7.3.1 Problem Definition and Literature Review

A footing system (e.g. railway track) is usually investigated in terms of two fundamental questions: first how much settlement would be induced under the applied load and second, what would be the bearing capacity of the system. A brief review of the approaches taken to address these two fundamental questions is given as follows.

The bearing capacity of surface footings on granular soils has been a challenging problem approached experimentally, analytically and numerically by numerous researchers. The most widely used equation to estimate the bearing capacity of surface footings on cohesionless soil was proposed by Terzaghi (1943) employing a semi-empirical bearing capacity factor N_γ:

$$q_u = \frac{1}{2}\gamma B N_\gamma \tag{7.42}$$

where γ and B are the soil unit weight and footing width respectively. N_γ (Meyerhof, 1963; Vesić, 1973; Hansen, 1970) is classically considered to be a function of a constant friction angle ϕ, implying linearity of q_u with footing width. Nevertheless, several experimental observations (e.g. Golder, 1941; Ovesen, 1975; Kutter *et al.*, 1988) showed that the bearing capacity does not, in general, increase linearly with footing width. This

phenomenon was described as a scale effect describing the decrease in N_γ with increasing footing width.

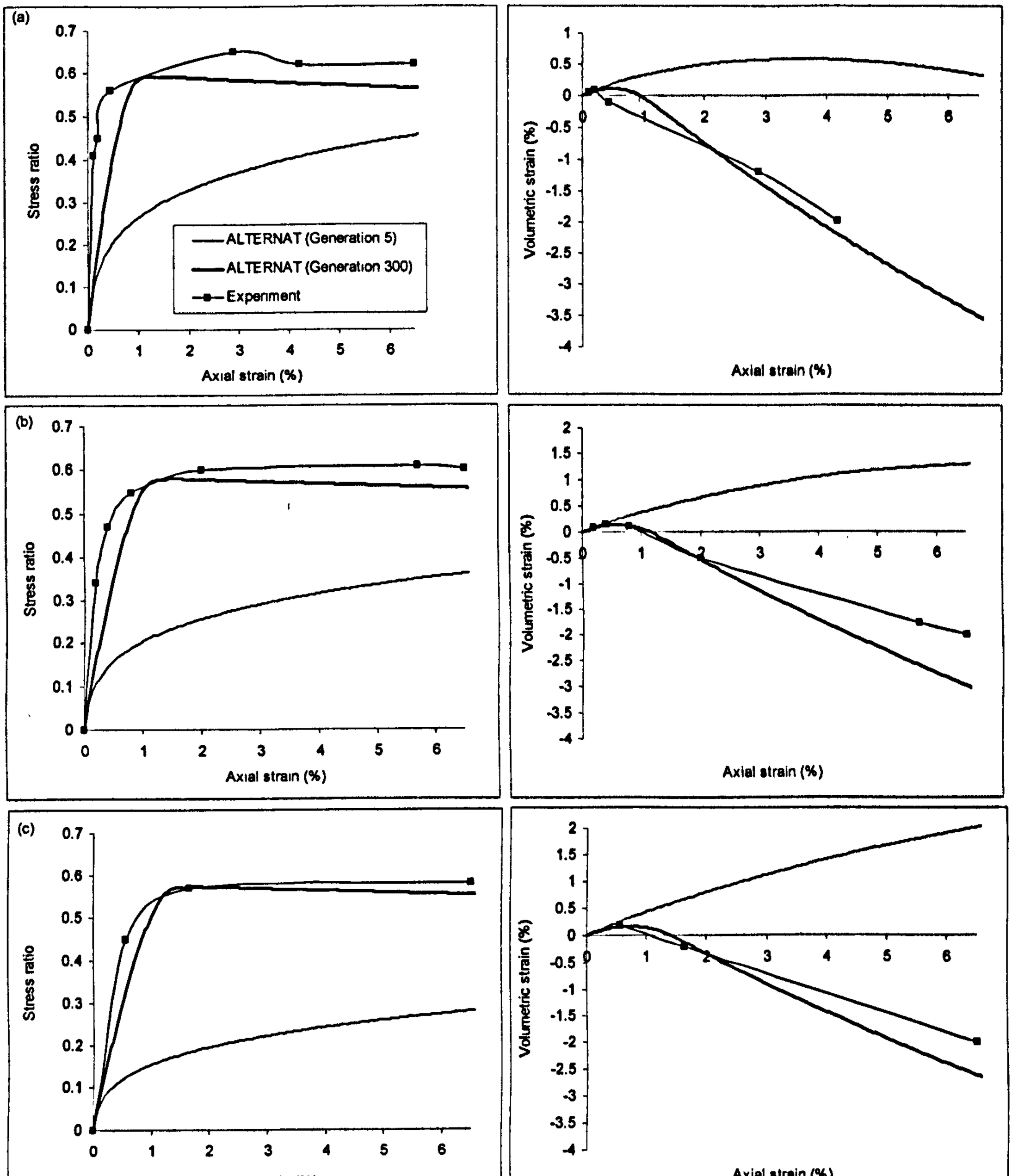

Figure 7.10. Improvement of simulation capability of ALTERNAT with generations for drain triaxial response of Toyoura sand at Dr=70% (a) $\sigma_c = 98$ kPa (b) $\sigma_c = 196$ kPa (c) $\sigma_c = 392$ kPa

De Beer (1965) explained that the scale effect may be primarily the result of a decrease in the friction angle with increasing mean effective stress and a grain size effect produced by progressive failure. However, further studies indicated that grain size changes caused by progressive failure have no significant effect on bearing capacity (Hettler and Gudehus, 1988). Muh (1963) described the progressive failure effect in a different way. By gradually increasing the footing load the shear strength is not simultaneously mobilized at all points on the slip surface. At first it is mobilised at points of highest shear strains, progressing then to other points in the soil body along the developing slip plane. This implies that in the failure state, while some points on the slip surface just reach failure, other points are experiencing strain softening or strain hardening behaviour. By performing centrifuge tests, Aiban and Znidarčić (1995) observed this effect and showed that the assumption of the peak friction angle in classical formulae overestimates the ultimate bearing capacity. Perkins and Madson (2000) noted that the presented results of Yamaguchi *et al.* (1976;1977) indicated that progressive failure becomes more prominent with increasing footing width, or confining pressure. However, in some experiments the potential for progressive failure, being defined by differences between the peak and residual strength of the soil, was more significant as the footing width decreased according to observations from shear tests on dense sands (Yamaguchi *et al.*, 1976). Perkins and Madson (2000) described the two counteracting mechanisms and pointed out the difficulty in predicting the point at which one effect dominates the other. They proposed that the combination of the two mechanisms can be described in terms of the strength-dilatancy of the granular soil.

Such complex solutions, accounting for the pressure dependency of shear strength, post peak behaviour and dilatancy (nonassociativity in the context of plasticity theory), cannot be addressed analytically but need numerical approaches. It eventually necessitates using an advanced soil model within a numerical programme for the determination of the bearing capacity of cohesionless soils. As noted by Banimahd and Woodward (2006), most of the previous numerical analyses have, however, been performed on relatively simple models. Griffiths (1982) conducted a finite element analysis on rigid shallow foundations using an elastic-perfectly plastic model with a Mohr-Coulomb failure surface, reporting good agreement between analytical and numerical results. Nevertheless, he discussed the difficulties in obtaining reasonable solutions for N_γ for friction angles greater than 35^0, partly because of high shear concentrations beneath the footing edge (termed as the

singularity problem) which require considerable stress redistribution. Considering the same kind of model, numerical limit analyses were also performed using finite elements (Hijiaj *et al*, 2005) and finite difference methods (Ukritchon *et al*., 2003). Furthermore, Griffiths (1982) and Woodward and Berenji (2001) investigated Terzaghi's superposition theory and stated that it can be used with confidence, provided that accurate values of the bearing capacity factors are known. Woodward and Griffiths (1998) clearly showed that simple models cannot predict reductions in N_γ with footing width, emphasizing the mesh effects. The sensitivity of the solution to the meshing and singularity has also been discussed by De Borst and Vermeer (1984) and Frydman and Burd (1997).

Simonini (1993) and Uneo *et al.* (1998) implemented a simple stress level dependent non-linear failure criterion, and observed the scale effects on N_γ, although they did not address dilatancy and post-peak behavioural effects. However, the effect of non-associativity has been discussed by several researchers using elastic perfectly plastic models with linear failure surfaces (i.e. considering a non stress dependent friction angle). Performing finite element analysis, De Borst and Vermeer (1984) stated that the bearing capacity of strip and smooth circular footings depend very little on the angle of dilatancy, similar to the findings of Davis and Booker (1973) and Zienkiewicz *et al.*(1975). However, Manoharan and Dasgupta (1995) and Frydman and Burd(1997) commented that this independency is valid for low friction angles only ($\phi < 30^0$); they showed that N_γ decreases when non-normality increases for $\phi > 30^0$ and a greater effect is expected for higher friction angles. These outcomes were later confirmed for both circular footings (Erikson and Drescher, 2002) and strip footings (Yin *et al.*, 2001).

Even if the bearing capacity is sufficiently high, serviceability of the corresponding superstructure may be of concern as granular soil foundations can still exhibit considerable settlement in a short peroid, i.e. immediately after load application. The critical settlement is often reached before the ultimate failure state of the foundation is achieved and therefore controls the design process in many cases. Numerous studies have concentrated on the prediction of shallow footing settlement on granular soils, mostly using linear elastic approaches. As the undisturbed sampling of such soils is very difficult, these methods are based mainly on in-situ tests results, including Standard Penetration Test (SPT), Cone penetration Test (CPT), Dilatometer Modulus Test (DMT) and Pressure Meter Test (PMT).

They usually estimate the soil compressibility with considerations of footing size and unit load (e.g. Papadopoulos 1992; Burland and Burbidge, 1985; De Beer, 1965).

Many of the existing methods incorporate relatively simple assumptions and can therefore fail to give consistent results with respect to actual observations (Poulos, 1999). Jardine *et al.* (1986) commented that "although linear elasticity remains a convenient tool for expressing measurements of soil stiffness, unless the nonlinear nature of soils is taken into account, soil-structure interaction computations and the interpretation of the field measurements can be misleading". Using a finite element analysis with a nonlinear hyperbolic constitutive relationship, Lee and Salgado (2002) showed that the conventional CPT based approach (Schmertmann *et al.*, 1978), which assumes linear elasticity, cannot accurately predict the settlement of shallow foundations on sands. They indicated that the soil stiffness is highly dependent on the stress-strain characteristics and density. Non-linearity in the stress-strain behaviour of shallow foundations on sand and its effect on the prediction of settlement were also confirmed by Lehane and Fahey (2002).

These modifications have significantly improved settlement prediction. However, Fuch and Kaliakin (2000) stated that elasticity-based approaches alone cannot capture all aspects of settlement response. It has been shown experimentally that the limit of purely elastic behaviour of granular soils ends at a small shear strain level (Bellotti *et al.*, 1989) and consequently local plastic zones can be developed in the soil under the footings at working loads. By performing finite element analysis of rigid surface footings, and considering non-linear elastic perfect plastic and linear elastic models, Jardine *et al.* (1986) observed a plastic zone formed at the footing edge at very small loads which influenced the displacement and stress distributions. As a consequence of these plastic zones, some areas inside the loading bulb beneath the footing may undergo post peak strain softening behaviour, even in a tolerable range of footing settlement. As plasticity starts to evolve in a granular media, the plastic flow rule and yielding criteria may substantially affect the deformation characteristics of the footing. For example, in granular soils, associated flow rules usually lead to excessive dilation and hence non-associated flow rules are preferred (Woodward, 2001).

As ALTERNAT realistically accounts for stress dependency of the friction angle, strain-softening-hardening and non-associativity, it constitutes an appropriate soil constitutive model to be used in studying the footing problem which exhibits a complicated behaviour as discussed above. Bearing capacity and settlement characteristics of a granular surface foundation are studied using a finite element code in which ALTERNAT is implemented in the next sections. The numerical considerations which are taken into account in the footing simulations are discussed first.

7.3.2 Numerical Considerations

7.3.2.1 Mesh Considerations

Owing to symmetry, only one half of the footing is considered, as shown in Figure (7.11). The dimensions of the mesh are chosen to be 10B×10B, where B is the footing diameter or width (strip footings). Analyses were performed to ensure that the finite element domain contained the failure surface and that the whole mechanism was not constrained by the finite element boundaries.

Bearing resistance is mobilized by applying equal displacement increments to the nodes beneath one half of the footing. As discussed by Griffiths (1982), displacement control provides numerical convenience, better stability, less iterations and represents physical reality. Applying equal displacement increments implies a rigid foundation; a flexible foundation can be modelled by imposing equal force increments to the footing nodes.

According to Woodward and Griffiths (1998), the numerical values of bearing capacity are significantly affected by the ratio of the footing width to depth of the first row of elements (B/D). While an adaptive approach can be utilized, they commented that a uniform mesh of constant ratio B/D > 6 gave reasonable results. In the present study, B/D =6.67 is chosen after performing initial analyses to verify this observation.

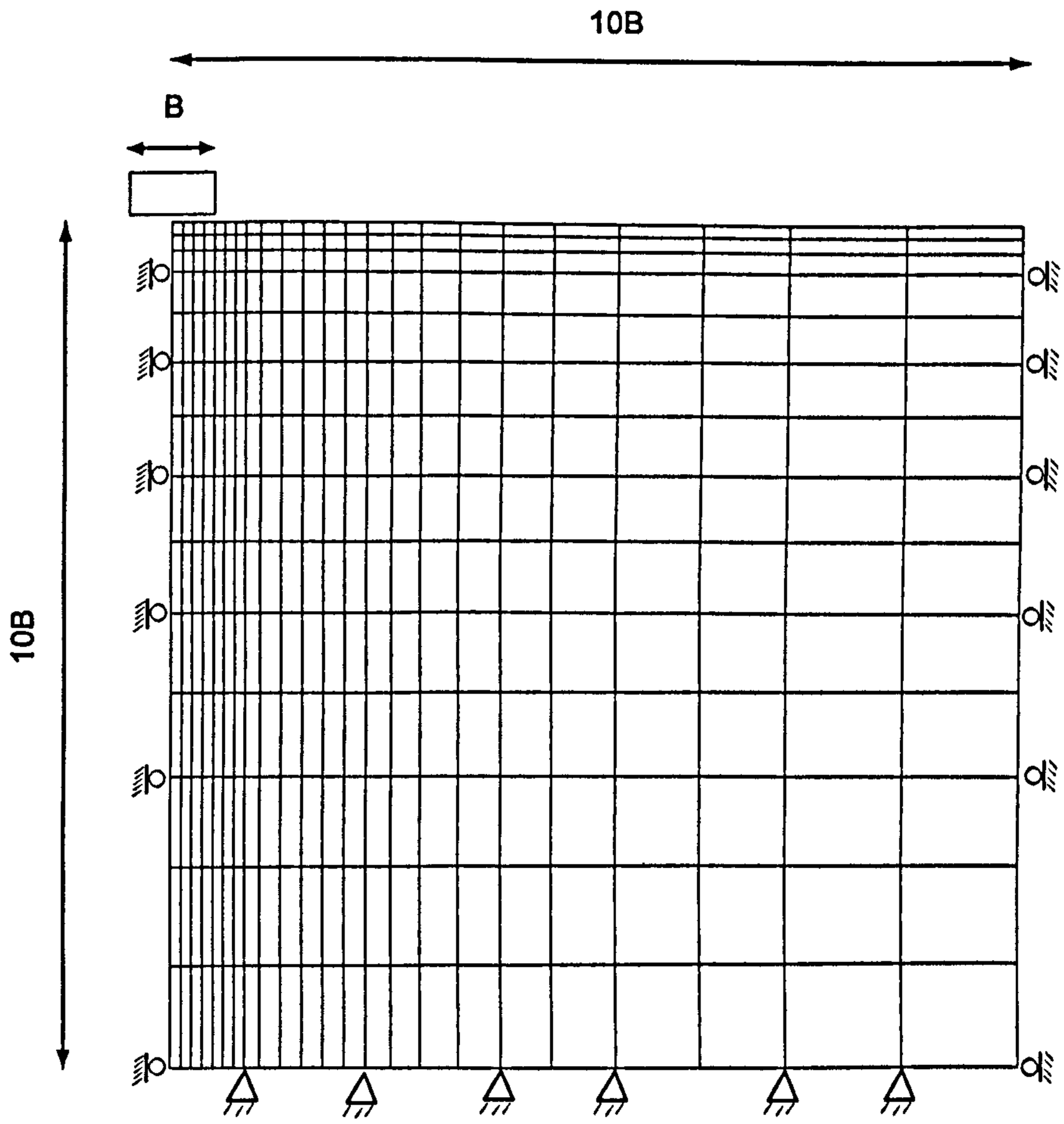

Figure 7.11. Finite element mesh used for foundation studies

7.3.2.2 Footing Edge Singularity

Even with the use of finer meshes close to the footing edge, the footing edge singularity can generate significant numerical problems during the simulation of granular surface foundations. Just outside the footing edge the mean stress is zero (or close to), hence the shear strength is close to zero. However, the mean stress directly under the footing significantly increases as the footing is loaded, giving an increase in the mobilized shear stress. These abrupt changes (discontinuities) in the stress field lead to large out of balance forces, causing significant convergence problems. These problems can be treated using either special elements that account for the discontinuity (Van Langen and Vermeer, 1991; Shiau *et al.* , 2003; Hjiaj *et al.*, 2005) or by applying a stress redistribution algorithm

(Griffiths, 1982 and Frydman and Burd, 1997). In this work, a stress redistribution approach is proposed to prevent large out of balance forces in this zone.

If the singularity is developing, the constitutive model is effectively switched off and any additional outer balanced incremental stresses are redistributed to adjacent Gauss points according to the following relationship (Banimahd and Woodward, 2006):

$$F_{corr} = \int_{A} [B]^{T} [D^{e(p)}] \{\Delta\varepsilon\} dA \tag{7.43}$$

where $[D^{e(p)}]$ is the elastic (plastic) stiffness matrix for that Gauss point, i.e. either a plastic, elasto-plastic or elastic stiffness matrix can be applied in the redistribution process. [B] is the displacement-strain matrix. $\Delta\varepsilon$ and A are the predicted strain increment and the elemental area respectively. Figure (7.12) shows typical pressure-normalized settlement (i.e. settlement normalized by footing diameter) curves from the footing analyses using different stress redistribution methods. It is clear that while the numerical analysis has not converged using no stress redistribution, both elastic and plastic redistributions give good convergence leading to similar peak results.

7.3.2.3 Computation of the Footing Pressure and Ultimate Bearing Capacity

Footing pressure is calculated using three different methods. The first method simply averages the vertical component of the Gauss point stresses (σ_y) directly under footing:

$$q_{avg} = \frac{\sum_{1}^{2n} R \times \sigma_y}{2n} - S_{int} \tag{7.44}$$

where n is the number of direct contact elements and R is the element scaling factor for axi-symmetric analysis. A correction for the initial surcharge (S_{int}) is made. The second method

(Equation 7.45) determines the equivalent vertical nodal forces (F_y) for the direct footing contact elements only (n).

$$q_{bts} = \frac{\sum_{1}^{n} F_y}{A_f} - S_{\text{int}} \qquad \text{where,} \quad F_y = \int_A B^T \sigma dA \tag{7.45}$$

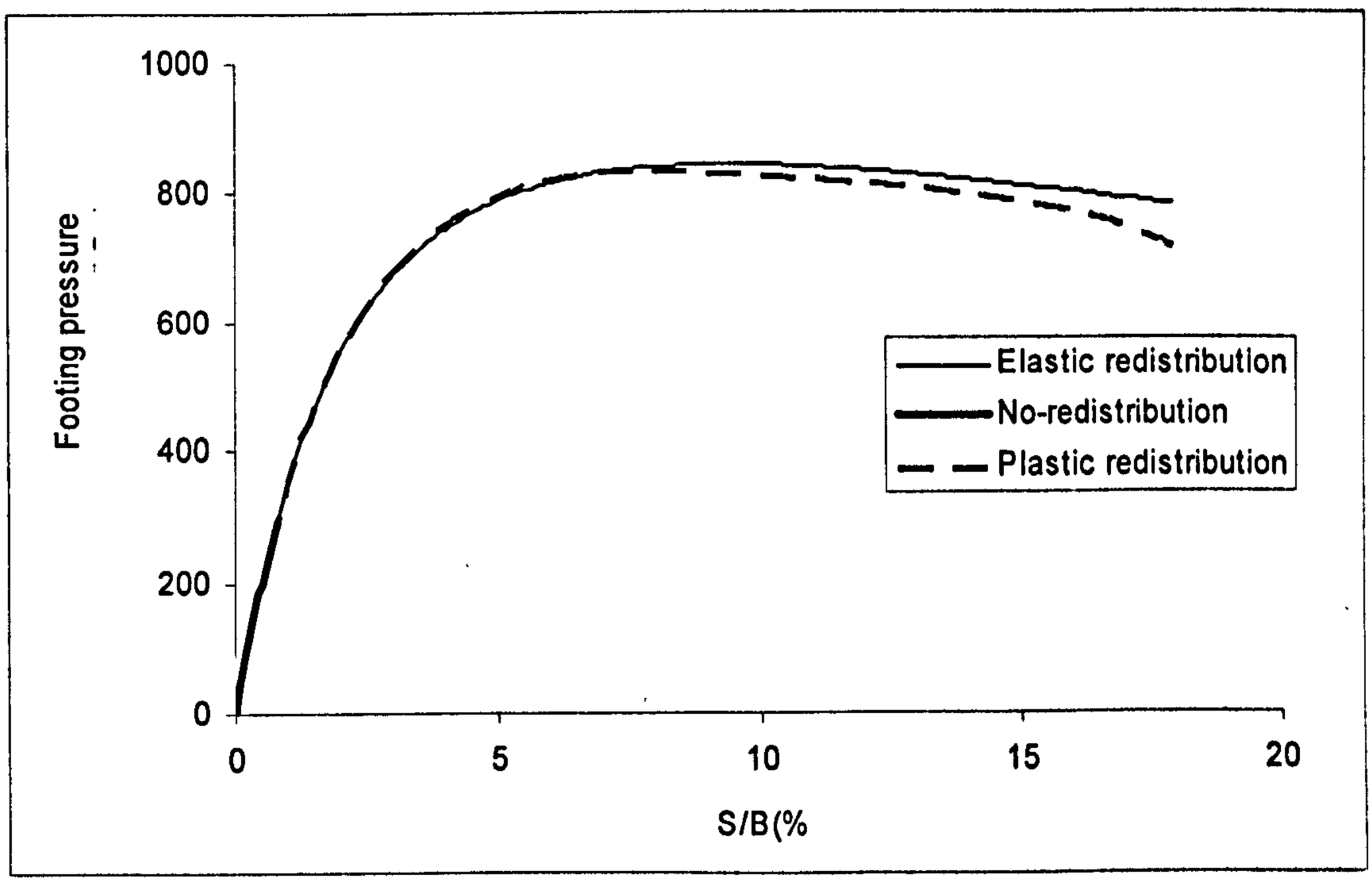

Figure7.12. The effect of stress redistribution methods on typical footing response (Banimahd and Woodward, 2006)

m and A_f are the number of surface elements and the area of the footing respectively. A is elemental area. The third method (Equation 7.46) also includes the stress contribution from the adjacent elements to the footing edge.

$$q_{btsa} = \frac{\sum_{1}^{m} F_y}{A_f} - S_{\text{int}} \tag{7.46}$$

As shown in Figure (7.13), these three different formulas give remarkably similar results after applying stress redistribution. Agreement of the results in equations (7.45) and (7.46) particularly underlines the fact that adjacent elements to the footing edge contribute very little to the bearing capacity of the footing due to a discontinuous stress field which exists around the footing edge. This shows good performance of the applied stress redistribution method for the singularity.

The ultimate bearing capacity is defined as the maximum computed pressure beneath the footing. In displacement controlled analysis, failure is considered as the state after which the displacement-footing pressure curve levels out or softens despite further displacement increments. N_γ is then calculated as follows:

$$N_\gamma = \left(\frac{2q}{\gamma B}\right)_{\max} \tag{7.47}$$

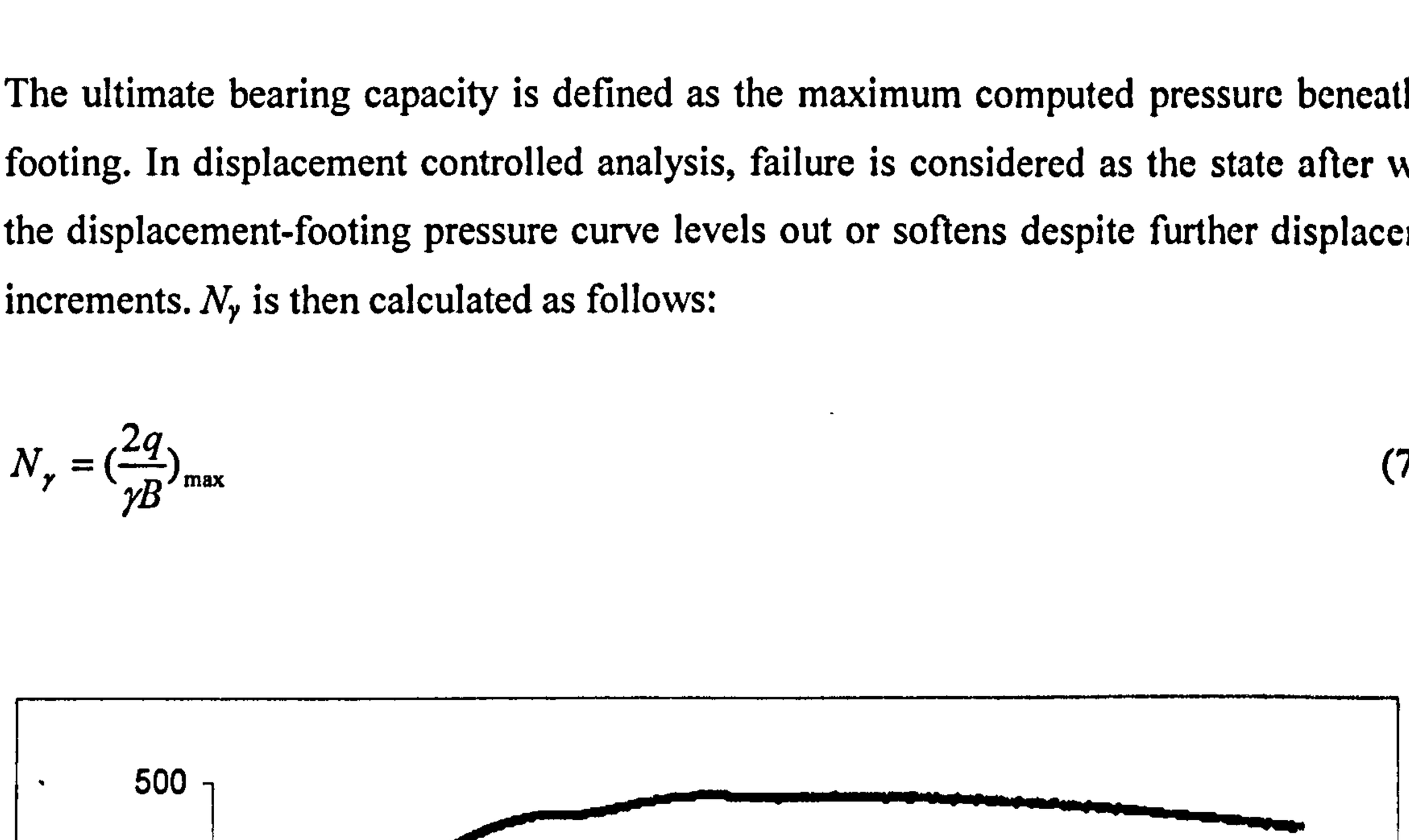

Figure 7.13. Typical footing responses for different methods of footing pressure calculations (Banimahd and Woodward, 2006)

7.3.3 Modelling Versus Experiments

In the current study, a set of footing loading tests is used to evaluate the present modelling approach. These tests were performed at the Texas A&M University campus for the spread footing prediction symposium, i.e. the Settlement 94 ASCE Special Conference (Briaud and Gibbens, 1994). The footings are square and are of 3, 2.5, 1.5 and 1 metre widths. The underlying soil is predominantly Tan silty sand (TSS) down to a depth of 11m with fine content varying with depth, from 2% to 30%. The footings were then founded at a depth of 0.76 m. Owing to the upper soil removal and geologic conditions of the site (coastal plain), the soil is considerably over-consolidated. Full details of the soil characteristics and test procedure can be found in Briaud and Gibbens (1994).

Among others, Lee and Salgado (2002) showed that a square footing can be numerically approximated as an axisymmetric one of the same area with no important precision loss. All footing systems are therefore modelled by the proposed finite element model as rough circular footings lying on a layer of the TSS. The footing embedment is simulated by applying equivalent pressure on the upper mesh boundary. ALTERNAT is calibrated to the available drained compression tests on Tan silty sands (Figure 7.14). Figure (7.15) gives the finite element analysis of the footing versus experiment results. It is clearly observed that the proposed approach predicts the deformation behaviour of the footings satisfactorily.

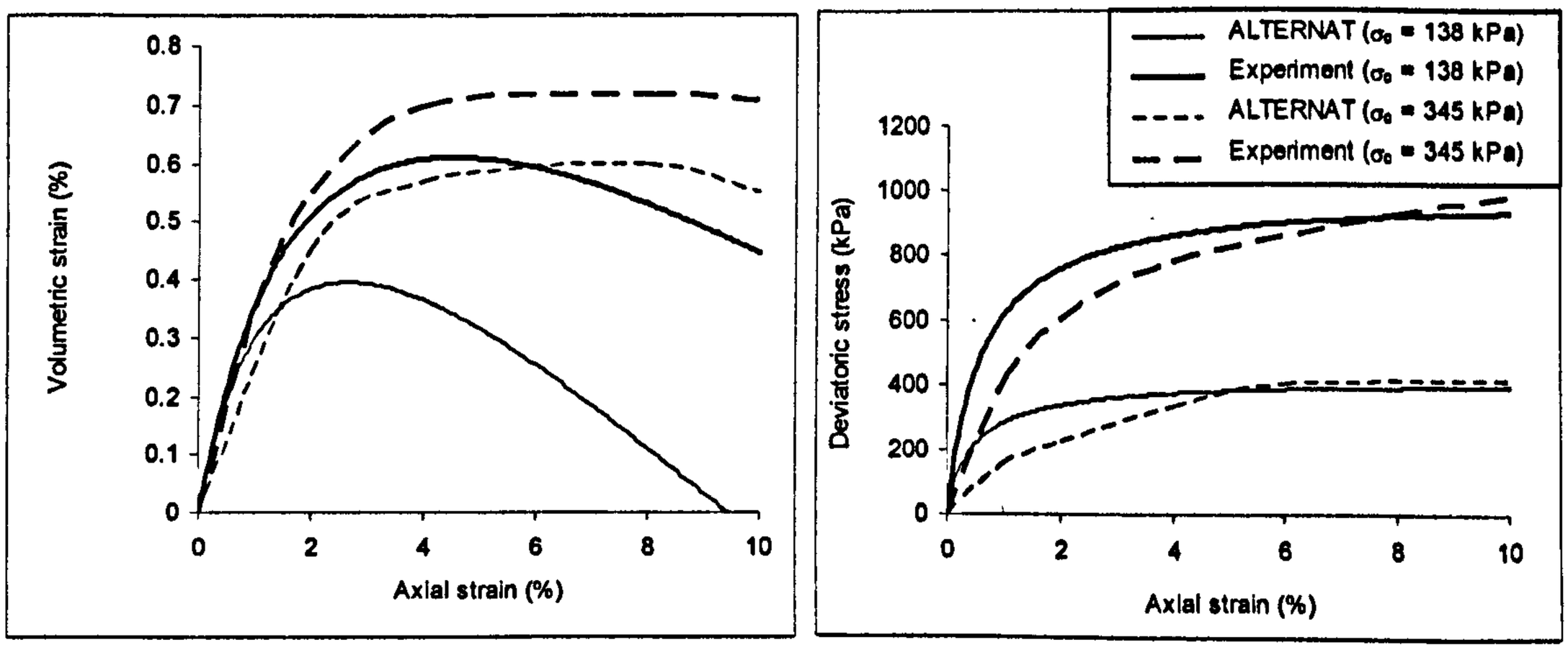

Figure 7.14. ALTERNAT response against drained triaxial results for Tan silty sand

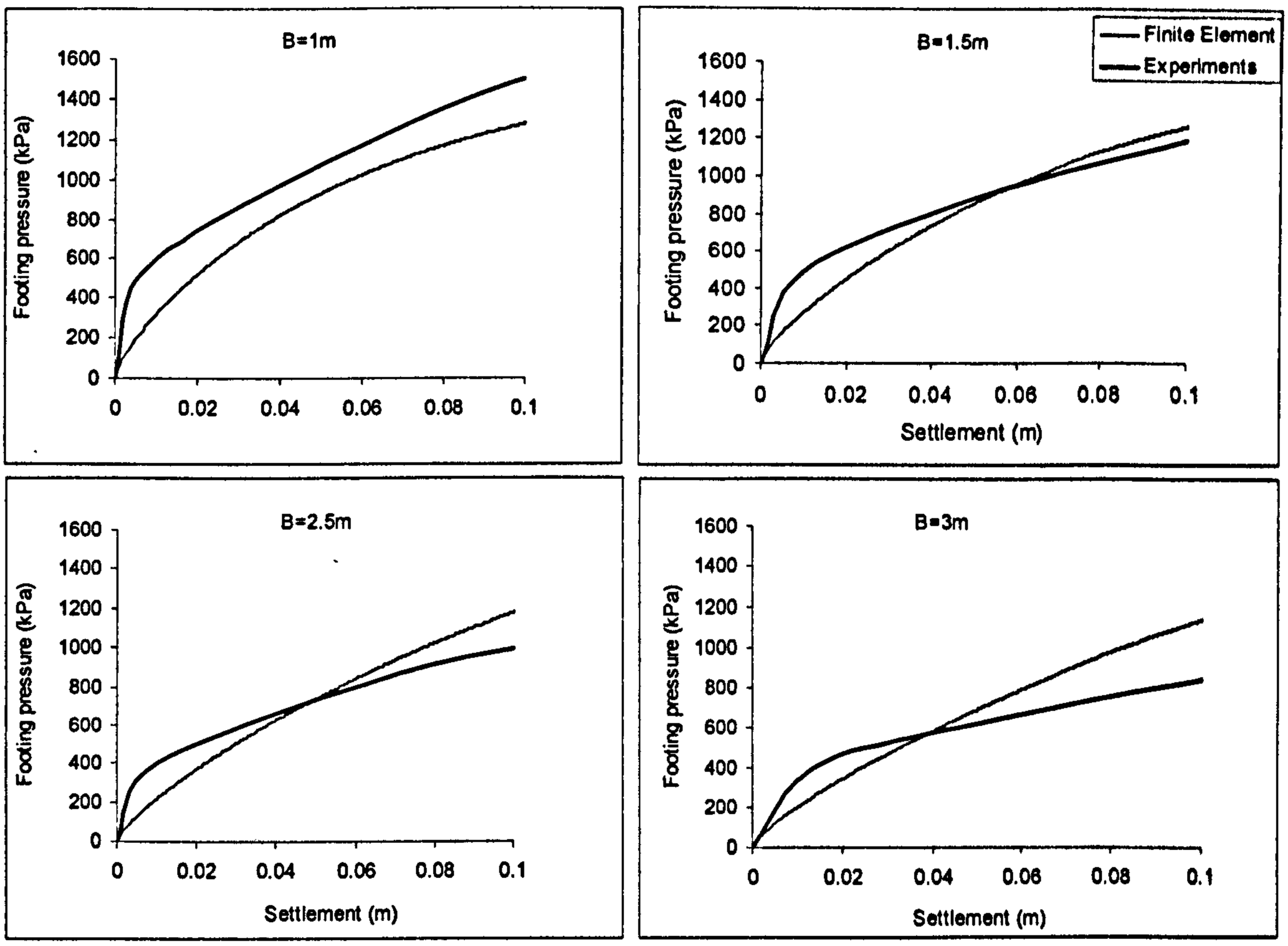

Figure 7.15. Simulated against measured responses of a square footing on Tan silty sand

7.3.4 Effect of Initial Isotropy

The self weight is included in a non-embedded footing system. The vertical stress therefore increases linearly with depth from zero at surface. The effect of lateral earth pressure at rest coefficient (K_0) is shown, as a typical foundation response, in Figure (7.16). According to Figure (7.16), at very small displacements, the effect of K_0 seems to be limited. At a medium displacement level, the effect of K_0 is more pronounced; a decrease in K_0 increases the footing settlement at a given footing pressure. In terms of bearing capacity, a slight decrease is also observed with decreases in K_0, as shown in Figure (7.17). In this study, the effect of K_0 is not studied further and hence initial isotropy is assumed.

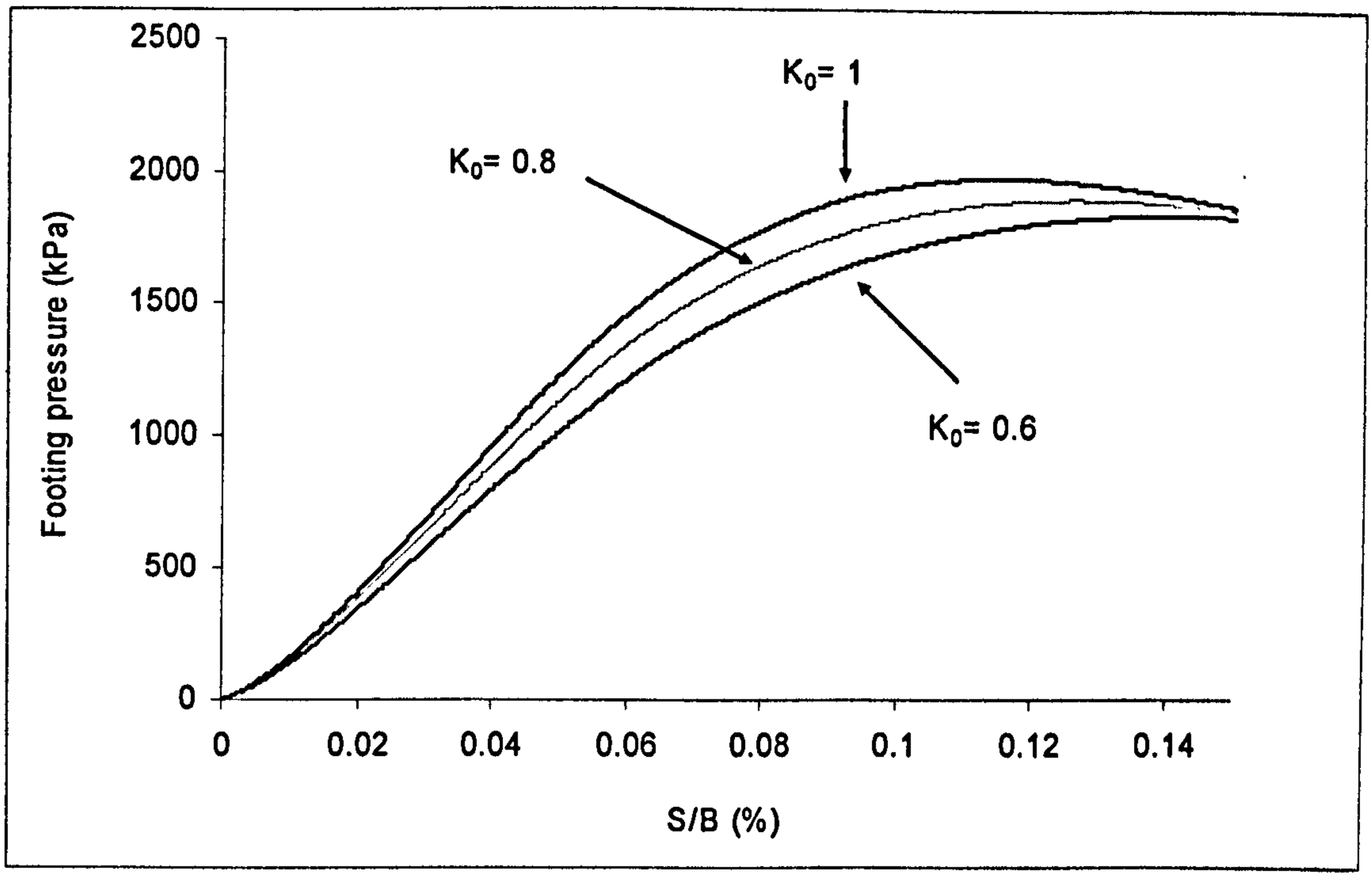

Figure 7.16. Effect of initial anisotropy on the settlement behaviour of a rough circular footing (B=3m) on Toyoura sand at D_r=70%

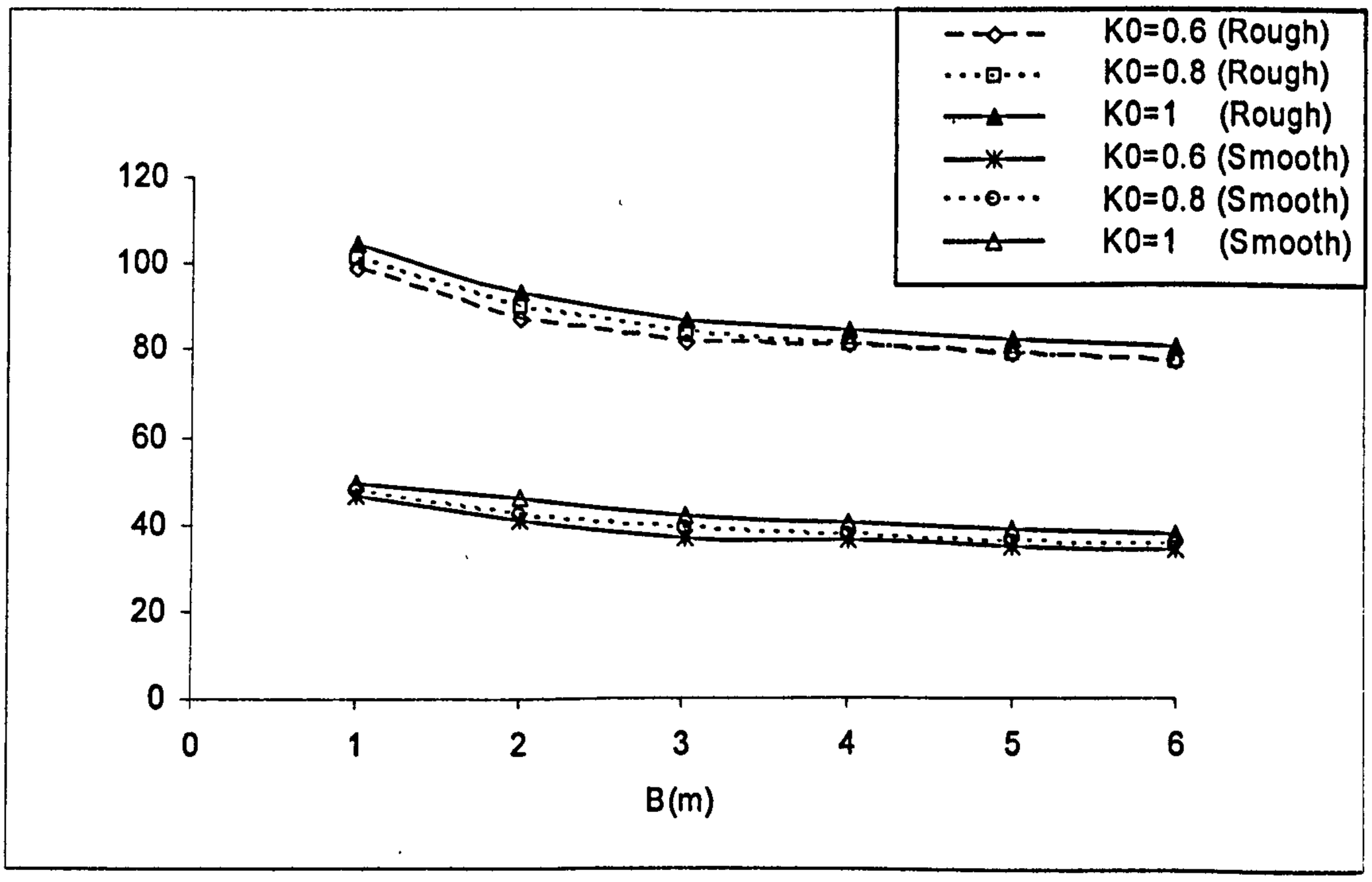

Figure 7.17. Effect of initial anisotropy on the bearing capacity factor N_γ for circular footings on Toyoura sand (D_r=70%) (Banimahd and Woodward, 2006)

7.3.5 Effect of Footing Size and Soil Density on N_γ

Figures (7.18a and 7.18b) show the N_γ analysis results for circular foundations at different diameters in both the smooth and rough cases. For smooth footings, the nodes underneath the footing are free to move horizontally. However, the horizontal movement of these nodes are restrained for rough footings. As expected, N_γ decreases as the diameter increases in both cases. An increase in N_γ with increases in initial relative density, which is caused by the increase in the internal friction angle and a decrease in the strain level at which dilative behaviour commences (Maeda and Miura, 1999a and b), is also observed. More dilative behaviour is observed in denser sands. The effect of density on the dilation of granular foundations at failure is shown in Figures (7.19) and (7.20) (negative volumetric strain denotes dilation). A detailed simulation of granular footing behaviour is therefore achieved when both the friction angle and the dilation rate change, as a result of changing mean stress and density. The scale effects are also observed in plane-strain cases (strip footings) for Nevada, Ersak and Hostun sands, as shown in Figure (7.21).

7.3.6 Effect of Roughness and Shape on The Computation of N_γ

The effect of roughness and shape on N_γ is investigated by considering the following factors:

$$F_r = \frac{N_{\gamma(smooth)}}{N_{\gamma(rough)}} \tag{7.48}$$

$$F_s = \frac{N_{\gamma(circular)}}{N_{\gamma(strip)}} \tag{7.49}$$

where F_r and F_s are roughness and shape factors respectively.

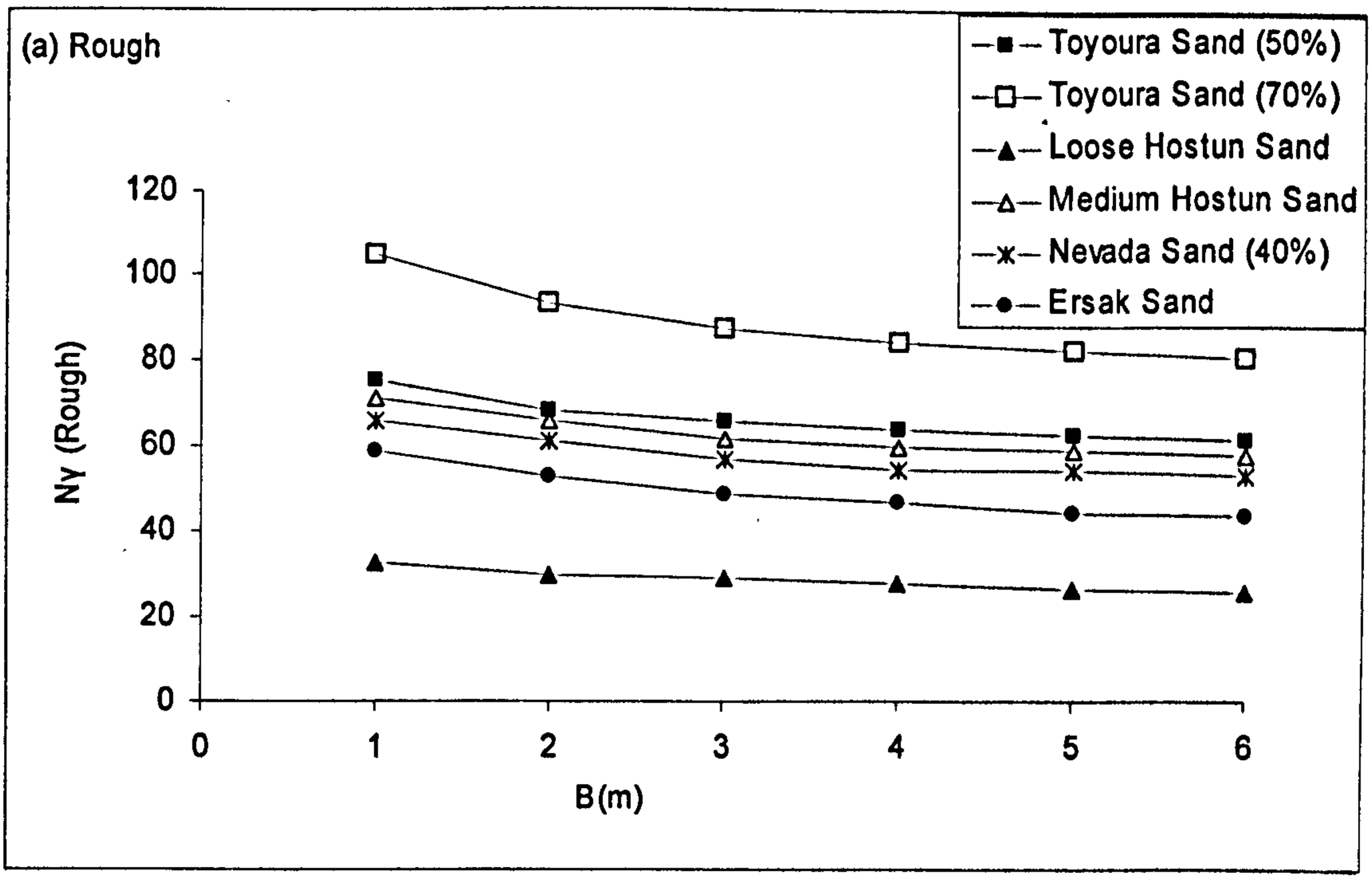

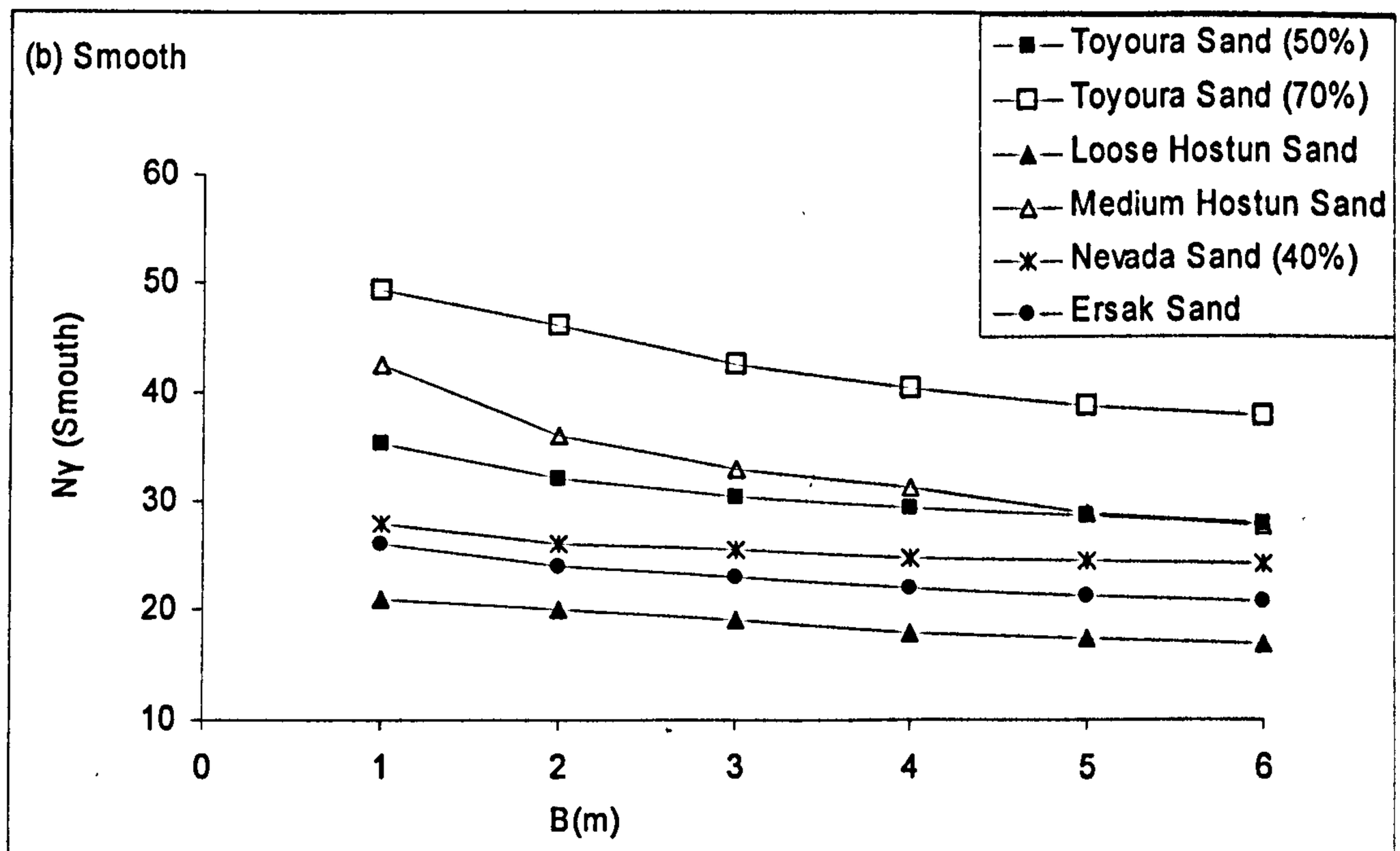

Figure 7.18. The effect of circular footing size on the bearing capacity factor N_γ (a) rough (b) smooth (Banimahd and Woodward, 2006)

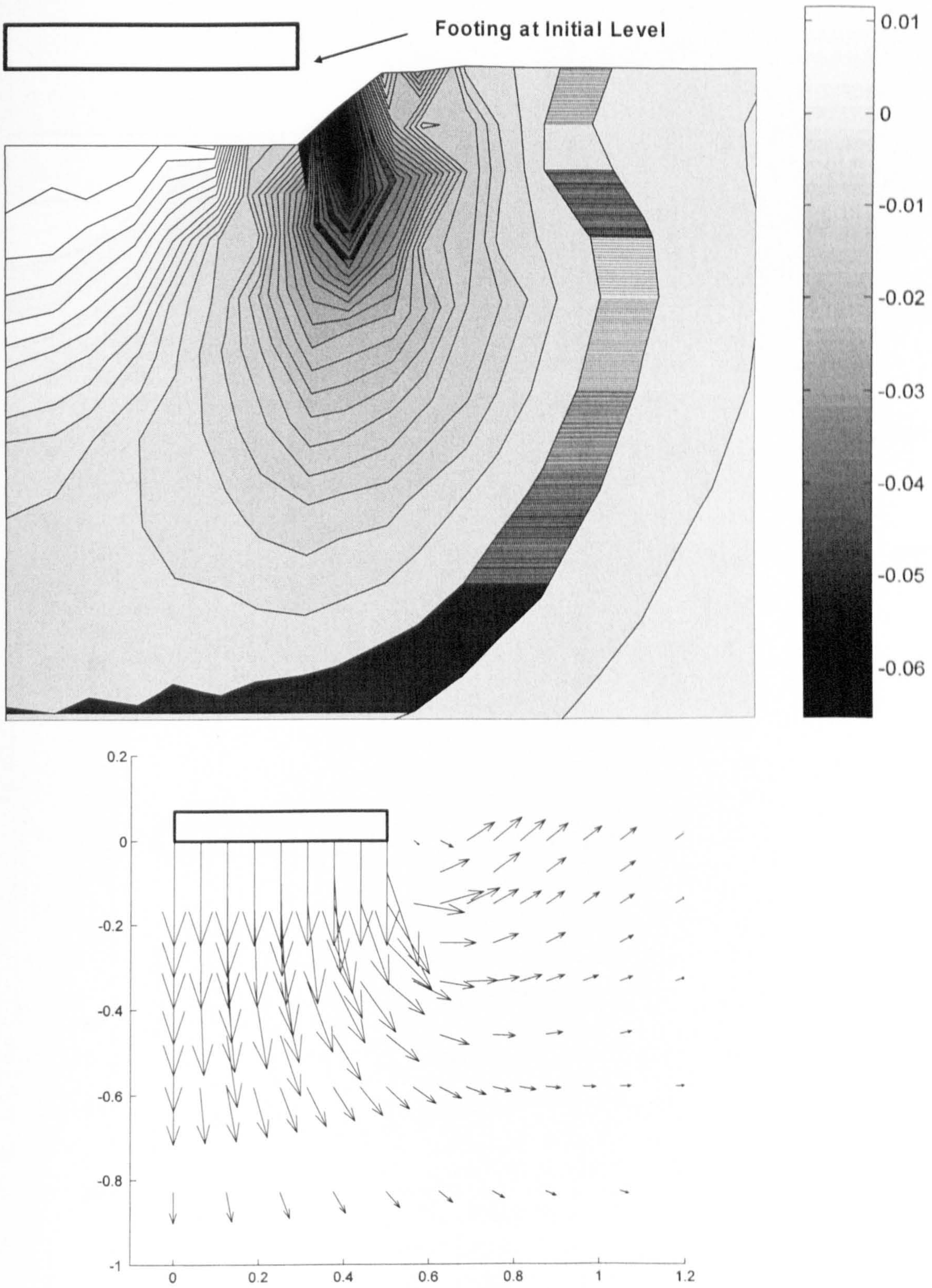

Figure 7.19. Volumetric strain contours and displacement vectors of a rough circular footing at the failure state (B=1 m) on Toyoura sand (D_r=50%) (Banimahd and Woodward, 2006)

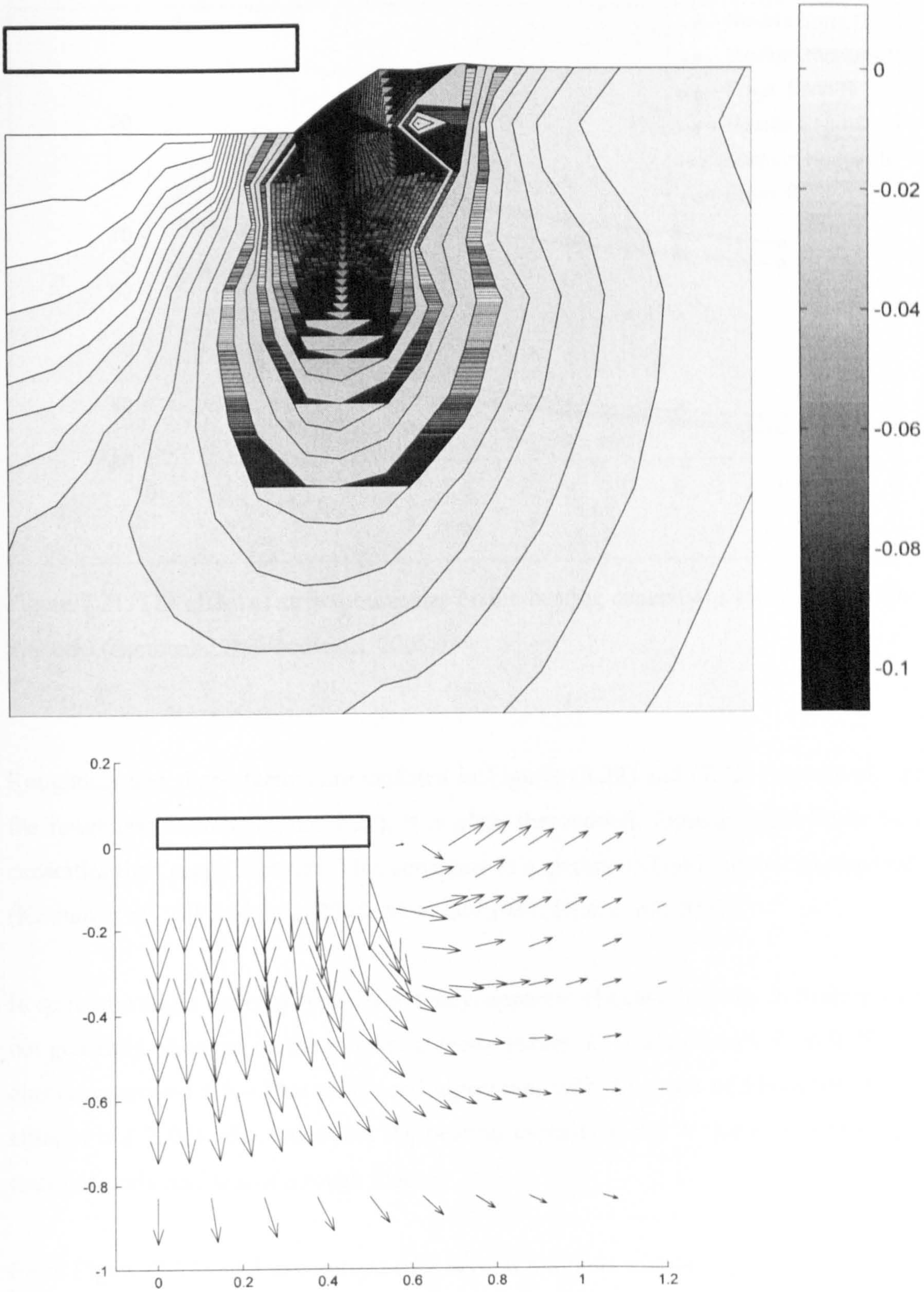

Figure 7.20. Volumetric strain contours and displacement vectors of a rough circular footing at the failure state (B=1 m) on Toyoura sand (D_r=70%) (Banimahd & Woodward, 2006)

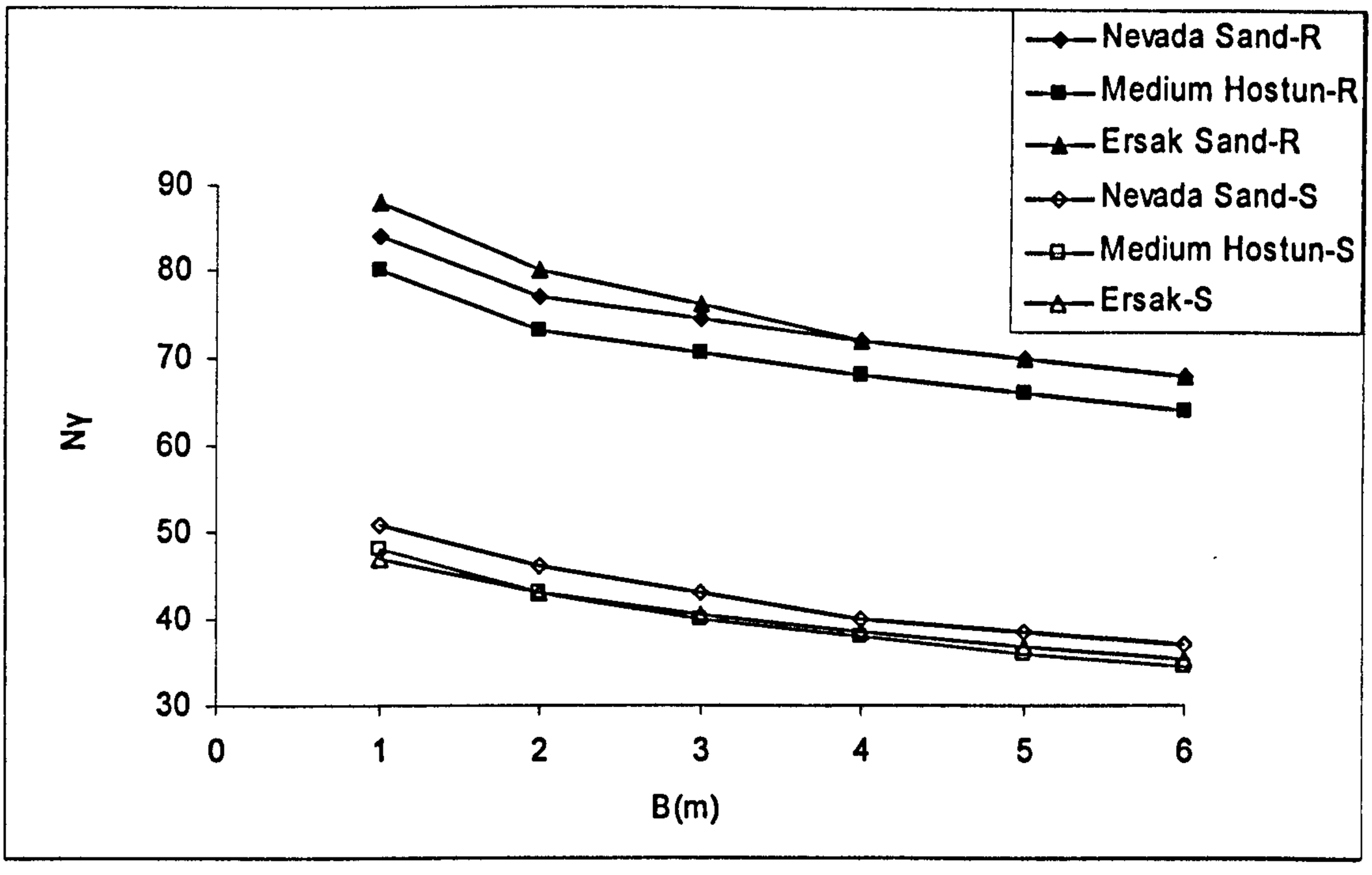

Figure 7.21. The effect of strip footing size on the bearing capacity factor N_γ (R: Rough S: Smooth) (Banimahd & Woodward, 2006)

Roughness and shape factors are depicted in Figures (7.22) and (7.23) respectively. From the roughness factors (Figure 7.22), it is clear that smooth footings yield lower bearing capacities than rough footings. This conforms to experimental and theoretical observations (Kimura *et al.*, 1985; Kumar, 2004; Meyerhof 1951; Hjiaj *et al.*, 2005).

In spite of a slight material type dependency, apparent effects of density or footing size are not generally observed on the roughness factor values. F_r varies from 0.42 to 0.67, mostly clustering around 0.5. This is in good agreement with the work of Meyerhof, 1951 and Hjiaj *et al.*(2005) who found that the bearing capacity factor N_γ for a smooth footing is approximately half that of a rough footing.

From Figure (7.23), and in common with several previous studies (e.g. De Beer, 1970), the bearing capacity factor N_γ for circular footings is less than that of strip footings. The shape factor (F_s) does not appear to depend on the footing size, but appears to vary for different

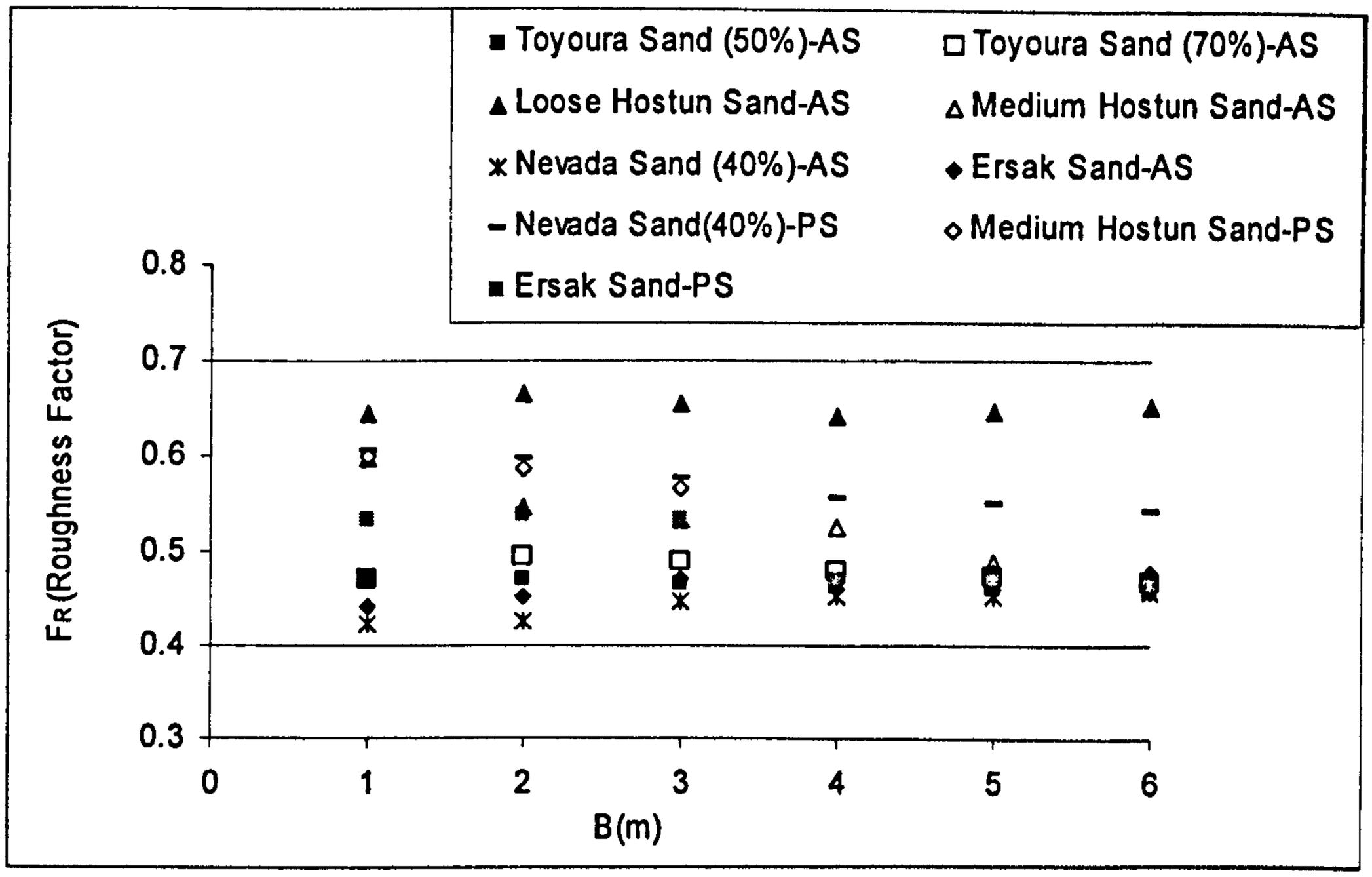

Figure 7.22. Roughness Factor (AS: Axi-Symmetric- PS: Plane Strain) (Banimahd and Woodward, 2006)

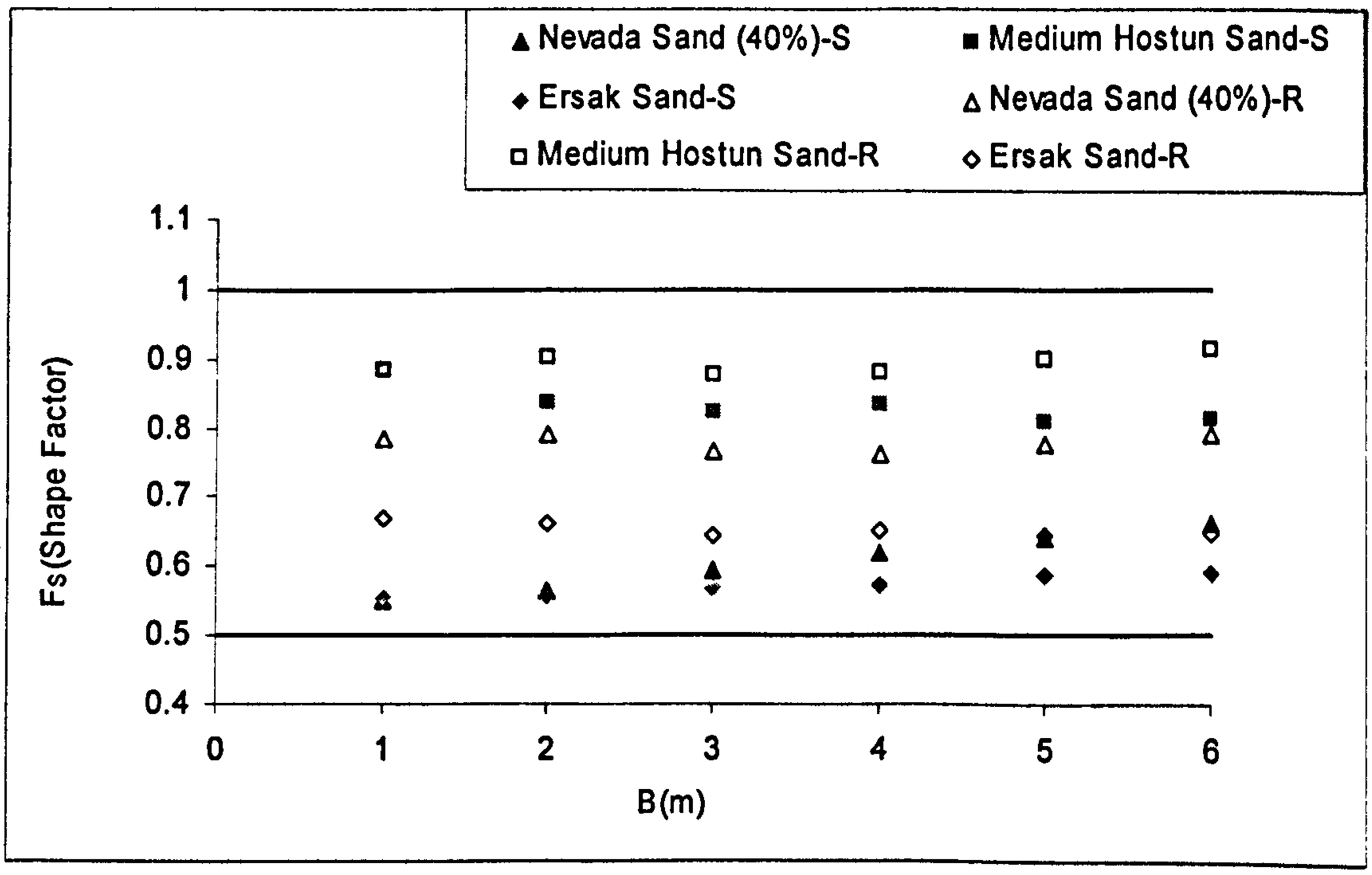

Figure 7.23. Shape Factor (S: Smooth- R: Rough) (Banimahd and Woodward, 2006)

types of granular materials, ranging from 0.55 to 0.91. However, a value of 0.6, as proposed by De Beer (1970) can be used for the shape factor in the general case.

7.3.7 Settlement Characteristics

Figures (7.24) and (7.25) give the axi-symmetric footing responses on Toyoura sand at relative densities of 50% and 70% respectively. At a relative density of 50% relative density the footing behaves in a strain-hardening way, whereas post-peak strain softening is observed on the response of the footing at a relative density of 70%. The strain softening response of the footing on the denser sand can be attributed to its dilatational behaviour, as discussed in Section 7.3.5. As expected, the bigger the footing size, the higher the settlement observed for a given unit load. Denser sand (D_r=70%) also experiences lower settlement than that of looser sand (D_r=50%).

The effect of roughness is also presented in Figures (7.24) and (7.25). The effect of roughness is observed to be generally more pronounced as settlement increases. At relatively large settlements, the rough footing behaves more stiffly than the smooth footing, leading to higher ultimate bearing pressures, as studied previously.

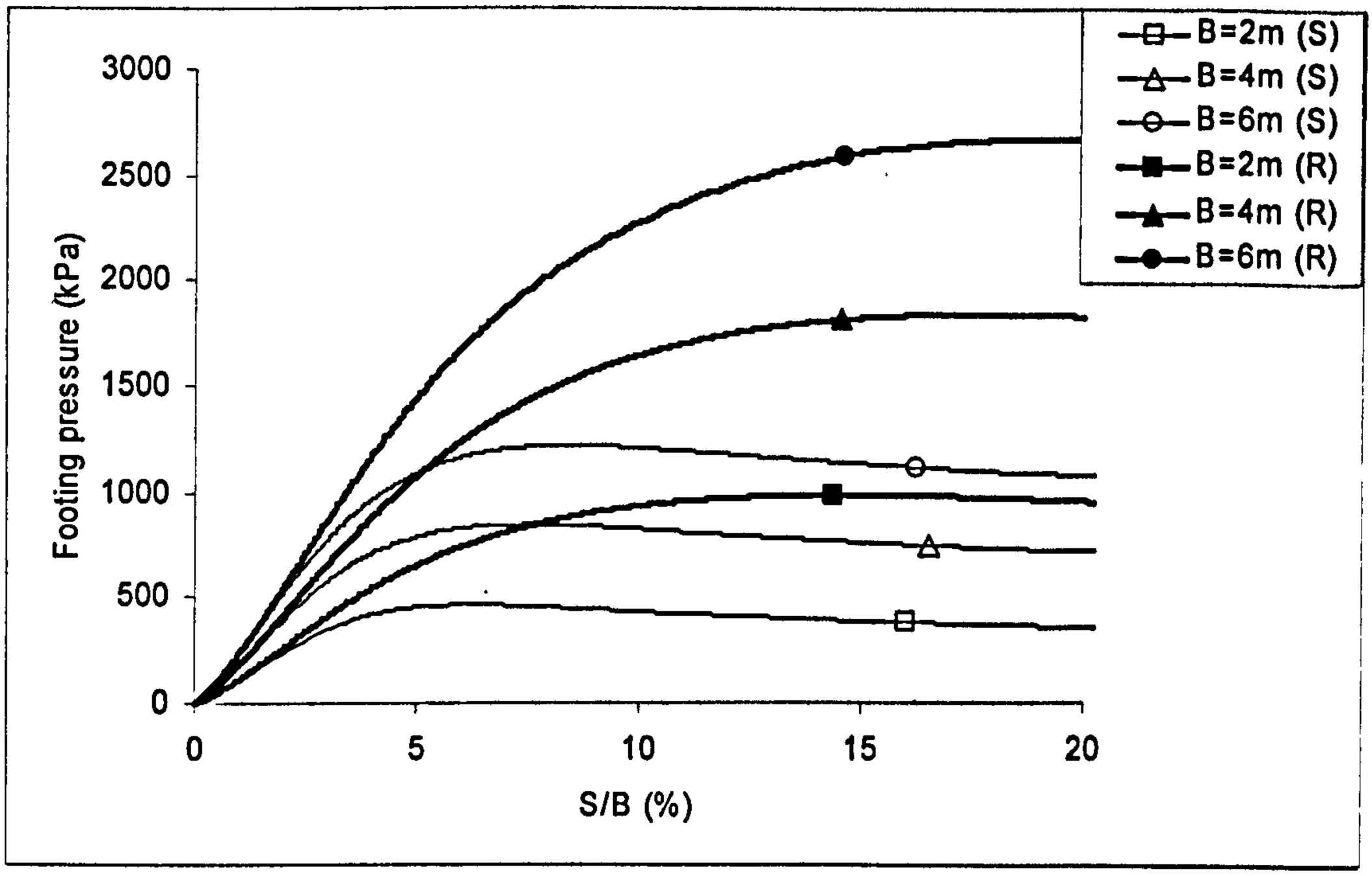

Figure 7.24. Settlement behaviour of a circular footing on Toyoura sand at *Dr*=50% (R: Rough S: Smooth)

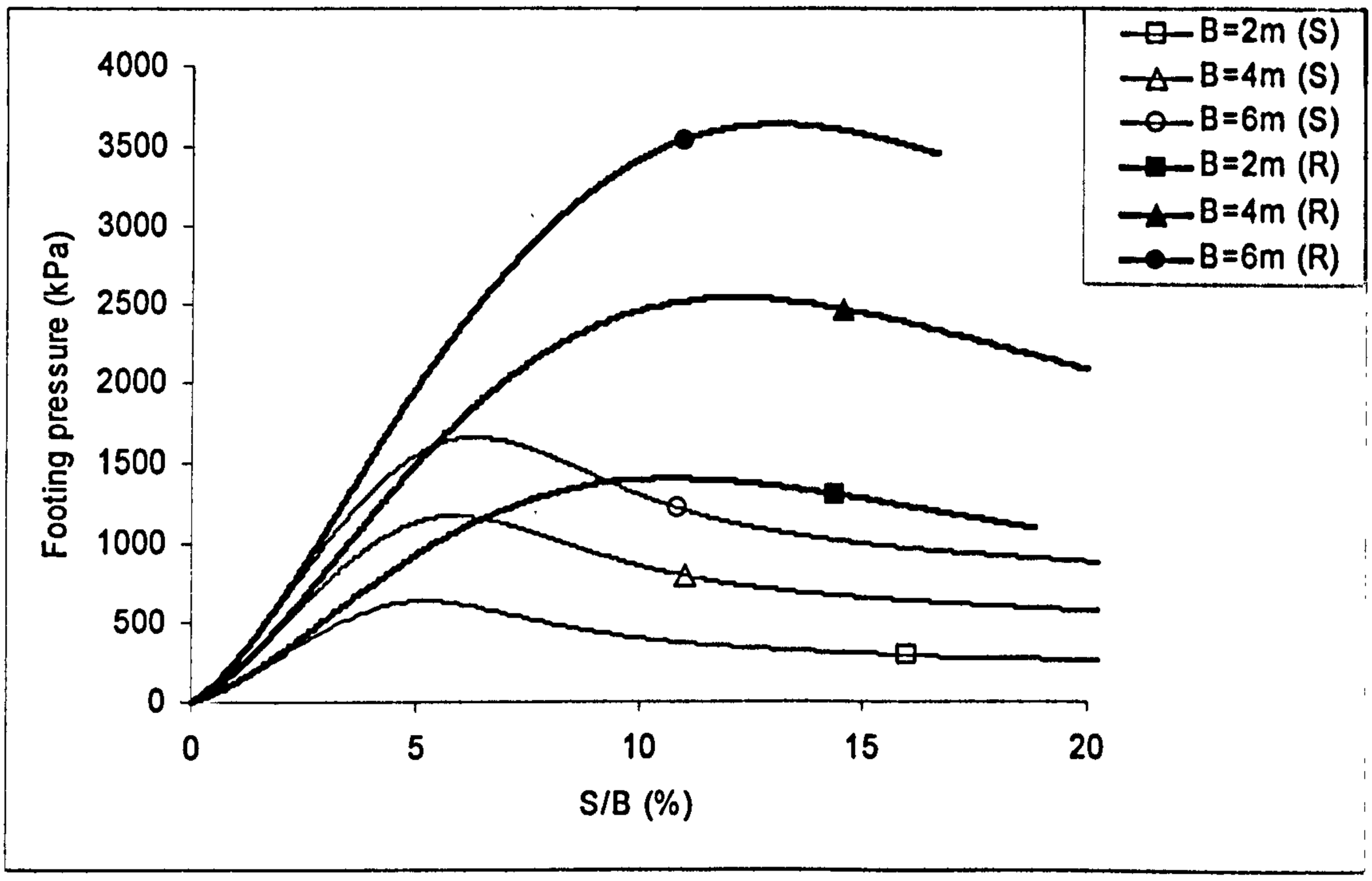

Figure 7.25. Settlement behaviour of a circular footing on Toyoura sand at *Dr*=70% (R: Rough S: Smooth)

According to Figures (7.24) and (7.25), there is a settlement level before which the footing roughness has a limited effect on the foundation response. This settlement level is seen to be about 2% of the footing diameter for all soil densities and footing sizes considered in Figures (7.24) and (7.25). It can therefore be said that the footing response up to a tolerable settlement of 25 mm for common structures (Terzaghi and Peck, 1967; Becker, 1996) remains practically unaffected by roughness if the footing diameter is large (B>2). In addition, as the footing size increases, the settlement level after which the roughness affects the footing response also increases, implying that the response of the footing remains almost unaffected by roughness up to a relatively large settlement for large footings. For example, for a footing diameter of 6 metres, the settlement of the footing up to about 120 mm remains insensitive to the roughness of the footing, which is around 5 times higher than the tolerable settlement in practice.

Subgrade compressibility is defined as the secant of the pressure-settlement curve, i.e. the given settlement to the corresponding pressure (Burland and Burbridge, 1985). Subgrade compressibility of the present settlement analysis for Toyoura sand (TOY) and Mia-Liao silty sand (MLS), at a settlement level of 25 mm, is plotted in Figure (7.26) for rough footings. The compressibility increases nonlinearly with footing size. As can be seen in Figure (7.26), increasing the density lowers the compressibility of the subgrade, when comparing footings on Toyoura sand at densities of 50% and 70%. The Mia-Liao silty sand also exhibits more compressibility when compared to a clean sand (Toyoura sand) at a given relative density (here Dr=50%), which can be attributed mainly to the fine presence (e.g. Huang *et al.* 1999).

Figures (7.27a-d) give the vertical strain distribution under rough and smooth circular footings on Tan silty sands (D_r =55%) at different settlement levels, footing size and roughness, according to the present finite element study (positive sign denotes compression in this figure). The zone in which strains change in consequence to the loading is slightly deeper for rough footings when compared to smooth ones. However, it is apparantly 2B for all cases irrespective of settlement level and roughness. The influence depth of 2B, for circular footings, as suggested by Schmertmann *et al.* (1978), is therefore justified for settlement calculations in practical applications.

7.3.8 Allowable Bearing Pressure

As discussed previously, in practice tolerable settlement and consequently its corresponding bearing pressure (allowable bearing pressure) often control the design process. Figure (7.28) represents the footing size effect on the allowable bearing pressure (referenced to 25 mm settlement). The allowable bearing pressure decreases as the footing size increases. As expected, a higher density sand gives higher allowable bearing pressures than a lower density one (as expected), and this effect is more substantial for smaller footings (B<2). Over-consolidated granular soils can also bear a higher bearing pressure when compared with normally consolidated soils at a given density (Tan Silty Sand versus MLS and Toyoura Sand). Rough footings give slightly higher allowable bearing capacity; however the footing roughness effect practically diminishes for footing diameters larger than 3m, as shown in Figure (7.28).

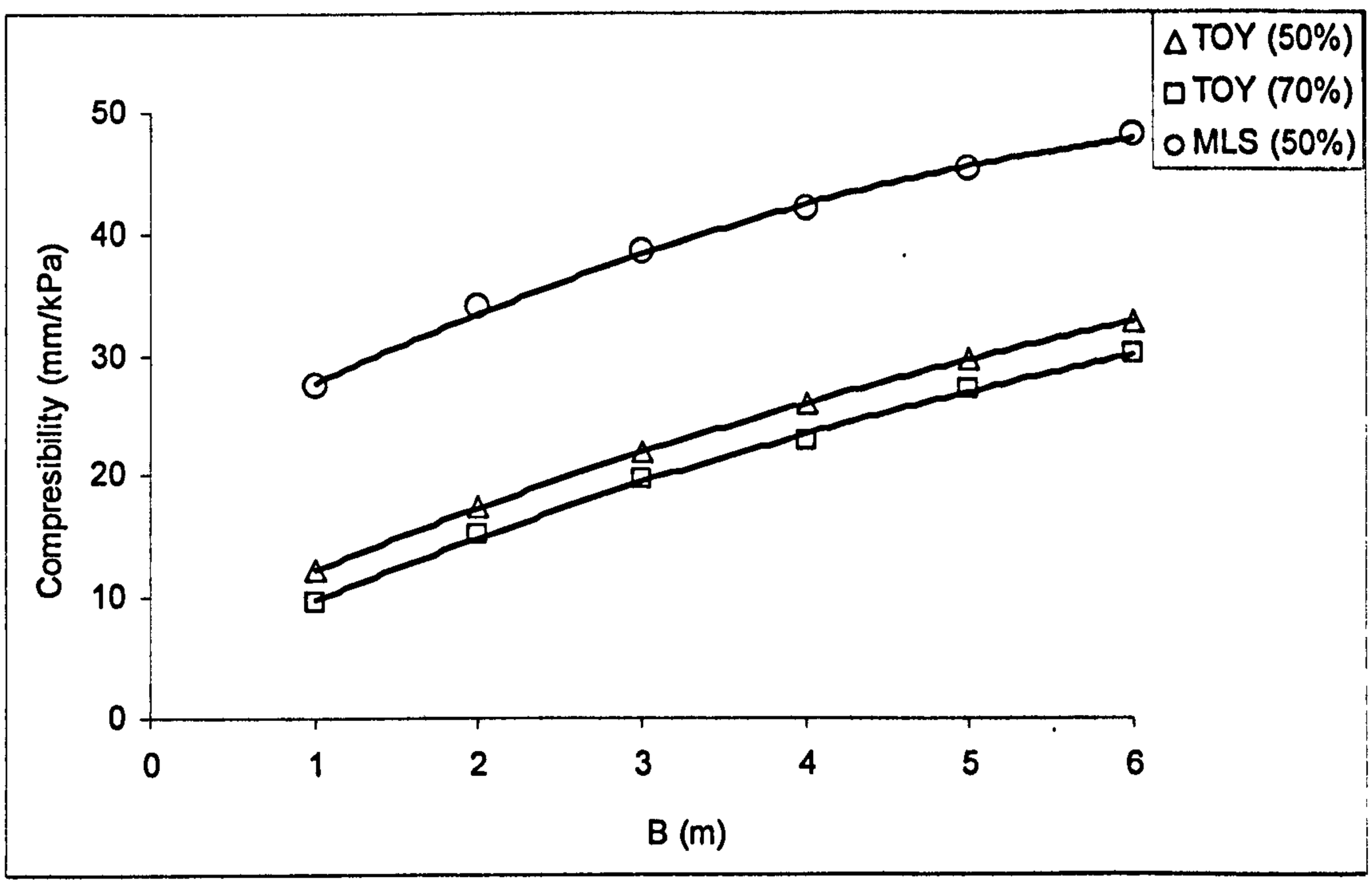

Figure 7.26. Compressibility of the granular soils under a circular footing

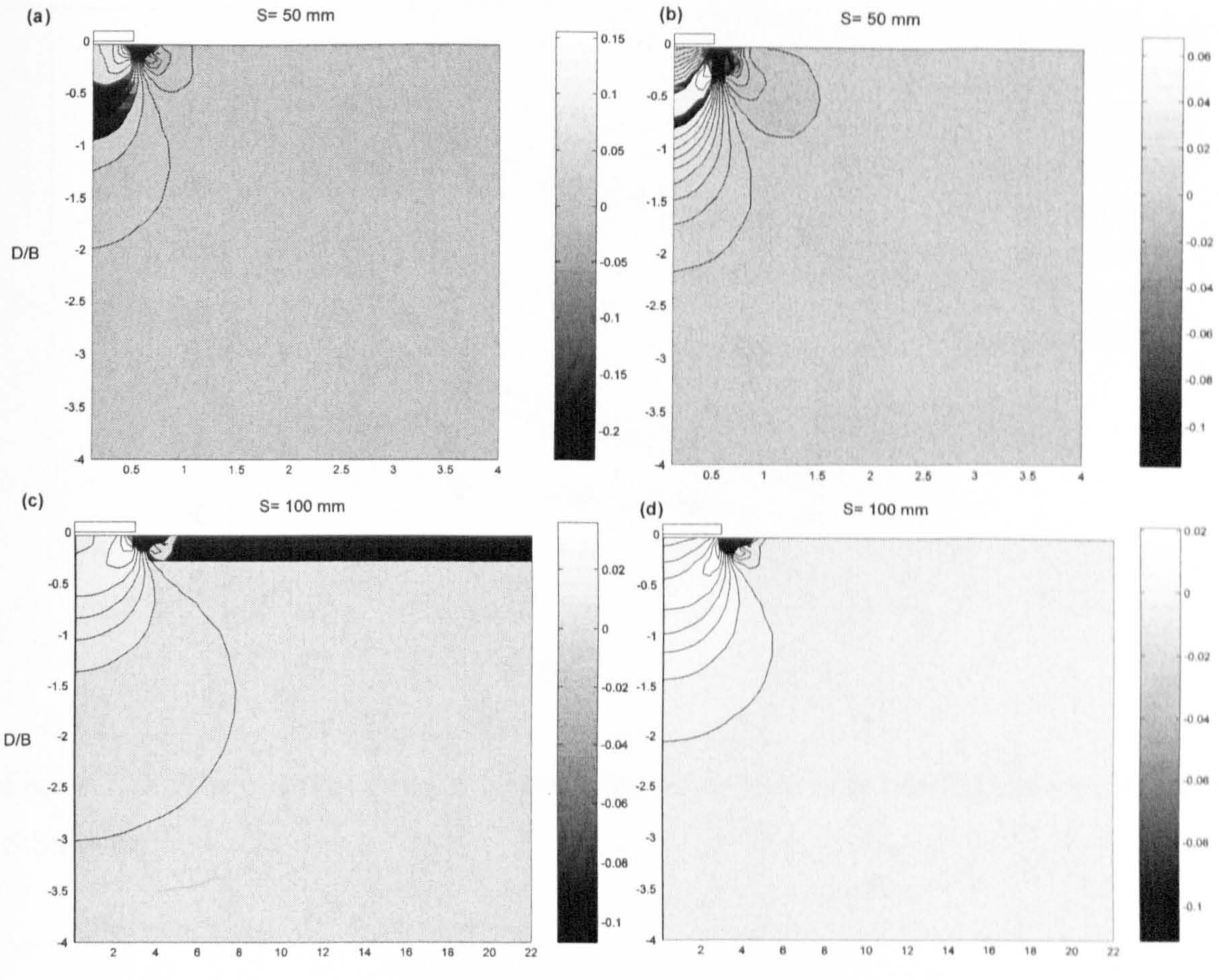

Figure 7.27. Vertical strain distribution under the footing on TSS (a) Smooth (B=1) (b) Rough (B=1) (c) Smooth (B=6) (d) Rough (B=6)

In Figure (7.29), as the footing size decreases, the ratio of the allowable bearing pressure to the ultimate bearing capacity (q_b/q_u) increases, suggesting that bearing capacity is more likely to control smaller footing design. The same trends are seen for smooth footings. Increasing the density of Toyoura sand (from D_r=50% to 70%) slightly lowers the ratio (q_b/q_u) as also observed by Lee and Salgado (2005). Similarly, higher fine content decreases the ratio (q_b/q_u), when comparing the ratio (q_b/q_u) values for Tan sand, MLS and Toyoura sands. Therefore, it is generally seen that the higher fine content and lower density raise the likelihood of the footing settlement to be the critical issue in the design process.

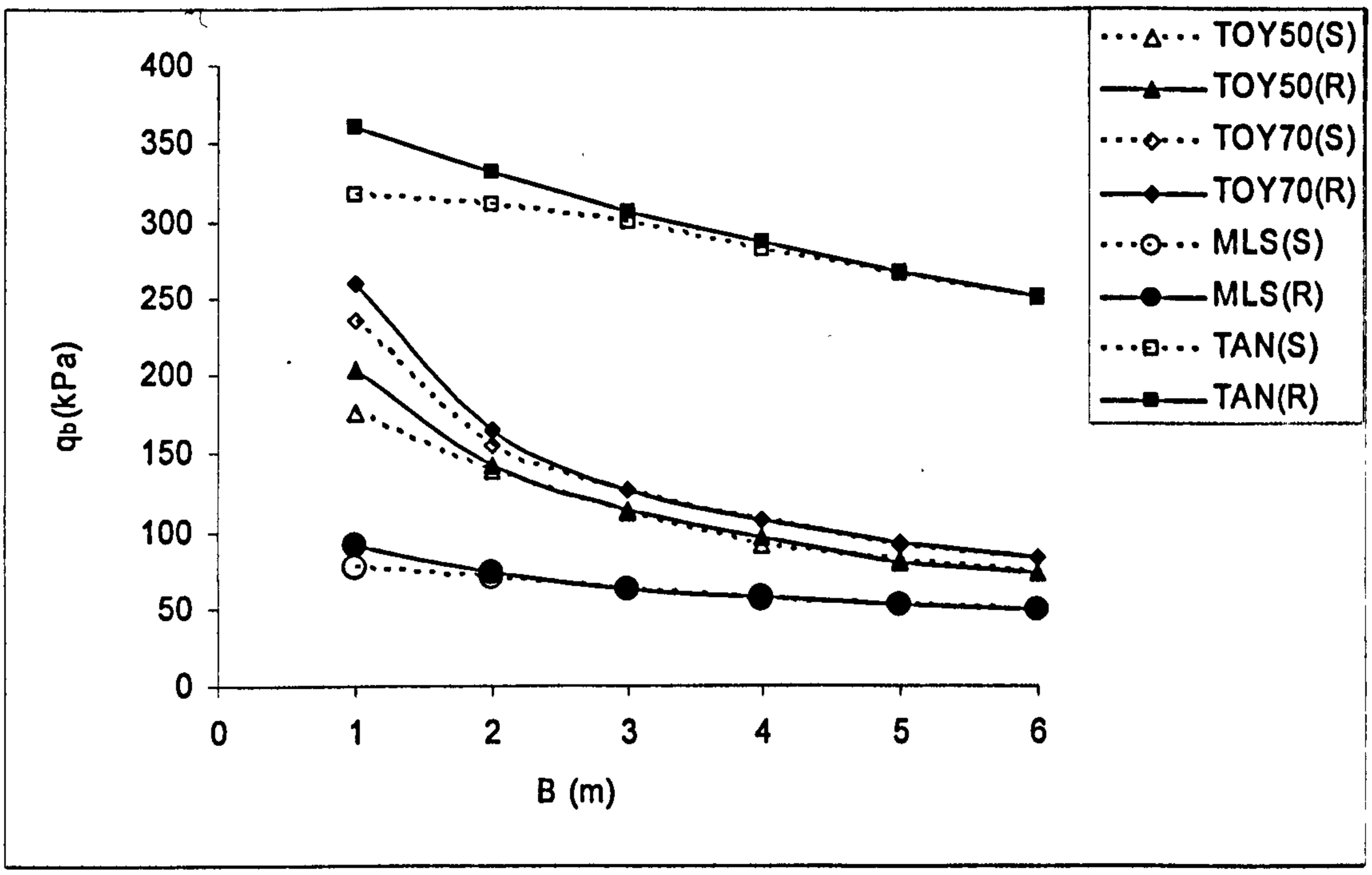

Figure 7.28. The effect of circular footing size on the allowable bearing pressure (R:Rough S:Smooth)

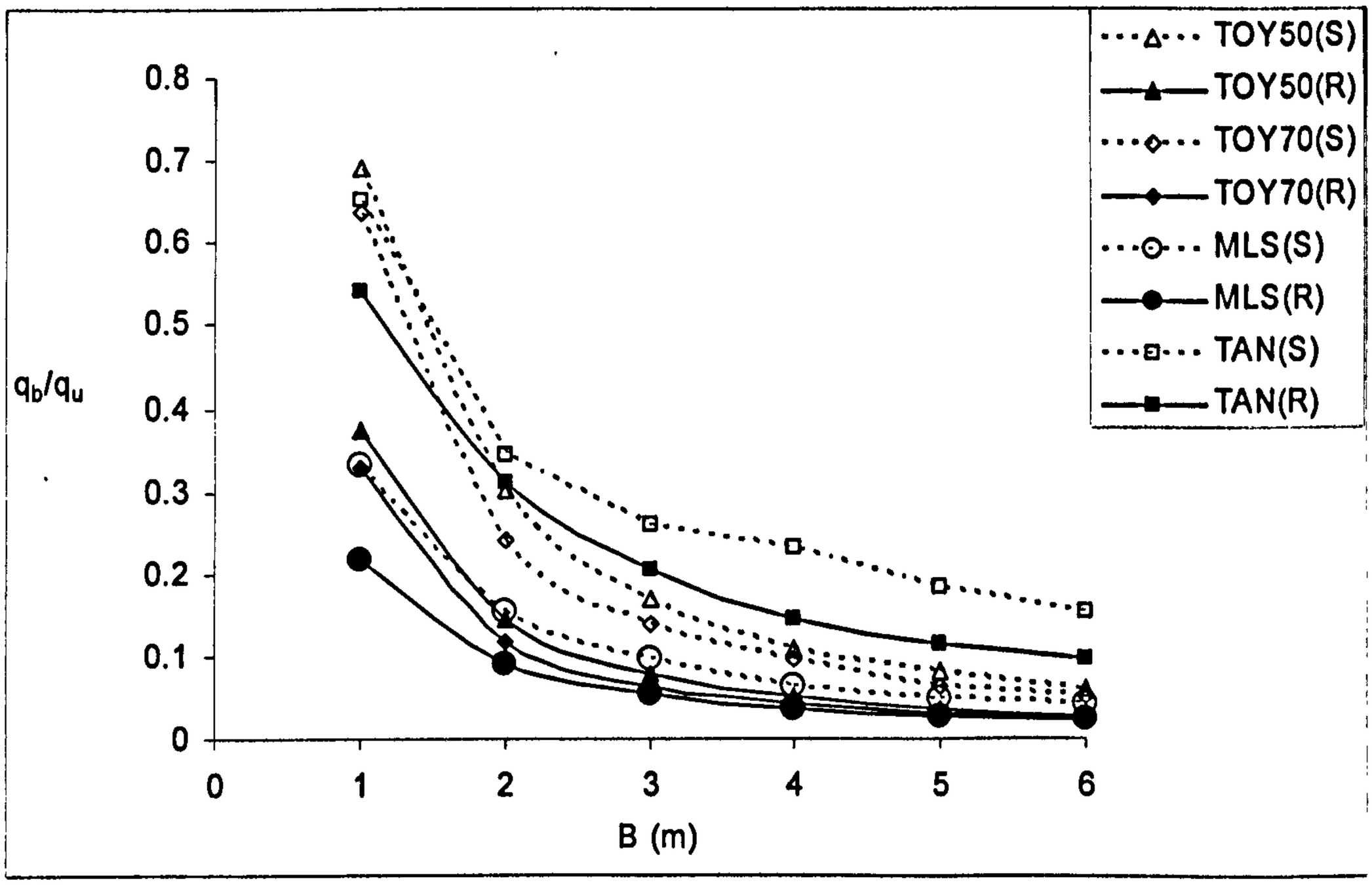

Figure 7.29. The effect of circular footing size on the ratio of allowable bearing pressure to ultimate bearing capacity (R:Rough S:Smooth)

These observations generally confirm the statement of Perkins and Madson (2001) in that the bearing capacity will most likely be the governing design consideration for sandy soils of high relative densities, and for lower relative densities, settlement will typically be of more concern. According to Figure (7.29), for both smooth and rough cases, the settlement is the governing design criterion for sandy soil of density up to 70%. The settlement will also probably be the main design criterion for smoother footings than for rough footings, especially for smaller foundations.

Figure (7.30) gives the stress ratio (t/s) distribution under a rough circular footing of 1m in diameter for both MLS and Toyoura sands (Dr=50%) at a settlement of 100 mm. Toyoura sand is at its ultimate bearing strength at this settlement level, and the affected depth has extended to 2B. It is not the case with MLS; the failure point occurs at much higher settlement and the affected depth is just less than 1B; this will extend to 2B at failure (see Section 7.3.9.3). This clearly shows that the soil stress-strain behaviour dictates, to a larger extent, whether the settlement or bearing capacity controls the design. If 100 mm is assumed to be the allowable settlement, while the bearing capacity is the controlling design parameter for the footing on Toyoura sand, settlement is the major criterion for a silty sand of the same density.

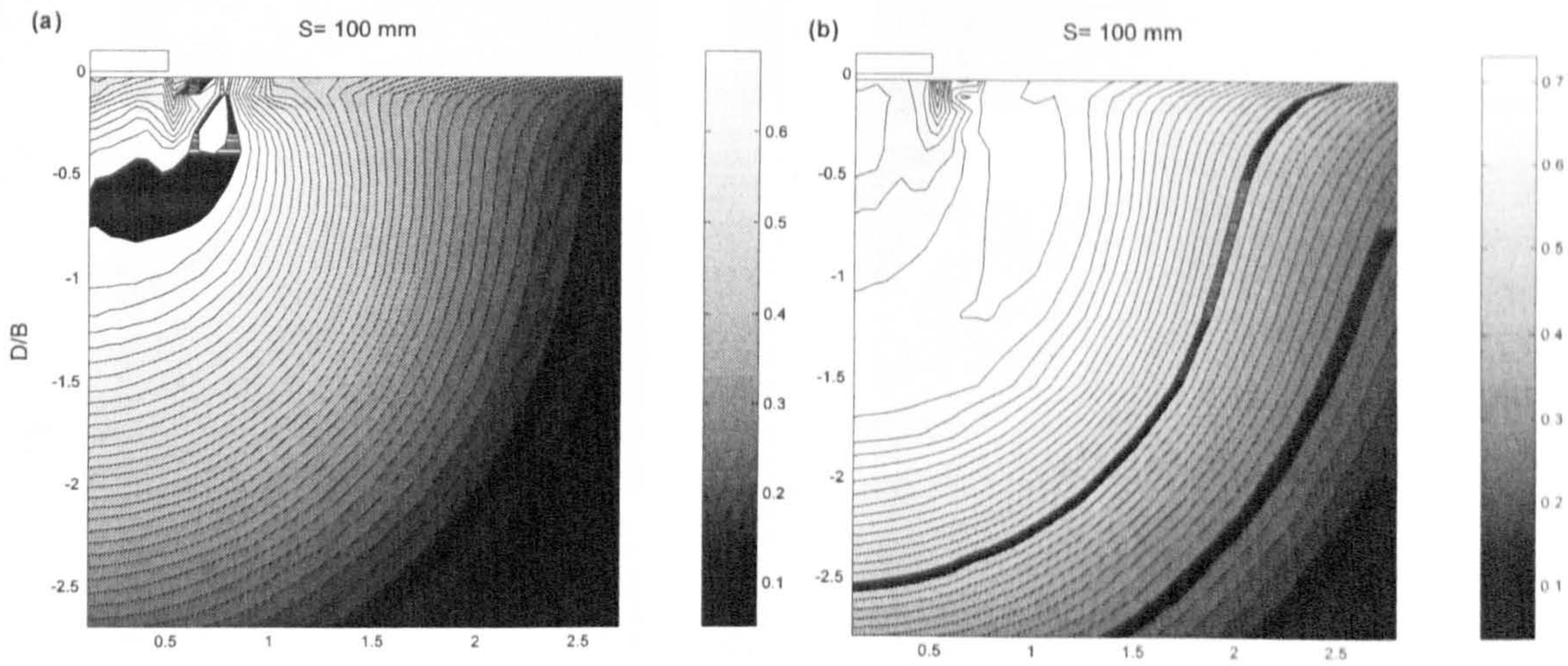

Figure 7.30. Stress ratio distribution under a rough circular footing (B=1) on (a) MLS (b)Toyoura sand at D_r=50%

At a lower level of settlement (25 mm), the depth of the affected area seems to be insensitive to the stress-strain characteristics for the cases studied. Figure (7.31) presents stress ratio contours under a circular footing at an allowable settlement level of 25mm. It is clearly seen that the roughness and compressibility have a relatively minor influence on the depth of influence at this settlement level, although as seen, the depth is slightly lower for smooth footings than for rough ones, and is slightly higher in Toyoura sand at a density of 50% than that in the MLS at the same density. As far as the allowable bearing response of the foundation is concerned, assuming the depth of influence to be equal to the footing diameter as proposed by Lee and Salgado (2002), it is found to be appropriate. It should, however, be noted that if higher settlement levels are considered allowable, the slip zone may be extended up to 2 times the footing diameter for rough footings (see Figure 7.30b).

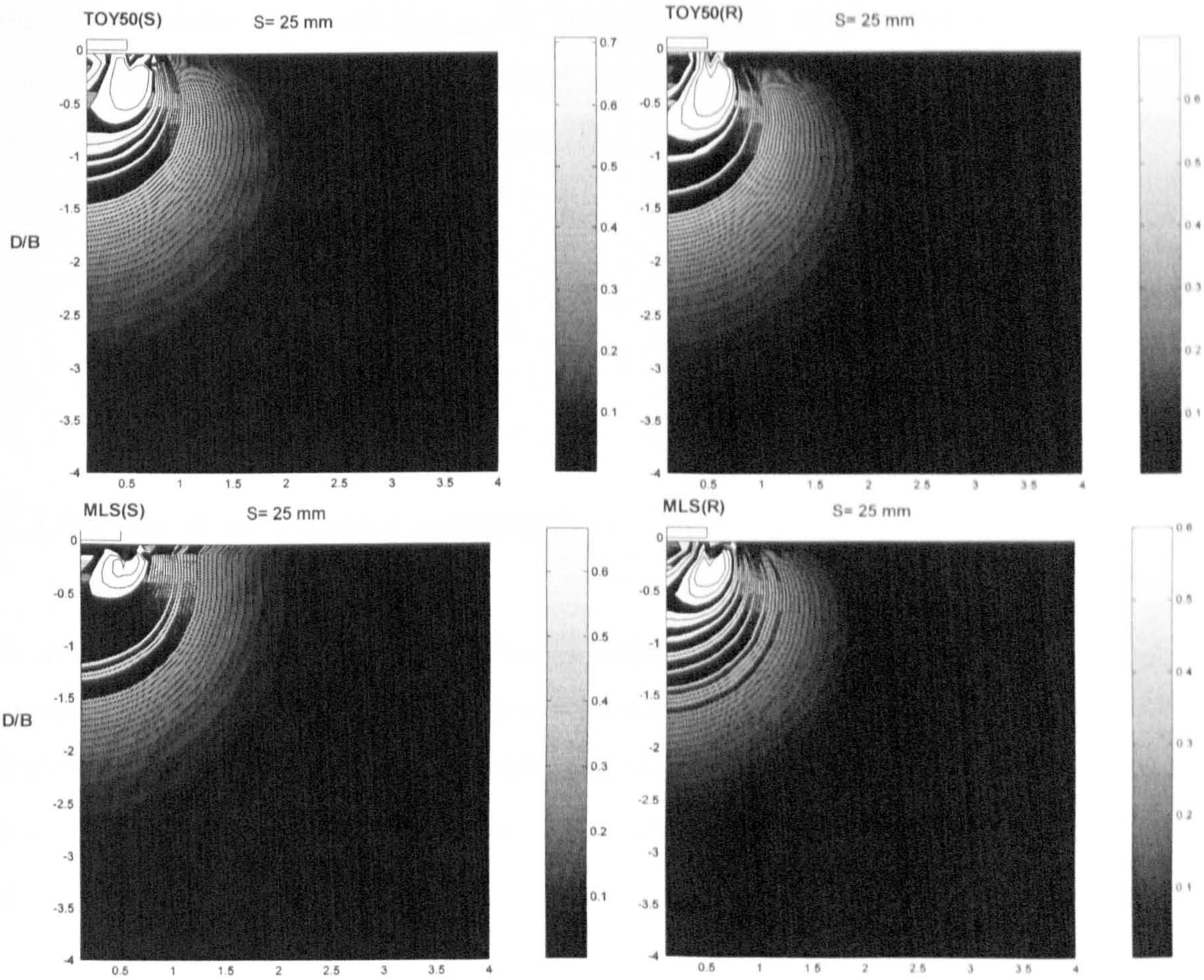

Figure 7.31. Stress ratio (t/s) contour under a circular footing (B=1m) (R:Rough S:Smooth)

7.3.9 Failure Mechanism

7.3.9.1 Progressive Failure

The granular foundation failure surface is not mobilized simultaneously, but in a progressive manner, so-called "progressive failure". As commented by Perkins and Madson (2000), the consequence of this phenomenon is that when the peak bearing capacity of the foundation is reached, only part of the material along the slip surface may be contributing to the shear strength at the peak friction angle, whereas the remaining parts contribute to the shear strength based on the critical state friction angle (or somewhere in between). They considered two limit cases in their work, an upper and a lower limit, in which all points along the failure surface generate strength corresponding to either the peak or constant volume (critical state) friction angles (at appropriate confining pressures). It was reasoned in their experiments that the ultimate bearing capacity factors (N_γ) were bracketed between these two limits: $N_{\gamma\text{-}cv}$ and $N_{\gamma\text{-}peak}$. By determining the relative position of the bearing capacity values with respect to these limits, an index of progressive failure was defined as a measure of progressive failure 'dominancy':

$$I_{pf} = \frac{N_{\gamma-peak} - N_{\gamma-experiment}}{N_{\gamma-peak} - N_{\gamma-cv}} \tag{7.50}$$

7.3.9.2 Relative Density Approach

A simple semi-empirical method, namely a relative density approach, was then proposed to estimate the ultimate bearing capacity of relatively dense sands, accounting for scale effects and progressive failure. This approach uses the Bolton (1986) expression for the peak friction angle (ϕ'_{peak}), based on a constant critical state friction angle (ϕ'_{cv}) and a relative dilatancy index:

$$\phi'_{peak} = \phi'_{cv} + AI_R \tag{7.51}$$

where A is an empirical constant depending on the strain restraints. The relative dilatancy index (I_R) is a function of the effective stress confinement (p') and the relative density of the soil (D_r):

$$I_R = D_r(Q - \ln p') - R \tag{7.52}$$

where, Q and R are empirical material constants with values of 10 and 1 respectively. First, an appropriate value of p' is determined through an iterative process for the soil beneath the foundation undergoing failure. The bearing capacity factors N_γ, corresponding to a peak friction angle ($N_{\gamma\text{-}peak}$) and a critical state friction angle ($N_{\gamma\text{-}cv}$), are then calculated from the upper bound solution as proposed by Chen (1975) for rough footings. An index of progressive failure (I_{pf}) is consequently correlated by a best-fit linear regression from the relative dilatancy index (I_R) for medium or high density sands:

$$I_{pf} = 0.044 I_R + 0.65 \tag{7.53}$$

The ultimate bearing capacity factor N_γ is then predicted as follows:

$$N_\gamma = N_{\gamma-peak} - I_{pf}(N_{\gamma-peak} - N_{\gamma-cv}) \tag{7.54}$$

Although not stated explicitly by Perkins and Madson (2000), it should be noted that this empirical method predicts the ultimate bearing capacity of 'relatively' rough footings, since the corresponding Authors' experimental database included mostly the relatively rough cases.

7.3.9.3 Numerical Study of Progressive Failure

The finite element responses for the different circular footing sizes, resting on Toyoura sand (ϕ'_{cv}=32^0) at a relative density of 70%, are plotted in Figure (7.32) against both the empirical results and the available centrifuge test results for relatively rough footings (Ueno *et al.*, 1994). As shown in Figure (7.32), a consistent set of numerical analysis results for

rough footings are observed when compared with the experimental results. The corresponding numerical results are also bracketed between $N_{\gamma\text{-}cv}$ and $N_{\gamma\text{-}peak}$. The roughness effects are again re-emphasized here by observing that N_γ for the smooth footings can fall to the lowest value of N_γ in rough cases when the critical state friction angle ($N_{\gamma\text{-}cv}$) is assumed.

Figure (7.33) presents the progressive failure index (I_{pf}) for the different circular footing sizes resting on Toyoura sand ($\phi'_{cv}=32^0$) at two different relative densities (50% and 70%) and Nevada sand ($\phi'_{cv}=33^0$) at a relative density of 40%. As can be clearly observed, I_{pf} increases with increasing I_R for Toyoura sand (D_r = 50% and 70%), indicating that progressive failure becomes more pronounced as the relative density increases, or the footing size decreases. Equation (7.52) reflects this trend. However, for Nevada sand at D_r=40% relative density, a decrease in the progressive failure index is observed as I_R increases. From the work of Yamaguchi *et al.* (1976,1977), also discussed by Perkins and Madson (2000), these different trends imply two counteracting mechanisms:

1- The potential for progressive failure, being defined by the difference between the peak and the residual strength of the soil, gets more significant as the relative density increases or the footing size decreases (here, for Toyoura sands, at D_r=50%-70%).

2- The progressive failure dominancy, defined by non-uniformity of shear strain and mobilized friction angle in the soil at the failure state, becomes more prominent in looser soil, increasing as the footing size increases (here, Nevada sand, D_r=40%).

A unified solution for different density and stress levels should address both mechanisms and be able to determine when one dominates the other. It is related to the strength-dilatancy characteristics of the soil (Perkins and Madson, 2000), which has been well represented by the proposed finite element solution using the kinematic model.

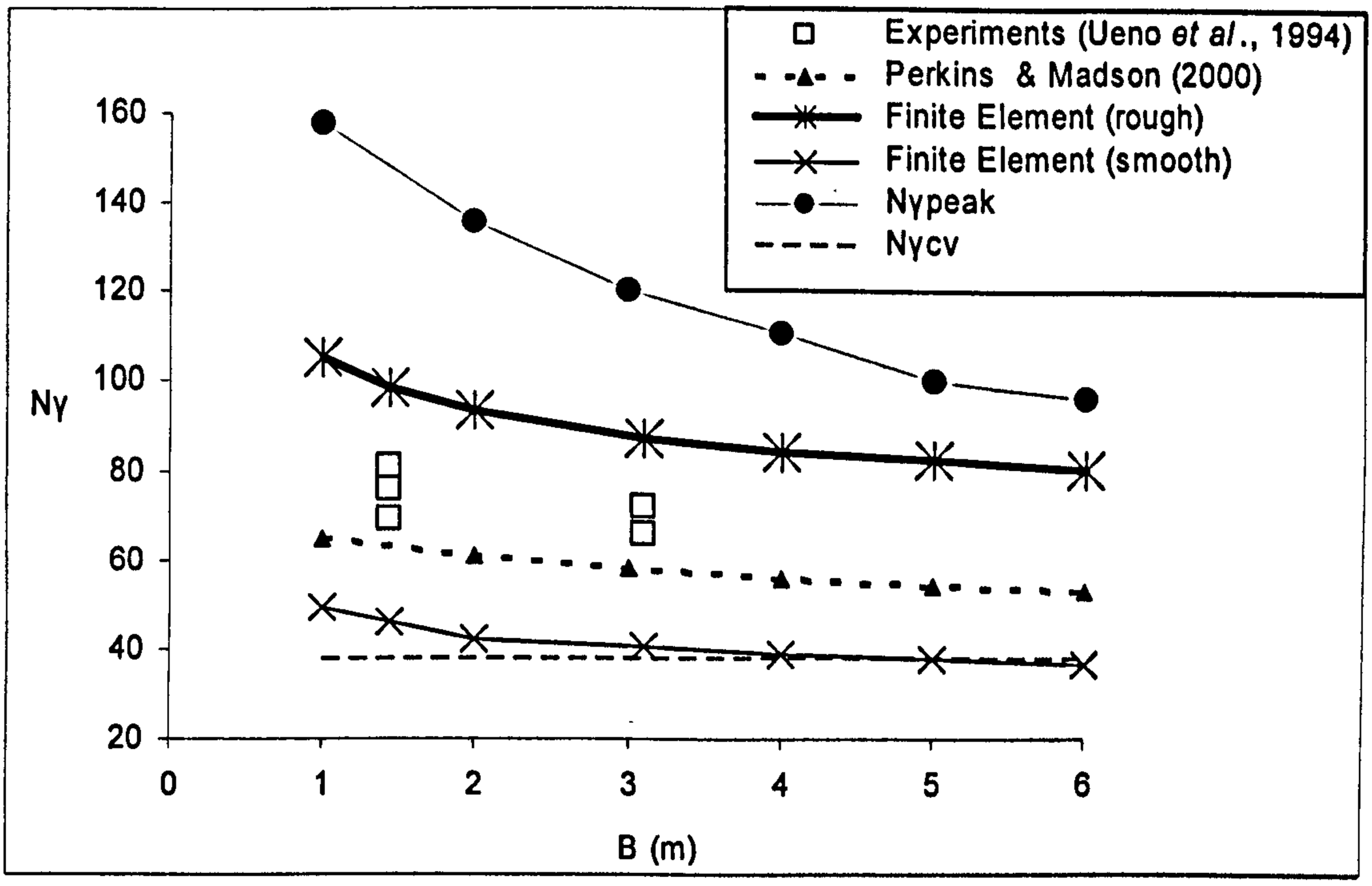

Figure 7.32. Finite element results plotted against both experiments and an empirical methods for circular footings on Toyoura sand (D_r = 70%) (Banimahd and Woodward, 2006)

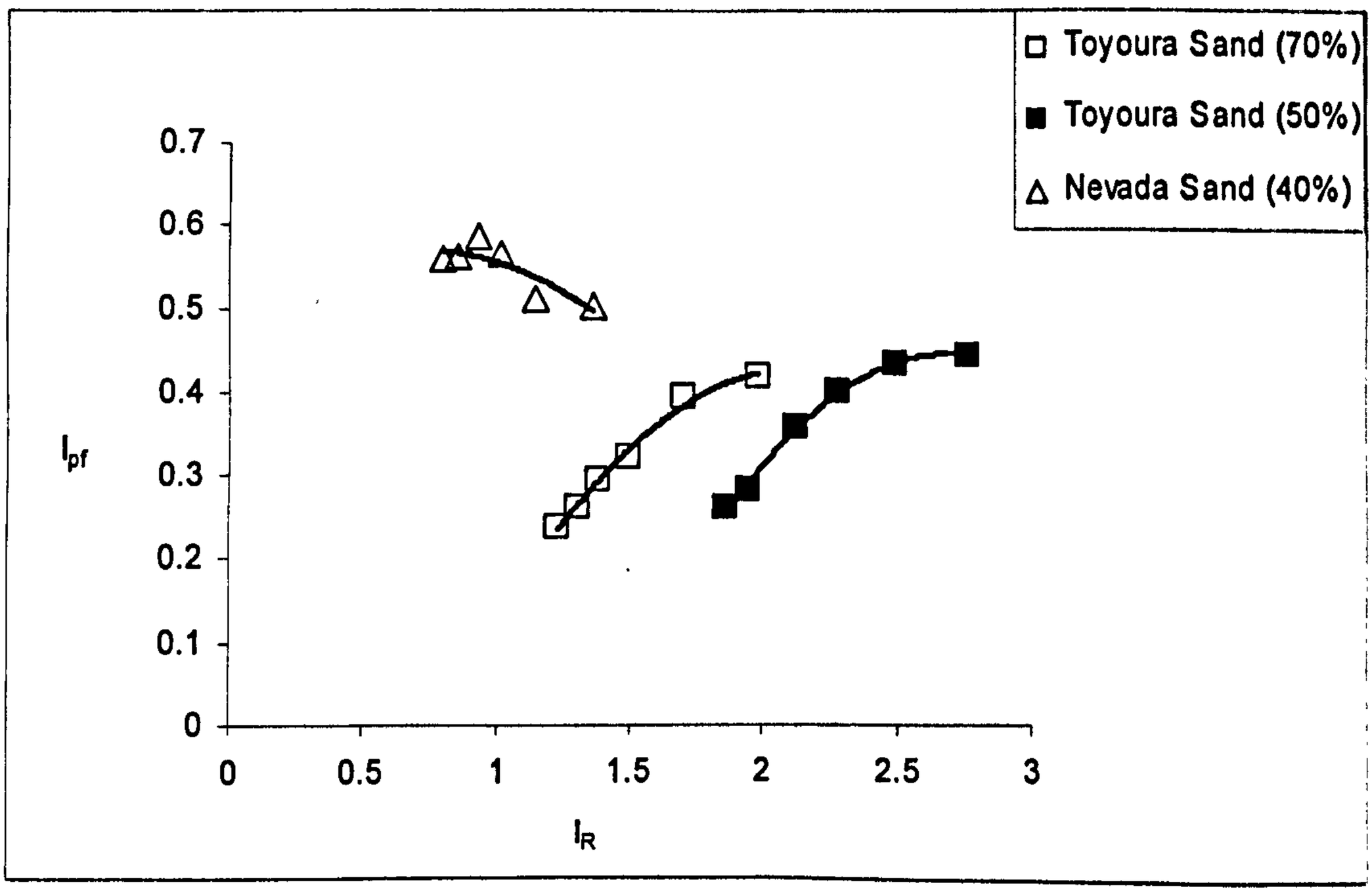

Figure 7.33. Progressive Failure Index of circular footings on Toyoura sand (D_r = 50% and 70%) and Nevada Sand (D_r = 40%) (Banimahd and Woodward, 2006)

The progressive nature of the failure mechanism is shown in Figure (7.34). When the footing is initially loaded, an area near the edge of the footing experiences a high shear stress ratio and fails in the early stages (the singularity effect). This area then spreads downwards into the soil until the failure zone reaches its maximum extent at which the ultimate failure state is achieved. In the post failure state, the depth of the failure zone remains relatively constant and the stress is redistributed within the failure zone itself. The evolution of failure, as shown in Figure (7.34), conforms very well with Meyerhof's explanation of the failure process (Meyerhof, 1955). By comparing Figures (7.34) and (7.35), it can be observed that the depth of the failure zone increases proportionally with footing size. Furthermore, Figure (7.34) also shows that the failure extent for rough footings is deeper than that of smooth footings. According to Figures (7.34) and (7.35), the depth of influence at failure is about 2B and 1.5B for rough and smooth circular footings respectively.

7.4 Cyclic Behaviour of Granular Soil Using ALTERNAT

As discussed in Chapter 2, permanent settlement will be developed in railway tracks under many passages of trains; this originates mainly from the settlement of the granular layers (ballast and sub-ballast) under the associated cyclic loading. To predict granular layer settlement, empirical relationships are frequently used in practice; these are reviewed in Chapter 2. As was seen in the previous section for the foundation problem, the behaviour of the granular system comprises complicated mechanisms, even under monotonic loading, which cannot be correctly represented by a simple empirical relationship, and an advanced constitutive model, such as ALTERNAT, is required. In the present section, the sole aim is to demonstrate the capability of ALTERNAT to simulate the cyclic response of granular systems. Detailed simulations of settlement characteristics of railway track are beyond the scope of this research and will not be covered here. However, a methodology is proposed which can integrate the dynamic finite element track model developed in the present research and ALTERNAT to simulate life-long performance of railway track.

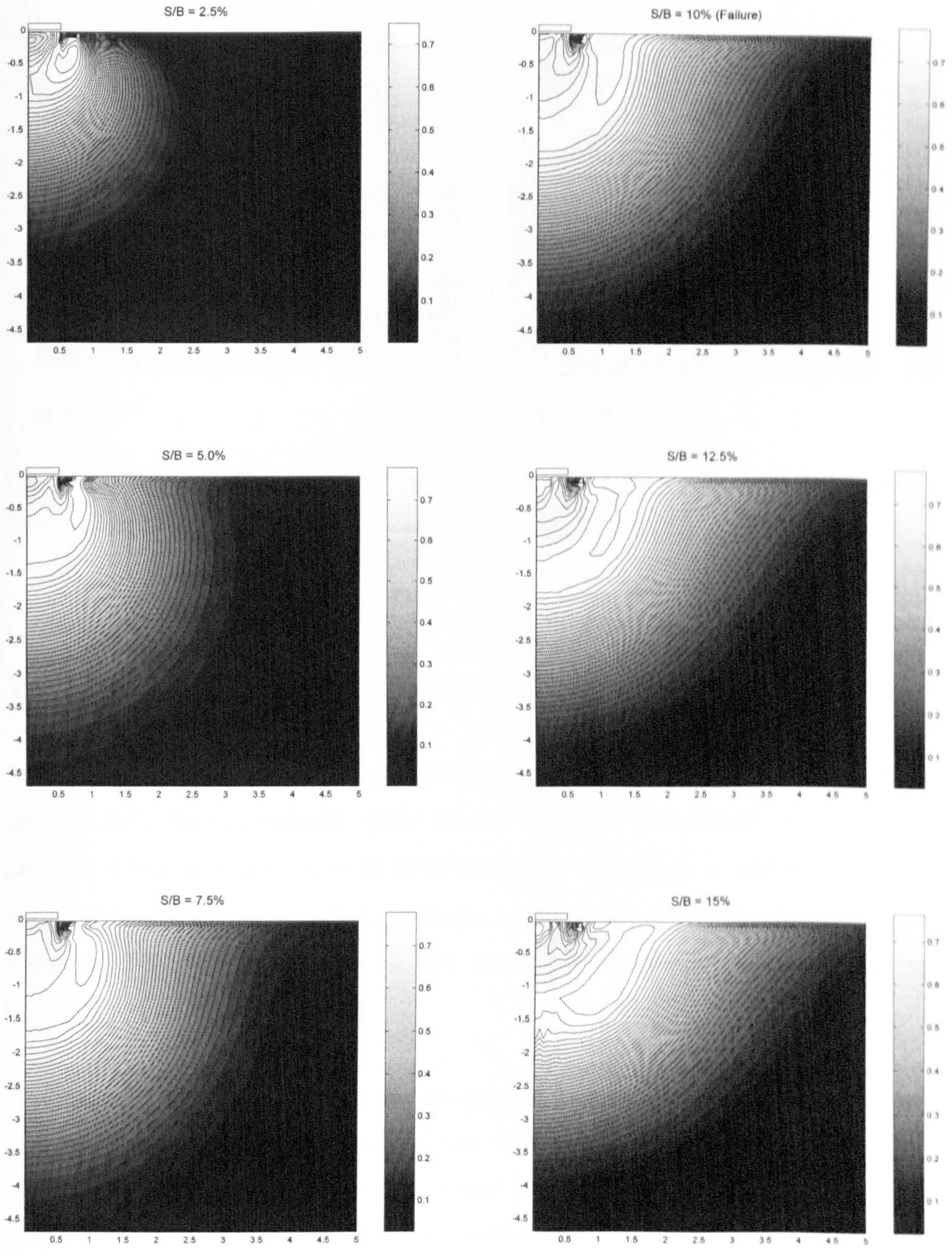

Figure 7.34 Stress ratio (t/s) contours at different stages of loading for a rough circular footing (B=1) on Toyoura sand (D_r = 70%) (Banimahd and Woodward, 2006)

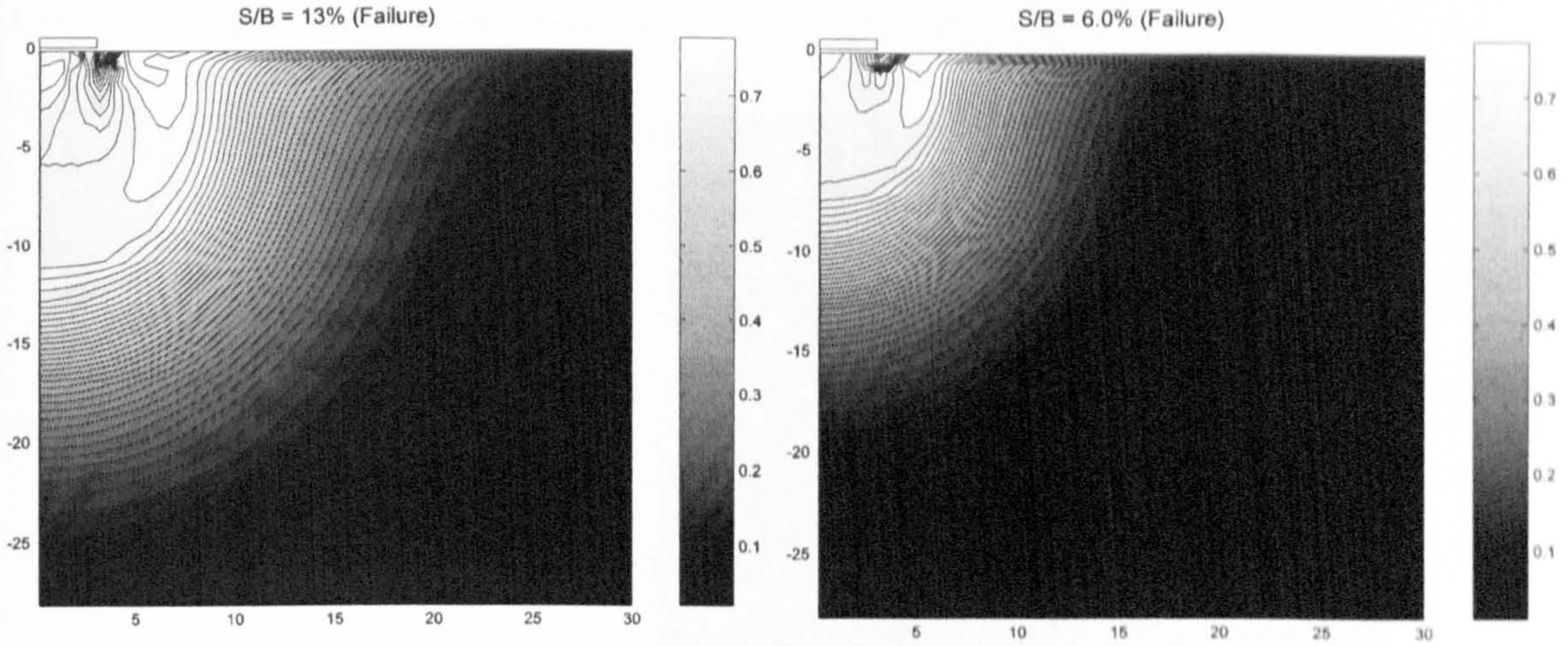

Figure 7.35. Stress ratio (t/s) contours at failure states for a circular footing (B=6) on Toyoura sand (D_r = 70%) (Banimahd and Woodward, 2006)

7.4.1 Cyclic Response of a Granular Soil

In order to show the capability of ALTERNAT when representing the cyclic response of a granular soil, the conventional cyclic triaxial condition is assumed; i.e. the confining pressure is kept constant ($\sigma_c = 50$ kPa) and cyclic axial stress is applied. As shown in Figure (7.36), Nevada sand is first cycled at a cyclic stress ratio of 0.35. After this the sand is cycled at a cyclic stress ratio of 0.96, representing very high axle loads, leading to overstressing of the granular soil.

Figures (7.37) and (7.38) illustrate that the granular soil has densified during the first 3000 load cycles towards an asymptotic resilient state. However, when the magnitude of the cyclic load increases (generating near failure conditions), the soil recommences plastic straining towards a new resilient state. This is in compliance with observations on track; i.e. if the load or train speed is increased, the increased track forces generate additional movements leading to increased maintenance.

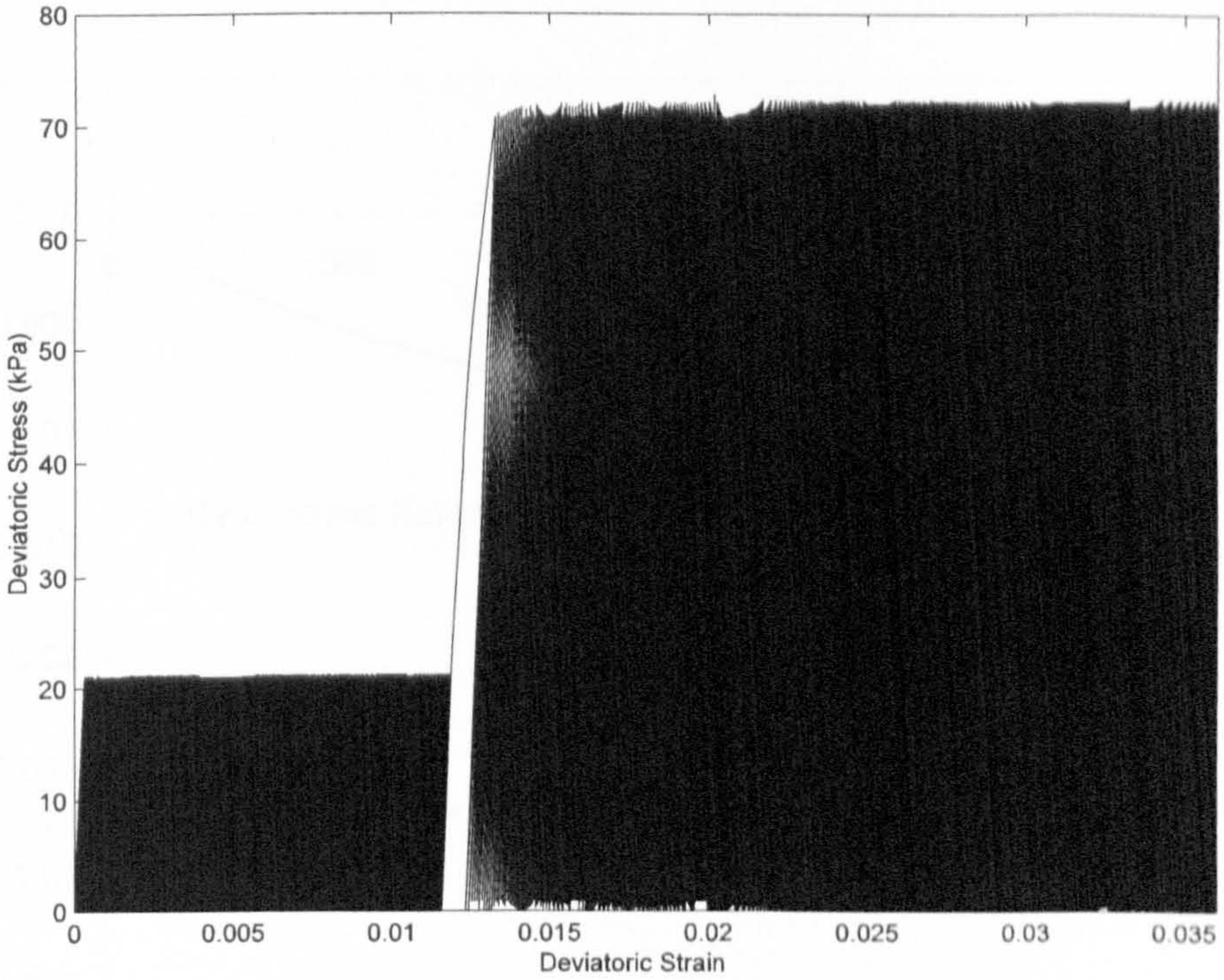

Figure 7.36. Illustration of cyclic deviatoric load applied on Nevada sand (conventional triaxial condition, $\sigma_c = 50$ kPa)

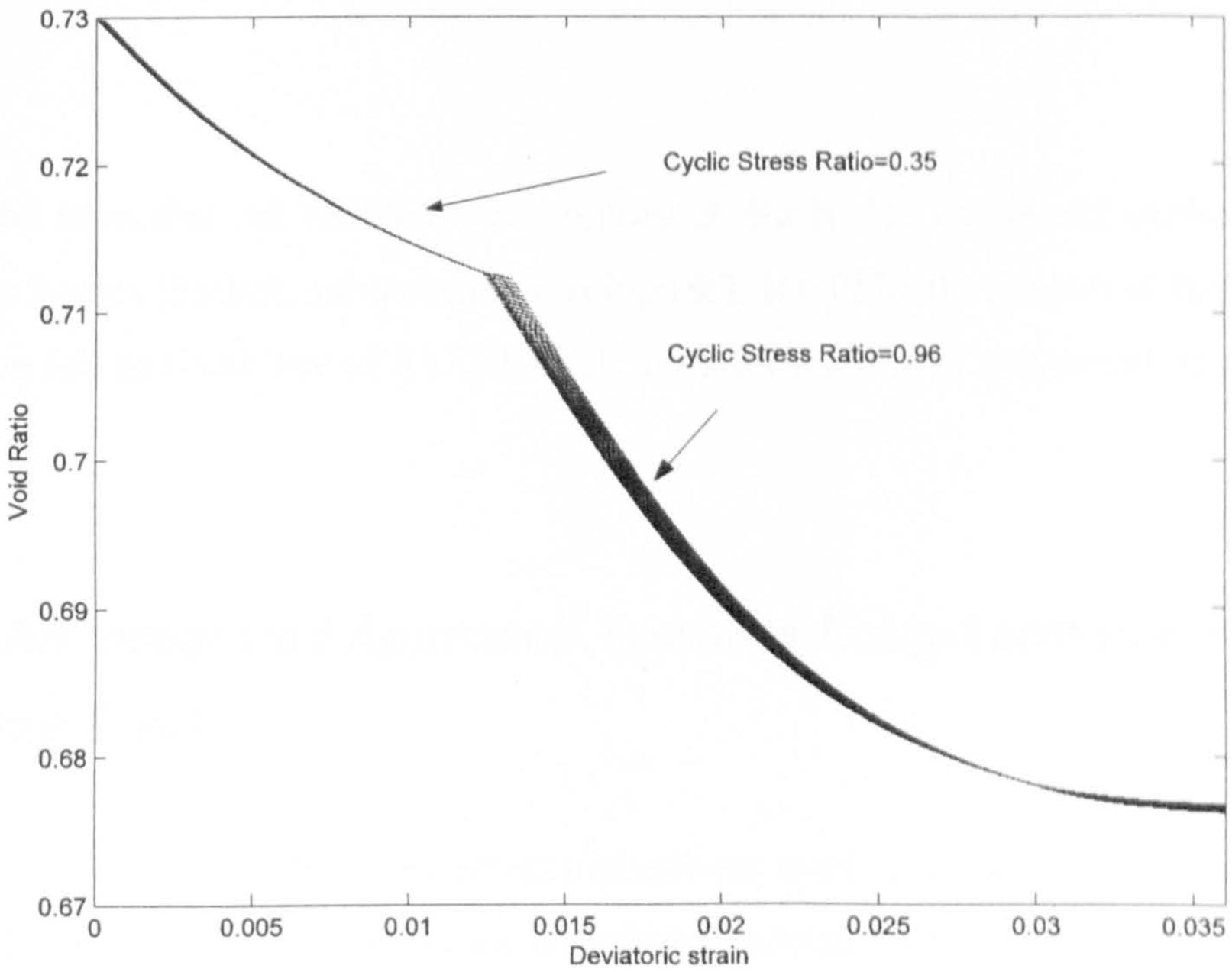

Figure 7.37. Effect of mixed cyclic loading on the void ratio of Nevada sand (conventional triaxial condition, $\sigma_c = 50$ kPa)

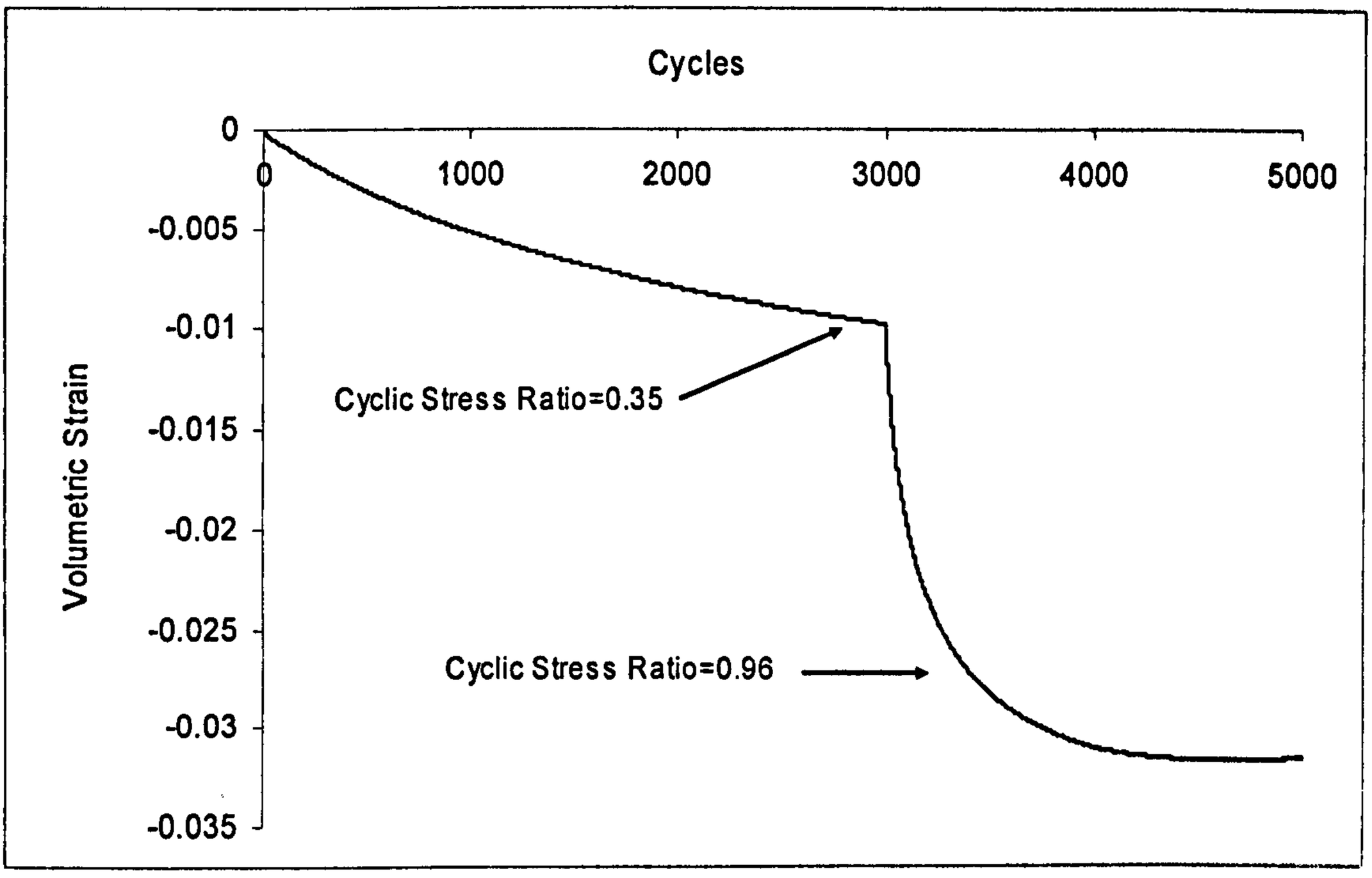

Figure 7.38. Effect of mixed cyclic loading on the volumetric strain of Nevada sand (conventional triaxial condition, $\sigma_c = 50$ kPa)

It can be seen that ALTERNAT can represent the basic features of cyclic behaviour of granular bodies (ballast, subballast and subgrade). It will be the subject of future research to show the full applicability of ALTERNAT in the simulation of settlement of railway tracks.

7.4.2 An Integrated Approach Towards Long-Term Performance of Railway Track

The development of uneven settlements in railway track will increase the dynamic load on the track according to the train-track interaction mechanics presented in Chapter 6. Higher stress levels generate higher settlements which can again affect the dynamic load and hence deterioration rate of the track. To model such a mechanism, it is not practically possible to run a number of dynamic finite element coupled train-track simulations, in which an

advanced elasto-plastic constitutive soil model is implemented due to the considerably high cost of computation, in terms of run time. Another approach is however possible. For a single passage of a train, when the response of track can be generally assumed to be mainly resilient, a nonlinear resilient finite element model (as developed in the present research) can simulate the induced stress in substructure to a good precision. The constitutive model, ALTERNAT, can then be used to predict the settlement over a number of the computed stress cycles, which represent the passages of trains. This could be done simply through applying the stress to a single finite element (or a column of elements representing the substructure layer) in which ALTERNAT is implemented. Mixed traffic can also be modelled by running two dynamic simulations with different train axle loads, and feeding the varying induced stresses into the finite element(s) within which ALTERNAT is implemented. The settlement generated after many passages of the trains can then be introduced to the dynamic finite element model in the form of an irregularity, as presented in Chapter 6. The dynamic train-track model with a new irregularity profile is then run to simulate the new induced stress level in the subgrade, which is then fed back into cyclic settlement model (based on ALTERNAT); the constitutive model is then used to predict the new settlement. In this way, it will be possible to simulate the long-term performance of railway track with respect to substructure behaviour, and to optimize the railway track system in terms of the required maintenance regime, for design purposes. It is also possible to plan the maintenance in terms of the maintenance intervals needed to keep the track geometry at an acceptable level. This integrated approach is shown in Figure (7.39).

The practicality of this proposed integrated approach is not being investigated here and will be subject of future research.

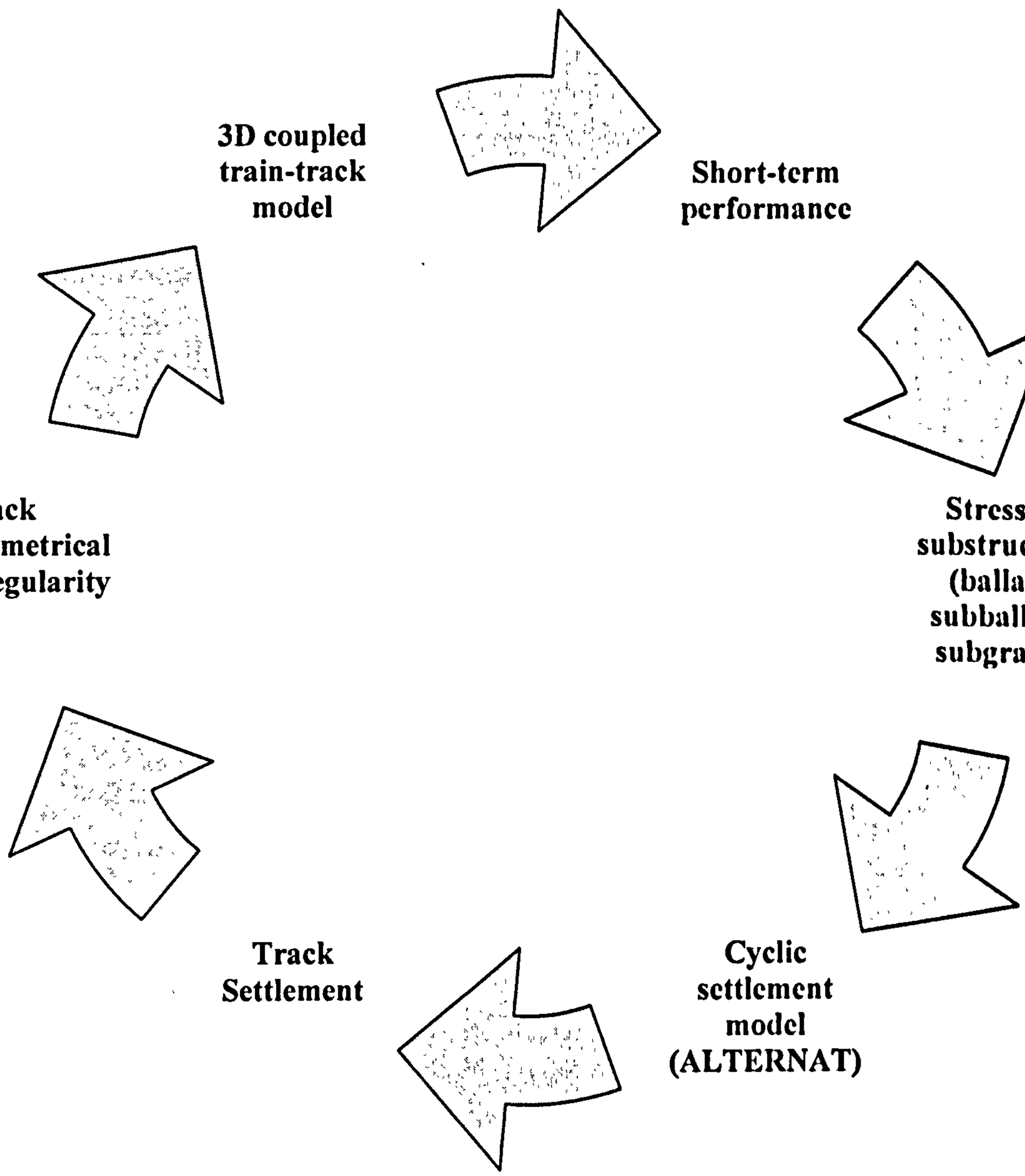

Figure. 7.39. An integrated approach towards life-long performance of railway track

7.5 Conclusion

The substructure of railway tracks is under complicated and high stress regimes, owing to increasing train speeds, heavier axle loads and mixed passenger-freight traffic. It was argued that empirical relationships cannot represent the behaviour of railway track properly under these conditions, and an advanced constitutive soil model should be employed. An

example of such a constitutive model, namely ALTERNAT, was described in this chapter along with a calibration procedure which was developed to determine the model parameters based on lab test results. This constitutive model takes into account the elastic nonlinearity, non-associatively and strain hardening-softening behaviour of the granular soil. It also simulates densification and cyclic mobility under cyclic regimes. As surface footings can represent railway track systems (e.g. sleeper on ballast and slab track on subgrades) and can be researched using data available in the literature, a comprehensive study of surface footings, in terms of both settlement and failure characteristics, was conducted using a finite element code in which ALTERNAT was implemented. In order to understand fully the mechanism of granular foundation systems, different granular materials were considered and the fundamental features of granular foundations were numerically studied and compared against experimental trends. The findings gave invaluable insights into the behaviour of surface footings, which are highly applicable for the monotonic response of railway track. The outcomes of the study are summarised below:

- The scale effect on bearing capacity factor N_γ was confirmed. As the footing size increases N_γ decreases.

- The bearing capacity factor increases as the relative density increases. Smooth footings yield a lower bearing capacity than the equivalent rough footings. While varying slightly with material type, the ratio of the smooth footing bearing capacity to the rough footing bearing capacity was approximately 0.5.

- Dilative behaviour of dense sand was well presented. More dilation is observed in denser sand under the footing, which resulted in a post-peak strain softening response.

- Circular footings yield a lower bearing capacity factor N_γ than those of the equivalent strip footings. The shape factor appears to be material dependent and does not apparently depend on footing size. However, a value of 0.6, as proposed by De Beer (1970), can be applied in the general case.

- Granular foundations fail progressively. The depth of the failure zone is proportional to the footing size. A rough footing exhibits a deeper failure mechanism than a smooth footing. The failure zone depths are about 2 and 1.5 times the foundation diameter for rough and smooth circular footings respectively.

- In a similar manner to observations from experiments, two counteracting progressive failure mechanisms are observed: an increase in the progressive failure potential with decreasing footing size for relatively dense sands, and an increase in the progressive failure dominancy with increasing footing size in loose sands.

- The effect of roughness is observed to be generally more pronounced as settlement increases. The settlement level, before which the settlement is practically not affected by roughness, is seen to be about 2% of the footing diameter for all the different densities and footing sizes considered. The footing response up to tolerable settlement of 25 mm for common structures is practically unaffected by roughness for larger footings (B>2; B is footing diameter). In addition, as the footing size increases, the settlement level after which the roughness affects the footing response increases, implying that the response of the footing remains almost unaffected by roughness up to a relatively large settlement.

- For settlement calculations, the depth of influence, at which the vertical strain mostly affects the settlement, is numerically found to be around 2B for axi-symmetric footings, confirming conventional assumptions, irrespective of soil density and footing roughness.

- Higher compressible sandy soils (lower density, higher fines content) give higher settlement for a given unit load. For a given settlement level (before the failure point and higher than the allowable settlement level), the slip zone is generally deeper in lower compressible sandy soil than ones in high compressible sandy

soil. Lower compressible soil fails at lower settlement levels than higher compressible soils, under a given footing.

- At an allowable settlement level (S=25mm), the slip zone depth can be assumed to be equal to the footing diameter in both rough and smooth cases for circular footings in all cases.

- As density decreases and fine content increases, the ratio between the allowable bearing pressure and ultimate bearing pressure decreases. Therefore it can be said that higher compressibility (lower density, higher fines content) generally raises the likelihood of the settlement to be the critical issue in the design. Roughly speaking, for a density lower than 70%, settlement is usually found to be the major concern.

- As the footing size increases the ratio between the allowable bearing pressure and ultimate bearing pressure decreases, and hence the chance that the settlement controls the design process increases.

- The allowable bearing pressure decreases with the footing size. The increase in density and the decrease in fine content would decrease the allowable bearing pressure. The effect of density seems to be more pronounced for smaller footings (B<2). Rough footings have higher allowable bearing pressure than the equivalent smooth footings. The effect of footing roughness seems to diminish for large foundations (B>2 m)

ALTERNAT was also used to study briefly the cyclic behaviour of granular soil, and it was demonstrated that it will represent the basic features of the cyclic response under a varying conventional triaxial cyclic loading. For future research, an approach was also proposed to integrate a three-dimension coupled train-track finite element model and ALTERNAT to simulate the life-long performance of railway tracks.

CHAPTER 8

CONCLUSIONS AND RECOMMENDATIONS

8.1 Conclusions

In this thesis, a series of models was developed based on the finite element method to study coupled train-railway track systems. A three-dimensional dynamic model, which incorporates all track components such as the multi-layered ground, sleepers and rails was first developed. In this model, non-reflecting boundaries and nonlinear constitutive relationships for the subgrade and ballast were implemented. The train was modelled as a combination of rigid masses, dashpots and springs. The train and track were coupled at the wheel-rail contact points employing a nonlinear-contact theory which incorporates the rail surface irregularities and the possibility of wheel-rail separation. The dynamic problem of the coupled track-train system was solved in the time domain using a modified explicit integration technique. Using the developed three-dimensional model, the effects of train speed and stiffness nonlinearity in the subgrade and ballast were studied in terms of track displacement and the stress & vibration level in the substructure. Based on these studies, a modified design algorithm was suggested for high speed tracks to minimize railway track maintenance levels.

Stiffness transitions between plain track and bridge abutment/ tunnel bases were also studied. Using a three-dimensional finite element model, the effect of the stiffness changes and a fault presence in the transition zone were investigated in terms of rail/wheel interaction force, stress in the ballast and subgrade, and the train body acceleration; which is considered to be a passenger comfort index. A simple train-irregularity model was also developed which computes the train response to any given irregularities, such as deflection

difference induced in a transition zone caused by stiffness changes. Using this train-irregularity model, the effects of the transition length, the train speed on the wheel/rail interaction force, and the passenger comfort level in the transition zones were studied. Furthermore, the relationships between the geometrical properties of the transition curves, which represent the change in the deflection between soft and stiff sides of transition, and the maximum dynamic force, were investigated. The design principles for transition zones and available site observations were critically studied against the outcome of transition studies conducted in the present chapter, and modifications were suggested towards the sustainable design of transitions.

It was also discussed that the simple empirical models, used mostly to predict track settlement, do not take into account complicated mechanisms of stress-strain response of the substructure, especially under the high and varying stress regimes generated by high speed and heavy trains, and mixed passenger-freight traffic. It was argued that an advanced constitutive soil model should therefore be employed in the context of the finite element method to simulate the track geo-system response appropriately. Such a constitutive soil model should address the stress state dependent stiffness/strength, strain hardening and softening, dilation mechanism, and progressive nature of failure, as occurs in the soil. An example of such a constitutive model, namely ALTERNAT, was described and a procedure was also developed, based on an optimization technique, to calibrate this model against the experimental data. Monotonic response of shallow footings were extensively studied using a finite element code incorporating ALTERNAT. As the surface footing can represent the track system (e.g. sleeper on ballast, slab track on subgrade), these studies provided invaluable insights into the factors affecting the settlement and bearing capacity of the track geo-system. The cyclic response of a granular soil was also briefly studied, and it was shown that ALTERNAT can simulate the basic features of the cyclic response of granular soils under train loadings. By employing the ALTERNAT cyclic settlement model and the three dimensional dynamic finite element model, an integrated approach was proposed for future studies towards the prediction of long-term performance of railway track.

The major findings of this research are listed below:

- The performance of classical explicit and Zhai's modified explicit schemes (Zhai, 1996) for time integration were compared for two benchmark problems with known solutions, and it was shown that Zhai's method performs better, especially if the time step is large.

- In order to implement nonlinear resilient constitutive relationships in an explicit dynamic track model, iterations may be needed at every time step (especially when the time step is relatively large) to find the appropriate resilient modulus, as the nonlinear resilient modulus of ballast and subrade are typically related to the stress state. An equivalent strain state based relationship for the nonlinear resilient modulus of both the subgrade and ballast was developed which eliminates the iterations and can be directly used in an explicit dynamic finite element model, such as the one developed in this research.

- Using the three-dimensional track model, an increase in track displacement, vibration and stress in the ballast, and stress in subgrade was observed. Softer subgrades induce higher track displacements at a given train speed for a given ballast stiffness and depth.

- The presence of track critical velocity (V_{cr}) was confirmed. It was shown that this is around the Rayleigh wave velocity of the subgrade for conventional tracks. Stiffer and deeper ballast layers will improve the track response, especially as the train speed approaches and passes the track critical velocity. However, owing to the nonlinearity and degradation of the ballast stiffness and tensionless nature of ballast, the improvement coming from the ballast layer in the high speed range may not be as high as expected.

- It was observed that the track response is essentially static for conventional tracks when the train speed is lower than 50% of critical track velocity.

- The track maintenance of the ballast layer was studied, based on the vibration level in the ballast (particle velocity), deviatoric stress level in the ballast and subgrade and the so-called plastic ratio in the ballast layer (induced stress ratio in the ballast normalised to the stress ratio at static failure, according to the Mohr-Coulomb criterion). It was mentioned that plastic settlement in the subgrade is mainly a function of deviatoric stress. The plastic settlement in the ballast is however, related to the stress ratio (the ratio of deviatoric stress to mean stress). If the stress ratio approaches the stress ratio at failure, i.e. the plastic ratio approaches one, more plastic deformation would be generated and more frequent maintenance is needed. Based on three–dimensional finite element simulations, the following observations were made:

  - Deeper and stiffer ballast layers will reduce the stress level in the subgrade and vibration in ballast and thereby reduce track maintenance. Their effect is more pronounced at higher speed. Ballast stiffness degradation and tensionless nature of ballast may however, limit this improvement to a considerable degree.

  - Increasing the train speed will result in a higher vibration and deviatoric stress level in the ballast and in the subgrade. A higher train speed also generally increases the plastic ratio in the ballast layer. It can therefore be said that a track under a higher speed regime requires more frequent maintenance. At a given train speed, softer subgrades cause higher vibration and stress levels in the ballast. Therefore tracks with softer subgrades need more maintenance.

  - The required maintenance level was categorised into three classes: low maintenance ($V<0.50\ V_{cr}$), high maintenance ($0.50\ V_{cr} < V < 0.70\ V_{cr}$) and severe deterioration ($V > 0.70\ V_{cr}$) regions. It was discussed that in a high maintenance zone the treatment of ballast would be enough, whereas in a severe deterioration zone the subgrade also needs to be treated. On this basis, 70% of the track critical velocity can be treated as the track speed limit.

- It was discussed that traditional design approaches are based mainly on reducing the stress or plastic settlement level in subgrade to an acceptable level, and hence they do not address the train speed effect and track maintenance requirements appropriately. Based on three dimensional dynamic modelling of railway track, a design procedure was proposed which takes into account track critical velocity, the stress and vibration level in the ballast, along with stress level in subgrade. According to this design procedure, it is also possible to design track treatments and to establish whether the subgrade or ballast (or both) needs to be improved.

- Substructure nonlinearity was also studied. It was indicated that the nonlinear constitutive relationship for a clayey subgrade should reflect the decrease in resilient modulus with devaitoric stress. It was also discussed that ballast stiffness would increase with mean stress and slightly increase with deviatoric stress (as a result of dilation in a confined space) for low train speeds, when relatively low stresses are induced in the ballast (in the case of a track under a passenger train). Ballast stiffness degradation with deviatoric stress/strain however becomes dominant at higher speeds as the deviatoric stress in the ballast increases considerably. Nonlinear models were calibrated to reflect the hardening and softening effects of the deviatoric stress on the ballast stiffness. Several nonlinear simulations were conducted, using a three-dimensional dynamic finite element track model (track under a moving passenger coach) and the following trends were noted:

  - Based on finite element simulations with nonlinear subgrades and linear ballast, it was seen that the effect of subgrade nonlinearity was increased with the increase in the train speed. A linear subgrade model may underestimate or overestimate - depending on whether lower or upper bound stiffness is considered - the track critical velocity, and the track response and maintenance level in terms of vibration and induced plastic ratio in the ballast.

- In order to study the effect of ballast nonlinearity, finite element simulations with linear subgrade and nonlinear ballast were conducted. At low to medium speed, the effect of ballast nonlinearity seems to be limited. However, as train speed increases further, nonlinearity of the ballast significantly increased the displacement, vibration and asymmetry of displacement field when compared with linear simulations with upper bound stiffness. In addition, the induced stress in subgrade was considerably higher in nonlinear simulations when compared with linear simulations.

- Higher deviatoric stresses in the subgrade, predicted from nonlinear simulations (nonlinear ballast), causes a larger degradation in the resilient stiffness of the subgrade (e.g. according to power model, Equation 5.23). In the presence of ballast nonlinearity, a higher impact on subgrade nonlinearity may therefore be expected. The nonlinearity of the subgrade would also affect the stress state in the ballast and therefore boost the effect of ballast nonlinearity. The effect of ballast and subgrade nonlinearity may be considerable, even at low speeds for freight trains owing to their heavy axles and consequently higher induced stresses in the ballast and subgrade. .

• Using a three-dimensional coupled train-track finite element model, train-track interaction with special reference to stiffness transition near bridges and tunnels were investigated. The following observations were made:

- The oscillations of wheel/rail interaction force caused by discrete sleeper support were investigated for a straight plain track (free of geometrical and/or substructural stiffness irregularities) with varying subgrade stiffness. It was seen that the maximum load exerted on the track increases as the train speed increases and subgrade stiffness decreases.

- Based on the simulations conducted by the coupled train-track model, it was seen that the increase in train speed, and having a softer subgrade, increases the interaction force in the transition zone and affects the passenger comfort

adversely. The increase in dynamic train load in the transition zone was attributed to the excitation of the train, caused by the deflection difference between the soft and rigid sides of the transition. It was indicated that in the presence of no track fault, the change in stiffness on its own does not usually cause a major problem, especially at low to medium speeds.

- The presence of a track fault (e.g. wet spot, voided area) was seen to be the major source of the increase in interaction force and passenger discomfort in the transition zone. The dynamic interaction force and train body acceleration were considerably higher for faulted transitions compared with non-faulted ones in a similar condition. In addition, it was observed that the stress level in the ballast and subgrade in the vicinity of fault is significantly higher than the stress level in similar positions on non-faulted track. It was concluded that the presence of a fault in the transition zone would result in fast deterioration of the track geometry and consequently frequent track maintenance.

- It was indicated that the train-track mechanism in a typical non-faulted transition zone is caused mainly by the response of the train wheels to irregularities produced in the transition zone as a result of stiffness changes. It was therefore concluded that a train model passing a transition curve, which represents a deflection change in the transition zone, would essentially simulate the transition problem, as far as train-track interaction is concerned. Using the train-irregularity model, an extensive parametric study was then conducted on the transition problem in terms of the deflection difference between soft and stiff sides, train speed, and the length in which this difference is traversed (deflection spanning length). The following observations were made:

- Comparing the interaction forces and train body accelerations induced when a pseudo full train or quarter train passed a typical transition, it was observed that while the quarter train and pseudo full train model give approximately the same interaction force, the vertical train body acceleration generated in the full train model is considerably lower than the acceleration generated in a quarter train

model. Such differences in responses were explained through the mechanism governing these two different variables. The interaction force is, to a large extent, governed by the unsprung mass of the wheel. On this basis, the interaction force response of the quarter and pseudo full train models was expected to be similar. Regarding the vertical acceleration of the train body, the suspension system (dampers and springs in the train models), and masses of the car body and pitching of the train are the major players, which are differently represented in the pseudo full and quarter train models. In the pseudo full train model, all dampers connected to the coach and bogies participate, to a different degree, to dissipate the wheel excitation. Accordingly, the level of damping associated with the coach is considerably higher in the pseudo full train model than the quarter train model, which clearly explains why the body acceleration is substantially lower than that of the quarter train model. It was suggested that the pseudo full train model should then be used if passenger comfort is the main subject of study.

- It was seen that the higher the deflection difference between soft and rigid sides of the transition (coming from resilient and permanent settlements), the higher the interaction force and train body acceleration would be for a given spanning length and train speed.

- For a given deflection difference, as the train speed increases then generally longer spanning lengths are required to keep the interaction force and train body acceleration under the permissible levels. In other words, longer spanning length would reduce the dynamic interaction force and train body acceleration for a given deflection difference at a given train speed

- An increase in train speed would increase the interaction force and train body acceleration for a given deflection difference and spanning length.

- It was indicated that deflection difference in a range of a few millimetres coming from the resilient behaviour of a conventional track (train speed lower than 70% of track critical velocity), would not increase the interaction force

considerably, provided a short spanning length is present. Permanent settlement of the track can, however, create a deflection difference in the range of centimetres, which can cause high dynamic load and progressive deterioration of track geometry.

- In terms of spanning length, to keep the dynamic force under a permissible level, a relatively short spanning length provided by a smooth stiffness change is required to span the resilient deflection difference on the soft and stiff sides of the transition (L= 4 m); however, this length increases up to 10 m for high speed cases, if a large defection difference is induced by permanent settlement on the softer side.

- Regarding the train body acceleration, as a passenger comfort index, the prominent effect of deflection difference is also observed on passenger comfort; as the deflection increases, there is a significant increase in train body acceleration and consequently, deterioration of passenger comfort is noted. At least 4 metres of spanning length, suggested based on the dynamic amplification factor for resilient deflection difference (as a result of stiffness difference), is enough to provide a comfortable ride, even if the most restrictive criterion is considered (0.05g). For higher deflection differences (coming from plastic settlement in the substructure), the spanning length should be much longer to satisfy even the least restrictive criterion (0.2g). It also seems that passenger comfort criteria are more difficult to fulfil than the interaction load criterion, especially for high speed cases. Spanning length may need to be even as long as 30 millimetres to satisfy the least restrictive criterion of maximum train body acceleration in the case of high deflection differences (in order of centimetres) and high train speed. Accumulation of permanent deformation in the transition zone, which is the cause of a high deflection difference, should therefore be essentially prevented (or limited) in a high speed track in order to ensure a comfortable ride with shorter spanning lengths. It should also be noted that it is partially down to high speed train design to provide an enhanced suspension system to improve passenger comfort at high speed operations. In practice high

speed trains are specifically designed to give a high quality ride under their operational conditions.

- The dynamic interaction force in the transition zone was studied with respect to the first and second spatial derivatives of the transition curve at three different train speeds (V=30, 50 and 70 m/s). The relationship between the maximum dynamic force and maximum first derivative and second derivative appears to be represented by linear relationships. As expected, increases in the maximum first and second derivative of the transition curve generally result in a higher interaction force. It was also observed that, with the increase in train speed, the gradients of the lines representing the relationships between the first and second gradients of the transition curves and interaction forces also increases, confirming the profound effect of train speed on the dynamic force applied in the transition zone. It was indicated that although for low speed (V=30 m/s), the dynamic amplification of the train load can be satisfactorily correlated to the first derivative of the transition curve (the curve gradient), for higher speed cases, such a correlation starts to deteriorate and the second spatial derivative seems to provide better correlation to the dynamic amplification factor. It is therefore proposed that the second spatial derivative of transition curves can be used for assessment of smoothness of the transition curve, regarding the load exerted on the transition zone, especially for medium to high speed tracks (V>30 m/s).

- The transition design principles were critically reviewed against the findings in the present research, and it was suggested that the design of a transition zone should be based on minimizing potential track faults and permanent deformation in these zones, rather than simply providing a smoother track stiffness change. Regarding the length of the transition, in addition to deflection spanning length, a run-in and run-off length (before and after the spanning length respectively) should be considered to limit the generation of plasticity and related track faults originating from excitation of the train coach when it is on the transition or past the transition. The run-off length was particularly important, as low frequency oscillations of wheel/rail interaction force, when the train coach passed a transition curve, were

noted to continue over a relatively long distance after the spanning length had finished.

- In order to fully understand the mechanism of a granular foundation system, such as railway track (sleeper on ballast or slab track on granular subgrade are surface footings), different granular materials were considered and fundamental features of the granular foundations were numerically studied and compared against experimental trends. As a classical problem, the surface footings have been investigated for several decades and hence a large amount of data exists in this area, which was utilised to evaluate the performance of ALTERNAT in simulating the monotonic response of a geotechnical system (i.e. granular footings). The finding gave invaluable insights into the behaviour of surface footings which is applicable for the monotonic response of railway track. A successful simulation of the monotonic response of surface footing was therefore seen as an important step towards the application of ALTERNAT to model the long-term monotonic and cyclic response of railway track. The outcomes of the study are summarised below:

  - Before employing the constitutive model to study a specific problem (here footing problem), it should be calibrated, i.e. the model parameters should be determined in order to represent a given soil stress-strain behaviour. A calibration procedure was developed to calibrate ALTERNAT against experimental data, based on an optimisation technique, namely a micro genetic algorithm. A calibration procedure was treated as an optimization problem in which the model parameters were determined through minimizing the defined error function, representing the difference between simulated and measured responses for available experimental test sets. The successful application of the procedure in the calibration of ALTERNAT was demonstrated. This procedure is totally independent of the constitutive model, and can overcome the limitations of having a large number of material parameters.

  - The scale effect on the bearing capacity factor N_γ was confirmed. As the footing size increases N_γ decreases.

- The bearing capacity factor increases as the relative density increases. Smooth footings yield a lower bearing capacity than the equivalent rough footings. While varying slightly with material type, the ratio of the smooth footing bearing capacity to the rough footing bearing capacity was approximately 0.5.

- The dilative behaviour of dense sand was well presented. More dilation is observed in denser sand under the footing, which resulted in a post-peak strain softening response.

- Circular footings yield a lower bearing capacity factor N_γ than those of the equivalent strip footings. The shape factor appears to be material dependent and does not apparently depend on footing size. However, a value of 0.6, as proposed by De Beer (1970), can be applied in the general case.

- Granular foundations fail progressively. The depth of the failure zone is proportional to the footing size. A rough footing exhibits a deeper failure mechanism than a smooth footing. The failure zone depths are about 2 and 1.5 times the foundation diameter for rough and smooth circular footings respectively.

- In a manner similar to observations from experiments, two counteracting progressive failure mechanisms are observed: an increase in the progressive failure potential with decreasing footing size for relatively dense sands, and an increase in the progressive failure dominancy with increasing footing size in loose sands.

- The effect of roughness is observed to be generally more pronounced as settlement increases. The settlement level, before which the settlement is practically not affected by roughness, is seen to be about 2% of the footing diameter for all different densities and footing sizes considered. The footing response up to a tolerable settlement of 25 mm for common structures is practically unaffected by roughness for larger footings (B>2; B is footing diameter). In addition, as the footing size increases, the settlement level after

which the roughness affects the footing response also increases, implying that the response of the footing remains almost unaffected by roughness up to a relatively large settlement.

- For settlement calculations, the depth of influence at which the vertical strain mostly affects the settlement is numerically found to be around 2B for axi-symmetric footings, confirming conventional assumptions, irrespective of soil density and footing roughness.

- Higher compressible sandy soils (lower density, higher fine content) give higher settlement for a given unit load. For a given settlement level (before the failure point and higher than the allowable settlement level) the slip zone is generally deeper in lower compressible sandy soil than one in high compressible sandy soil. Lower compressible soils fail at lower settlement levels than higher compressible soils, under a given footing.

- At an allowable settlement level (S=25mm), the slip zone depth can be assumed to equal the footing diameter in both rough and smooth cases for circular footings in all cases.

- As density decreases and fine content increases, the ratio between the allowable bearing pressure and ultimate bearing pressure decreases. Therefore it can be said that higher compressibility (lower density, higher fines content) generally raises the likelihood of the settlement being the critical issue in the design. Roughly speaking, for a density lower than 70%, settlement is usually found to be the major concern.

- As the footing size increases the ratio between the allowable bearing pressure and ultimate bearing pressure decreases, and hence the chance that the settlement controls the design process increases.

- The allowable bearing pressure decreases with the footing size. The increase in density and the decrease in fine content would decrease the allowable bearing

pressure. The effect of density seems to be more pronounced for smaller footings (B<2). Rough footings have higher allowable bearing pressure than the equivalent smooth footings. The effect of footing roughness seems to diminish for large foundations (B>2 m).

- ALTERNAT was also used to study briefly the cyclic behaviour of granular soil, and it was demonstrated that it will represent the basic features of the cyclic response under a varying conventional triaxial cyclic load. For future research, an approach was proposed to integrate a three-dimensional coupled train-track finite element model and cyclic settlement model (based on ALTERNAT) to simulate the life-long performance of railway tracks.

8.2 Recommendations for Future Research

The following areas are recommended for further research:

- A typical simulation of a coupled train-track is time consuming using conventional computers. It is therefore suggested that the developed code be paralyzed. Using the paralyzed code, the following studies can be made:

  - Wave propagation at high speeds, the effect of the embankment on wave propagation.

  - The effect of mitigation techniques, such as infilled trenches, on wave propagation in railway track and vibration level on the surrounding area. e.g. in the buildings in the vicinity of railway tracks.

  - Sleeper voiding effects on track response in the transition zone. Fine meshing is required around the voided sleeper(s). Contact elements need to be incorporated to simulate sleeper-ballast contact and loss of contact for voided sleepers. In addition, a two-point rail-wheel contact mechanism may

need to be implemented. Voiding development and growth in the ballast can be simulated utilizing the integrated coupled train-track dynamic model and cyclic settlement model (based on ALTERNAT).

- Modelling soil improvement techniques, such as stone columns and application of geosynthetics on the track response in the finite element framework.

- It is well-known that the Lysmer boundary does not absorb the Rayleigh wave properly. A more appropriate yet simple boundary condition needs to be developed for railway track modelling at high speeds.

- Experimental observations show a considerable particle breakage in the ballast when it is under high pressure. Constitutive models like ALTERNAT do not take into account the effect of particle breakage. Research should be done to incorporate its effect in ALTERNAT. The modified constitutive model can then be used to study the effect of particle breakage on densification and settlement of the granular layer.

- Three dimensional footing analyses need to be conducted to study the loading-deformation and failure mechanism of the sleeper on ballast. The effect of different parameters such as sleeper size, roughness, stiffness and flexural properties of sleeper (e.g. for wooden, concrete and steel sleepers) can be investigated.

- Full application of the proposed approach towards long-term performance of track needs to be researched. The stress level in the ballast (or substructure in general), obtained from the three-dimensional coupled train-track model, can be fed into the ALTERNAT cyclic settlement model in which ALTERNAT is calibrated (e.g. to ballast, sub-ballast, subgrade). The cyclic model includes a single finite element representing, e.g., ballast under the sleeper or a column of finite elements representing the substructure layer. The stress input to the cyclic model can be in the form of stress components which are converted to nodal forces which will be applied as boundary conditions to the mesh. The cyclic model is then cycled to a number which represents the given number of train passages and hence predicts the

permanent settlement under the sleeper after the given number of train passages. The predicted permanent settlements will then be fed back into the dynamic coupled train-track model as an irregularity profile. The dynamic model, with the new irregularity profile, is then used to predict the new stress state in the substructure which is then fed into the cyclic model, to estimate the permanent settlement generated after a certain number of train passages. In this way, it will be possible to simulate the long-term performance of railway track with respect to substructure behaviour, and optimize the railway track system in terms of required maintenance, for design purposes. It is also possible to plan the ballast maintenance, in terms of maintenance intervals required to keep the track geometry at an acceptable level. It would also be ideal if the numerical research was accompanied by full laboratory and site measurements (e.g. field tests and instrumentations, geophysical investigations) so that a full understanding of the track mechanics, in terms of maintenance requirements, can be developed.

References

Aiban, A.S., and Znidarčić, D., 1995. Centrifugal modelling of bearing capacity of shallow foundations on sands. Journal of Geotechnical Engineering, ASCE, 121(10): 704-711.

Allen, J.J., 1973. The Effect of non-constant lateral pressure of the resilient response of granular materials, Ph.D. Thesis, University of Illinois, Urbana, Illinois, USA.

Allen, J.J., and Thompson, M.R., 1974. Resilient response of granular materials subjected to time-dependent lateral stresses. Transportation Research Record, 510(1-13).

Alva-Hurtado, J. E., 1980. A methodology to predict the elastic and inelastic behaviour of railroad ballast, PhD Thesis, Univertisy of Massachusetts, Amherst, Massachusetts.

Alva-Hurtado, J.E., and Selig, E. T., 1981. Permanent strain behaviour of railroad ballast, Proceedings of the 10th International Conference on Soil Mechanics and Foundation Engineering, Stockholm, Sweden, pp. 543-546.

American Railway Engineering Association (AREA), 1996. Manual for railway engineering, Washington.

Andersen, L., and Nielsen, S.R.K., 2003. Boundary element analysis of the steady state response of an elastic half-space to a moving force on its surface. Engineering Analysis with Boundary Elements, 27(1): 23-38.

Arulmoli, K., Muraleetharan, K. K., Hossain, M. M. and. Fruth, L. S., 1992. VELACS, Verification of liquefaction analysis by centrifuge studies, laboratory testing program, soil data report, The Earth Technology Corporation, CA.

Banimahd, M., and Woodward, P. K. , 2006. Load-displacement and bearing capacity of foundations on granular soils using a multi-surface kinematic constitutive soil model. International Journal for Numerical and Analytical Methods in Geomechanics, 30(9): 865 - 886.

Banimahd, M., and Woodward, P.K., 2007. 3-dimensional finite element modelling of railway transitions, Proceedings of 9th International Conference on Railway Engineering, London, UK.

Barksdale, R.D., 1972. Laboratory evaluation of rutting in base course materials, Proceedings of 3rd International Conference on Structural Design of Asphalt Pavements, pp. 161-174.

Becker, D., 1996. 18th Canadian geotechnical colloquium: limit states design for foundation part1. An overview of the foundation design process. Canadian Geotechnical Journal, 33(6): 956-983.

Bellotti, R., Ghionna, V., Jamiolkowski, M., Robertson, P.K., and Peterson, R.W. , 1989. Interpretation of moduli from self-boring pressuremeter tests in sand. Géotechnique, 39(2): 269-292.

Beskos, D.E., 1997. Boundary element methods in dynamic analysis: Part II. Applied Mechanics Review, 50(3): 149-197.

Bodare, A., 1993. markvibrationer i samband med tagtrafik, program for forskningproject (In Swidish), Division of Soil and Rock Mechanics, Department of Civil and Environmental Engineering, Royal Institute of technology, Stockholm, Sweden.

Bolton, M.D., 1986. The strength and dilatancy of sands. Géotechnique, 36(1): 65-78.

Boyce, J.R., Brown, S. F., and Pell, P. S., 1976. The resilient behaviour of a granular material under repeated loading. Proceedings of Australian Road Research Board, 8: 8-19.

Boyce, J.R., 1980. A non-linear model for the elastic behaviour of granular materials under repeated loading, Proceedings of International Symposium on Soils Under Cyclic and Transient Loading, Swansea, UK., pp. 285-294.

Brecciaroli, F., and Kolisoja, P., 2006. Deformation behaviour of railway embankment materials under repeated loading, Literature review, Finish Railway Administration, Helsinki, Finland.

Briaud, J.L., and Gibbens, R., 1994. Test and prediction results for five large spread footings on sand, Proceedings of a prediction symposium sponsored by the Federal Highway Administration at the occasion of the settlement '94 ASCE Conference at Texas A&M University, ASCE, Geotechnical Special Publication, No. 41, pp. 92-128.

Brough, M.J., Ghataora, G. S., Stirling, A. B., Madelin, K. B., Rogers C. D. F., and Chapman D. N. , 2003. Investigation of railway track subgrade. I: In-situ assessment. Proceedings of ICE: Transport, 156 (3): 145-154.

Brown, S.F., and Pell, P.S., 1967. An experimental investigation of the stresses, strains and deflections in a layered pavement structure subjected to dynamic loads, Proceedings of 2nd International Conference on Structural Design of Asphalt Pavements, Ann Arbor, USA, pp. 487-504.

Brown, S.F., Lashine, A.K.F., and Hyde, A.F.L., 1975. Repeated load triaxial testing of silty clay. Geotechnique, 25(1): 95-114.

Brown, S.F., and Hyde, A.F.L, 1975. Significance of cyclic confining stress in repeated load triaxial testing of granular material. Transportation Research Record, 537: 49-58.

Brown, S.F., 1979. The characterization of cohesive soils for flexible pavement design, Design Parameters in Geotechnical Engineering, British Geotechnical Society, London, UK, pp. 15-22.

Brown, S.F., and Selig, E.T., 1991. The design of pavement and rail track foundations. Cyclic loading of soils: from theory to design, M.P.O'Reilly, and S.F. Brown (Eds), Von Nostrand Reinhold, N.Y., pp. 249-305.

Brown, S.F., and Dawson, A. R., 1992. Two stage mechanistic approach to asphalt pavement design, Proceedings of 7th International Conference on Asphalt Pavements, Vol. 1, International Society for Asphalt Pavements, University of Nottingham, Nottingham, UK, pp. 16-34.

Brown, S.F., 1996. Soil mechanics in pavement engineering, 36th Rankine Lecture of the British Geotechnical Society. Geotechnique, 46(3): 383-426.

Burland, J.B., and Burbridge, M.C., 1985. Settlement of foundations on sand and gravel. Century Celebration of Glasgow and West of Scotland, Proceedings of Institution of Civil Engineers: 1325-1381.

Burmister, D.M., 1945. The general theory of stresses and displacements in layered soil systems. Journal of Applied Physics, 16: 89–94 126-127; 296-302.

Burrow, M.P.N., Bowness D., and Ghataora, G.S., 2007. A comparison of railway track foundation design methods. Proceedings of the Institution of Mechanical Engineers Part F: Journal of Rail and Rapid Transit (Special Issue on Rail Research UK), 221: 1-12.

Cai, Z., Raymond, G.P., AND Bathust, R.J., 1994. Estimate of static track modulus using elastic foundation models. Transportation Research Record: 65-71.

Carroll, D.L., 1996. Genetic Algorithms and Optimizing Chemical Oxygen-Iodine Lasers, Proceedings of Conference on Developments in Theoretical and Applied Mechanics, The University of Alabama, USA, pp. 411-424.

Caughey, T.K., 1960. Classical normal modes in damped linear systems. Journal of Applied Mechanics, ASME, 27: 269–271.

Chang, S.C., Adegoke, C.W., and Selig, E.T., 1980. Geotrack model for railroad track performance. Journal of Geotechnical Engineering, ASCE, 106(GT11): 1201-1217.

Chen, W.F., 1975. Limit analysis and soil plasticity. Elsevier Science.

Cheung, L.W., 1994. Laboratory assessment of pavement foundation materials, PhD thesis, University of Nottingham, Nottingham, U.K.

Chuhan, Z., and Chongbin, Z. , 1987. Coupling method of finite and infinite elements for strip foundation. Earthquake Engineering and Structural Dynamics 15: 839–851.

Clark, C.W., 1957. Track loading fundamentals-parts 1-7. Railway Gazette, 106.

Clark, M., McCann, D.M., and Forde M.C., 2002. Infrared thermographic investigation of railway track ballast. NDT&E International, 35: 83-94.

Clark, M., Gordon, M., and Forde M.C., 2004. Issues over high-speed non-invasive monitoring of railway trackbed. NDT&E International 37: 131–139.

Cook, R.D., Malkus, D.S. Plesha, M.E., and Witt, R.J., 2002. Concepts and applications of finite element analysis. John Wiley and Sons.

Correia, A.G., 2004. Evaluation of mechanical properties of unbound granular materials for pavements and rail tracks, Keynote Lecture, International Seminar on Geotechnics in Pavement and Railway Design and Construction, Athens, Greece.

Cundal, P.A., Kunar, R.R., Carpenter P.C., and Marti, J. , 1978. Solution of infinite dynamic problems by finite modelling in the time domain, Proceedings of 2nd International Conference on Applied Numerical Modelling Madrid, Spain.

Dahlberg, T., 2001. Some railroad settlement models-a critical review. Proceedings of Institution of Mechanical Engineers, Part F, Journal of Rail and Rapid Transit, 215: 289-300.

Dahlberg, T., 2006. Track issues, Handbook of Railway Vehicle Dynamics, S. Iwnicki (Ed). Taylor & Francis, pp. 144-175.

Davis, E.H., and Booker, J.R. , 1973. Some adaptations of classical plasticity theory for soil stability problems, Proceedings of Symposium on Role of Plasticity in soil Mechanics, Cambridge, England, pp. 24-41.

De Beer, E.E., 1965. Bearing capacity and settlement of shallow foundations on sand, Proceedings of Symposium on Bearing Capacity and Settlements of Foundations, Duke University, Durham, N.C., pp. 15-33.

De Beer, E.E., 1970. Experimental determination of the shape factors and the bearing capacity factors of sand. Géotechnique, 20(4): 387-411.

De Borst, R., and Vermeer, P.A. , 1984. Possibilities and limitation of finite elements for limit analysis. Géotechnique, 34(2): 199-210.

De Man, A.P., 2002. DYNATRACK: A survey of dynamic railway, track properties and their quality. Ph.D. Thesis, Delft University of Technology, Delft, the Netherlands.

Dieterman, H., and Metrikine, A., 1997. Steady-state displacement of a beam on an elastic half-space due to a uniformly moving constant load. European Journal of Mechanics A/Solids, 16(2): 295-306.

Dobry, R., and Vucetic, M., 1987. Dynamic properties and seismic response of soft clay deposits, Proceedings of International Symposium on Geotechnical Engineering for soft soils, Mexico City, Mexico, pp. 51-87.

Drumm, E.C., Baoting-Paku, Y., and Pierce, T.J., 1991. Estimation of subgrade resilient modulus from standard tests. Journal of Geotechnical Engineering, ASCE, 116(5): 774-789.

Eberson, W., Trevizo, M.C., and Selig, E.T. , 1993. Effect of low track modulus on track performance, Proceedings of the Fifth International Heavy Haul Conference, China, pp. 379–388.

Eisenmann, J., and Rump, R., 1997. Ein Schotteroberban für hohe Geschwindigkeiten (In German). Eisenbahntechnische Rundschan, 3: 99-107.

El Horsi, M.S., 1984. Contribution a l'etude des propriete mecanique des materiaux (in French), Thesis d'Etat, University of Paris, Paris, France.

Elfino, M.K., and Davidson, J.L., 1989. Modelling field moisture in resilient moduli testing, Resilient Moduli of Soils: Laboratory Conditions, ASCE Geotechnical Special publications, No.24, pp. 31-51.

Erikson, H.L., and Drescher, A., 2002. Bearing capacity of circular footings. Journal of Geotechnical and Geoenvironmental Engineering, ASCE, 128(1): 38-43.

Esveld, 2001. Modern Railway Track. MRT Productions.

Frederick, C.O., and Round, D.J. , 1984. Vertical train loading, track technology for the next decade. Vehicle System Dynamics, Special Supplement, 24: 222-233.

European Committee for Standardization, 1995. EUROCODE 1: Basis of Design and Actions on Structures. Part 3: Traffic Loads on Bridges, ENV 1991-3.

Frost, M.W., Fleming, P.R., and Rogers, D. F. C., 2004. Cyclic triaxial tests on clay subgrades for analytical pavement design. Journal of Transportation Engineering, ASCE, 130(3): 378-386.

Fryba, L., 1999. Vibration of solids and structure under moving loads. Groningen, Noordhoof.

Frydman, S., and Burd, H.J., 1997. Numerical studies of bearing capacity factor Nγ. Journal of Geotechnical and Geoenvironmental Engineering, ASCE, 123(1): 20-29.

Fuchs, C., and Kaliakin, V.N. , 2000. Footing settlement simulations: modelling considerations, Proceedings of EM2000, 14th Engineering Mechanics Conference, ASCE, Austin, TX.

Gallagher, G.P., Leiper, Q., Williamson, R., Clark, M.R., and Forde, M.C. , 1999. The application of time domain ground penetrating radar to evaluate railway track ballast. NDT&E International, 32: 463–468.

Goldberg, D.E., 1989. Genetic Algorithms in Search, Optimization and Machine Learning. Addison-Wesley.

Golder, H.Q., 1941. The ultimate bearing pressure of rectangular footings. Proceedings of the Institution of Civil Engineers, 17: 161-174.

Grandil, J., and Ramondence, P., 1990. The dynamic behaviour of railways on high-speed lines, SNCF, Paris.

Grassie, S.L., Gregory, R. W., Harrison, D. and Johnson, K. L., 1982. The dynamic response of railway track to high frequency vertical excitation. Proceedings of Institution of Mechanical Engineers, Part C: Journal of Mechanical Engineering Science, 24: 77-90.

Griffiths, D.V., 1982. Computation of bearing capacity factors using finite elements. Géotechnique, 32(3): 195-202.

Gudishala, R., 2004. Development of resilient modulus prediction models for base and subgrade pavement layers from in situ devices test results, MSc Thesis, Louisiana State University, Louisiana, USA.

Hall, L., 2000. Simulations and analyses of train-induced ground vibrations, a comparative study of two and three-dimensional calculations with actual measurements, PhD Thesis, Royal Institute of Technology, Sweden.

Hall, L., 2003. Simulations and analyses of train-induced ground vibrations in finite element models. Soil Dynamics and Earthquake Engineering 23: 403–413.

Hansen, J.B., 1970. A revised and extended formula for bearing capacity. Bulletin of Danish Geotechnical Institute, 28:5-11.

Haynes, J.G., and Yoder, E.J., 1963. Effect of repeated loading on gravel and crushed stone base course materials used in the AASHO (American Association of State Highway Officials) road test. Highway Research Record, 39.

Heath, D.L., Shenton, M. J., Sparrow, R. W., and Waters, J. M., 1972. Design of conventional rail track foundations. Proceedings of Institution of Civil Engineers, 51: 251–267.

Hettler, A., and Gudehus, G., 1988. Influence of the foundation width on the bearing capacity factor. Soils and Foundations, 28(4): 81-92.

Hicks, R.G., 1970. Factors influencing the resilient properties of granular materials, Ph.D. Thesis, University of California, Berkeley, CA

Hicks, R.G., and Monismith, C.L., 1971. Factors influencing the resilient response of granular materials. Highway Research Record, 345: 15-31.

Hinton, E., Rock, T., and Zienkiewicz, O.C., 1976. A note on mass lumping and related processes in the finite element method. Earthquake Engineering and Structural Dynamics, 4: 245-249.

Hjiaj, M., Lyamin, A.V., and Sloan, S.W., 2005. Numerical limit analysis solutions for the bearing capacity factor Nγ. International Journal of Solids and Structures, 42: 1681-1704.

Hornych, P., Kazai, A., and Piau, J.M., 1998. Study of the resilient behaviour of unbound granular materials, Proceedings of 5th International Conference on the Bearing Capacity of Roads and Airfields, Trondhein, Norway, pp. 1277-1287.

Huang, A.B., Hsu, H.H. and Chang, J.W., 1999. The behaviour of a compressible silty fine sand. Canadian Geotechnical Journal, 36: 88-101.

Huang, Y.H., Lin, C., Deng, X., and Rose, J., 1984. KENTRACK, A Computer Program for Hot-Mix Asphalt and Conventional Ballast Railway Track beds, Asphalt Institute (Publication RR-84-1) and National Asphalt Pavement Association (Publication QIP-105).

Hugenschmidt, J., 2000. Railway track inspection using GPR. Journal of Applied Geophysics 43: 147–155.

Hung, H.H., and Yang, B.Y., 2001. A review of researches in ground-born vibrations with emphasis on those induced by trains. Proceedings of National Research Council, China, 25(1): 1-16.

Hunt, G.A., 1994. Analysis of requirements for railway construction on soft ground, Technical Report LR TM 031, British Rail Research, London, UK.

International Union of Railways, 1994. Earthworks and track-bed layers for railway lines. UIC Code 719 R, Paris, France.

Ishibashi, I., and Zhang , X. , 1993. Unified dynamic shear moduli and damping ratios of sand and clay. Soils and Foundations, 33(1): 182-191.

Jardine, R.J., Potts, D.M., A.B., Fourie, and J.B., Burland, 1986. Studies of the influence of non-linear stress-strain characteristics in soil-structure interaction. Géotechnique, 36(3): 377-396.

Jenkins, H.H., Stephenson, J.E., Clayton, G.A., Morland, G.W., and Lyon, D., 1974. The effect of track and vehicle parameters on wheel/rail vertical dynamic forces. Railway Engineering Journal, 3: 2-16.

Johnson, K.L., 1985. Contact mechanics. Cambridge University Press.

Jones, C.J.C., and Block, J. R., 1996. Prediction of ground vibration from freight trains. Journal of Sound and Vibration, 193(1): 205-213.

Jones, D.V., Laghrouche, O. and Le Houdec, D., 1994. A study of the active isolation of traffic vibrations using a coupled finite and infinite elements model, Proceedings of Conference on Advances in Computational Method for Simulation, Edinburgh, UK, pp. 165-170.

Jones, D.V., Le Houedec, D., and Petyt, M., 1998. Ground vibrations due to a rectangular harmonic load. Journal of Sound and Vibration, 212(1): 61-74.

Jong, G., 1976. Rowe's stress-dilatancy relation based on friction. Geotechnique, 26(3): 527-534.

Ju, S.H., and Lin, H.T. , 2004. Analysis of train-induced vibrations and vibration reduction schemes above and below critical Rayleigh speeds by finite element method. Soil Dynamics and Earthquake Engineering, 24(12): 993-1002.

Ju, S.H., 2007. Finite element analysis of structure-borne vibration from high-speed train. Soil Dynamics and Earthquake Engineering, 27: 259–273.

Kaynia, A.M., Madhus, C., and Zackrisson, P., 2000. Ground vibration from high-speed trains: prediction and countermeasure. Journal of Geotechnical and Geoenvironmental Engineering, 126 (6): 531–537.

Kenney, J.T., 1954. Steady-state vibrations of beam on elastic foundation for moving load. Journal of Applied Mechanics, 76: 359-364.

Kerr, A., and Moroney, B.E.., 1993. Track transition problems and remedies. Proceedings of American Railway Engineering, 94: 267-298.

Kerr, A.D., 1987. On the vertical modulus in a standard railway track analysis. Rail International, November Issue.

Kerr, A.D., and Eberhardt, A.W., 1992. The stress analysis of railroad track with nonlinear base response. Rail International, March Issue.

Kerr, A.D., 2000. On the determination of the rail support modulus k. International Journal of Solids and Structures, 37: 4335-4351.

Kimura, T., Kusakabe, O., and Saitoh K., 1985. Geotechnical model tests of bearing capacity problems in a centrifuge. Géotechnique, 35(1): 33-45.

Knutson, M., and Thompson, M.R., 1977. Resilient response of railway ballast. Transport Research Record, Transportation Research Board, 651: 31-39.

Kokusho, T., Yoshida, Y. and Esashi Y. , 1982. Dynamic properties of soft clay for wide strain range. Soils and Foundations, 20(2): 45-60.

Kolisoja, P., 1994. Large scale dynamic triaxial tests with coarse grained aggregates, Proceedings of 4th International Conference on the Bearing Capacity of Roads and Airfields, Minneapolis, USA.

Kolisoja, P., 1997. Resilient deformation characteristics of granular materials. Ph.D. Thesis, Tampere University of Technology, Tampere, Finland.

Kramer, S.L., 1996. Geotechnical earthquake engineering. Prentice Hall.

Krishnakumar, K., 1989. Micro-genetic algorithms for stationary and non-stationary function optimization, SPIE Proceedings of Intelligent Control and Adaptive Systems, pp. 289-296.

Krylov, V.V., Dawson, A. R., Heelis, M. E. and Collop, A. C., 2000. Rail movement and ground waves caused by high-speed trains approaching track-soil critical velocities. Proceedings of Institution of Mechanical Engineers, Part F: Journal of Rail and Rapid Transit, 214(2): 107-116.

Kumar, J., 2004. Effect of footing-soil interface friction on bearing capacity factor Nγ. Géotechnique, 54(10): 677-680.

Kutter, B.L., Abghari, A., and Cheney, J.A., 1988. Strength parameters for bearing capacity of sand. Journal of Geotechnical Engineering. ASCE, 114(4): 491-497.

Lade, P.V., and Duncan, J.M. , 1975. Elasto-plastic stress-strain theory for cohesionless soils. Journal of Geotechnical Engineering, ASCE, 107(GT10): 1037-1053.

Lade, P.V., 1977. Elasto-plastic stress-strain theory for cohessionless soil with curved yield surface. International Journal of Solids and Structures, 13: 1019-1035.

Lade, P.V., 1979. Three-dimensional stress-strain behaviour and modelling of soils, Heft 4, Serie Grundbau, Institute of Soil and Foundation Engineering, Ruhr University of Bochum. Germany.

Lade, P.V., and Nelson, R.B., 1987. Modelling the elastic behaviour of granular materials. International Journal for Numerical and Analytical Methods in Geomechanics, 11: 521-542.

Lane, G.S., 1982. The effect of track and traffic parameters on the development of track vertical roughness, Proceedings of 2nd International Heavy Haul Railway Engineering Conference, Colorado, USA, pp. 395-405.

Lee, J., and Salgado, R. , 2002. Estimation of footing settlement in sand. International Journal of Geomechanics, ASCE, 2(1): 1-28.

Lee, J., and Salgado, R., 2005. Estimation of bearing capacity of circular footings on sands based on cone penetration test. Journal of Geotechnical and Geoenvironmental Engineering, ASCE, 131(4): 442-452.

Lee, W., Altschaeffl, A. G. and White, T. D. , 1997. Resilient modulus of cohesive soils. Journal of Geotechnical and Geoenvironmental Engineering, ASCE, 123(2): 131 – 136.

Lehane, B., and Fahey, M. , 2002. A simplified nonlinear settlement prediction model for foundations on sand. Canadian Geotechnical Journal, 39: 293-303.

Lei, X., and Mao, L., 2001. Dynamic analysis of the track structure of a high speed railway using finite elements. Proceedings of Institution of Mechanical Engineers, Part F: Journal of Rail and Rapid Transit, 215: 301-309.

Lei, X., and Noda, N.A., 2002. Analyses of dynamic response of vehicle and track coupling system with random irregularity of track vertical profile. Journal of Sound and Vibration, 258 147–165.

Lei, X., and Mao, L., 2003. Dynamic response analyses of vehicle and track coupled system on track transition of conventional high speed railway. Journal of Sound and Vibration, 271: 1133-1146.

Lekarp, F., and Dawson, A., 1998. Modelling permanent deformation behaviour of unbound granular materials. Construction and Building Material, 12(1): 9-18.

Lekarp, F., Isacsson, U., and Dawson, A., 2000a. State of the art. I: Resilient response of unbound aggregates. Journal of Transportation Engineering, ASCE, 126(1): 66-75.

Lekarp, F., Isacsson,U., and Dawson A., 2000b. State of the art. II: Permanent strain response of unbound aggregates. Journal of Transportation Engineering, ASCE, 126(1): 76-83.

Lentz, R.W., and Baladi, G. Y. , 1981. Constitutive equation for permanent strain of sand subjected to cyclic loading. Transport Research Record, 810: 50-54.

Li, D., and Selig, E. T., 1994. Resilient modulus for fine-grained subgrade soil. Journal of Geotechnical Engineering, 120(6): 939-957.

Li, D., and Selig, E.T., 1996. Cumulative plastic deformation for fine-grained subgrade soils. Journal of Geotechnical Engineering, ASCE, 122(12): 1006-1013.

Li, D., Sussman, T. R., and Selig, E. T., 1996. Procedure for railway track granular layer thickness determination, Report no. R-898, Association of American Railroads, Transportation Technology Center, Pueblo, Colorado, USA.

Li, D., and Selig, E. T., 1998a. Method for railroad track foundation design. I: development

Journal of Geotechnical and Geoenvironmental Engineering, ASCE 124(4): 316–322.

Li, D., and Selig, E. T., 1998b. Method for railroad track foundation design. II: applications. Journal of Geotechnical and Geoenvironmental Engineering, ASCE, 124(4): 323-332.

Li, D., and Davis, D., 2005. Transition of railroad bridge approaches. Journal of Geotechnical and Geoenvironmental Engineering, 131(11): 1392-1398.

Liang, B., Zhu, D., and CAI, Y. , 2001. Dynamic analysis of the vehicle-subgrade model of a vertical coupled system. Journal of Sound and Vibration, 245(1): 79-92.

Lundqvist, A., and Dahlberg, T, 2005. Load impact on railway track due to unsupported sleepers. Proceedings of Institution of Mechanical Engineers, Part F: Journal of Rail and Rapid Transit, 219(2): 67-77.

Luo, Y., Yin, H., and Hua, C., 1996. The dynamic response of railway ballast to the action of trains moving at different speeds. Proceedings of Institution of Mechanical Engineers, Part F: Journal of Rail and Rapid Transit, 210: 95-101.

Lyon, D., 1972. The calculation of track forces due to dipped rail joints, wheel flats and rail welds, Second ORE Colloquium on Technical Computer Programs.

Lysmer, J., and Kuhlemeyer, R.L., 1969. Finite dynamic model for infinite media. Journal of the Engineering Mechanics, ASCE, 95(EM4): 859–877.

Madshus, C., and Kaynia, A.M., 2000. High–speed trains on soft ground: dynamic behaviour at critical speed. Journal of Sound and Vibration, 231(3): 689-701.

Madshus, C., Lacasse, S., Kaynia, A and Hårvik L. , 2004. Geodynamic challenges in high speed railway projects, International Conference on Geotechnical Engineering For Transportation projects, ASCE, CA, pp. 192-215.

Maeda, K., and Miura, K., 1999a. Confining stress dependency of mechanical properties of sands. Soils and Foundations, 39(1): 53-68.

Maeda, K., and Miura, K. , 1999b. Relative density dependency of mechanical properties of sands. Soils and foundations, 39(1): 69-80.

Mair, I.R., 1976. The rail as a beam on a stiffening elastic foundation Rail International, No.8.

Malik, A.K., Chandra, S., and Singh, A.B., 2006. Steady-state response of an elastically supported infinite beam to a moving load. Journal of Sound and Vibration, 291: 1148-1169.

Manoharan, N., and Dasgupta, S.P., 1995. Bearing capacity of surface footings by finite elements. Computers and Structures, 54(4): 563-586.

Maree, J.H., Freeme, C. R., Van Zyl, N. J., and Savage, P. F. , 1982. The permanent deformation of pavements with untreated crushed stone bases as measured in heavy vehicle simulator tests., Proceedings of 11th Australian Road Research Board Conference, pp. 16–28.

Mayhew, H.C., 1983. Resilient properties of unbound road base under repeated triaxial loading, Transport and Road Research Laboratory, Crowthorne, UK.

Meimon, Y., Corte, J.F., Fargeix, D. and Flavigny, E., 1991. Validation de modéles pour le calcul des fondation superficielles (In French), Proceeding of 10th European Conference on Soil Mechanics & Foundation Engineering, Florence, Italy.

Meyerhof, G.G., 1951. The ultimate bearing capacity of foundations. Géotechnique, 2(4): 301-332.

Meyerhof, G.G., 1955. Influence of roughness of base and ground-water conditions on the ultimate bearing capacity of foundations. Géotechnique, 6: 227-242.

Meyerhof, G.G., 1963. Some recent research on the bearing capacity of foundations. Canadian Geotechnical Journal, NRC, 1(1): 16-26.

Miller, G.F.G., Pursey, H., 1954. On the partition of energy between elastic waves in a semi-infinite solid. Proceedings of the Royal Society, London, UK, 2333: 55-69.

Mitry, F.G., 1964. Determination of the modulus of resilient deformation of untreated base course materials, Ph.D. Thesis, University of California, Berkeley, California, USA.

Molenkamp, F., 1982. Kinematic model for alternating loading ALTERNAT, GM Report CO-218598, Delft Geotechnics.

Molenkamp, F., 1987. Elasto-plastic model for the simulation of liquefaction under alternating loading, Department of Civil Engineering, University of Ottawa.

Molenkamp, F., 1988. A simple model for isotropic non-linear elasticity of frictional materials. International Journal for Numerical and Analytical Methods in Geomechanics, 12: 467-475.

Molenkamp, F., 1990. Reformulation of ALTERNAT to minimise numerical drift due to cyclic loading, University of Manchester.

Molenkamp, F., 1992. Application of non-linear elastic model. International Journal for Numerical and Analytical Methods in Geomechanics, 16: 131-150.

Monismith, C.L., Seed, H.B., Mitry, F.G., and Chan, C.K. , 1967. Prediction of pavement deflections from laboratory tests, Proceedings of 2nd International Conference on Structural Design of Asphalt Pavements, Ann Arbor, USA., pp. 109-140.

Monismith, C.L., Ogawa, N. and Freeme, C.R., 1975. Permanent deformation characteristics of subgrade soil due to repeated loading. Transport Research Record, 537: 1-17.

Moore, W.M., Britton, S.C., and Scrivner, F.H., 1970. A laboratory study of the relation of stress to strain for a crushed limestone base material, Research Report 99-5F, Study 2-8-65-99, Texas Transportation Institute, Texas A and M University, Texas, USA.

Moossazadeh, J., and Witczak, M.W. , 1981. Prediction of subgrade moduli for soil that exhibits nonlinear behaviour. Transport Research Record, 810: 9-17.

Muhs, E., 1963. Über die zullässige bellastung nichtibindiger böden. Mittielungen der Deutschen Forschungsgesellshaft Für bodenmechanik(Degebo), Heft 16 (in German), Berlin. Germany.

Network Rail, 2005. Company Code of Practice, Formation treatments NR/SB/TRK/9039, Network Rail, London , UK.

Nielsen, J.C.O., and Abrahamsson, T.J.S 1992. Coupling of physical and modal components for analysis of moving nonlinear dynamic systems on general beam structures. International Journal for Numerical Methods in Engineering, 33: 1843-1859.

Nielson, J.C.O., and Igeland, A. 1995. Vertical dynamic interaction between train and track—influence of wheel and track imperfections. Journal of Sound and Vibration, 187: 825-839.

Ovesen, N.K., 1975. Centrifugal testing applied to bearing capacity problems of footings on sand. Géotechnique, 25(2): 394-401.

Paolucci, R., and Spinelli, D. , 2006. Ground Motion Induced by Train Passage. Journal of Engineering Mechanics, ASCE, 132(2): 201-210.

Papadopoulos, B.P., 1992. Settlements of shallow foundations on cohesionless soils. Journal of Geotechnical Engineering , ASCE, 118(3): 377-393.

Pappin, J.W., and Brown, S.F., 1980. Resilient stress-strain behaviour of a crushed rock, Proceedings of International Symposium on Soils under Cyclic and Transient Loading, Swansea, UK, pp. 169-177.

Paute, J.L., Hornych, P., and Benaben, J. P., 1996. Repeated load triaxial testing of granular materials in the French network of Laboratories des Ponts et Chausse'es. Proceedings of Eureapian Symposium on Flexible Pavements, , Lisbon, Portugal, pp. 53–64.

Perkins, S.W., and Madson, C.R. , 2000. Bearing Capacity of shallow foundations on sands: a relative density approach. Journal of Geotechnical and Geoenvironmental Engineering, ASCE, 126(16): 521-530.

Picoux, B., Rotinat, R., Regoin, J.P., Le Houedec, D., 2003. Prediction and measurements of vibrations from a railway track lying on a peaty ground. Journal of Sound and Vibration, 267(3): 575-589.

Pita, A.L., Teixeira, P.F., and Robuste F., 2004. High speed and track deterioration: the role of vertical stiffness of the track. Proceedings of Institution of Mechanical Engineers, Part F: Journal of Rail and Rapid Transit, 218: 31-40.

Popp, K., Kruse, H., and Kaiser, I., 1999. Vehicle-track dynamics in the mid-frequency range Vehicle System Dynamics, 31: 423-464..

Poulos, H.G., 1999. Common procedures for foundation settlement analysis-are they adequate? , Proceedings of 8th Australia New Zealand Conference on Geomechanics, pp. 3-25.

Prud'Homme, 1978. A. Ligne a grande vitesse Paris-Sud-Est (In French), Annls Inst. Techq Batiment Trav.

Rada, G., and Witczak, M.W., 1981. Comprehensive evaluation of laboratory resilient moduli results for granular materials. Transportation Research Record, 810: 23-33.

Radampola, S.S., 2006. Evaluation and modelling performance of capping layer in rail track substructure, PhD Thesis, University of Central Queensland, Australia.

Raymond, G.P., 1985. Design for railroad ballast and subgrade support. Journal of Geotechnical Engineering, 104(1): 45-59.

Santha, B.L., 1994. Resilient Modulus of subgrade soils: comparison of two constitutive equations. Tranasport Research Record, 1462: 79-90.

Sato, Y., 1977. Study on high-frequency vibration in track operated with high-speed train. JNR Quarterly Report: 109-114.

Sato, Y., 1995. Japanese studies on deterioration of ballasted track. Vehicle System Dynamics, 24(Suppl.): 197–208.

Sato, Y., 1997. Optimization of track maintenance work on ballasted track, Proceedings of the World Congress on Railway Research (WCRR '97), Florence, Italy, pp. 405–411.

Schmertmann, J.H., Hartman, J.P., and Brown, P.R., 1978. Improved strain influence factor diagrams. Journal of Geotechnical Engineering , ASCE, 104(GT8): 1131-1135.

Schooleman, R.B., 1996. Overgang kunstwerk-aardebaan voor de hoge-snelheidslijn (In dutch), Report 7-96-110-10, Technical University of Delft, Delft, Netherland.

Seed, H.B., Chan, C. K., and Lee, C. E. , 1962. Resilience characteristics of subgrade soils and their relation to fatigue failures in asphalt pavements, Proceedings of International Conference. on the Structural Design of Asphalt Pavements, University of Michigan, Ann Arbor, USA, pp. 611–636.

Seed, H.B., Mitry, F.G., Monismith, C.L., and Chan, C.K., 1967. Prediction of flexible pavement deflections from laboratory repeated load tests, National Cooperative Highway Research Program, Report No. 35.

Seed, H.B., and Idriss, I.M. , 1970. Soil moduli and damping factors for dynamic response Analyses, Report No. EERC 70-10, Earthquake Engineering Research Center, University of California, CA.

Selig, E.T., and Waters, J.M. , 1994. Track geotechnology and substructure management Thomas Telford.

Shahu, J.T., Kameswara Rao, N.S.V., and Yudhbir 1999. Parametric study of resilient response of tracks with a subballast layer. Canadian Geotechnical Journal, 36(6): 1137-1150.

Sheng, X., Jones, C.J.C., Petyt, M., 1999. Ground vibration generated by a harmonic load acting on a railway track. Journal of Sound and Vibration, 225(1): 3–28.

Shenton, M.J., 1985. Ballast deformation and track deterioration, Proceedings of the Conference on Track Technology, University of Nottingham, pp. 253–265.

Shiau, J.S., Lyamin, A.V., and Sloan S.W. , 2003. Bearing capacity of a sand layer on clay by finite element limit analysis. Canadian Geotechnical Journal, NRC, 40: 900-915.

Simonini, P., 1993. Influence of relative density and stress level on the bearing capacity of sands. International Journal for Numerical and Analytical Methods in Geomechanics, 17(871-890).

Singh, S.K., and Kuo J.T., 1970. Response of an elastic half space to uniformly moving circular surface load. Journal of Applied Mechanics, ASME: 109-115.

Smith, I.M., Griffiths, D.V., 1997. Programming the finite element method. Wiley, N.Y.

Smith, W.S. and Nair, K, 1973. Development of procedures for characterization of untreated granular base course materials and asphalt treated base course materials, Report No. FHWA-RD-74-61, Federal Highway Administration, Washington, D.C., USA.

Sneddon, R.v., 1988. Reilient modulus testing of 14 Nebraska Soils, University of Nebraska, Lincoln, USA.

Srinivasan, M., 1969. Modern permanent way. Somaiga Publications, Bombay, India.

Steenbergen, M., 2006. Modelling of wheels and rail discontinuities in dynamic wheel-rail contact analysis Vehicle System Dynamics, 44(10): 763-787.

Steenbergen, M.J.M.M., and Esveld C., 2006. Rail weld geometry and assessment concepts. Proceedings of Institution of Mechanical Engineers, Part F: Journal of Rail and Rapid Transit, 220: 257-271.

Stewart, H.E., O'Rourke, T.D., 1988. Load factor method for dynamic track loading. Journal of Transportation Engineering, ASCE, 114(1): 21-39.

Suiker, A.S.J., and Elsveld, C., 1997. Stiffness transition subjected to instantaneous moving load passages, Proceedings, 6th International Heavy Haul Conference, South Africa pp. 1194-1205.

Suiker, A.S.J., and de Borst, R., 1999. Critical response of a granular railway track under high train velocities. In: P.S. Pande (Editor), Proceedings of Numerical Models in geomechanics-NUMOG VII, Graz, Austria, pp. 297-302.

Suiker, A.S.J., 2002. The mechanical behaviour of ballasted railway tracks, PhD Thesis, Delft University of Technology, The Netherlands.

Sun, L., 2002. A closed-form solution of beam on viscoelastic subgrade subjected to moving loads. Computers & Structures, 80(1):1-8.

Sun, Y.Q., and Dhanasekar, M., 2002. A dynamic model for the vertical interaction of the rail track and wagon system. International Journal of Solids and Structures 39: 1337–1359.

Sweere, G.T.H., 1990. Unbound granular bases for roads. Ph.D. Thesis, University of Delft, Delft, The Netherlands.

Takagi, R., 2005. High-speed railway: The last 10 years. Japan Railway and Transport Review, 40: 4-7.

Talbot, A.N., 1918. Stresses in railraod tracks, Report of the Special Committee on Stresses in Railroad Track, American Railway Engineering Association (AREA).

Talbot, A.N., 1920. Stresses in railraod tracks, Report of the Special Committee on Stresses in Railroad Track, American Railway Engineering Association (AREA).

Terzaghi, K., 1943. Theoretical soil mechanics. John Wiley and Sons, Inc., N.Y.

Terzaghi, K., and Peck, R.B., 1967. Soil Mechanics in engineering practice, Wiley, NY

Thom, N.H., 1988. Design of road foundations, Ph.D. Thesis, University of Nottingham, Nottingham, UK.

Thom, N.H., and Brown, S. F. , 1988. The effect of grading and density on the mechanical properties of a crushed dolomitic limestone, Proceedings of 14th Australian Road Research Board Conference, Materials and Testing, pp. 94-100.

Thompson, D.R., and Woodward, P.K., 2004. Track stiffness management usign the Xitrack geocomposite. Permanent Way Institution Journal, 122(3): 135-138.

Thompson, M.R., and Robnett, Q.L., 1979. Resilient properties of subgrade soil. Journal of Transportation Engineering, ASCE, 105(1): 71-89.

Timoshenko, S., and Langer, B.F., 1926. Method of analysis of statical and dynamical stresses in rail, Proceedings of 2nd International Congress for Applied Mechanics, Zürich, Switzerland.

Timoshenko, S., and Langer, B.F., 1932. Stresses in railroad track. Transactions, ASME, 54.

Ueno, K., Miura, K., and Maeda, Y., 1998. Prediction of ultimate bearing capacity of surface footings with regard to size effects. Soils and Foundations, 38(3): 165-178.

Ukritchon, B., Whittle A. J. and Klangvijit C., 2003. Calculation of bearing capacity factor Nγ using numerical limit analyses. Journal of Geotechnical and Geoenvironmental Engineering, ASCE, 129(6): 468-474.

Uneo, K., Nakatomi, T., Mito, K. and Kusakabe, O. , 1994. Influence of initial conditions on bearing characteristics of sand, Proceedings of International Conference of Centrifuge '94, Singapore, pp. 541-546.

Uzan, J., 1985. Characterization of Granular Materials. Transportation Research Record, 1022: 52-59.

Uzan, J., 1992. Resilient characterization of pavement materials. International Journal for Numerical and Analytical Methods in Geomechanics, 16(6): 453-459.

Van Langen, H., and Vermeer, P.A., 1991. Interface elements for singular plasticity points. International Journal for Numerical Method and Analytical method in Geomechanics, 15: 301-305.

Vesic, A.B., and Johnson, W.H., 1963. Model studies of beams on silt subgrade. Journal of the Soil Mechanics and Foundation Division, ASCE, 89(1): 1-31.

Vesić, A.S., 1973. Analysis of ultimate loads of shallow foundations. Journal of Soil Mechanics and Foundation Division. ASCE, 99(1): 45-73.

Vucetic, M., and Dobry, R., 1991. Effect of soil plasticity on cyclic response. Journal of Geotechnical Engineering, ASCE, 117(1): 89-107.

Vuong, B., 1992. Influence of density and moisture content on dynamic stress strain behaviour of a low plasticity crushed rock. Road and Transportation Research, 1(2): 88-100.

Werkmeister, S., 2003. Permanent deformation behaviour of unbound granular materials in pavement constructions, Ph.D. Thesis, Dresden University of Technology, Dresden, Germany.

Witczak, M.W., and Uzan, J., 1988. The Universal Airport Pavement Design System, Granular Material Characterization, Report No.1, University of Maryland, Maryland, USA.

Woldringh, R.F., and New, B.M. , 1999. Embankment design for high speed trains on soft soils, Proceedings of Geotechnical Engineering for Transportation Infrastructure, Amsterdam, Netherland.

Wolf, J.P., and Song, C., 1996. Finite element modelling of unbounded media. John Wiley & Sons, N.Y., USA.

Wolf, H., 1992. The elasto-plastic behaviour of granular pavement layers in South Africa, PhD Thesis, University of Pretoria, South Africa.

Woods, R.D., 1968. Screening of surface waves in soils. Journal of Soil Mechanics and Foundation Division, ASCE, 94(SM4): 951-979.

Woodward, P.K., 1993. Earthquake engineering and advanced constitutive modelling in geomechanics by finite elements, PhD Thesis, Department of Civil Engineering, University of Manchester.

Woodward, P.K., and Griffiths, D.V. , 1998. Observation on the computation of the bearing capacity factor Nγ by finite elements. Géotechnique, 48(1): 137-141.

Woodward, P.K., and Molenkamp, F. , 1999. Application of an advanced multi-surface kinematic constitutive soil model. International Journal for Numerical and Analytical Methods in Geomechanics, 23(15): 1995-2043.

Woodward, P.K., and Berenji, A.P. , 2001. Advanced numerical investigation of Terzaghi superposition theory. Advances in Engineering Software, 32: 797-804.

Woodward, P.K., 2001. Advanced numerical modelling of granular soil, Advanced Numerical Applications and Plasticity in Geomechanics, D.V.Griffiths and G.Gioda (Eds). Springer, pp. 277-333.

Woodward, P.K., Nicholl, G. and Zettor, B., 2004. Application of XiTRACK GeoComposite technology to Bletchley points on the west coast main line, 7th International Conference on Railway Engineering.

Woodward, P.K., Zettor, B., Kaddouri, A., and Banimahd, M., 2005. Advanced nonlinear dynamic finite element modelling of railway track behaviour, Proceedings of 8th International Confrence on Railway Engineering, London, UK.

Woodward, P.K., Boyd, P., and Banimahd M., 2007a. XiTRACK reinforcement of tunnel railway tracks from floating to fixed geometry in a day, 9th International Confrence on Railway Engineering, London, UK.

Woodward, P.K., Boyd, P. , Spiers, J. and Banimahd M., 2007b. XiTRACK reinforcement of Keadby canal drawbridge. 9th International Conference on Railway Engineering, London, UK.

Woodward, P.K., and Nesnas, K., 2000. Analysing the behaviour of footing on sand using an advanced constitutive soil model, Research Report, EPSRC Grant GR/L75498.

WJRC (West Japan Railway Company), 2002a. Construction and maintenance standards for commuter and local railway track, Osaka, Japan.

WJRC (West Japan Railway Company), 2002b. Construction and maintenance standards for Shinkansen track. West Japan Railway Company, Osaka, Japan.

Wu, T.X., and Thompson D.J., 2002. A hybrid model for the noise generation due to railway wheel flats. Journal of Sound and Vibration, 251: 115-139.

Wu, T.X., and Thompson D.J., 2003. On the impact noise generation due to a wheel passing over rail joints. journal of Sound and Vibration, 267 485–496.

Yamaguchi, H., Kimura T., and Fujii N., 1976. On the influence of progressive failure on the bearing capacity of shallow foundation in dense sand. Soils and Foundations, 16(4): 11-22.

Yamaguchi, H., Kimura T., and Fujii N. , 1977. On the scale effect of footings in dense sand, Proceeding of the 9th International Conference on Soil Mechanics and Foundation Engineering, pp. 795-798.

Yerli, H.R., Kacinb, S., Kocaka, S. , 2003. A parallel finite–infinite element model for two-dimensional soil–structure interaction problems. Soil Dynamics and Earthquake Engineering , 23: 249–253.

Yin, J.H., Wang Y.J. and Salvadurai A.P.S. , 2001. Influence of non-associativity on the bearing capacity of a strip footing. Journal of Geotechnical and Geoenvironmental Engineering, ASCE, 127(11): 985-989.

Yokota, K., and Konno, M., 1980. Dynamic Poisson's ratio of soil, Proceedings of 7th world Conference on Earthquake Engineering, Istanbul, Turkey, pp. 475-478.

Zerwer, A., Cascante, G., and Hutchinson, J., 2002. Parameter Estimation in Finite Element Simulations of Rayleigh Waves. Journal of Geotechnical and Geoenvironmental Engineering, ASCE, 128(3): 250-261.

Zhai W. and Cai, Z., 1997. Dynamic interaction between a lumped mass vehicle and a discretely supported continuous rail track. Computers & Structures 63: 987-997.

Zhai, W.M., 1996. Two simple integration methods for large-scale dynamic problems in engineering. International Journal for Numerical Methods in Engineering, 39(24): 4199-4214.

Zhai, W.M., and True, H., 1999. Vehicle-track dynamics on a ramp and on the bridge: simulation and measurements. Vehicle System Dynamics, Supplement 33: 604-615.

Zhai, W.M., Cai, C. B., Wang, Q.C., Lu, Z. W. and Wu, X. S., 2001. Dynamic effects of vehicles on tracks in the case of raising train speeds. Proceeding of Institution of Mechanical Engineers, Part F: Journal of Rail and Rapid Transit, 215(2): 125-135.

Zhai, W.M., Wang, K. Y., and Lin, J. H., 2004. Modelling and experiment of railway ballast vibrations Journal of Sound and Vibration 270(4-5): 673-683

Zienkiewicz, O.C., Humpheson, C., and Lewis, R.W. , 1975. Associated and non-associated viscoplasticity and plasticity in soil mechanics. Géotechnique, 25(4): 671-689.